MELT WATER RETENTION PROCESSES IN SNOW AND FIRN ON ICE SHEETS AND GLACIERS: OBSERVATIONS AND MODELING

EDITED BY: W. Tad Pfeffer, Jason E. Box, Robert S. Fausto and Horst Machguth

PUBLISHED IN: Frontiers in Earth Science

frontiers Research Topics

ISSN 1664-8714
ISBN 978-2-88945-619-2
DOI 10.3389/978-2-88945-619-2

About Frontiers

Frontiers is more than just an open-access publisher of scholarly articles: it is a pioneering approach to the world of academia, radically improving the way scholarly research is managed. The grand vision of Frontiers is a world where all people have an equal opportunity to seek, share and generate knowledge. Frontiers provides immediate and permanent online open access to all its publications, but this alone is not enough to realize our grand goals.

Frontiers Journal Series

The Frontiers Journal Series is a multi-tier and interdisciplinary set of open-access, online journals, promising a paradigm shift from the current review, selection and dissemination processes in academic publishing. All Frontiers journals are driven by researchers for researchers; therefore, they constitute a service to the scholarly community. At the same time, the Frontiers Journal Series operates on a revolutionary invention, the tiered publishing system, initially addressing specific communities of scholars, and gradually climbing up to broader public understanding, thus serving the interests of the lay society, too.

Dedication to Quality

Each Frontiers article is a landmark of the highest quality, thanks to genuinely collaborative interactions between authors and review editors, who include some of the world's best academicians. Research must be certified by peers before entering a stream of knowledge that may eventually reach the public - and shape society; therefore, Frontiers only applies the most rigorous and unbiased reviews.
Frontiers revolutionizes research publishing by freely delivering the most outstanding research, evaluated with no bias from both the academic and social point of view. By applying the most advanced information technologies, Frontiers is catapulting scholarly publishing into a new generation.

What are Frontiers Research Topics?

Frontiers Research Topics are very popular trademarks of the Frontiers Journals Series: they are collections of at least ten articles, all centered on a particular subject. With their unique mix of varied contributions from Original Research to Review Articles, Frontiers Research Topics unify the most influential researchers, the latest key findings and historical advances in a hot research area! Find out more on how to host your own Frontiers Research Topic or contribute to one as an author by contacting the Frontiers Editorial Office: researchtopics@frontiersin.org

MELT WATER RETENTION PROCESSES IN SNOW AND FIRN ON ICE SHEETS AND GLACIERS: OBSERVATIONS AND MODELING

Topic Editors:
W. Tad Pfeffer, University of Colorado at Boulder, United States
Jason E. Box, Geological Survey of Denmark and Greenland GEUS, Denmark
Robert S. Fausto, Geological Survey of Denmark and Greenland GEUS, Denmark
Horst Machguth, University of Fribourg, Switzerland

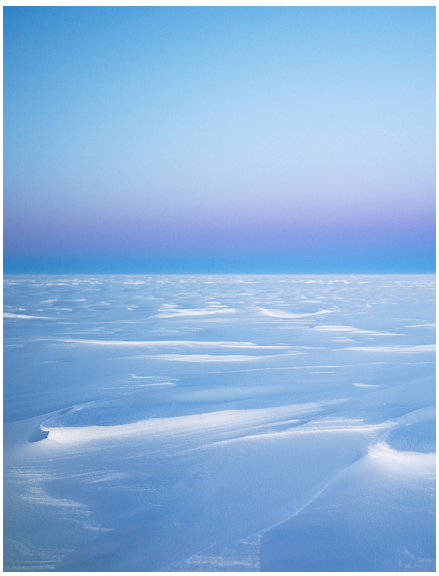

Evening light over the Greenland Ice Sheet, close to the abandoned DYE-2 radar station. Surface melt at the DYE-2 site has increased over the last two decades and the site has become an important location to study changes in the Greenland firn. Image: Horst Machguth, licensed under CC-BY.

Melt takes place where the surface of glaciers or ice sheets interacts with the atmosphere. While the processes governing surface melt are fairly well understood, the pathways of the meltwater, from its origin to the moment it leaves a glacier system, remain enigmatic. It is not even guaranteed that meltwater leaves a glacier or ice sheet. On Greenland, for example, only slightly more than 50% of the meltwater runs off. The remainder mostly refreezes within the so-called firn cover of the ice sheet.

This eBook contains 11 studies which tackle the challenge of understanding meltwater retention in snow and firn from various angles. The studies focus both on mountain glaciers and on the Greenland ice sheet and address challenges such as measuring firn properties, quantifying their influence on meltwater retention, modelling firn processes and meltwater refreezing as well as unravelling the mechanisms within the recently discovered Greenland firn aquifers.

Citation: Pfeffer, W. T., Box, J. E., Fausto, R. S., Machguth H., eds (2018). Melt Water Retention Processes in Snow and Firn on Ice Sheets and Glaciers: Observations and Modeling. Lausanne: Frontiers Media. doi: 10.3389/978-2-88945-619-2

Table of Contents

THE GREENLAND FIRN AQUIFERS

frontiers in Earth Science

EDITORIAL
published: 30 July 2018
doi: 10.3389/feart.2018.00105

Editorial: Melt Water Retention Processes in Snow and Firn on Ice Sheets and Glaciers: Observations and Modeling

Horst Machguth[1]*, *Jason E. Box*[2], *Robert S. Fausto*[2] and *William Tad Pfeffer*[3]

[1] Department of Geosciences, University of Fribourg, Fribourg, Switzerland, [2] Geological Survey of Denmark and Greenland GEUS, København, Denmark, [3] Cooperative Institute for Research in Environmental Sciences, University of Colorado, Boulder, CO, United States

Keywords: ice sheets, glaciers, retention, percolation, refreezing, cold content, surface mass balance

Editorial on the Research Topic

Melt Water Retention Processes in Snow and Firn on Ice Sheets and Glaciers: Observations and Modeling

INTRODUCTION

More than half of Greenland's current annual mass loss is attributed to runoff from surface melt (Enderlin et al., 2014; van den Broeke et al., 2016). While this already suggests that melt plays an important role in Greenland's mass balance, it is worth noting that only slightly more than half of the surface melt runs off in today's climate (Steger et al.). The remaining half of the meltwater produced is retained in firn and snow and does not contribute to runoff. If the fraction of retained meltwater were to decrease, the impact of surface melt on ice sheet mass balance could become much larger. Compared to Greenland, Antarctic surface melt is comparatively very small and has limited direct impact on mass balance. However, a process called hydrofracturing provides even smaller amounts of meltwater with a potentially powerful lever on Antarctic sea level contribution; meltwater that accumulates in crevasses promotes growth of fractures and reduces the stability of Antarctic ice shelves (Kuipers Munneke et al., 2014; Pollard et al., 2015), potentially leading to their detachment. While the break-off of an ice shelf can have a strong impact on the flow of the glaciers feeding the former ice shelf (Mercer, 1978), there are also more subtle ways by which meltwater and meltwater retention in snow and firn influence ice dynamics. The release of latent heat upon refreezing efficiently warms snow or firn while heat conduction and advection expand the warming signal. This effect, termed cryo-hydrological warming (Phillips et al., 2010; Lüthi et al., 2015), raises temperature, associated viscosity and consequently flow velocity of glaciers and ice sheets (Colgan et al., 2015).

This brief review highlights why understanding meltwater retention processes is crucial to anticipate future changes in ice sheets and glaciers in a warming world. The 11 studies of this *Frontiers in Earth Sciences Research Topic* examine various aspects of meltwater retention in snow and firn. In the following, we separate research progress and challenges into three categories: *measuring firn properties*, *modeling firn structure and meltwater retention,* and unraveling the mechanisms associated with the *Greenland firn aquifers*.

OPEN ACCESS

Edited and reviewed by:
Regine Hock,
University of Alaska Fairbanks, United States

***Correspondence:**
Horst Machguth
horst.machguth@unifr.ch

Specialty section:
This article was submitted to Cryospheric Sciences, a section of the journal Frontiers in Earth Science

Received: *18 June 2018*
Accepted: *05 July 2018*
Published: *30 July 2018*

Citation:
Machguth H, Box JE, Fausto RS and Pfeffer WT (2018) Editorial: Melt Water Retention Processes in Snow and Firn on Ice Sheets and Glaciers: Observations and Modeling. Front. Earth Sci. 6:105. doi: 10.3389/feart.2018.00105

MEASURING FIRN PROPERTIES

Measuring the firn meltwater retention process and its influence on land ice hydrology is inherently challenging as the major processes take place at the subsurface in a spatially heterogeneous manner. While a large body of work on snow hydrology exists (e.g., Colbeck, 1972; Hirashima et al., 2014), the firn of glaciers and ice sheets comprises scales and structures not usually identified in seasonal snow, and are produced by multi-year processes also not known from seasonal snow studies. Hence, dedicated measurements of firn hydrology can complement snow studies. Sommers et al. address firn water through their approach of *in situ* pneumatic measurements of firn permeability. While earlier research (e.g., Albert et al., 1996) focused on dry firn, they studied firn regularly exposed to melt. Sommers et al. adds to an increasing number of innovative *in situ* measurements of melting firn, such as for example direct observation of percolating meltwater by means of ground penetrating radar (Heilig et al., 2018). Samimi and Marshall examine firn meltwater retention from the perspective of a temperate mountain glacier. Through direct measurement of temperature and water content, they find that temperate snow and firn does not retain meltwater directly, but overnight refreezing of meltwater consumes about 10–15% of the melt energy available the subsequent day. Samimi and Marshall thus underline the importance of short-term cycles of melt and freezing which even influence mass balance of bare ice areas of the Greenland ice sheet (Smith et al., 2017).

MODELING OF FIRN STRUCTURE AND MELTWATER RETENTION

Meltwater retention in snow and firn moderates Greenland ice sheet mass loss and global sea level (Pfeffer et al., 1991; Janssens and Huybrechts, 2000). This global impact stands in stark contrast to the small-scale variability of meltwater percolation and retention that manifests itself in the complexity of firn structures (Brown et al., 2011). Modelers generally invoke a concept where vertical percolation is described as either (i) a homogeneously progressing wetting front in isothermal snow and firn at 0°C, or (ii) heterogeneous flow in advance of a uniform wetting front in a matrix at sub-freezing temperatures. van Pelt et al., Steger et al., and Langen et al. apply firn meltwater models to assess future relevance of retention processes on a synthetic Arctic glacier and to quantify the present-day role of meltwater retention on the Greenland ice sheet. Langen et al. show their model achieving agreement with observed firn stratigraphy and mass balance while Steger et al. conclude that Greenland's snow and firn currently retain 41–46% of all liquid water (mainly melt but also including rain). All three studies, however, invoke homogeneous percolation and leave the issue of heterogeneous flow as poorly understood. Models of heterogeneous percolation exist (Hirashima et al., 2014; Wever et al., 2016) but they are computationally expensive and validation of model output is challenged by uncertainties of basic input parameters such as fresh-snow density (Steger et al.). These challenges are addressed by Marchenko et al. who suggest a simple empirical parametrization of preferential flow and by Fausto et al. who analyzed a large set of firn and snow data to improve estimates of Greenland snow density.

FIRN AQUIFERS

In spring 2011 in a little studied region of southeast Greenland, a group of researchers were surprised when their drill emerged from its borehole dripping with water (Forster et al., 2014). Finding liquid water in the firn before the melt season had even started was a surprise and inspired a new Greenland research field in perennial firn aquifers. Model simulations exhibit skill in indicating the location of firn aquifers (Forster et al., 2014; Langen et al.) and indicate that the east Greenland aquifer could be a recent phenomenon that formed following strong melt in summer 2010 (Steger et al.). The hydrology of the aquifers is subject to ongoing research, applying seismic methods to determine aquifer thickness and volume, (Montgomery et al.), or slug testing to measure hydraulic conductivity. (Miller et al.). The amount of water contained in the aquifers remains poorly constrained, but the total estimated area of at least 22,000 km^2 (Miège et al., 2016) makes firn aquifers potentially significant contributors to global sea level change. In this context, the findings of Poinar et al. are relevant because they suggest that aquifers infiltrate through the hydrofracturing of crevasses down to the bed, which connect to the ice sheet discharge system.

SYNTHESIS

The study of meltwater retention has been stimulated by recent discoveries such as the Greenland firn aquifers and studies indicating high importance of surface mass balance in sea level scenarios. To further improve understanding of the processes and their relevance in mass balance of glaciers and ice sheets, Van As et al. performed an expert solicitation to point out major hurdles. The survey responses show that the community identifies research priorities in (i) measuring and modeling the spatial heterogeneity of processes, (ii) assessing the permeability of different types of firn to percolating meltwater, and (iii) in improving surface boundary conditions for modeling. It is promising that the 11 manuscripts of this eBook address all three of the challenges identified by the expert pool.

AUTHOR CONTRIBUTIONS

HM led the authorship of this article. JB, WP, and RF provided text input.

FUNDING

This article was partially supported by the Independent Research Fund of Denmark grant FNU 4002-00234. HM is partially supported by the Swiss National Science Foundation grant 200021_169453.

ACKNOWLEDGMENTS

We thank all authors and reviewers for their contribution to the research topic on *Melt Water Retention Processes in Snow and Firn on Ice Sheets and Glaciers: Observations and Modeling*. We also thank the funding agencies that supported the studies presented in this eBook.

REFERENCES

Albert, M. R., Arons, E. M., and Davis, R. E. (1996). "Firn Properties Affecting Gas Exchange at Summit, Greenland: Ventilation Possibilities," in *Chemical Exchange Between the Atmosphere and Polar Snow,* eds E. W. Wolff and R. C. Bales (Berlin; Heidelberg: Springer), 561–565

Brown, J., Harper, J., Pfeffer, W., Humphrey, N., and Bradford, J. (2011). High resolution study of layering within the percolation and soaked facies of the Greenland ice sheet. *Ann. Glaciol.* 52, 35–41. doi: 10.3189/172756411799096286

Colbeck, S. C. (1972). A theory of water percolation in snow. *J. Glaciol.* 11, 369–385

Colgan, W., Sommers, A., Rajaram, H., Abdalati, W., and Frahm, J. (2015). Considering thermal-viscous collapse of the Greenland ice sheet. *Earth's Future* 3, 252–267. doi: 10.1002/2015EF000301

Enderlin, E., Howat, I., Jeong, S., Noh, M., van Angelen, J., and van den Broeke, M. (2014). An improved mass budget for the Greenland ice sheet. *Geophys. Res. Lett.* 41, 866–872. doi: 10.1002/2013gl059010

Forster, R. R., Box, J. E., van den Broeke, M. R., Miège, C., Burgess, E. W., van Angelen, J. H., et al. (2014). Extensive liquid meltwater storage in firn within the Greenland ice sheet. *Nat. Geosci.* 7, 95–98. doi: 10.1038/ngeo2043

Heilig, A., Eisen, O., MacFerrin, M., Tedesco, M., and Fettweis, X. (2018). Seasonal monitoring of melt and accumulation within the deep percolation zone of the Greenland Ice Sheet and comparison with simulations of regional climate modeling. *Cryosphere.* 12, 1851–1186. doi: 10.5194/tc-12-1851-2018

Hirashima, H., Yamaguchi, S., and Katsushima, T. (2014). A multi-dimensional water transport model to reproduce preferential flow in the snowpack. *Cold Reg. Sci. Technol.* 108, 80–90. doi: 10.1016/j.coldregions.2014.09.004

Janssens, I., and Huybrechts, P. (2000). The treatment of meltwater retention in mass-balance parameterisations of the Greenland ice sheet. *Ann. Glaciol.* 31, 133–140. doi: 10.3189/172756400781819941

Kuipers Munneke, P., Ligtenberg, S. R. M., van den Broeke, M. R., and Vaughan, D. G. (2014). Firn air depletion as a precursor of Antarctic ice-shelf collapse. *J. Glaciol.* 60, 205–214. doi: 10.3189/2014JoG13J183

Lüthi, M. P., Ryser, C., Andrews, L. C., Catania, G. A., Funk, M., Hawley, R. L., et al. (2015). Heat sources within the Greenland Ice Sheet: dissipation, temperate paleo-firn and cryo-hydrologic warming. *Cryosphere* 9, 245–253. doi: 10.5194/tc-9-245-2015

Mercer, J. (1978). West Antarctic ice sheet and CO2 greenhouse effect: a threat of disaster. *Nature* 271, 321–325

Miège, C., Forster, R. R., Brucker, L., Koenig, L. S., Solomon, D. K., Paden, J. D., et al. (2016). Spatial extent and temporal variability of Greenland firn aquifers detected by ground and airborne radars. *J. Geophys. Res.* 121, 2381–2398. doi: 10.1002/2016JF003869

Pfeffer, W., Meier, M., and Illangasekare, T. H. (1991). Retention of Greenland Runoff by Refreezing: implications for projected future sea level change. *J. Geophys. Res.* 96, 22117–22124

Phillips, T., Rajaram, H., and Steffen, K. (2010). Cryo-hydrologic warming: a potential mechanism for rapid thermal response of ice sheets. *Geophys. Res. Lett.* 37:L20503. doi: 10.1029/2010GL044397

Pollard, D., DeConto, R. M., and Alley, R. B. (2015). Potential Antarctic Ice Sheet retreat driven by hydrofracturing and ice cliff failure. *Earth Planet. Sci. Lett.* 412, 112–121. doi: 10.1016/j.epsl.2014.12.035

Smith, L. C., Yang, K., Pitcher, L. H., Overstreet, B. T., Chu, V. W., Rennermalm, A. K., et al. (2017). Direct measurements of meltwater runoff on the Greenland ice sheet surface. *Proc. Natl. Acad. Sci. U.S.A.* 114, E10622–E10631. doi: 10.1073/pnas.1707743114

van den Broeke, M., Enderlin, E., Howat, I., Kuipers Munneke, P., Noël, B., van de Berg, W. J., et al. (2016). On the recent contribution of the Greenland ice sheet to sea level change. *Cryosphere* 10, 1933–1946. doi: 10.5194/tc-10-1933-2016

Wever, N., Würzer, S., Fierz, C., and Lehning, M. (2016). Simulating ice layer formation under the presence of preferential flow in layered snowpacks. *Cryosphere* 10, 2731–2744. doi: 10.5194/tc-2016-185

Conflict of Interest Statement: The authors declare that the research was conducted in the absence of any commercial or financial relationships that could be construed as a potential conflict of interest.

frontiers in Earth Science

PERSPECTIVE
published: 29 November 2016
doi: 10.3389/feart.2016.00101

Challenges of Quantifying Meltwater Retention in Snow and Firn: An Expert Elicitation

*Dirk van As *, Jason E. Box and Robert S. Fausto*

Department of Glaciology and Climate, Geological Survey of Denmark and Greenland, Copenhagen, Denmark

Thirty-four experts took part in a survey of the most important and challenging topics in the field of meltwater retention in snow and firn, to reveal those topics that present the largest potential for scientific advancement. The most important and challenging topic to the expert panel is spatial heterogeneity of percolation, both in measurement and model studies. Studying percolation blocking by ice layering, particularly in modeling, also provides large potential for science advancement, as well as hydraulic conductivity and capillary forces in snow/firn. Model studies can benefit from improved initialization, and improved calculation of accumulation and liquid water at the surface. Firn coring should be performed more often, though we argue that also data that are relatively simple to collect, but of great importance to retention such as surface accumulation, density and temperature, are too sparse due to the high logistical expenses involved in field campaigns. Generally speaking, retention changes are expected to be of importance to the climatic (surface) mass balance and thus ice loss in coming decades, more so for Greenland than Antarctica or ice masses elsewhere.

Keywords: snow, firn, melt, percolation, retention, refreezing, spatial heterogeneity, ice layer blocking

OPEN ACCESS

Edited by:
Martin Hoelzle,
University of Fribourg, Switzerland

Reviewed by:
Shad O'Neel,
USGS Alaska Science Center, USA
Christoph Schneider,
Humboldt University of Berlin, Germany

****Correspondence:***
Dirk van As
dva@geus.dk

Specialty section:
This article was submitted to Cryospheric Sciences, a section of the journal Frontiers in Earth Science

Received: *20 September 2016*
Accepted: *09 November 2016*
Published: *29 November 2016*

Citation:
van As D, Box JE and Fausto RS (2016) Challenges of Quantifying Meltwater Retention in Snow and Firn: An Expert Elicitation. Front. Earth Sci. 4:101. doi: 10.3389/feart.2016.00101

INTRODUCTION

The mass balances of ice sheets, ice caps, and glaciers worldwide include one large mass input, namely snow accumulation. Yet depending on the location, several large mass loss components exist such as ice-dynamic mass transfer to the oceans, basal melting, surface meltwater runoff, and sublimation. Globally, the loss components are found to out-compete the gains in the current climate, which is largely attributed to increased melting at the air-ice and ocean-ice interfaces, also impacting ice dynamic discharge (IPCC, 2013).

Surface runoff occurs when melting, rainfall, and condensation exceed evaporation and retention in snow, firn, porous ice, and supraglacial lakes (Cuffey and Paterson, 2010). Our ability to determine surface runoff thus depends on our ability to determine several entirely independent processes, each with their own complexities. Out of these processes, retention of water in snow, firn or ice may not be the largest contributor averaged over an entire glacier, ice cap or ice sheet, yet regionally (in the *percolation area*) it can be large enough to accommodate all liquid water that percolates into the surface layer (e.g., Benson, 1962). At lower elevations, the snow and firn (or even porous ice) periodically gets overwhelmed by liquid water in the *runoff area*. Challenges in determining runoff are largest due to the uncertainties in quantifying retention in snow and firn, as this is the only component that takes place at depth (in the order of meters), thus out of sight and reach of basic, direct observational methods (Harper et al., 2012). Indirect methods have existed for

decades, such as determining changes in density/stratigraphy from repeat snow pits (e.g., Techel and Pielmeier, 2011) or firn cores (e.g., Vallelonga et al., 2014), continuous subsurface temperature measurements for capturing the release of latent heat from refreezing (Humphrey et al., 2012; Charalampidis et al., 2016), or radar systems capable of identifying strong reflectors in porous snow or firn as ice layers (e.g., Koenig et al., 2016). Such methods are excellent for determining the location and quantity of the retained mass, but do not allow us to track and comprehend all physical processes involved in percolation and refreezing. This then limits our ability to model these processes with accuracy.

Whereas part of the difficulty in studying retention stems from not being able to track water movement through snow/firn with detail without altering the medium itself by digging pits or drilling cores, another aspect is the memory of the system. Namely, when meltwater refreezes it will impact future percolation due to changes in snow/firn density and temperature (Bezeau et al., 2013). This continues until the layer and the changes it caused in the snow/firn, migrated downward far enough to escape the direct influence of surface processes, i.e., the maximum percolation depth (Harper et al., 2012). Depending on the net accumulation rate (Mosley-Thompson et al., 2001), this can take many years. So if a model is forced by inaccurate surface energy quantities, or initialized with inaccurate snow/firn densities and temperatures, or struggles representing physical processes such as gravitational densification (Arthern et al., 2010; Morris and Wingham, 2014), thermal conduction (Sturm et al., 1997), and movement of liquid water (Colbeck, 1974; Hirashima et al., 2010), then not only the first retention event may be calculated inaccurately, but in a cascade effect all retention events may be affected. The impact on the climatic mass balance can be substantial for instance when consecutive high melt seasons occur, with ice layer formation shifting conditions in favor of surface runoff as opposed to percolation (Machguth et al., 2016).

In this paper, we aim to identify the most crucial topics in meltwater retention in order to reveal the largest potential for scientific advancement in this field. We apply expert elicitation, which is common practice in investigations with high uncertainty due to the lack of data, for instance in case of rare events or future predictions. In glaciology the expert survey methodology was applied e.g., in estimating future sea level contributions from the ice sheets (Bamber and Aspinall, 2013). Our approach differs in that we will not attempt quantification of meltwater retention in snow and firn through expert elicitation.

METHODS

The questionnaire used to conduct the expert elicitation on meltwater retention in snow and firn, consisted of 18 entries listing snow/firn processes and properties (**Table 1**). On a scale of 1–10, 10 being highest, the expert was asked to rate each topic in terms of: (1) importance to meltwater retention, (2) difficulty level in measuring with accuracy, and (3) difficulty level in modeling with accuracy (providing ratings R_{ret1-3} for each topic/question). Also, the expert was asked to rate "the importance of the change in meltwater retention in snow and firn in a warming climate on decadal time scales for mass loss from" (1) Antarctica, (2) Greenland, and (3) other glaciated regions (ratings R_{reg1-3}). In case of substantial doubt the expert was asked not to provide an answer. In order to be able to assess the expert levels of the sources, the questionnaire also asked for the self-assessed (1) expert level on the topic of meltwater retention in snow and firn, (2) experience level performing firn measurements, (3) experience level modeling meltwater retention in snow and firn (ratings R_{exp1-3}), and (4) the years (Y) since (or until) obtaining a Ph.D. degree.

We invited those present at the "Workshop on observing and modeling meltwater retention processes in snow and firn on ice sheets and glaciers" hosted by the Geological Survey of Denmark and Greenland (GEUS) on 1–3 June 2016, and other known topical experts to take part in the survey. With the aim of publishing the results indicated on the questionnaire, all subjects gave their written consent by returning the document. The expert panel of 34 excludes the first author of this study. On average, the retention expert level is found to be 6.4 ($R_{exp1,av}$). Experience levels are lower for modeling of retention ($R_{exp2,av} = 5.6$), and particularly for measuring ($R_{exp3,av} = 4.9$), the latter of which is likely related to the high cost associated with field expeditions.

We apply expert weighting to each answer by multiplication with an individual expert factor, calculated as:

$$F_{exp} = \left(\frac{R_{exp}}{R_{exp,av}} + \frac{Y + 10}{Y_{av} + 10} \right) / 2 \quad (1)$$

Note, that the self-assessed expert level and scientific seniority weigh equally in calculating one's expert level. Ratings R_{ret1} and R_{reg1-3} are weighted using expert level rating R_{exp1}, ratings R_{ret2} using R_{exp2}, and ratings R_{ret3} using R_{exp3}. Expert factors vary between 0.29 and 2.18, a factor of 7.4 difference.

Likewise, we apply importance weighting by multiplication with the importance factor of each snow/firn topic:

$$F_{imp} = \frac{R_{ret1,EW}}{R_{ret1,EW,av}} \quad (2)$$

where $R_{ret1,EW}$ is the expert-weighted importance averaged over all experts. Importance factors range between 0.67 and 1.26.

Using these methods, we obtain averages and expert-weighted (EW) averages for every surveyed snow/firn topic, in terms of their importance to meltwater retention, and their difficulty to quantify by means of measuring and modeling (**Table 1**). We also present expert- and importance-weighted (EIW) averages of the difficulties in measuring and modeling. Note, that after the weighting values can exceed the 1–10 range.

RESULTS

The 34 experts attributed average values between 4.4 and 8.5 with an overall average of 6.7 to the importance of snow/firn topics (**Table 1**). Expert weighting has little impact on the average (6.8), nor on the ranking of the importance of processes/properties. Surface accumulation (8.6) and the availability of liquid water at

TABLE 1 | Expert judgment assessment of snow/firn processes and properties relevant to retention.

Topic	Importance to snow/firn processes			Difficulty level in measuring with accuracy				Difficulty level in modeling with accuracy			
	Av	*SD*	EW	Av	*SD*	EW	EIW	Av	*SD*	EW	EIW
Surface water (melt+rain)	8.4[2]	1.4	8.4[2]	5.6	2.4	5.5	6.7	5.8	2.1	5.7	7.0
Surface accumulation	8.5[1]	1.3	8.6[1]	4.6	1.8	4.7	5.9	5.8	1.7	5.8	7.3[4]
Surface accumulation density	6.8	1.5	6.9	5.4	2.7	5.3	5.3	5.7	1.9	5.9	5.9
Surface temperature	7.2	1.9	7.2	3.0	1.9	3.3	3.5	4.5	1.6	4.5	4.7
Surface albedo (melt-albedo feedback)	7.3[5]	1.6	7.3[5]	4.0	2.0	4.3	4.6	5.9	1.3	5.9	6.3
Near-surface solar radiation penetration	5.4	2.1	5.6	7.2	1.7	7.4	6.1	6.3	2.0	6.6	5.4
Near-surface ventilation by wind	4.4	1.9	4.6	7.3[4]	2.0	7.8[4]	5.2	7.3[4]	1.9	7.3[4]	4.9
Grain size	6.4	1.5	6.5	5.1	1.9	5.2	5.0	6.7	2.0	6.8	6.5
Gravitational densification	6.2	1.6	6.3	5.6	1.9	5.8	5.3	4.6	1.7	4.7	4.3
Heat conduction	6.5	1.5	6.6	5.3	1.8	5.5	5.3	4.8	2.0	5.0	4.8
Capillary forces acting on liquid water	6.4	1.6	6.7	7.7[2]	1.6	8.2[2]	8.0[4]	7.0[5]	2.1	7.3[5]	7.2[5]
Hydraulic conductivity	6.8	1.6	7.1	7.4[3]	1.5	8.1[3]	8.5[2]	7.3[3]	1.6	7.7[3]	8.0[3]
Blocking of meltwater percolation by ice layering	7.5[4]	1.5	7.7[4]	7.2	1.9	7.3	8.2[3]	8.3[2]	1.3	8.5[2]	9.5[2]
Spatial heterogeneity of meltwater percolation	7.6[3]	1.6	7.9[3]	7.9[1]	2.1	8.6[1]	9.9[1]	8.6[1]	1.7	9.1[1]	10.5[1]
Deep firn processes / lower boundary conditions	4.9	2.0	5.3	7.3[5]	2.1	7.6[5]	5.9	6.5	2.4	6.8	5.3
Spatial (vertical) resolution	–	–	–	5.9	2.2	6.6	6.6	5.3	2.1	5.7	5.7
Time resolution (capability of resolving relevant cycles)	–	–	–	6.4	2.2	6.7	6.7[5]	5.2	1.9	5.7	5.7
Model initialization	–	–	–	–	–	–	–	6.6	1.7	7.0	7.0
Average	6.7	1.6	6.8	6.1	2.0	6.3	6.3	6.2	1.8	6.4	6.4

Listed are the arithmetic-mean averages (Av), standard deviations (SD), expert-weighted averages (EW), and expert- and importance-weighted averages (EIW) of the expert ratings on a scale of 1–10. Ranks 1–5 indicating highest values are in superscript.

the surface (8.4) are considered most important, followed by the spatial heterogeneity of meltwater percolation (7.9), percolation blocking by ice layering (7.7), and surface albedo through the melt-albedo feedback (7.3). Least important of the selected topics is considered to be near-surface ventilation by wind (4.6).

EW-values of the difficulty level in measuring the snow/firn processes/properties vary considerably (**Table 1**). Whereas measuring surface temperature (or in fact any surface variable) is considered relatively straightforward (3.3), measuring the spatial heterogeneity of meltwater percolation is judged to be the largest challenge (8.6). Other large challenges are found in measuring the effect of capillary forces on liquid water (8.2), hydraulic conductivity (8.1), ventilation by wind (7.8), and processes occurring in the bottom half of the firn (7.6).

Also in modeling, surface temperature is considered least difficult to determine with accuracy (4.5), and spatial heterogeneity most difficult (9.1, **Table 1**). The top five modeling challenges align well with the high ranking observational challenges, except that the modeling of percolation blocking by ice layering ranks second (8.5). On average, measuring and modeling retention-related topics (6.4) are judged to be equally complicated (6.3 vs. 6.4).

In **Figure 1A**, we identify four quadrants in a plot of importance vs. difficulty of the survey topics. Most topics are located in the quadrants of high importance and low difficulty, or low importance and high difficulty. Three topics are judged to be of above-average importance and difficulty: spatial heterogeneity in, and blocking of, meltwater percolation, and the hydraulic conductivity of the snow/firn.

EIW-values confirm that these three are top ranking both in measuring and modeling (**Table 1**, **Figure 1B**). Also the topic of capillary forces acting on liquid water ranks high (8.0 and 7.2). The top five in measuring is completed by temporal resolution, i.e., the difficulty in resolving relevant firn process cycles from repeat cores. In modeling, surface accumulation has a top-ranking EIW-value (7.3).

Finally, we turn to the question on how important meltwater retention in snow/firn is to the change in the mass balance of ice masses around the globe in coming decades (R_{reg1-3}). This expert judgment assessment indicates that, on these timescales, retention may be an important factor for ice loss from Antarctica (5.2), Greenland (8.4), and glaciated regions elsewhere (6.5).

DISCUSSION

On some topics nearly all experts agree as shown by a small standard deviation (**Table 1**). For instance, all but one expert assess the modeling of meltwater percolation blocking by ice layers to be difficult (7–10), resulting in a small standard deviation of 1.3. In the other extreme, in judging the difficulty

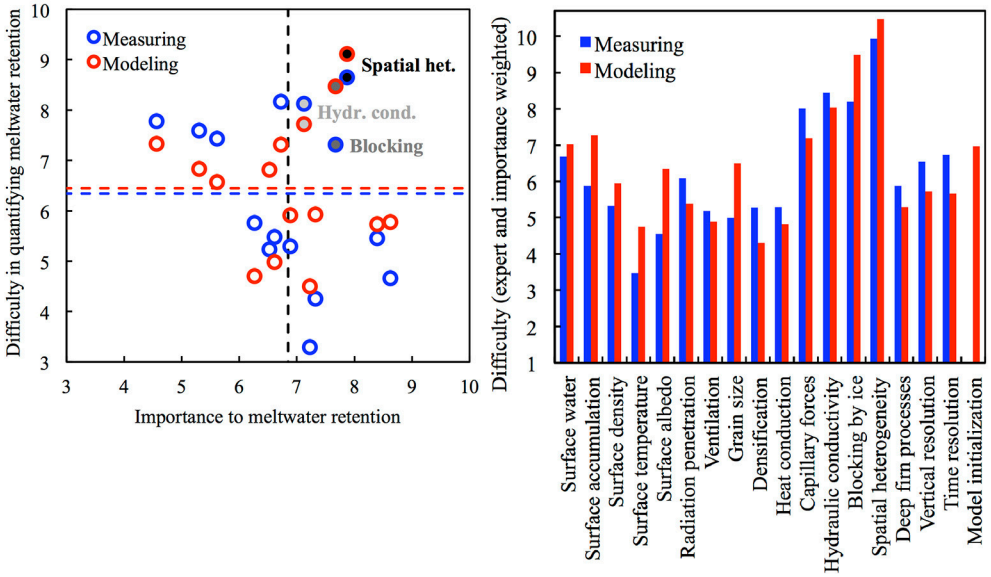

FIGURE 1 | (A) The expert-weighted difficulty in quantifying aspect in observational (blue) and modeling (red) studies of meltwater retention in snow and firn, plotted against their expert-weighted importance. Dashed lines represent average values. **(B)** The expert- and importance-weighted difficulty in measuring (blue) and modeling (red) studies. Ratings were provided on a scale of 1–10.

level of measuring surface accumulation density, a considerable disagreement is found with entries over the entire 1–10 range, resulting in a larger standard deviation of 2.7. To remedy the situation in which the less experienced potentially increase disagreement, we added weight to the opinions of those with more experience in the field of retention by calculating expert factors for all survey partakers, based on the expert's seniority level and self-assessed expert levels (see Methods Section). The calculation is arguably arbitrary, and therefore kept simple. However, we find that expert weighting does not significantly change the average topic score; expert weighting contributes between −0.16 and +0.71 with an average of +0.22 to the R_{ret} questions. Therefore, the results are expert-level insensitive, because the survey part takers with a below-average expert level generally agree with their more experienced peers. The adjustment through importance weighting is larger with adjustment between −2.59 (snow/firn ventilation being difficult to measure, but not important for retention studies) and +1.49 (surface accumulation being somewhat difficult to model, but very important for retention studies), yet the average importance-adjustment is negligible at −0.04.

If a topic related to meltwater retention in snow/firn is considered to be both important and difficult to assess, we regard this as a topic in which the largest scientific advances can be made. These topics have an above-average EIW score (**Table 1**). Yet, we also need to consider the topics that are important, but less difficult to quantify. In retention modeling, these topics leave little room for advancement. On the other hand, in measuring, an additional challenge exists in reaching the often remote and inaccessible accumulation areas of glaciers and ice caps/sheets. So while the measurement may be relatively simple, observational data remain sparse due to high logistical expense. A data shortage is also reflected in the experts' opinion that relevant cycles in retention are not well-resolved by repeat firn coring (**Table 1**). Therefore, we argue that also the relatively simple, yet important, measurements should be targeted for scientific advancement in retention. Strikingly, these are all the measurements of surface variables listed in **Table 1** (surface water, accumulation, density, temperature, and albedo) for which automated solutions exist or can be developed, such as equipping weather stations (e.g., Mölg et al., 2008; Van As et al., 2011) with radiometers, sonic rangers, and snow-water-equivalent sensors.

With sparsity of observational data, it becomes of primary importance that existing data are available to everyone. Excellent examples of publicly available databases containing firn data exist (e.g., the SUMup database; Koenig et al., 2016), and efforts should be made by the global glaciological community to expand those databases. Likewise, only few models are capable of detailed calculations of meltwater retention in snow and firn. The more the model codes become available to the entire research community, the more researchers can build on previous efforts, and the largest the scientific advancement will be.

CONCLUSION

In this study, we used the results of 34 experts that took part in an expert elicitation of meltwater retention in snow and firn, to identify those snow/firn processes and properties that are both important and challenging to quantify, thus providing the largest potential for scientific advancement. We applied expert- and importance-weighting, only the latter of which proved influential.

We find the following topics to present the largest potential for scientific advancement, both in measuring and modeling:

- spatial heterogeneity of meltwater percolation in snow/firn,
- blocking of percolating meltwater by ice layers, especially in model studies,
- hydraulic conductivity,
- and capillary forces acting on liquid water.

Additionally, in modeling the following topics are worthy of further emphasis:

- quantifying surface water,
- quantifying accumulation,
- and model initialization.

Based on the survey results, we also argue for:

- obtaining more firn cores and to sample them in more detail,
- and measuring surface variables (liquid water, accumulation, density, temperature, and albedo) at more sites, since data sparsity is not caused by the difficulty of the measurement itself, but by the difficulty in getting to the accumulation areas of glaciers and ice caps/sheets.

In a final question on the future change of retention due to climate change, the expert panel answered that in the coming decades, meltwater retention is expected to be of importance to mass loss in glaciated regions worldwide, especially in Greenland.

AUTHOR CONTRIBUTIONS

DV, RF, and JB conceived the study. DV compiled the questionnaire, analyzed the data, and wrote the text with contributions by JB and RF.

ACKNOWLEDGMENTS

We are grateful to the anonymous experts taking part in this study. Support for this study was provided by Denmark's Nature and Universe grant DFF 4002-00234 through the Retain project (retain.geus.dk) and the Danish Energy Agency (www.ENS.dk) through the Programme for Monitoring of the Greenland Ice Sheet (www.PROMICE.dk). This study with human subjects was carried out in accordance with the ethical guidelines by the Geological Survey of Denmark and Greenland (GEUS).

REFERENCES

Arthern, R. J., Vaughan, D. G., Rankin, A. M., Mulvaney, R., and Thomas, E. R. (2010). *In situ* measurements of Antarctic snow compaction compared with predictions of models. *J. Geophys. Res.* 115:F03011. doi: 10.1029/2009JF001306

Bamber, J. L., and Aspinall, W. P. (2013). An expert judgement assessment of future sea level rise from the ice sheets. *Nat. Clim. Change* 3, 424–427. doi: 10.1038/nclimate1778

Benson, C. S. (1962). *Stratigraphic Studies in the Snow and Firn of the Greenland Ice Sheet*. Research Report 70, SIPRE.

Bezeau, P., Sharp, M., Burgess, D., and Gascon, G. (2013). Firn profile changes in response to extreme 21st-century melting at Devon Ice Cap, Nunavut, Canada. *J. Glaciol.* 59, 981–991. doi: 10.3189/2013JoG12J208

Charalampidis, C., Van As, D., Colgan, W. T., Fausto, R. S., MacFerrin, M., and Machguth, H. (2016). Thermal tracing of retained meltwater in the lower accumulation area of the southwestern Greenland ice sheet. *Ann. Glaciol.* 57. doi: 10.1017/aog.2016.2. Available online at: https://www.igsoc.org/annals/57/72/accepted.html

Colbeck, S. C. (1974). The capillary effects on water percolation in homogeneous snow. *J. Glaciol.* 13, 85–97.

Cuffey, K. M., and Paterson, W. S. B. (2010). *The Physics of Glaciers*. Burlington, MA: Academic Press, 704.

Harper, J., Humphrey, N., Pfeffer, W. T., Brown, J., and Fettweis, X. (2012). Greenland ice-sheet contribution to sea-level rise buffered by meltwater storage in firn. *Nature* 491, 240–243. doi: 10.1038/nature11566

Hirashima, H., Yamaguchi, S., Sato, A., and Lehning, M. (2010). Numerical modeling of liquid water movement through layered snow based on new measurements of the water retention curve. *Cold Regions Sci. Technol.* 64, 94–103. doi: 10.1016/j.coldregions.2010.09.003

Humphrey, N. F., Harper, J. T., and Pfeffer, W. T. (2012). Thermal tracking of meltwater retention in Greenland's accumulation area. *J. Geophys. Res.* 117:F01010. doi: 10.1029/2011JF002083

IPCC (2013). "Climate change 2013: the physical science basis," in *Contribution of Working Group I to the Fifth Assessment Report of the Intergovernmental Panel on Climate Change*, eds T. F. Stocker, D. Qin, G.-K. Plattner, M. Tignor, S. K. Allen, J. Boschung, A. Nauels, Y. Xia, V. Bex, and P. M. Midgley (Cambridge; New York, NY: Cambridge University Press), 1535.

Koenig, L. S., Ivanoff, A., Alexander, P. M., MacGregor, J. A., Fettweis, X., Panzer, B., et al. (2016). Annual Greenland accumulation rates (2009–2012) from airborne snow radar. *Cryosphere* 10, 1739–1752. doi: 10.5194/tc-10-1739-2016

Machguth, H., MacFerrin, M., Van As, D., Box, J. E., Charalampidis, C., Colgan, W., et al. (2016). Greenland meltwater storage in firn limited by near-surface ice formation. *Nat. Clim. Change* 6, 390–393. doi: 10.1038/nclimate2899

Mölg, T., Cullen, N. J., Hardy, D. R., Kaser, G., and Klok, L. (2008). Mass balance of a slope glacier on Kilimanjaro and its sensitivity to climate. *Int. J. Climatol.* 28, 881–892. doi: 10.1002/joc.1589

Morris, E. M., and Wingham, D. J. (2014). Densification of polar snow: measurements, modeling, and implications for altimetry. *J. Geophys. Res.* 119, 349–365. doi: 10.1002/2013JF002898

Mosley-Thompson, E., McConnell, J. R., Bales, R. C., Lin, P. N., Steffen, K., Thompson, L. G., et al. (2001). Local to regional-scale variability of annual net accumulation on the Greenland ice sheet from PARCA cores. *J. Geophys. Res.* 106, 33839–33851. doi: 10.1029/2001JD900067

Sturm, M., Holmgren, J., Konig, M., and Morris, K. (1997). The thermal conductivity of seasonal snow. *J. Glaciol.* 43, 26–41.

Techel, F., and Pielmeier, C. (2011). Point observations of liquid water content in wet snow–investigating methodical, spatial and temporal aspects. *Cryosphere* 5, 405–418. doi: 10.5194/tc-5-405-2011

Vallelonga, P., Christianson, K., Alley, R. B., Anandakrishnan, S., Christian, J. E. M., Dahl-Jensen, D., et al. (2014). Initial results from geophysical surveys and shallow coring of the Northeast Greenland Ice Stream (NEGIS). *Cryosphere* 8, 1275–1287. doi: 10.5194/tc-8-1275-2014

Van As, D., Fausto, R. S., and PROMICE Project Team (2011). Programme for Monitoring of the Greenland Ice Sheet (PROMICE): first temperature and ablation records. *Geol. Surv. Den. Greenland Bull.* 23, 73–76.

Conflict of Interest Statement: The authors declare that the research was conducted in the absence of any commercial or financial relationships that could be construed as a potential conflict of interest.

frontiers in Earth Science

ORIGINAL RESEARCH
published: 07 February 2017
doi: 10.3389/feart.2017.00006

Diurnal Cycles of Meltwater Percolation, Refreezing, and Drainage in the Supraglacial Snowpack of Haig Glacier, Canadian Rocky Mountains

Samira Samimi and Shawn J. Marshall*

Department of Geography, University of Calgary, Calgary, AB, Canada

Meltwater refreezing and storage in the supraglacial snowpack can reduce and delay meltwater runoff from glaciers. These are well-established processes in polar environments, but the importance of meltwater refreezing and the efficiency of meltwater drainage are uncertain on temperate alpine glaciers. To examine these processes and quantify their importance on a mid-latitude mountain glacier, we measured the temperature and meltwater content in the upper 50 cm of the supraglacial snowpack of Haig Glacier in the Canadian Rocky Mountains. Thermistors and Time Domain Reflectometry (TDR) probes were installed at 10-cm intervals at two sites in the glacier accumulation area from May to September, 2015. A Denoth meter was used to make point measurements for comparison with the TDR inferences of snowpack dielectric properties. These data are supplemented by automatic weather station data, used to calculate surface melt rates and drive a model of subsurface temperature, refreezing, and drainage. We observed a strong diurnal cycle in snow water content throughout the summer melt season, but subsurface refreezing was only significant in May; after this, overnight refreezing was restricted to a thin surface layer of the snowpack. Overnight decreases in water content after May are associated with meltwater percolation and drainage. There was negligible meltwater retention in the snow on a daily basis, but the refrozen water does represent an "energy sink," with 10–15% of the available melt energy diverted to melting refrozen meltwater. This reduces the total meltwater runoff from the site, even though no meltwater is retained in the system.

Keywords: meltwater retention, TDR, temperate glacier, hydraulic conductivity, snow water content, glacier hydrology, canadian rockies, refreezing

OPEN ACCESS

Edited by:
Jason Eric Box,
Geological Survey of Denmark and Greenland, Denmark

Reviewed by:
Qiao Liu,
Institute of Mountain Hazards and Environment (CAS), China
Ward Van Pelt,
Uppsala University, Sweden

****Correspondence:***
Samira Samimi
samira.samimi@ucalgary.ca

Specialty section:
This article was submitted to Cryospheric Sciences, a section of the journal Frontiers in Earth Science

Received: *22 September 2016*
Accepted: *18 January 2017*
Published: *07 February 2017*

Citation:
Samimi S and Marshall SJ (2017) Diurnal Cycles of Meltwater Percolation, Refreezing, and Drainage in the Supraglacial Snowpack of Haig Glacier, Canadian Rocky Mountains. Front. Earth Sci. 5:6. doi: 10.3389/feart.2017.00006

INTRODUCTION

Glacier meltwater represents a significant water resource in many of the world's mountain regions (e.g., Huss, 2011; Jost et al., 2012; Mark et al., 2015; Soruco et al., 2015). Mountain glaciers act as short- and long-term water reservoirs, retaining snow cover throughout the year and storing this as firn and ice on timescales of decades to centuries. This storage reservoir can be tapped in warm, dry periods, when the seasonal snowpack is depleted and water supplied by rainfall and snow melt may

not be available to provide a vital source of water for mountain rivers, maintaining minimum flows (Fountain and Tangborn, 1985; Jansson et al., 2003) and regulating stream temperatures (Moore et al., 2009).

Estimates of glacier contributions to streamflow commonly assume that 100% of surface melt runs off of the glacier, contributing to river flows with minimal delays (e.g., Huss, 2011; Marshall et al., 2011). In some situations, it may be valid to assume that glacier melt contributes to downstream flow with negligible storage or losses, such that total monthly melt can be compared with the monthly runoff. However, meltwater runoff is subject to delays and storage within the subglacial, englacial, and supraglacial systems, particularly during the early melt season (Willis et al., 2002) when meltwater is stored in the pore space of seasonal snow and firn (Fountain, 1996; Fountain and Walder, 1998; Schneider, 2000). Meltwater can also be stored as a layer of slush on top of the impermeable ice (e.g., Koenig et al., 2014).

The importance of these processes in temperate mountain glaciers is uncertain. Temperate mountain glaciers are commonly steep and are efficiently drained from mid- to late-summer, with well-developed channel systems that deliver meltwater to proglacial streams in a matter of hours (e.g., Shea et al., 2005).

The winter snowpack and firn aquifer can store large quantities of water (Östling and Hooke, 1986; Fountain and Walder, 1998; Schneider, 2000; Koenig et al., 2014). For instance, 10 meters of snow and firn with a 5% water content by volume equates to 500 mm of water, which is a significant fraction of summer melt in the accumulation area of most temperate mountain glaciers. If this aquifer is recharged each summer, this can represent a delay in meltwater runoff from the glacier system with a timescale of weeks to months. Hydrological models of glaciers need to include these processes of meltwater refreezing and storage in the snow and firn, to better represent the timing of glacier contributions to streamflow.

With the acknowledged importance of meltwater percolation, storage, and refreezing in glacier mass and energy balance (e.g., Pfeffer et al., 1991; Schneider and Jansson, 2004; Reijmer et al., 2012), extensive recent effort has gone into methods to measure and model these processes in snow and firn. Direct measurements of snow liquid water content are rare in glacier studies, but point measurements have been made using capacitance plates (Denoth, 1994) or other means to infer water content from the dielectric permittivity, such as snow forks (e.g., Pfeffer and Humphrey, 1998), and these methods appear sensitive enough to infer volumetric water content changes of ∼1% in snow (Techel and Pielmeier, 2011). Upward-looking radar systems are now being used to continuously monitor meltwater percolation, after successful introduction of this technology in snow avalanche and snow hydrology applications (e.g., Heilig et al., 2009, 2015; Mitterer et al., 2011b; Schmid et al., 2014).

Models of meltwater percolation processes, including preferential flow, are also improving rapidly, particularly within SNOWPACK (Hirashima et al., 2010; Mitterer et al., 2011a,b; Wever et al., 2015). For glacier and ice sheet applications, coupled energy balance and snow/firn hydrology models have also been developed to quantify the effects of meltwater refreezing and retention on glacier mass balance (e.g., Van Pelt et al., 2012; Reijmer et al., 2012). *In situ* data are still needed to calibrate and evaluate these models, and to address the complexities of preferential flow paths in layered and cold snowpacks (e.g., piping, sills). Drainage and refreezing processes are probably simpler in the case of temperate mountain glaciers, but this has not been thoroughly considered. Our main objective here is to quantify the potential importance of meltwater refreezing and retention for a mid-latitude mountain glacier.

Meltwater refreezing can also be important to the glacier energy and mass balance, with the potential for overnight refreezing to reduce seasonal runoff. When meltwater that is in the surface snow or is pooled on the glacier surface refreezes overnight or due to a cold-weather system, it consumes energy to re-warm and re-melt this ice once the surface energy balance returns to a positive state. Where this happens every night, this can lead to "recycling" of meltwater, with energy being used to melt the same water several times, and projected glacier meltwater production will exceed the actual runoff. This process has been posited to be significant for mountains glaciers (Marshall, 2014), but it is unknown whether it is important to total summer runoff and mass balance.

Here we report on measurements of meltwater percolation, storage, and refreezing in the supraglacial snowpack of Haig Glacier in the Canadian Rocky Mountains. We used Time Domain Reflectometry (TDR) and thermistor probes to measure water content of the upper 50 cm of the surface snowpack at two sites on the upper glacier from May through September, 2015. In conjunction with automatic weather station (AWS) data and a model of surface energy balance and melt, we examine meltwater storage, refreezing and drainage within the snowpack, and the implications for the surface energy balance and glacier runoff.

The paper is organized as follows: Section Methods provides details of the field site, instrumentation, measurement protocols, and a brief review of TDR applications to measure soil and snow water content. We provide some detail because, to our knowledge, automatically-recording TDR probes have not previously been used to monitor snow or firn hydrology on glaciers. Section Results presents our results and Section Discussion discusses the broader implication of our measurements, methods, and findings.

METHODS

Field Site

Haig Glacier (50°43′′N, 115°18′′W) is a small mountain glacier located approximately 100 km southwest of Calgary, Alberta in the Canadian Rocky Mountains (**Figure 1**). It is the main outlet of a small icefield that lies on the continental divide. The central flowline is 2.7 km in length, with an elevation range from 2435 to 2840 m, and the median elevation of the glacier is 2662 m. Glaciological and meteorological studies on Haig Glacier were established in August 2000 and more details on the energy and mass balance regime are given in Marshall (2014).

The glacier is influenced by a mixture of continental and Pacific climates. The melt season at this site usually runs from May until September, with intermittent snow and freeze-up events throughout the summer. Average winter snow

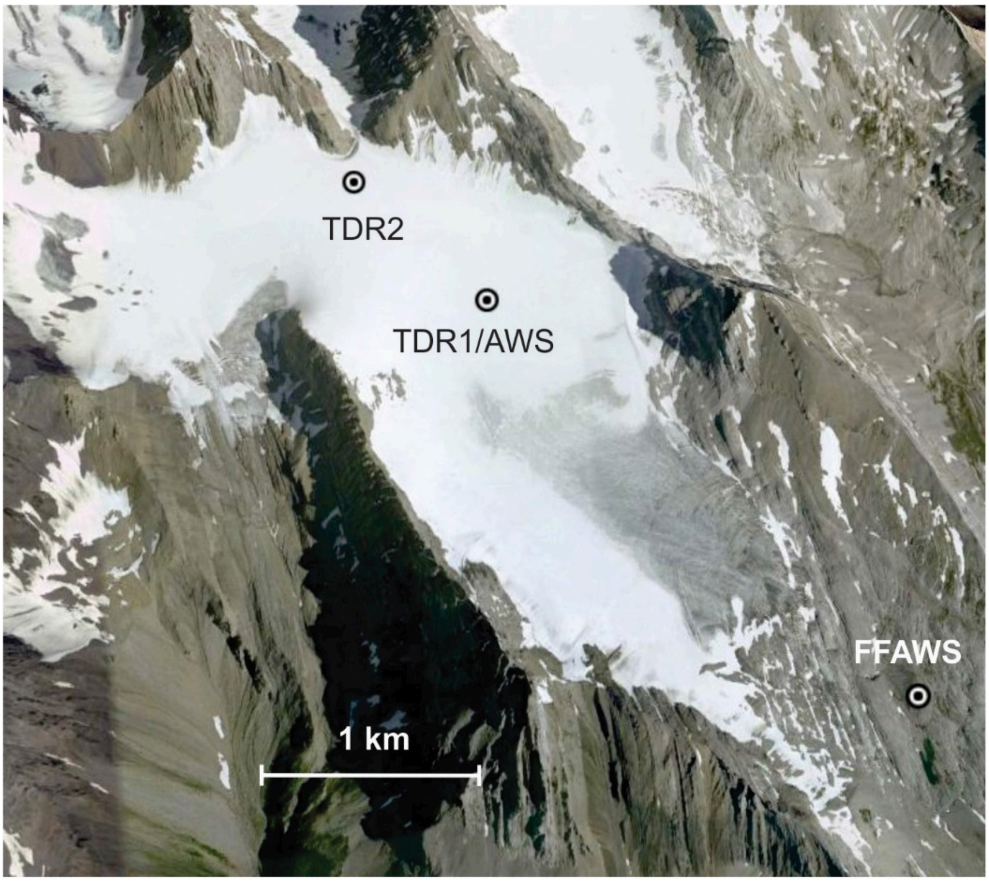

FIGURE 1 | Map of Haig Glacier, Canadian Rocky Mountains, indicating the weather station (AWS), forefield weather station (FFAWS), and TDR sites used in this study. TDR1 is at an elevation of 2700 m and TDR2 is at 2820 m.

accumulation on the upper glacier was 1700 mm water equivalent (w.e.) from 2002 to 2013, and the average glacier accumulation over this period was 1360 mm w.e. (Marshall, 2014). Summer mass balance averaged −2350 mm w.e. from 2002 to 2013. Of the summer runoff, an average of 42% was derived from firn and ice and 58% comes from seasonal snow melt. Glacier mass balance data reported by Marshall (2014) show net mass balance has been negative every year since the Haig Glacier study was initiated in 2000, with an average value of −960 mm w.e. per year from 2002 to 2013. The glacier accumulation area is shrinking, with complete loss of the winter snowpack on six summers since 2000, but some firn still remains above an elevation of about 2720 m.

TDR Methods

To monitor meltwater retention and refreezing in the supraglacial snowpack, we installed TDR probes on the upper glacier in summer 2015. TDR is a method of measuring water content and electrical conductivity based on relative permittivity (dielectric constant) of water, and is a well-established tool in soil hydrology studies. This method was applied to measure soil water content by Topp et al. (1980). Here we applied TDR to snow with only two modifications: we change the window for collecting the waveforms in the datalogger program, and equations specific to snow are needed to relate dielectric to snow water content.

With TDR probes, electromagnetic charges (EM waves) are sent along a conductive rod with length L. The probe contains three parallel metal rods that are inserted in the snow. The two-way travel time, t, is measured to determine how long it takes for the wave to reflect back from the end of the rod, a distance $2L$. Propagation velocity $v = 2L/t$. Snow is a dielectric medium, which allows no net flow of electric charge but experiences a displacement of charges in response to the imposed electric field. This affects the propagation velocity of the wave in the snow, particularly in the presence of liquid water. Wave speed decreases in proportion to the relative permittivity of the snow surrounding the probe, ε_s, following $v = c/\ \varepsilon_s\ ^{1/2}$ (e.g., Topp and Davis, 1985). Here $c = 3 \times 10^8$ m s^{-1} is the speed of light, the propagation velocity of electro-magnetic waves in a vacuum.

Snow is a porous medium that is made up of a mixture of ice, air, and liquid water. The dielectric properties of snow vary because the dielectric permittivity of air, ice, and water differ markedly: $\varepsilon_a = 1$, $\varepsilon_i = 3.2$, and $\varepsilon_w = 80$. Hence, the dielectric permittivity of snow increases strongly with liquid water content,

making ε_s a sensitive indicator of snow moisture. For porosity q and volumetric liquid water fraction θ_w, the bulk density of the snow is

$$\rho_s = \rho_i\ (1-\theta) + \rho_a\,(\theta-\theta_w) + \rho_w\theta_w, \tag{1}$$

Where ρ_i is the density of ice crystals in the snow matrix and ρ_a and ρ_w are the densities of air and water. The dry density, ρ_d, is calculated from Equation (1) when $\theta_w = 0$. When the snow is dry (e.g., on our first field visit in May), $\rho_s = \rho_d$ and this can be measured directly. When the snow is wet, an estimate of θ_w is needed to calculate dry density from field measurements of ρ_s. Snow density and water content both influence dielectric permittivity because solid and liquid water molecules are polarized in the presence of an electric field, and a greater mass of these molecules creates more polarization and a higher relative permittivity.

Measured dielectric permittivity needs to be converted to water content based on a dielectric mixing model. There are different approaches for this. Empirical equations that relate TDR-derived dielectric permittivity to liquid water content have been developed for soils (e.g., Topp et al., 1980; Ledieu et al., 1986), but these are not appropriate for snow or firn. Tiuri et al. (1984) introduce empirical equations that relate the dielectric permittivity to dry snow density and snow water content. Stein et al. (1997) and Schneebeli et al. (1998) discuss the application of TDR probes in snow. Several studies employ the Looyenga mixing model (Looyenga, 1965) to relate dielectric permittivity to water content in firn and ice (e.g., Macheret et al., 1993; Murray et al., 2000; Van Pelt et al., 2014; Christianson et al., 2015). The Looyenga mixing model estimates water content as a function of the dry density, following:

$$\varepsilon_d^{1/3} = 1 + \frac{\rho_d}{\rho_i}\left(\varepsilon_i^{1/3} - 1\right), \tag{2}$$

and

$$\theta_w = \left(\varepsilon_s^{1/3} - \varepsilon_d^{1/3}\right) / \left(\varepsilon_w^{1/3} - \varepsilon_d^{1/3}\right). \tag{3}$$

To apply Equation (3), e_s is measured by the TDR and e_d is calculated from Equation (2), using the dry density based on snow density measurements and Equation (1). This requires an estimate of water content in Equation (1); we base this on the coincident field measurements of snow density and the TDR-inferred θ_w, so the calculation is iterative, but dry density estimates are not strongly sensitive to small variations in θ_w. Variables ε_w, ε_i and ρ_i are constants.

As an alternative to the Looyenga model, we also consider a linear mixing model that is based on the volume-averaged index of refraction (Birchak et al., 1974), following

$$\theta_w = \frac{\varepsilon_s^{1/2} - \varepsilon_i^{1/2}\,(1-\theta)\ -\ \varepsilon_a^{1/2}\theta}{\varepsilon_w^{1/2} - \varepsilon_a^{1/2}}. \tag{4}$$

Recent snow radar studies (e.g., Heilig et al., 2015) also apply an exponent of 0.5 in the dielectric mixing model. This relation more directly relates to the volume-averaged wave velocity that is measured by the TDR, which is a function of $\varepsilon_s{}^{1/2}$ (Birchak et al., 1974). To evaluate which model works better, we compare the estimates of θ_w from Equation (3, 4) with measurements from a Denoth meter (Denoth, 1994), a capacitance sensor that is commonly used for snow moisture measurements. This is an analog sensor, so comparisons are limited to point measurements that were done on two site visits in summer 2015. Data from the Denoth meter were collected every 2 h in snow layers beside the TDR sensors.

Field Experiment Design

Four TDR probes were installed in the upper 50 cm of the seasonal snowpack in the accumulation area of the Haig glacier, 10 cm vertically apart from each other to monitor the vertical movement of percolated melt water. Beside each probe we installed a thermistor to monitor the temperature in the snowpack. The study sites are indicated in **Figures 1**, **2** shows an example of the field setup. TDR pits were filled up with snow once the probes were installed. The data logger recorded the data every 30 min and it was collected every 3–4 weeks. Site visits and details of the TDR installation are given in **Table 1**. Our first visit was in mid-May, prior to the onset of meltwater runoff. Snow pits were dug to the previous summer surface at sites TDR1 and TDR2 and sampled every 10 cm for density with a 100-cc box-cutter snow sampler. The snowpack was isothermal. Snow depths at sites TDR1 and TDR2 were 302 and 356 cm, respectively, with snow-water equivalents of 1270 and 1450 mm. The average snow density at TDR1 was 420 kg m^{-3} in May, and 450 kg m^{-3} in the upper 50 cm. Corresponding May values at site TDR2 were 410 and 460 kg m^{-3}.

The TDR probes and thermistors melted out over a few days after each installation, so the data are only valid for 2–8 days after we left the field, depending on the melt rates. On each visit we dug a new pit, reinstalled the probes, and measured the snow densities in each 10-cm layer. Haig Glacier experienced an extreme melt year in 2015 and lost all of its winter snowpack by the second week of August. The snow at our initial study site, TDR1, was gone on July 21, so in our late-July visit we relocated to site TDR2, where about 60 cm of snow remained. Firn was exposed at site TDR2 at the time of our August visit. We could not dig into the firn, so probes were inserted vertically, all sampling the upper 30-cm of the firn. There were 20 cm of fresh snow at the time of instrument takedown and removal on Sept 21.

An automatic weather station (AWS) was installed at site TDR1 from May 12-September 21. **Table 2** lists the instruments mounted on the AWS and in the TDR pits. AWS data are used to monitor the snow-surface height, which indicates the time of melt-out for the sensors, and also as input to a model of surface energy balance. The net energy at the glacier surface is a function of the energy fluxes at the surface-atmosphere interface,

$$Q_N = Q_s\,(1-\alpha) + Q_L^{\downarrow} - Q_L^{\uparrow} + Q_H + Q_E + Q_C \tag{5}$$

Where Q_S is the incoming shortwave radiation, α is the surface albedo, $Q_L^{\downarrow}$ and $Q_L^{\uparrow}$ are the incoming and outgoing longwave radiation, Q_H and Q_E are the sensible and latent heat fluxes,

FIGURE 2 | Photograph of the TDR field setup. TDR sensors and thermistors were installed with 10-cm spacing in the upper 50 cm of the snowpack. A Denoth meter was used to make point measurements for comparison with the TDR.

TABLE 1 | Field visits and TDR setup, summer 2015.

Visits	Day in 2015	Site	Depth (cm)	Density (kg m^{-3})
1	May 13	TDR1	20, 30, 40, 50	450
2	June 9	TDR1	5, 15, 25, 35	470
3	July 9	TDR1	10, 20, 30, 40	495
4	July 31	TDR2	10, 20, 30, 40	510
5	Aug 12	TDR2	30 (vertical)	600

TABLE 2 | Sensors installed on the automatic weather station (AWS) and in the TDR pits in summer 2015.

AWS sensors	Instrument	Comments
Temperature	HC-S3-XT	
Relative Humidity	HC-S3-XT	
Barometric pressure	RM Young 61250V	
Wind speed/Direction	RM Young 05103	
Short wave radiation	Kipp and Zonen CNR1	Spectral range 0.35-2.50 μm
Long wave radiation	Kipp and Zonen CNR1	Spectral range 5-50 μm
Snow surface height	SR50A sonic ranger	
TDR sensor		
Model	TDR100	
Multiplexing	SDMX50	
TDR Probes	CS605	3-rod probe, 30 cm length, 0.476-cm diameter
Thermistors	107 T	

Qc is the conductive heat flux from the snow/ice to the surface. All energy fluxes have units W m^{-2}. Radiation fluxes are measured directly. The turbulent fluxes are modeled using a bulk aerodynamic approach that uses AWS temperature, humidity, and wind speed (Marshall 2014), and the conductive heat flux is modeled using a multi-layered subsurface snow/firn/ice model to 10-m depth (Ebrahimi and Marshall, 2016). This is the approximate depth of penetration of the annual temperature wave (Cuffey and Paterson, 2010).

When Q_N is positive and the surface temperature is below 0°C, net energy goes to heating the surface layer of the snow/ice, a 10-cm layer within the subsurface model. If the surface is at 0°C, positive net energy goes to melting, following

$$m = Q_N/(\rho_w L_f), \tag{6}$$

Where m is the melt rate (m s^{-1}), and L_f is the latent heat of fusion. If net energy is negative, any liquid water that is present will refreeze and then the surface layer will cool.

The surface energy balance is a boundary condition for the subsurface model, which describes the coupled snow thermodynamics and hydrology. Subsurface temperatures are modeled as a function of heat conduction and meltwater refreezing, following

$$\rho_s c_s \frac{\partial T}{\partial t} = \frac{\partial}{\partial z}\left(-k_t \frac{\partial T}{\partial z}\right) + \varphi_t, \tag{7}$$

Where ρ_s, c_s, and k_t are the density, heat capacity, and thermal conductivity of the subsurface snow, firn, or ice and $\varphi_t(z)$ is a local source term that accounts for latent heat of refreezing,

$$\varphi_t = \rho_w L_f \dot{r}/\Delta z \tag{8}$$

The refreezing rate $\dot{r}$ has units m s^{-1}, φ_t has units W m^{-3}, and Δz is the thickness of the layer in which the meltwater refreezes.

Refreezing is calculated within the subsurface thermal model. We track the volumetric liquid water fraction, θ_w, in the snow/firn pore space, and if conductive energy loss occurs in a subsurface layer where liquid water is present, this energy is diverted to latent enthalpy of freezing, rather than cooling the snow. Temperatures cannot drop below 0°C until $\theta_w = 0$. Liquid water is converted to ice in the subsurface layer.

The surface energy balance in Equation (5) also gives melt totals every 30 min, which are used in conjunction with the TDR data to examine meltwater drainage and storage in the upper 50 cm of the snowpack. To calculate the meltwater drainage fluxes at each depth, z, we use a simple model of water balance based on the change in measured water content, assuming that the surface meltwater percolates locally. We did not account for rainfall, although this is a potentially important contribution to the snow water content at times. There were no rain events during the data intervals that we analyse here.

For snow layers with thickness Δz and with θ_w expressed as the fractional water content, the amount of water in a given layer is equal to $\theta_w\ \Delta z$. In our study $\Delta z = 0.1$ m and the water content $\theta_w\ \Delta z$ can be expressed in meters. Define the meltwater percolation rate to be q_w and a local ϑ_w refreezing rate $\dot{r}$, as above, each with units m s^{-1}. The local water balance in each subsurface layer is then:

$$\frac{d\theta_w}{dt} = -\nabla q_w - \frac{\dot{r}}{\Delta z} = \frac{1}{\Delta z}\left(q_{wu} - q_{wl} - \dot{r}\right) \qquad (9)$$

where, and q_{wu} and q_{wl} refer to the meltwater flux into (upper boundary) and out of (lower boundary) the layer and any water that refreezes is distributed over the layer Δz. We assume that all meltwater flow is vertical (gravitational drainage with no horizontal advection), such that the flux divergence in Equation (9) can be calculated from the vertical derivative.

Meltwater fluxes are estimated by solving Equation (9), given independent estimates of the snow water content (from the TDR measurements) and internal refreezing. The flux into the top layer is equal to the melt rate, modeled from Equation (6). At all layer boundaries below this, q_w is calculated from Equation (9), using measured value of $d\theta_w/dt$ and model estimates of ϑ_w in each layer. Refreezing is calculated within the subsurface model; if there is an energy deficit in a layer, available liquid water will freeze before the subsurface layer can cool below 0°C. This drainage model is used to characterize percolation timescales and the effective hydraulic conductivity of the snowpack.

RESULTS

AWS data for the summer are plotted in **Figure 3**, to give a quantitative sense of the summer weather. Air temperatures fluctuated around 0°C during mid-May, but mostly stayed above the melting point, even overnight, from June through August (JJA) (**Figure 3A**). The average JJA temperature was 6.0°C, compared to a normal of 4.7°C at this altitude on the glacier (2002–2014). All JJA days, and 122 out of 131 days for the whole period, had maximum temperatures above 0°C. In contrast, only 20 out of 92 JJA days saw minimum temperatures below 0°C.

The warm temperatures and sunny conditions (**Figure 3B**) drove high melt rates, with a positive feedback from a below-normal surface albedo (green line in **Figure 3B**). Albedo was low due to the early exposure of glacier ice as well as a heavy layer of impurities from forest-fire fallout; the warm, dry weather also made for a strong fire season in British Columbia, upwind of Haig Glacier, and this darkened the glacier surface. The average JJA albedo at site TDR1 was 0.46, and the bare-ice value through late July and August was 0.11. Albedo was temporarily refreshed by intermittent summer snow events through this period, which effectively shut down the melt for 1–2 days (**Figure 3C**).

The melt season on the upper glacier ended abruptly around August 31, with new snow arriving and persisting in the upper accumulation area. Small amounts of melting continued during warm intervals in September, but restricted to the new snow at the AWS site. Despite this relatively early onset of winter, cumulative ablation at the AWS site was about 5 m (**Figure 3D**), or 2700 mm w.e. Net mass balance at the site was −1470 mm w.e. and the glacier-wide value for 2014–2015 was about −2200 mm w.e.

The complete loss of snow and the warm conditions in the accumulation area made for an interesting summer, if not ideal for examining meltwater refreezing and storage in the snow. Analysis of our TDR data therefore concentrates on the spring and early summer. On the positive side, the warm summer and high melt rates provide a good example of meltwater drainage and refreezing processes under these conditions.

Denoth-meter data collected on the June and July visits confirms that the TDR is reliably measuring water content, but with uncertainty in the relation between dielectric permittivity and snow water content. **Figure 4A** plots θ_w values at 10-cm depth from the Denoth meter and the two TDR mixing models that we apply, Equations (3, 4), for a series of bi-hourly measurements from July 7 to 9. The three methods show the same diurnal cycle, but Equation (4) gives us a closer match to the Denoth meter. The Looyenga mixing model give a 4% higher volumetric water content than the other two methods. The full set of TDR vs. Denoth data is plotted in **Figure 4B**. There is considerable scatter but the Birchak mixing model, Equation (4), is generally closer to the Denoth-meter readings and gives lower values of θ_w, more in accord with values reported elsewhere for melting snow (e.g., Kawashima et al., 1993; Niang et al., 2006). Based on this comparison, we use the linear mixing model to estimate θ_w from the TDR data for our analyses.

TDR Results

There are strong diurnal cycles in temperature during the early melt season, with overnight temperatures dropping below 0°C (**Figure 3A**). **Figure 5** gives a detailed view of air temperature, net energy (Equation 5), and the subsurface thermistor and TDR data for the period May 16–23. Melt rates were relatively low during this period, up to 20 mm w.e. d^{-1} (**Figure 3C**), and sensors were installed from 20 to 50 cm depth, so data remain valid for more than a week before the top sensor melted out. There were clear-sky conditions from May 18 to

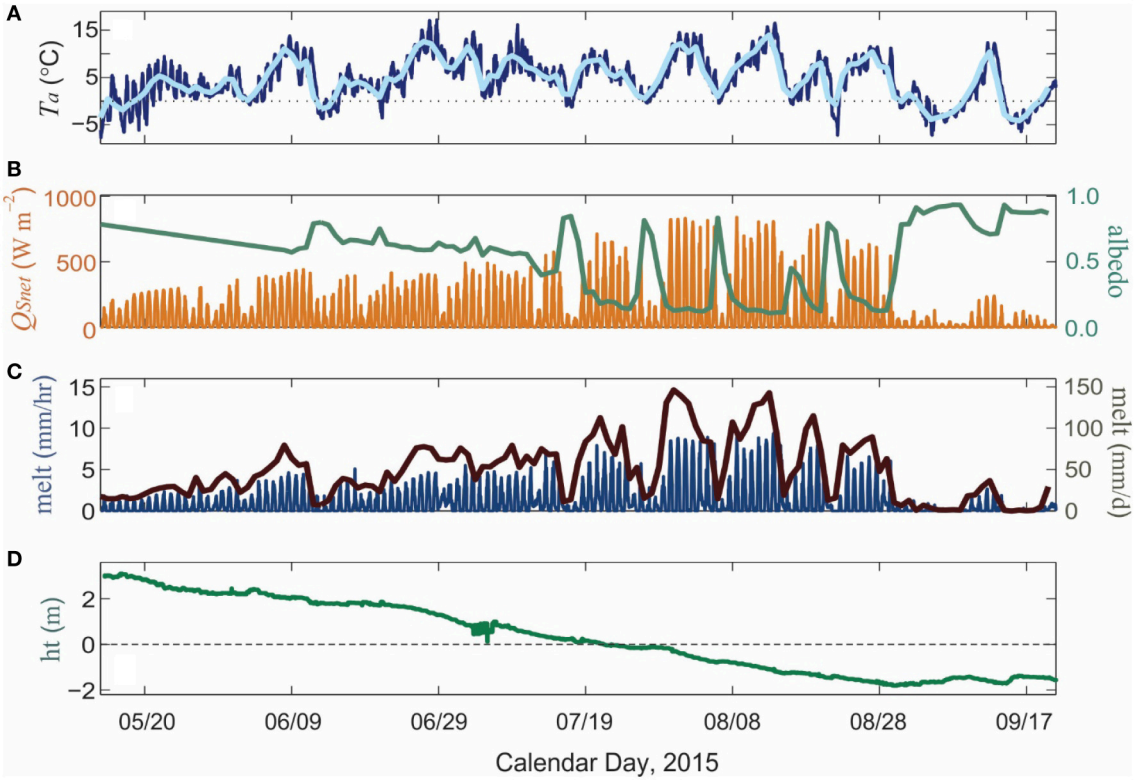

FIGURE 3 | Meteorological observations at the Haig Glacier AWS site, May 13-Sept 21, 2015. (A) Air temperature, 30-min (dark blue) and daily mean (light blue). **(B)** Net shortwave radiation (orange) and daily mean albedo (green). **(C)** modeled melt, hourly (dark blue), and daily total (brown). **(D)** SR50 snow/ice surface height. Negative values indicate glacier ice ablation.

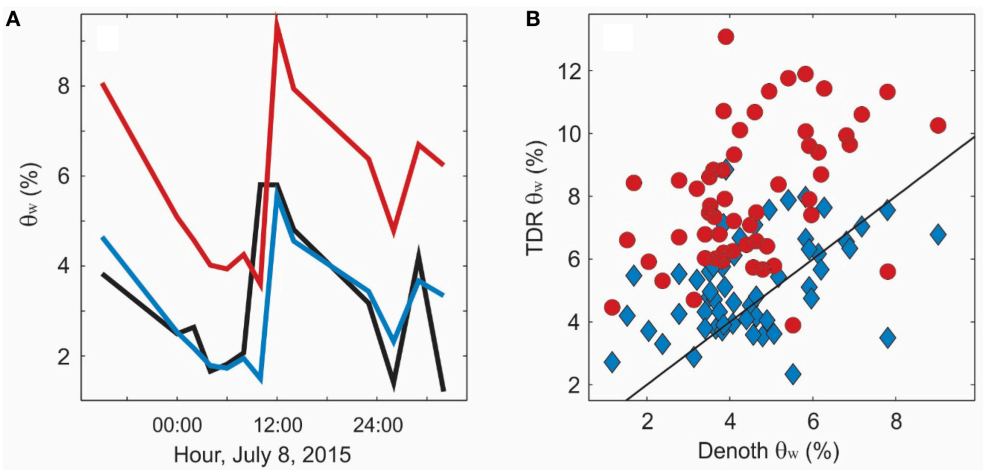

FIGURE 4 | Comparison of volumetric water content, θ_w, derived from a Denoth meter vs. the TDR probes. Water volume with the TDR probes is calculated from the measured dielectric coefficient using a linear (blue) and Layoonga (red) mixing models. **(A)** Temporal evolution of snow water content at 10-cm depth below the surface. **(B)** Available Denoth-meter data vs. TDR-derived θ_w values from site visits on July 7–8 and July 30–31.

23, evident in the shortwave radiation record (**Figure 5B**), and this drove strong overnight cooling (**Figure 5A**). Net energy was negative overnight during this period (**Figure 5B**) and the snowpack refroze to between 30 and 40 cm depth (**Figure 5C**). The top two thermistors recorded minimum temperatures of about −5 and −3°C overnight, and later in this week the lower two thermistors also registered sub-freezing temperatures. By this point, after May 21, more than 10 cm of ablation

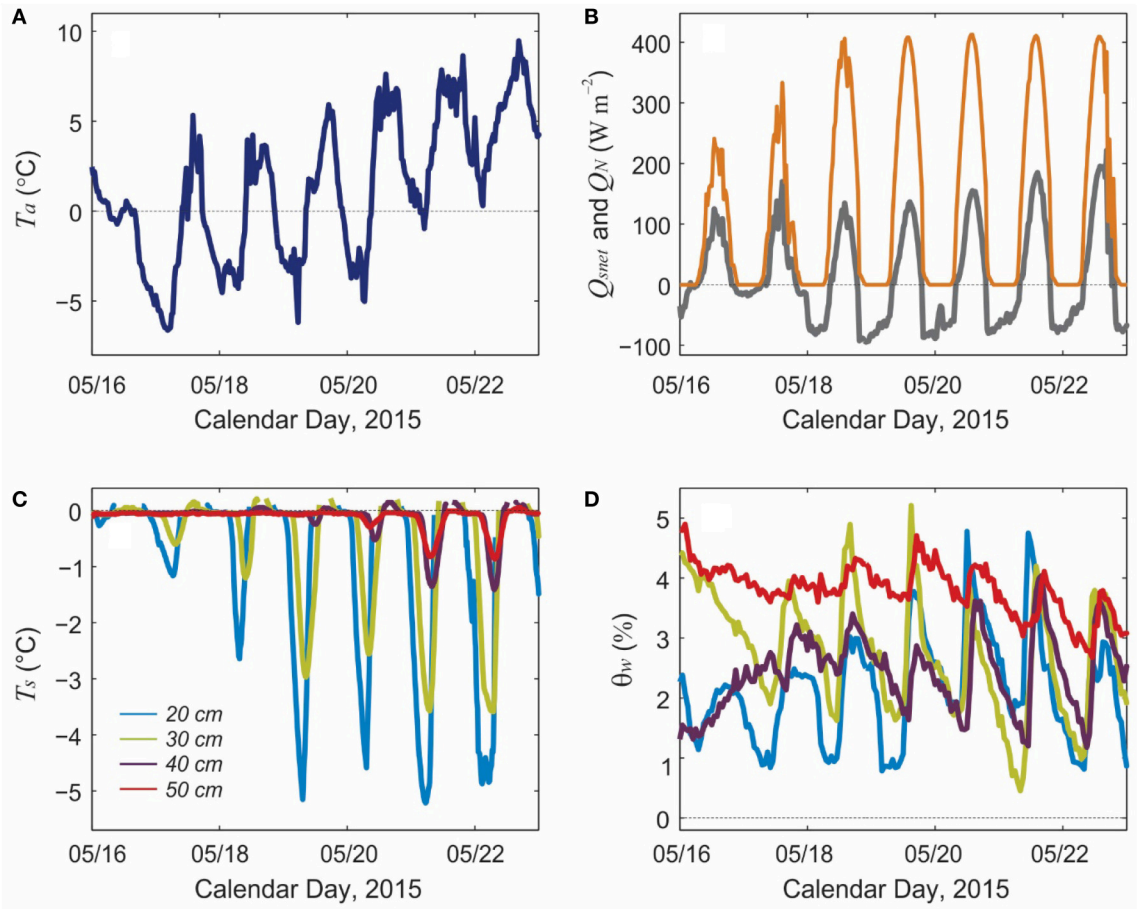

FIGURE 5 | Meteorological and snowpack conditions from May 15-22, 2015. (A) Air temperature, °C. **(B)** Net shortwave radiation (orange) and net energy (gray), W m^{-2}. **(C)** Snow temperatures (°C) and **(D)** TDR-derived water content (%) at 20, 30, 40, and 50 cm depth.

had occurred and these two sensors were within 40 cm of the surface.

The TDR data (**Figure 5D**) show diurnal cycles, in good accord with the temperature data and net energy, with water content between 1 and 5%. There are overnight minima and daytime maxima in snow water content, but with some lags relative to the shortwave radiation and net energy. The lowest values of θ_w are recorded in the early morning, ca. 06:00–09:00, followed by a rapid rise and mid-afternoon peak in θ_w around 15:00–16:00. This is consistent with overnight refreezing, as indicated by the thermistors, followed by shortwave-driven thawing and surface melting during the day. The overnight phase change in the snowpack has some inertia. Delays in the freezing-front migration to depth are also clear in the thermistor data. The deepest thermistor/TDR pair, at 50 cm, have different behavior through this period, remaining at 0°C for most of this time with only small diurnal cycles in θ_w. Water content remains near 4%, and only starts to drop below this as the sensor depth shoals over the last 2 days.

TDR-inferred water content does not drop to 0 as should be the case with deep overnight refreezing. We attribute this to errors in the TDR measurements and in our equations that relate water content to the measured dielectric permittivity. Results indicate an uncertainty of ∼2% in the measurements, with a positive bias; this bias is about two times higher with the Looyenga mixing model. Similar results are reported by Pfeffer and Humphrey (1998) with snow-fork based snow water content measurements in Greenland: liquid water contents of 2–3% at sub-freezing temperatures. This implies a potential positive bias in the sensor, at least at low water contents. In soil studies, Jones et al. (2002) report an uncertainty of 1–2% in TDR-based water content estimates. In contrast, Schneebeli et al. (1998) document no evidence of a systematic bias in comparisons of TDR results with Denoth meter measurements in snow.

Figure 6 plots comparable data for the full study period, illustrating the seasonal evolution of the net energy, melt rates, and snow water content. The time scale is not continuous, as we have only 2–8 days of valid data following each site visit/station reset. Thermistor data indicate that they rarely drop below 0°C following the May visit; the snowpack remained at the melting point subsequent to May, although a thin refrozen surface crust set up overnight during all of our site visits.

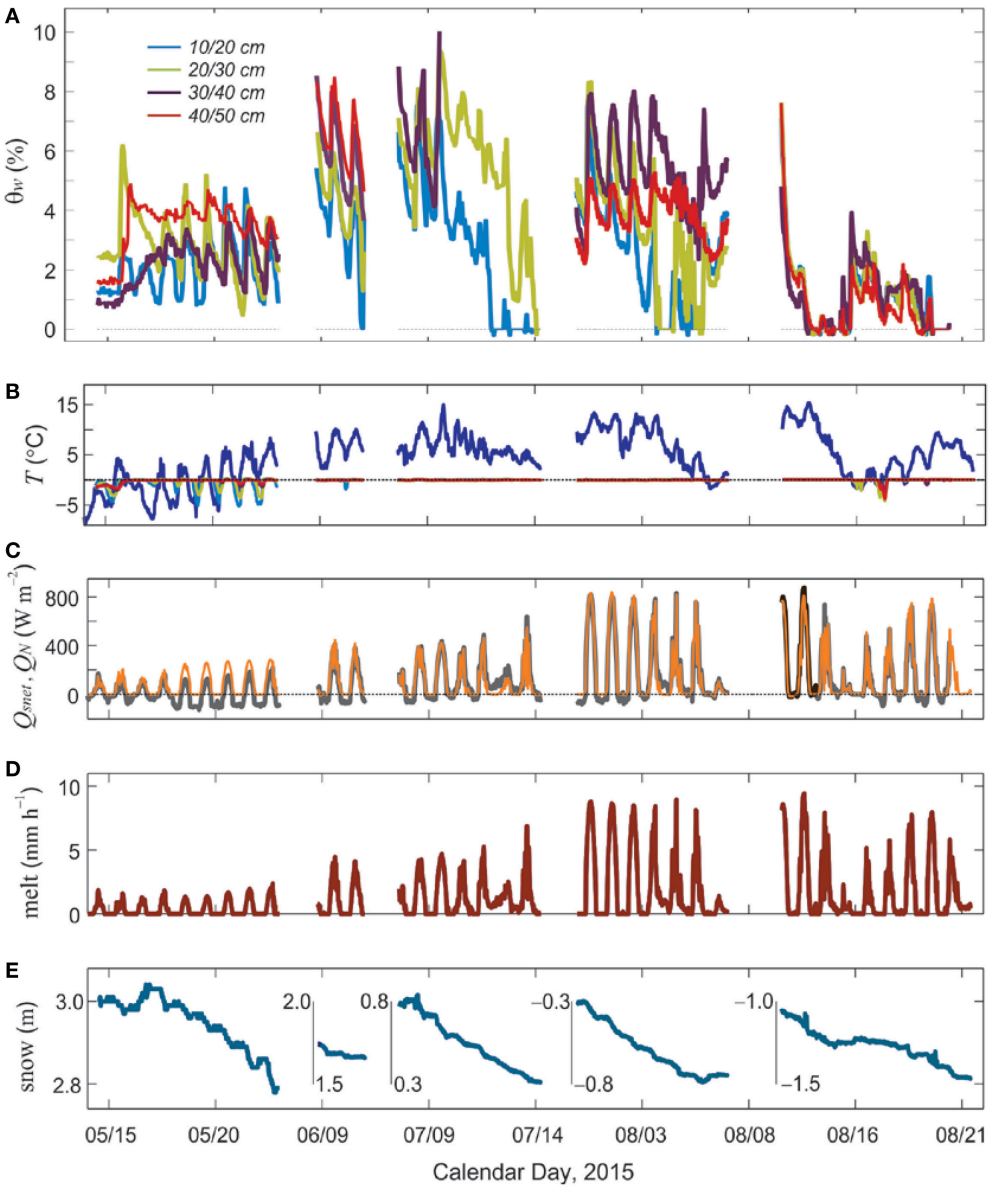

FIGURE 6 | (A) TDR-derived snow water content in the upper 50 cm of the seasonal snow and firn and **(B–E)** weather conditions over the five study periods, summer 2015. **(B)** Air (dark blue) and snow temperatures, °C. Thermistor depths and colors are the same as in **(A)**. **(C)** Net shortwave radiation (orange) and net energy (gray), W m^{-2}. **(D)** Modelled melt rates, mm h^{-1}. **(E)** Snow surface height (m). Negative values indicate ice ablation.

Snow water content varies from 0 to 10% in the main summer melt season, June through August, with strong diurnal cycles throughout the record, at all depths. Daytime values are typically in the range of 5–7%. Based on the thermistor data and shallow snow pits that we excavated during our visits, there is no evidence of overnight refreezing through this period. The diurnal cycles are driven instead by strong daytime melting and overnight drainage, once the meltwater is reduced or shut off for the night. The lowest water content tends to be near the surface, with θ_w increasing with depth, although this is not always the case. The deepest sensor in the August data (40 cm; red line in **Figure 6A**) records less water content than the sensors at 20–30 cm, but this is an exception in our data. Overnight water content in summer is around 4%. This probably corresponds to irreducible water content being held by capillary forces in snow pack.

During the July visit, only about 50 cm of snow remained at site TDR1 and there was a 10-cm thick layer of water at the base of the snowpack, visible in **Figure 2**. This water ponded at the ice-snow interface as a result of the impermeable glacier ice and a low slope at our study site, ca. 3°, which limits down glacier supraglacial drainage when there is still snow present. This layer of pure water and the overlying slush caused problems for our

lowest TDR sensor, at 40 cm; it reported off-scale and no data are available from this sensor, so it is not plotted in **Figure 6A**. Our program for the TDR time window and waveform probably did not extend to high enough water contents to allow for useful data. Sensor 3, at 30 cm, also gave off-scale readings after two days. Sensor 1, at 10 cm, drops to 0 on July 12, at which time it has melted out and is lying on the snow surface. Sensor 2 follows suit the next day. The same behavior is seen in the August data.

While the sensors are in place, discharge at each level can be modeled through the local water balance, following Equation (9). Results of this simple drainage calculation are shown in **Figure 7** for the periods where all four sensors were operational. Drainage is calculated every 30 min and expressed in units of mm h^{-1}. The plots show both total melt (Equation 6) and the drainage (melt minus refreezing).

In May there is a lag between the melt and drainage and drainage is always less than the total melt. This is consistent with the observed refreezing during the night and the partitioning of positive net energy between warming the snowpack and generating meltwater at the surface. When net energy becomes positive in the morning, it takes several hours to warm up and thaw the near-surface ice layers in the snowpack. Drainage peaks several hours after the peak melt, and continues overnight after the surface meltwater shuts off. By mid-summer all the meltwater is draining with little lag, which indicates negligible storage. Drainage in May is about 2 mm h^{-1}, increasing to 10–12 mm h^{-1} in July and August.

To better quantify the delays in drainage, we calculate the lagged correlation between melt and drainage at each depth. **Figure 8** plots the correlation results for lags of up to 8 h in May, June, and August, the time periods shown in **Figure 7**. In the top two layers (upper 20 cm), the maximum correlation is at a lag of 1 h in each case, which indicates that the meltwater is flushing through quickly. At depths of 30 to 50 cm, the maximum correlation increases to 3–4 h in May. Lags also increase with depth in June and August, but the correlations are stronger and the lag is reduced to 1 h in August. This indicates more rapid drainage and a tight coupling between the melt rates and drainage in the upper 40 cm of the snowpack. Unlike in May, there is negligible storage on hourly time scales.

DISCUSSION

Uncertainties

There are several sources of uncertainty in the data and the model applied to infer water content from the measured dielectric. The TDR probes need to be well-coupled with the snow for a clean signal, and this may not always be the case, particularly as the snow becomes very wet. Snow density measurements and the associated porosity inferences have some uncertainty, as do all of the meteorological data that drive the melt model. The surface energy balance calculations require assumptions about the turbulent heat transfer (e.g., stability, surface roughness values). We neglect rainfall in this study, but we were at the site during the observation periods (e.g., **Figure 6**), and are confident that there was no rainfall during these periods. However, a more complete model should include liquid precipitation along with meltwater as a water source at the upper boundary in Equation (9).

The largest source of uncertainty is associated with conversion of the measured dielectric permittivity to θ_w. The Birchak et al. (1974) mixing model gives better estimates of θ_w than the Looyenga (1965) model with our data, but we still see θ_w values of ∼2% when the near-surface snow was clearly refrozen, with temperatures of −5°C. This implies an uncertainty of about 2%, but also a potential positive bias in the measurements and/or mixing model. We are not certain about why the Looyenga model gives such high numbers. It has been successfully applied to saturated firn and ice (e.g., Macheret et al., 1993; Murray et al., 2000; Christianson et al., 2015) and snow (Niang et al., 2006). It may be that the geometry of water in the unsaturated pore space is inconsistent with the assumption of spherically-packed inclusions in the Looyenga mixing model.

Our comparisons with the Denoth meter assume no horizontal variations in snow-water content, such that we can compare adjacent measurements. The snow was highly homogeneous during our field work, so this may not be problematic.

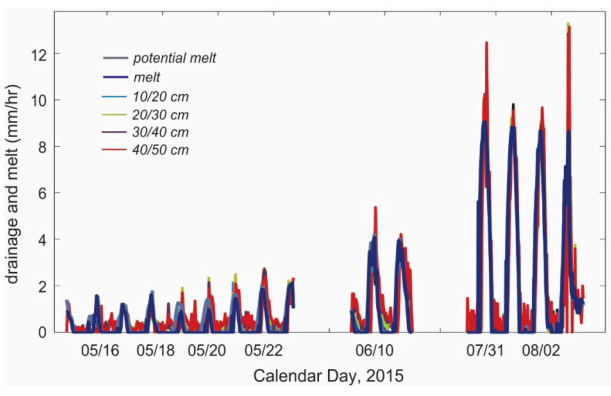

FIGURE 7 | Modelled meltwater production and measured drainage for the TDR study periods in summer 2015.

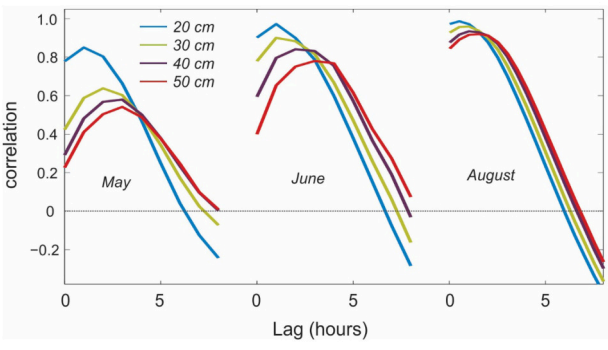

FIGURE 8 | Lag in surface meltwater production vs. drainage at different depths.

Perhaps more critical is the implicit assumption that the TDR measurements are not impacted by excavating the snow pit. The snow pits were filled in after the sensors were installed, but this is still a disrupted environment, potentially favorable to surface water infiltration. The TDR probes are 30 cm long and they were inserted in the shaded wall, so they are sampling undisturbed snow. The overlying snow was also left undisturbed. Because slopes are low at this site, we assume purely vertical percolation of the meltwater (i.e., no horizontal advection), and we also did not witness any surface water flow at the two TDR sites. Meltwater drainage was through local gravitational percolation, with no visible piping, channeling, or preferential pathways. For these reasons, we don't believe that the snow being sampled by the TDR probes was influenced by the snow pit or aberrant hydrological behavior.

Implications for Supraglacial Hydrology and Glacier Mass Balance

The TDR data give an insightful representation of meltwater percolation and drainage in the supraglacial snowpack and its evolution through the summer melt season. Infiltration and drainage through the isothermal snow pack are fast processes, with percolation speeds of order 1–10 mm h^{-1} (**Figure 7**). The time lag for the meltwater wave to propagate through the upper 50 cm of the snowpack is up to a 4 h in the early melt season and 1–2 h in July and August (**Figure 8**). The higher lags in May are associated with overnight refreezing of the meltwater in the upper 40 cm of the snowpack. Over a 24-h timescale, all of the meltwater drains, even in the early melt season. Within the uncertainty of our measurements, we see no evidence of meltwater storage in the upper 50 cm of the snowpack on daily to seasonal timescales, after initial wetting of the snowpack.

We model the meltwater drainage as Darcian flow, with hydraulic conductivity k_h and hydraulic head $h = z$. For gravitational drainage in this case, $k_h = q_w$. Our measured drainage rates give effective hydraulic conductivities of 3×10^{-7} m s^{-1} in May and 3×10^{-6} m s^{-1} July. The snowpack is unsaturated and these are not necessarily limiting values; they are set by the melt rates, and flow rates higher than this could possibly be accommodated. These values are low relative to firn estimates of $1–5 \times 10^{-5}$ m s^{-1} in the review of Fountain and Walder (1998). However, our values are consistent with the saturated permeability value of $\kappa_S \sim 2 \times 10^{-9}$ m^2 reported by Colbeck and Anderson (1982) for snow with a density of 500 kg m^{-3}. This corresponds to a saturated hydraulic conductivity of $k_S \sim 10^{-2}$ m s^{-1}. Applying the equations of Hirashima et al. (2010) for unsaturated water flow in snow, the corresponding unsaturated hydraulic conductivity is $k_h \sim 3 \times 10^{-6}$ m s^{-1}, in accord with our summer data.

Continuous measurements of snow water content and meltwater percolation in mountain snowpacks over the spring melt season are available from impedance sensors (Mitterer et al., 2011a) and upward-looking radar (Heilig et al., 2015; Wever et al., 2015), supplemented by lysimeter measurements of drainage at the base of the snowpack. These studies offer additional insight into wetting front propagation and drainage timescales, although hydraulic conductivities are not reported. Drainage rates reported by Mitterer et al. (2011a) reach 40 mm d^{-1} in late May, through a 1–1.5 m snowpack, corresponding to an effective hydraulic conductivity of 5×10^{-7} m s^{-1}. Similarly, snowpack drainage rates of ∼4 mm h^{-1} in Wever et al. (2015) and up to 60 mm d^{-1} in Heilig et al. (2015) equate to snowpack-integrated hydraulic conductivities of 10^{-6} and 7×10^{-7} m s^{-1}, respectively. These values are consistent with our data and may also be minimum values, reflecting the ability of the ripened summer snowpack to transport all of the meltwater that is generated at the surface.

Our diurnal cycles of snow water content are similar to those in Mitterer et al. (2011a), who record daily θ_w variations between 4 to 8%. This suggests an irreducible water content of 4%, with daytime increases in pore water and drainage on a timescale of hours, giving complete overnight drainage. In contrast, Heilig et al. (2015) report lower values of θ_w (typically 2–4%) and more muted diurnal cycles, with an amplitude of 1–2%. Modeling of water drainage with SNOWPACK within these studies considering different formulations for meltwater percolation in mountain snowpacks, such that hydraulic conductivity is a function of numerous variables such as snow grain size and density, with no single value reported. Our results appear to be in accord with these previous observational and modeling studies of isothermal alpine snowpacks.

If we assume the snowpack to be homogeneous, such that percolation processes and the effective hydraulic conductivity are uniform with depth, these values imply that meltwater drains through the full summer snowpack to the firn or ice interface in less than a day. While we do not have deep sensors to confirm this, the summer snowpack, once temperate, has uniform density (constant within measurement uncertainty), with coarse, rounded grains and no layered structure, akin to the summer snowpack conditions reported by Wever et al. (2015). Hence, the upper 50 cm of the snowpack is likely representative. This is untrue in the early melt season, when the snowpack is still cold and there is strong overnight refreezing, but after mid-May during our study the snowpack was wetted, and there was negligible meltwater retention at our site. Meltwater can still be delayed and stored in the firn or in the englacial and subglacial systems, so we cannot make conclusions about meltwater retention in the full glacier hydrological system.

Figure 9 plots the predictions of a meltwater drainage model through the full melt season at the AWS site, based on Darcian drainage with a hydraulic conductivity of 10^{-6} m s^{-1}. The model includes a subsurface temperature solution and a calculation of meltwater refreezing. During the first ∼2 weeks of the study period (**Figure 9**), the near-surface snow cooled down overnight (**Figure 5**), much of the daily meltwater refroze, and it took several hours to warm up and thaw the surface layer the following morning. Local drainage did not commence until the afternoon and in the model, the meltwater did not reach the base of the snowpack and begin to drain until May 21 (**Figure 9**). Following this, drainage kept pace with melting for the rest of the summer. Overnight refreezing took place through most of the summer, until the snowpack was gone in August (**Figure 9**), but after mid-May the overnight refreezing was primarily associated with the

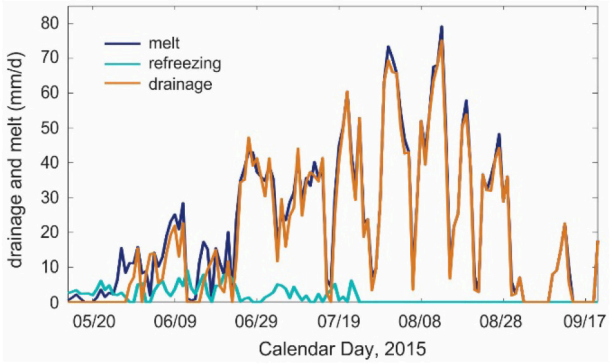

FIGURE 9 | Daily total melt (blue), refreezing (marine), and runoff (orange) calculated from the subsurface drainage model at the Haig Glacier AWS site, summer 2015.

irreducible water content of the snowpack in the near-surface, i.e. the water that is retained by capillary pressure. We assume the irreducible water content to be 3–4% by volume (7% of available pore space, after Colbeck, 1974 and Coléou and Lesaffre, 1998). This water refreezes at night or during cold periods if net energy is negative, but the associated latent heat release keeps the snowpack isothermal in mid-summer.

Total summer melt in **Figure 9** is equal to 2960 mm w.e., with 2700 mm w.e. of drainage and 260 mm w.e. of refreezing. The deficit in drainage relative to melt is because some of this melt (about 260 mm w.e., or 9%) is "recycled" meltwater. In contrast to polar environments, little or no refrozen water is retained, since this thaws during the day and drains. Some meltwater may be retained in the system in September or October, within the fresh autumn snow that starts to accumulate on the glacier.

Our results depend on the assumed irreducible water content. If this is taken to be 6%, total summer melt, drainage, and refreezing are equal to 2940, 2620, and 320 mm w.e., respectively. For a value of 2%, the corresponding values are 3000, 2820, and 180 mm w.e. Within this range, this amounts to a drainage deficit of 6–11% relative to total summer melt. Drainage increases when there is less refreezing, since more of the available melt energy is committed to fresh surface melt rather than re-melting of the water that has refrozen. Total summer melt also increases slightly because the transition from snow to lower-albedo glacier ice occurs sooner.

Our results imply that meltwater refreezing has a significant (order 10%) impact on the summer surface mass balance on this glacier, even though there is negligible meltwater retention or internal accumulation in the seasonal snow. The refreezing process may be even more important for mountains glaciers at higher altitudes and latitudes. Temperatures and melt rates were also unusually high at our site in summer 2015; it was one of the most negative mass balance years on record in the Canadian Rocky Mountains. Caution is therefore needed in extending our refreezing observations to other summers.

When refreezing did occur at our site, it delayed the meltwater drainage by a few hours and it also consumed some of the available melt energy the subsequent day, reducing the daily drainage. This latter effect is the one that is of greatest interest for mountain glacier mass and energy balance. As an example, we calculate that 51 mm w.e. of meltwater refroze in the period May 16–23. The latent energy required to re-thaw this refrozen meltwater amounts to 17.0 MJ m^{-2}, relative to a total positive net energy of 27.4 MJ m^{-2} that was available for melt over that period. An additional 8.2 MJ m^{-2} of the available net energy was consumed to warm up the snowpack to the melting point, leaving only 2.2 MJ m^{-2} available for "new" surface melt.

Internal snowpack refreezing releases latent heat, so this energy is available and contributes to the net snowpack energy (adding to the surface energy flux in Equation 5). Some of this serves to warm the snowpack, and some of it is dissipated to the atmosphere through conductive heat fluxes to the surface and subsequent radiative and convective cooling. When this occurs at night, under conditions of negative net energy, this energy is essentially lost to the system. The latent energy added to the near-surface snowpack during refreezing often keeps the snow close to or at the melting point, which indirectly adds to the melting the subsequent day.

The numbers from May 16 to 23 are not representative of the entire summer. At this time, the average air and surface snow temperatures were 1.7 and -2.6°C, respectively, conducive to refreezing. The corresponding numbers over the full study period, May 13–Sept 21, were 4.6 and −0.8°C, and the subsurface snowpack was isothermal for most of the summer. The total energy committed to thawing refrozen meltwater over the full period was 99 MJ m^{-2}, 9% of the total available positive energy of 1141 MJ m^{-2}. For the full melt season, the modeled runoff of 2880 mm w.e. corresponds to a latent energy of 965 MJ m^{-2}, or 85% of available positive energy. The remaining 15% of available energy was used to warm the snowpack and thaw "recycled" meltwater. This enthalpy sink is a potentially important effect during cool summers and in colder environments.

Recommendations for Application of TDR in Glacier Hydrology

Conventional TDR probes are able to measure snow water content at the levels seen in the supraglacial snowpack (a few %). As these are easily deployed in combination with a data logger, continuous monitoring is possible, providing insight into diurnal and seasonal cycles of meltwater storage and drainage in the snowpack. Deployment in vertical networks, similar to what is conventionally done in thermistor arrays, allows water fluxes to be estimated, including both vertical drainage and local "source/sink" effects associated with internal refreezing.

To our knowledge, this is the first application of TDR to track meltwater percolation and drainage in the supraglacial snowpack. Continuous measurements have been made in seasonal snowpacks using upward-looking radar (e.g., Heilig et al., 2009, 2015; Mitterer et al., 2011b; Schmid et al., 2014) and impedance cables (Mitterer et al., 2011a), and numerous studies have used point-sampling methods to infer dielectric permittivity, such as Denoth meters or snow forks (e.g., Pfeffer and Humphrey, 1998; Techel and Pielmeier, 2011). TDR offers the possibility to record continuously at multiple levels in the

snowpack, but TDR has not been thoroughly explored in snow or glacier hydrology. Schneebeli et al. (1998) note the potential of TDR probes for quantification of snow liquid water content, but the difficulty in calibrating against known water content in the field. This is a challenge, given the sensitivity and uncertainty in the mixing models, but there is a high sensitivity to temporal and spatial variations in snow water content, which should be possible to exploit.

This method holds promise for further study in different glacial environments, but several improvements are possible from our exploratory work at Haig Glacier. Melt-out of the sensors makes it difficult to get continuous data on temperate glaciers, but this will be less of a problem in colder environments, such as polar regions. For work on temperate glaciers, with high summer melt rates, we recommend additional sensors that go deeper into the snowpack, to permit a longer study window for each deployment. The Campbell Scientific setup permits 8 TDR probes per multiplexer, so 8 or 16 probes could be installed at a site. A spacing of 20 cm would be reasonable, to track the meltwater to a depth up of to 3 m. It would be insightful to excavate into the underlying firn, to instrument across the snow-firn transition.

We also suggest that a second pit be instrumented proximal to the first, e.g., 10 m away, to provide a replicate under similar snowpack and meteorological conditions. Horizontal snowpack and hydrological variability are known to be high in polar environments (e.g., Rennermalm et al., 2013), and are also documented in temperate alpine snowpacks (e.g., Techel and Pielmeier, 2011; Heilig et al., 2015). The supraglacial snow at our site is homogeneous in density and grain size in the summer months, with no evidence of preferential flow paths, but it is not clear how representative a single point is with respect to water content and wetting front propagation. Detailed spatial studies such as those of Techel and Pielmeier (2011) would be insightful, and might reveal a seasonal evolution of the spatial structure.

We also recommend a comparison of TDR-derived dielectric permittivity with inferences from high-frequency radar, particularly with upward-looking radar studies (Mitterer et al., 2011b; Schmid et al., 2014; Heilig et al., 2015). The two techniques appear complementary for tracking the wetting front propagation in space and time. This may also help to elucidate the most appropriate mixing model to convert dielectric permittivity to snow water content, which is something that remains unclear. The Looyenga (1965) mixing model is based on the geometry of spherically-packed water inclusions, and the expected bulk dielectric properties vary strongly with the shape of inclusions (Sihvola et al., 1985). The TDR field setup is intrinsically two-dimensional, with axially symmetric (i.e., cylindrical) electromagnetic fields operating over a vertical cross-section of the snow. For spherical water droplets of radius r in cross-section, the response can be expected to vary as $1/r^2$ rather than $1/r^3$, which may explain why we find better results with the mixing model of Birchak et al. (1974). The Birchak model can also be thought of as a volumetric average of the complex index of refraction, which relates to the wave speed (proportional to $\varepsilon_s{}^{-1/2}$), so this approach seems logical. Nonetheless, the Looyenga mixing model is commonly applied in firn hydrology (e.g., Christianson et al., 2015), and has been recommended over the Birchak model on theoretical grounds (Sihvola et al., 1985) and in previous snow research (Niang et al., 2006). Results are very sensitive to the choice of mixing model, so further study is needed here.

CONCLUSIONS

We demonstrate that data-logging TDR instrumentation is able to monitor the temporal evolution of water content in a supraglacial snowpack. This has the potential to be a valuable tool to contribute to the growing interest in understanding and quantifying meltwater retention in glaciers and ice sheets. Vertical TDR arrays provide information about percolation velocities in snow, hydraulic conductivity, and internal refreezing. They can be deployed at multiple verticals, together with thermistor arrays, in a way that mimics numerical models of snow thermal and hydrological evolution (e.g., with 10 or 20-cm layers), providing direct data on snow temperature, water content, and water balance for model calibration and evaluation.

The diurnal cycle, water content, and drainage rates in our data affirm the ability of TDR measurements to capture small amounts of liquid water in snow, but more work is needed with *in situ* snow or firn sampled to find the best mixing model to convert measured dielectric permittivity to snow water content. Based on our estimates of overnight liquid water content in frozen and well-drained snowpacks, we estimate an uncertainty of about 2% in our estimates of water content, with a positive bias at low values of θ_w. This is based on the Birchak et al. (1974) mixing model; the Looyenga (1965) mixing model overestimates θ_w by ∼4% in our data, and may not be well-suited to unsaturated snow.

Bearing these caveats on the mixing model in mind, we record liquid water contents from 0 to 12% in the supraglacial snowpack over the course of the summer, increasing from typical values of ∼4% in the early melt season to ∼10% in July and August. Meltwater refreezing in May occurred to a depth of about 35 cm, but we see no evidence of internal refreezing from June to August. The snowpack remained isothermal, but a thin refrozen surface crust developed on most nights. Liquid water retained in the pore spaces through capillary pressure may have refrozen over night near the snow surface, with the associated latent heat release keeping the snow at 0°C.

There are strong diurnal cycles in snow liquid water content throughout the summer, which we attribute to refreezing in May and efficient overnight drainage for the rest of the melt season. There is negligible meltwater storage on daily timescales; after initial wetting of the snowpack, all meltwater drains to depth. Drainage lags of 3–4 h are evident in the May snowpack over the upper 50 cm, decreasing to ∼1 h in July. The effective hydraulic conductivity for the meltwater percolation is of order 10^{-6} m s^{-1}.

The measurements over five different periods in summer 2015 inform a model of subsurface temperature evolution and meltwater drainage for the full summer. This provides initial estimates of meltwater retention and the importance of internal refreezing for this temperate alpine glacier. We conclude that

meltwater retention in the seasonal snow is a negligible process when it comes to the glacier mass balance—no meltwater is retained in the supraglacial system. However, refreezing dose have a significant impact on meltwater runoff and summer mass balance by creating an effective "energy sink"; meltwater that refreezes overnight needs to thaw, such that energy is consumed to melt the same snow/ice more than once. We estimate that 85% of available melt energy was used to generate meltwater runoff (i.e., an efficiency of 85%). The remaining 15% is diverted to warming the snow/ice and thawing the refrozen meltwater. Re-melting accounts for about 9% of the positive net energy and snowpack warming consumes 6%. Models that neglect these processes will overestimate glacier runoff.

Future work is needed on several fronts. Spatial variability, deeper vertical structure, and firn layers need to be examined on mountain glaciers. The same processes need to be examined for colder alpine environments and in cold snow and firn in polar ice masses. The methods that we introduce should work well in these settings, but the importance of refreezing for glacier mass and energy balance can be expected to be much more significant.

AUTHOR CONTRIBUTIONS

All authors listed, have made substantial, direct and intellectual contribution to the work, and approved it for publication.

ACKNOWLEDGMENTS

The Haig Glacier study is supported by the Natural Sciences and Engineering Research Council (NSERC) of Canada. This manuscript is a contribution to the NSERC-funded Changing Cold Regions Network. We thank Rick Smith of the University of Calgary Weather Research Station for technical support. Mick Lack and Mike Norton of WinSport Canada kindly assist in our access to the Haig Glacier research site. We thank two reviewers for their insightful comments, which greatly improved this paper.

REFERENCES

Birchak, J. R., Gardner, C. G., Hipp, J. E., and Victor, J. M. (1974). High dielectric constant microwave probes for sensing soil moisture. *Proc. IEEE* 62, 93–98. doi: 10.1109/PROC.1974.9388

Christianson, K., Kohler, J., Alley, R. B., Nuth, C., and Pelt, W. J. (2015). Dynamic perennial firn aquifer on an Arctic glacier. *Geophys. Res. Lett.* 42, 1418–1426. doi: 10.1002/2014GL062806

Colbeck, S. C. (1974). The capillary effects on water percolation in homogeneous snow. *J. Glaciol.* 13, 85–97.

Colbeck, S. C., and Anderson, E. (1982). The permeability of a melting snow cover. *Water Resour. Res.* 18, 904–908. doi: 10.1029/WR018i004p00904

Coléou, C., and Lesaffre, B. (1998). Irreducible water saturation in snow: experimental results in a cold laboratory. *Ann. Glaciol.* 26, 64–68.

Cuffey, K. M., and Paterson, W. S. B. (2010). *The Physics of Glaciers, 4th Edn.* Burlington, ON: Butterworth-Heinemann/Elsevier.

Denoth, A. (1994). An electronic device for long-term snow wetness recording. *Ann. Glaciol.* 19, 104–106.

Ebrahimi, S., and Marshall, S. J. (2016). Surface energy balance sensitivity to meteorological variability on Haig Glacier, Canadian Rocky Mountains. *Cryosphere* 10, 2799–2819. doi: 10.5194/tc-10-2799-2016

Fountain, A. G. (1996). Effect of snow and firn hydrology on the physical and chemical characteristics of glacial runoff. *Hydrol. Process.* 10, 509–521. doi: 10.1002/(SICI)1099-1085(199604)10:4<509::AID-HYP389>3.0.CO;2-3

Fountain, A. G., and Tangborn, W. V. (1985). The effect of glaciers on streamflow variations. *Water Resour. Res.* 21, 579–586. doi: 10.1029/WR021i004p00579

Fountain, A. G., and Walder, J. S. (1998). Water flow through temperate glaciers. *Rev. Geophys.* 36, 299–328. doi: 10.1029/97RG03579

Heilig, A., Mitterer, C., Schmid, L., Wever, N., Schweizer, J., Marshall, H.-P., et al. (2015). Seasonal and diurnal cycles of liquid water in snow—Measurements and modeling. *J. Geophys. Res. Earth Surf.* 120, 2139–2154. doi: 10.1002/2015jf003593

Heilig, A., Schneebeli, M., and Eisen, O. (2009). Upward-looking ground-penetrating radar for monitoring snowpack stratigraphy. *Cold Reg. Sci. Technol.* 59, 152–162. doi: 10.1016/j.coldregions.2009.07.008

Hirashima, H., Yamaguchi, S., Sato, A., and Lehning, M. (2010). Numerical modelling of liquid water movement through layered snow based on new measurements of the water retention curve. *Cold Reg. Sci. Technol.* 64, 94–103. doi: 10.1016/j.coldregions.2010.09.003

Huss, M. (2011). Present and future contribution of glacier storage change to runoff from macroscale drainage basins in Europe. *Water Resour. Res.* 47:W07511. doi: 10.1029/2010WR010299

Jansson, P., Hock, R., and Schneider, T. (2003). The concept of glacier storage: a review. *J. Hydrol.* 282, 116–129. doi: 10.1016/S0022-1694(03)00258-0

Jones, S. B., Wraith, J. M., and Or, D. (2002). Time Domain Reflectometry (TDR) measurement principles and applications. *Hydrol. Process.* 16, 141–153. doi: 10.1002/hyp.513

Jost, G., Moore, R. D., Menounos, B., and Wheate, R. (2012). Quantifying the contribution of glacier runoff to streamflow in the upper Columbia River Basin, Canada. *Hydrol. Earth Syst. Sci.* 16, 849–860. doi: 10.5194/hess-16-849-2012

Kawashima, K., Yamada, T., and Wakahama, G. (1993). Investigations of internal structure and transformational processes from firn to ice in a perennial snow patch. *Ann. Glaciol.* 18, 117–122.

Koenig, L. S., Miège, C., Forster, R. R., and Brucker, L. (2014). Initial *in situ* measurements of perennial meltwater storage in the Greenland firn aquifer. *Geophys. Res. Lett.* 41, 81–85. doi: 10.1002/2013GL058083

Ledieu, J., De Ridder, P., De Clerck, P., and Dautrebande, S. (1986). A method of measuring soil moisture by time-domain reflectometry. *J. Hydrol.* 88, 319–328. doi: 10.1016/0022-1694(86)90097-1

Looyenga, H. (1965). Dielectric constants of heterogeneous mixtures. *Physica* 31, 401–406. doi: 10.1016/0031-8914(65)90045-5

Macheret, Y., Moskalevsky, M. Y., and Vasilenko, E. V. (1993). Velocity of radio waves in glaciers as an indicator of their hydrothermal state, structure and regime. *J. Glaciol.* 39, 373–384.

Mark, B. G., Baraer, M., Fernandez, A., Immerzeel, W., Moore, R. D., and Weingartner, R. (2015). "Glaciers as water resources," in *The High Mountain Cryosphere,* eds C. Huggel et al. (Cambridge: Cambridge University Press), 184–203.

Marshall, S. J. (2014). Meltwater run-off from Haig Glacier, Canadian Rocky Mountains, 2002–2013. *Hydrol. Earth Syst. Sci.* 18, 5181–5200. doi: 10.5194/hess-18-5181-2014

Marshall, S. J., White, E. C., Demuth, M. N., Bolch, T., Wheate, R., Menounos, B., et al. (2011). Glacier water resources on the eastern slopes of the Canadian Rocky Mountains. *Can. Water Resour. J.* 36, 109–134. doi: 10.4296/cwrj3602823

Mitterer, C., Heilig, A., Schweizer, J., and Eisen, O. (2011b). Upward-looking ground-penetrating radar for measuring wet-snow properties. *Cold Reg. Sci. Technol.* 69, 129–138. doi: 10.1016/j.coldregions.2011.06.003

Mitterer, C., Hirashima, H., and Schweizer, J. (2011a). Wet-snow instabilities: comparison of measured and modelled liquid water content and snow stratigraphy. *Ann. Glaciol.* 52, 201–208. doi: 10.3189/172756411797252077

Östling, M., and Hooke R. L. (1986). Water storage in Storglaciären, Kebnekaise, Sweden. *Geogr. Ann. Ser. A Phys. Geogr.* 68, 279–290. doi: 10.2307/521521

Moore, R. D., Fleming, S. W., Menounos, B., Wheate, R., Fountain, A., Stahl, K., et al. (2009). Glacier change in western North America: influences on

hydrology, geomorphic hazards and water quality. *Hydrol. Process.* 23, 42–61. doi: 10.1002/hyp.7162

Murray, T., Stuart, G. W., Fry, M., Gamble, N. H., and Crabtree, M. D. (2000). Englacial water distribution in a temperate glacier from surface and borehole radar velocity analysis. *J. Glaciol.* 46, 389–398. doi: 10.3189/172756500781833188

Niang, M., Bernier, M., Stacheder, M., Brandelik, A., and Van Bochove, E. (2006). Influence of snow temperature interpolation algorithm and dielectric mixing-model coefficient on density and liquid water content determination in a cold seasonal snow pack. *Subsurf. Sensing Technol. Appl.* 7, 1–22. doi: 10.1007/s11220-006-0020-9

Pfeffer, W. T., and Humphrey, N. F. (1998). Formation of ice layers by infiltration and refreezing of meltwater. *Ann. Glaciol.* 26, 83–91.

Pfeffer, W. T., Meier, M. F., and Illangasekare T. H. (1991). Retention of Greenland runoff by refreezing: implications for projected future sea level change. *J. Geophys. Res.* 96, 22117–22124. doi: 10.1029/91JC02502

Reijmer, C. H., van den Broeke, M. R., Fettweis, X., Ettema, J., and Stap, L. B. (2012). Refreezing on the Greenland ice sheet: a comparison of parameterizations. *Cryosphere* 6, 743–762. doi: 10.5194/tc-6-743-2012

Rennermalm, A. K., Moustafa, S. E., Mioduszewski, J., Chu, V. W., Forster, R. R., Hagedorn, B. et al. (2013). Understanding Greenland ice sheet hydrology using an integrated multi-scale approach. *Environ. Res. Lett.* 8:015017. doi: 10.1088/1748-9326/8/1/015017

Schmid, L., Heilig, A., Mitterer, C., Schweizer, J., Maurer, H., Okorn, R., et al. (2014). Continuous snowpack monitoring using upward-looking ground-penetrating radar technology. *J. Glaciol.* 60, 509–525. doi: 10.3189/2014JoG13J084

Schneebeli, M., Coléou, C., Touvier, F., and Lesaffre, B. (1998). Measurement of density and wetness in snow using time-domain reflectometry. *Ann. Glaciol.* 26, 69–72.

Schneider, T. (2000). Hydrological processes in the wet-snow zone of glacier: a review. *Z. Gletscherkd. Glazialgeol.* 36, 89–105.

Schneider, T., and Jansson, P. (2004). Internal accumulation in firn and its significance for the mass balance of Storglaciären, Sweden. *J. Glaciol.* 50, 25–34. doi: 10.3189/172756504781830277

Shea, J. M., Anslow, F. S., and Marshall, S. J. (2005). Hydrometeorological relationships on Haig Glacier, Alberta, Canada. *Ann. Glaciol.* 40, 52–60. doi: 10.3189/172756405781813465

Sihvola, A., Nyfors, E., and Tiuri, M. (1985). Mixing formula and experimental results for the dielectric constant of snow. *J. Glaciol.* 31, 163–170.

Soruco, A., Vincent, C., Rabatel, A., Francou, B., Thibert, E., Sicart, J. E., et al. (2015). Contribution of glacier runoff to water resources of La Paz city, Bolivia (16 S). *Ann. Glaciol.* 56, 147–154. doi: 10.3189/2015AoG70A001

Stein, J., Laberge, G., and Lévesque, D. (1997). Monitoring the dry density and the liquid water content of snow using time domain reflectometry (TDR). *Cold Reg. Sci. Technol.* 25, 123–136. doi: 10.1016/S0165-232X(96)00022-5

Techel, F., and Pielmeier, C. (2011). Point observations of liquid water content in wet snow –investigating methodical, spatial and temporal aspects. *Cryosphere* 5, 405–418. doi: 10.5194/tc-5-405-2011

Tiuri, M., Sihvola, A., Nyfors, E., and Hallikaiken, M. (1984). The complex dielectric constant of snow at microwave frequencies. *IEEE J. Oceanic Eng.* 9, 377–382. doi: 10.1109/JOE.1984.1145645

Topp, G. C., and Davis, J. L. (1985). Measurement of soil water content using time-domain reflectometry (TDR): a field evaluation. *Soil Sci. Soc. Am. J.* 49, 19–24. doi: 10.2136/sssaj1985.03615995004900010003x

Topp, G. C., Davis, J. L., and Annan, A. P. (1980). Electromagnetic determination of soil water content: measurements in coaxial transmission lines. *Water Resour. Res.* 16, 574–582. doi: 10.1029/WR016i003p00574

Van Pelt, W. J. J., Oerlemans, J., Reijmer, C. H., Pohjola, V. A., Pettersson, R., and van Angelen, J. H. (2012). Simulating melt, runoff and refreezing on Nordenskiöldbreen, Svalbard, using a coupled snow and energy balance model. *Cryosphere* 6, 641–659. doi: 10.5194/tc-6-641-2012

Van Pelt, W. J. J., Pettersson, R., Pohjola, V. A., Marchenko, S., Claremar, B., and Oerlemans, J. (2014). Inverse estimation of snow accumulation along a radar transect on Nordenskiöldbreen, Svalbard. *J. Geophys. Res. Earth Surf.* 119, 816–835. doi: 10.1002/2013JF003040

Wever, N., Schmid, L., Heilig, A., Eisen, O., Fierz, C., and Lehning, M. (2015). Verification of the multi-layer SNOWPACK model with different water transport schemes. *Cryosphere* 9, 2271–2293. doi: 10.5194/tc-9-2271-2015

Willis, I. C., Arnold, N. S., and Brock, B. W. (2002). Effect of snowpack removal on energy balance, melt and runoff in a small supraglacial catchment. *Hydrol. Process.* 16, 2721–2749. doi: 10.1002/hyp.1067

Conflict of Interest Statement: The authors declare that the research was conducted in the absence of any commercial or financial relationships that could be construed as a potential conflict of interest.

frontiers in Earth Science

ORIGINAL RESEARCH
published: 03 March 2017
doi: 10.3389/feart.2017.00020

Inferring Firn Permeability from Pneumatic Testing: A Case Study on the Greenland Ice Sheet

Aleah N. Sommers[1], Harihar Rajaram[1], Eliezer P. Weber[2], Michael J. MacFerrin[3], William T. Colgan[4] and C. Max Stevens[5]*

[1] Department of Civil, Environmental, and Architectural Engineering, University of Colorado at Boulder, Boulder, CO, USA, [2] Apex Companies, LLC, Boulder, CO, USA, [3] Cooperative Institute for Research in Environmental Science, University of Colorado at Boulder, Boulder, CO, USA, [4] Department of Earth and Space Science and Engineering, York University, Toronto, ON, Canada, [5] Department of Earth and Space Sciences, University of Washington, Seattle, WA, USA

Across the accumulation zone of the Greenland ice sheet, summer temperatures can be sufficiently warm to cause widespread melting, as was the case in July 2012 when the entire ice sheet experienced a brief episode of enhanced surface ablation. The resulting meltwater percolates into the firn and refreezes, to create ice lenses, and layers within the firn column. This is an important process to consider when estimating the surface mass balance of the ice sheet. The rate of meltwater percolation depends on the permeability of the firn, a property that is not well constrained in the presence of refrozen ice layers and lenses. We present a novel, inexpensive method for measuring *in-situ* firn permeability using pneumatic testing, a well-established technique used in environmental engineering and hydrology. To illustrate the capabilities of this method, we estimate both horizontal and vertical permeability from pilot tests at six sites on the Greenland ice sheet: KAN-U, DYE-2, EKT, NASA-SE, Saddle, and EastGRIP. These sites cover a range of conditions from mostly dry firn (EastGRIP), to firn with several ice layers and lenses from refrozen meltwater (Saddle, NASA-SE, EKT), to firn with extensive ice layers (DYE-2 and KAN-U). The estimated permeability in firn without refrozen ice layers at EastGRIP agrees well with the range previously reported using an air permeameter to measure permeability through firn core samples at Summit, Greenland. At sites with ice lenses or layers, we find high degrees of anisotropy, with vertical permeability much lower than horizontal permeability. Pneumatic testing is a promising and low-cost technique for measuring firn permeability, particularly as meltwater production increases in the accumulation zone and ice layers and lenses from refrozen melt layers become more prevalent. In these initial proof-of-concept tests, the estimated permeabilities represent effective permeability at the meter scale. With appropriately higher vacuum pressures and more detailed monitoring, effective permeabilities over a larger scale may be quantified reliably, and multiple measurements during a season and across multiple years could improve understanding of the evolving firn structure and permeability. The technique is also suitable for broad application in Antarctica and other glaciers and ice caps.

Keywords: permeability, firn, snow, Greenland, pneumatic testing, ice lenses, anisotropy

OPEN ACCESS

Edited by:
Alun Hubbard,
Aberystwyth University, UK

Reviewed by:
Nander Wever,
École Polytechnique Fédérale de Lausanne (EPFL), Switzerland
Stefan Ligtenberg,
Utrecht University, Netherlands

****Correspondence:***
Aleah N. Sommers
aleah.sommers@colorado.edu

Specialty section:
This article was submitted to Cryospheric Sciences, a section of the journal Frontiers in Earth Science

Received: *01 September 2016*
Accepted: *16 February 2017*
Published: *03 March 2017*

Citation:
Sommers AN, Rajaram H, Weber EP, MacFerrin MJ, Colgan WT and Stevens CM (2017) Inferring Firn Permeability from Pneumatic Testing: A Case Study on the Greenland Ice Sheet. Front. Earth Sci. 5:20. doi: 10.3389/feart.2017.00020

INTRODUCTION

The Greenland Ice Sheet has been losing mass at an accelerated rate in recent years and is a significant contributor to sea level rise (e.g., Krabill et al., 2004; Velicogna and Wahr, 2006; Rignot et al., 2011; Fettweis et al., 2013). Accurate modeling of the surface mass balance of the ice sheet is essential for predicting its contribution to sea level rise over the next century. Percolation and refreezing of meltwater in firn occurs across much of the ice sheet accumulation area and influences runoff, which is a significant component of the surface mass balance. Accurately modeling percolation and refreezing requires an estimate of firn permeability (e.g., Colbeck, 1975; Ambach et al., 1981; Marsh and Woo, 1985).

Permeability (units of length^2) is an intrinsic property of a porous medium that characterizes the connectivity of pore spaces and describes the ability of a fluid (such as air or water) to flow through the material. The hydraulic conductivity (units of length time^{-1}) of a porous medium for flow of water is, in fact, related to the intrinsic permeability as follows (Bear, 1972):

$$K = k\frac{\rho g}{\mu} \tag{1}$$

Where K is the hydraulic conductivity, k is the intrinsic permeability of the material, ρ is bulk density of water, g is acceleration due to gravity, and μ is the dynamic viscosity of water. More generally, Equation (1) also provides a relationship for the conductivity to any fluid, including air. In firn, meltwater percolation can change the material structure through melting and refreezing, along with grain metamorphic processes. Firn permeability, then, is a material property that evolves with time, and a measurement of air permeability in firn from a short-duration pneumatic test reflects a snapshot in time of intrinsic permeability of the current material structure (which is useful and necessary for modeling meltwater percolation).

In heterogeneous media, the large-scale effective permeability typically exhibits anisotropy, i.e., direction-dependent permeability that requires a tensorial representation (e.g., Bear, 1972; Colbeck, 1975; Albert et al., 1996; Calonne et al., 2012). Firn is an anisotropic porous medium, particularly due to the presence of solid refrozen ice layers, ice lenses, or distinct wind crust layers (ice layers defined as being continuous on a snow pit scale, ice lenses as discontinuous; Fierz et al., 2009).

Although hydraulic conductivity (K) is most directly relevant to meltwater infiltration and transport models, it can be inferred from intrinsic permeability (k) measurements according to Equation (1). It is common to measure k using air as a fluid. Previous field studies have employed various techniques to measure the air permeability of seasonal snow, as well as firn samples collected in polar regions. Early permeability measurements using progressive compression were conducted by Bader (1939) and Bender (1957). Shimizu (1970) developed a dual-cylinder air permeameter to characterize permeability of snow in Hokkaido, Japan. Sommerfeld and Rocchio (1993) used a permeameter with a conditioning column to measure permeability of seasonal snow in Wyoming, USA. A similar design to the dual-cylinder permeameter of Shimizu (1970) was adopted to measure permeability of snow and firn at different depths at Summit, Greenland (Albert et al., 1996; Albert and Shultz, 2002; Luciano and Albert, 2002; Adolph and Albert, 2014) and in Antarctica (Courville et al., 2007, 2010; Hörhold et al., 2009). Recent studies have included other approaches as well: Courville et al. (2010) compared measured permeability with permeability estimated from microtomography and Lattice-Boltzmann modeling, and Calonne et al. (2012) used three-dimensional images of snow microstructure to estimate the full permeability tensor at the core scale for numerous samples of seasonal snow and Antarctic firn. These studies all measured or estimated permeability of extracted core samples, which would not necessarily accurately represent the field-scale effective permeability in the presence of ice layers and lenses of varying horizontal extent.

Given the implications of increased meltwater percolation in Greenland's firn and to account for ice lenses of varying horizontal extent, it is important to consider *in-situ* field permeability measurements rather than measurements from isolated core samples, and whether these measurements can resolve anisotropy directly. Most of the aforementioned studies involving Greenland firn considered only vertical permeability, with the exceptions of Albert et al. (1996), in which striking differences between horizontal and vertical permeability were observed in samples from the top 1 m of snow at Summit, and Luciano and Albert (2002), who measured both horizontal and vertical permeability in selected sections of a 13 m core at Summit, with distinct directional differences throughout the depth. Since Summit rarely experiences melt (i.e., refrozen ice lenses do not occur), these studies provide excellent reference datasets for permeability measurements of dry Greenland firn without the influence of refrozen ice lenses. In Vermont, USA, Albert and Perron (2000) found that vertical permeability across ice layers and surface crust was significantly lower than in the rest of the snowpack, and we expect that refrozen ice lenses in Greenland firn would exhibit similar properties.

As meltwater production on the Greenland Ice Sheet increases with warming air temperatures, new ice lenses will likely form at higher elevations, affecting the large-scale effective permeability of Greenland firn. This directly affects its percolation and retention capacity, and accordingly its sea level rise buffering capacity (Pfeffer et al., 1991; Harper et al., 2012). An open question associated with climate change is: *How will firn permeability, meltwater percolation, and refreezing rates change with increased meltwater production and more, or thicker, ice lenses, and layers?* Extending that line of thought, *how much meltwater can be retained in the firn as opposed to draining from the ice sheet?* Recent observations have shown that at locations experiencing increased melt, ice lenses can build up to form sufficiently thick layers that become impermeable to further meltwater percolation, yielding surface runoff in areas that could previously absorb the summer meltwater by means of vertical percolation (Charalampidis et al., 2016; Machguth et al., 2016; Mikkelsen et al., 2016). To better infer the consequences of these changes, cost-effective approaches to measuring *in-situ* field permeability are needed. Multiple

measurements within a season and annually will also help to improve understanding of evolving permeability, and will help to constrain refreezing and the formation of ice lenses and layers.

Here we present a relatively simple and inexpensive method for measuring *in-situ* firn permeability using pneumatic testing. This technique is frequently used to characterize permeability of anisotropic soil, gravel, and rock formations in the design of soil vapor extraction systems for environmental remediation (Weinig, 1992). In April–May 2016, before the onset of the melt season, we conducted a field campaign to test the method at six sites on the Greenland Ice Sheet. The method is described below, followed by an explanation of how the tests were analyzed and permeability values inferred. The results presented here are primarily intended as proof of concept to demonstrate the utility of our method, while also highlighting the potential for more expansive application to explore the spatial and temporal distribution of poorly constrained firn permeability values used in surface mass balance models for Greenland, Antarctica, and other ice caps and alpine glaciers.

METHODS

Pneumatic Testing Method and Field Setup

Pneumatic testing is a well-established technique for characterizing the permeability of soil, gravel, and rock, in the context of designing soil vapor extraction systems for environmental remediation (e.g., Johnson et al., 1990; Weinig, 1992). The method involves drilling boreholes, applying suction with a vacuum at known depth below an airtight seal in one borehole, and monitoring the air pressure response below a seal at known depth in another borehole some distance from the applied vacuum. A similar procedure can be customized for application to snow and firn. A schematic of this setup is shown in **Figure 1**, and a photograph of the field setup is shown in **Figure 2**.

We conducted tests at six locations on the Greenland Ice Sheet, with varying prevalence of ice lenses and layers in the stratigraphy, at various vacuum and monitoring point depths down to approximately 4 m depth at each site. The monitoring borehole was drilled at a radial distance of 1 m from the vacuum hole. We drilled boreholes by hand using a Kovacs Mark II coring drill for the vacuum hole and a Kovacs ice auger for the monitoring hole. Inflatable rubber plugs (Cherne Muni-Ball models 262,010 and 262,064) were used to seal the holes at depth. The plugs were inflated through tubes connected to a bicycle pump at the surface. Airflow through the snow and firn was induced using a portable wet/dry vacuum (Ridgid model WD4522) powered by a generator (Honda model EU2000T1A1). The flow rate of air was measured using a thermal anemometer (Dwyer model 471B). Pressure responses were recorded using analog differential pressure gauges (Dwyer Series 2000 Magnehelic) as well as a digital pressure transducer (Dwyer Series 607-3) connected to a Campbell Scientific CR1000 datalogger.

Alternative Setup—Drilling into a Firn Pit Wall

A modified experimental orientation was also employed at DYE-2 in south Greenland. In this case, boreholes were drilled horizontally into a large firn pit wall. A schematic of the vacuum and monitoring borehole orientation is shown in **Figure 3**, and a photograph is shown in **Figure 4**. The vacuum was applied 1 m deep into the wall, in a layer of firn bounded above by a 5 cm-thick ice layer and below by a 20 cm-thick ice layer (horizontal extent of the ice layers into the wall is unknown). For these tests, pressure responses were measured in sealed monitoring boreholes drilled 1 m deep into the wall at three locations: 1 m away in the same layer of firn as the vacuum (Monitoring Borehole 1), 20 cm above the upper ice layer (Monitoring Borehole 2), and 20 cm below the thicker, lower ice layer (Monitoring Borehole 3).

Analytical Solution for Air Flow through Firn

Permeability can be inferred from pneumatic field tests by considering analytical solutions for steady-state air flow through a porous, anisotropic medium (e.g., Shan et al., 1992). We treat air flow through snow and firn as Darcian flow of an ideal gas with constant viscosity and composition, and we assume the system to be isothermal. For the pressure solution, it is convenient to define a transformed variable u related to pressure (Collins, 1961):

$$u = P_a^2 - P^2 \tag{2}$$

where P_a is the ambient atmospheric pressure, and P is pressure at a given point in the snow or firn. It can be shown that under steady flow conditions, u satisfies the Laplace equation (Bear, 1972):

$$\nabla \cdot (\boldsymbol{k} \nabla u) = 0 \tag{3}$$

where $\boldsymbol{k}$ is the air permeability tensor. The analytical solution for u during our pneumatic tests is obtained from the solution of the three-dimensional Laplace equation with the vacuum treated as a point sink in spherical coordinates. To account for the constant-pressure surface boundary open to the atmosphere, we use the method of images, a well-established technique for the solution of the Laplace equation for flow toward a source/sink in semi-infinite or finite domains (e.g., Jeans, 1908; Milne-Thomson, 1938; Bear, 1972). With the vacuum (a pressure "sink") applied at depth z_0, adding an "image source" at height z_0 above the surface forms a line of symmetry to ensure that $u = 0$ at the surface, where atmospheric pressure acts. Using a rescaled vertical coordinate to transform an anisotropic medium to an equivalent isotropic medium (Bear, 1972; Shan et al., 1992) yields:

$$u(r,z) = \frac{Q}{4\pi\sqrt{k_r k_z}} \left[\frac{1}{\sqrt{r^2 + \frac{k_r}{k_z}(z - z_0)^2}} - \frac{1}{\sqrt{r^2 + \frac{k_r}{k_z}(z + z_0)^2}} \right] \tag{4}$$

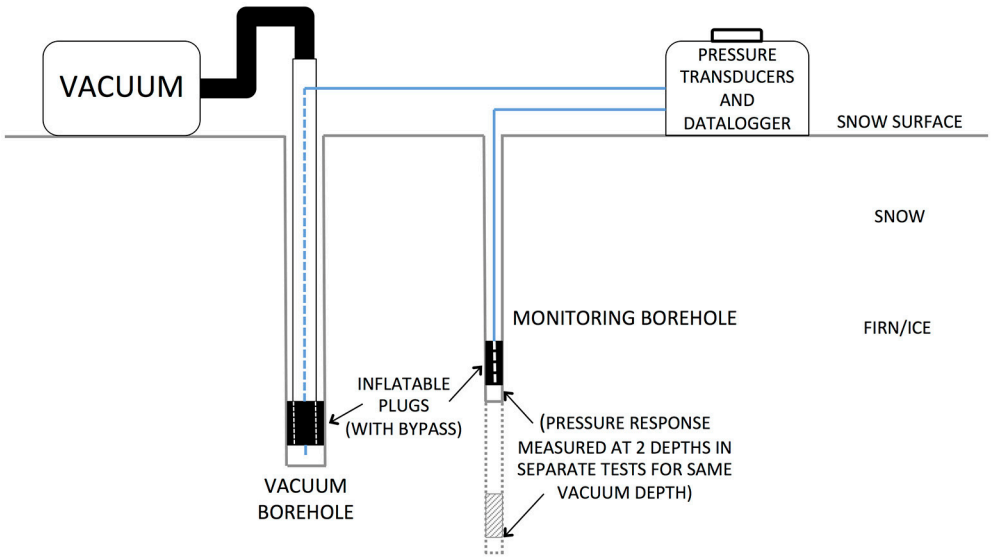

FIGURE 1 | Schematic of pneumatic testing field setup. Vacuum is applied at depth in one borehole below a seal and the resulting pressure response is measured below a seal in another borehole, through tubing connected to a pressure gauge on the surface. For each depth of applied vacuum, pressure responses at two monitoring depths are recorded in separate tests.

where r is radial distance from the vacuum hole, z is depth below the surface, Q is volumetric air flow rate, k_r is radial (horizontal) permeability, k_z is vertical permeability, and z_0 is the depth at which vacuum is applied. Note that this solution assumes a tensorial permeability that is constant (not spatially variable) within the domain, corresponding to an assumed constant heterogeneous firn pack for each test. In reality, firn structure may vary substantially across a depth range of a few meters; tests at multiple depths at each site capture the influence of these variations. **Figure 5** presents an example pressure response field and air flow streamlines based on this solution for one of our pneumatic tests. Using two monitoring points for each vacuum depth, horizontal, and vertical permeability values are inferred by fitting the analytical $u(r,z)$ field (Equation 4) to observed differential pressure responses by employing a least-squares optimization scheme (MATLAB nonlinear least-squares solver *lsqnonlin*). By dividing the equations for these two monitoring points, $u_1(r_1,z_1)/u_2(r_2,z_2)$, it is also possible to directly solve for the anisotropy ratio k_r/k_z. Comparing the value of k_r/k_z obtained directly with that inferred from optimization serves as a useful check of the reliability of optimization results.

The solution for u can be modified to incorporate an impermeable layer at some depth rather than treating the domain as semi-infinite below the surface; with multiple boundaries, the method of images becomes more complicated. In this case, we need to apply an image source to account for the constant-pressure surface boundary as before, and also apply an image sink below the impermeable boundary to effectively cancel out the flux at that boundary. But the image source above the surface then creates an unbalanced flux across the lower boundary, and the image sink below the impermeable boundary creates a pressure drop at the surface, violating the boundary conditions, requiring additional images sources/sinks. For each pair of images added, these imbalances persist; the solution by the method of images with two boundaries thus requires an infinite series of images (Bear, 1972; Shan et al., 1992). The resulting series solution is convergent because the later images in the series are increasingly farther away from the finite domain of interest. Designating the impermeable boundary at the depth of the first ice layer with thickness ~20 cm or greater (according to stratigraphy from cores drilled at each site), we found that this had no effect on the pressure solution in our test domain, suggesting that the shallowest extensive ice layer is too deep to influence the pressure response in the overlying firn and thinner refrozen melt layers. The solution for u can also be modified to treat the vacuum

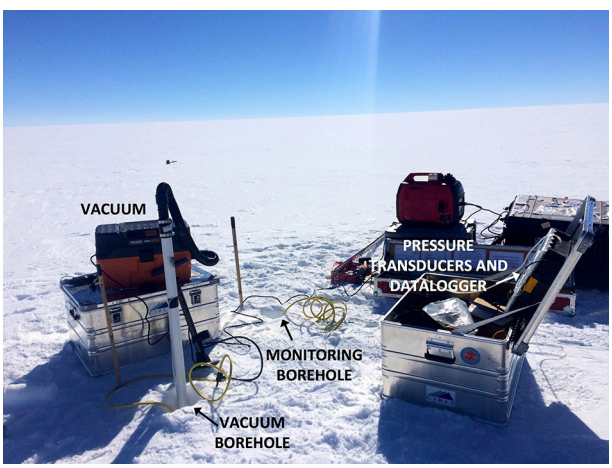

FIGURE 2 | Photograph of pneumatic testing field setup.

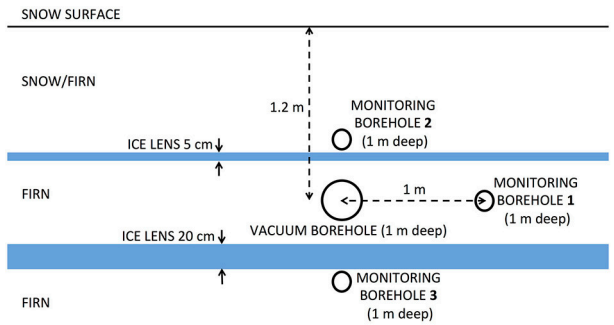

FIGURE 3 | Schematic of alternative pneumatic test setup, drilling boreholes horizontally into a firn pit wall at DYE-2. Vacuum was applied in a sealed borehole drilled 1 m horizontally into a layer of firn bounded above and below by ice layers as observed in the pit wall. Pressure response to the vacuum was measured in sealed boreholes at three locations: (1) in the same layer of firn, (2) above a 5 cm-thick ice layer, and (3) below a 20 cm-thick ice layer. The monitoring point located above the thinner (5 cm) ice layer from the vacuum exhibited a lower pressure response compared to the response in the same layer of firn as the vacuum, and the monitoring point across the thicker (20 cm) ice layer from the vacuum exhibited a negligible response.

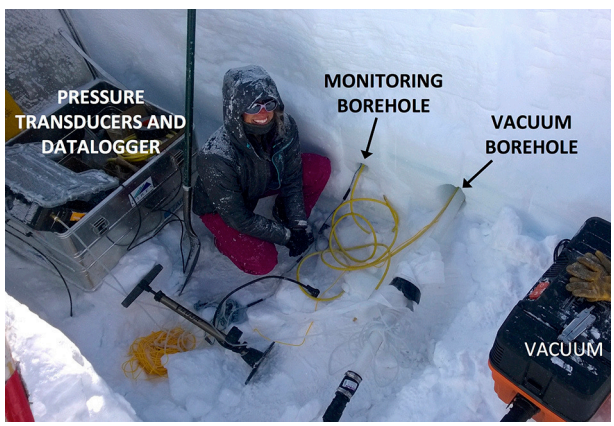

FIGURE 4 | Photograph of alternative pneumatic test setup, drilling boreholes horizontally into a firn pit wall at DYE-2.

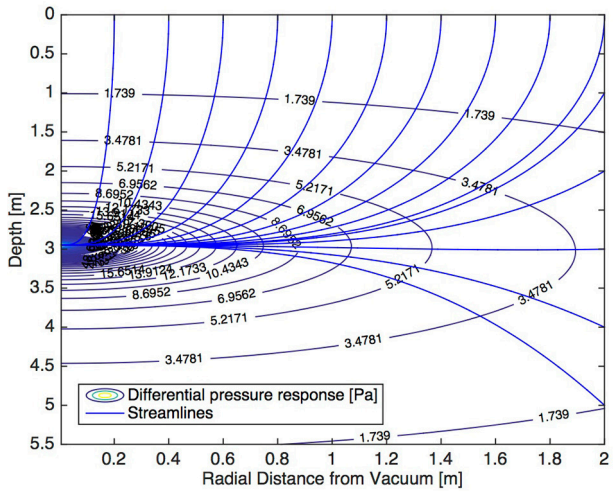

FIGURE 5 | Sample pressure field due to air flow induced by a vacuum in one of our pneumatic tests. In this example, the vacuum is applied at 3 m depth. Snow surface is at the top of the plot. Labeled contour lines show the differential pressure response. Blue lines indicate air flow streamlines.

as a line sink in the small section of open borehole below the plug, rather than as a point sink (Shan et al., 1992). The permeability values inferred using these modified analyses fell in the same range and exhibited the same anisotropy patterns as those obtained using the simpler solution (Equation 4) for a point-source in a semi-infinite domain.

RESULTS

Inferred Firn Permeability and Anisotropy at Six Sites on the Greenland Ice Sheet with Different Stratigraphy

We pilot tested this method for inferring firn permeability from pneumatic testing in April–May 2016 before the onset of melt at six sites on the Greenland Ice Sheet (**Figure 6**). Site characteristics and specific test dates are listed in **Table 1**. Five of the sites (KAN-U, DYE-2, EKT, NASA-SE, and Saddle) are situated in south Greenland, near the Arctic Circle. These sites experience melt in some or most years; ice layers and lenses were observed in the firn cores drilled at each location and in snow pits. Ice layers are particularly abundant at KAN-U, which experiences the most melt of these five sites, and also at DYE-2. The sixth site, EastGRIP, is located farther north than the other sites and very rarely experiences melt, rendering it a useful control site for permeability of dry firn in the absence of refrozen lenses.

Using the analytical solution for air flow and optimization methods for parameter estimation described in Section Analytical Solution for air Flow through Firn, horizontal and vertical permeability were inferred for each test conducted at the field sites. **Figure 7** presents the horizontal (k_r, dashed line) and vertical (k_z, solid line) permeability profiles for five sites, along with the depth of ice layers and lenses at each site (indicated by horizontal dark blue lines, as recorded from stratigraphy analysis of a firn core drilled near the pneumatic test site at each location). The horizontal extent of ice layers and lenses is not known. Permeability at KAN-U was investigated separately because of the thick ice layer at that site, and will be described below in Section Permeability in a Thick Ice Layer. The colored shading in **Figure 7** represents possible ranges of k_r and k_z due to uncertainty in flow rate measurement. The depth range associated with each permeability estimate (vertical extent of the lines) corresponds to the depths of the two monitoring points where pressure response was measured for a given applied vacuum depth. In most cases, horizontal permeability is greater than vertical permeability. For tests that span several ice layers or lenses, this anisotropy is more pronounced, which intuitively makes sense: it is more difficult for air to flow vertically through ice layers, or around ice lenses, than to flow horizontally through

TABLE 1 | Characteristics for sites on the Greenland ice sheet where permeability tests were conducted.

Site	KAN-U	Dye-2	EKT	Saddle	NASA-SE	EastGRIP	Summit
Latitude (deg)	67.000	66.473	66.985	65.999	66.480	75.627	72.580
Longitude (deg)	−47.023	−46.283	−44.394	−44.500	−42.500	−35.942	−38.505
Elevation (m)	1812	2092	2343	2457	2389	2675	3199
Mean annual temperature (deg C)	−16.7	−18.4	−21.0	−21.0	−20.7	−30.6	−30.2
Test Date (2016)	28 April	9 May	2 May	6 May	4 May	16 May	N/A

Characteristics for Summit are also shown for comparison. Mean annual temperature is the mean annual air temperature for 1979–2014 from MAR 3.5.2 (Fettweis et al., 2013) forced by ERA Interim.

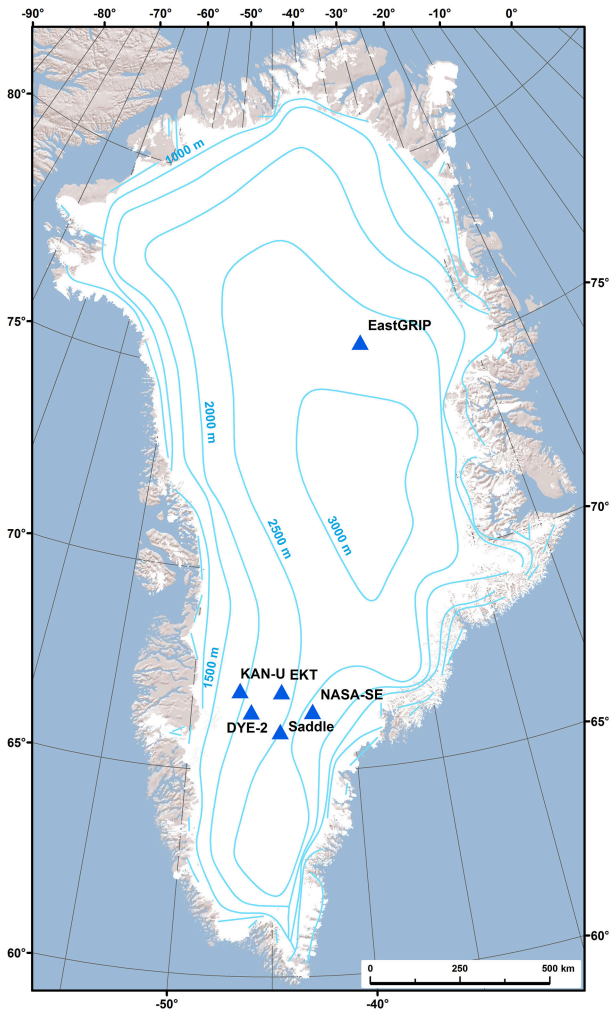

FIGURE 6 | Map of field sites on the Greenland Ice Sheet where pneumatic tests were conducted in spring 2016. Labeled contours indicate ice surface elevation.

the firn between layers. In some of the tests that span several ice layers or lenses (see the middle test at EKT, the middle and deepest tests at NASA-SE, the deepest test at Saddle, and the deepest test at DYE-2), the vertical permeability is very low ($<1 \times 10^{-10}$ m^2). In other tests that span ice layers or lenses, however, the vertical permeability is not quite so low (for example, the top test at DYE-2 and the top and middle tests at Saddle). This distinction may be related to the horizontal extent of individual ice lenses, which was not measured. In contrast to the high anisotropy of tests spanning several ice layers, horizontal and vertical permeability at EastGRIP are more similar in magnitude, with vertical permeability even being slightly higher than horizontal permeability in the deeper tests at that location. It is reasonable to find low anisotropy here, considering that EastGRIP has very few ice lenses; the deeper tests span dry firn without even thin refrozen ice lenses. In the absence of ice lenses, it is possible to have higher vertical permeability than horizontal permeability due to metamorphic processes at the grain scale (Luciano and Albert, 2002; Calonne et al., 2012).

In **Table 2**, we compare the anisotropy ratio k_r/k_z inferred from optimization with k_r/k_z from the direct solution of u_1/u_2 described in Section Analytical Solution for Air Flow through Firn. The results agree closely, with the exception of four tests that exhibit extremely high anisotropy across ice layers. For these tests that span several ice layers from which we infer very small k_z values from optimization (and correspondingly large anisotropy ratios), a direct solution for the anisotropy ratio k_r/k_z is not found due to its large magnitude (the equations for u_1 and u_2 each approach $1/\infty$, so u_1/u_2 becomes similar to dividing zero by zero). This implies that the inferred values for k_r and k_z from optimization are more uncertain in these cases, but the overall inference of very low vertical permeability and high anisotropy across ice layers remains valid.

Permeability in a Thick Ice Layer

Our lowest-elevation field site is KAN-U, which experiences the most melt each summer and, as a result, has the most prevalent refrozen ice layers. Firn cores drilled in spring 2016 at this site revealed a continuous solid ice layer from a depth of approximately 1.4–8 m. This configuration provides a unique field setup to illustrate the capabilities of our pneumatic test method for inferring permeability in the presence of thick sections of refrozen ice layers. At this site, differential pressure response was measured in a single borehole at the point of applied vacuum for incremental depths, from 0.2 m down to 2.0 m, shown in **Figure 8A**. An abrupt transition in the generated suction is apparent when the vacuum is applied in "solid" ice (below 1.4 m). The differential pressure measured at 1.8 m and 2.0 m is equal to that measured with the vacuum hose completely

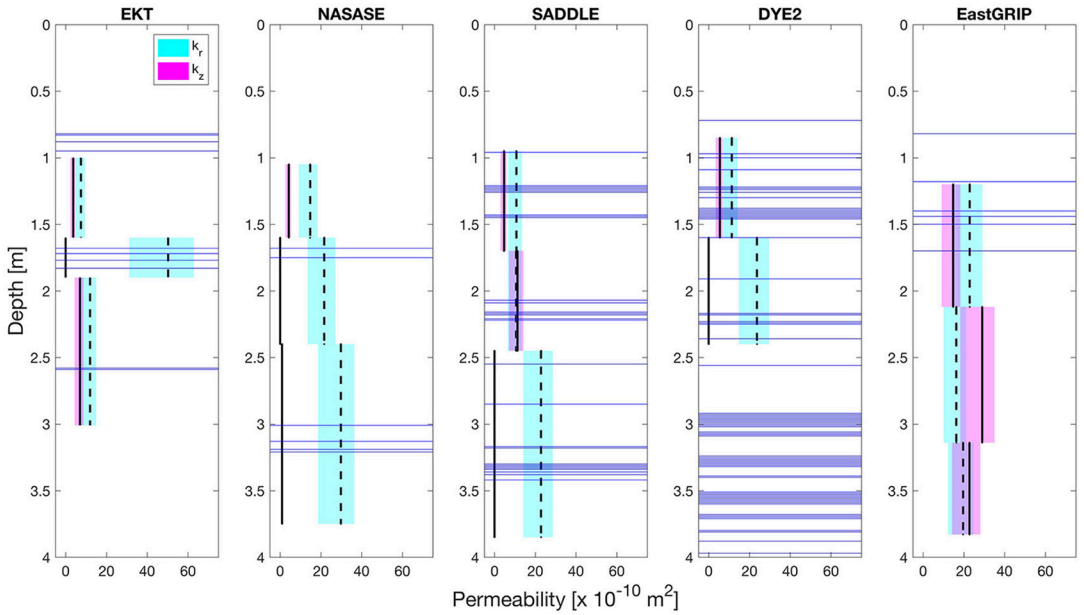

FIGURE 7 | Inferred horizontal (k_r) and vertical (k_z) firn permeability values at five sites on the Greenland Ice Sheet. The vertical depth range for each estimate corresponds to the depth between the two monitoring point depths where differential pressure was measured for each vacuum depth. Horizontal dark blue lines indicate the depths of ice layers and lenses observed in cores at each site. Cyan and magenta shading represents inferred permeability limits based on the range of airflow rates produced by the vacuum in the field. In some cases that span several ice layers, the inferred vertical permeability is very low ($k_z < 1 \times 10^{-10}$ m^2, essentially impermeable).

TABLE 2 | Anisotropy ratio (k_r/k_z) for each test inferred from optimization and by direct solution.

Test ID	Vacuum depth [m]	Monitoring depths [m]	k_r/k_z (optimization)	k_r/k_z (direct solution)
EKT 1	1.00	1.00, 1.60	2.0	2.0
EKT 2	2.10	1.60, 1.90	3.3×10^6	N/A
EKT 3	2.95	1.90, 3.01	1.7	1.7
NASA-SE 1	1.05	1.05, 1.60	3.5	3.4
NASA-SE 2	1.95	1.60, 2.40	620	N/A
NASA-SE 3	2.85	2.40, 3.75	31.1	31.9
SADDLE 1	1.00	0.95, 1.70	2.3	2.3
SADDLE 2	2.00	1.70, 2.45	0.9	0.9
SADDLE 3	3.10	2.45, 3.85	1.2×10^6	N/A
DYE-2 1	1.00	0.85, 1.60	2.1	2.0
DYE-2 2	2.05	1.60, 2.40	8.3×10^5	N/A
EastGRIP 1	0.90	1.20, 2.12	1.6	1.6
EastGRIP 2	2.01	2.12, 3.14	0.6	0.5
EastGRIP 3	2.90	3.14, 3.83	0.9	0.9

Test ID labels identify the site name and test number (numbered from shallowest to deepest). For the majority of the tests, k_r/k_z inferred by optimization agrees closely with k_r/k_z from the direct solution. Four tests that span several ice layers (EKT 2, NASA-SE 2, SADDLE 3, and DYE-2 2) exhibit extraordinarily high anisotropy, essentially implying negligible vertical permeability. For these cases, the direct solution for k_r/k_z breaks down numerically. This reflects a higher level of uncertainty for k_r and k_z inferred from optimization for these tests, but the general inference of high anisotropy and very low vertical permeability across the ice layers holds.

sealed, indicating that: (a) the thick refrozen ice layer is nearly impermeable, and (b) the inflatable plugs achieve a good seal against the borehole walls. Permeability values can be inferred from this test scenario using the analytical solution described in Section Analytical Solution for Air Flow through Firn. In this case, we consider the differential pressure measured just below the vacuum, and treat that pressure as uniform on a small sphere (with radius 5 cm) representing the open space in the vacuum below the borehole. For the two monitoring points needed for the analysis, we select two points on this sphere and employ the optimization methods for parameter estimation as described previously. **Figure 8B** presents horizontal and vertical permeability values inferred from the field tests at KAN-U. The results support what we might expect in this situation. In the top meter of snow and firn (with a few minor ice layers and lenses), horizontal permeability is greater than vertical permeability, but even the horizontal permeability is relatively low compared to our other sites ($<5 \times 10^{-10}$ m^2). Both horizontal and vertical permeability generally decrease further with depth, and both become very small ($<0.3 \times 10^{-10}$ m^2) in the thick ice below 1.5 m. This indicates that the meters-thick ice layer significantly decreases the permeability.

Pneumatic Tests into a Firn Pit Wall

We also conducted three additional tests at DYE-2 with the alternative test orientation involving boreholes drilled horizontally into a snow pit wall (shown in **Figures 3**, **4**). First, the pressure response was observed in a borehole sealed 1 m deep, located 1 m radially away from the vacuum borehole, in the same layer of firn bounded by the ice layers (labeled Monitoring Borehole 1 in **Figure 3**); the measured differential pressure response here was 12.4 Pa. Next, the pressure was monitored in

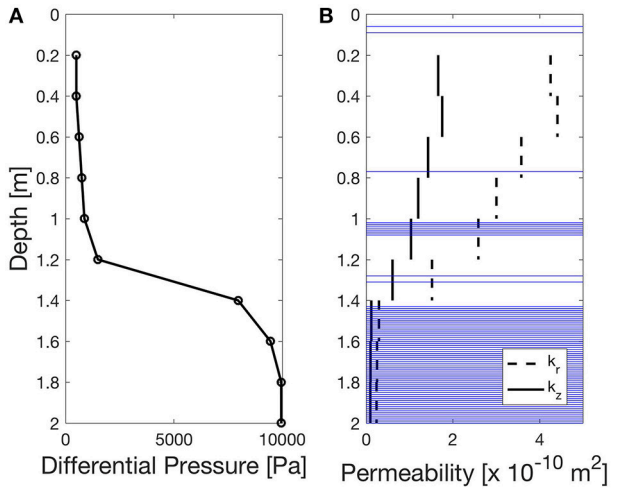

FIGURE 8 | (A) Differential pressure measured in vacuum tests at KAN-U. **(B)** Inferred horizontal (k_r) and vertical (k_z) permeability values (depth of refrozen ice layers and lenses shown as blue horizontal lines). In both the differential pressures and permeability values, an abrupt transition is apparent between 1.2 and 1.4 m depth, corresponding to the transition to solid refrozen ice that extends from ~1.4 to 8 m at this site. The differential pressure measured at 1.8 m and 2.0 m is equal to that measured for a nearly perfect vacuum (i.e., sealing the vacuum hose). In the snow and firn above the thick ice, k_r is greater than k_z, and both generally decrease with depth until the transition to thick ice, where both become very small, reflecting the effective impermeability of the refrozen ice.

a borehole just above the 5 cm ice layer (Monitoring Borehole 2). In this case the differential pressure was 8.7 Pa, suggesting that this ice layer interferes with air flow but is not completely impermeable (the horizontal extent of the ice layer into the wall is unknown). For the third test (Monitoring Borehole 3), the pressure response was measured below the 20 cm-thick ice layer below the vacuum. The differential pressure response here was 1.2 Pa—a very small response, suggesting that the 20 cm-thick ice layer substantially diminishes vertical permeability.

TABLE 3 | Inferred permeability with 95% confidence intervals associated with the optimization method for parameter estimation.

Test ID	k_r [$m^2 \times 10^{-10}$] (95% confidence)	k_z [$m^2 \times 10^{-10}$] (95% confidence)
EKT 1	7.518 (7.498, 7.537)	3.723 (3.717, 3.730)
EKT 2	50.32 (33.79, 66.86)	3.055×10^{-5} (−1.321, 1.322)
EKT 3	12.00 (11.99, 12.02)	7.043 (7.036, 7.049)
NASA-SE 1	14.807 (14.805, 14.809)	4.268 (4.267, 4.268)
NASA-SE 2	21.68 (−9.251, 52.61)	0.035 (−7.754, 7.825)
NASA-SE 3	29.85 (29.48, 30.22)	0.961 (0.800, 1.123)
SADDLE 1	10.77 (10.73, 10.82)	4.724 (4.710, 4.738)
SADDLE 2	10.63 (10.45, 10.82)	11.30 (11.16, 11.44)
SADDLE 3	22.84 (−14.73, 60.40)	3.793×10^{-5} (−30.98, 30.98)
DYE-2 1	11.38 (11.35, 11.40)	5.518 (5.510, 5.526)
DYE-2 2	23.72 (−40.57, 88.02)	4.325×10^{-10} (−16.19, 16.19)
EastGRIP 1	22.86 (21.16, 24.57)	14.75 (13.95, 15.55)
EastGRIP 2	16.28 (15.50, 17.06)	29.03 (28.07, 29.99)
EastGRIP 3	19.67 (19.50, 19.83)	22.75 (22.56, 22.94)

In most cases, the confidence intervals are narrow, indicative of a true optimum found in the solution. Values shaded in gray correspond to tests that span several ice layers, with very low vertical permeability. The confidence intervals for these highlighted cases are large, without a unique solution. This suggests that the assumption of an effective homogeneous anisotropic material to represent the firn/ice combination in these cases is not fully appropriate, and it is apparent that the ice layers act as impermeable boundaries.

DISCUSSION

Comparison to Previously Published Values

Permeability measurements for Greenland firn have been previously published for Summit (Albert et al., 1996; Albert and Shultz, 2002; Luciano and Albert, 2002; Adolph and Albert, 2014). We attempted to conduct pneumatic tests at Summit during our field campaign, but suffered equipment failure in the extreme cold during our only opportunity for these tests (−33°C, with freezing fog). Our northern field site at EastGRIP, however, can be reasonably compared to Summit with similar surface temperatures (see **Table 1**); both sites experience very little melt and so consist of mainly dry firn. When they have occasionally experienced melt in the last several years (for example, in the high melt year 2012), the refrozen melt layers are very thin, on the order of 1–2 mm. Average snow and firn density measured in the top 3 m at Summit and EastGRIP in 2016 indicate densities approximately 21% higher at EastGRIP, owing primarily to lower accumulation rates. Adolph and Albert (2014) found, however, that there was not a direct relationship between permeability and density at Summit (for near-surface firn), so this difference in density does not necessarily undermine a comparison of permeabilities at the two sites.

The vertical permeability values measured for the top 3 m of snow and firn at Summit in 2000 typically fell between 2 and 100×10^{-10} m^2 (Albert and Shultz, 2002). Albert et al. (1996) published both horizontal and vertical permeability for the top meter of snow at Summit, with values for both ranging between 2 and 60×10^{-10} m^2. Horizontal and vertical permeability values were also reported at Summit by Luciano and Albert (2002), with a range of 10–65 $\times 10^{-10}$ m^2. At EastGRIP, we infer vertical permeability (k_z) in the range 10–40 $\times 10^{-10}$ m^2, and horizontal permeability (k_r) of 10–30 $\times 10^{-10}$ m^2, which are consistent with the range reported for dry snow and firn at Summit. For our two deeper tests at EastGRIP (below 2 m), we infer vertical permeability to be slightly higher than horizontal permeability (k_r/k_z of 0.9 and 0.6 for the two depths, respectively); Luciano and

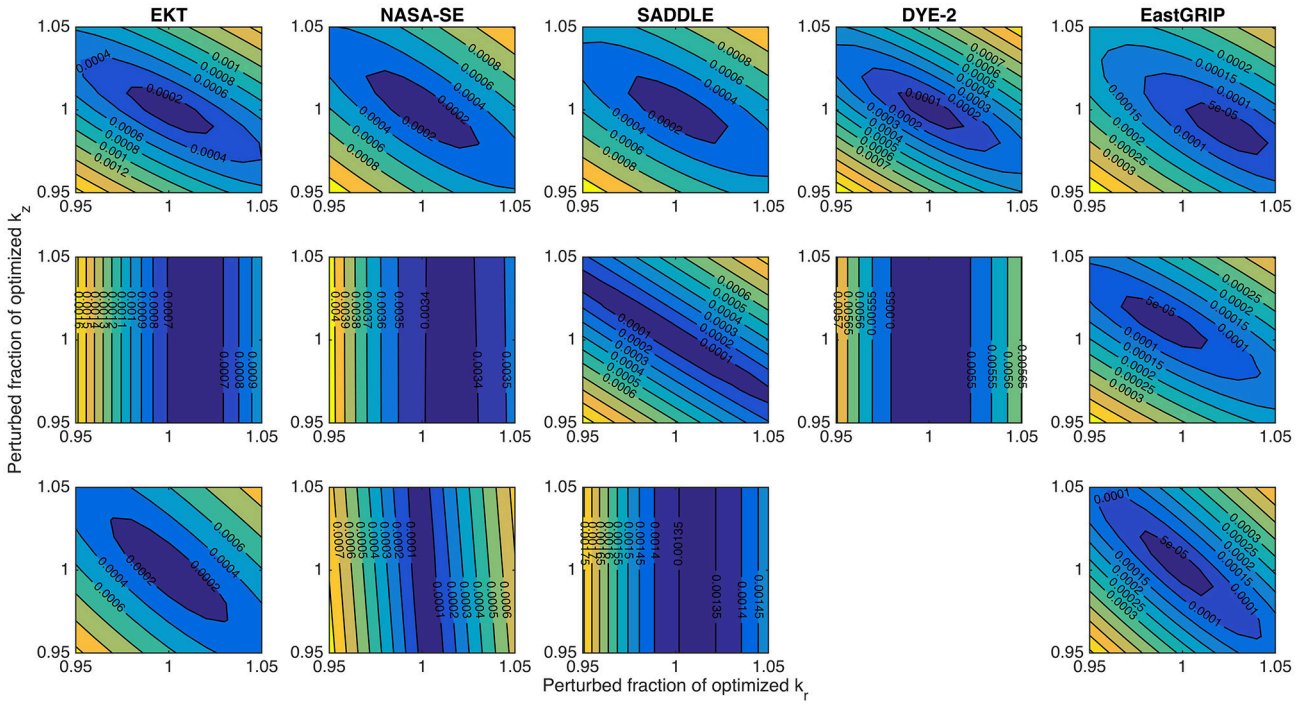

FIGURE 9 | Root-mean-square error (RMSE) in pressure response for each pneumatic test are obtained by perturbing about the optimal estimates of permeabilities. Tests are shown for each site in order of depth. In most cases, a clear optimum is apparent near the center of the plot. The tilt of the RMSE contour lines indicates a dependence in the solution between k_r and k_z. In several cases (EKT 2, NASA-SE 2, NASA-SE 3, SADDLE 3, DYE-2 2), there is not a clear RMSE optimum. These cases correspond to tests that span several ice layers, with very low vertical permeability. The assumption of an effective homogeneous anisotropic material in these cases does not adequately represent the behavior resulting from distinct impermeable layers and results in higher uncertainties for k_r estimates for these tests.

Albert (2002) also found slightly higher vertical than horizontal permeability for comparable depths in dry firn at Summit. This anisotropy is likely due to firn microstructure; for example, Calonne et al. (2012) measured higher vertical than horizontal permeability (k_r/k_z ~0.6) in evolved depth hoar.

Uncertainty in Permeability Estimates

We wish to clearly articulate sources of error and uncertainty in our measurements and analysis. In this section we present confidence intervals associated with optimization for the inferred permeability values, the uncertainty associated with measurement error, and discuss practical difficulties that were encountered during the field tests.

Uncertainty Associated with Optimization

In Section Inferred Firn Permeability and Anisotropy at Six Sites on the Greenland Ice Sheet with Different Stratigraphy, we inferred permeability based on optimal fitting of our measured pressure responses with an analytical solution for air flow through an anisotropic porous medium. From the optimization process (using the MATLAB nonlinear least-squares solver *lsqnonlin,* https://www.mathworks.com/help/optim/ug/lsqnonlin.html), we obtain 95% confidence intervals associated with each inferred permeability value using the MATLAB function *nlparci* (https://www.mathworks.com/help/stats/nlparci.html, which uses the optimized parameter estimates, residuals, and Jacobian generated by *lsqnonlin*). **Table 3** presents k_r and k_z inferred for each pneumatic test along with these confidence intervals. In most cases, the confidence intervals are narrow ($<2 \times 10^{-10}$ m^2), indicating a clear optimum solution. In some cases, however, the confidence intervals are relatively large (up to 60×10^{-10} m^2), and may even include nonphysical negative permeability values. These nonconforming cases correspond to tests that span several ice layers or lenses within the firn. The broad confidence intervals suggest that the assumption of a semi-infinite effective/equivalent homogeneous medium is not physically representative in these cases, where sets of distinct ice layers may act like impermeable boundaries.

To help confirm the robustness of the k_r and k_z estimates, sensitivity analysis of the root-mean-squared error (RMSE) between predictions and observations was performed by perturbing each parameter estimate (k_r and k_z) by ±5% about the optimal estimate. The contours of RMSE in parameter space visualize how well-defined the optima are, and also determine whether there are interactions between the parameter estimates. **Figure 9** presents the resulting RMSE contours in measured pressure responses for each perturbation combination. In most cases, a clear optimum is apparent near the center of the contour plot. The RMSE contours are tilted, however, indicating

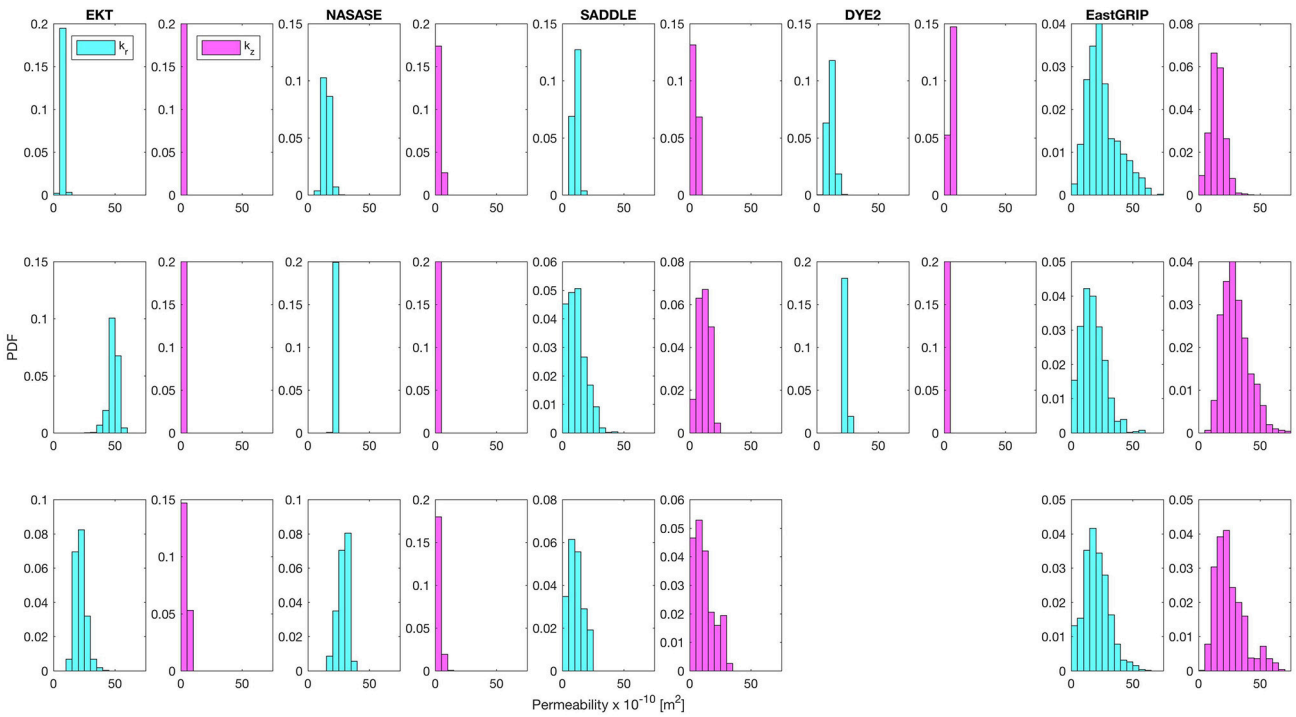

FIGURE 10 | Permeability inferred from pneumatic tests with perturbations of measured pressure responses to account for measurement error. Assuming a normal distribution of measurement error with $\mu = 0$, $\sigma = 0.5$ Pa, we applied the optimization solution to find k_r and k_z for 1,000 randomly sampled errors for each pneumatic test. The resulting probability density function (PDF) of k_r and k_z for each test at each site is shown. Referencing the ice layer/lens depths shown in **Figure 7**, these distributions support the finding that in general, $k_r > k_z$ in the presence of ice layers or lenses. At EastGRIP, k_r and k_z are more similar in magnitude. Broader PDF distributions correspond to tests in which low pressure responses were observed, making these tests more sensitive to measurement error.

some dependence between the k_r and k_z estimates (for two independent variables, the contours would appear as circles or ellipses with major and minor axes aligned with the horizontal or vertical axes). In some cases, there is no clear center to the RMSE contours, but rather the contour lines are vertical or near vertical; these cases correspond to those tests that span several ice layers and are essentially impermeable to vertical flow. The shape of the pressure RMSE contours in these cases shows that the RMSE is relatively insensitive to estimates of k_z (note that k_z is very small in these cases, with correspondingly small perturbations). As discussed previously, the optimized permeability is less well constrained for these cases that span several ice layers.

Uncertainty Due to Measurement Error

During our pneumatic tests, steady-state pressure responses were read from analog differential pressure gauges and recorded by hand in a field notebook. Because pressure responses to the vacuum are small (in the range of 1–10 Pa), any fluctuations due to wind or a slight tilt of the gauge box can cause unintended errors. All efforts were made in the field to eliminate these errors. Where possible, manually recorded pressure responses were also verified and confirmed by the digitally recorded pressure responses on the datalogger. Some tests were not recorded digitally due to power supply challenges in cold conditions. A comparison of steady-state differential pressures for all tests with both a digital and manual record reveals close agreement and only minor discrepancies between the two, with a median difference of 0.5 Pa. To estimate the uncertainty in inferred permeability associated with possible measurement error, we assume the error to be normally distributed with standard deviation $\sigma = 0.5$ Pa. We perturb the observed pressure responses for each pneumatic test with a random sample of 1,000 errors from this normal distribution and solve for the corresponding optimized k_r and k_z for each of the perturbations. **Figure 10** presents the probability density function (PDF) for k_r and k_z for each test depth at each site. These distributions fall within the same range as seen before (5–60 $\times$ 10^{-10} m^2 for k_r, and 0–30 $\times$ 10^{-10} m^2 for k_z), and support the general patterns discussed above in Section Inferred Firn Permeability and Anisotropy at Six Sites on the Greenland Ice Sheet with Different Stratigraphy. In the presence of ice layers and lenses, k_r is typically greater than k_z. At EastGRIP, k_r and k_z are more similar in magnitude. Tests with a wider distribution spread correspond to tests in which the measured pressure response was low, making them more sensitive to pressure measurement error.

Equipment Challenges and Flow Rate Uncertainty

The thermal anemometer we used for measuring flow rate was damaged and ceased to function partway through the field campaign after exposure to particularly cold conditions (below -24°C). The flow measurements that were recorded successfully prior to its damage, however, correspond to a fairly narrow

range of 3.5–7.0 ms^{-1}. Because of this uncertainty (and also the general fluctuating nature of thermal anemometer flow rate measurement), shaded error bars on the inferred permeability values presented in **Figure 7** are included to reflect the range in flow rate generated by the portable wet/dry vacuum. Permeability values corresponding to the mean measured flow rate (5.1 ms^{-1}) are indicated as solid (k_z) or dashed (k_r) black lines on the figure.

The inflatable rubber plugs used to seal the boreholes at depth were inflated through tubes connected to a bicycle pump at the surface. The integrity of the seals against the borehole walls is important. On especially cold days (below −20°C), the tube connections to the pump contracted and required constant vigilance to ensure proper seals were maintained. Only tests in which solid hand-tight seals (tugging on the attached tubing yielded no movement) held in both the vacuum and monitoring boreholes for the duration of a test were recorded and used in the analysis above. If a seal was lost, the plug and equipment noticeably dropped to rest at the bottom of the borehole. In future applications, a portable air compressor could be used to maintain and ensure constant pressure in the plugs, and more expensive custom silicone plugs could be used, with temperature ratings for all connections and equipment down to −40°C. While it is certainly preferable to conduct the pneumatic tests in less extreme cold, logistics in the field do not always allow for such fair-weather flexibility.

Conclusions and Recommendations for Future Work

From these initial tests on the Greenland Ice Sheet, we have found *in-situ* pneumatic testing to be a promising method that can be used to infer horizontal and vertical firn permeability in the field. Accurate permeability estimates are necessary for meltwater infiltration, transport, and retention models that estimate runoff, a key component of surface mass balance. In general, we find higher anisotropy in firn permeability across refrozen ice layers and lenses than in dry firn. In the presence of ice layers and lenses, vertical permeability ranges from 0–30 × 10^{-10} m^2, with horizontal permeability on the order of 5–60 × 10^{-10} m^2. In dry firn without refrozen lenses or layers, both vertical and horizontal permeability range between approximately 10–30 × 10^{-10} m^2.

Researchers using this method in future campaigns could employ more pressure transducers at various monitoring depths and distances from the vacuum for each test to generate a more complete picture of the permeability structure at a given site. To avoid being limited by temperature conditions during available test opportunities during a field campaign, all equipment should be rated down to −40°C Additionally, a stronger vacuum motor could potentially be used to stimulate measureable pressure responses farther away from the vacuum (taking care not to destroy the firn structure itself). Finally, it would be particularly illuminating to examine in detail the change in permeability over multiple years at locations on the Greenland Ice Sheet with increasing meltwater production. Such a study has the potential to clarify changes accompanying increased ice layer and ice lens formation that results from a warming climate, with ramifications for meltwater percolation and surface mass balance of the entire ice sheet. This technique is also suitable for broad application in Antarctica and other glaciers and ice caps.

AUTHOR CONTRIBUTIONS

AS designed, built, and tested the equipment, performed field experiments, analyzed data, and wrote the majority of the manuscript. HR provided guidance in the experimental design and various analysis techniques, and assisted in writing the manuscript. EW was involved in the conceptual and technical design, helped build the field setup, conducted preliminary tests in Colorado, and provided valuable insight on soil-vapor-extraction system design. MM offered the opportunity to collaborate in Greenland to conduct the field tests, assisted in manuscript preparation, and provided encouragement and expertise on all firn-related matters. WC and CS assisted in field experiments in Greenland, helped design site-specific tests, and were involved in preparation of the manuscript.

FUNDING

This work was funded primarily by a Dean's Graduate Student Research Grant from the Graduate School at the University of Colorado. Additional support was provided by an American Geophysical Union Cryosphere Innovation Award for Students, a NASA Earth and Space Sciences Fellowship (NNX14AL24H), and an Innovative Seed Grant from the University of Colorado. Logistical support was provided in collaboration with the FirnCover project (NASA ROSES grant NNX15AC62G).

ACKNOWLEDGMENTS

Many thanks to the FirnCover 2016 team for support and camaraderie in the field (MM, CS, WC, Darren Hill, Baptiste Vandecrux, Shawn Marshall, Samira Samimi, Achim Heilig, Bastian Gerling, and Leander Gambal), and also to CH2MHill Polar Field Services.

REFERENCES

Adolph, A. C., and Albert, M. R. (2014). Gas diffusivity and permeability through the firn column at Summit, Greenland: measurements and comparison to microstructural properties. *Cryosphere* 8, 319–328. doi: 10.5194/tc-8-319-2014

Albert, M. R., Arons, E. M., and Davis, R. E. (1996). "Firn properties affecting gas exchange at Summit, Greenland: ventilation possibilities," in *Chemical Exchange between the Atmosphere and Polar Snow*, eds E. W. Wolff and R. C. Bales (Berlin; Heidelberg: Springer), 561–565.

Albert, M. R., and Perron, F. E. (2000). Ice layer and surface crust permeability in a seasonal snow pack. *Hydrol. Process.* 14, 3207–3214. doi: 10.1002/1099-1085(20001230)14:18%3C3207::AID-HYP196%3E3.3.CO;2-3

Albert, M. R., and Shultz, E. F. (2002). Snow and firn properties and air–snow transport processes at Summit, Greenland. *Atmos. Environ.* 36, 2789–2797. doi: 10.1016/S1352-2310(02)00119-X

Ambach, W., Blumthaler, M., and Kirchlechner, P. (1981). Application of the gravity flow theory to the percolation of melt water through firn. *J. Glaciol.* 27, 67–75.

Bader, H. (1939). "Mineralogische und strukturelle Charakterisierung des Schnees und seiner Metamorphose," in *Der Schnee und seine Metamorphose*, eds H. Bader, J. Neher, O. Eckel, C. Thams, R. Haefeli (Bern: Kummerly & Frey), 1–61. (Beiträge zur Geologie der Schweiz, Geotechnische Serie Hydrologie 3, Transl. Tienhaven, J. C. V., 1954: Snow and its metamorphism, SIPRE Translations, 14: 1–55).

Bear, J. (1972). *Dynamics of Fluids in Porous Materials*. New York, NY: Elsevier.

Bender, J. A. (1957). *Air Permeability of Snow*. US Army Snow Ice and Permafrost Research Establishment. Wilmette, IL: Corps of Engineers.

Calonne, N., Geindreau, C., Flin, F., Morin, S., Lesaffre, B., Du Roscoat, S. R., et al. (2012). 3-D image-based numerical computations of snow permeability: links to specific surface area, density, and microstructural anisotropy. *Cryosphere* 6, 939–951. doi: 10.5194/tc-6-939-2012

Charalampidis, C., van As, D., Colgan, W., Fausto, R., MacFerrin, M., and Machguth, H. (2016). Thermal tracing of retained meltwater in the lower accumulation area of the southwestern Greenland ice sheet. *Ann. Glaciol.* 57, 1–10. doi: 10.1017/aog.2016.2

Colbeck, S. C. (1975). A theory for water flow through a layered snowpack. *Water Res. Res.* 11, 261–266.

Collins, R. E. (1961). *Flow of Fluids through Porous Media*. New York, NY: Reinhold.

Courville, Z. R., Albert, M. R., Fahnestock, M. A., Cathles, L. M., and Shuman, C. A. (2007). Impacts of an accumulation hiatus on the physical properties of firn at a low-accumulation polar site. *J. Geophys. Res.* 112. doi: 10.1029/2005JF000429

Courville, Z., Hörhold, M., Hopkins, M., and Albert, M. (2010). Lattice-Boltzmann modeling of the air permeability of polar firn. *J. Geophys. Res.* 115:F04032. doi: 10.1029/2009JF001549

Fettweis, X., Franco, B., Tedesco, M., van Angelen, J. H., Lenaerts, J. T. M., van den Broeke, M. R., et al. (2013). Estimating the Greenland ice sheet surface mass balance contribution to future sea level rise using the regional atmospheric climate model MAR. *Cryosphere* 7, 469–489. doi: 10.5194/tc-7-469-2013

Fierz, C., Armstrong, R. L., Durand, Y., Etchevers, P., Greene, E., McClung, D. M., et al. (2009). "The International classification for seasonal snow on the ground," in *IHP-VII Technical Documents in Hydrology N°83, IACS Contribution N°1, UNESCO-IHP* (Paris).

Harper, J., Humphrey, N., Pfeffer, W. T., Brown, J., and Fettweis, X. (2012). Greenland ice-sheet contribution to sea-level rise buffered by meltwater storage in firn. *Nature* 491, 240–243. doi: 10.1038/nature11566

Hörhold, M. W., Albert, M. R., and Freitag, J. (2009). The impact of accumulation rate on anisotropy and air permeability of polar firn at a high-accumulation site. *J. Glaciol.* 55, 625–630. doi: 10.3189/002214309789471021

Jeans, J. H. (1908). *The Mathematical Theory of Electricity and Magnetism*. Cambridge: University Press.

Johnson, P. C., Stanley, C. C., Kemblowski, M. W., Byers, D. L., and Colthart, J. D. (1990). A practical approach to the design, operation, and monitoring of *in situ* soil-venting systems. *Groundwater Monit. Remediation* 10, 159–178.

Krabill, W., Hanna, E., Huybrechts, P., Abdalati, W., Cappelen, J., Csatho, B., et al. (2004). Greenland ice sheet: increased coastal thinning. *Geophys. Res. Lett.* 31:L24402. doi: 10.1029/2004GL021533

Luciano, G. L., and Albert, M. R. (2002). Bidirectional permeability measurements of polar firn. *Ann. Glaciol.* 35, 63–66. doi: 10.3189/172756402781817095

Machguth, H., MacFerrin, M., van As, D., Charalampidis, C., Colgan, W., Fausto, R. S., et al. (2016). Greenland meltwater storage in firn limited by near-surface ice formation. *Nat. Clim. Chang.* 6, 390–393. doi: 10.1038/nclimate2899

Marsh, P., and Woo, M. K. (1985). Meltwater movement in natural heterogeneous snow covers. *Water Resour. Res.* 21, 1710–1716.

Mikkelsen, A. B., Hubbard, A., MacFerrin, M., Box, J. E., Doyle, S. H., Fitzpatrick, A., et al. (2016). Extraordinary runoff from the Greenland ice sheet in 2012 amplified by hypsometry and depleted firn retention. *Cryosphere* 10, 1147–1159. doi: 10.5194/tc-10-1147-2016

Milne-Thomson, L. M. (1938). *Theoretical Hydrodynamics*. New York, NY: Macmillan.

Pfeffer, W. T., Meier, M. F., and Illangasekare, T. H. (1991). Retention of Greenland runoff by refreezing: implications for projected future sea level change. *J. Geophys. Res.* 96, 22117–22124. doi: 10.1029/91JC02502

Rignot, E., Velicogna, I., Van den Broeke, M. R., Monaghan, A., and Lenaerts, J. T. M. (2011). Acceleration of the contribution of the Greenland and Antarctic ice sheets to sea level rise. *Geophys. Res. Lett.* 38:L05503. doi: 10.1029/2011GL046583

Shan, C., Falta, R. W., and Javandel, I. (1992). Analytical solutions for steady state gas flow to a soil vapor extraction well. *Water Resour. Res.* 28, 1105–1120. doi: 10.1029/91WR02986

Shimizu, H. (1970). Air permeability of deposited snow. *Contrib. Inst. Low Temperature Sci. A* 22, 1–32.

Sommerfeld, R. A., and Rocchio, J. E. (1993). Permeability measurements on new and equitemperature snow. *Water Res. Res.* 29, 2485–2490. doi: 10.1029/93WR01071

Velicogna, I., and Wahr, J. (2006). Acceleration of Greenland ice mass loss in spring 2004. *Nature* 443, 329–331. doi: 10.1038/nature05168

Weinig, W. T. (1992). "Monitoring the vadose zone during pneumatic pumping tests," in *Proceedings of the Sixth National Outdoor Action Conference, National Ground Water Association* (Westerville, OH), 133–146.

Conflict of Interest Statement: The authors declare that the research was conducted in the absence of any commercial or financial relationships that could be construed as a potential conflict of interest.

frontiers in Earth Science

METHODS
published: 07 May 2018
doi: 10.3389/feart.2018.00051

A Snow Density Dataset for Improving Surface Boundary Conditions in Greenland Ice Sheet Firn Modeling

Robert S. Fausto[1], Jason E. Box[1], Baptiste Vandecrux[1,2], Dirk van As[1], Konrad Steffen[3,4,5], Michael J. MacFerrin[6], Horst Machguth[7,8], William Colgan[1,6], Lora S. Koenig[9], Daniel McGrath[10], Charalampos Charalampidis[11] and Roger J. Braithwaite[12]*

[1] Geological Survey of Denmark and Greenland, Copenhagen, Denmark, [2] Arctic Technology Centre, Technical University of Denmark, Lyngby, Denmark, [3] Swiss Federal Research Institute WSL, Birmensdorf, Switzerland, [4] Swiss Federal Institute of Technology, Zurich, Switzerland, [5] Swiss Federal Institute of Technology, Lausanne, Switzerland, [6] Cooperative Institute for Research in Environmental Sciences, University of Colorado Boulder, Boulder, NV, United States, [7] Department of Geography, University of Zurich, Zurich, Switzerland, [8] Department of Geosciences, University of Fribourg, Fribourg, Switzerland, [9] National Snow and Ice Data Center, University of Colorado, Boulder, NV, United States, [10] Geosciences Department, Colorado State University, Fort Collins, CO, United States, [11] Bavarian Academy of Sciences and Humanities, Munich, Germany, [12] University of Manchester, Manchester, United Kingdom

OPEN ACCESS

Edited by:
Timothy C. Bartholomaus, University of Idaho, United States

Reviewed by:
Xavier Fettweis, University of Liège, Belgium
Marco Möller, University of Bremen, Germany
Clément Miège, University of Utah, United States

***Correspondence:**
Robert S. Fausto
rsf@geus.dk

Specialty section:
This article was submitted to Cryospheric Sciences, a section of the journal Frontiers in Earth Science

Received: *13 October 2017*
Accepted: *18 April 2018*
Published: *07 May 2018*

Citation:
Fausto RS, Box JE, Vandecrux B, van As D, Steffen K, MacFerrin MJ, Machguth H, Colgan W, Koenig LS, McGrath D, Charalampidis C and Braithwaite RJ (2018) A Snow Density Dataset for Improving Surface Boundary Conditions in Greenland Ice Sheet Firn Modeling. Front. Earth Sci. 6:51. doi: 10.3389/feart.2018.00051

The surface snow density of glaciers and ice sheets is of fundamental importance in converting volume to mass in both altimetry and surface mass balance studies, yet it is often poorly constrained. Site-specific surface snow densities are typically derived from empirical relations based on temperature and wind speed. These parameterizations commonly calculate the average density of the top meter of snow, thereby systematically overestimating snow density at the actual surface. Therefore, constraining surface snow density to the top 0.1 m can improve boundary conditions in high-resolution firn-evolution modeling. We have compiled an extensive dataset of 200 point measurements of surface snow density from firn cores and snow pits on the Greenland ice sheet. We find that surface snow density within 0.1 m of the surface has an average value of 315 kg m^{-3} with a standard deviation of 44 kg m^{-3}, and has an insignificant annual air temperature dependency. We demonstrate that two widely-used surface snow density parameterizations dependent on temperature systematically overestimate surface snow density over the Greenland ice sheet by 17–19%, and that using a constant density of 315 kg m^{-3} may give superior results when applied in surface mass budget modeling.

Keywords: snow surface density, firn, Greenland, parameterization, surface mass budget, model boundary condition

INTRODUCTION

The mass budget of the Greenland ice sheet has grown increasingly negative during the past two decades (e.g., Kjeldsen et al., 2015; Van den Broeke et al., 2016). There is a strong impetus to constrain critical processes in order to reduce uncertainties in mass balance estimates (e.g., Shepherd et al., 2012; IPCC, 2013; Khan et al., 2015). In particular, an improved understanding of

ice-sheet-wide snow and firn properties can reduce uncertainties in: remotely-sensed or modeled ice sheet mass budget (e.g., Van den Broeke et al., 2016), identifying internal layers for calculating accumulation rates from combined radar and firn core surveys (Hawley et al., 2006, 2014; de la Peña et al., 2010; Miège et al., 2013; Karlsson et al., 2016; Koenig et al., 2016; Overly et al., 2016; Lewis et al., 2017), and quantifying meltwater retention (Harper et al., 2012; Humphrey et al., 2012; Machguth et al., 2016) and accumulation rates (López-Moreno et al., 2016; Schaller et al., 2016) from firn cores and snow pits. Improved estimates of surface snow density, which serves as an important boundary condition in firn densification modeling, can reduce uncertainties in mass budget studies (e.g., Sørensen et al., 2011; Csatho et al., 2014; Hurkmans et al., 2014; Morris and Wingham, 2014; Colgan et al., 2015) that convert remotely-sensed volume changes to mass changes based on either depth-density profile relations or surface snow density parameterizations. Ice sheet models that assess the surface mass budget, such as SICOPOLIS (Greve et al., 2011) or PISM (Aschwanden et al., 2012), are also limited by uncertainties in surface snow density. Fausto et al. (2009) found that the inclusion of firn densification in SICOPOLIS through a physical description of the retention capacity yields a 10% increase in the accuracy of the present-day surface mass budget.

Regional climate models calculate firn densification (e.g., Vionnet et al., 2012; Langen et al., 2015; Steger et al., 2017), but are limited by uncertainties in surface snow density feeding into their subsurface schemes. Some models use surface snow density parameterizations based on temperature to implicitly account for spatiotemporal variability (e.g., Reeh et al., 2005; Kuipers Munneke et al., 2015). Other models use parameterizations that depend on wind speed (e.g., Gallée et al., 2013) or a combination of air temperature and wind speed (e.g., Vionnet et al., 2012), while for instance Langen et al. (2015) used a constant surface snow density value.

The parameterizations based on temperatures rely on *in-situ* firn measurements with a coarse vertical resolution. For instance, Reeh et al. (2005) used a firn model to infer surface snow density from the 10-m firn temperature and depth-density profiles, while Kuipers Munneke et al. (2015) used the average density of the top meter of snow/firn, which would systematically overestimate surface snow density in regional climate model studies (Steger et al., 2017) if interpreted as the surface value. Most firn-evolution models operate at a centimeter-scale vertical resolution, requiring a surface snow density boundary condition derived at a resolution finer that 1 m. Using observational data sampled at high vertical resolution, one can derive the true surface value and avoid systematically overestimating surface snow density and consequently the density of the entire firn column. More accurate firn density-depth profiles yield improvements for mass budget studies of the Greenland ice sheet (e.g., Li and Zwally, 2011; Ligtenberg et al., 2011; Simonsen et al., 2013; Csatho et al., 2014; Overly et al., 2016; Steger et al., 2017).

The aim of this study is to present a spatially extensive density dataset for the Greenland ice sheet derived from 200 density-profile measurements, and to investigate the observed spatiotemporal variability for the top 0.1 m of snow/firn. In an application of this dataset, we quantify the performance of the observation-based temperature-dependent surface snow density parameterizations by Kuipers Munneke et al. (2015) and Reeh et al. (2005) that are often used as boundary conditions in surface mass budget studies of the Greenland ice sheet (e.g., Csatho et al., 2014; Steger et al., 2017).

METHODS

Dataset

Our surface density dataset consists of 200 point observations, along with the geographic location, annual air temperature and annual accumulation rate for these locations. The oldest surface density data were collected by Benson (1962) in 1954 in Northwest Greenland at latitudes between 70° to 77° N (Appendix C). These measurements include annual accumulation rates and 10 m firn temperatures reported by Mock and Weeks (1965) (Appendix A). Data from both the percolation and ablation areas of the southern and western ice sheet sections near 61.3° N (Nordbo Gletscher) and 69.7° N (Paakitsoq), respectively, were collected by Braithwaite et al. (1982, 1994). Our dataset also includes data from the Program for Arctic Regional Climate Assessment (PARCA) (Mosley-Thompson et al., 2001; Thomas and Investigators, 2001). Further, the SUrface Mass balance and snow depth on sea ice working grouP (SUMuP) provided accumulation rates, snow depths and density values at various sites on the ice sheet (Koenig et al., 2013; Montgomery et al., 2018), including observations from a study of Greenland accumulation (Hawley et al., 2014) and firn aquifers (Forster et al., 2013; Koenig et al., 2014; Miège et al., 2016). We gathered annual air temperatures, accumulation rates, and density observations from snow pits and firn cores from the Greenland Climate Network (GC-Net) (Steffen et al., 1996), the Programme for Monitoring of the Greenland Ice Sheet (PROMICE) (Van As et al., 2016b), and the Arctic Circle Traverses (ACTs) (e.g., Machguth et al., 2016). Lastly, we also included observations by Schaller et al. (2016) from the NEEM to EGRIP traverse, and from the López-Moreno et al. (2016) Greenland circumnavigation. Accumulation rates in the database are not long-term averages, but represent the preceding year's snowfall. **Figure 1** provides a map of all measurement locations. All data are available as Supplementary Material. **Figure 2a** illustrates that 28% of the observations were taken in the mid-1950s, only 2% were taken in the 1980s and 1990s, while 70% were obtained between 1999 and 2016. 94% of the measurements were gathered at elevations exceeding 1,000 m above sea level (**Figure 2d**).

Defining the surface layer as the upper 0.1 m of snow yields that in most cases the surface layer was deposited in multiple snowfall events, except for areas located at relatively low elevations in the south and southeast of the ice sheet, where individual precipitation events typically produce more than 0.1 m of snow (Burgess et al., 2010). Where possible, the annual air temperature was calculated as the average over the 365 days prior to the date for which the surface snow density was determined. Where air temperature measurements are not available, i.e., for the older data by Benson (1962) and Braithwaite et al. (1994),

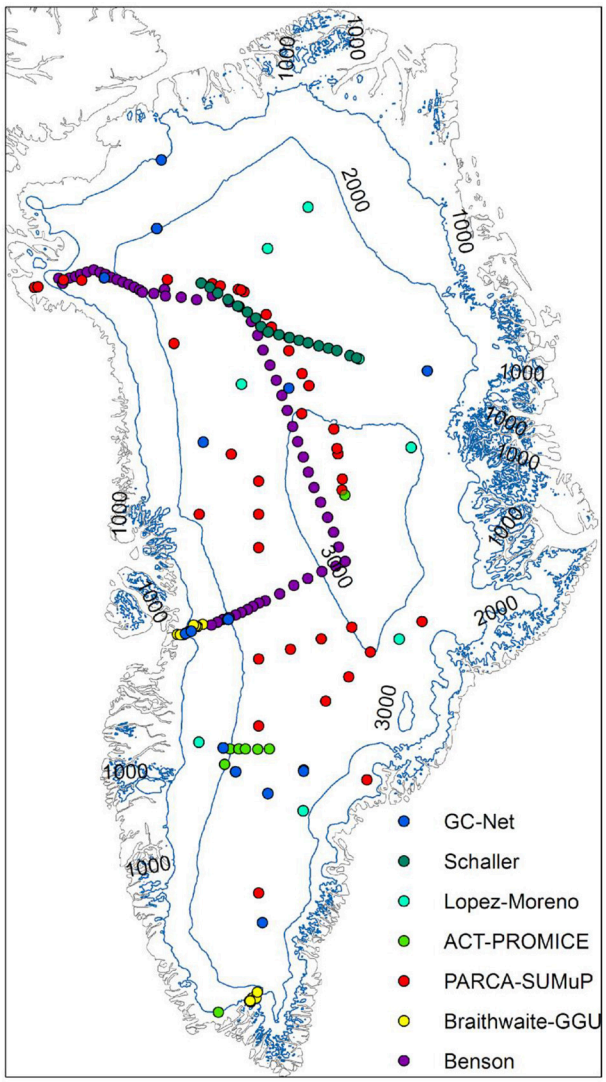

FIGURE 1 | Locations of all surface snow density measurement locations in our dataset. Contours lines indicate elevations in meters above sea level.

but firn-core temperatures were, we use 10 m firn temperature as annual air temperature following e.g., Reeh et al. (2005), Polashenski et al. (2014), and Kuipers Munneke et al. (2015). This is a fair approximation since 10 m firn temperatures reflect the conductive temperature wave propagation in places with little or no melt (Benson, 1962). Though valid for the earlier observations in our dataset, recent increases in ice sheet melt area have reduced the dry snow facies of the ice sheet (McGrath et al., 2013) and therefore the applicability of this methodology.

Commonly, snow/firn was sampled in snow pits using a fixed volume cutter at 0.05–0.1 m vertical resolution. These samples were weighed using a variety of scales. When density data were derived from a core, the snow was extracted from the core barrel and typically sub-sampled into 0.1 m sections before being weighed. Conger and McClung (2009) investigated measurement errors of several different density cutters and conclude that measurement accuracy was within 3–12%. They also conclude that the absolute measurement uncertainty is within 11% of true density. A discussion of density cutters by Proksch et al. (2016) reaches a similar uncertainty of 9%. For the data in our database, sampling uncertainty is not documented in any of the field campaigns, however it seems reasonable to assume that surface snow density is known within 10%. Typically, this measurement uncertainty is smaller than the spatial variability in surface snow density in the vicinity of the measurement location (e.g., Proksch et al., 2015). We argue that the point measurements in our dataset do not represent fresh snow, as the persistent katabatic winds in Greenland compact surface snow within days after snowfall (e.g., Liston et al., 2007).

Firn Model Initialization

We test a surface snow density parameterization for the Greenland ice sheet that is dependent on temperature, similar to commonly used parameterizations by Kuipers Munneke et al. (2015) and Reeh et al. (2005). We assume a linear dependence of surface snow density (ρ) in kg m^{-3} on annual air temperature (T_a) in °C, in what we refer to as parameterization P1:

$$\rho = A + B \cdot T_a \quad (1)$$

We determine the fit coefficients by orthogonal linear regression to all available T_a values in our dataset, and find a best fit for A = 362.1 and B = 2.78 (**Table 1**) for the top 0.1 m of snow. Kuipers Munneke et al. (2015) determined the coefficients of Equation (1) using annual surface temperature T_s in °C simulated by RACMO2.3 and the average density of the uppermost 1 m of snow/firn, and found what we here refer to as parameterization P2:

$$\rho_{KM15} = 481 + 4.834 \cdot T_s \quad (2)$$

Reeh et al. (2005) derived surface snow density as a function of the 10-m firn temperature (T_f) from the near-surface part of their depth-density profiles by determining the load at 5 m depth, as calculated by their model, so that it fits the corresponding load derived from the measured depth-density profiles (parameterization P3):

$$\rho_{R05} = 625 + 18.7 \cdot T_f + 0.293 \cdot T_f^2 \quad (3)$$

There is a ca. 40% overlap between our dataset and the data feeding into the Kuipers Munneke et al. (2015) and Reeh et al. (2005) parameterizations that stems from them also using the Benson (1962), Braithwaite et al. (1994), and PARCA (Mosley-Thompson et al., 2001) datasets.

To highlight the importance of sampling depth ranges in producing an observationally-based boundary condition for firn models in Greenland, we also test P1 (Equation 1) using the average density of the top 0.2 and 0.5 m of snow/firn in our analysis (**Table 1**). We theorize that, by using density data obtained as close to the surface as possible, we avoid introducing a systematic bias due to compaction. Yet by focusing only on the top layer of snow/firn, we likely introduce more scatter in our results due to additional variability by single weather events. We investigate such considerations below.

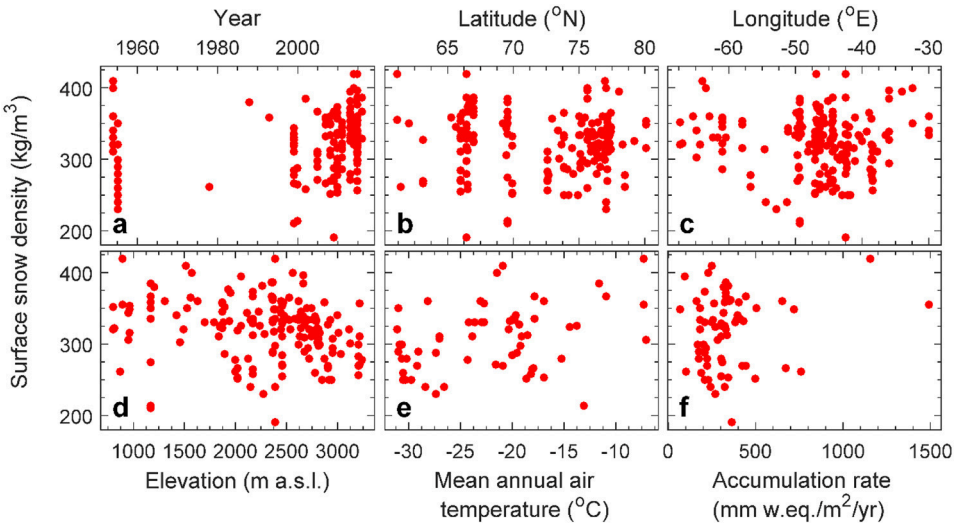

FIGURE 2 | Density of the top 0.1 m of snow plotted against site- and campaign-specific parameters: **(a)** year, **(b)** latitude, **(c)** longitude, **(d)** elevation, **(e)** annual mean near-surface air temperature, and **(f)** accumulation rate.

TABLE 1 | Fit coefficients and statistics for parameterization P1 (Equation 1).

Depth range (m)	A	B	Correlation (R^2)	Number of observations
0–0.1	362.1	2.78	0.12	91
0–0.2	363.0	2.21	0.14	91
0–0.5	358.4	1.30	0.08	91

RESULTS

Surface snow density in our 200-value database ranges between 190 and 420 kg m^{-3}, with an average of 315 kg m^{-3} and associated standard deviation of 44 kg m^{-3} (**Figure 3**, **Table 2**). Using the 10% measurement uncertainty range chosen in the methods section, we determine the average uncertainty to be ± 32 kg m^{-3}. The measurement uncertainty is smaller than the 44 kg m^{-3} standard deviation, which demonstrates a significant natural variability in the top 0.1 m of snow most likely due to differences in precipitation events and influences from weather in general. Yet the variability in surface snow density could also depend on location or annual air temperature as investigated below.

There is no significant temporal trend in surface snow density (**Figure 2a**), indicating that the relatively large timespan over which measurements were collected does not introduce a bias. **Figure 2** also illustrates that surface snow density is not significantly correlated with latitude, longitude, elevation, nor annual accumulation rate. Remarkably, also annual air temperature does not prove to be a strong predictor of surface snow density (**Figure 2e**). Even in a stepwise linear regression we find that no combination of variables in our database adequately predicts the surface snow density (results not presented). We quantify the poor predictive skill of annual air temperature in all three parameterizations in **Table 3**, showing root mean square error (RMSE) values for the top 0.1 m of snow to be 42–84 kg m^{-3}, with mean biases of + 19% (P2) and +17% (P3). For the 0–0.1 m depth range, RMSE values for P2 and P3, are respectively a factor of 2.0 and 1.8 higher than those for our P1 parameterization (**Table 3**).

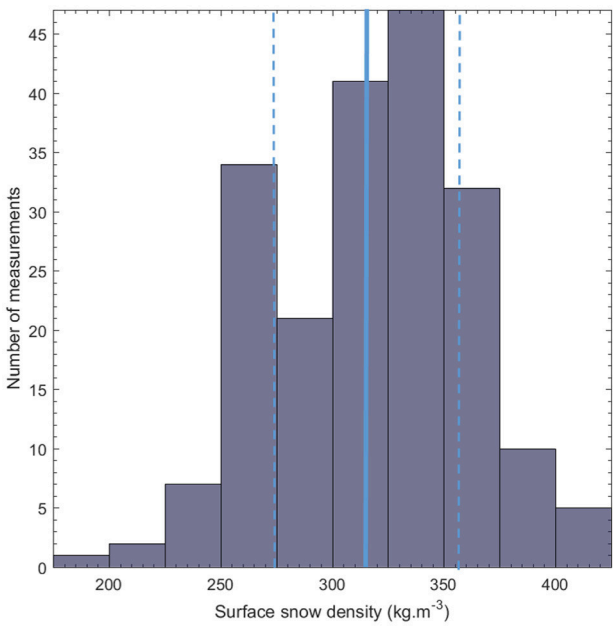

FIGURE 3 | Number of surface snow density measurements over the Greenland ice sheet. Blue solid and dashed lines indicate the average and standard deviation of the dataset, respectively.

TABLE 2 | Surface snow density dataset metadata for three depth ranges.

Depth range (m)	0–0.1	0–0.2	0–0.5
Number of observations	200	206	231
Minimum (kg m^{-3})	191	170	256
Maximum (kg m^{-3})	420	478	510
Average (kg m^{-3})	315	324	341
Median (kg m^{-3})	321	325	336
Standard deviation (kg m^{-3})	44	41	37

TABLE 3 | Root-mean-square error (RMSE), mean bias and RMSE ratio values for parameterizations using annual mean air temperature: P1 (this study), P2 (Kuipers Munneke et al., 2015) and P3 (Reeh et al., 2005).

ρ parameterization	Depth range (m)	RMSE (kg m^{-3})	Mean bias (kg m^{-3})	RMSE ratio P2/P1	RSME ratio P3/P1
P1	0–0.1	42	0	2.0	1.8
P1	0–0.2	30	0	2.2	2.1
P1	0–0.5	24	0	2.2	2.1
P2	0–0.1	84	72 (19%)	–	–
P2	0–0.2	67	58 (15%)	–	–
P2	0–0.5	53	42 (11%)	–	–
P3	0–0.1	76	62 (17%)	–	–
P3	0–0.2	63	48 (13%)	–	–
P3	0–0.5	50	32 (8%)	–	–

Average snow/firn density increases from 315 to 341 kg m^{-3} as the averaging depth range increases from 0.1 to 0.5 m (**Table 2**). Simultaneously, the standard deviation decreases indicative of a reduction in small-scale spatial variability (**Table 2**), i.e., differences in snow/firn density profiles are growing smaller due to compaction and as the relative influence of single weather events reduces. As a result of using larger depth ranges yielding larger average densities, the performance of parameterizations P2 and P3 increases judging from reducing RMSE values, but they still overestimate the average density of the top 0.5 m of snow/firn by 11% (P2) and 8% (P3) (**Table 3**). Even taking into account that T_a (Equation 1) typically exceeds T_s (Equation 2) by a few degrees does not make up for more than 10 kg m^{-3} of the P2 overestimate.

Figure 4 illustrates the dependence of surface snow density on annual air temperature for the top 0.1, 0.2, and 0.5 m of snow/firn, confirming that (1) air temperature is a poor predictor of surface snow density, (2) variability of surface snow density decreases with increasing depth range, (3) existing temperature-based parameterizations tend to overestimate surface snow density, (4) especially for snow density nearest the surface, and revealing that (5) the predictive skill of parameterizations P2 and P3 is poorest for annual temperatures exceeding −20°C. Consequently, we judge that using a single constant value to represent surface snow density on the Greenland ice sheet may be preferred over using a temperature-dependent parameterization.

DISCUSSION

Depth Range

We use a smaller depth range to better represent surface snow density than previous studies. Assessing density closer to the surface is important for producing a more accurate upper boundary condition to be used in firn evolution models that would produce too high firn densities along the entire depth profile. **Figure 4**, **Table 3** confirm that using relatively large depth ranges in determining a surface snow density parameterization results in overestimated values by Kuipers Munneke et al. (2015) and Reeh et al. (2005). Our smallest tested depth range of 0–0.1 m reveals larger natural variability, but would not introduce a considerable systematic bias in firn evolution modeling even if a vertical grid resolution finer than 0.1 m is used. In surface mass balance modeling, the choice of vertical resolution of the subsurface directly influences the calculation of key variables, such as the meltwater retention capacity of the snow/firn column. The more variable density in the top 0.1 m of snow compared to the top 0.2 m (factor of 1.4 more variable) or 0.5 m (1.8), is due to the influence of single precipitation events and subsequent weather forcing. We contend that this increased variability is preferable over the introduction of a systematic bias in surface mass balance modeling.

The top of the snowpack compacts rapidly after snowfall (e.g., Brun et al., 1997; Liston et al., 2007), as the crystal structure of freshly deposited snow breaks down within days due to wind and redistribution of drifting snow (e.g., Kotlyakov, 1961; Kojima, 1967; Pahaut, 1976). Surface snow densification by wind, which generally only influences the top 0.1 m, becomes insignificant after a few days (Brun et al., 1997). For most or all observations in our dataset, we can safely assume that wind compaction has occurred already. Therefore, our dataset and resulting products should not be used in models to prescribe or validate fresh snow densities (e.g., Vionnet et al., 2012), but rather to define the upper boundary condition (i.e., minimum density) in firn evolution models that do not calculate micro-scale snow physics and densification by wind, snow drift and redistribution.

In regions where large snowfall events occur, such as in south Greenland, density measurements of the top 0.1 m of snow may reflect the conditions during one snowfall event and subsequent weather-dependent densification prior to measurement. All of the snow-density measurements in our database were taken in spring and summer, meaning that our average and parameterization may be seasonally biased. Dibb and Fahnestock (2004) investigated the seasonality of the surface snow density at Summit in Greenland, and found a seasonal standard deviation of 30% in density in the top 0.03 m of snow as determined from 22 measurements during a two-year period. However, seasonal variation in the surface snow density is likely to increase with elevation (Brun et al., 1997) with standard deviation values lower than 30% in regions away from the three dome sites in Greenland where persistent katabatic winds and their influence on snow compaction do not occur (e.g., Noël et al., 2014). In general, katabatic winds are strongest in winter due to surface radiative cooling, and at lower elevations (below 2,000 m above sea level) due to larger surface slopes (e.g., Van As et al., 2013; Noël et al.,

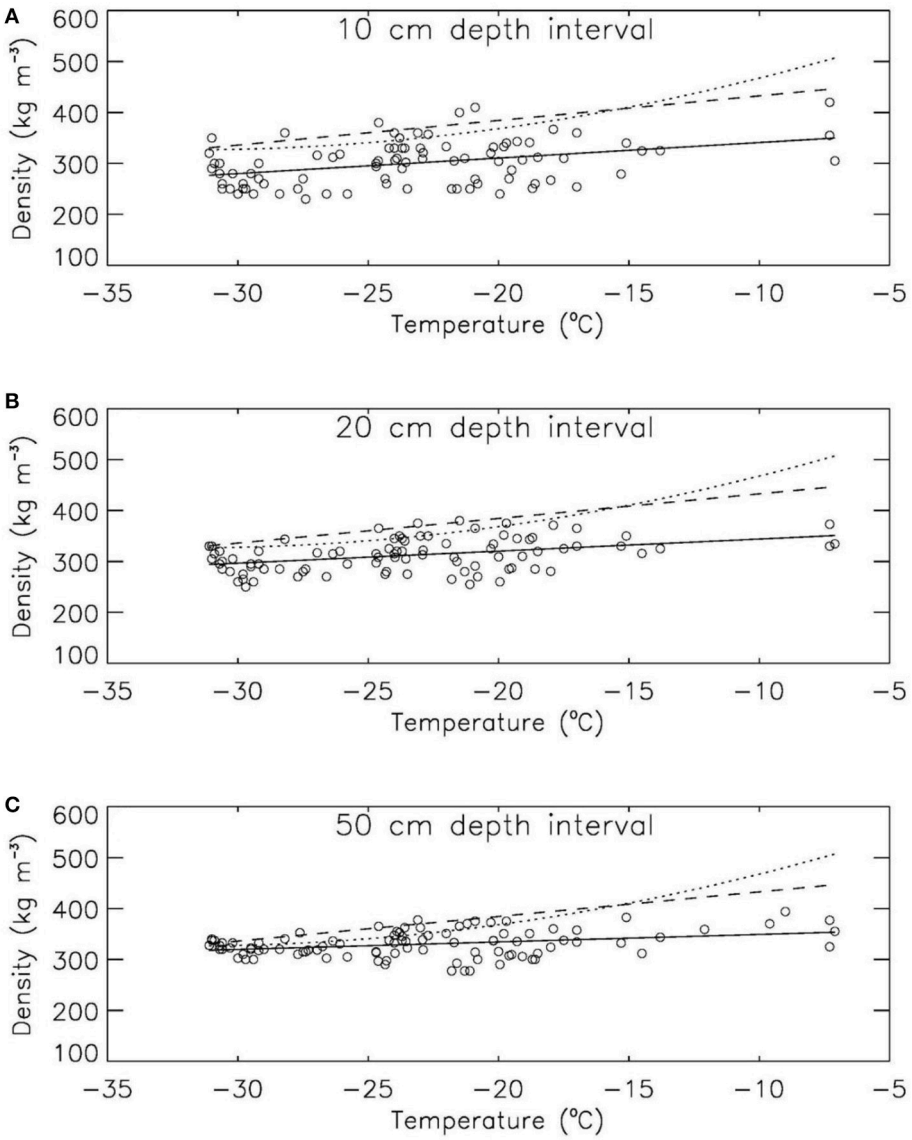

FIGURE 4 | Orthogonal linear regression fits (solid lines) for temperature-dependent parameterization P1 (**Table 1**) for **(A)** depth range 0–0.1 m, **(B)** depth range 0–0.2 m, and **(C)** depth range 0–0.5 m. Circles represent our observational dataset. Parameterizations by Kuipers Munneke et al. (2015) and Reeh et al. (2005) are plotted as dashed and dotted lines, respectively.

2014), resulting in wind-packing of fresh surface snow within days.

Temperature Dependence

Higher air temperatures result in higher snow and firn densities through increased compaction (Zwally and Li, 2002). It is therefore desirable to ensure that parameterizations of surface snow density remain appropriate even as the climate changes (e.g., Reeh et al., 2005; Morris and Wingham, 2014). Studies of Greenland accumulation rates and firn properties document a recent densification in the overall firn column and attribute it to climate warming (e.g., de la Peña et al., 2015; Charalampidis et al., 2016a; Machguth et al., 2016; Overly et al., 2016). If we assume that temperature-dependent densification processes are responsible for the transformation of freshly-fallen snow to the surface snow densities of our dataset, the inclusion of temperature as a variable in a parameterization (Equation 1) explicitly accounts for atmospheric warming. In this case, a parameterization is better capable of representing changing surface conditions due to climate variability. For instance, our temperature-dependent parameterization suggests that the observed 2.7°C warming at Summit over the period 1982–2011 (McGrath et al., 2013) had lead to a local surface snow density increase of 8 kg m^{-3}. But even a large temperature increase of 10°C anywhere in Greenland would only cause a densification of 28 kg m^{-3} in the top 0.1 m of snow, which

is smaller than the 32 kg m^{-3} measurement uncertainty and 44 kg m^{-3} standard deviation of the dataset (**Table 2**). For larger depth ranges the temperature sensitivity (*B*-values in P1, see **Table 2**) is considerably smaller and thus more insignificant given the measurement uncertainty and natural variability. The insignificant densification as a result of warming supports the notion that temperature is a poor predictor of the variability of surface snow density in the top 0.1, 0.2, and 0.5 m of snow/firn, and that using a constant value may be preferable in some applications.

Modeling Implications and Limitations

The choice of a surface snow density boundary condition influences calculations of available pore space by models simulating the surface mass budget of the Greenland ice sheet. Steger et al. (2017) discussed the limitations and inaccuracies of their Greenland ice sheet surface mass budget simulations by regional climate model RACMO2.3, and conclude that the Kuipers Munneke et al. (2015) parameterization systematically overestimates surface snow density, impacting pore space available for refreezing at depth. Langen et al. (2015) and Charalampidis et al. (2016b) applied a constant surface snow density value of 330 kg m^{-3} in regional climate model HIRHAM5, while Langen et al. (2017) applied a parameterization depending on latitude, longitude and elevation, derived from our dataset, in a new model version. The latter study found that the parameterization yields an ice-sheet-wide average of surface snow density that is 7% lower than using a constant density value of 330 kg m^{-3}, signifying a higher meltwater retention capacity in the snow and firn. Langen et al. (2017) also documented that the firn density profiles simulated by HIRHAM5 using their parameterization satisfactorily resemble measured profiles. Yet based on our own findings we suspect that using a constant surface snow density value of 315 $\pm$ 32 kg m^{-3} as boundary condition, a value 5% lower than that used by Langen et al. (2015), should perform equally well in Greenland-wide surface mass budget simulations.

Using our dataset for the top 0.1 m of snow, as opposed to using those for larger depth ranges, comes at the cost of a higher variability (standard deviation in **Table 2**) due to a larger influence of meteorology-dependent processes like snow drift (Brun et al., 1997; Hörhold et al., 2011; Koenig et al., 2016). The larger variability could also stem from snowfall events depositing more than 0.1 m of snow. Layers below the top 0.1 m are not much influenced by wind compaction, snow drift and redistribution, and will primarily be subject to the less efficient densification through rounding or settling of snow grains from vapor fluxes in the subsurface layers (e.g., Albert and Shultz, 2002). Surface mass budget models using our constant value of 315 kg m^{-3} for the top 0.1 m of snow may therefore misrepresent relatively low-density layers below 0.1 m depth deposited during large snowfall events. Regions where snowfall may exceed 0.1 m in single events are typically located at lower elevations on the southern and southeastern parts of the ice sheet (e.g., Burgess et al., 2010).

Our dataset has sparse coverage in the northern and eastern sectors of the ice sheet, possibly introducing a spatial bias in our results. **Figure 5** illustrates that the elevation distribution of our measurement locations broadly reflects the overall area-elevation distribution of the ice sheet as determined from the GIMP digital elevation model (Howat et al., 2014). Some lower elevation ranges (1,000–1,750 m above sea level) are relatively underrepresented in our dataset, while some higher elevation ranges are comparatively overrepresented. Our parameterization could benefit from acquiring additional measurements from elevations between 1,000 and 1,750 m above sea level, i.e., in the lower percolation area of the ice sheet (Benson, 1962). The lower percolation area is considered crucial for properly determining the surface mass budget, as firn properties influencing meltwater retention capacity vary substantially across the ice sheet (Van As et al., 2016a; Langen et al., 2017).

CONCLUSIONS

We constructed a dataset of surface snow density for the top 0.1, 0.2, and 0.5 m of snow/firn on the Greenland ice sheet based on 200 *in situ* measurements collected during the 1953–2016 timespan. We found that only the annual air temperature has a weak predictive skill of surface snow density in the construction of a temperature-dependent parameterization. Our parameterization yields surface snow densities of 32–72 kg m^{-3} (8–19%) lower than earlier parameterizations do, thus beyond the 32 kg m^{-3} measurement uncertainty range. Yet since the natural variability in surface snow density is found to be large with e.g., a 44 kg m^{-3} standard deviation for the top 0.1 m of snow, the temperature sensitivity of surface snow density is not found to be significant, indicating that an average surface snow density of 315 kg m^{-3} could be the preferred choice as a boundary

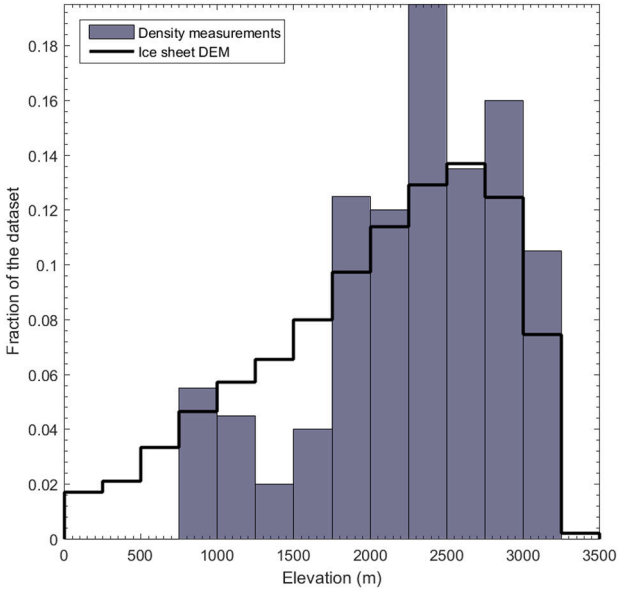

FIGURE 5 | Elevation distribution of the surface snow density measurement locations compared to the area-elevation distribution of the entire Greenland ice sheet.

condition for models calculating the surface mass budget of the Greenland ice sheet.

AUTHOR CONTRIBUTIONS

RF conceived the study and wrote the manuscript; BV and RF did the statistical analysis. All authors contributed with field data and continuously discussed the results and developed the analysis further.

ACKNOWLEDGMENTS

This work was supported by the Danish Research Council Grant FNU 4002-00234 and the Programme for Monitoring of the Greenland Ice Sheet (www.promice.dk). The author team would like to thank all the reviewers and scientific editor, T. Bartholomaus, for help and constructive criticism, which improved the manuscript significantly. We acknowledge J. T. M. Lenaerts for a collegial review and valuable comments. LK was supported by NASA Cryospheric Sciences program NASA Award NNX1 5AC62G.

SUPPLEMENTARY MATERIAL

The Supplementary Material for this article can be found online at: https://www.frontiersin.org/articles/10.3389/feart.2018.00051/full#supplementary-material

Data Sheet 1 | Surface density dataset consists of point observations (0–10, 0–20, 0–50 cm), along with the geographic location, annual air temperature and annual accumulation rates.

REFERENCES

Albert, M. R., and Shultz, E. F. (2002). Snow and firn properties and air-snow transport processes at Summit, Greenland. *Atmos. Environ.* 36, 2789–2797. doi: 10.1016/S1352-2310(02)00119-X

Aschwanden, A., Bueler, E., Khroulev, C., and Blatter, H. (2012). An enthalpy formulation for glaciers and ice sheets. *J. Glaciol.* 58, 441–457. doi: 10.3189/2012JoG11J088

Benson, C. S. (1962). Stratigraphic studies in the snow and firn of the Greenland ice sheet. *SIPRE. Res. Rep.* 70, 1–93.

Braithwaite, R. J., Clement, P., and Clausen, H. (1982). Inferences from a 19 m firn core, Nordbogletscher, South Greenland. *Rapp. Grønlands Geol. Unders.* 110, 96–98.

Braithwaite, R. J., Laternser, M., and Pfeffer, W. T. (1994). Variations of near-surface firn density in the lower accumulation area of the Greenland ice sheet, Pakitsoq, West Greenland. *J. Glaciol.* 40, 477–485. doi: 10.1017/S002214300001234X

Brun, E., Martin, E., and Spiridonov, V. (1997). Coupling a multi-layered snow model with a GCM. *Ann. Glaciol.* 25, 66–72. doi: 10.3189/S0260305500013811

Burgess, E. W., Forster, R. R., Box, J. E., Mosley-Thompson, E., Bromwich, D. H., Bales, R. C., et al. (2010). A spatially calibrated model of annual accumulation rate on the Greenland ice sheet (1958–2007). *J. Geophys. Res. Earth Surf.* 115:F02004. doi: 10.1029/2009JF001293

Charalampidis, C., Van As, D., Colgan, W. T., Fausto, R. S., Macferrin, M., and Machguth, H. (2016a). Thermal tracing of retained meltwater in the lower accumulation area of the Southwestern Greenland ice sheet. *Ann. Glaciol.* 57, 1–10. doi: 10.1017/aog.2016.2

Charalampidis, C., Van As, D., Langen, P. L., Fausto, R. S., Vandecrux, B., and Box, J. E. (2016b). Regional climate-model performance in Greenland firn derived from *in situ* observations. *Geol. Surv. Denmark Greenland Bull.* 35, 75–78.

Colgan, W., Abdalati, W., Citterio, M., Csatho, B., Fettweis, X., Luthcke, S., et al. (2015). Hybrid glacier inventory, Gravimetry and Altimetry (HIGA) mass balance product for Greenland and the Canadian Arctic. *Rem. Sens. Environ.* 168, 24–39. doi: 10.1016/j.rse.2015.06.016

Conger, S. M., and McClung, D. M. (2009). Comparison of density cutters for snow profile observations. *J. Glaciol.* 55, 163–169. doi: 10.3189/002214309788609038

Csatho, B. M., Schenk, A. F., Van der Veen, C. J., Babonis, G., Duncan, K., Rezvanbehbahani, S., et al. (2014). Laser altimetry reveals complex pattern of Greenland ice sheet dynamics. *Proc. Nat. Acad. Sci. U.S.A.* 111, 18478–18483. doi: 10.1073/pnas.1411680112

de la Peña, S., Howat, I. M., Nienow, P. W., Van den Broeke, M. R., Mosley-Thompson, E., Price, S. F., et al. (2015). Changes in the firn structure of the western Greenland ice sheet caused by recent warming. *Cryosphere* 9, 1203–1211. doi: 10.5194/tc-9-1203-2015

de la Peña, S., Nienow, P., Shepherd, A., Helm, V., Mair, D., Hanna, E., et al. (2010). Spatially extensive estimates of annual accumulation in the dry snow zone of the Greenland ice sheet determined from radar altimetry. Cryosph*ere* 4, 467–474. doi: 10.5194/tc-4-467-2010

Dibb, J. E., and Fahnestock, M. (2004). Snow accumulation, surface height change, and firn densification at Summit, Greenland: insights from 2 years of *in situ* observation. *J. Geophys. Res.* 109:D24113. doi: 10.1029/2003JD004300

Fausto, R. S., Ahlstrøm, A., Van As, D., Johnsen, S. J., Langen, P. L., and Steffen, K. (2009). Improving surface boundary conditions with focus on coupling snow densification and meltwater retention in large-scale ice-sheet models of Greenland. *J. Glaciol.* 55, 869–878. doi: 10.3189/002214309790152537

Forster, R. R., Box, J. E., Van den Broeke, M. R., Miège, C., Burgess, E. W., Van Angelen, J. H., et al. (2013). Perennial liquid water discovered in Greenland firn layer. *Nat. Geosci.* 7, 95–98. doi: 10.1038/ngeo2043

Gallée, H., Trouvilliez, A., Agosta, C., Genthon, C., Favier, V., and Naaim-Bouvet, F. (2013). Transport of snow by the wind: a comparison between observations in Adélie Land, Antarctica, and simulations made with the regional climate model MAR. *Bound Lay. Meteorol.* 146, 133–147. doi: 10.1007/s10546-012-9764-z

Greve, R., Saito, F., and Abe-Ouchi, A. (2011). Initial results of the SeaRISE numerical experiments with the models SICOPOLIS and IcIES for the Greenland Ice Sheet. *Ann. Glaciol.* 52, 23–30. doi: 10.3189/172756411797252068

Harper, J., Humphrey, N., Pfeffer, W. T., Brown, J., and Fettweis, X. (2012). Greenland ice-sheet contribution to sea-level rise buffered by meltwater storage in firn. *Nature* 491, 240–243. doi: 10.1038/nature11566

Hawley, R. L., Courville, Z. R., Kehrl, L. M., Lutz, E. R., Osterberg, E. C., Overly, T. B., et al. (2014). Recent accumulation variability in Northwest Greenland from GPR and shallow cores along the Greenland inland traverse. *J. Glaciol.* 60, 375–382. doi: 10.3189/2014JoG13J141

Hawley, R. L., Morris, E. M., Cullen, R., Nixdorf, U., Shepherd, A. P., and Wingham, D. J. (2006). ASIRAS airborne radar resolves internal annual layers in the dry-snow zone of Greenland. *Geophys. Res. Lett.* 33:L04502. doi: 10.1029/2005GL025147

Hörhold, M. W., Kipfstuhl, S., Wilhelms, F., Freitag, J., and Frenzel, A. (2011). The densification of layered polar firn. *J. Geophys. Res.* 116:F01001. doi: 10.1029/2009JF001630

Howat, I. M., Negrete, A., and Smith, B. E. (2014). The Greenland Ice Mapping Project (GIMP) land classification and surface elevation datasets. *Cryosphere* 8, 1509–1518. doi: 10.5194/tc-8-1509-2014

Humphrey, N. F., Harper, J. T., and Pfeffer, W. T. (2012). Thermal tracking of meltwater retention in Greenland's accumulation area. *J. Geophys. Res. Earth Surf.* 117:F01010. doi: 10.1029/2011JF002083

Hurkmans, R. T. W. L., Bamber, J. L., Davis, C. H., Joughin, I. R., Khvorostovsky, K. S., Smith, B. S., et al. (2014). Time-evolving mass loss of the Greenland ice sheet from satellite altimetry. *Cryosphere* 8, 1725–1740. doi: 10.5194/tc-8-1725-2014

IPCC. (2013). *Climate Change 2013: the Physical Science Basis*. Contribution of Working Group I to the Fifth Assessment Report of the Intergovernmental Panel on Climate Change, eds T. F. Stocker, D. Qin, G.-K. Plattner, M. Tignor, S. K. Allen, J. Boschung et al. (Cambridge, New York, NY: Cambridge University Press), 1535.

Karlsson, N. B., Eisen, O., Dahl-Jensen, D., Freitag, J., Kipfstuhl, S., Lewis, C., et al. (2016). Accumulation rates during 1311-2011 CE in north-central Greenland derived from air-borne radar data. *Front. Earth Sci*. 4:97. doi: 10.3389/feart.2016.00097

Khan, S. A., Aschwanden, A., Bjørk, A. A., Wahr Kjeldsen, K. K., and Kjær, K. H. (2015). Greenland ice sheet mass balance: a review. *Rep. Prog. Phys*. 78:046801. doi: 10.1088/0034-4885/78/4/046801

Kjeldsen, K. K., Korsgaard, N. J., Bjørk, A. A., Khan, S. A., Box, J. E., Funder, S., et al. (2015). Spatial and temporal distribution of mass loss from the Greenland ice sheet since AD 1900. *Nature* 528, 396–400. doi: 10.1038/nature16183

Koenig, L., Box, J., and Kurtz, N. (2013). Improving surface mass balance over ice sheets and snow depth on sea ice. *Eos Trans. AGU* 94:100. doi: 10.1002/2013EO100006

Koenig, L. S., Ivanoff, A., Alexander, P. M., MacGregor, J. A., Fettweis, X., Panzer, B., et al. (2016). Annual Greenland accumulation rates (2009–2012) from airborne snow radar. *Cryosphere* 10, 1739–1752. doi: 10.5194/tc-10-1739-2016

Koenig, L. S., Miège, C., Forster, R. R., and Brucker, L. (2014). Initial *in situ* measurements of perennial meltwater storage in the Greenland firn aquifer. *Geophys. Res. Lett*. 41, 81–85. doi: 10.1002/2013GL058083

Kojima, K. (1967). "Densification of seasonal snow cover," in *Physics of Snow and Ice*, ed. H. Oura (Sapporo: Institute of Low Temperature Science, Hokkaido University), 929–952.

Kotlyakov, V. M. (1961). Results of a study of the process of formation and structure of the upper layer of the ice sheet in eastern Antarctica. *Antarctic Glaciol.* 55, 88–99.

Kuipers Munneke, P., Ligtenberg, S. R. M., Noël, B. P. Y., Howat, I. M., Box, J. E., Mosley-Thompson, E., et al. (2015). Elevation change of the Greenland ice sheet due to surface mass balance and firn processes 1960–2014. *Cryosphere* 9, 2009–2025. doi: 10.5194/tc-9-2009-2015

Langen, P. L., Fausto, R. S., Vandecrux, B., Mottram, R. H., and Box, J. E. (2017). Liquid water flow and retention on the Greenland ice sheet in the regional climate model HIRHAM5: local and large-scale impacts. *Front. Earth Sci*. 4:110. doi: 10.3389/feart.2016.00110

Langen, P. L., Mottram, R. H., Christensen, J. H., Boberg, F., Rodehacke, C. B., Stendel, M., et al. (2015). Quantifying energy and mass fluxes controlling Godthåbsfjord freshwater input in a 5 km simulation (1991–2012). *J. Climate*. 28, 3694–3713. doi: 10.1175/JCLI-D-14-00271.1

Lewis, G., Osterberg, E., Hawley, R., Whitmore, B., Marshall, H. P., and Box, J. E. (2017). Regional Greenland accumulation variability from operation IceBridge airborne accumulation radar. *Cryosphere* 11, 773–788. doi: 10.5194/tc-11-773-2017

Li, J., and Zwally, H. J. (2011). Modeling of firn compaction for estimating ice-sheet mass change from observed ice-sheet elevation change. *Ann. Glaciol*. 52, 1–7. doi: 10.3189/172756411799096321

Ligtenberg, S. R. M., Helsen, M. M., and Van den Broeke, M. R. (2011). An improved semi-empirical model for the densification of Antarctic firn. *Cryosphere* 5, 809–819. doi: 10.5194/tc-5-809-2011

Liston, G. E., Haehnel, R. B., Sturm, M., Hiemstra, C. A., Berezovskaya, S., and Tabler, R. D. (2007). Simulating complex snow distributions in windy environments using SnowTran-3D. *J. Glaciol*. 53, 241–256. doi: 10.3189/172756507782202865

López-Moreno, J. I., Olivera-Marañón, M., Zabalza, J., and Larramendi, R. H. (2016). Snowpack observations from a circumnavigation of the Greenland Ice Sheet. *Cuad. Invest. Geográf.* 42, 369–381.

Machguth, H., MacFerrin, M., Van As, D., Box, J. E., Charalampidis, C., Colgan, W., et al. (2016). Greenland meltwater storage in firn limited by near-surface ice formation. *Nat. Clim. Change* 6, 390–393. doi: 10.1038/nclimate2899

McGrath, D., Colgan, W., Bayou, N., Muto, A., and Steffen, K. (2013). Recent warming at Summit, Greenland: global context and implications. *Geophys. Res. Lett.* 40, 2091–2096. doi: 10.1002/grl.50456

Miège, C., Forster, R. R., Box, J. E., Burgess, E. W., McConnell, J. R., Pasteris, D. R., et al. (2013). Southeast Greenland high accumulation rates derived from firn cores and ground-penetrating radar. *Ann. Glaciol*. 54, 322–332. doi: 10.3189/2013AoG63A358

Miège, C., Forster, R. R., Brucker, L., Koenig, L. S., Solomon, D. K., Paden, J. D., et al. (2016). Spatial extent and temporal variability of Greenland firn aquifers detected by ground and airborne radars. *J. Geophys. Res. Earth Surf*. 121, 2381–2398. doi: 10.1002/2016JF003869

Mock, S. J., and Weeks, W. F. (1965). The distribution of ten-meter snow temperatures on the Greenland ice sheet. *CRREL Rep*. 170, 1–44.

Montgomery, L., Koenig, L., and Alexander, P. (2018). The SUMup Dataset: compiled measurements of surface mass balance components over ice sheets and sea ice with preliminary analysis over Greenland. *Earth Syst. Sci. Data Discuss*. doi: 10.5194/essd-2018-21

Morris, E. M., and Wingham, D. J. (2014). Densification of polar snow: measurements, modeling, and implications for altimetry. *J. Geophys. Res. Earth Surf*. 119, 349–365. doi: 10.1002/2013JF002898

Mosley-Thompson, E., McConnell, J. R., Bales, R. C., Li, Z., Lin, P.-N., Steffens, K., et al. (2001). Local to regional scale variability of annual net accumulation on the Greenland ice sheet from PARCA cores. *J. Geophys. Res.*106, 33839–33851. doi: 10.1029/2001JD900067

Noël, B., Fettweis, X., Van de Berg, W. J., Van den Broeke, M. R., and Erpicum, M. (2014). Sensitivity of Greenland ice sheet surface mass balance to perturbations in sea surface temperature and sea ice cover: a study with the regional climate model MAR. *Cryosphere* 8, 1871–1883. doi: 10.5194/tc-8-1871-2014

Overly, T. B., Hawley, R. L., Helm, V., Morris, E. M., and Chaudhary, R. N. (2016). Greenland annual accumulation along the EGIG line, 1959-2004, from ASIRAS airborne radar and neutron-probe density measurements. *Cryosphere* 10, 1679–1694. doi: 10.5194/tc-10-1679-2016

Pahaut, E. (1976). *La Métamorphose des Cristaux de Neige (Snow crystal metamorphosis), 96, Monographies de la Météorologie Nationale*. Paris: Météo France.

Polashenski, C., Courville, Z., Benson, C., Wagner, A., Chen, J., Wong, G., et al. (2014). Observations of pronounced Greenland ice sheet firn warming and implications for runoff production. *Geophys. Res. Lett*. 41, 4238–4246. doi: 10.1002/2014GL059806

Proksch, M., Löwe, H., and Schneebeli, M. (2015). Density, specific surface area, and correlation length of snow measured by high-resolution penetrometry. *J. Geophys. Res. Earth Surf.* 120, 346–362, doi: 10.1002/2014JF003266

Proksch, M., Rutter, N., Fierz, C., and Schneebeli, M. (2016). Intercomparison of snow density measurements: bias, precision, and vertical resolution .*Cryosphere* 10, 371–384. doi: 10.5194/tc-10-371-2016

Reeh, N., Fisher, D. A., Koerner, R. M., and Clausen, H. B. (2005). An empirical firn-densification model comprising ice lenses. *Ann. Glaciol*. 42, 101–106. doi: 10.3189/172756405781812871

Schaller, C. F., Freitag, J., Kipfstuhl, S., Laepple, T., Steen-Larsen, H. C., and Eisen, O. (2016). A representative density profile of the North Greenland snowpack. *Cryosphere* 10, 1991–2002. doi: 10.5194/tc-10-1991-2016

Shepherd, A., Ivins, E. R., Geruo, A., Barletta, V. R., Bentley, M. J., Bettadpur, S., et al. (2012). A reconciled estimate of ice-sheet mass budget. *Science* 338, 1183–1189. doi: 10.1126/science.1228102

Simonsen, S. B., Stenseng, L., Adalgeirsdóttir, G., Fausto, R. S., Hvidberg, C. S., and Lucas-Picher, P. (2013). Assessing a multilayered dynamic firn-compaction model for Greenland with ASIRAS radar measurements. *J. Glaciol*. 59, 545–558. doi: 10.3189/2013JoG12J158

Sørensen, L. S., Simonsen, S. B., Nielsen, K., Lucas-Picher, P., Spada, G., Adalgeirsdottir, G., et al. (2011). Mass balance of the Greenland ice sheet (2003–2008) from ICESat data: the impact of interpolation, sampling and firn density. *Cryosphere* 5, 173–186. doi: 10.5194/tc-5-173-2011

Steffen, K., Box, J. E., and Abdalati, W. (1996). "Greenland climate network: GC-Net," in *CRREL 96-27 Special Report on Glaciers, Ice Sheets and Volcanoes*, ed S. C. Colbeck, 98–103.

Steger, C. R., Reijmer, C. H., Van den Broeke, M. R., Wever, N., Forster, R. R., Koenig, L. S., et al. (2017). Firn meltwater retention on the Greenland ice sheet: a model comparison. *Front. Earth Sci.* 5:3. doi: 10.3389/feart.2017.00003

Thomas, R. H., and PARCA Investigators (2001). Program for Arctic Regional Climate Assessment (PARCA): goals, key findings, and future directions. *J. Geophys. Res.* 106, 33691–33705. doi: 10.1029/2001JD900042

Van As, D., Box, J. E., and Fausto, R. S. (2016a). Challenges of quantifying meltwater retention in snow and firn: an expert elicitation. *Front. Earth Sci.* 4:101. doi: 10.3389/feart.2016.00101

Van As, D., Fausto, R. S., Cappelen, J., Machguth, H., Van de Wal, R. S. W., and the PROMICE project team (2016b). Placing Greenland ice sheet ablation measurements in a multi-decadal context. *Geol. Surv. Denmark Greenland Bull.* 35, 71–74.

Van As, D., Fausto, R. S., Colgan, W. T., Box, J. E., Ahlstrøm, A. P., Andersen, S. B., et al. (2013). Darkening of the Greenland ice sheet due to the melt albedo feedback observed at PROMICE weather stations. *Geol. Surv. Denmark Greenland Bull.* 28, 69–72.

Van den Broeke, M. R., Enderlin, E. M., Howat, I. M., Kuipers Munneke, P., Noël, B. P. Y., Van de Berg, W. J., et al. (2016). On the recent contribution of the Greenland ice sheet to sea level change. *Cryosphere* 10, 1933–1946. doi: 10.5194/tc-10-1933-2016

Vionnet, V., Brun, E., Morin, S., Boone, A., Faroux, S., Le Moigne, P., et al. (2012). The detailed snowpack scheme Crocus and its implementation in SURFEX v7. 2. *Geosci. Model. Dev.* 5, 773–791. doi: 10.5194/gmd-5-773-2012

Zwally, H. J., and Li, J. (2002). Seasonal and interannual variations of firn densification and ice-sheet surface elevation at the Greenland summit. *J. Glaciol.* 48, 199–207. doi: 10.3189/172756502781831403

Conflict of Interest Statement: The authors declare that the research was conducted in the absence of any commercial or financial relationships that could be construed as a potential conflict of interest.

The reviewer, CM, declared a past collaboration with two of the authors, JB and LK, to the handling editor.

frontiers in Earth Science

ORIGINAL RESEARCH
published: 25 November 2016
doi: 10.3389/feart.2016.00102

The Changing Impact of Snow Conditions and Refreezing on the Mass Balance of an Idealized Svalbard Glacier

Ward J. J. van Pelt[1]*, *Veijo A. Pohjola*[1] and *Carleen H. Reijmer*[2]

[1] Department of Earth Sciences, Uppsala University, Uppsala, Sweden, [2] Institute for Marine and Atmospheric Research Utrecht, Utrecht University, Utrecht, Netherlands

Glacier surface melt and runoff depend strongly on seasonal and perennial snow (firn) conditions. Not only does the presence of snow and firn directly affect melt rates by reflecting solar radiation, it may also act as a buffer against mass loss by storing melt water in refrozen or liquid form. In Svalbard, ongoing and projected amplified climate change with respect to the global mean change has severe implications for the state of snow and firn and its impact on glacier mass loss. Model experiments with a coupled surface energy balance—firn model were done to investigate the climatic mass balance and the changing role of snow and firn conditions for an idealized Svalbard glacier. A climate forcing for the past, present and future (1984–2104) is constructed, based on observational data from Svalbard Airport and a seasonally dependent projection scenario. With this forcing we mimic conditions for a typical inland Svalbard glacier. Results illustrate ongoing and future firn degradation in response to an elevational retreat of the equilibrium line altitude (ELA) of 31 m decade^{-1}. The temperate firn zone is found to retreat and expand, while cold ice in the ablation zone warms considerably. In response to pronounced winter warming and an associated increase in winter rainfall, the current prevalence of refreezing during the melt season gradually shifts to the winter season in a future climate. Sensitivity tests reveal that in a present and future climate the density and thermodynamic structure of Svalbard glaciers are heavily influenced by refreezing. Refreezing acts as a net buffer against mass loss. However, the net mass balance change after refreezing is substantially smaller than the amount of refreezing itself, which can be ascribed to melt-enhancing effects after refreezing, which partly offset the primary mass-retaining effect of refreezing.

Keywords: Svalbard, mass balance, snow, future, climate change, refreezing

OPEN ACCESS

Edited by:
Horst Machguth, University of Zurich, Switzerland

Reviewed by:
Koji Fujita, Nagoya University, Japan
Kjetil Schanke Aas, University of Oslo, Norway

***Correspondence:**
Ward J. J. van Pelt
ward.van.pelt@geo.uu.se

Specialty section:
This article was submitted to Cryospheric Sciences, a section of the journal Frontiers in Earth Science

Received: *29 August 2016*
Accepted: *11 November 2016*
Published: *25 November 2016*

Citation:
van Pelt WJJ, Pohjola VA and Reijmer CH (2016) The Changing Impact of Snow Conditions and Refreezing on the Mass Balance of an Idealized Svalbard Glacier. Front. Earth Sci. 4:102. doi: 10.3389/feart.2016.00102

1. INTRODUCTION

During the most recent decades, Arctic temperatures have increased at an amplified rate compared to the global mean (ACIA, 2005; IPCC, 2013), which has been ascribed to retreating sea-ice cover and resulting ice—atmosphere feedbacks (Serreze and Francis, 2006; Bintanja and van der Linden, 2013). Additionally, precipitation in the Arctic has increased in recent decades in response to

atmospheric moistening (Min et al., 2008; Zhang et al., 2012). Increases in both precipitation and temperature in the Arctic are projected to accelerate during the remainder of the twenty-first century (Bengtsson et al., 2011; Bintanja and Selten, 2014).

The climate on the high-Arctic archipelago of Svalbard, located at the northern end of the Atlantic warm water current, is highly sensitive to variability and trends in winter-time sea-ice extent (Divine and Dick, 2006; Day et al., 2012), as well as changes in atmospheric circulation patterns (Hanssen-Bauer and Førland, 1998). Observed temperatures at Svalbard Airport, Longyearbyen, between 1898–2012 show a marked positive mean trend of 0.26°C decade^{-1} (Nordli et al., 2014). A strong seasonal contrast prevails in observed temperature trends with markedly more pronounced warming in winter/spring than in summer (Førland et al., 2011; Bintanja and van der Linden, 2013; Nordli et al., 2014). Observational precipitation records in Svalbard since the early and mid-twentieth century reveal weakly positive trends, with low significance due to substantial local-scale and instrumental uncertainty (Førland and Hanssen-Bauer, 2000). Projections for Svalbard, based on empirical downscaling, indicate a continued modest precipitation increase and a three times higher warming rate up to the year 2100 than observed over the last 100 years (Førland et al., 2011).

Changing temperature and precipitation conditions affect the energy and mass balance of Svalbard glaciers. Estimates of the multi-decadal mass balance of all Svalbard glaciers, disregarding frontal ablation, are close to zero with values ranging between −0.05 m w.e. a^{-1} for 1979–2013 (Lang et al., 2015) and 0.08 m w.e. a^{-1} for 1957–2014 (Østby et al., in review). Frontal calving of tide-water glaciers is a substantial mass loss term and has been estimated at −0.18 m w.e. a^{-1} for 2000–2006 (Blaszczyk et al., 2009). Altogether, recent warming has enhanced glacier thinning, which has been estimated at −0.59 m a^{-1} for 1961–2005, based on airborne/satellite altimetry for six glaciers around Svalbard (James et al., 2012). As a dynamic response to glacier thinning, glaciers in Svalbard have shrunk by 7% of their total area during the past 30 years for a sample of around 400 glaciers (Nuth et al., 2013).

The interaction between a glacier surface, the atmosphere above and the underlying snow/firn determines the climatic mass balance. The climatic mass balance is defined as the sum of the surface mass balance, due to surface accumulation and ablation, and the internal mass balance (Cogley et al., 2011). Rising temperature induces more surface melting, but the timing and rate of melt water discharge depends strongly on the presence and state of seasonal snow and firn. Snow acts as a buffer against mass loss due to its mirroring effect on solar radiation, which reduces heat absorption and surface melt, and because it can store percolating melt water in either solid (refrozen) or liquid form. Refreezing of percolating and stored water in snow and firn contributes significantly to the mass balance of glaciers and ice sheets and has a pronounced impact on subsurface temperature and density (Jania et al., 1996; Wright et al., 2007; Reijmer et al., 2012). It is generally most pronounced in accumulation zones and peaks in spring when first melt enters the cold snow pack and in fall when the cold wave induces refreezing of stored liquid water.

While there has been much focus on the direct mass-retaining effect of refreezing (e.g., Pfeffer et al., 1991; Reijmer et al., 2012), there has been considerably less attention for the role of indirect effects after refreezing. The primary mass balance effect of refreezing is to retain melt/rain water in refrozen form, thereby reducing the fraction of melt/rain water that runs off. At the same time heat release and solid mass retention by refreezing affect the thermodynamic state and stratigraphy of the snow pack, thereby affecting the conductive heat flux and potentially the surface albedo, which in turn influence surface melt and runoff. A detailed assessment of the impact of refreezing on the mass balance of glaciers requires a coupled treatment of surface and snow processes, and is highly relevant for modeling melt and discharge of Arctic glaciers.

In a warming climate, higher melt rates lead to firn densification and thinning, ultimately causing a retreat of the perennial snow cover to higher elevations. Rapid near-surface densification in lower accumulation zones in south-west Greenland (Machguth et al., 2016) and western Svalbard (Van Pelt and Kohler, 2015) are manifestations of this. Shrinking accumulation zones (1) amplify melt rates in summer due to increased bare-ice exposure (ice—albedo feedback), and (2) reduce the potential for melt water retention by refreezing. Both effects reduce the buffering role of snow and firn against mass loss in a warming climate (e.g., Van Angelen et al., 2013; Van Pelt and Kohler, 2015).

Our aim with this study is to investigate the changing state of snow and firn conditions in Svalbard and its impact on glacier mass loss in a past, present and future climate (1984–2104). Numerical simulations are done with a coupled surface energy balance—firn model (EBFM; Van Pelt et al., 2012; Van Pelt and Kohler, 2015), on a synthetic elevation-dependent grid. We attempt to simulate evolving surface and snow/firn conditions along the centerline of an idealized inland Svalbard glacier. Such a set-up facilitates an analysis with a focus on the process understanding and helps to identify the role of feedback mechanisms. The constructed climate forcing relies on variability from the Svalbard Airport meteorological station, a seasonally-dependent future projection scenario (Førland et al., 2011), and observation-based elevation lapse rates. The model, climate forcing and experimental setup are described in Section 2. Model results are analyzed and discussed in Section 3. Finally, conclusions and recommendations are given in Section 4.

2. METHODS

2.1. Model

A coupled energy balance—firn model (EBFM) is used to perform simulations on a synthetic elevation dependent grid. Here, we briefly summarize the main qualitative model aspects; for a more complete overview of the coupled model and its implementation, see Van Pelt et al. (2012) and Van Pelt and Kohler (2015) and references therein. The model has previously been used to study the mass balance and firn evolution of Nordenskiöldbreen in central Svalbard (Van Pelt et al., 2012, 2013, 2014; Vega et al., 2016), and Kongsvegen and

Holtedahlfonna in western Svalbard (Christianson et al., 2015; Van Pelt and Kohler, 2015).

Driven by meteorological fields, at every model time-step a surface energy balance model sums the heat fluxes at the surface in order to determine the surface temperature and the energy involved in melting:

$$Q_{\text{melt}} = Q_{\text{sw}} + Q_{\text{lw}} + Q_{\text{turb}} + Q_{\text{ghf}} + Q_{\text{rain}}, \quad (1)$$

where Q_{melt} is the energy available for melt, Q_{sw} is the net shortwave radiation, Q_{lw} is the net longwave radiation, Q_{turb} is the turbulent heat exchange by the latent and sensible heat flux, Q_{ghf} is the conductive ground heat flux, and Q_{rain} is the energy supplied by rainfall. The surface temperature is limited to 0°C, any excess energy results in melting of the surface layer ($Q_{\text{melt}} > 0$). Formulations of the individual energy fluxes can be found in Klok and Oerlemans (2002); a qualitative description of the individual fluxes is given below.

In order to solve the surface energy balance climate input of air temperature, relative humidity, cloud cover and precipitation is required by this model. Cloud cover, temperature and relative humidity affect the incoming shortwave radiation, which depends on the top-of-atmosphere radiation, atmospheric transmissivity and the grid orientation (Klok and Oerlemans, 2002). Reflected shortwave radiation is determined by the albedo, following a snow depth and age dependent formulation (Oerlemans and Knap, 1998). Incoming longwave radiation is formulated as a function of cloud cover, relative humidity and air temperature (Konzelmann et al., 1994), while the Stefan-Boltzmann law for a black body describes emitted longwave radiation. The description of turbulent sensible and latent heat exchange uses bulk equations by Oerlemans and Grisogono (2002), requiring climate input of air temperature and relative humidity, respectively. The ground heat flux represents conduction between the surface skin layer and the underlying snow/ice and can take both signs depending on the near-surface temperature gradient. Finally, the heat supplied by rainfall depends on air temperature and is generally a small term. The model distinguishes between snow and rainfall by using a gradual (linear) transition from snow to rain between air temperatures of 0.5 and 2.5°C; hence, at a temperature of 1.5°C precipitation consists of 50% rain and snow (Van Pelt et al., 2012).

Energy and mass exchange at the surface provides an upper boundary condition for the subsurface model, tracking the evolution and vertical distribution of temperature, density and water content. The multi-layer subsurface model is based on Reijmer and Hock (2008) and later modified and extended by Van Pelt et al. (2012). The energy consumed in melting the surface may be released again as latent heat below the surface when percolating or stored water refreezes in snow or firn layers. The subsurface model solves the thermodynamic equation, accounting for heat conduction and refreezing:

$$\rho c_p(T)\frac{\partial T}{\partial t} = \frac{\partial}{\partial z}\left(\kappa(\rho)\frac{\partial T}{\partial z}\right) + \frac{RL}{d}, \quad (2)$$

where T is the layer temperature, ρ the layer density, $c_p(T)$ the specific heat capacity, $\kappa(\rho)$ the effective conductivity, R the refreezing rate (kg m^{-2} s^{-1}), L the latent heat of fusion and d the layer thickness. The subsurface model additionally solves the densification equation, considering refreezing and gravitational packing of the snow $G(\rho, T)$ (Ligtenberg et al., 2011):

$$\frac{\partial \rho}{\partial t} = G(\rho, T) + \frac{R}{d}. \quad (3)$$

Vertical water transport and refreezing is simulated using a bucket scheme (Greuell and Konzelmann, 1994; Reijmer and Hock, 2008; Van Pelt et al., 2012). Storage of percolating water occurs in two forms: (1) on its way down a small amount of water is held in temperate layers against capillary forces (irreducible water), and (2) water accumulates on top of impermeable ice to form a layer of slush water, thereby filling the remaining pore space. Runoff occurs at the firn-ice transition and is instantaneous in the case of bare-ice exposure and according to a slope-dependent time-scale for standing slush water within the snow-pack (Reijmer and Hock, 2008).

The climatic mass balance is a direct measure for mass changes resulting from the interaction of atmosphere, glacier surface and the underlying snow/firn (Cogley et al., 2011). It is therefore effectively a measure for mass change at and below the surface, down to the base of the snow or firn pack (if present). The climatic mass balance is defined here as the sum of mass gain, through precipitation and condensation/riming, and mass loss, through runoff and evaporation/sublimation. Refreezing may act as a buffer against mass loss where a firn/snowpack is present, as it reduces the amount of melt water that runs off. In our experiments the climatic mass balance is assumed to be equal to the sum of mass changes above the base of the model domain at 15–20 m depth; any potential refreezing below this depth is regarded as negligible.

2.2. Climate Forcing

2.2.1. Temporal Variability

In order to run the coupled model, meteorological input of precipitation, air temperature, cloud cover and relative humidity is required at a sub-daily temporal resolution. Meteorological data of the above parameters, collected at the coastal meteorological station at Svalbard Airport at 28 m a.s.l., Longyearbyen (Norwegian Meteorological Institute, eKlima.no) are used as time-series for 1975–2014. Six-hourly observations of temperature, cloud cover and relative humidity were interpolated to the 3-h model resolution, whereas observed 12-h precipitation sums were split into 3-h bins. The average temperature between 1 September 1975 and 31 August 2014 was equal to −5.0 °C, precipitation summed to 191 mm a^{-1}, mean relative humidity was equal to 74%, and average cloud cover was 64%.

Time-series of winter (DJF), spring (MAM), summer (JJA) and autumn (SON) mean observed temperature and precipitation between 1975–2014 (first 39 years in **Figure 1**), show a clear inhomogeneity in observed seasonal temperature trends. Over the observation period 1975–2014, winter warming (2.2°C decade^{-1}) exceeds summer warming (0.5°C decade^{-1}) by a factor of four. Much stronger winter than summer warming, referred to as Arctic winter warming (AWW), is one of the key

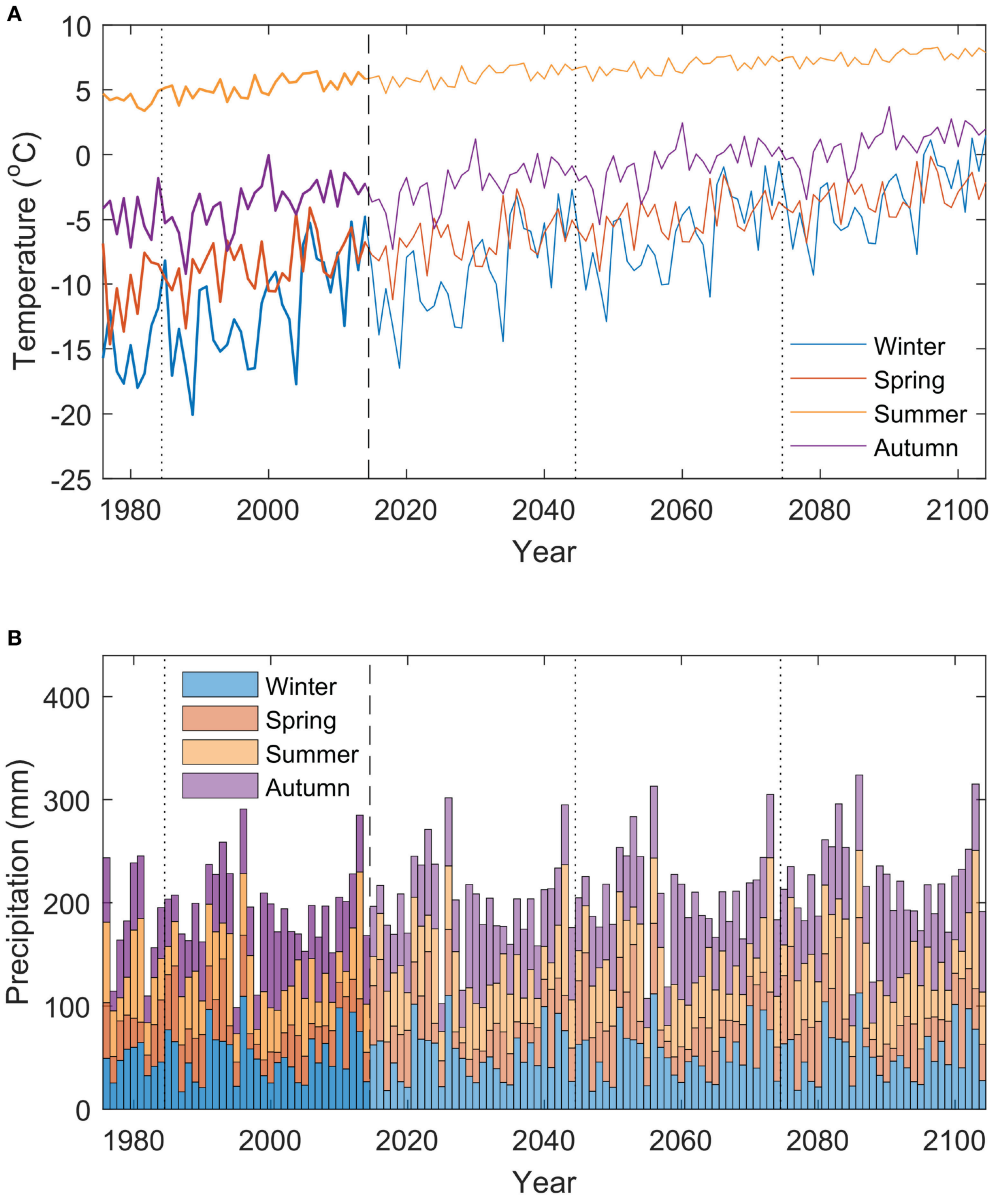

FIGURE 1 | Time-series of observed and projected winter (DJF), spring (MAM), summer (JJA) and autumn (SON) temperature (A) and precipitation **(B)** for the period 1975–2104.

features of Arctic Amplification and has been ascribed to the retreat of sea ice and the resulting ice—atmosphere feedbacks (Serreze and Francis, 2006; Bintanja and van der Linden, 2013).

Førland et al. (2011) used the NorACIA (Norwegian Arctic Climate Impact Assessment) regional climate model, with input from six atmosphere ocean general circulation model (AOGCM) simulations for a range of emission scenarios (A1B, A2, and B2), to simulate the past (1961–1990) and future (2071–2100) climate in the Svalbard region. The ensemble results present seasonal temperature and precipitation trends between 1961–1990 and 2071–2100, yielding linear seasonal temperature trends for Svalbard Airport of 1.0 (DJF), 0.6 (MAM), 0.3 (JJA) and 0.5°C decade^{-1} (SON) and precipitation trends of 0.4 (DJF), 2.6 (MAM), 1.0 (JJA), and 1.9 % decade^{-1} (SON) (Førland et al., 2011).

In addition to seasonal inhomogeneity in warming, at intra-seasonal time-scales (days to weeks) cold spells are found to warm faster than warm spells. This is apparent when comparing trends per season of above-average (upper 50%) and below-average (lower 50%) temperatures in the 1975–2014 Svalbard Airport record, as shown in **Figure 2**. Below-average temperatures were found to increase 1.5 (DJF), 2.1 (MAM), 2.1 (JJA), and 1.6 (SON) times faster than above-average temperatures, which indicates more rapid warming of cold spells for all seasons.

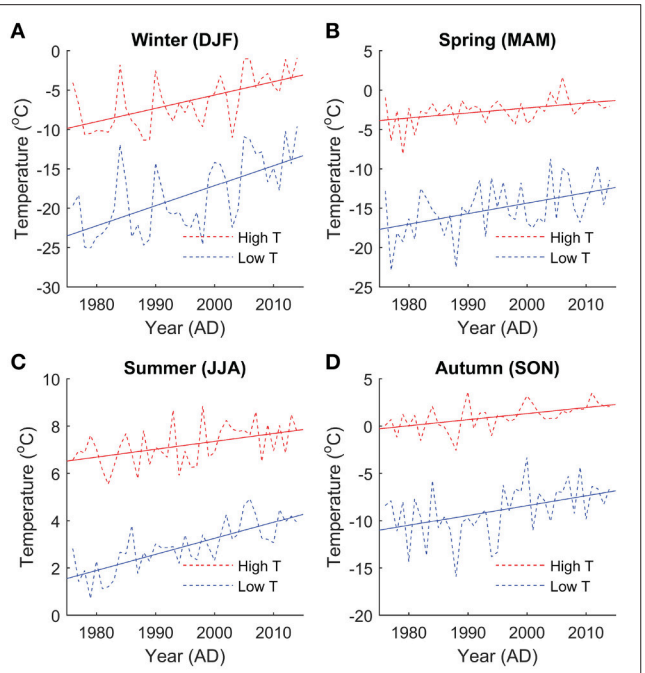

FIGURE 2 | Time-series of winter (DJF; A), spring (MAM; **B**), summer (JJA; **C**) and autumn (SON; **D**) temperature at Svalbard Airport for the period 1975–2104, averaged per year for above-average (upper 50%; dashed red line) and below-average (lower 50%; dashed blue line) values.

In order to extend the 1975–2014 climate forcing into the future, we first repeat variability of temperature, precipitation, cloud cover and relative humidity, observed at Svalbard Airport between 1984–2014, three times to cover the period 2014–2104. In a next step, we impose seasonal trends in temperature and precipitation, according to Førland et al. (2011). Finally, for the temperature projection we additionally account for the aforementioned inhomogeneity in warming of cold and warm spells, as observed in the Svalbard Airport record. More specifically, the following steps are applied to generate future time-series for temperature, precipitation, cloud cover and relative humidity:

1. Observed 3-h time-series of temperature, precipitation, cloud cover and relative humidity during the 30-year reference period (1984–2014), are repeated three times into the future to cover the 90-year period from 1 September 2014 to 31 August 2104.
2. Seasonal trends of temperature and precipitation in Førland et al. (2011) are imposed on the future time-series. Seasonally inhomogeneous trends are already present in the reference climate (1984–2014) and thus also within the repeated future 30-year blocks. Therefore, for every season corrections for seasonally inhomogeneous warming are applied per 30-year block, i.e., an entire 30-year block is shifted to conform with the change applicable for the midpoint of the 30-year period. After trend application, mean seasonal temperatures between 2015 and 2104 increase by 8.6 (DJF), 5.2 (MAM), 2.3 (JJA), and 4.6 °C (SON), and seasonal precipitation rates rise by 3 (DJF), 23 (MAM), 9 (JJA), and 17% (SON), in line with projections in Førland et al. (2011).
3. Inhomogeneity of warming of cold and warm spells within seasons during the observational period (**Figure 2**), is assumed to persist in a future climate. A time-dependent temperature correction is implemented by multiplying the seasonal trends applied in step 2 by a time-dependent function, which is <1 for above-average temperatures and >1 for below-average temperatures. The function is equal to $1 + \Delta T(t) * C_T$, where $\Delta T(t)$ is the temperature deviation at time-step t from the 30-year running seasonal mean, and C_T (in K^{-1}) is a seasonally-dependent coefficient, which represents the fractional change of the seasonal trend per degree temperature deviation from the 30-year running seasonal mean. With seasonal values of C_T of -0.034 (DJF), -0.057 (MAM), -0.160 (JJA), and -0.048 K^{-1} (SON) continuation of the observed inhomogeneity at Svalbard Airport between 1975–2014 (**Figure 2**) is assured in the future temperature scenario.

The resulting time-series of seasonally averaged temperature and precipitation for 1975–2104 are shown in **Figure 1**. The projected climate scenario includes changes in temperature and precipitation variability. Stronger winter than summer warming reduces the magnitude of the annual temperature cycle (**Figure 1A**). Additionally, more pronounced warming of cold than warm spells leads to a reduction of short-term (intra-seasonal) temperature variability. The latter is also responsible for the decrease of inter-annual variability in seasonal temperatures (**Figure 1A**), since relatively warm seasons (compared to the 30-year mean) will experience a weaker warming trend than relatively cold seasons. Finally, seasonal precipitation trends cause the magnitude of individual precipitation events to increase, while the frequency of precipitation events remains unchanged in the projected climate.

The above described approach to generate meteorological time-series provides a strong alternative to using climate output from a single future realization of a RCM, which is prone to substantial uncertainty given the generally large spread between individual RCM projection runs. The current approach also has some limitations. While we incorporate expected changes in the magnitude of temperature and precipitation variability, no potential long-term changes in the frequency and distribution of weather events are accounted for. For example, an increased frequency of heavy-precipitation events in the Northern hemisphere has been suggested (Min et al., 2011), although a recent analysis of extreme precipitation events in Svalbard reveals no significant trends over the most recent decades (Serreze et al., 2015). Furthermore, we do not account for potential trends in cloud cover and relative humidity, due to a current lack of constraints of long-term trends of these variables. This is believed to have a minor impact on the presented results, since (summer) temperature and precipitation are assumed to be the dominant factors influencing the climatic mass balance and snow/firn development. To test sensitivity of the model results to different climate

scenarios, a set of climate sensitivity experiments is performed (Section 3.5).

2.2.2. Elevation Dependence

Experiments are performed on an elevation-dependent model grid, representing the centerline of a typical inland Svalbard glacier. Constructed time-series of temperature, precipitation, cloud cover and relative humidity (Section 2.2.1) apply at sea-level elevation. An elevation-dependent climate forcing is constructed by applying lapse rates for temperature and precipitation, using values typical for Svalbard glaciers. Based on previous estimates of temperature lapse rates in Svalbard which range between $-0.0040°C\ m^{-1}$ (Gardner et al., 2009) and $-0.0066°C\ m^{-1}$ (Nuth et al., 2012), we use a constant mean temperature lapse rate of $-0.0053°C\ m^{-1}$. We apply an average precipitation lapse rate of 0.97 mm w.e. $a^{-1}\ m^{-1}$, based on GPR measurements in 1997–1999 in different regions on Svalbard (Sand et al., 2003; Winther et al., 2003). Winter stake balance measurements on Holtedahlfonna in western Svalbard (Baumberger, 2007; Nuth et al., 2012; Van Pelt and Kohler, 2015) and Nordenskiöldbreen in central Svalbard (Van Pelt et al., 2012, 2014) reveal that precipitation remains constant above an approximate elevation of 800–1000 m a.s.l. Based on this, we set the elevation above which the precipitation lapse rate reduces to zero at 900 m a.s.l. No elevation lapse rates were applied for relative humidity and cloud cover.

2.3. Model Setup and Experiments

Forced with 3-h climate input (Section 2.2), we perform time-dependent experiments with EBFM (Section 2.1), on a model grid covering an altitudinal range of 0–1500 m a.s.l. An altitudinal grid spacing of 25 m is used. The subsurface model uses a moving grid consisting of 200 vertical layers with a maximum layer thickness of 10 cm; depending on surface mass fluxes layers will be added or removed at the surface and base of the vertical model domain (Van Pelt and Kohler, 2015). In contrast to a fixed grid, a moving grid avoids averaging of layer properties and assures layer properties do not suffer from numerical diffusion. The model uses a 3-h time-step, except in the calculation of subsurface heat conduction, for which adaptive time-stepping is used to assure numerical stability. In the calculation of the incoming solar radiation, we assume the surface to be flat, we neglect any shading by surrounding topography, and set the geographic position to the approximate location of Longyearbyen in central Svalbard (78°12′ N, 15°26′ E). We adopt the same model parameter setup for simulating the energy balance and subsurface conditions as in Van Pelt and Kohler (2015). In Van Pelt and Kohler (2015) surface energy balance parameters have been calibrated to optimize model performance against stake and weather station data on glaciers around Kongsfjorden in western Svalbard. Calibrated constants include the aerosol transmissivity coefficient (affects incoming solar radiation), fresh snow and ice albedo (affects reflected solar radiation), emissivity exponents for clear-sky and overcast conditions (affects incoming longwave radiation), and the turbulent exchange coefficient (affecting turbulent heat exchange). Simulated subsurface density and temperature profiles have been validated against observational data in Van Pelt et al. (2014) and Van Pelt and Kohler (2015). We do not account for any glacier dynamics, i.e., zero horizontal ice flow is assumed, which implies slight potential offsets (increasing with depth) of the presented vertical profiles. Given the shallow depth of the vertical model (up to 20 m), we believe the impact of ice flow on our results is likely to be small.

Experiments performed with EBFM cover the 120-year period between 1 September 1984 and 31 August 2104. Realistic simulation of subsurface conditions in the first years of the experiments requires initialized subsurface temperature, density and water content conditions at the start of the simulations (Van Pelt et al., 2012; Van Pelt and Kohler, 2015). To generate initial conditions, we perform a spin-up procedure in which the model is looped three times over the spin-up period 1975–1984, with meteorological input at sea-level from the Svalbard Airport record and lapse rates given in Section 2.2.2. Final output of an initialization run is used as input for the next iteration. During the 27-year spin-up procedure a snow and firn pack develops and deep density, temperature and liquid water storage approach a state consistent with the mean surface forcing between 1975–1984. Final output of the third initialization run provides initial conditions for the experiments starting 1 September 1984. Long-term runs done with EBFM include a standard run, using the above-described standard model settings, and a set of sensitivity experiments, in which the model is run without refreezing (Section 3.4) and perturbed settings for the climate scenario and elevation lapse rates (Section 3.5).

3. RESULTS AND DISCUSSION

In this section we will present results of the model experiments. We start with a discussion of the long-term subsurface evolution at a site in the lower accumulation zone (Section 3.1). Next, we present elevation profiles of the mass balance, refreezing and subsurface conditions (Section 3.2). Thereafter, the changing role of refreezing in a future climate is discussed (Section 3.3), followed by an assessment of the impact of refreezing on the mass balance and subsurface conditions (Section 3.4). Finally, we present the outcome of climate sensitivity experiments (Section 3.5).

3.1. Subsurface Evolution

Increasing melt and rain water percolation in snow and firn in a future climate impacts the subsurface thermodynamics, stratigraphy and water storage. To illustrate the consequences of ongoing and projected climate conditions on the state of snow/firn, we first focus on the simulated firn evolution for a site at an elevation of 800 m a.s.l. for the periods 2010–2014, 2040–2044, 2070–2074, and 2100–2014 (**Figure 3**).

In a present-day climate, the site at 800 m a.s.l. is located in the lower accumulation zone and a thick (>10 m) firn pack is present at this elevation (**Figure 3A**). Heat release by refreezing of percolating water quickly removes the winter cold content at the start of the melt season (**Figure 3B**). Melt-freeze cycles during the melt season cause rapid near-surface densification, leading to the formation of a summer surface with elevated density every melt season (**Figure 3A**). At this elevation, melt water percolates

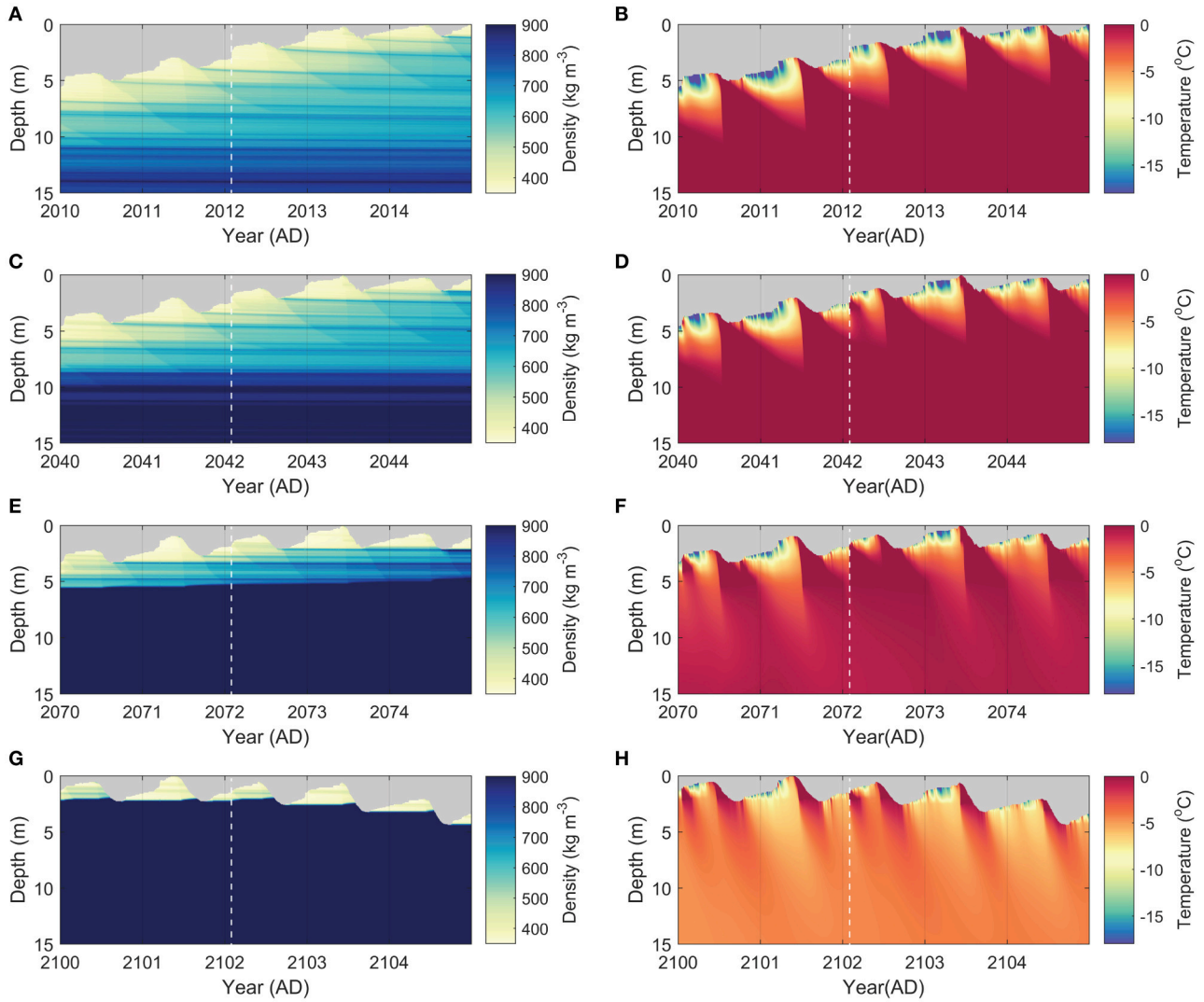

FIGURE 3 | Subsurface density (left) and temperature (right) during the four periods 2010–2014 (A,B), 2040–2044 **(C,D)**, 2070–2074 **(E,F)** and 2100–2104 **(G,H)** at an elevation of 800 m a.s.l. A vertical offset is applied for surface height changes with positive (negative) offsets representing surface height increase (decrease). Surface height changes are defined with respect to the base of the model domain and hence incorporate the effect of firn compaction. Depth on the y-axis is the depth with respect to the highest surface height in the 5-year period. Year labels and tick marks on the x-axis are given at 1 January of the indicated year. The white dashed line marks the onset of the rainfall event in February 2012, 2042, 2072, and 2102.

throughout the firn column every summer season (**Figure 3B**), filling a fraction of the pore space with irreducible water. During the winter season, refreezing occurs at increasing depth as stored irreducible water gradually freezes in response to surface and firn cooling. Winter-time cooling only removes stored water by refreezing in the first meters, which causes the deeper firn to remain temperate (**Figure 3B**). Firn densification in the first few meters is dominated by the effect of refreezing; deeper down, gravitational settling becomes a dominant factor (**Figure 3A**).

In a future climate, higher summer melt rates and continued densification by refreezing and settling cause the firn pack to rapidly thin in the first decades and to disappear by the end of the twenty-first century (**Figures 3C,E,G**). Toward the end of the twenty-first century, this site at 800 m a.s.l. turns into ablation area, resulting in a net annual surface height lowering, absence of firn, and seasonal snow accumulation on top of the impermeable ice in winter (**Figure 3G**). The shallow firn—ice transition depth in the last decades limits deep water storage and refreezing, which causes deep temperatures to become non-temperate (**Figure 3H**). In addition to the lack of refreezing, the higher conductivity of ice compared to snow promotes more rapid winter-time cooling. Warm spells in winter and associated rainfall cause (additional) winter-time refreezing, removing part of the cold content in the upper meters. A clear example of this is seen in February 2012, 2042, 2072, and 2102; heavy winter rainfall causes deep percolation and refreezing, thereby substantially affecting subsurface temperatures (**Figures 3D,F,H**) and snow stratigraphy in subsequent months (**Figures 3C,E,G**).

With winter warming being more pronounced than summer warming, the frequency of winter rainfall events is projected to increase, having a major impact on the seasonal distribution of refreezing and the thermodynamic state of snow and firn, as will be further discussed in Section 3.3.

3.2. Elevation Profiles

Next, we discuss the mass balance and subsurface conditions for an elevation range of 0 to 1500 m a.s.l. Time-series of deep firn temperature (at 15-m depth) and bulk density (mean of first 10 m) are shown in **Figure 4**. Time-series of ELA, superposed in **Figure 4**, indicate a slightly non-linear increase from 500–600 m a.s.l. during the reference period (1984–2014) to 800–900 m a.s.l. during the final 30 years of the simulation (2074–2104). A mean linear trend of 31 m a.s.l. decade^{-1} was found, summing to a total ELA increase of 367 m a.s.l. over the simulation period. A comparison of ELA during the reference period to regional values presented in Hagen et al. (2003) and Möller et al. (2016) reveals that simulated ELA is more representative of the relatively dry inland regions in central Spitsbergen, than the wet coastal regions. This can in part be explained by the use of climate input from Svalbard Airport, located in central Spitsbergen, as a sea-level forcing.

The thermodynamic structure of Svalbard glaciers is strongly influenced by latent heat release after refreezing, which is dominant in the lower accumulation zone where deep percolation and water storage can occur ((Van Pelt and Kohler, 2015); Østby et al., in review). The current and projected thermodynamic structure with cold deep subsurface temperatures in the ablation area and temperate conditions in the lower accumulation area is common for Svalbard glaciers (Björnsson et al., 1996; Pettersson, 2004). It is noteworthy that the simulated subsurface temperature development during the reference period (1984–2014) resembles what has recently been observed at a high elevation site (1200 m a.s.l.) on Nordenskiöldbreen in central Spitsbergen. Observed temperatures at 12 m depth in a medium-length borehole in 1998 (Van de Wal et al., 2002) and in a shallow borehole in 2012 (Van Pelt et al., 2014) revealed a warming from cold to temperate conditions, which is in line with the simulated results shown in **Figure 4A**.

At high elevations in the accumulation zone the percolation depth of melt/rain water is limited and the winter cold wave is sufficiently strong to refreeze all stored water in the course of the winter season. This is not the case in the lower accumulation zone, where water stored deep in the firn (at more than a few meter depth) may survive the winter cooling. At these elevations temperate deep firn conditions remain and in case discharge through crevasses and moulins is low, deep firn water reservoirs (perennial firn aquifers) can potentially develop on top of the impermeable ice. As shown by Kuipers Munneke et al. (2014) the formation of deep perennial temperate firn requires moderate to high melt rates and high accumulation rates. After the discovery of perennial firn aquifers in Greenland (Forster et al., 2013), similar deep firn water reservoirs have recently been detected in ground-penetrating radar data in Svalbard in the accumulation zones on Lomonosovfonna (R. Pettersson, personal communication, 2016) and Holtedahlfonna (Christianson et al., 2015). Without appropriate physics in the model to simulate firn aquifer build-up and dynamics, we limit ourselves to identifying locations of potential firn aquifer development.

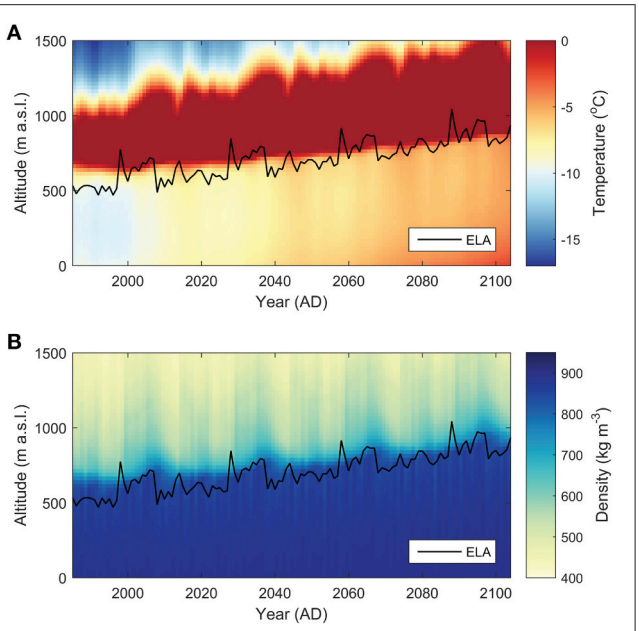

FIGURE 4 | Time-series of annual mean subsurface temperature at 15-m depth (A) and mean density in the first 10 m **(B)** between 1984 and 2104, plotted as a function of elevation. The black line shows the evolution of the ELA. Years on the x-axis are defined between 1 September (preceding year) and 31 August.

The projected subsurface development in **Figure 4A** reveals substantial warming of deep (ice) temperatures in the ablation area in response to increasing surface temperatures. The elevation band with temperate firn conditions in the lower accumulation zone is found to (1) migrate upwards in response to ELA retreat, and (2) to cover a larger elevation range in a warming climate (**Figure 4A**). Increased melt rates cause firn degradation and gradual depletion (**Figure 4B**), causing the firn line to migrate upwards with a delay of typically a few years relative to the rising ELA. The time-delay between ELA rise, firn line retreat and upward extension of the temperate firn zone is an indicator of the sensitivity of firn conditions to changing surface conditions. Widening of the temperate firn zone (**Figure 4A**) can be explained by an increased significance of rainfall at high elevations, as well as to preferential winter warming, causing a reduction of subsurface cold content at the start of the melt season.

Elevation profiles of mass balance for the periods 1984–2014, 2014–2044, 2044–2074, and 2074–2104 in **Figure 5A** reveal slightly accelerating upward migration of the ELA. The mean ELA equals 564 m a.s.l. for 1984–2014, 644 m a.s.l. for 2014–2044, 733 m a.s.l. for 2044–2074, and 831 m a.s.l. for 2075–2104. In line with the accelerated ELA rise, the mass balance sensitivity in the ablation area is found to increase in a future climate causing

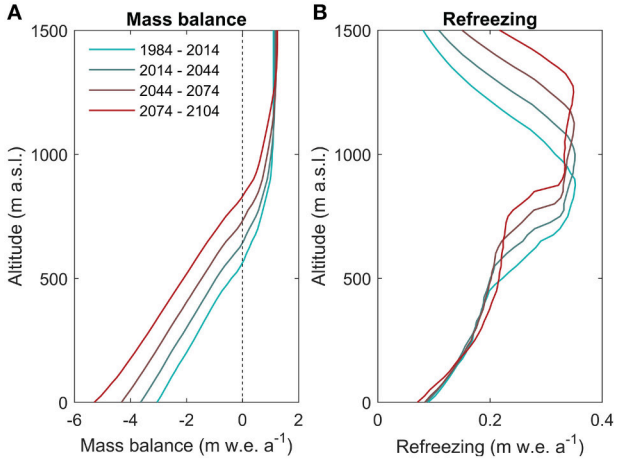

FIGURE 5 | Elevation profiles of the mass balance (A) and refreezing **(B)** averaged for the periods 1984–2014, 2014–2044, 2044–2074, and 2074–2104. Refreezing in **(B)** represents total refreezing within the vertical model domain extending down to a depth of 15–20 m.

accelerated mass loss toward the end of the simulation period (**Figure 5A**). Elevation profiles of refreezing (**Figure 5B**) show values ranging between 0.07 and 0.35 m w.e. a^{-1} for all periods, with patterns consistently showing a maximum of refreezing in the lower accumulation zone, in line with previous findings for all Svalbard glaciers (Østby et al., in review) and for individual glaciers in central Svalbard (Van Pelt et al., 2012) and western Svalbard (Van Pelt and Kohler, 2015). A similar distribution with a maximum of refreezing in the accumulation zone has also been shown in other regions, such as on the Tibetan Plateau (Fujita et al., 1996). Comparing height-profiles of refreezing between periods reveals an upward shift of the maximum in time in line with the projected firn line retreat. Widening in time of the elevation band with highest refreezing rates is apparent and explains the aforementioned extension of the temperate firn zone (**Figure 4A**).

3.3. Seasonality of Refreezing

Next, we discuss changes in the seasonal pattern of refreezing. The seasonal distribution of refreezing at elevations of 300, 600, and 900 m a.s.l., averaged over three different periods (1984–2014, 2029–2059, and 2074–2104), is shown in **Figure 6**. During the reference period (1984–2014, **Figure 6A**), refreezing of melt or rain water is typically most pronounced during the melt season when first melt enters cold seasonal snow or firn, and due to melt-freeze cycles following the daily cycle in temperature and insolation (Colbeck, 1987; Pfeffer and Humphrey, 1998). In the accumulation zone at 900 m a.s.l., a substantial fraction of the total refreezing occurs outside the melt season (**Figure 6A**) and can be ascribed to refreezing of stored irreducible water, continuing throughout the winter season. During the reference period, small amounts of winter-time refreezing occur at 300 m a.s.l. and can be attributed to rare rainfall events. During the melt season, refreezing at 300 m a.s.l. is mostly concentrated in June-July, when first melt enters the initially cold seasonal snow pack, which disappears in the course of the melt season; higher up, refreezing continues throughout the melt season (**Figure 6A**).

In a future climate, refreezing is projected to become less substantial during the melt season and more significant during the winter season at all three elevations (**Figures 6B,C**). Pronounced winter warming leads to an increased frequency of warm spells with positive temperature excursions, causing increased rainfall occurrence in winter. Latent heat release after refreezing of rain water in winter snow causes snow and firn to warm considerably, which has major implications for the thermodynamic profile and substantially reduces the cold content at the start of the melt season. As a result, refreezing during the melt season will decrease at the expense of winter-time refreezing. An example of this is shown in **Figure 3** after a heavy rainfall event in February 2012, 2042, 2072, and 2102.

In contrast to rainfall, surface melting in a warming climate remains very small in winter, mostly due to low or absent solar radiation. For 2074–2104, the ratio of summed melt to summed rainfall between November and March ranges from 3% at 900 m a.s.l. to 20% at 300 m a.s.l., respectively, which confirms that increased future winter-time refreezing is mostly induced by rain events.

3.4. Impact of Refreezing on Subsurface Conditions and Mass Balance

Refreezing of melt and rain water in snow and firn is known to exert a major influence on subsurface temperature and density profiles, and it has been shown to provide a substantial buffer against mass loss of Arctic glaciers (e.g., Wright et al., 2007; Van Angelen et al., 2013). In order to investigate the impact of refreezing on the mass balance, as well as subsurface thermodynamics and stratigraphy, we performed an additional experiment (1984–2104) in which the effects of refreezing are ignored. More specifically, in this experiment we do not allow for any solid mass retention and heat release by refreezing. As a result, all available melt and rain water at the surface will eventually run off; liquid water storage as irreducible water or slush water may still occur and delays runoff. Results of the two runs, averaged over the whole simulation period, are compared in **Figure 7**.

Elevation profiles for the refreezing and no-refreezing runs show a major impact of refreezing on temperatures at 15-m depth, particularly in the lower accumulation zone (**Figure 7A**). Without refreezing subsurface temperature is only governed by heat conduction and the vertical mass flux and shows a nearly linear decrease with elevation as a result of atmospheric cooling with elevation. Differences of up to 10°C are apparent in the lower accumulation zone. In the ablation area, the impact of refreezing on 15-m subsurface temperature is negligible. Here, heat released by refreezing in seasonal snow is to a large extent removed through melting and discharge of the snow layer.

Without refreezing the vertical density profile in the accumulation zone is determined by gravitational settling and surface accumulation. Solid mass retention by refreezing increases long-term mean bulk density in the upper 10 m by up to 117 kg m^{-3} in the lower accumulation zone (**Figure 7B**).

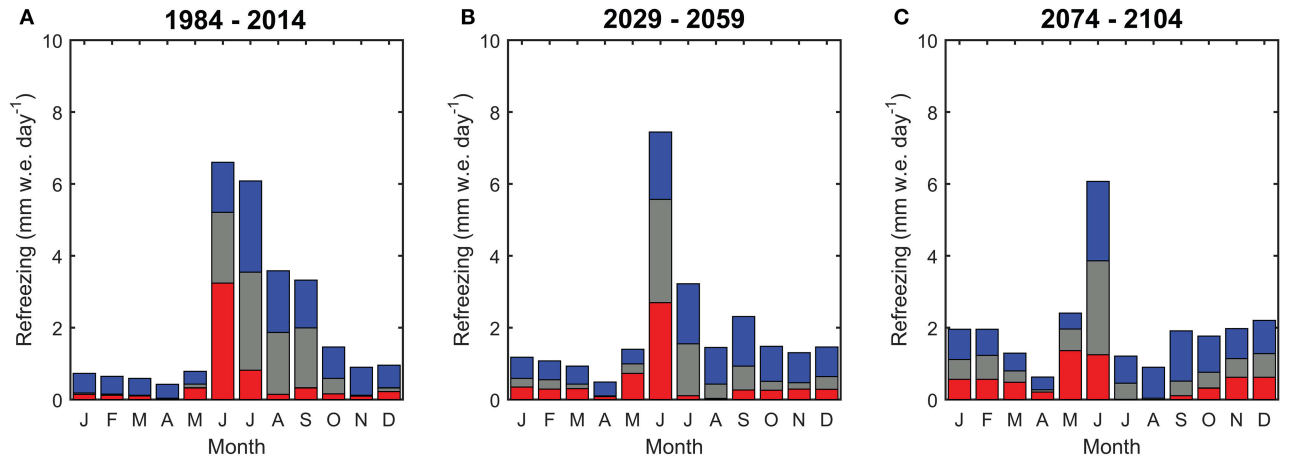

FIGURE 6 | The 30-year mean seasonal distribution of refreezing for the periods 1984–2014 (A), 2029–2059 **(B)**, and 2074–2104 **(C)** at elevations of 300, 600, and 900 m a.s.l.

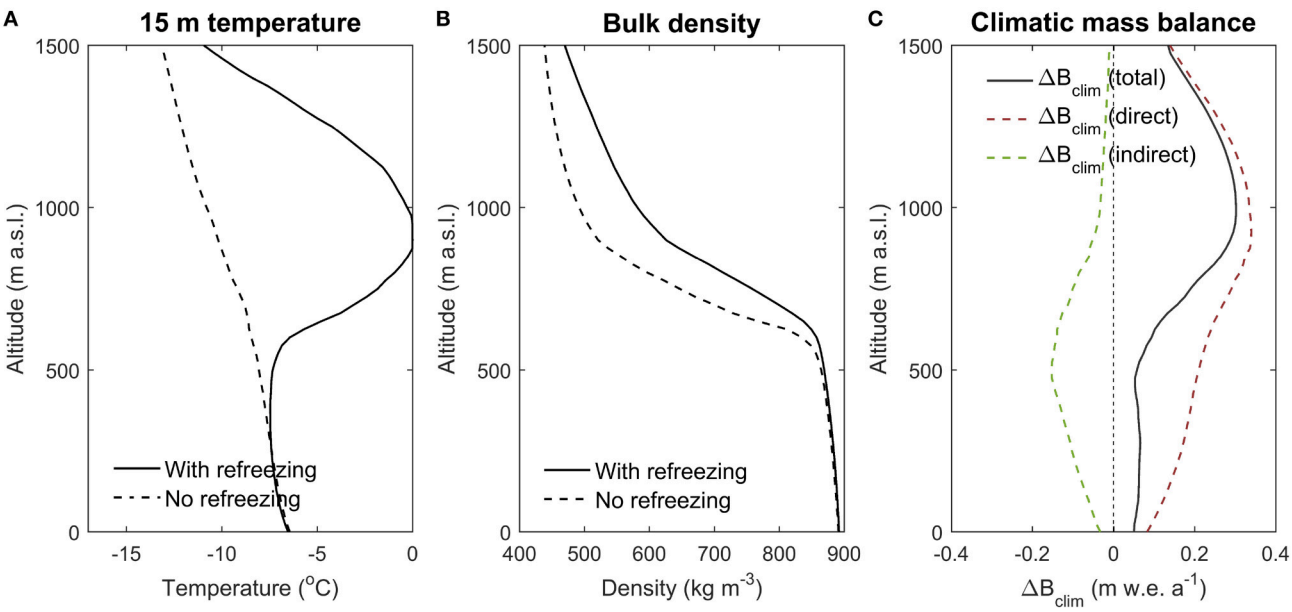

FIGURE 7 | Elevation profiles of subsurface (15-m) temperature (A) and bulk density in the upper 10 m **(B)**, averaged for the period 1984–2104, for a run with and without refreezing. In **(C)** the net mass balance impact of refreezing is shown and is split into contributions from direct and indirect effects; ΔB_{clim} (total) is calculated by subtracting climatic mass balance of the no-refreezing run from the refreezing run, ΔB_{clim} (direct) is the direct effect of refreezing on the climatic mass balance and is equal to total refreezing in the vertical column, and ΔB_{clim} (indirect) represents the indirect impact of refreezing on the climatic mass balance related to firn heating and densification.

Averaged over the simulation period and the elevation range 900–1500 m a.s.l., i.e., above the maximum firn line elevation, we find relative contributions to total densification of compaction and refreezing of 64 and 36%, respectively.

Refreezing of percolating or stored water reduces the amount of melt and rain water that runs off, which implies a positive direct impact on the mass balance. However, due to indirect effects after refreezing, as a result of firn heating and densification, the impact of refreezing on the climatic mass balance is not necessarily equal to the amount of refreezing itself. Firstly, heat release during refreezing increases subsurface temperatures, inducing a more positive (or less negative) conductive heat flux at the surface, with the positive flux direction defined toward the surface. A more positive conductive heat flux at the surface may result in higher melt rates as surface temperatures are more readily raised to melting point. Secondly, refreezing adds solid mass to the snow pack and may create ice layers, which, when exposed at the surface, lowers the surface

albedo and enhances melt rates. Thirdly, the mass addition by refreezing may prolong the lifetime of seasonal snow and thus reduces the period of bare-ice exposure in summer, thereby reducing surface melt. In order to quantify the net impact of refreezing on the climatic mass balance, we calculate the difference between the climatic mass balance (B_{clim}) in the refreezing and no-refreezing experiments (ΔB_{clim}; "refreezing" minus "no-refreezing"; black line in **Figure 7C**). The total ΔB_{clim} (black line) is positive at all elevations (**Figure 7C**), indicating a general positive impact of refreezing on the mass balance. The direct ΔB_{clim} (red line) refers to the direct mass retaining effect of refreezing, and is equal to the amount of refreezing itself (equivalent to the mean of the four lines in **Figure 5B**). By differencing the total and direct mass balance effect of refreezing, we estimate the net indirect effect of refreezing (green line in **Figure 7C**). The net indirect impact of refreezing is the summed effect of the three aforementioned indirect effects; this sensitivity experiment does not allow us to further distinguish individual contributions. The net impact of indirect effects on the mass balance is negative, which indicates that the positive indirect effect (potential prolongation of snow cover) is more than compensated for by negative indirect effects (melt enhancement due to snow pack heating and ice layer formation). A maximum net impact of indirect effects is found in the high ablation area at an approximate elevation of 500 m a.s.l. Averaged over the 0–1500 m a.s.l. elevation range, the mass balance effect of refreezing is 31% smaller than refreezing itself.

3.5. Climate Sensitivity

The above results are sensitive to the chosen future climate scenario, described in Section 2.2. To quantify this sensitivity we performed additional runs for the period 1984–2104 with perturbed precipitation and temperature trends. Sensitivity experiments include runs with zero long-term seasonal trends in temperature ("no ΔT" scenario) and precipitation ("no ΔP" scenario), and runs in which seasonal trends are doubled for temperature ("double ΔT" scenario) and precipitation ("double ΔP" scenario). We additionally perform an experiment in which inhomogeneity in warming of warm and cold spells is ignored ("no spell correction scenario"). For the "no ΔT," "double ΔT," "no ΔP" and "double ΔP" scenarios, sensitivity of the mass balance, deep temperature (15-m) and bulk density (0–10 m) is shown in **Figure 8**. For all experiments sensitivity values, averaged over the elevation range 0–1500 m a.s.l., are presented in **Table 1**.

Due to relatively weak trends for precipitation in the standard run, the mass balance, deep temperature and bulk density are all found to be much more sensitive to perturbations of the temperature scenario than perturbations of the precipitation scenario (**Table 1**; **Figure 8**). Averaged over the 0–1500 m a.s.l. elevation range the mass balance responds about twice as strong to doubling of future seasonal temperature trends than to a no-change scenario, which indicates a strong non-linearity of the mass balance sensitivity to temperature changes (**Table 1**). The mass balance sensitivity to temperature changes is highest in the ablation zone and decreases with elevation (**Figure 8A**), in line with previous findings in Van Pelt et al. (2012). In a "double ΔT" scenario a mean future ELA for the period 2014–2104 of 1125 m a.s.l., and 1330 m a.s.l. for the period 2074–2104, would imply that nearly all glaciers in Svalbard would have maximum elevations below the ELA toward the end of the twenty-first century (Nuth et al., 2013). Finally, ignoring inhomogeneity in warming of cold and warm spells ("no spell correction scenario") has a modest negative impact on the simulated elevation-averaged mass balance (**Table 1**); in this sensitivity experiment, seasonal warm extremes are amplified leading to higher summer melt rates, thereby enhancing future mass loss.

Deep temperatures and bulk densities in a "double ΔT" scenario, averaged over the period 2014–2104, are strongly influenced by rapid upward migration of the ELA, which effectively smooths out the elevation-dependent variability seen in the "no ΔT" scenario, in which long-term trends in the ELA are absent (**Figure 8B**). Doubling of temperature trends causes pronounced subsurface warming with respect to the standard run (**Table 1**), yet cold deep temperature conditions remain in the ablation area even during the last 30 years of the simulation. Based on the above, it seems very unlikely that the general thermodynamic structure with cold deep temperatures in the ablation area and temperate conditions in the lower accumulation zone will change in the near-future. The impact of the "no spell correction scenario" on elevation-averaged deep temperatures is small, while the impact on density is substantial (**Table 1**). The latter can be ascribed to an increased significance of rainfall and subsequent refreezing in winter due to higher temperatures during warm spells.

As described in Section 2.2.2, we use fixed elevation lapse rates for temperature and precipitation. In practice, temperature and precipitation lapse rates may vary in space and we test the sensitivity of the modeled results to typical lapse rate perturbations representing regional variability across Svalbard. The magnitude of the chosen temperature lapse rate perturbations (± 0.0010°C m^{-1}), relative to the standard value of -0.0053°C m^{-1}, reflects variability in reported values across Svalbard, ranging from -0.0040 (Gardner et al., 2009) to -0.0066°C m^{-1} (Nuth et al., 2012). Sand et al. (2003) reported precipitation lapse rates for Svalbard ranging from 0 to 2.6 mm w.e. a^{-1} m^{-1}; based on this, we perform sensitivity experiments with the standard value (0.97 mm w.e. a^{-1} m^{-1}) perturbed by ± 1.0 mm w.e. a^{-1} m^{-1}. Sensitivity results are averaged over the period 2014–2104 for the elevation range 0–1500 m a.s.l., and summarized in **Table 2**. The mass balance, deep temperature and bulk density are most sensitive to the applied perturbations of the precipitation lapse rate. The impact of temperature lapse rate perturbations is typically about half the impact of the precipitation lapse rate perturbations. **Table 2** further reveals that the mass balance is more sensitive to positive temperature and negative precipitation lapse rate changes than to perturbations of opposite sign. Furthermore, the high impact of negatively perturbing the precipitation lapse rate can be ascribed to low precipitation for the whole elevation range in this experiment, which has a severe impact on firn area extent, subsurface temperature and density. Altogether, the above suggests larger regional variability in mass balance and subsurface conditions

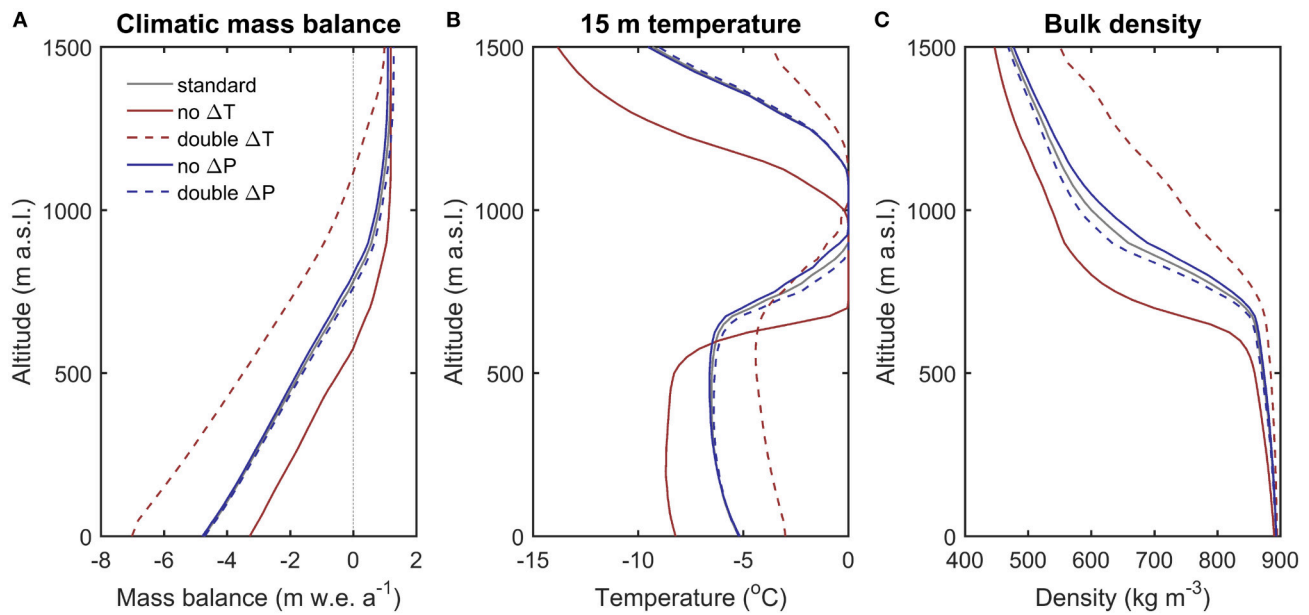

FIGURE 8 | Sensitivity of the 2014–2104 mean climatic mass balance (A), 15-m subsurface temperature **(B)** and the 0–10 m bulk density **(C)** for a range of future climate scenarios.

TABLE 1 | Sensitivity of the 2014–2104 mean climatic mass balance (B_{clim}), 15-m deep temperature (T_{deep}) and 0–10 m bulk density (ρ_{bulk}) to different temperature and precipitation scenarios.

Experiment	B_{clim} (m w.e. a^{-1})	ΔB_{clim} (m w.e. a^{-1})	T_{deep} (°C)	ΔT_{deep} (°C)	ρ_{bulk} (kg m^{-3})	$\Delta\rho_{bulk}$ (kg m^{-3})
Standard	−0.79	–	−4.18	–	729	–
No ΔT	−0.06	+0.73	−6.21	−2.03	681	−48
Double ΔT	−2.26	−1.47	−2.57	+1.61	792	+63
No ΔP	−0.88	−0.09	−4.31	−0.13	737	+9
Double ΔP	−0.71	+0.08	−4.03	+0.15	721	−7
No spell correction	−1.23	−0.44	−4.01	+0.17	763	+34

Calculated values are averaged values over the elevation range 0–1500 m a.s.l. ΔB_{clim}, ΔT_{deep}, and $\Delta\rho_{bulk}$ represent differences of B_{clim}, T_{deep}, and ρ_{bulk} relative to the standard run (perturbation run minus standard run).

TABLE 2 | Sensitivity of the 2014–2104 mean climatic mass balance (B_{clim}), 15-m deep temperature (T_{deep}) and 0–10 m bulk density (ρ_{bulk}) to different lapse rates for temperature (γ_T) and precipitation (γ_P).

Experiment	Standard lapse rate	Perturbation	B_{clim} (m w.e. a^{-1})	ΔB_{clim} (m w.e. a^{-1})	T_{deep} (°C)	ΔT_{deep} (°C)	ρ_{bulk} (kg m^{-3})	$\Delta\rho_{bulk}$ (kg m^{-3})
Standard			−0.79		−4.18		729	
γ_T	−0.0053 K m^{-1}	−0.0010	−0.55	+0.25	−5.59	−1.41	692	−36
		+0.0010	−1.15	−0.36	−3.54	+0.64	774	+45
γ_P	0.97 mm w.e. a^{-1} m^{-1}	−1	−1.86	−1.07	−8.21	−4.03	862	+133
		+1	−0.09	+0.70	−2.90	+1.28	668	−61

Calculated values are averaged values over the elevation range 0–1500 m a.s.l. ΔB_{clim}, ΔT_{deep}, and $\Delta\rho_{bulk}$ represent differences of B_{clim}, T_{deep}, and ρ_{bulk} relative to the standard run (perturbation run minus standard run).

can be expected from spatial variation of precipitation lapse rates rather than temperature lapse rates.

4. CONCLUSIONS

Model experiments with a coupled surface energy balance—firn model (EBFM) were done to investigate the climatic mass balance and the changing role of snow and firn conditions in an idealized Svalbard glacier setting. A climate forcing is generated on an elevation-dependent grid for the past, present and future (1984–2104), based on observational data from Svalbard Airport, observation-based elevation lapse rates, and a seasonally dependent projection scenario from an ensemble of future RCM runs. Experiments include a standard run and a set of sensitivity experiments to quantify the impact of refreezing and to assess sensitivity of the results to the chosen climate scenario and elevation lapse rates.

Results illustrate ongoing and future firn degradation and (delayed) firn line retreat in response to an upward ELA migration of 31 m a.s.l. decade^{-1} between 1984–2104. In a future climate, the elevation band with temperate deep firn in the lower accumulation area, caused by deep percolation, liquid water storage and year-round refreezing, is found to migrate upwards and expand. The cold ablation area warms considerably, yet remains non-temperate toward the end of the twenty-first century. In a future climate, refreezing remains of similar significance, with maximum refreezing rates occurring in the (retreating) lower accumulation zone. In response to pronounced winter warming and an associated increase in winter rainfall, the current prevalence of refreezing during the melt season gradually shifts to the winter season in a future climate. This can be ascribed to more frequent and substantial heat release in the winter snow pack after rainfall events, which in turn reduces the refreezing potential at the start of the melt season.

Comparison of the standard run and a no-refreezing experiment reveals that in a present and future climate the density and thermodynamic structure of Svalbard glaciers are heavily influenced by solid mass retention and heat release after refreezing. By computing the mass balance difference of the refreezing and no-refreezing experiments, we further quantified the mass balance impact of refreezing. The total mass balance effect is found to be positive at all elevations, indicating refreezing acts as a net buffer against mass loss. However, the mass balance effect of refreezing is found to be 31% smaller than mass retention by refreezing itself. This discrepancy is caused by indirect effects after refreezing, related to snow/firn heating, density changes and snow cover changes, which collectively have a negative mass balance impact that partly offsets the mass gain through melt water retention.

Climate sensitivity experiments with perturbed climate scenarios indicate a much higher sensitivity of mass balance, subsurface temperature and bulk density to the prescribed temperature than the precipitation scenario. Experiments with perturbed elevation lapse rates, based on observed regional variability across Svalbard, show a higher sensitivity of the results to precipitation lapse rate changes than to temperature lapse rate perturbations.

Our main aim with this work was to assess the role of snow/firn conditions and refreezing on the mass balance of glaciers in rapidly changing Svalbard climate. For this we chose an idealized elevation-dependent grid, which facilitated the presented analysis with a focus on process-understanding and a discussion of the role of feedbacks. Overall, the results indicate a decisive role for transient snow and firn conditions, and in particular refreezing, on glacier mass loss. This motivates the coupling of surface models to detailed snow models accounting for the subsurface thermodynamic, density and water content evolution in large-scale applications.

AUTHOR CONTRIBUTIONS

WvP performed the model experiments and wrote the manuscript. WvP, VP, and CR discussed the approach and model outcome. VP and CR provided thorough comments and feedback on the manuscript that helped to improve the manuscript quality.

ACKNOWLEDGMENTS

Meteorological data from the Svalbard Airport weather station were downloaded from the eKlima portal (www.eklima.no), provided by the Norwegian Meteorological Institute. We thank colleagues at Uppsala University, and in particular S. Marchenko, for discussion, comments and suggestions which have helped to improve the manuscript. Finally, we thank the reviewers and editor for their insightful feedback that has helped to improve the manuscript.

REFERENCES

ACIA (2005). *Arctic Climate Impact Assessment - Scientific Report*. New York, NY: Cambridge University Press.

Baumberger, A. (2007). *Massebalans på Kronebreen/Holtedahlfonna, Svalbard - kontrollerende faktorer*. Master thesis, University of Oslo.

Bengtsson, L., Hodges, K. I., Koumoutsaris, S., Zahn, M., and Keenlyside, N. (2011). The changing atmospheric water cycle in Polar Regions in a warmer climate. *Tellus A* 63A, 907–920. doi: 10.1111/j.1600-0870.2011.00534.x

Bintanja, R., and Selten, F. M. (2014). Future increases in Arctic precipitation linked to local evaporation and sea-ice retreat. *Nature* 509, 479–482. doi: 10.1038/nature13259

Bintanja, R., and van der Linden, E. C. (2013). The changing seasonal climate in the Arctic. *Sci. Rep.* 3, 1–8. doi: 10.1038/srep01556

Björnsson, H., Gjessing, Y., Hamran, S.-E., Hagen, J. O., Liestøl, O., Palsson, F., et al. (1996). The thermal regime of sub-polar glaciers mapped by multi-frequency radio-echo sounding. *J. Glaciol.* 42, 23–32.

Blaszczyk, M., Jania, J. A., and Hagen, J. O. (2009). Tidewater glaciers of Svalbard: recent changes and estimates of calving fluxes. *Polish Polar Res.* 30, 85–142.

Christianson, K., Kohler, J., Alley, R. B., Nuth, C., and Van Pelt, W. J. (2015). Dynamic perennial firn aquifer on an Arctic glacier. *Geophys. Res. Lett.* 42, 1418–1426. doi: 10.1002/2014GL062806

Cogley, J. G., Hock, R., Rasmussen, L. A., Arendt, A. A., Bauder, A., Braithwaite, R. J., et al. (2011). *Glossary of Glacier Mass Balance and Related Terms*.

Technical report, IHP-VII Technical Documents in Hydrology No. 86, IACS Contribution No. 2, UNESCO-IHP, Paris.

Colbeck, S. C. (1987). "A review of the metamorphism and classification of seasonal snow cover crystals," in *Avalanche Formation, Movement and Effects, Proceedings of the Davos Symposium, September 1986*.

Day, J. J., Bamber, J. L., Valdes, P. J., and Kohler, J. (2012). The impact of a seasonally ice free Arctic Ocean on the temperature, precipitation and surface mass balance of Svalbard. *Cryosphere* 6, 35–50. doi: 10.5194/tc-6-35-2012

Divine, D. V., and Dick, C. (2006). Historical variability of sea ice edge position in the Nordic Seas. *J. Geophys. Res.* 111:C01001. doi: 10.1029/2004JC002851

Førland, E. J., Benestad, R., Hanssen-Bauer, I., Haugen, J. E., and Skaugen, T. E. (2011). Temperature and precipitation development at svalbard 1900–2100. *Adv. Meteorol.* 2011, 1–14. doi: 10.1155/2011/893790

Førland, E. J., and Hanssen-Bauer, I. (2000). Increased precipitation in the Norwegian Arctic: true or false? *Clim. Change* 46, 485–509. doi: 10.1023/A:1005613304674

Forster, R. R., Box, J. E., Van den Broeke, M. R., Miège, C., Burgess, E. W., Van Angelen, J. H., et al. (2013). Extensive liquid meltwater storage in firn within the Greenland ice sheet. *Nat. Geosci.* 7, 95–98. doi: 10.1038/ngeo2043

Fujita, K., Seko, K., Ageta, Y., Jianchen, P., and Tandong, Y. (1996). Superimposed ice in glacier mass balance on the Tibetan Plateau. *J. Glaciol.* 42, 454–460.

Gardner, A. S., Sharp, M. J., Koerner, R. M., Labine, C., Boon, S., Marshall, S. J., et al. (2009). Near-surface temperature lapse rates over Arctic glaciers and their implications for temperature downscaling. *J. Climate* 22, 4281–4298. doi: 10.1175/2009JCLI2845.1

Greuell, W., and Konzelmann, T. (1994). Numerical modelling of the energy balance and the englacial temperature of the Greenland Ice Sheet. Calculations for the ETH-Camp location (West Greenland, 1155 m a.s.l.). *Glob. Planet. Change* 9, 91–114. doi: 10.1016/0921-8181(94)90010-8

Hagen, J. O., Kohler, J., Melvold, K., and Winther, J.-G. (2003). Glaciers in Svalbard: mass balance, runoff and freshwater flux. *Polar Res.* 22, 145–159. doi: 10.1111/j.1751-8369.2003.tb00104.x

Hanssen-Bauer, I., and Førland, E. (1998). Long-term trends in precipitation and temperature in the Norwegian Arctic: can they be explained by changes in atmospheric circulation patterns? *Clim. Res.* 10, 143–153. doi: 10.3354/cr010143

IPCC (2013). *Climate Change 2013: The Physical Science Basis. Contribution of Working Group I to the Fifth Assessment Report of the Intergovernmental Panel on Climate Change [Stocker, T.F., D. Qin, G. - K. Plattner, M. Tignor, S.K. Allen, J. Bosc hung, A. Nauels, Y. X*. Cambridge; New York: Cambridge University Press.

James, T. D., Murray, T., Barrand, N. E., Sykes, H. J., Fox, A. J., and King, M. A. (2012). Observations of enhanced thinning in the upper reaches of Svalbard glaciers. *Cryosphere* 6, 1369–1381. doi: 10.5194/tc-6-1369-2012

Jania, J., Mochnacki, D., and Gadek, B. (1996). The thermal structure of Hansbreen, a tidewater glacier in southern Spitsbergen, Svalbard. *Polar Res.* 15, 53–66. doi: 10.1111/j.1751-8369.1996.tb00458.x

Klok, E. L., and Oerlemans, J. (2002). Model study of the spatial distribution of the energy and mass balance of Morteratschgletscher, Switzerland. *J. Glaciol.* 48, 505–518. doi: 10.3189/172756502781831133

Konzelmann, T., van de Wal, R., Greuell, W., Bintanja, R., Henneken, E., and Abeouchi, A. (1994). Parameterization of global and longwave incoming radiation for the Greenland Ice Sheet. *Glob. Planet. Change* 9, 143–164. doi: 10.1016/0921-8181(94)90013-2

Kuipers Munneke, P., M. Ligtenberg, S. R., Van den Broeke, M. R., Van Angelen, J. H., and Forster, R. R. (2014). Explaining the presence of perennial liquid water bodies in the firn of the Greenland Ice Sheet. *Geophys. Res. Lett.* 41, 476–483. doi: 10.1002/2013GL058389

Lang, C., Fettweis, X., and Erpicum, M. (2015). Stable climate and surface mass balance in Svalbard over 1979-2013 despite the Arctic warming. *Cryosphere* 9, 83–101. doi: 10.5194/tc-9-83-2015

Ligtenberg, S. R. M., Helsen, M. M., and Van Den Broeke, M. R. (2011). An improved semi-empirical model for the densification of Antarctic firn. *Cryosphere* 5, 809–819. doi: 10.5194/tc-5-809-2011

Machguth, H., MacFerrin, M., Van As, D., Box, J. E., Charalampidis, C., Colgan, W., et al. (2016). Greenland meltwater storage in firn limited by near-surface ice formation. *Nat. Clim. Change* 6, 390–393. doi: 10.1038/nclimate2899

Min, S.-K., Zhang, X., and Zwiers, F. (2008). Human-induced Arctic moistening. *Science (New York, N.Y.)* 320, 518–520. doi: 10.1126/science.1153468

Min, S.-K., Zhang, X., Zwiers, F. W., and Hegerl, G. C. (2011). Human contribution to more-intense precipitation extremes. *Nature* 470, 378–381. doi: 10.1038/nature09763

Möller, M., Obleitner, F., Reijmer, C. H., Pohjola, V. A., Głowacki, P., and Kohler, J. (2016). Adjustment of regional climate model output for modeling the climatic mass balance of all glaciers on Svalbard. *J. Geophys. Res. Atmospheres*. 121, 5411–5429. doi: 10.1002/2015JD024380

Nordli, Ø., Przybylak, R., Ogilvie, A. E., and Isaksen, K. (2014). Long-term temperature trends and variability on Spitsbergen: the extended Svalbard Airport temperature series, 1898–2012. *Polar Res.* 33:21349. doi: 10.3402/polar.v33.21349

Nuth, C., Kohler, J., König, M., Von Deschwanden, A., Hagen, J. O., Kääb, A., et al. (2013). Decadal changes from a multi-temporal glacier inventory of Svalbard. *Cryosphere* 7, 1603–1621. doi: 10.5194/tc-7-1603-2013

Nuth, C., Schuler, T. V., Kohler, J., Altena, B., and Hagen, J. O. (2012). Estimating the long-term calving flux of Kronebreen, Svalbard, from geodetic elevation changes and mass-balance modelling. *J. Glaciol.* 58, 119–133. doi: 10.3189/2012JoG11J036

Oerlemans, J., and Grisogono, B. (2002). Glacier winds and parameterization of the related surface heat fluxes. *Tellus* 54A, 440–452. doi: 10.1034/j.1600-0870.2002.201398.x

Oerlemans, J., and Knap, W. H. (1998). A 1 year record of global radiation and albedo in the ablation zone of Morteratschgletscher, Switzerland. *J. Glaciol.* 44, 231–238.

Pettersson, R. (2004). *Dynamics of the Cold Surface Layer of Polythermal storglaciären, Sweden*. Ph.D. thesis, Stockholm University, Department of Physical Geography and Quaternary Geology. Stockholm University Dissertation Series.

Pfeffer, W. T., and Humphrey, N. (1998). Formation of ice layers by infiltration and refreezing of meltwater. *Ann. Glaciol.* 26, 83–91.

Pfeffer, W. T., Meier, M. F., and Illangasekare, T. H. (1991). Retention of Greenland runoff by refreezing: implications for projected future sea level change. *J. Geophys. Res.* 96, 117–122. doi: 10.1029/91JC02502

Reijmer, C. H., and Hock, R. (2008). Internal accumulation on Storglaciären, Sweden, in a multi-layer snow model coupled to a distributed energy- and mass-balance model. *J. Glaciol.* 54, 61–72. doi: 10.3189/002214308784409161

Reijmer, C. H., Van Den Broeke, M. R., Fettweis, X., Ettema, J., and Stap, L. B. (2012). Refreezing on the Greenland ice sheet: a comparison of parameterizations. *Cryosphere* 6, 743–762. doi: 10.5194/tc-6-743-2012

Sand, K., Winther, J.-G., Marechal, D., Bruland, O., and Melvold, K. (2003). Regional variations of snow accumulation on spitsbergen, svalbard, 1997-99. *Nordic Hydrol.* 34, 17–32.

Serreze, M. C., Crawford, A. D., and Barrett, A. P. (2015). Extreme daily precipitation events at Spitsbergen, an Arctic Island. *Int. J. Climatol.* 35, 4574–4588. doi: 10.1002/joc.4308

Serreze, M. C., and Francis, J. A. (2006). The Arctic amplification debate. *Clim. Change* 76, 241–264. doi: 10.1007/s10584-005-9017-y

Van Angelen, J. H., Lenaerts, J. T. M., Van den Broeke, M. R., Fettweis, X., and Van Meijgaard, E. (2013). Rapid loss of firn pore space accelerates 21st century Greenland mass loss. *Geophys. Res. Lett.* 40, 2109–2113. doi: 10.1002/grl.50490

Van de Wal, R. S. W., Mulvaney, R., Isaksson, E., Moore, J. C., Pinglot, J. F., Pohjola, V. A., et al. (2002). Reconstruction of the historical temperature trend from measurements in a medium-length borehole on the Lomonosovfonna plateau, Svalbard. *Ann. Glaciol.* 35, 371–378. doi: 10.3189/172756402781816979

Van Pelt, W. J. J., and Kohler, J. (2015). Modelling the long-term mass balance and firn evolution of glaciers around Kongsfjorden, Svalbard. *J. Glaciol.* 61, 731–744. doi: 10.3189/2015JoG14J223

Van Pelt, W. J. J., Oerlemans, J., Reijmer, C. H., Pettersson, R., Pohjola, V. A., Isaksson, E., et al. (2013). An iterative inverse method to estimate basal topography and initialize ice flow models. *Cryosphere* 7, 987–1006. doi: 10.5194/tc-7-987-2013

Van Pelt, W. J. J., Oerlemans, J., Reijmer, C. H., Pohjola, V. A., Pettersson, R., and Van Angelen, J. H. (2012). Simulating melt, runoff and refreezing on

Nordenskiöldbreen, Svalbard, using a coupled snow and energy balance model. *Cryosphere* 6, 641–659. doi: 10.5194/tc-6-641-2012

Van Pelt, W. J. J., Pettersson, R., Pohjola, V. A., Marchenko, S., Claremar, B., and Oerlemans, J. (2014). Inverse estimation of snow accumulation along a radar transect on Nordenskiöldbreen, Svalbard. *J. Geophys. Res. Earth Surf.* 119, 816–835. doi: 10.1002/2013JF003040

Vega, C. P., Pohjola, V. A., Beaudon, E., Claremar, B., Van Pelt, W. J. J., Pettersson, R., et al. (2016). A synthetic ice core approach to estimate ion relocation in an ice field site experiencing periodical melt: a case study on Lomonosovfonna, Svalbard. *Cryosphere* 10, 961–976. doi: 10.5194/tc-10-961-2016

Winther, J.-G., Bruland, O., Sand, K., Gerland, S., Marechal, D., Ivanov, B., et al. (2003). Snow research in Svalbard – an overview. *Polar Res.* 22, 125–144. doi: 10.1111/j.1751-8369.2003.tb00103.x

Wright, A. P., Wadham, J. L., Siegert, M. J., Luckman, A., Kohler, J., and Nuttall, A.-M. (2007). Modeling the refreezing of meltwater as superimposed ice on a high Arctic glacier: a comparison of approaches. *J. Geophys. Res.* 112:F04016. doi: 10.1029/2007jf000818

Zhang, X., He, J., Zhang, J., Polyakov, I., Gerdes, R., Inoue, J., et al. (2012). Enhanced poleward moisture transport and amplified northern high-latitude wetting trend. *Nat. Clim. Change* 3, 47–51. doi: 10.1038/nclimate1631

Conflict of Interest Statement: The authors declare that the research was conducted in the absence of any commercial or financial relationships that could be construed as a potential conflict of interest.

frontiers in Earth Science

ORIGINAL RESEARCH
published: 09 March 2017
doi: 10.3389/feart.2017.00016

Parameterizing Deep Water Percolation Improves Subsurface Temperature Simulations by a Multilayer Firn Model

Sergey Marchenko[1,2], Ward J. J. van Pelt[1], Björn Claremar[1], Veijo Pohjola[1], Rickard Pettersson[1], Horst Machguth[3] and Carleen Reijmer[4]*

[1] Department of Earth Sciences, Uppsala University, Uppsala, Sweden, [2] Department of Geophysics, The University Centre in Svalbard, Longyearbyen, Norway, [3] Department of Geography, University of Zurich, Zurich, Switzerland, [4] Institute for Marine and Atmosphere Research, Utrecht University, Utrecht, Netherlands

OPEN ACCESS

Edited by:
Michael Lehning,
École Polytechnique Fédérale de Lausanne (EPFL), Switzerland

Reviewed by:
Hiroyuki Hirashima,
National Research Institute for Earth Science and Disaster Resilience, Japan
Nander Wever,
École Polytechnique Fédérale de Lausanne (EPFL), Switzerland

***Correspondence:**
Sergey Marchenko
sergey.marchenko@geo.uu.se

Specialty section:
This article was submitted to Cryospheric Sciences, a section of the journal Frontiers in Earth Science

Received: *28 September 2016*
Accepted: *07 February 2017*
Published: *09 March 2017*

Citation:
Marchenko S, van Pelt WJJ, Claremar B, Pohjola V, Pettersson R, Machguth H and Reijmer C (2017) Parameterizing Deep Water Percolation Improves Subsurface Temperature Simulations by a Multilayer Firn Model. Front. Earth Sci. 5:16. doi: 10.3389/feart.2017.00016

Deep preferential percolation of melt water in snow and firn brings water lower along the vertical profile than a laterally homogeneous wetting front. This widely recognized process is an important source of uncertainty in simulations of subsurface temperature, density, and water content in seasonal snow and in firn packs on glaciers and ice sheets. However, observation and quantification of preferential flow is challenging and therefore it is not accounted for by most of the contemporary snow/firn models. Here we use temperature measurements in the accumulation zone of Lomonosovfonna, Svalbard, done in April 2012–2015 using multiple thermistor strings to describe the process of water percolation in snow and firn. Effects of water flow through the snow and firn profile are further explored using a coupled surface energy balance - firn model forced by the output of the regional climate model WRF. *In situ* air temperature, radiation, and surface height change measurements are used to constrain the surface energy and mass fluxes. To account for the effects of preferential water flow in snow and firn we test a set of depth-dependent functions allocating a certain fraction of the melt water available at the surface to each snow/firn layer. Experiments are performed for a range of characteristic percolation depths and results indicate a reduction in root mean square difference between the modeled and measured temperature by up to a factor of two compared to the results from the default water infiltration scheme. This illustrates the significance of accounting for preferential water percolation to simulate subsurface conditions. The suggested approach to parameterization of the preferential water flow requires low additional computational cost and can be implemented in layered snow/firn models applied both at local and regional scales, for distributed domains with multiple mesh points.

Keywords: firn, firn modeling, preferential flow, internal accumulation, Lomonosovfonna, Svalbard, firn water content

1. INTRODUCTION

Glaciers and ice sheets occupy a substantial fraction of mountain ranges and polar areas and are important components in the system of feedbacks linking the atmosphere, land, and ocean. Glaciers are sensitive to environmental perturbations and are often used as indicators of the past and present climate changes (e.g., Meese et al., 1994; Haeberli et al., 2007). The observed global air temperature rise during the twentieth and twenty-first century (Vaughan et al., 2013) leads to elevated rates of melt water production on glaciers. According to recent estimates one third of the observed rate of the sea level rise is explained by the accelerated rate of mass loss from the Greenland and Antarctic ice sheets, another third is coming from the glaciers and ice caps (Church et al., 2011).

One of the uncertainty sources in the estimates of the contribution of glaciers and ice sheets to the sea-level rise stems from the fact that the melt water generated at the glacier surface does not necessarily lead to runoff. Liquid water can refreeze (e.g., Pfeffer et al., 1991; Machguth et al., 2016) or be stored in the firn pores forming perennial firn aquifers (e.g., Forster et al., 2014; Christianson et al., 2015). Refreezing effectively reduces the amount of melt water that runs off and is most significant in the accumulation zone (e.g., Van Pelt et al., 2012). At the same time, the release of latent heat accompanying refreezing effectively warms the snow and firn column (e.g., Zdanowicz et al., 2012). Once the snow and firn profile is temperate and water cannot be accommodated in the pores, excess water contributes to runoff and eventually to the sea level rise. Firn line retreat to higher elevation and consecutive shrinking of accumulation zones in a warming climate lead to an overall reduction of refreezing, which implies an acceleration of glacier runoff (e.g., van Angelen et al., 2013; Van Pelt et al., 2016). Thus it is important to understand the processes involved in the mass and energy exchange at and below the glacier surface to explain the observed changes in the Earth's ice cover and predict its role in a changing climate.

Multi-layer snow and firn models have been used for description of the mass and energy fluxes in the uppermost tens of meters below the glacier surface. Depending on their exact implementation they may include descriptions of snow precipitation and wind drift, metamorphism, gravitational settling, conductive heat transport, water infiltration, refreezing, and runoff. These processes determine the evolution of the state variables like temperature, grain size and structure, density and water content. The models are typically forced either by observational data or by the surface schemes describing the energy and mass fluxes at the surface to which they are coupled through albedo, ground heat flux, and other feedbacks. For instance, the firn model initially suggested by Greuell and Oerlemans (1986) and developed further by several studies (e.g., Greuell and Konzelmann, 1994; Reijmer and Hock, 2008; Van Pelt et al., 2012) was successfully used in energy/mass balance studies on glaciers and ice sheets (e.g., Bassford et al., 2006; Reijmer et al., 2012; Van Pelt and Kohler, 2015). The CROCUS (Brun et al., 1989) and SNOWPACK (Bartelt and Lehning, 2002) models were originally designed for seasonal snow studies but were also successfully utilized for thicker snow, firn and ice packs (Obleitner and Lehning, 2004; Fettweis, 2007; Gascon et al., 2014; Lang et al., 2015).

Most models assume that the vertical water percolation is laterally uniform and is regulated by two properties of each layer: refreezing capacity and the potential of capillary and adhesive forces to hold water against gravity. However, field and laboratory observations suggest considerable horizontal gradients in the rate of vertical water flow. At certain points concentration of water flow occurs and water infiltrates deeper than the background wetting front forming preferential flow paths. Occurrence of the latter in porous soils infiltrated by water is widely acknowledged (e.g., Hill and Parlange, 1972; Hendrickx and Flury, 2001). Existence of the preferential flow paths in snow and firn has been shown by numerous stratigraphical studies using dye tracing experiments and thick sections (McGurk and Marsh, 1995; Schneebeli, 1995; Bøggild, 2000; Waldner et al., 2004; Campbell et al., 2006; Williams et al., 2010). Further evidences have been provided by temperature tracking of water refreezing events (Sturm and Holmgren, 1993; Conway and Benedict, 1994; Pfeffer and Humphrey, 1996; Humphrey et al., 2012; Cox et al., 2015), radar surveys (Albert et al., 1999; Williams et al., 2000), and observations at the melting snow surface (Williams et al., 1999).

It is important to account for the preferential water flow in estimates of the energy and mass fluxes at glaciers as the mechanism can bring water to the deep snow and firn layers. Deep water percolation serves as an effective way to increase the temperature in deep snow and firn layers through the release of latent heat. A model assuming no preferential flow is likely to overestimate the density gradient with depth and produce a colder subsurface temperature profile than what exists in reality (Gascon et al., 2014), especially at the onset of the melt season (Steger et al., 2017). These effects may results in biased estimates of energy and mass fluxes at and below the surface.

A number of attempts have been undertaken to parameterize preferential flow in snow models. An approach used in one dimensional models is to divide the water available at the surface between two wetting fronts corresponding to the laterally uniform and preferential water flow. For constraining that division, Marsh and Woo (1984b, 1985) used data from multiple lysimeters. Katsushima et al. (2009) and Wever et al. (2016) applied thresholds based on the water content of snow to allocate water to the matrix and preferential flow domains. An alternative approach was suggested by Bøggild (2000) who allowed melt water to affect only a fraction of the profile's refreezing and retention capacity rising from 0.22 (Marsh and Woo, 1984a) to 1 over time. To induce preferential water flow in multidimensional snow models Illangasekare et al. (1990) and Hirashima et al. (2014) perturbed the spatial distribution of subsurface density and grain size.

It has been shown that using the above-mentioned approaches allows simulating preferential flow paths that are intuitively expected in a cold snow pack with a melting surface and qualitatively comply with the empirical evidences. However, constraining the parameters used in the models for characterizing snow and firn (e.g., hydraulic conductivity, water entry pressure, size and shape of snow grains and pores, scale of their spatial heterogeneities) is challenging as reliable high resolution datasets

on the spatial variability of snow properties are complicated to retrieve and hence scarce. The fine scale of the processes involved in preferential water flow currently limits the applicability of 2D and 3D snow models with detailed physics in snow/firn simulations at larger scales. However, for distributed regional scale modeling of the mass and energy fluxes at glaciers the details of water infiltration processes might be of limited importance, while accurate estimation of the effect of water percolation on the evolution of the bulk density and temperature is more crucial.

The purpose of the present article is to find an efficient way to describe preferential water flow in snow and firn and by this to increase model performance in reproducing observed subsurface temperature evolution. It is based on the field data on temperature evolution in the upper 12 m of the snow and firn pack measured at Lomononosovfonna, Svalbard, during 2012–2014 by nine thermistor strings horizontally separated by 3–8.5 m. The results of measurements are compared with the temperature simulations using a multilayer snow and firn model (Van Pelt et al., 2012; Van Pelt and Kohler, 2015). A simple routine for describing the effects of preferential water percolation on snow and firn conditions is implemented and tuned to minimize the error between the simulated and observed temperature evolutions. Sensitivity of the model to different infiltration schemes, depths of water percolation and surface melt rate is tested and discussed. Finally, we discuss the potential development of deep percolation schemes and their implementation in firn models, which will help to reduce the uncertainty in simulated subsurface conditions.

2. STUDY SITE

Lomonosovfonna is a >500 km^2 ice field in the central part of the Spitsbergen island, Svalbard, nourishing several outlet glaciers including Nordenskiöldbreen (**Figure 1**). During the twentieth to twenty-first century the archipelago has seen a pronounced rise in air temperature (Førland et al., 2011; Nordli et al., 2014), glacier retreat (Nuth et al., 2013), and thinning (Moholdt et al., 2010; Nuth et al., 2010; James et al., 2012). At the summit of Lomonosovfonna the surface temperature experienced a rise of *ca* 2–3°C during the twentieth century (Van de Wal et al., 2002). Recent decades at Lomonosovfonna and Nordenskiöldbreen are dominated by an amplified and seasonally-dependent warming and the mean annual air temperature increased by more than 1°C during 1989–2010. The resulting glacier-averaged mass balance during this period was calculated to be -0.39 m w.e. yr^{-1} (Van Pelt et al., 2012).

The study site is in the accumulation zone of the Lomonosovfonna ice field on a flat spot at 78.824°N, 17.432°E, 1,200 m a.s.l., well above the equilibrium line, which for Nordenskiöldbreen was estimated to be at 719 m a.s.l. (Van Pelt et al., 2012). The local glacier thickness derived from a GPR survey is 192 ± 5.1 m (Pettersson, 2009, unpublished data) and the thickness of the firn layer according to coring results was around 20 m in 2009 (Wendl, 2014). Recent modeling results in the area showed that at the elevation of our study site the melt rate during 1989–2010 was on average $\approx$0.34 m w.e. yr^{-1} (Van Pelt et al., 2012). Accumulation at Lomonosovfonna is affected by the wind drift (Pälli et al., 2002; Van Pelt et al., 2014) and measured rates range between 0.58 ± 0.13 and $\approx$0.75 m w.e. yr^{-1} (Van Pelt et al., 2014; Wendl et al., 2015). Subsurface temperature measurements at Lomonosovfonna during summer season were carried out in 1965 (Zinger et al., 1966), 1980 (Zagorodnov and Zotikov, 1980), and more recently by Marchenko et al. (2017). While in Marchenko et al. (2017) the focus was on subsurface density and stratigraphy, in this study the analysis concentrates on the subsurface temperature evolution.

3. DATA

3.1. AWS and Stake Measurements

For monitoring of the surface energy and mass fluxes an automatic weather station (AWS) was installed at Lomonosovfonna in April 2013 and reinstalled in April 2014 and 2015. Air temperature was measured every 3 h during 23 April–17 August in 2013 and 29 April 2014–1 May 2015. Downwelling and upwelling fluxes of short- and long-wave radiation (SW↓, SW↑, LW↓, LW↑, respectively) were measured every 30 min and averaged values were recorded every 3 h during 23 April–14 July 2013 and 28 April–26 August 2014. Details on the used instruments are given in the **Table 1**.

The AWS data were filtered to exclude potentially erroneous values from the analysis. Firstly, we discarded the values collected at battery voltage below the limits provided by the manufacturers of the corresponding instruments. Secondly, values outside of the feasible range were rejected: for air temperature this was <-40 and >10°C, for SW↓ and SW↑ this was <0 and >800 W m^{-2} and for LW↓ <0 and >350 W m^{-2}. Additional constraints were also applied to LW↑ assuming that the glacier surface cannot be colder than -50°C and warmer than 0°C. The minimal (140 W m^{-2}) and maximum (316 W m^{-2}) values for the fluxes were calculated using the Stefan-Boltzmann law assuming a surface emissivity of 1, as:

$$LW\uparrow = \sigma \cdot T^4,$$

where $\sigma = 5.67 \cdot 10^{-8}$ Wm^{-2}K^{-4} and T is the surface temperature in Kelvin. Radiation measurements are prone to significant biases due to deposition of rime on the sensors. Values possibly measured during periods dominated by riming were interpreted from occasional decreases in short wave radiative fluxes accompanied by a small difference between LW↓ and LW↑ and excluded from the analysis.

Measurements of snow depth and snow surface height at stake S11 during field campaigns in April 2012–2015 (**Figure 1**) are also used for validation of the simulated surface energy and mass fluxes. Although, the stake is situated at a distance of 1.5 km from our site, results from radar surveys (Van Pelt et al., 2014) suggest that there is no significant gradient in net annual accumulation rate between the two sites. Measurements at the stake yield estimates of accumulation during the period from August (when the summer surface is formed) to April and the net surface mass flux between two field campaigns. It has to be noted, that the measurements also include the effect of snow and firn settling. Winter accumulation rate measurements include the effect of snow settling that occurs above the previous summer surface and

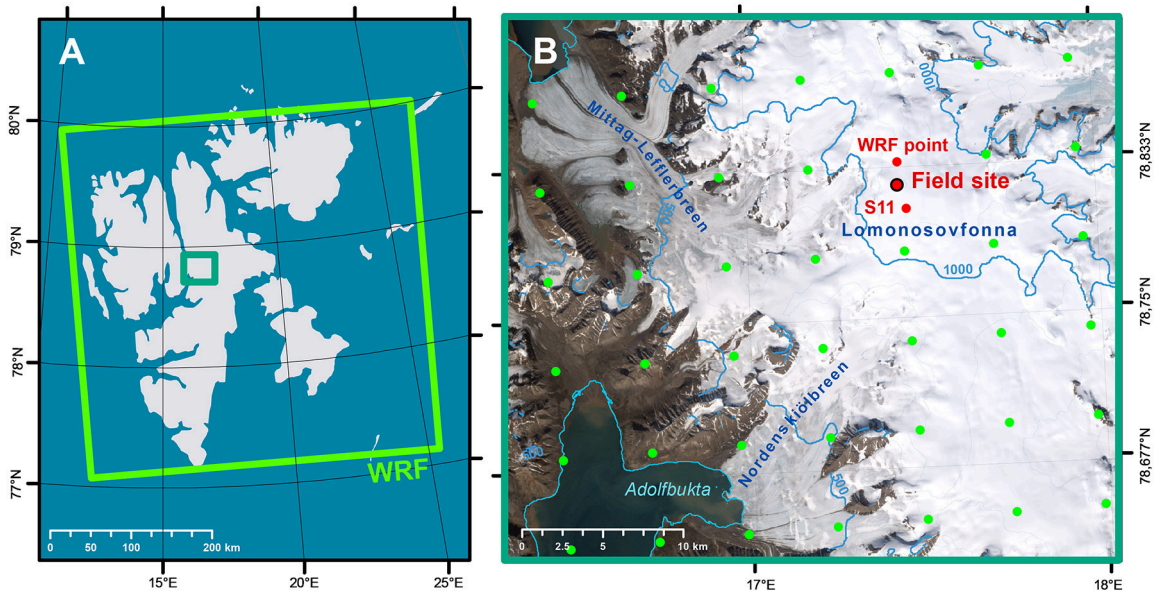

FIGURE 1 | (A) Svalbard archipelago, large green polygon shows the extent of WRF domain, smaller dark-green polygon marks the area shown in **(B)**. **(B)** Lomonosovfonna and its outlet glaciers. Green dots show locations of the WRF domain nodes; large red dot marks location of the AWS and thermistor strings (detailed sketch of installation is found in Marchenko et al., 2017: thermistor strings were installed in boreholes 1–9); smaller red dots show the WRF domain node, output for which was used to force the surface energy balance model and location of the stake S11. Background - true color satellite image LANDSAT ETM+ from 13 July 2002, contour lines and coastline data is provided by the Norwegian Polar Institute.

TABLE 1 | Instruments used for measurements of the air temperature, radiative energy fluxes, and subsurface temperature.

Parameters		22 April 2012	22 April 2013	17 April 2014
Data logger		Campbell Scientific CR10X		
Air temperature		–	Vaisala HMP45A	Rotronic HC2S3
Radiative energy fluxes		–	Kipp and Zonen CNR1	Kipp and Zonen CNR4
Snow and firn temperature	Thermistors	RTI-electronics ACC-003,5 kOhm at 25°C	Betatherm 100K6A1i, 100 kOhm at 25°C	
	Reference resistors	Rho Point 8G16D, 10 kOhm	Rho Point 8G16D, 100 kOhm	
	Excitation voltage, mV	280	900	

net annual accumulation measurements can be expected to be influenced by the gravitational densification occurring above the stake bottom. The latter can reach significant values as the in 2012 the stake bottom was at 8 m below the surface.

3.2. Snow and Firn Density

Firn density was measured in four cores drilled in April 2012–2014 by a Kovacs corer. The lengths of the cores were 9.9, 11.3 and 13.6 m. Details on the routines applied for extraction and processing of the cores were presented by Marchenko et al. (2017). For the further analysis the density profiles originally measured with a high vertical resolution were smoothed using a 1 m running average filter to exclude spikes caused by thin and likely not laterally consistent ice layers (Marchenko et al., 2017) and to ensure mass conservation.

3.3. Snow and Firn Temperature

Multiple thermistor strings were used to continuously record the evolution of the snow and firn temperature. In April 2012, 2013, and 2014 nine custom manufactured thermistor strings were installed in holes drilled by Kovacs auger with a 5.5 cm diameter. The depths of sensors on the strings are presented in **Figure 2**. The strings were installed in a 3 × 3 square grid pattern with 3 m separation between neighboring holes. To minimize preferential percolation of melt water along the cables, the holes were backfilled with drill chips and surface snow.

Each thermistor was connected in series with a reference temperature stable resistor to form a resistive half bridge. Precisely measured excitation voltage was applied to the circuit and the voltage drop over reference resistor was measured using a data logger. To increase the number of channels scanned by the logger several relay multiplexors were connected to it. Details on the applied electrical schemes are listed in the **Table 1**. During post-processing the voltages measured by the data logger were first converted to resistances and then to temperature values using the manufacturer guidelines.

The resulting datasets span the periods 22 April–9 October in 2012, 23 April–12 July in 2013, and 17 April 2014–11 April 2015. Time gaps between the periods covered by subsurface

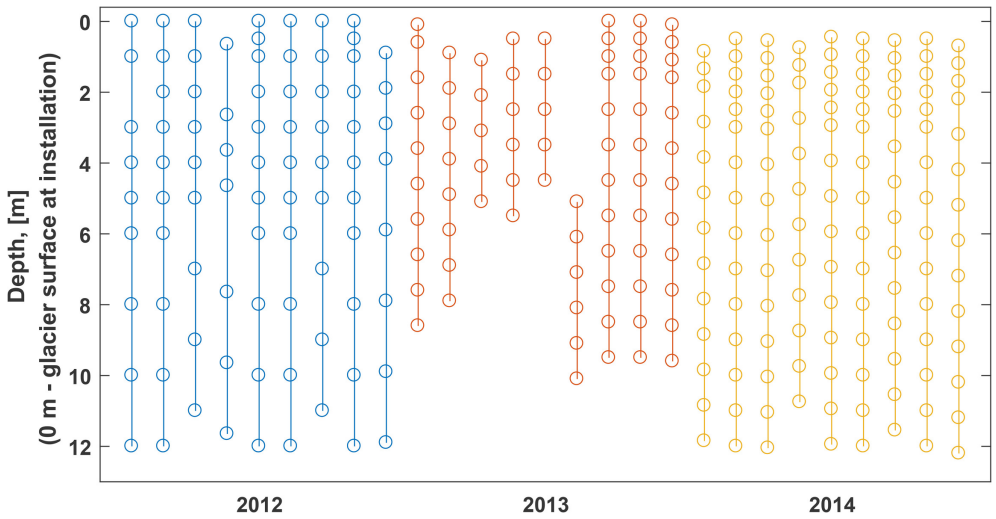

FIGURE 2 | Depths of thermistors installed in April 2012 (blue), April 2013 (red), and April 2014 (yellow) referenced to the glacier surface at installation.

temperature monitoring are explained by the technical problems that occurred during summer 2012 (rapid battery drainage) and 2013 (flooding of the equipment case by melt water). To facilitate the comparison of firn temperature measured by multiple thermistor strings the data from individual strings were first interpolated to a common depth grid using shape-preserving piecewise cubic interpolation. In the next step, the resulting datasets were horizontally averaged to obtain a more spatially representative dataset for each year. We also define three time intervals with rapid subsurface temperature changes subjectively estimated from the results of measurements and interpreted as being driven by the release of latent heat from refreezing water: 2 June–25 September in 2012, 3 June–12 July in 2013, and 4 July–21 September in 2014. These time intervals are used in the further analysis of field data and for its comparison with the model outputs.

4. MODELING

4.1. Regional Climate Model WRF

The Weather Research and Forecast (WRF) regional climate model (Skamarock et al., 2008) has been previously shown to successfully reproduce the evolution of meteorological parameters measured by weather stations in Svalbard (Claremar et al., 2012; Aas et al., 2015, 2016). WRF was forced by ERA Interim weather re-analysis data (Dee et al., 2011) with the spatial resolution of 0.75°, the sea surface temperature and sea ice data from the Operational Sea Surface Temperature and Sea Ice Analysis dataset (Donlon et al., 2012) with 0.05° resolution. We used the dataset on land terrain elevation from the US Geological Survey, while glacier mask was provided by the Norwegian Polar Institute (Nuth et al., 2010). The following modules were used in WRF: land surface scheme NOAH-MP (Niu et al., 2011), turbulence scheme MYNN-2.5 (Nakanishi and Niino, 2006), radiation parameterization RRTMG (Iacono et al., 2008), cumulus convection from Grell and Dévényi (2002) and the double-moment micro-physics scheme from Morrison et al. (2005). The WRF model was run for a domain covering almost the entire Svalbard archipelago (**Figure 1A**) on a spatial resolution of 5.5 km (**Figure 1B**). For the further analysis we used four WRF output variables for the domain point that is closest to our study site and lies at 1,053 m a.s.l. (**Figure 1B**). Air temperature and relative humidity, precipitation and fractional cloud cover accounting for the presence of clouds in all atmospheric levels produced by WRF at 3 h temporal resolution serve as input for the coupled surface energy balance–firn model described below. Despite an elevation difference between the observation site and the model grid point of around 150 m a negative air temperature bias with respect to AWS measurements was found. However, no lapse rate based correction is applied as further discussed in Section 5.1.

4.2. Coupled Surface Energy Balance - Firn Model

To simulate the evolution of the surface and subsurface energy and mass fluxes we apply a model previously used for glaciers on Svalbard (Van Pelt et al., 2012, 2014; Van Pelt and Kohler, 2015). The model consists of two parts describing processes at and below the surface. The surface scheme developed along the lines of Klok and Oerlemans (2002) describes the energy and mass fluxes at the glacier surface and solves for the skin temperature, melt rate, and accumulation. The one dimensional subsurface scheme is based on the model presented by Greuell and Konzelmann (1994) modified by Reijmer and Hock (2008) and Van Pelt et al. (2012) to incorporate updated physics of liquid water storage, gravitational compaction, and heat conduction.

4.2.1. Surface Energy and Mass Fluxes

The surface scheme accounts for the following mass fluxes at the surface: accumulation due to solid precipitation and riming

and mass loss due to melt and sublimation. The energy fluxes (in W m^{-2}) at the surface are described by the equation:

$$Q_m = SW_{net} + LW_{net} + Q_s + Q_{lat} + Q_{rain} + Q_{sub},$$

where Q_m is the energy available for melt, SW_{net} and LW_{net} are the short and long wave radiation balances, respectively, Q_s and Q_{lat} are the sensible and latent turbulent heat fluxes, Q_{rain} is the energy supplied by rainfall, Q_{sub} is the subsurface conductive heat flux. Detailed information on the formulations for individual energy fluxes can be found in Klok and Oerlemans (2002) and Van Pelt et al. (2012) and references therein.

On each time step the surface energy balance scheme estimates the above listed fluxes and solves for the surface temperature. In case the resulting value exceeds 0°C, it is reset to ice melt temperature and the fluxes dependent on surface temperature (LW_{net}, Q_s, Q_{lat}, and Q_{sub}) are recomputed to produce the Q_m.

4.2.2. Firn Model

At each time step the subsurface model simulates temperature (T, °C), density (ρ, kg m^{-3}) and "wet" gravimetric water content ($\theta_w = m_w/m_{tot}$, grav.%, where m_w is the mass of water and m_{tot} is the total mass) of multiple snow, firn and ice layers. The model uses a moving grid in which the boundaries between layers are kept constant over time (Lagrangian scheme). That allows to take into account the effects of vertical advection of snow and firn layers with respect to the surface induced by mass fluxes at the surface. Gravitational settling of the layers is described following Ligtenberg et al. (2011): density of the layers increases with time as a function of the accumulation rate and local subsurface temperature. Conductive heat exchange in the profile is described by the Fourier's law with the conductivity of individual layers parameterized as a function of their density following Calonne et al. (2011). It is assumed that at the lower boundary of the model domain the heat flux equals zero. Although, the simulations are performed for a *ca.* 25 m thick domain, the output only for the upper 12 m is analyzed in detail, as the vertical extent of the empirical dataset on subsurface temperature and density is limited.

Refreezing of surface liquid water strongly influences the subsurface conditions. The routines applied to describe the processes at each time step of the model are described in **Figure 3**. The original subsurface scheme is built following the widely applied "bucket" approach and is referred to below as the "default water infiltration scheme." According to it all water is first allocated to the topmost layer after which its downwards propagation is estimated. Water is allowed to advance to the underlying layer when the refreezing capacity (*RC* in **Figure 3**) of the current one is eliminated and the gravimetric water content exceeds the maximum gravimetric water content (or water holding capacity—*WHC* in **Figure 3**) — potential of capillary and adhesive forces to retain water against gravity. Water holding capacity of snow and firn is parameterized as a function of density following Schneider and Jansson (2004) and decreases from 11 to 2 grav. % with the density rise from 350 to 900 kg m^{-3}. Temperature and density of subsurface layers changes in response to the refreezing of water. The

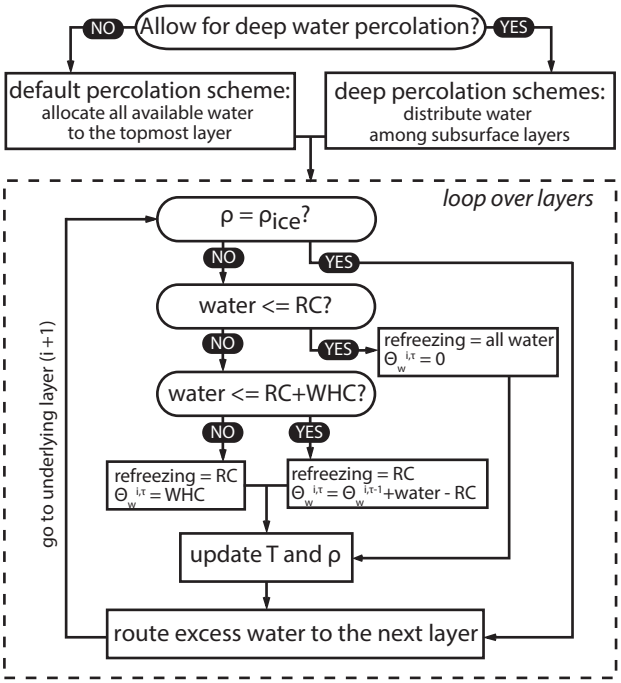

FIGURE 3 | Schematic diagram illustrating routines executed to assess the influence of liquid water refreezing on the temperature (*T*), density (ρ), and water content (θ_W) of subsurface layers at one time step (τ). RC, refreezing capacity defined by the layer's temperature and density; WHC, water holding capacity defined by the potential of capillary and adhesive forces to retain water within a layer against gravity.

model also describes buildup of slush water layer on top of the lowermost solid ice layer that is assumed to be impermeable and superimposed ice formation as a result of freezing of the slush layer. However, in our case no slush water is generated in the upper 15 m as density never reaches the density of ice there. Runoff is possible either from the bottom of the domain or from the slush layer as a function of time (Zuo and Oerlemans, 1996).

4.2.3. Deep Water Infiltration Schemes

Motivated by previous studies pointing to the highly inhomogeneous pattern of water flow in snow (e.g., Williams et al., 2010) and associated uncertainties in simulating the subsurface mass and energy fluxes (e.g., Gascon et al., 2014; Langen et al., 2017; Steger et al., 2017) we implement different parameterizations of the deep water percolation in snow and firn. Preferential water flow essentially concentrates water flow at certain parts of the snow and firn profile even if water supply at the surface exhibits no lateral variability (e.g., Katsushima et al., 2013). This effect is schematically illustrated by **Figure 4A**, which, however, is not based on field or simulation data. In a horizontally averaged 1-D case the phenomena can be expressed by allowing fractions of surface water to penetrate to different depths.

In each model time step the mass of liquid water available at the surface is distributed among the subsurface layers before the effect of refreezing is assessed (**Figure 3**). The distribution is

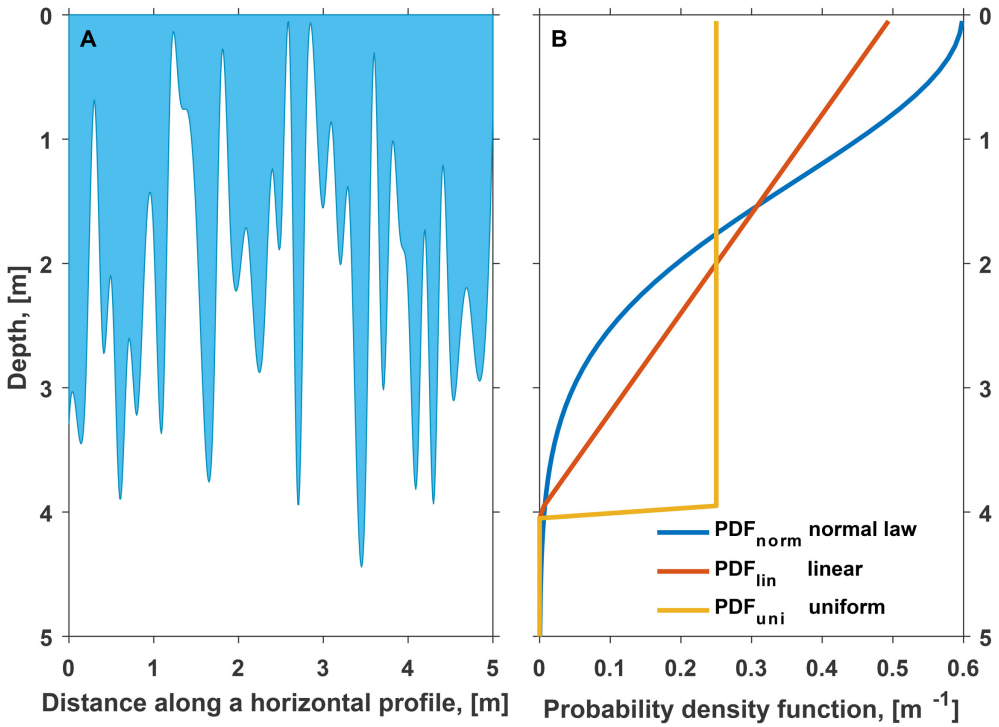

FIGURE 4 | (A) A schematic representation of preferential water flow in a snow and firn pack - blue color shows the wet part of an imaginative snow pit wall. Vertical and horizontal scales and the shape of the "wetting front" are chosen arbitrarily for illustrative purposes. **(B)** Probability density functions corresponding to the deep water infiltration schemes implemented in the firn model. Values along the horizontal axis can also be interpreted as the fractions of surficial water that would be allocated to a 1 m thick firn layer found at a specific depth.

governed by a probability density function $PDF(z, z_{lim})$, where argument z (m) is depth and z_{lim} (m) is the single tuning parameter—the depth below which no (or only a small fraction) liquid water is allocated. Since liquid water is generated at the surface it was assumed that deeper layers generally receive less water and the $PDF(z, z_{lim})$ function decreases with depth. We test three different implementations of this probabilistic approach with different shapes of the $PDF(z, z_{lim})$ function. Corresponding curves are presented in **Figure 4B**. In contrast to the default infiltration scheme, the tested deep percolation routines allow for instantaneous percolation below 0°C level, thereby mimicking the effect of piping at the lateral scale of several meters.

Uniform water infiltration scheme (yellow curve in **Figure 4B**) assumes that water is equally distributed above z_{lim} and no water is allowed to infiltrate below this level:

$$PDF_{uni}(z, z_{lim}) = \begin{cases} \frac{1}{z_{lim}}, & \text{if } z < z_{lim} \\ 0, & \text{otherwise} \end{cases}$$

According to the linear water infiltration scheme (red curve in **Figure 4B**) the $PDF(z, z_{lim})$ function decreases with depth at a constant rate and reaches 0 at z_{lim}:

$$PDF_{lin}(z, z_{lim}) = \begin{cases} \frac{2(z_{lim}-z)}{z_{lim}^2}, & \text{if } z < z_{lim} \\ 0, & \text{otherwise} \end{cases}$$

The normal law water infiltration scheme (blue curve in **Figure 4B**) distributes the water mass according to the corresponding probability density function with the standard deviation $\sigma = z_{lim}/3$, implying that 99.7% of the water stays above z_{lim}:

$$PDF_{norm}(z, z_{lim}) = 2\frac{\exp(-\frac{z^2}{2\sigma^2})}{\sigma\sqrt{2\pi}},$$

Thus with the same z_{lim} value the relative amount of surficial water allocated to the firn layers just above z_{lim} is maximum for the uniform infiltration scheme and minimal for the normal-law percolation. Using the above defined $PDF(z, z_{lim})$ functions we estimate the fraction of the surface water that is added to subsurface layer i with thickness dz_i as:

$$k^i = PDF(z_i, z_{lim}) \cdot dz_i.$$

The suggested schemes describing deep water percolation do not incorporate the physical details of the water transport processes occurring in snow and firn but are rather a statistical description of the horizontally-averaged effect of deep percolation on firn conditions at the scale of several meters. Although, we optimize the model to minimize the mismatch with the averaged temperature evolution measured on a 6 × 6 m plot, the results may also be useful for larger scale applications.

4.3. Model Setup

We set the values of the tuning parameters in the surface energy balance scheme such as the aerosol transmissivity exponent, emissivity exponent at clear-sky and overcast conditions, turbulent exchange coefficient following Van Pelt et al. (2012), who carried extensive calibration experiments at Nordenskiöldbreen and Lomonosovfonna using the data from an AWS at 600 m a.s.l. and readings at multiple stakes. In line with Van Pelt et al. (2014) the value of the fresh snow albedo was set to 0.89, which also resulted in best fit between the simulated and measured LW↑.

The coupled energy balance-firn model was run for a single point at the study site (**Figure 1B**) with a 3 h temporal resolution during 1 April 2012–1 May 2015. The subsurface scheme is based on a one-dimensional vertical domain comprising 250 layers with an initially uniform thickness of 0.1 m. The firn model is initiated by the temperature and density profiles measured in April 2012. On the 23^{d} and 18th April 2013 and 2014, respectively, the simulated density and temperature distributions are reset to the values measured on the corresponding dates to minimize cumulative errors. The gravimetric liquid water content in the profile is reset accordingly to ensure that no liquid water is present in layers at subfreezing temperature.

To explore the effect of deep water percolation on the simulated snow and firn temperature evolution the infiltration schemes described in Section 4.2.3 were implemented and tested for a range of z_{lim} values: 0.1 m and 0.5–25 m with a step of 0.5 m. We also investigate the model response to perturbation of the surface energy balance by an additional term E_+ set to −5 and 5 W m^{-2}, which corresponds to a *ca.* 22% decrease and a *ca.* 27% increase in surface melt rate, respectively. For the default infiltration scheme additional experiments were also performed for a range of E_+ values up to 50 W m^{-2}.

5. RESULTS

5.1. Surface Energy Fluxes

The simulated surface conditions at Lomonosovfonna are validated by comparing the output of the WRF model and of the surface energy balance scheme with the AWS and stake measurements. The measured and simulated evolution of air temperature is presented in **Figure 5**. The modeled mean annual temperature at the study site during April 2012–April 2015 is −11.7°C and shows a pronounced seasonal cycle. In summer months the temperature reaches a few degrees above zero while during cold spells in winter it can drop down to −30°C (**Figure 5A**). The WRF model reproduces well the observed air temperature (**Figure 5B**, **Table 2**) with a root mean square difference (RMSD) of just below 2°C and an underestimation by −0.44°C averaged over the period of observation.

Agreement between the simulated and measured radiative energy fluxes is illustrated by the scatter plots in **Figure 6**. The mean deviation and RMSD values between the measured and modeled LW↓ values are 9 and 39 W m^{-2}, respectively (**Table 2**). The cloud of points in **Figure 6A** describing the model performance in reproducing the LW↓ can visually be divided into three parts. The points lying along the diagonal line correspond to a good match between the measured and simulated values, while the points occurring above and below the diagonal line indicate respectively over- and under-estimation of the energy flux by the model. Since, the LW↓ flux is heavily dependent on the cloud cover (e.g., Klok and Oerlemans, 2002; Stephens, 2005), we suggest that the three clusters of points are respectively

TABLE 2 | Model performance in reproducing the air temperature (T_a) and radiative fluxes measured at the AWS (see Figures 5, 6).

Parameter	*k*	*b*	*r*	RMSD	MD
T_a	0.94	−0.9	0.97	1.9	−0.4
LW↓	0.63	105.0	0.65	38.9	9.2
LW↑	0.89	31.7	0.89	11.4	1.7
SW↓	0.64	60.0	0.78	83.6	−18.7
SW↑	0.65	57.6	0.75	81.9	−9.9

k and b are the parameters in the linear fit: $S = k \cdot M + b$ (where S and M are the simulated and measured values), r is the Pearson correlation coefficient, RMSD is the root mean square difference and MD is the mean difference (bias) between the simulated and measured values.

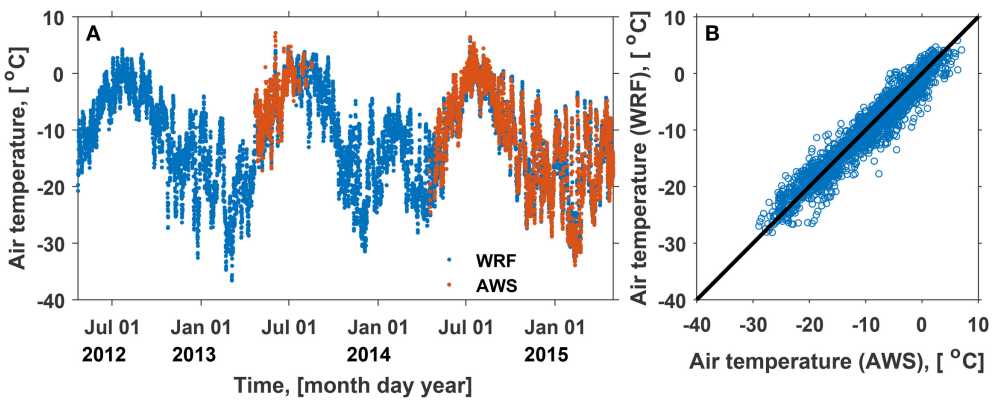

FIGURE 5 | Air temperature at the Lomonosovfonna ice field in April 2012–2015. (A) Values simulated using the regional climate model WRF (blue), AWS measurements (red). **(B)** Scatter plot illustrating the agreement between the simulated and measured values.

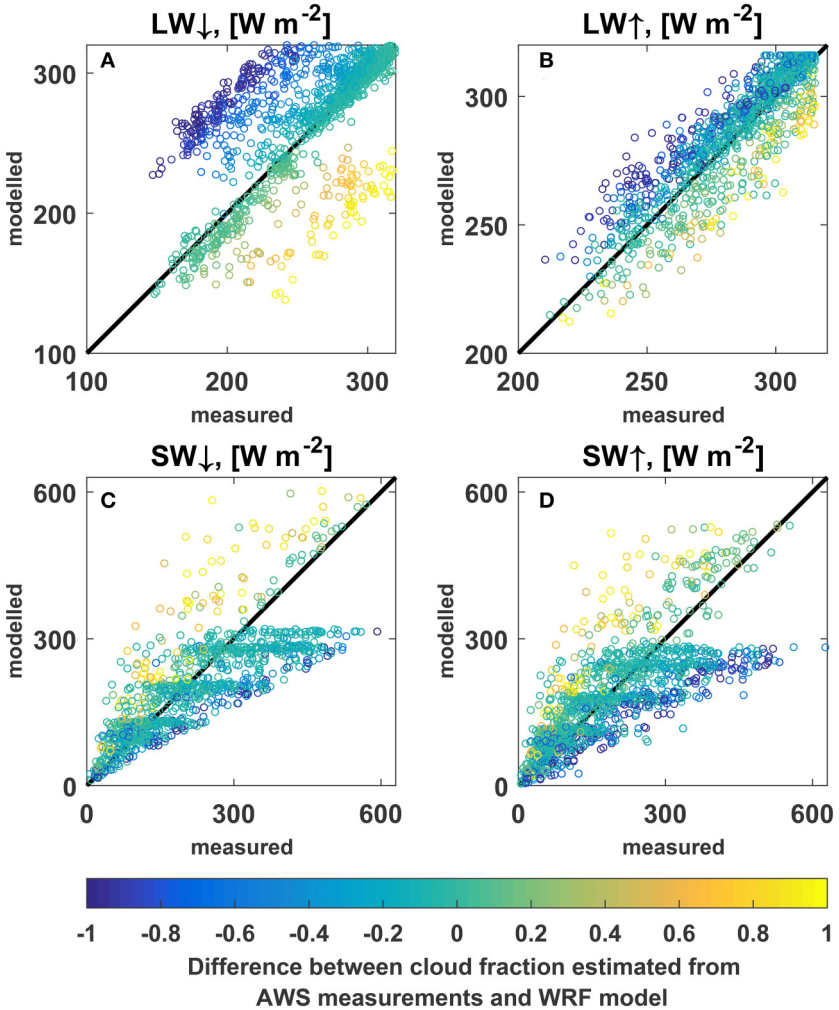

FIGURE 6 | Scatter plots illustrating the agreement between the measured and simulated intensities of the radiative energy fluxes at the Lomonosovfonna ice field during 23 April–14 July 2013 and 28 April–26 August 2014. (A) Long wave downwelling radiation. **(B)** Long wave upwelling radiation. **(C)** Short wave downwelling radiation. **(D)** Short wave upwelling radiation.

explained by: small errors, over- and underestimation of the cloud cover (n) by the WRF model.

This interpretation of LW↓ scatter plot (**Figure 6A**) is supported by an independent estimation of the n values based on the LW↓ and air temperature measurements at the AWS following the approach of Kuipers Munneke et al. (2011) which assumes a linear dependence between these two parameters for any given air temperature. The resulting differences between the AWS-estimated and WRF-predicted cloud cover fractions are shown as the color code of points in **Figure 6**. Overestimation of the cloud cover by the WRF model indeed results in artificially high LW↓ values and occurs more often than underestimation. The upper cluster of points in **Figure 6A** is significantly larger than the lower and the mean cloud cover fraction estimated from the LW↓ and air temperature measurements is 0.65, while the average of WRF derived values for the same period is 0.85.

The mean differences between the simulated and measured short wave radiative flux values (**Figures 6C,D**; **Table 2**) are −19 and −10 W m^{-2} for the downwelling and upwelling components, respectively, although RMSD are considerably larger and are above 80 W m^{-2}. We also find that the mean daily albedo (i.e., the averaged relation between mean daily SW↑ and SW↓ values) produced by the model (0.88) is significantly higher than the corresponding measured value (0.80), which is most probably explained by the measurement uncertainties related to the tilt of the AWS mast and riming of sensors. Overestimation of the cloud cover in the forcing data results in reduced SW↓ values, while when the WRF model underestimates the cloud cover, SW↓ is too high (**Figure 6C**).

The negative effect of the overestimated cloud cover on SW↓ is more than compensated by the positive effect on the LW↓. **Figure 7** illustrates the cumulative melt produced by the model during the 3 year period. It is apparent that the model forced by

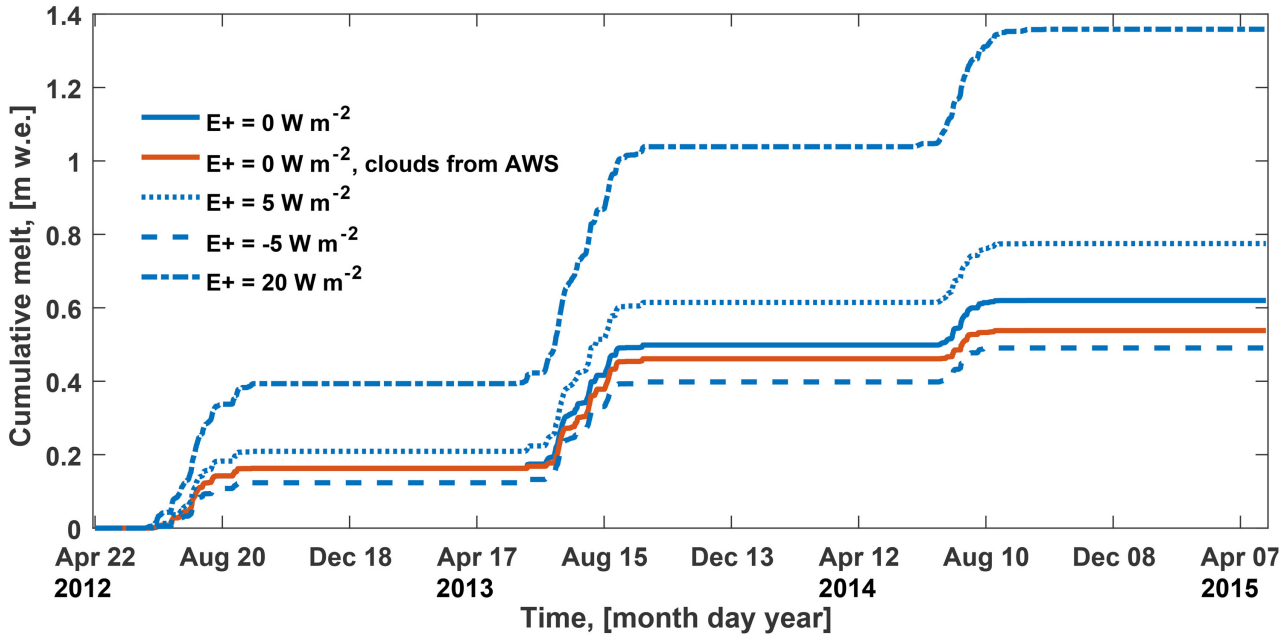

FIGURE 7 | Simulated cumulative melt rate at the Lomonosovfonna ice field in April 2012–2015 for different forcings and settings of the energy balance scheme. Blue lines are used when cloud forcing is provided by WRF, red - cloud forcing is approximated following Kuipers Munneke et al. (2011) using AWS measurements of LW↓ and air temperature, when those are available, when not WRF output is used.

overall lower *n* values based on AWS measurements, when those are available, produces significantly less melt water compared to the reference run done using the cloud cover from WRF (solid red and blue curves on **Figure 7** correspondingly). The effect is also seen in **Figure 6B** illustrating the agreement between measured and simulated LW↑: overestimation of cloud cover by WRF also results in higher simulated LW↑ values than measured by the radiometer (blue points).

The upwelling long wave radiative energy flux appears to be in close agreement with the measurements (**Figure 6B**, **Table 2**). LW↑ is a function of the surface temperature and is defined by the sum of all energy fluxes at the surface. High correlation (0.89) between the modeled and measured LW↑ (**Table 2**) hence suggests the high accuracy of simulated surface temperature, timing of melt events and also of the melt rate, assuming that the physics of energy fluxes above subfreezing and melting surfaces are similar. In absence of data to directly validate melt rate at the site this provides an important indirect source of validation of simulated melt rates. The absence of a clear bias in simulated surface temperature can be ascribed to compensating effects of the uncertainties in simulated cloud cover (overall positive), air temperature and surface albedo (negative), and turbulent fluxes.

The average winter (*ca.* August to April) and annual surface height change measured at stake S11 in April 2012–2015 is 1.8 and 1.3 m correspondingly. The average simulated surface height change during the period starting at the surface's lowermost position in July–September (12, 8, and 26 August 2012, 2013, and 2014) and ending at the day when the stake is revisited in April next year is 1.7 m. Estimation of snow gravitational settling during the time following Ligtenberg et al. (2011) yields *ca.* 0.1 m and thus the surface height change is reduced to 1.6 m. The average annual increment in the surface height during April 2012–April 2015 is 1.7 m. If snow and firn settling above the layer that in April 2012 is at the depth of 8 m (stake length below the surface) is taken into account following Ligtenberg et al. (2011) the value decreases to 1.3 m. The close agreement between modeled and observed dynamics of the surface height suggests decent performance of the surface scheme forced by the WRF model output in reproducing the energy and mass fluxes at our field site on Lomonosovfonna.

The amount of melt water produced by the reference run of the model (blue solid curve in **Figure 7**) in 2013 (0.34 m w. e.) is significantly larger than in 2012 (0.16 m w. e.) and in 2014 (0.12 m w. e.). This finding agrees with glacier-averaged stake mass balance data for Nordenskiöldbreen (unpublished data described in Van Pelt et al., 2012) according to which the summer mass balance in 2012, 2013, and 2014 was −0.37, −0.79, and −0.35 m w.e., respectively.

5.2. Observed Snow and Firn Temperature Evolution

The measured snow and firn temperature evolution averaged over all thermistor strings installed in each of the field campaigns is presented in **Figure 8A**. The vertical depth scale is corrected using the modeled change in the surface height and thickness of subsurface layers to account for the accumulation and ablation at the surface and gravitational settling below it.

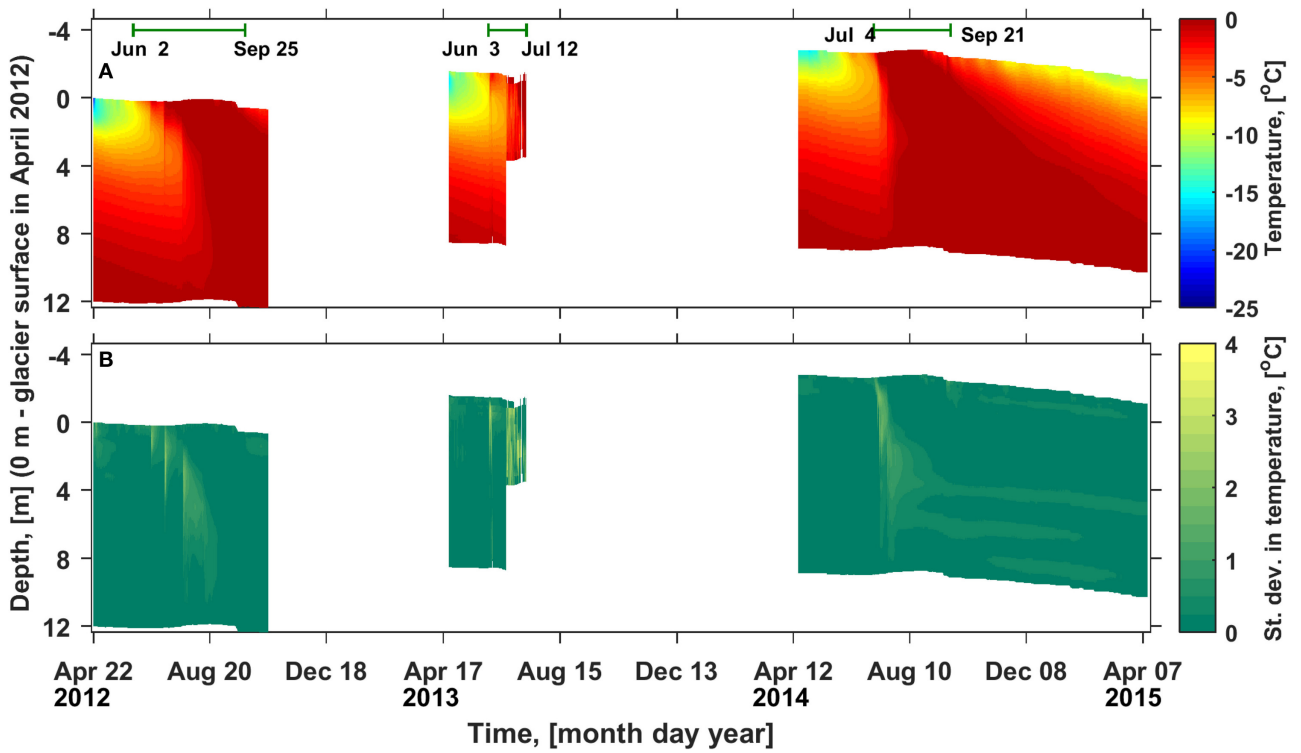

FIGURE 8 | Evolution of the snow and firn temperature measured at the Lomonosovfonna ice field in April 2012–2015. The depth scale was corrected using the model output to account for the accumulation/melt at the surface and gravitational settling below it. **(A)** Temperature values interpolated to a finer mesh (0.1 m between grid nodes) and averaged over all thermistor strings installed in each of the field campaigns. Green bars in the upper part of the panes mark the time intervals used in calculations presented in **Figures 9**, **11**. **(B)** Evolution of the standard deviation in snow and firn temperature at one depth used here as a measure of the horizontal temperature gradients.

In April of each year temperature increases from *ca* −15°C at the surface to 0°C at *ca* 10 m depth (**Figure 8A**). Data from June and July 2012 and 2013 shows that warming of the profile occurred in several steps associated with events of intensive melt at the surface (**Figure 7**). The entire profile was temperate by August 24 in 2012 and by August 9 in 2014. Data for the later part of the summer season in 2013 is not available, however, considering the high melt rates simulated for that year (**Figure 7**), it can be expected that the upper 12 m of the firn profile became temperate even earlier than in the other two years. Snow and firn temperature evolution during the autumn and winter months was only measured in 2014. It is apparent that in the absence of surface melt starting from the first days of September, the layer of temperate snow and firn is eliminated due to the conductive heat flux toward the cooling surface.

To characterize the lateral variability of the snow and firn temperature measured simultaneously at the same depth standard deviations for corresponding sets of values from multiple thermistor strings were calculated (**Figure 8B**). The standard deviations reach up to 4°C and during all three melt seasons the areas with increased lateral variability in snow and firn temperature descend to greater depth over time following the 0°C isotherm, where intensive refreezing can be expected. The observation can be related to the horizontal gradients in the rate of downward water flux and associated migration of maxima in lateral temperature variability. It is particularly obvious during the ablation season in 2012, when the melt water generated at the surface during the first warm spell on the 20th June reached no deeper than 2 m, while the consecutive ablation events on the 4th and 23rd July likely brought the water deeper: to 5 and 9 m at maximum, respectively. In 2014 increased lateral variability in snow and firn temperature is also observed during the autumn and winter months at 4.2, 6.3, and 8.5 m (**Figure 8**). Referenced to the glacier surface in April 2014 these depths correspond to 7, 9.1, and 11.3 m. The phenomena can be related to perched horizons with increased water content that have a horizontal extent less than the plot covered by our thermistor measurements (6×6 m). In April 2014 Marchenko et al. (2017) found multiple ice layers at 7, 8, 9, and 10.8 m depth in three boreholes where the thermistor strings used in present study were installed afterwards. These ice layers could have acted as impermeable horizons and retained water which locally inhibited the cold wave penetration.

The occasional high lateral temperature gradients during the 3 years of observations at Lomonosovfonna indicate a possible uncertainty in subsurface temperature measurements performed at single locations in accumulation zones of glaciers. Higher values of the standard deviations (**Figure 8B**) during the summer period suggest that the largest uncertainty can be expected during

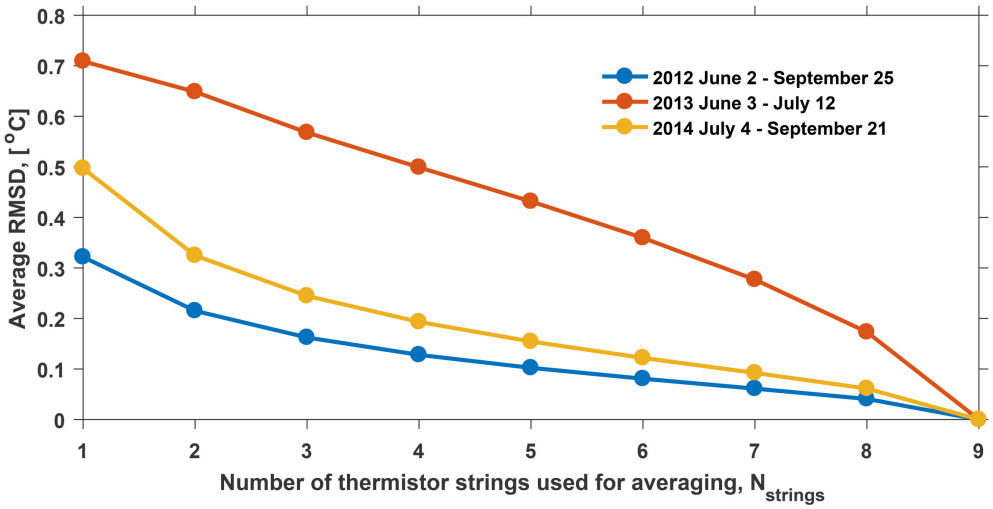

FIGURE 9 | Sensitivity of the measurements of subsurface temperature evolution during the summer period to the number of thermistor strings ($N_{strings}$) expressed as the averaged RMSD between the reference dataset ($N_{strings} = 9$) and averages of different number of thermistor strings ($N_{strings} = 1...9$).

liquid water infiltration in the snow and firn. Data from multiple thermistor strings installed in close vicinity of each other and monitored simultaneously during three melt seasons allows to investigate the effect of averaging the measured temperature evolution over a varying number of thermistor strings.

Firstly for each of the three periods with rapid subsurface temperature changes (see the green bars in **Figure 8A**) a reference dataset was defined as an average of all nine thermistor strings available ($N_{strings} = 9$). Secondly, multiple sample datasets were constructed by averaging data from $N_{strings} = 1...9$ thermistor strings. The resulting average RMSD between the reference and the samples are presented in **Figure 9**. For the 2012 and 2014 datasets the RMSD value decreases from ≈0.4°C for single thermistor string to ≈0.25°C for 3 strings, while the RMSD for larger $N_{strings}$ values decrease at a slower rate. For the dataset collected in 2013 the RMSD values also show a decrease with the number of strings but the values are generally higher and the concave pattern in lacking. We relate these observations to the shorter period of measurements and a lesser number of thermistors scanned during the season (see **Figure 2**) and note that the subsurface temperature dataset collected during 2013 is the most uncertain. Thus it becomes apparent that monitoring the summer evolution of subsurface temperature using multiple thermistor strings is beneficial as the resulting laterally averaged dataset is more representative for the study site.

5.3. Modeling Snow and Firn Temperature Evolution

Figure 10 presents the evolution of snow and firn temperature simulated with $E_+ = 0$ W m^{-2} and using the conventional water percolation scheme not allowing for deep water infiltration (**Figure 10A**) along with the corresponding deviations from the measurements (**Figure 10B**) and simulated gravimetric water content (**Figure 10C**). The general pattern of subsurface temperature evolution agrees with the results of measurements. In May and June a gradual warming occurs due to the increase of air temperature. Between mid-June and July infiltrating water causes a fast downward expansion of the temperate snow and firn layer. Evolution of the water content profile follows the firn temperature changes: water saturates the potential of the capillary and adhesive forces immediately after the layer in question becomes temperate. In September, after surface melt ceases, the subsurface profile gradually cools, and the water suspended in pores is refrozen. The temperature below ≈10–12 m remains always at 0°C, it is set to the observed state every April and the conductive cold wave does not reach that deep during 1 year.

Despite the general agreement between the simulated and measured subsurface temperature, the vertical extent and strength of perturbations in the snow and firn temperature deviate considerably from the observations (**Figure 10B**) with the simulated profile being generally colder. The difference between the simulated and measured temperature reaches up to 12.5 and −8°C. While only 0.3% of the RMSD values are >1°C, 42.3% of the deviations are below −1°C. Biases are the largest in July, when high surface melt rate results in fast and deep water infiltration, which is not captured by the firn model in its default configuration. Positive errors in simulated temperature occur very seldom and are restricted to the upper 1 m of the profile. We note that the depth of elevated negative anomalies increases over time as the deeper firn layers become temperate under the influence of infiltrating water. By the end of all three simulated ablation seasons the subsurface profile did not reach the temperate state. Cold firn was still present below 2 m depth in 2012 and 2014, and below 6.5 m in 2013, when the surface melt rate was higher and the temperate near-surface firn layer almost connected with the deep temperate firn.

Next we explore the sensitivity of the firn model results to different water infiltration schemes and the value of the

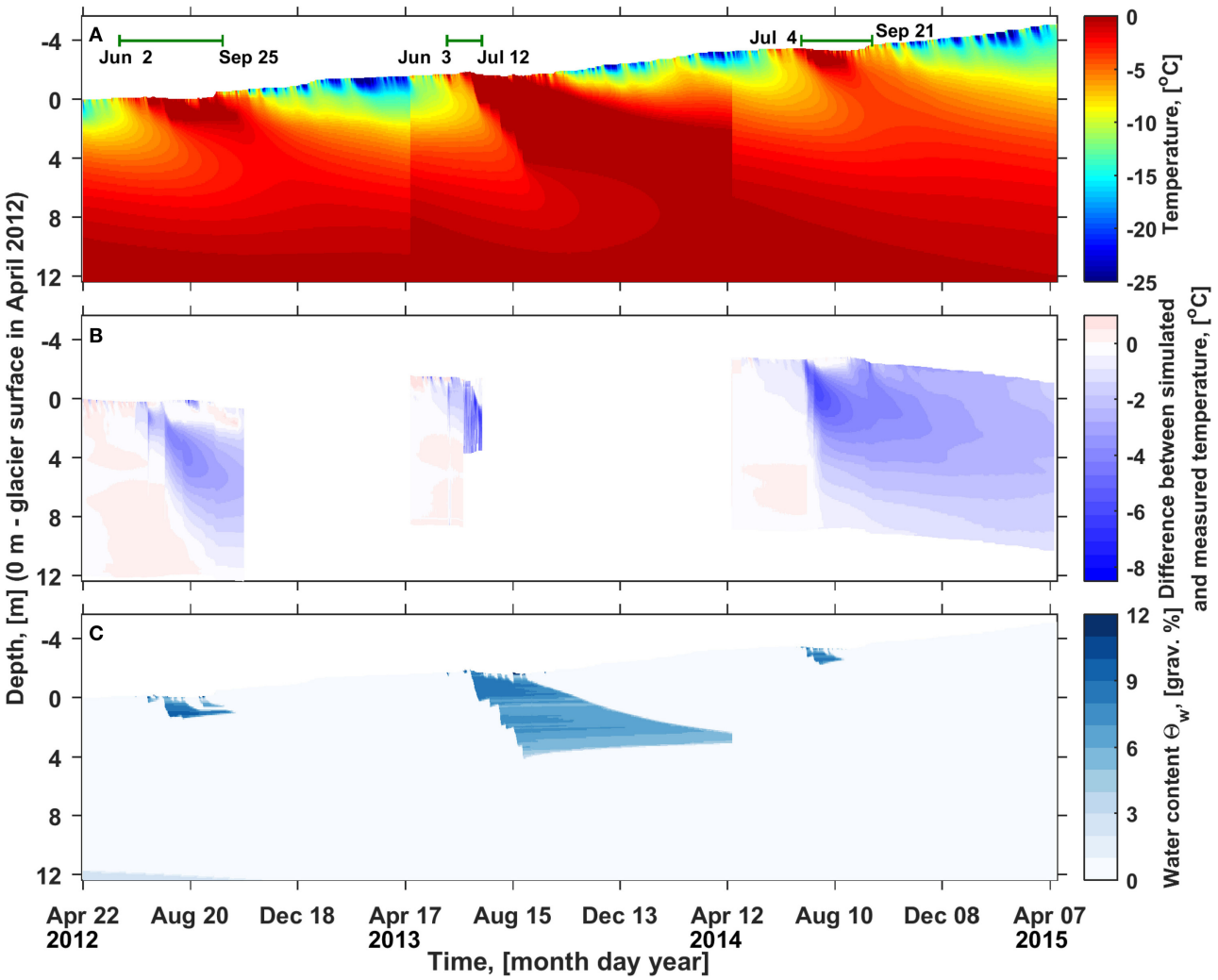

FIGURE 10 | (A) Evolution of the snow and firn temperature simulated using $E_+ = 0$ W m^{-2} and the default water infiltration scheme. Green bars in the upper part of the panel mark the time intervals used in calculations presented in **Figure 11**. Resetting the simulated temperature profile to the measured values on the 23rd, 18th, and 16th April 2013, 2014, and 2015, respectively causes the sudden shifts in temperature evolution. **(B)** Difference between the simulated **(A)** and measured (**Figure 8A**) temperature evolution. Values larger than 1°C constitute *ca* 0.33% and are shown as 1°C. **(C)** Evolution of the simulated gravimetric water content (Θ_W)

percolation depth z_{lim}. The RMSD between simulated and measured subsurface temperature during the periods of rapid changes (**Figure 11**) is 1.5–2.8°C for the default infiltration scheme and all three deep infiltrations schemes with z_{lim} set to 0.1 m. With the increase of z_{lim} to 25 m the RMSD values in all cases exhibit a gradual decrease approximately by a factor of 2 and a subsequent increase almost to the initial values. The presence of a minimum in each case suggests that implementation of the deep water percolation scheme significantly improves the firn model performance in reproducing the measured subsurface temperature evolution. The z_{lim} values corresponding to the minimal RMSD between the simulated and measured temperature evolution lie in a wide range from 4.5 to 12 m for different years and parameterizations, with a consistent pattern of the uniform percolation exhibiting the smallest values (4.5–6 m) and the normal law percolation the largest (7.5–12 m). At the same time, the minimal RMSD values reached for the different infiltration schemes vary only slightly.

Sensitivity experiments for the default configuration of the firn model revealed that decreasing the amount of melt ($E_+ = -5$ W m^{-2}) results in slightly higher values of the RMSD between the simulated and measured temperature evolution. Higher melt rates ($E_+ > 0$ W m^{-2}) improve the model performance (**Figure 11**). While a moderate perturbation of $E_+ = 5$ W m^{-2} results only in a slight reduction of the RMSD, with significantly higher E_+ values it is possible to reach a similar effect as by implementation of the deep percolation schemes. However, that is only possible with $E_+ = 20$ W m^{-2} in 2012, $E_+ = 22$ W m^{-2} in 2013, and $E_+ = 32$ W m^{-2} in 2014, which corresponds to increase in the annual melt amount by a factor 2.2, 1.9, and 4.2

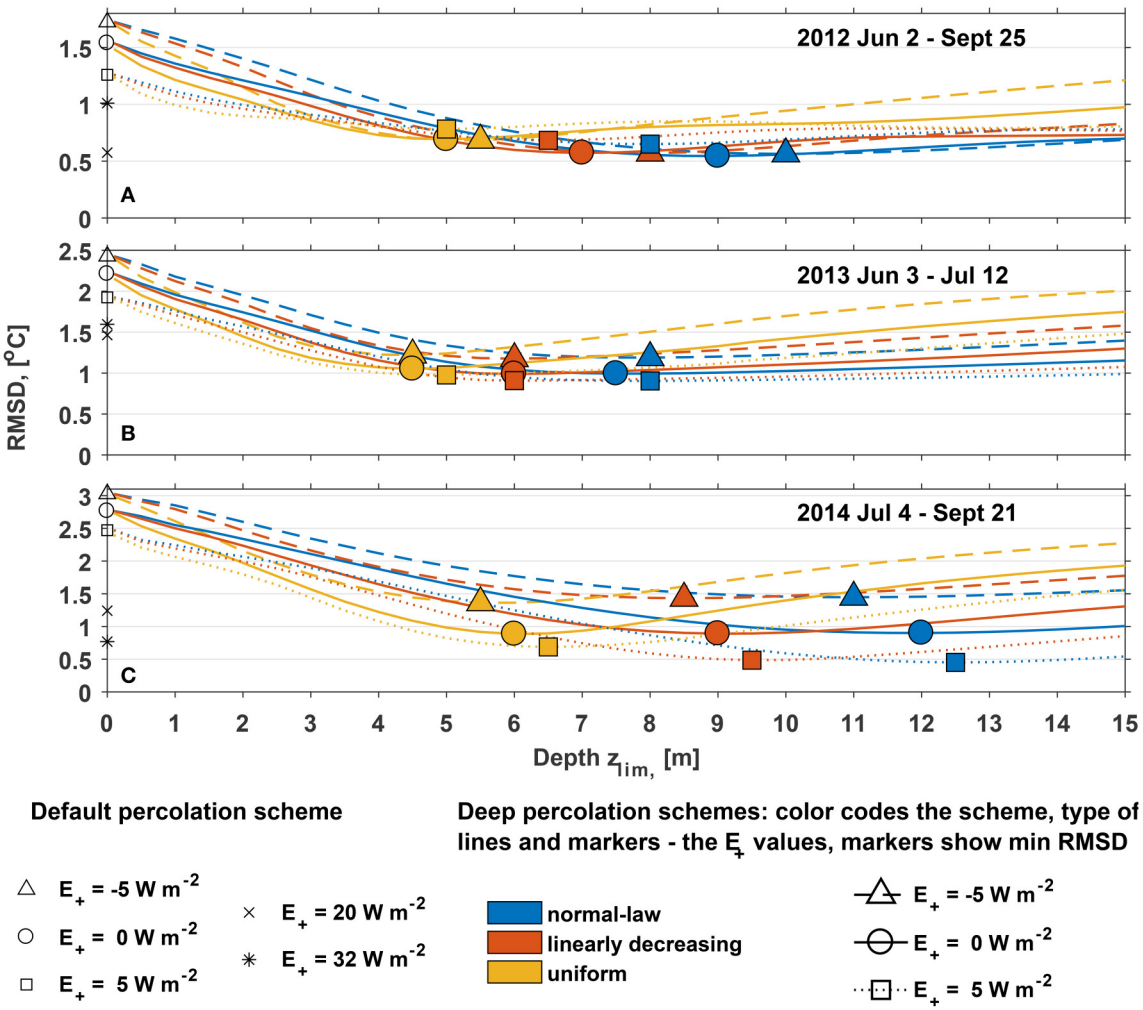

FIGURE 11 | Sensitivity of the RMSD between the simulated and measured summer subsurface temperature on the type of the infiltration scheme, depth z_{lim} to which liquid water is allowed to infiltrate and parameter E_+ regulating the energy available for melt. (A) 2 June–25 September 2012; **(B)** 3 June–12 July 2013; **(C)** 4 July–21 September 2014. Note the difference in the limits of the vertical axis. Black markers in each panel show the RMSD for the default water infiltration scheme, blue color shows the results for "normal law," red for the "linear" and yellow for the "uniform" infiltration laws. Markers show location of the minima in RMSD for each of the $RMSD = f(z_{lim})$ functions. Type of the line and marker code tuning of the surface energy balance model: solid lines and circles for $E_+ = 0\,\mathrm{W\,m^{-2}}$, dashed lines and triangles for $E_+ = -5\,\mathrm{W\,m^{-2}}$ and dotted lines and squares for $E_+ = 5\,\mathrm{W\,m^{-2}}$.

for the 3 years, respectively. Given the above described model performance in reproducing the observed energy and mass fluxes at the surface the major underestimation of melt rates seems unrealistic.

In most cases for any given z_{lim} value in the deep infiltration schemes setting E_+ to $-5\,\mathrm{W\,m^{-2}}$ (dashed lines) results in the highest RMSD values, while $E_+ = 5\,\mathrm{W\,m^{-2}}$ (dotted lines) leads to the minimal errors. However, the minimal RMSD values obtained with different settings of E_+ for the deep percolation schemes exhibit this dependence only in 2014, while in 2012 and 2013 the performance of the firn model depends only slightly on the settings of the surface melt rate.

Figure 12 presents the snow and firn temperature evolution simulated using $E_+ = 0\,\mathrm{W\,m^{-2}}$ and the uniform law percolation scheme with z_{lim}=5 m, which is the average of the three z_{lim} values resulting in minimal RMSD for that scheme in 2012, 2013 and 2014. The misfit between the simulated and measured temperature evolution (**Figure 12B**) still reaches −8 and 12.5°C, but the corresponding time and depth ranges are rather limited. Only 2.3% of the values are >1°C and 13.6% are below −1°C, which is much lower than what was produced by the firn model in its default configuration (**Figure 10B**). A notable overestimation of the firn temperature occurs in July 2012, while in the other two seasons firn temperature is slightly underestimated. The firn profile reaches the temperate conditions by the end of ablation seasons in 2012 and in 2013 in line with the observations. However, in summer 2014 increase of the deep firn temperature remains underestimated. A better match is found with E_+ set to $5\,\mathrm{W\,m^{-2}}$ (blue square in **Figure 11C**) but a considerable cold firn layer is still present by the end of ablation season, suggesting

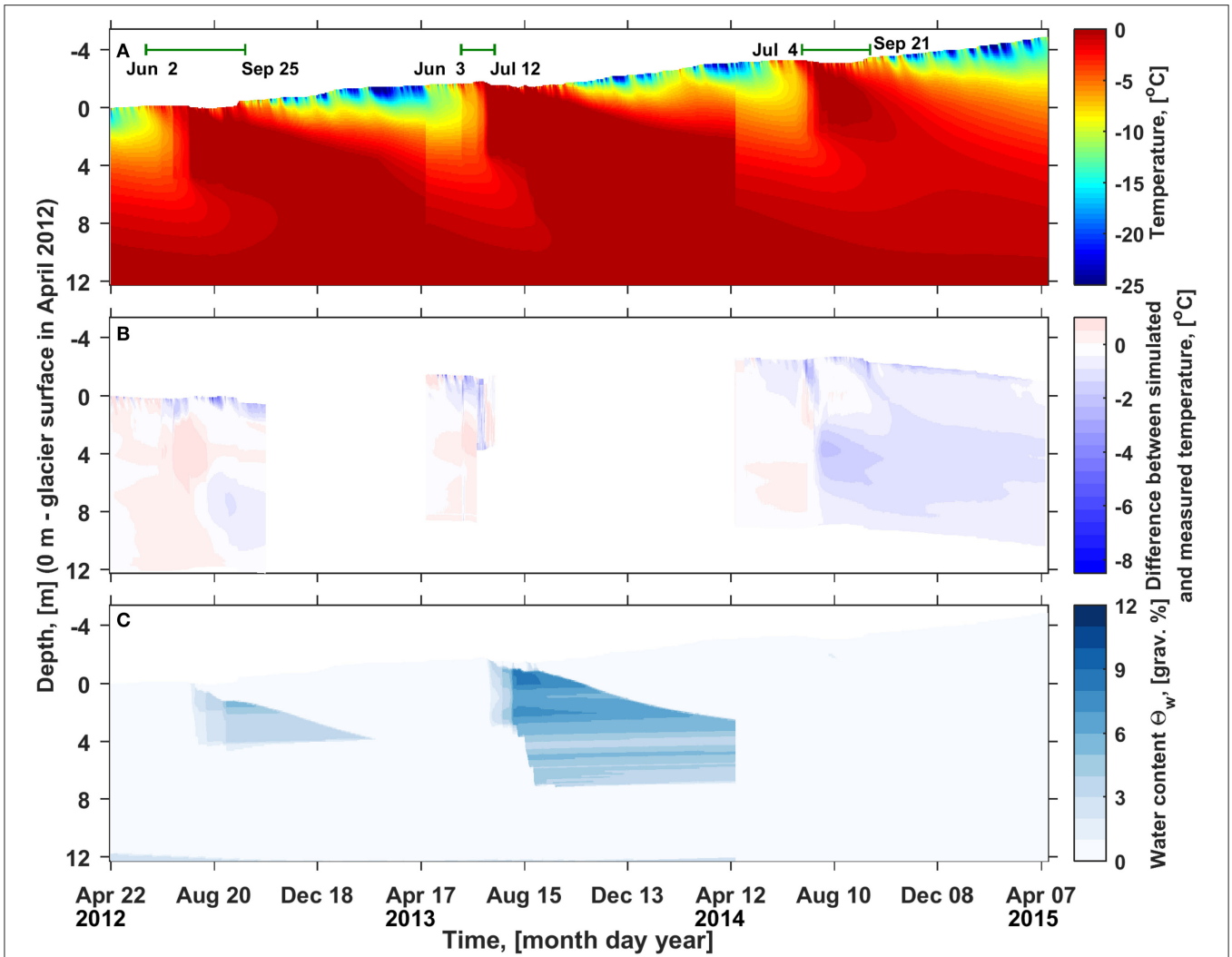

FIGURE 12 | (A) Evolution of the snow and firn temperature simulated using $E_+ = 0\ \mathrm{W\,m^{-2}}$ and the uniform law water infiltration scheme with z_{lim}=5 m, corresponding to the average of z_{lim} values resulting in minimal RMSD for the summer seasons 2012 – 2014. Green bars in the upper part of the panel mark the time intervals used in calculations presented in **Figure 11**. Resetting the simulated temperature profile to the measured values on the 23rd, 18th, and 16th April 2013, 2014, and 2015, respectively causes the sudden shifts in temperature evolution. **(B)** Difference between the simulated **(A)** and measured (**Figure 8A**) temperature evolution. Values larger than 1°C constitute ca 2.3% and are shown as 1°C. **(C)** Evolution of the simulated gravimetric water content (Θ_w). Note: the color scales are the same as in **Figure 10**.

that simulated melt rates are likely underestimated during this ablation period. The firn gravimetric water content (**Figure 12C**) follows the downwards propagation of the 0°C level but is considerably lower than in the case of default water percolations scheme (**Figure 10C**). The density profile is similar in both model realizations, suggesting no difference in the maximum gravimetric water content, and, consequently, significantly lower saturation values in case deep water percolation is assumed.

6. DISCUSSION

The air temperature simulated by WRF for the point at 1053 m a.s.l. is on average 0.4°C lower than the values measured by the AWS at 1,200 m a.s.l. even though an opposite tendency can be expected from the elevation difference of ≈150 m and published lapse rate values for Svalbard of 4–6.6°C km^{-1} (Wright et al., 2005; Nuth et al., 2012). Given the high correlation coefficient (0.97, see **Table 2**) between the measured and modeled values we conclude that in accordance with earlier results from Svalbard (Claremar et al., 2012; Aas et al., 2015, 2016) the WRF model demonstrated a prominent skill in reproducing the observed air temperature with a tendency for its underestimation.

The cloud cover generated by WRF clearly exceeds the approximations based on the AWS measurements of LW↓ and air temperature following Kuipers Munneke et al. (2011). In contrast with our findings, Aas et al. (2015) reported underestimation of the cloud optical depth at Ny Ålesund (20 m a.s.l.) and Etonbreen (370 m a.s.l., Austfonna). That inconsistency may be explained by the fact that our study site is at a considerably higher elevation.

We find that monitoring the evolution of subsurface temperature using multiple thermistor strings scanned simultaneously and installed in close vicinity from each other is advantageous. It allows to derive a more spatially representative dataset by averaging data from several strings. The latter is of particular relevance during the period of melt water infiltration occurring not homogeneously and resulting in the highest standard deviations in temperature measured at the same depth (**Figure 8B**). The shape of the $RMSD = f(N_{strings})$ function (**Figure 9**) suggests that representativity can be significantly improved by increasing the number of strings to 3 or 4. The typical values of RMSD between the reference and averages of different number of thermistor strings (**Figure 9**) are consistently and significantly lower than the RMSD between the simulated and measured subsurface temperature (**Figure 11**). This justifies utilization of the empirical data for constraining the suggested schemes describing deep water percolation and validating the modeling results. In a broader context it also proves the potential of temperature tracking of melt water in snow and firn packs (Conway and Benedict, 1994; Pfeffer and Humphrey, 1996; Humphrey et al., 2012; Cox et al., 2015; Charalampidis et al., 2016).

Subsurface temperature measurements at Lomonosovfonna provide evidence of warming that occurred during the last decades. The firn temperature measured at 10 m depth in August 1965 (Zinger et al., 1966, 1,050 m a.s.l.) and 1976 (Zagorodnov and Zotikov, 1980, 1,120 m a.s.l.) was in the range of −3 to −2°C and the seasonal temperate surface layer reached the maximum depth of 2–3 m. This suggests that the upper reaches of the ice field, at that time, belonged to the cold firn zone according to the classification of Shumskii (1964). However, our results show that by the end of the ablation seasons 2012–2014 the firn at Lomonosovfonna was temperate down to 10 m meaning that the study site is now in the warm firn zone and runoff may occur.

Reproducing these observations appears to be challenging for the firn model with the default configuration of the water infiltration scheme (**Figure 10**). By the end of all three ablation seasons the simulated subsurface profile still contained thick layers of firn at subfreezing temperature, which eliminates the possibility of runoff. Underestimation of the snow and firn temperature also results in errors in the simulated conductive heat flux below the surface and consequently biased estimations of other components of the surface energy balance. Additionally, a higher viscosity of too cold firn and ice (Cuffey and Paterson, 2010) may induce biases in long-term simulations of glacier dynamics.

Increasing the surface melt rate by 27% by setting E_+ to 5 W m^{-2} resulted only in moderate decrease of the RMSD between the simulated and measured firn temperature and did not produce a warm firn pack by the end of ablation seasons 2012–2014. Larger perturbations (E_+ = 20, 22, and 32 W m^{-2} in 2012–2014) significantly reducing the RMSD between the simulated and measured subsurface temperature evolution seem unlikely. Serious changes in the settings of the surface energy balance scheme result in reduction of the performance in validation of the model output against data from stake S11 and the AWS, particularly the LW↑ measurements. The spatial and temporal dynamics of the errors in simulated subsurface temperature evolution (**Figure 10B**) had the same principal characteristics as evolution of the standard deviations in temperature measured at the same depth (**Figure 8B**). Altogether this suggests that in conditions of short ablation period at Lomonosovfonna the latent heat of infiltrating and refreezing water heats up the subsurface profile more effectively than it is possible within the default infiltration scheme.

The tested deep percolation schemes allowed to significantly reduce the RMSD between the simulated and measured temperature evolution (**Figures 11**, **12B**). The deep infiltration schemes result in more effective heating of the subsurface profile by the latent heat of refreezing water due to two mechanisms. Firstly, water going deeper releases latent heat at greater distance from the surface, where temperature gradients are low, and conductive heat exchange is not effective. At the same time, the upper part of the profile is allowed to maintain subfreezing temperature longer and by this be more readily warmed up by conduction from the melting surface. Secondly, by allowing a fraction of water to go past the upper firn horizons the potential of capillary and adhesive forces to retain some of the water in the upper layers is underused.

Two dimensional empirical data on the volumetric liquid water content of the seasonal snow packs presented by Techel and Pielmeier (2011) evidences that even though the source of liquid water is at the surface and the dominant flow is directed downwards, perched pockets with increased liquid water content can be present within snow pack along with pockets with reduced liquid water content. Thus the estimates of snow water holding capacity obtained by measuring the liquid mass retained by the sample after being entirely soaked and then drained (Coléou and Lesaffre, 1998; Schneider and Jansson, 2004) may be not immediately applicable in 1D snow and firn models at the onset of the water infiltration. Measurements of the volumetric water content in seasonal snow using upward directed radar conducted by Heilig et al. (2015) yielded the values of <2 vol. % at the onset of outflow from the snow pack registered by lysimeter. Converted to the relative gravimetric water content this corresponds to 6 grav. % assuming the density of 350 kg m^{-3}, which is significantly lower than the 10.7 grav. % resulting from the Schneider and Jansson (2004) parameterization. Earlier Reijmer et al. (2012) used a low water holding capacity value (2 grav. %) within the SOMARS model similar to the one used in present study to mimic the effect of preferential flow on subsurface conditions. However, such approach has the drawback of producing too high runoff rates once the water refreezing and retention capacity of the profile is exhausted.

The minimal RMSDs between the simulated and measured subsurface temperature (**Figure 11**) are consistently found with the largest z_{lim} values for the normal law infiltration (7.5–12 m) and with the smallest z_{lim} for the uniform scheme (4.5–6 m). This behavior of the firn model is explained by the properties of the probability density functions (**Figure 4B**). With the same settings of the z_{lim} parameter the uniform infiltration scheme allocates most water between $z_{lim}/2$ and z_{lim}, while the normal

infiltration implies that the smallest amount of water reaches that deep. It can be noted that the high horizontal gradients in subsurface temperature (**Figure 8B**) were observed in the depth range that is most close to the z_{lim} values resulting in minimal RMSD derived using the uniform infiltration scheme (**Figure 11**). That is particularly apparent for the data from 2012. Therefore, we suggest that this pattern of water percolation most closely reproduces the subsurface water flow.

It has to be mentioned that constraining of the shape of the $PDF(z, z_{lim})$ function and of the z_{lim} values largely relies on the extensive subsurface temperature dataset collected at Lomonosovfonna. Implementation of the suggested approach to parameterization of the deep water percolation for other areas or time periods will require additional temperature measurements for validation of the model output. That might be rather challenging in case the firn model is run on a distributed grid.

In the same time the logic of the deep water infiltration parameterization is simple to implement and allows for further development. Potentially additional parameters can be incorporated in the suggested deep percolation functions for a more realistic description of the effect of preferential water flow. Firstly, the utilized assumption of a constant in time z_{lim} value is in contrast with the results of temperature measurements. From **Figure 8B** it is apparent that the maximum depth of water percolation increases over the course of a melt season, which calls for implementation of a time dependence in the model. Secondly, the rate of water infiltration is known to be strongly dependent on the water supply. This is the result of the positive feedbacks: between the relative water conductivity and the water saturation of snow for unsaturated flow (Colbeck, 1972) and between the hydraulic conductivity and grain size of snow for saturated flow (Shimizu, 1970). It is, however, not obvious whether preferential water flow is more pronounced under conditions of high surface melt. While it was found to be the case in soils (Glass et al., 1989), according to the experimental studies, sieved snow was not more prone to preferential water infiltration under high water supply rates (Katsushima et al., 2013). According to our results high water supply rates at the surface are associated with a less pronounced concentration of the flow in the snow and firn pack: in 2013 when most melt water was produced during the ablation period (**Figure 7**), the optimal z_{lim} values are minimal (**Figure 11**) and in 2014 the opposite situation is observed. Finally, subsurface density distribution (ice layers, snow/firn grain-size contrasts, etc.) greatly influences the pattern of water infiltration (Marsh and Woo, 1984a; Fierz et al., 2009), which could be taken into account by incorporating additional arguments in the model.

7. CONCLUSIONS

Evolution of subsurface temperature at 1200 m a.s.l. on Lomonosovfonna, Svalbard, was studied during April 2012–2015 using field measurements by multiple thermistor strings and simulations using a coupled surface energy balance–multilayer firn model. Climate forcing for the model is provided by output of the regional scale climate model WRF and the initial subsurface temperature and density distributions are approximated from field data. Simulated mass and energy fluxes at the surface are validated against stake and AWS data.

The snow and firn pack is found to be heavily influenced by liquid water refreezing during the summer period and associated release of the latent heat. By the end of ablation seasons 2012–2014 the upper 12 m of the snow and firn pack were isothermal at 0°C. Compared to the earlier measurements at the ice field, our results provide an evidence of the subsurface warming that occurred during the last decades. The horizontal gradients in subsurface temperature were largest during the period of active melt water infiltration in July and migrated downwards over time. They are interpreted as being associated with the preferential flow paths in firn below the background wetting front. As a consequence of inhomogeneous water flow in snow and firn the measurements from single thermistor strings may be not representative for the area. On the basis of measurements done simultaneously in nine closely placed thermistor strings during two melt seasons we suggest that averaging data from 3 to 4 thermistor strings can significantly increase reliability of the summer temperature data.

Firn model with the default configuration of the water infiltration scheme consistently produced an overall too cold firn profile during the summer seasons 2012–2014. Performance of the subsurface temperature simulations is significantly improved by introduction of deep water infiltration schemes. We describe the effects of preferential water flow in snow and firn using a probability density function that distributes surficial water among subsurface layers relying on a single tuning parameter—depth z_{lim} to which liquid water is allowed to reach. Three different implementations of the approach were tested.

Introduction of the deep infiltration schemes reduced the RMSD between the simulated and measured temperature by about a factor of 2, more effectively than increasing the melt rate by 27% and in line with a melt increase of *ca* 200–400% for different years. The minimal RMSD values were reached with z_{lim} set to 4.5–12 m with the largest and smallest values consistently corresponding to the normal law and uniform infiltration schemes.

The mechanism behind the suggested approach to description of preferential water flow in one dimensional snow and firn models relies on the under-use of the potential of the upper layers to refreeze and retain water against gravity due to the capillary and adhesive forces. Given the simple logic and dependence on the sole parameter (z_{lim}), suggested deep infiltration schemes can be implemented in firn models applied at a wide range of spatial scales and allow further development by introduction of additional arguments.

AUTHOR CONTRIBUTIONS

VP, RP, CR, and SM designed the study. SM designed the field experiments, modeling strategy, was responsible for preparation, and updating of the manuscript. CR and WvP provided the coupled surface energy balance-firn model and facilitated its utilization and implementation of the deep infiltration schemes.

BC ran the WRF model and provided the forcing data for the coupled surface energy balance-firn model. SM, WvP, HM, RP, VP contributed to collection of the empirical data in the field campaigns. All authors contributed to the preparation of the manuscript and its critical revision.

ACKNOWLEDGMENTS

This publication is contribution 85 of the Nordic Centre of Excellence SVALI funded by the Nordic Top-level Research Initiative. Authors appreciate the constructive feedback provided by the Editor and two Reviewers, their efforts helped to significantly improve the manuscript. Funding was also provided by the Vetenskapsrådet grant 621-2014-3735 (VP). Authors acknowledge the Swedish Polar Research Secretariat, the Norwegian Polar Institute and the University Centre in Svalbard for logistical support of the field campaigns. Additional funding of the field operations was provided by the Ymer-80 foundation, Arctic Field Grant of the Research Council of Norway, Margit Althins stipend of the Royal Swedish Academy of Sciences.

REFERENCES

Aas, K. S., Berntsen, T. K., Boike, J., Etzelmüller, B., Kristjánsson, J. E., Maturilli, M., et al. (2015). A comparison between simulated and observed surface energy balance at the Svalbard archipelago. *J. Appl. Meteorol. Climatol.* 54, 1102–1119. doi: 10.1175/JAMC-D-14-0080.1

Aas, K. S., Dunse, T., Collier, E., Schuler, T. V., Berntsen, T. K., Kohler, J., et al. (2016). The climatic mass balance of Svalbard glaciers: a 10-year simulation with a coupled atmosphere–glacier mass balance model. *Cryosphere* 10, 1089–1104. doi: 10.5194/tc-10-1089-2016

Albert, M., Koh, G., and Perron, F. (1999). Radar investigations of melt pathways in a natural snowpack. *Hydrol. Process.* 13, 2991–3000. doi: 10.1002/(SICI)1099-1085(19991230)13:18<2991::AID-HYP10>3.0.CO;2-5

Bartelt, P., and Lehning, M. (2002). A physical SNOWPACK model for the Swiss avalanche warning: Part I: numerical model. *Cold Regions Sci. Technol.* 35, 123–145. doi: 10.1016/S0165-232X(02)00074-5

Bassford, R. P., Siegert, M. J., Dowdeswell, J. A., Oerlemans, J., Glazovsky, A. F., and Macheret, Y. Y. (2006). Quantifying the mass balance of ice caps on Severnaya Zemlya, Russian high Arctic I: climate and mass balance of the Vavilov ice cap. *Arctic Antarct. Alp. Res.* 38, 1–12. doi: 10.1657/1523-0430(2006)038[0001:QTMBOI]2.0.CO;2

Bøggild, C. E. (2000). Preferential flow and melt water retention in cold snow packs in West-Greenland. *Nordic Hydrol.* 31, 287–300. Available online at: http://hr.iwaponline.com/content/31/4-5/287

Brun, E., Martin, E., Simon, V., Gendre, C., and Coleou, C. (1989). An energy and mass model of snow cover suitable for operational avalanche forecasting. *J. Glaciol.* 35, 333–342. doi: 10.1017/S0022143000009254

Calonne, N., Flin, F., Morin, S., Lesaffre, B., du Roscoat, S. R., and Geindreau, C. (2011). Numerical and experimental investigations of the effective thermal conductivity of snow. *Geophys. Res. Lett.* 38, L23501. doi: 10.1029/2011GL049234

Campbell, F. M. A., Nienow, P. W., and Purves, R. S. (2006). Role of the supraglacial snowpack in mediating meltwater delivery to the glacier system as inferred from dye tracer investigations. *Hydrol. Process.* 20, 969–985. doi: 10.1002/hyp.6115

Charalampidis, C., van As, D., Colgan, W. T., Fausto, R. S., Macferrin, M., and Machguth, H. (2016). Thermal tracing of retained meltwater in the lower accumulation area of the southwestern Greenland ice sheet. *Ann. Glaciol.* 57, 1–10. doi: 10.1017/aog.2016.2

Christianson, K., Kohler, J., Alley, R. B., Nuth, C., and van Pelt, W. J. J. (2015). Dynamic perennial firn aquifer on an Arctic glacier. *Geophys. Res. Lett.* 42, 1418–1426. doi: 10.1002/2014GL062806

Church, J. A., White, N. J., Konikow, L. F., Domingues, C. M., Cogley, J. G., Rignot, E., et al. (2011). Revisiting the Earth's sea-level and energy budgets from 1961 to 2008. *Geophys. Res. Lett.* 38:L18601. doi: 10.1029/2011GL048794

Claremar, B., Obleitner, F., Reijmer, C., Pohjola, V., Waxegård, A., Karner, F., et al. (2012). Applying a mesoscale atmospheric model to Svalbard glaciers. *Adv. Meteorol.* 2012:22. doi: 10.1155/2012/321649

Colbeck, S. C. (1972). A theory of water percolation in snow. *J. Glaciol.* 11, 369–385. doi: 10.1017/S0022143000022346

Coléou, C., and Lesaffre, B. (1998). Irreducible water saturation in snow: experimental results in a cold laboratory. *Ann. Glaciol.* 26, 64–68. doi: 10.1017/S0260305500014579

Conway, H., and Benedict, R. (1994). Infiltration of water into snow. *Water Resour. Res.* 30, 641–649. doi: 10.1029/93WR03247

Cox, C., Humphrey, N., and Harper, J. (2015). Quantifying meltwater refreezing along a transect of sites on the Greenland ice sheet. *Cryosphere* 9, 691–701. doi: 10.5194/tc-9-691-2015

Cuffey, K., and Paterson, W. S. B. (2010). *The Physics of Glaciers*. Academic Press. Available online at: https://www.elsevier.com/books/the-physics-of-glaciers/cuffey/978-0-12-369461-4

Dee, D. P., Uppala, S. M., Simmons, A. J., Berrisford, P., Poli, P., Kobayashi, S., et al. (2011). The ERA-Interim reanalysis: configuration and performance of the data assimilation system. *Q. J. R. Meteorol. Soc.* 137, 553–597. doi: 10.1002/qj.828

Donlon, C. J., Martin, M., Stark, J., Roberts-Jones, J., Fiedler, E., and Wimmer, W. (2012). The Operational Sea Surface Temperature and Sea Ice Analysis (OSTIA) system. *Remote Sens. Environ.* 116, 140–158. Advanced Along Track Scanning Radiometer(AATSR) Special Issue. doi: 10.1016/j.rse.2010.10.017

Fettweis, X. (2007). Reconstruction of the 1979–2006 Greenland ice sheet surface mass balance using the regional climate model MAR. *Cryosphere* 1, 21–40. doi: 10.5194/tc-1-21-2007

Fierz, C., Armstrong, R., Durand, Y., Etchevers, P., Greene, E., McClung, D., et al. (2009). *The International Classification for Seasonal Snow on the Ground*. IHP-VII Technical Documents in Hydrology, No. 83, IACS contribution No. 1, UNESCO-IHP, Paris. Available online at: http://unesdoc.unesco.org/images/0018/001864/186462e.pdf

Førland, E. J., Benestad, R., Hanssen-Bauer, I., Erik, H. J., and Skaugen, T. E. (2011). Temperature and precipitation development at Svalbard 1900–2100. *Adv. Meteorol.* 2011:893790. doi: 10.1155/2011/893790

Forster, R. R., Box, J. E., van den Broeke, M. R., Miege, C., Burgess, E. W., van Angelen, J. H., et al. (2014). Extensive liquid meltwater storage in firn within the Greenland ice sheet. *Nat. Geosci.* 7, 95–98. doi: 10.1038/ngeo2043

Gascon, G., Sharp, M., Burgess, D., Bezeau, P., Bush, A. B., Morin, S., et al. (2014). How well is firn densification represented by a physically based multilayer model? Model evaluation for Devon Ice Cap, Nunavut, Canada. *J. Glaciol.* 60, 694–704. doi: 10.3189/2014JoG13J209

Glass, R. J., Steenhuis, T. S., and Parlange, J.-Y. (1989). Wetting front instability: 2. Experimental determination of relationships between system parameters and two-dimensional unstable flow field behavior in initially dry porous media. *Water Resour. Res.* 25, 1195–1207. doi: 10.1029/WR025i006p01195

Grell, G. A., and Dévényi, D. (2002). A generalized approach to parameterizing convection combining ensemble and data assimilation techniques. *Geophys. Res. Lett.* 29, 38.1–38.4. doi: 10.1029/2002GL015311

Greuell, W., and Konzelmann, T. (1994). Numerical modelling of the energy balance and the englacial temperature of the Greenland Ice Sheet. Calculations for the ETH-Camp location (West Greenland, 1155 m a.s.l.). *Global Planet. Change* 9, 91–114. doi: 10.1016/0921-8181(94)90010-8

Greuell, W., and Oerlemans, J. (1986). Sensitivity studies with a mass balance model including temperature profile calculations inside the glacier. *Z. Gletsch.kd. Glazialgeol.* 22, 101–124. Available online at: https://dspace.library.uu.nl/handle/1874/21035

Haeberli, W., Hoelzle, M., Paul, F., and Zemp, M. (2007). Integrated monitoring of mountain glaciers as key indicators of global climate change: the European Alps. *Ann. Glaciol.* 46, 150–160. doi: 10.3189/172756407782871512

Heilig, A., Mitterer, C., Schmid, L., Wever, N., Schweizer, J., Marshall, H.-P., et al. (2015). Seasonal and diurnal cycles of liquid water in snow measurements

and modeling. *J. Geophys. Res.* 120, 2139–2154. doi: 10.1002/2015JF003593

Hendrickx, J. M., and Flury, M. (2001). "Uniform and preferential flow mechanisms in the vadose zone," in *Conceptual Models of Flow and Transport in the Fractured Vadose Zone* (Washington, DC: The National Academies Press), 149–188. Available online at: https://www.nap.edu/catalog/10102/conceptual-models-of-flow-and-transport-in-the-fractured-vadose-zone

Hill, D. E., and Parlange, J.-Y. (1972). Wetting front instability in layered soils. *Soil Sci. Soc. Am. J.* 36, 697–702. doi: 10.2136/sssaj1972.03615995003600050010x

Hirashima, H., Yamaguchi, S., and Katsushima, T. (2014). A multi-dimensional water transport model to reproduce preferential flow in the snowpack. *Cold Regions Sci. Technol.* 108, 80–90. doi: 10.1016/j.coldregions.2014.09.004

Humphrey, N. F., Harper, J. T., and Pfeffer, W. T. (2012). Thermal tracking of meltwater retention in Greenland's accumulation area. *J. Geophys. Res. Earth Surf.* 117:F01010. doi: 10.1029/2011JF002083

Iacono, M. J., Delamere, J. S., Mlawer, E. J., Shephard, M. W., Clough, S. A., and Collins, W. D. (2008). Radiative forcing by long-lived greenhouse gases: calculations with the AER radiative transfer models. *J. Geophys. Res.* 113:D13103. doi: 10.1029/2008JD009944

Illangasekare, T. H., Walter, R. J., Meier, M. F., and Pfeffer, W. T. (1990). Modeling of meltwater infiltration in subfreezing snow. *Water Resour. Res.* 26, 1001–1012. doi: 10.1029/WR026i005p01001

James, T. D., Murray, T., Barrand, N. E., Sykes, H. J., Fox, A. J., and King, M. A. (2012). Observations of enhanced thinning in the upper reaches of Svalbard glaciers. *Cryosphere* 6, 1369–1381. doi: 10.5194/tc-6-1369-2012

Katsushima, T., Kumakura, T., and Takeuchi, Y. (2009). A multiple snow layer model including a parameterization of vertical water channel process in snowpack. *Cold Regions Sci. Technol.* 59, 143–151. doi: 10.1016/j.coldregions.2009.09.002

Katsushima, T., Yamaguchi, S., Kumakura, T., and Sato, A. (2013). Experimental analysis of preferential flow in dry snowpack. *Cold Regions Sci. Technol.* 85, 206–216. doi: 10.1016/j.coldregions.2012.09.012

Klok, E. L., and Oerlemans, J. (2002). Model study of the spatial distribution of the energy and mass balance of Morteratschgletscher, Switzerland. *J. Glaciol.* 48, 505–518. doi: 10.3189/172756502781831133

Kuipers Munneke, P., Reijmer, C. H., and van den Broeke, M. R. (2011). Assessing the retrieval of cloud properties from radiation measurements over snow and ice. *Int. J. Climatol.* 31, 756–769. doi: 10.1002/joc.2114

Lang, C., Fettweis, X., and Erpicum, M. (2015). Stable climate and surface mass balance in Svalbard over 1979 - 2013 despite the Arctic warming. *Cryosphere* 9, 83–101. doi: 10.5194/tc-9-83-2015

Langen, P. L., Fausto, R. S., Vandecrux, B., Mottram, R. H., and Box, J. E. (2017). Liquid water flow and retention on the Greenland ice sheet in the regional climate model HIRHAM5: local and large-scale impacts. *Front. Earth Sci.* 4:110. doi: 10.3389/feart.2016.00110

Ligtenberg, S. R. M., Helsen, M. M., and van den Broeke, M. R. (2011). An improved semi-empirical model for the densification of Antarctic firn. *Cryosphere* 5, 809–819. doi: 10.5194/tc-5-809-2011

Machguth, H., MacFerrin, M., van As, D., Box, J. E., Charalampidis, C., Colgan, W. T., et al. (2016). Greenland meltwater storage in firn limited by near-surface ice formation. *Nat. Clim. Change* 6, 390–393. doi: 10.1038/nclimate2899

Marchenko, S., Pohjola, V. A., Pettersson, R., van Pelt, W. J. J., Vega, C. P., Machguth, H., et al. (2017). A plot-scale study of firn stratigraphy at Lomonosovfonna, Svalbard, using ice cores, borehole video and GPR surveys in 2012–14. *J. Glaciol.* 63, 67–78. doi: 10.1017/jog.2016.118

Marsh, P., and Woo, M.-K. (1984a). Wetting front advance and freezing of meltwater within a snow cover: 1. Observations in the Canadian Arctic. *Water Resour. Res.* 20, 1853–1864. doi: 10.1029/WR020i012p01853

Marsh, P., and Woo, M.-K. (1984b). Wetting front advance and freezing of meltwater within a snow cover: 2. A simulation model. *Water Resour. Res.* 20, 1865–1874. doi: 10.1029/WR020i012p01865

Marsh, P., and Woo, M.-K. (1985). Meltwater movement in natural heterogeneous snow covers. *Water Resour. Res.* 21, 1710–1716. doi: 10.1029/WR021i011p01710

McGurk, B. J., and Marsh, P. (1995). "Flow-finger continuity in serial thick-sections in a melting sierran snowpack," in *Biogeochemistry of Seasonally Snow-Covered Catchments (Proceedings of a Boulder Symposium, July 1995) IAHS publ. no. 228*. Available online at: http://iahs.info/uploads/dms/iahs_228_0081.pdf

Meese, D. A., Gow, A. J., Grootes, P., Stuiver, M., Mayewski, P. A., Zielinski, G. A., et al. (1994). The accumulation record from the GISP2 core as an indicator of climate change throughout the Holocene. *Science* 266, 1680–1682. doi: 10.1126/science.266.5191.1680

Moholdt, G., Nuth, C., Hagen, J. O., and Kohler, J. (2010). Recent elevation changes of Svalbard glaciers derived from ICESat laser altimetry. *Remote Sens. Environ.* 114, 2756–2767. doi: 10.1016/j.rse.2010.06.008

Morrison, H., Curry, J. A., and Khvorostyanov, V. I. (2005). A new double-moment microphysics parameterization for application in cloud and climate models. Part I: description. *J. Atmos. Sci.* 62, 1665–1677. doi: 10.1175/JAS3446.1

Nakanishi, M., and Niino, H. (2006). An improved Mellor–Yamada level-3 model: its numerical stability and application to a regional prediction of advection fog. *Bound. Layer Meteorol.* 119, 397–407. doi: 10.1007/s10546-005-9030-8

Niu, G.-Y., Yang, Z.-L., Mitchell, K. E., Chen, F., Ek, M. B., Barlage, M., et al. (2011). The community Noah land surface model with multiparameterization options (Noah-MP): 1. model description and evaluation with local-scale measurements. *J. Geophys. Res.* 116:D12109. doi: 10.1029/2010JD015139

Nordli, Ø., Przybylak, R., Ogilvie, A., and Isaksen, K. (2014). Long-term temperature trends and variability on Spitsbergen: the extended Svalbard Airport temperature series, 1898–2012. *Polar Res.* 33:21349. doi: 10.3402/polar.v33.21349

Nuth, C., Kohler, J., König, M., von Deschwanden, A., Hagen, J. O., Kääb, A., et al. (2013). Decadal changes from a multi-temporal glacier inventory of Svalbard. *Cryosphere* 7, 1603–1621. doi: 10.5194/tc-7-1603-2013

Nuth, C., Moholdt, G., Kohler, J., Hagen, J. O., and Kääb, A. (2010). Svalbard glacier elevation changes and contribution to sea level rise. *J. Geophys. Res.* 115, F01008. doi: 10.1029/2008JF001223

Nuth, C., Schuler, T. V., Kohler, J., Altena, B., and Hagen, J. O. (2012). Estimating the long-term calving flux of Kronebreen, Svalbard, from geodetic elevation changes and mass-balance modelling. *J. Glaciol.* 58, 119–133. doi: 10.3189/2012JoG11J036

Obleitner, F., and Lehning, M. (2004). Measurement and simulation of snow and superimposed ice at the Kongsvegen glacier, Svalbard (Spitzbergen). *J. Geophys. Res.* 109:D04106. doi: 10.1029/2003JD003945

Pälli, A., Kohler, J. C., Isaksson, E., Moore, J. C., Pinglot, J. F., Pohjola, V. A., et al. (2002). Spatial and temporal variability of snow accumulation using ground-penetrating radar and ice cores on a Svalbard glacier. *J. Glaciol.* 48, 417–424. doi: 10.3189/172756502781831205

Pfeffer, W. T., and Humphrey, N. F. (1996). Determination of timing and location of water movement and ice-layer formation by temperature measurements in sub-freezing snow. *J. Glaciol.* 42, 292–304. doi: 10.1017/S0022143000004159

Pfeffer, W. T., Meier, M. F., and Illangasekare, T. H. (1991). Retention of Greenland runoff by refreezing: Implications for projected future sea level change. *J. Geophys. Res.* 96, 22117–22124. doi: 10.1029/91JC02502

Reijmer, C. H., and Hock, R. (2008). Internal accumulation on Storglaciären, Sweden, in a multi-layer snow model coupled to a distributed energy- and mass-balance model. *J. Glaciol.* 54, 61–72. doi: 10.3189/002214308784409161

Reijmer, C. H., van den Broeke, M. R., Fettweis, X., Ettema, J., and Stap, L. B. (2012). Refreezing on the Greenland ice sheet: a comparison of parameterizations. *Cryosphere* 6, 743–762. doi: 10.5194/tc-6-743-2012

Schneebeli, M. (1995). "Development and stability of preferential flow paths in a layered snowpack," in *Biogeochemistry of Seasonally Snow-Covered Catchments (Proceedings of a Boulder Symposium July 1995) IAHS Publ. no. 228*, 89–95. Available online at: http://iahs.info/uploads/dms/iahs_228_0089.pdf

Schneider, T., and Jansson, P. (2004). Internal accumulation in firn and its significance for the mass balance of Storglaciären, Sweden. *J. Glaciol.* 50, 25–34. doi: 10.3189/172756504781830277

Shimizu, H. (1970). "Air permeability of deposited snow," in *Contributions from the Institute of Low Temperature Science* A22, 1–32. Available online at: http://hdl.handle.net/2115/20234

Shumskii, P. A. (1964). "Zones of Ice Formation," in *Principles of structural glaciology*, ed P. F. Shvetsov (New York, NY: Dover Publications, Inc.), 407–440.

Skamarock, W., Klemp, J., Dudhia, J., Gill, D., Barker, D., Wang, W., et al. (2008). *A Description of the Advanced Research WRF Version 3*. Technical Report, NCAR Technical Note NCAR/TN-475+STR. Available online at: http://www2.mmm.ucar.edu/wrf/users/docs/arw_v3.pdf

Steger, C., Reijmer, C., Van Den Broeke, M., Wever, N., Forster, R., Koenig, L., et al. (2017). Firn meltwater retention on the Greenland ice sheet: a model comparison. *Front. Earth Sci.* 5:3. doi: 10.3389/feart.2017.00003

Stephens, G. L. (2005). Cloud feedbacks in the climate system: a critical review. *J. Clim.* 18, 237–273. doi: 10.1175/JCLI-3243.1

Sturm, M., and Holmgren, J. (1993). Rain-induced water percolation in snow as detected using heat flux transducers. *Water Resour. Res.* 29, 2323–2334. doi: 10.1029/93WR00609

Techel, F., and Pielmeier, C. (2011). Point observations of liquid water content in wet snow – investigating methodical, spatial and temporal aspects. *Cryosphere* 5, 405–418. doi: 10.5194/tc-5-405-2011

van Angelen, J. H., Lenaerts, J. T. M., van den Broeke, M. R., Fettweis, X., and van Meijgaard, E. (2013). Rapid loss of firn pore space accelerates 21st century Greenland mass loss. *Geophys. Res. Lett.* 40, 21092113. doi: 10.1002/grl.50490

Van de Wal, R. S. W., Mulvaney, R., Isaksson, E., Moore, J. C., Pinglot, J. F., Pohjola, V. A., et al. (2002). Reconstruction of the historical temperature trend from measurements in a medium-length borehole on the Lomonosovfonna plateau, Svalbard. *Ann. Glaciol.* 35, 371–378. doi: 10.3189/172756402781816979

Van Pelt, W., and Kohler, J. (2015). Modelling the long-term mass balance and firn evolution of Glaciers around Kongsfjorden, Svalbard. *J. Glaciol.* 61, 731–744. doi: 10.3189/2015JoG14J223

Van Pelt, W. J., Pettersson, R., Pohjola, V. A., Marchenko, S., Claremar, B., and Oerlemans, J. (2014). Inverse estimation of snow accumulation along a radar transect on Nordenskiöldbreen, Svalbard. *J. Geophys. Res.* 119, 816–835. doi: 10.1002/2013JF003040

Van Pelt, W. J. J., Oerlemans, J., Reijmer, C. H., Pohjola, V. A., Pettersson, R., and van Angelen, J. H. (2012). Simulating melt, runoff and refreezing on Nordenskiöldbreen, Svalbard, using a coupled snow and energy balance model. *Cryosphere* 6, 641–659. doi: 10.5194/tc-6-641-2012

Van Pelt, W. J. J., Pohjola, V. A., and Reijmer, C. H. (2016). The changing impact of snow conditions and refreezing on the mass balance of an idealized Svalbard glacier. *Front. Earth Sci.* 4:102. doi: 10.3389/feart.2016.00102

Vaughan, D. G., Comiso, J. C., Allison, I., Carrasco, J., Kaser, G., Kwok, R., et al. (2013). "Observations: Cryosphere, Chapter 4," in *Climate Change 2013: The Physical Science Basis. Contribution of Working Group I to the Fifth Assessment Report of the Intergovernmental Panel on Climate Change,* eds T. F. Stocker, D. Qin, G.-K. Plattner, M. Tignor, S. K. Allen, J. Boschung, A. Nauels, Y. Xia, V. Bex, and P. M. Midgley (Cambridge, UK; New York, NY: Cambridge University Press), 317–382. Available online at: http://ipcc.ch/pdf/assessment-report/ar5/wg1/WG1AR5_Chapter04_FINAL.pdf

Waldner, P. A., Schneebeli, M., Schultze-Zimmermann, U., and Flühler, H. (2004). Effect of snow structure on water flow and solute transport. *Hydrol. Process.* 18, 1271–1290. doi: 10.1002/hyp.1401

Wendl, I. A. (2014). *High resolution records of black carbon and other aerosol constituents from the Lomonosovfonna 2009 ice core*. Ph.D. thesis, Departement für Chemie und Biochemie der Universität Bern. Available online at: http://csold.unibe.ch/students/theses/phd/76.pdf

Wendl, I. A., Eichler, A., Isaksson, E., Martma, T., and Schwikowski, M. (2015). 800-year ice-core record of nitrogen deposition in Svalbard linked to ocean productivity and biogenic emissions. *Atmos. Chem. Phys.* 15, 7287–7300. doi: 10.5194/acp-15-7287-2015

Wever, N., Würzer, S., Fierz, C., and Lehning, M. (2016). Simulating ice layer formation under the presence of preferential flow in layered snowpacks. *Cryosphere* 10, 2731–2744. doi: 10.5194/tc-10-27 31-2016

Williams, M., Pfeffer, W., and Knoll, M. (2000). *Collaborative Experiment for Pulsed Radar Visualization of Water Flow Paths in Snow*. Boulder, CO: Technical Report, University of Colorado.

Williams, M. W., Erickson, T. A., and Petrzelka, J. L. (2010). Visualizing meltwater flow through snow at the centimetre-to-metre scale using a snow guillotine. *Hydrol. Process.* 24, 2098–2110. doi: 10.1002/hyp.7630

Williams, M. W., Sommerfeld, R., Massman, S., and Rikkers, M. (1999). Correlation lengths of meltwater flow through ripe snowpacks, colorado front range, USA. *Hydrol. Process.* 13, 1807–1826. doi: 10.1002/(SICI)1099-1085(199909)13:12/13<1807::AID-HYP891>3.0.CO;2-U

Wright, A., Wadham, J., Siegert, M., Luckman, A., and Kohler, J. (2005). Modelling the impact of superimposed ice on the mass balance of an Arctic glacier under scenarios of future climate change. *Ann. Glaciol.* 42, 277–283. doi: 10.3189/172756405781813104

Zagorodnov, V. S., and Zotikov, I. A. (1980). Core drilling at Spitsbergen (in Russian). *Materialy Glatsiologicheskih Issledovanii: Khronika, Obsujdeniya (Data of Glaciological Studies)* 40, 157–163.

Zdanowicz, C., Smetny-Sowa, A., Fisher, D., Schaffer, N., Copland, L., Eley, J., et al. (2012). Summer melt rates on Penny Ice Cap, Baffin Island: past and recent trends and implications for regional climate. *J. Geophys. Res.* 117:F02006. doi: 10.1029/2011JF002248

Zinger, Y. M., Koryakin, V. S., Lavrushin, Y. A., Markin, V. A., Mihalev, B. I., and Troitskiy, L. C. (1966). Study of glaciers at Spitsbergen by a Soviet expedition during summer 1965 (in Russian). *Materialy Glatsiologicheskih Issledovanii: Khronika, Obsujdeniya (Data of Glaciological Studies)* 12, 59–72.

Zuo, Z., and Oerlemans, J. (1996). Modelling albedo and specific balance of the Greenland ice sheet: calculations for the Søndre Strømjörd transect. *J. Glaciol.* 42, 305–317. doi: 10.1017/S00221430000 04160

Conflict of Interest Statement: The authors declare that the research was conducted in the absence of any commercial or financial relationships that could be construed as a potential conflict of interest.

The reviewer NW and handling Editor declared their shared affiliation, and the handling Editor states that the process nevertheless met the standards of a fair and objective review.

frontiers in Earth Science

METHODS
published: 12 January 2017
doi: 10.3389/feart.2016.00110

Liquid Water Flow and Retention on the Greenland Ice Sheet in the Regional Climate Model HIRHAM5: Local and Large-Scale Impacts

Peter L. Langen[1], Robert S. Fausto[2], Baptiste Vandecrux[2,3], Ruth H. Mottram[1] and Jason E. Box[2]*

[1] Climate and Arctic Research, Danish Meteorological Institute, Copenhagen, Denmark, [2] Geological Survey of Denmark and Greenland, Copenhagen, Denmark, [3] Arctic Technology Centre (ARTEK), Technical University of Denmark, Lyngby, Denmark

OPEN ACCESS

Edited by:
Marco Tedesco, NASA Goddard Institute for Space Studies-Columbia University, USA

Reviewed by:
Michiel Van Den Broeke, Utrecht University, Netherlands
Xavier Fettweis, University of Liège, Belgium
Patrick Alexander, NASA Goddard Institute for Space Studies, USA

***Correspondence:**
Peter L. Langen
pla@dmi.dk

Specialty section:
This article was submitted to Cryospheric Sciences, a section of the journal Frontiers in Earth Science

Received: *04 October 2016*
Accepted: *22 December 2016*
Published: *12 January 2017*

Citation:
Langen PL, Fausto RS, Vandecrux B, Mottram RH and Box JE (2017) Liquid Water Flow and Retention on the Greenland Ice Sheet in the Regional Climate Model HIRHAM5: Local and Large-Scale Impacts. Front. Earth Sci. 4:110. doi: 10.3389/feart.2016.00110

To improve Greenland Ice Sheet surface mass balance (SMB) simulation, the subsurface scheme of the HIRHAM5 regional climate model was extended to include snow densification, varying hydraulic conductivity, irreducible water saturation and other effects on snow liquid water percolation and retention. Sensitivity experiments to investigate the effects of the additions and the impact of different parameterization choices are presented. Compared with 68 accumulation area ice cores, the simulated mean annual net accumulation bias is −5% (correlation coefficient of 0.90). Modeled SMB in the ablation area compares favorably with 1041 PROMICE observations with regression slope of 0.95–0.97 (depending on model configuration), correlation coefficient of 0.75–0.86 and mean bias −3%. Weighting ablation area SMB biases at low- and high-elevation with the amount of runoff from these areas, we estimate ice sheet-wide mass loss biases in the ablation area at −5 and −7% using observed (MODIS-derived) and internally calculated albedo, respectively. Comparison with observed melt day counts shows that patterns of spatial (correlation ∼0.9) and temporal (correlation coefficient of ∼0.9) variability are realistically represented in the simulations. However, the model tends to underestimate the magnitude of inter-annual variability (regression slope ∼0.7) and overestimate that of spatial variability (slope ∼1.2). In terms of subsurface temperature structure and occurrence of perennial firn aquifers and perched ice layers, the most important model choices are the albedo implementation and irreducible water saturation parameterization. At one percolation area location, for instance, the internally calculated albedo yields too high subsurface temperatures below 5 m, but when using an implementation of irreducible saturation allowing higher values, an ice layer forms in 2011, reducing the deep warm bias in subsequent years. On the other hand, prior to the formation of the ice layer, observed albedos combined with lower irreducible saturation give the smallest bias. Perennial firn aquifers and perched ice layers occur in varying thickness and area for

different model parameter choices. While the occurrence of these features has an influence on the local-scale subsurface temperature, snow, ice and water fields, the Greenland-wide runoff and SMB are—in the model's current climate—dominated by the albedo implementation.

Keywords: liquid water percolation in firn, regional climate model, HIRHAM5 subsurface scheme, Greenland ice sheet runoff, Greenland ice sheet surface mass balance, Greenland ice sheet perched ice layers, Greenland ice sheet perennial firn aquifer

INTRODUCTION

Greenland ice sheet mass budget changes are among the largest sources of uncertainty in estimates of sea level rise under climate change (Church et al., 2013; Gregory et al., 2013). A key uncertainty in the mass budget is the degree of meltwater retention due to refreezing and capillary forces (e.g., Janssens and Huybrechts, 2000; Harper et al., 2012; Vernon et al., 2013; van As et al., 2016). As the climate has warmed, the zone where melt and rainfall occurs over the snowpack has expanded to higher elevations in the last decade (Howat et al., 2013; de la Peña et al., 2015). Observations from Polashenski et al. (2014) confirm that firn warming is a both long-term (>50 years) and widespread effect. Successive warm summers have also led to the formation of reduced permeability ice lens complexes that expand runoff into the accumulation area, e.g., at the KAN-U site at 1840 m a.s.l (above sea level) in 2012 (Machguth et al., 2016a). Accounting realistically for firn permeability will likely become increasingly important with continued climate warming, and we focus in this paper on representing the pathways of liquid water in snow and firn in a surface mass balance (SMB) model.

When melt or rainfall occurs at the surface of the snowpack, the water typically percolates deeper down and may be stored as liquid water or refrozen in the form of ice lenses (Benson, 1962; Braithwaite et al., 1992). The process by which water percolates in the snowpack was comprehensively described in a Darcian type flow model by Colbeck (1972). Melt percolation has been identified and observed across many glaciers, particularly in the Alps and the Arctic, where deep snow packs often exist overlying glacier ice (e.g., Müller, 1976; Braithwaite et al., 1994; Parry et al., 2007; Wright et al., 2007; Humphrey et al., 2012; Gascon et al., 2013; Polashenski et al., 2014). The meltwater penetration depth is controlled by the temperature and density of the snowpack. Snow/firn density controls the hydraulic conductivity, the pore spaces where water can be contained, and the thermal conductivity of the snow. Subsurface temperature has an important control on densification rate and, via layer cold content, determines if and how much liquid water will freeze.

Once liquid water is in the snowpack, if there is sufficient cold content, the water may refreeze, forming ice layers and pipes. Ice lenses appear to reduce percolation, acting as a barrier to "deep percolation," i.e., percolation below the previous year's accumulation (Machguth et al., 2016a). Refreezing releases latent heat and acts to warm the snowpack, a phenomenon that has been observed in the Greenland firn over the last 50 years (Polashenski et al., 2014) and seen in modeled snow packs in regional climate simulations (e.g., van den Broeke et al., 2009). However, under high accumulation rate and in locations with low surface slope, meltwater may remain unfrozen and locked in perennial firn aquifers (Forster et al., 2014; Koenig et al., 2014; Kuipers Munneke et al., 2014). Along with refrozen water, perennial firn aquifers have a potentially important delaying effect on sea level rise from Greenland ice in a warming world (Pfeffer et al., 1991). Percolation of meltwater into the snowpack is, however, limited by available pore space (Harper et al., 2012) and future projections by van Angelen et al. (2013) suggest that this pore space may be filled after just a few decades, leading to an acceleration of runoff.

The importance of accounting for these processes has driven the development of snow and firn models within SMB models. As liquid water retention and refreezing are spatially heterogeneous processes and occur at sub-grid scale, early models used parameterizations. Reeh (1989) assumed a fixed percentage of the winter accumulation was retained. Janssens and Huybrechts (2000), Pfeffer et al. (1991) and others developed parameterizations to quantify meltwater retention from a reduced number of variables. Only more recently have meltwater percolation and retention been physically described in firn and snowpack models both at ice sheet scale and in alpine environments (CROCUS, Vionnet et al., 2012; SNOWPACK, Wever et al., 2015). Similar physically-based representations have also been adapted into regional climate models RACMO and MAR (Fettweis, 2007; van den Broeke et al., 2009; Reijmer et al., 2012). The version of HIRHAM5 described in Langen et al. (2015) used a simplified representation of liquid water retention and refreezing.

Declining surface albedo feeding back with temperature and melt plays an important role for the mass balance (e.g., Box et al., 2012; van Angelen et al., 2014). The darkening may be associated both with a general warming (Tedesco et al., 2016) and with increasing amounts of light-absorbing impurities transported to the ice sheet (Dumont et al., 2014; Keegan et al., 2014) or from exposure of "dirty ice" (Tedesco et al., 2016). In any case, the representation of and interplay between albedo processes and subsurface meltwater and refreezing has important effects on the mass balance in a warming climate (van Angelen et al., 2012) including the lower accumulation area (Charalampidis et al., 2015).

In this paper we present results from a HIRHAM5 subsurface scheme which accounts for snow/firn density evolution and hydraulic conductivity and employs two different albedo implementations (described in Section Model Description and Simulations), allowing for formation of firn aquifers and perched impermeable ice layers. In Section Model Evaluation

Using Observations, we compare model results to observed net accumulation, SMB in the ablation area, melt extent and subsurface density profiles at multiple ice sheet locations. In addition, we compare simulations with observed subsurface temperature evolution at a single site in West Greenland. We then perform sensitivity tests and discuss the choices made in the model which are particularly important (Section Sensitivity Results). Conclusions are given in Section Conclusions.

MODEL DESCRIPTION AND SIMULATIONS

The regional climate model HIRHAM5 combines the dynamical core of the HIRLAM7 numerical weather forecasting model (Eerola, 2006) with physics schemes from the ECHAM5 general circulation model (Roeckner et al., 2003). Details of the configuration are in Christensen et al. (2006). In the all-Greenland domain employed here after Lucas-Picher et al. (2012), HIRHAM5 is run on a horizontal 0.05° × 0.05° rotated-pole grid corresponding roughly to 5.5 km resolution. The atmosphere has 31 levels in the vertical and a 90 s time step. On the lateral boundaries, the ERA-Interim reanalysis (Dee et al., 2011) provides 6 h atmospheric model-level fields of wind, temperature and humidity as well as surface pressure. Across ocean grid points, ERA-Interim sea surface temperatures and sea ice concentration are prescribed. The experiment covers 35 years (1980-2014).

Subsurface Scheme

At the surface, snow mass is updated with snowfall, rainfall, melt and deposition/sublimation at each subsurface scheme time step (1 h). Likewise, the surface temperature is updated via energy budget closure with radiative and turbulent surface energy exchange above and diffusive and advective heat exchange with subsurface layers. If the surface temperature exceeds 0°C, it is reset to 0°C and the excess energy supplies heat for melting (Langen et al., 2015).

The current subsurface model has a number of additions and extensions after the original five-layer ECHAM5 surface scheme (Roeckner et al., 2003) modified for use over glaciers and ice sheets by Langen et al. (2015). Advancements include densification, snow grain growth, snow state-dependent hydraulic conductivity, superimposed ice formation and irreducible water saturation as well as accommodation for water retention in excess of the irreducible saturation. In the following, we describe the details of the new features.

Vertical Discretization

The new subsurface scheme consists of a horizontal grid of non-interacting columns with 32 layers of time-constant water equivalent thicknesses. Each layer's thickness is divided into contributions from snow (p_s), ice (p_i), and liquid water (p_w); each having m w.e. units. While their relative magnitudes can vary through time, the sum of these three parameters equals the layer thickness and remains constant. The layer thicknesses increase exponentially with depth to increase resolution near the surface (N'th layer thickness $D_N = D_1\lambda^{N-1}$, with $D_1 = 0.065$ m and $\lambda = 1.173265$ chosen to give a full model depth of 60 m w.e. minimizing impacts of lower boundary conditions). The uppermost 2.2 m w.e. are thus represented by 12 layers with thicknesses varying from 6.5 to 37 cm w.e., while the top 10.4 m w.e. has 21 layers with thicknesses up to 1.6 m w.e. The lowest subsurface layer has a thickness of 9.2 m w.e.

As mass is added on top of the subsurface model (via snow, rainfall, condensation or deposition), the scheme advects mass downward to ensure the constant w.e. layer thicknesses. Likewise, when mass is removed from the column by runoff, evaporation or sublimation, mass is shifted up from an infinite ice reservoir below into the lowest model layer. This up- and down mass flux is accompanied by an associated vertical transfer of sensible heat, snow density, grain size and snow, water and ice fractions.

Temperature, Refreezing, and Superimposed Ice Formation

The original ECHAM5 heat diffusion solver (Roeckner et al., 2003) is modified to accommodate a density dependent snow thermal conductivity (Yen, 1981; Vionnet et al., 2012),

$$k_s = k_{ice}\left(\frac{\rho_s}{\rho_w}\right)^{1.88} \quad (1)$$

where k_{ice} is the ice thermal conductivity (in W m^{-1} K^{-1}) and ρ_s and ρ_w are, respectively, the densities of snow and water. The layer bulk thermal conductivity is calculated through a volume-weighted blending of k_s and k_{ice}. Accumulating snow is assumed to have the temperature of the upper layer, while rain is assumed have 0°C temperature, T_f. The possible energy source from rain with temperature above T_f is thus disregarded. The infinite sublayer, with which the lowest model layer exchanges heat, is set to the simulated local long-term mean near-surface air temperature. This infinite sublayer choice may lead to a slight overestimation of refreezing since the model-bottom will be kept cooler than near-surface layers in case of latent heat release from refreezing. Since the subsurface model is 60 m w.e. deep, the vertical temperature gradient and resulting heat diffusion associated with this bottom cooling will be minor.

The cold content, i.e., the energy required to heat the snow and ice mass to T_f, in each layer is used to freeze liquid water, transferring mass to the ice fraction. Refreezing is assumed to be instantaneous, thereby freezing as much water as is available or as cold content allows within a single time step. The temperature of the layer is raised by latent heat release to conserve energy. Superimposed ice formation occurs when liquid water resides in a temperate layer above an impermeable layer (description below) with a temperature below the freezing point. A downward heat flux at the layer interface is then calculated assuming that the cold, impermeable layer has a linear temperature profile between T_f at the interface and the mean layer temperature at the layer mid-point. This downward heat flux allows superimposed ice to form in the temperate layer and heats the impermeable layer beneath.

Water Saturation

The water saturation, S_w, is the volume of water per pore space volume and may be written in terms of masses as

$$S_w = \frac{p_w}{p_s}\frac{\rho_s\rho_i}{\rho_w(\rho_i-\rho_s)} \quad (2)$$

where $\rho_i = 917\,\mathrm{kg\,m^{-3}}$ is taken to be the density of ice and p_w and p_s are the layer masses of water and snow. The maximum water saturation that can be sustained by snow grain capillary tension is termed the irreducible water saturation, S_{wi}, with values employed in models varying widely. Colbeck (1974) found a value of 0.07 experimentally and Yamaguchi et al. (2010) found a value of 0.02, both for snow with a density of about $550\,\mathrm{kg\,m^{-3}}$. Coleou and Lesaffre (1998) experimented with variable densities and found an approximate relationship between porosity, $P = 1-\rho_s/\rho_i$, and the water per snow-plus-water mass irreducible liquid water content, W_{mi}:

$$W_{mi} = 0.057\frac{P}{1-P} + 0.017 = 0.057\frac{\rho_i-\rho_s}{\rho_s} + 0.017 \quad (3)$$

The quantity W_{mi} may be converted to S_{wi} through the relation

$$S_{wi} = \frac{W_{mi}}{(1-W_{mi})}\frac{\rho_s\rho_i}{\rho_w(\rho_i-\rho_s)} \quad (4)$$

As ρ_s increases, S_{wi} calculated in this manner initially decreases from ~0.10 at $100\,\mathrm{kg\,m^{-3}}$ to ~0.07 at $300\,\mathrm{kg\,m^{-3}}$. S_{wi} then increases to about ~0.085 at $600\,\mathrm{kg\,m^{-3}}$ and ~0.17 near $810\,\mathrm{kg\,m^{-3}}$ (**Figure 1**).

Vionnet et al. (2012) used an irreducible water saturation value of 0.05 in the Crocus/SURFEX model. As described by Reijmer et al. (2012), SOMARS/RACMO used 0.02 while Crocus/MAR used 0.06. Kuipers Munneke et al. (2014) used the Coleou and Lesaffre (1998) approach in their study of perennial firn aquifers with the Ligtenberg et al. (2011) firn model. To test the sensitivity toward this choice, we perform experiments with a fixed value of 0.02 along with values calculated based on the Coleou and Lesaffre (1998) parameterization.

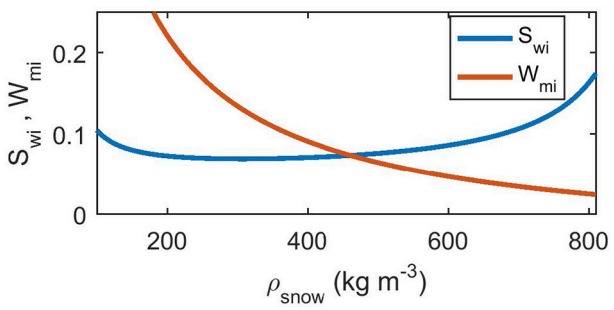

FIGURE 1 | Irreducible saturation, S_{wi}, and irreducible liquid water content, W_{mi} (water per snow-plus-water mass), as a function of snow density following the parameterization by Coleou and Lesaffre (1998).

Finally, given values of S_w and S_{wi}, we may calculate the effective liquid saturation,

$$\Theta = \frac{S_w - S_{wi}}{1-S_{wi}} \quad (5)$$

which becomes positive when the snow contains more water than can be permanently held by capillary forces alone.

Downward Flow of Liquid Water

In our treatment of vertical flow of liquid water through the snowpack, we closely follow the implementation by Hirashima et al. (2010). The governing equation for water flow, q ($\mathrm{m\,s^{-1}}$), is Darcy's law,

$$q = K\left(\frac{dh}{dz}+1\right) \quad (6)$$

where dh/dz is the vertical gradient in capillary suction, h (m units), and the second term (+1) represents gravity. The vertical coordinate, z, increases downwards. The hydraulic conductivity, K ($\mathrm{m\,s^{-1}}$), and the capillary suction are parameterized in terms of snow grain diameter, d_g (mm units), effective liquid saturation, Θ, and snow density, ρ_s, as follows. The hydraulic conductivity of snow is the product of the saturated and unsaturated conductivities, $K_{snow} = K_s K_r$, the former of which was determined by Shimizu (1970) to follow:

$$K_s = 0.077\frac{g}{\nu_w}\left(\frac{d_g}{1000}\right)^2 \exp(-0.0078\rho_s) \quad (7)$$

Here, g is the acceleration due to gravity and ν_w is the kinematic viscosity of water ($1.787\cdot10^{-6}\ \mathrm{m^2\,s^{-1}}$). Note that d_g has mm units. We thus divide by 1000 to get the diameter in m units in accordance with Calonne et al. (2012). In the van Genuchten (1980) parameterization of K_r and h used by Hirashima et al. (2010), two parameters (α and n) must be calculated,

$$\alpha = 7.3\,d_g + 1.9,\ n = 15.68\exp(-0.46\,d_g) + 1 \quad (8)$$

With these, and the quantity $m = 1 - 1/n$, we calculate,

$$K_r = \Theta^{\frac{1}{2}}\left[1-\left(1-\Theta^{\frac{1}{m}}\right)^m\right]^2 \quad (9)$$

$$h = \frac{1}{\alpha}\left(\Theta^{-\frac{1}{m}}-1\right)^{\frac{1}{n}} \quad (10)$$

As the layers in our subsurface model contain both snow and ice, we need to take into account the hydraulic conductivity reduction resulting from the presence of ice. Colbeck (1975) developed an analytical model for a snowpack with interspersed ice layers, and we employ it here for model layers with some ice fraction. The bulk hydraulic conductivity of the entire model layer is

$$K = K_{snow}\left[f_{snow} + (1-f_{snow})\frac{1+\frac{w_h}{w_{ice}}}{\frac{K_{ice}}{K_{snow}}+\frac{w_h}{w_{ice}}}\right] \quad (11)$$

where $f_{snow} = H_s/(H_s+H_i)$ is the fraction of the physical layer thickness which is snow (here, $H_s = p_s\rho_w/\rho_s$ and $H_i = p_i\rho_w/\rho_i$

are the physical thicknesses of the snow and ice fractions). The hydraulic conductivity of ice, K_{ice}, is assumed zero, and the fraction w_h/w_{ice} is the ratio between the width of holes in the ice and the width of the ice. A value of 1 for this fraction means that when ice is present in a layer, it has a horizontal extent of half the unit area. Here, it is essentially a tuning parameter that can decrease the hydraulic conductivity in the presence of ice and we perform experiments with w_h/w_{ice} values of 1 and 0.1.

Hirashima et al. (2010) introduced an implementation of Darcy's law that allows for longer time-steps at the cost of considering only downward flow, and the same is adopted here. The instantaneous flux, q_0, evaluated using beginning-of-time-step values for all the above quantities influencing K and h, will change during a long time step and taking $q_0\Delta t$ as the time-step total flux will be an overestimate; the total flux into a given layer will at most equal all the water beyond irreducible saturation in the layer above, or it will equal the amount that increases the vertical h-gradient sufficiently to obtain balance between the two terms in Darcy's law (Equation 6). That limiting amount, q_{lim}, is estimated iteratively and allows for calculation of the time-step integrated flux $q_{lim}\left[1-\exp\left(-\frac{q_0}{q_{lim}}\Delta t\right)\right]$ (Hirashima et al., 2010).

During our sensitivity experiments, we also employ a "NoDarcy" version of the code which ignores the delaying effect of hydraulic conductivity on the vertical flow, allowing all water in excess of the irreducible saturation to fully percolate within a single time step.

Impermeable Layers and Runoff

A layer is considered impermeable if its bulk dry density,

$$\rho_{bulk} = (p_s + p_i)\Big/\left(\frac{p_s}{\rho_s}+\frac{p_i}{\rho_i}\right) \tag{12}$$

exceeds a threshold of 810 kg m^{-3}. This value is lower than the classical value of pore close-off density at 830 kg m^{-3} (Cuffey and Paterson, 2010), since field studies (Gregory et al., 2014) show that in high-accumulation areas such as West Antarctic Ice Sheet (WAIS) divide (and presumably Greenland), impermeability occurs over a range of densities (780–840 kg m^{-3}) centered around an average of 810 kg m^{-3}. No water is allowed to flow to an impermeable layer from above and the same applies if a layer has its entire pore space filled ($S_w = 1$). For a layer above an impermeable layer, water that would otherwise have flowed downwards, through either the Darcy or NoDarcy mechanisms described above, becomes available to run off. However, it does not run off immediately. Instead, runoff, Q_{RO}, per time-step is calculated from the water in excess of the irreducible saturation, p_{liqex}, as:

$$Q_{RO} = p_{liqex}\frac{\Delta t}{\tau_{RO}} \tag{13}$$

where $\tau_{RO} = c_{RO,1} + c_{RO,2}\exp(-c_{RO,3}S)$ is a characteristic local runoff time-scale that increases as the surface slope, S (unit m m^{-1}), tends to zero (Zuo and Oerlemans, 1996). The coefficients $c_{RO,1}$, $c_{RO,2}$ and $c_{RO,3}$ are set to 0.33 day, 25 days and 140, respectively (as in CROCUS/MAR, Lefebre et al., 2003). With this delayed runoff, water in excess of irreducible saturation may linger in a layer until it forms superimposed ice on the layer beneath, runs off or refreezes.

There is currently no representation of horizontal flow or routing of meltwater in HIRHAM5. Once water runs off as described above, it exits the model domain.

Densification and Grain Growth

Re-writing Equation (5) in Vionnet et al. (2012), the time evolution of the snow density, ρ_s, is given as

$$\frac{d\rho_s}{dt} = \frac{\rho_s\sigma}{\eta} \tag{14}$$

where σ is the overburden pressure and η is the snow viscosity, parameterized as in Vionnet et al. (2012) Equation (7):

$$\eta = f_1 f_2 \eta_0 \frac{\rho_s}{c_\eta}\exp\left[a_\eta\,(T_f - T) + b_\eta\rho_s\right] \tag{15}$$

Here, $\eta_0 = 7.62237\cdot10^6$ kg s^{-1}, $a_\eta = 0.1$ K^{-1}, $b_\eta = 0.023$ m^3 kg^{-1}, $c_\eta = 250$ kg m^{-3} are identical to Vionnet et al. (2012), while f_2 is taken to be a constant of 4, neglecting the reduction in η for grain sizes smaller than about 0.3 mm. The effect of liquid water on viscosity and compaction rate enters in f_1 as,

$$f_1 = \frac{1}{1+60\frac{p_w}{p_s}\frac{\rho_s}{\rho_w}} \tag{16}$$

Freshly-fallen snow has an initial density parameterized through a linear regression of surface density observations onto surface elevation, z_{srf} (m a.s.l.), latitude, φ (degrees north), and longitude, λ (degrees east):

$$\rho_{s,f} = a_\rho + b_\rho z_{srf} + c_\rho\varphi + d_\rho\lambda \tag{17}$$

with $a_\rho = 328.35$ kg m^{-3}, $b_\rho = -0.049376$ kg m^{-4}, $c_\rho = 1.0427$ kg m^{-3} deg^{-1} and $d_\rho = -0.11186$ kg m^{-3} deg^{-1} (Fausto et al., in preparation).

The snow grain size diameter, d_g (in mm), used in the calculation of hydraulic conductivity is modeled following Katsushima et al. (2009) and Hirashima et al. (2010) in terms of the mass liquid water content in percent, $L = p_w/p_s\times100$, as

$$\frac{d}{dt}d_g = \frac{1}{d_g^2}\min\left(\frac{2}{\pi}\left[1.28\cdot10^{-8}\text{mm}^3\text{s}^{-1} + 4.22\cdot10^{-10}\text{mm}^3\text{s}^{-1}\times L^3\right],\ 6.94\cdot10^{-8}\text{mm}^3\text{s}^{-1}\right) \tag{18}$$

The first option, increasing with L^3, follows Brun (1989) for low liquid water content, while the second option depends only on the d_g^{-2} factor. As in Katsushima et al. (2009), we choose an initial value of 0.1 mm for the grain size diameter of freshly fallen snow.

Experimental Design

We perform sensitivity tests with multiple subsurface scheme versions and parameter settings, running the subsurface scheme offline from the HIRHAM5 atmospheric code by saving 6 h fields of surface fluxes of energy (downward short- and longwave radiation, latent and sensible heat fluxes) and snowfall, rainfall and sublimation mass fluxes from HIRHAM5. These fields are in turn read in to the offline subsurface code and interpolated to the 1 h time step employed there. The upward short- and longwave fluxes are calculated in the offline code based on albedo (see below) and surface temperature. Spin-up of the subsurface model is performed by taking an initial condition from a previous experiment and repeating the decade 1980-1989 (chosen since it precedes the warming in later decades) until transients in decadal means of runoff and subsurface temperatures have ceased, typically 50–100 years. A separate spin-up is performed for each sensitivity experiment. After spin-up, the transient 1980-2014 experiment is started from the final model state.

Surface albedo is crucial to determining melt energy and in turn the supply of subsurface liquid water and runoff. We perform sensitivity tests with two different implementations: (i) MODIS-derived daily gridded fields of observed surface albedo after Box et al. (2012, see Section Observational Data), hereafter "MOD," and (ii) surface albedo computed internally as in Langen et al. (2015), hereafter "LIN" referring to the linear function of temperature. The internally computed albedo thus employs a linear ramping of snow albedo between 0.85 below −5°C and 0.65 at 0°C for the upper-level temperature. The albedo of bare ice is constant at 0.4. Ice and snow albedos are blended for small snow depths using an exponential transition with an e-folding depth of 3.2 cm (as in Oerlemans and Knap, 1998).

Table 1 lists the sensitivity experiments with different combinations of albedo, water percolation mechanism, parameterization of S_{wi} and choice of w_h/w_{ice}. The experiments MOD-ref and LIN-ref, corresponding to a model with Darcy flow, S_{wi} parameterized following Coleou and Lesaffre (1998) and w_h/w_{ice} set to 1 (with either MODIS-derived or internally calculated albedo), are considered the reference setting.

TABLE 1 | Overview of sensitivity experiments with different choices of albedo implementation (MODIS-derived or linear formulation), water percolation mechanism (Darcy or NoDarcy), parameterization of irreducible water saturation, S_{wi} (fixed value of 0.02 or Coleou and Lesaffre, 1998, parameterization) and choice of w_h/w_{ice} (used in Equation 11).

Experiment	Darcy vs. NoDarcy	S_{wi}	w_h/w_{ice}	Albedo
MOD-ref	Darcy	CL	1.0	MODIS
MOD-w01	Darcy	CL	0.1	MODIS
MOD-Swi02	Darcy	0.02	1.0	MODIS
MOD-NoDarcy	NoDarcy	CL	–	MODIS
LIN-ref	Darcy	CL	1.0	Linear
LIN-Swi02	Darcy	0.02	1.0	Linear

The parameter w_h/w_{ice} is not relevant in NoDarcy.

MODEL EVALUATION USING OBSERVATIONS

In the following, we compare simulated and observed surface accumulation, SMB and surface melt day counts (Section Surface Mass Balance and Melt Extent) as well as subsurface temperature development at a single Programme for Monitoring of the Greenland Ice Sheet (PROMICE) site and subsurface density profiles at a collection of sites (Section Subsurface Temperature and Density). Throughout this study, we use the term SMB for the sum of surface accumulation and ablation, including internal accumulation within the surface snowpack due to refreezing and superimposed ice formation. We note that this term is sometimes also referred to as climatic mass balance (e.g., Cogley et al., 2011). The surface accumulation (and to some extent also ablation) is external to the subsurface model in the sense that accumulation is provided exclusively from the HIRHAM5 atmospheric model. The ablation is a result of the downward energy fluxes from HIRHAM5, but also the albedo calculated in the LIN simulations and specified in the MOD simulations at the top of the subsurface model. It furthermore depends on the subsurface energy flows and thus also on the other model choices.

Observational Data

MODIS Albedo

The Moderate Resolution Imaging Spectroradiometer (MODIS) MOD10A1 surface albedo used in the model is de-noised and smoothed as described by Box et al. (2012), whereby residual cloud artifacts are identified and rejected using running 11-day statistics in each pixel. Values that differ by more than two standard deviations from the 11-day mean are rejected unless they are within 0.04 of the median. Finally, the 11-day running median is used as the daily value. Given that data are only available since 2000, a daily MODIS-climatology based on the pre-darkening period 2000-2006 (see Tedesco et al., 2016) is used prior to 2000 (as in Fausto et al., 2016b).

Accumulation

A compilation of 86 ice cores providing annual w.e. net accumulation rate is available from Box et al. (2013), and spans elevations between 311 and 3188 m a.s.l. Here we select cores overlapping in time with our experiments and having elevations above 1000 m a.s.l. This gives a total of 68 cores (red circles in **Figure 2** and Supplementary Table S1) providing a sample across elevations and east-west and north-south differences.

Surface Mass Balance

Historical and contemporary SMB observations from all regions of Greenland compiled by Machguth et al. (2016b) under PROMICE are compared to daily simulated SMB. We use observations that overlap with our experiments and exclude sites that fall outside the model's glacier mask. The selection yields 1041 observations from 351 sites (blue circles in **Figure 2**). The time span of the SMB observations varies from months to years, although a full year or a 3-month ablation season are the most common. In our analyses (see **Table 2** and **Figure 4**) these

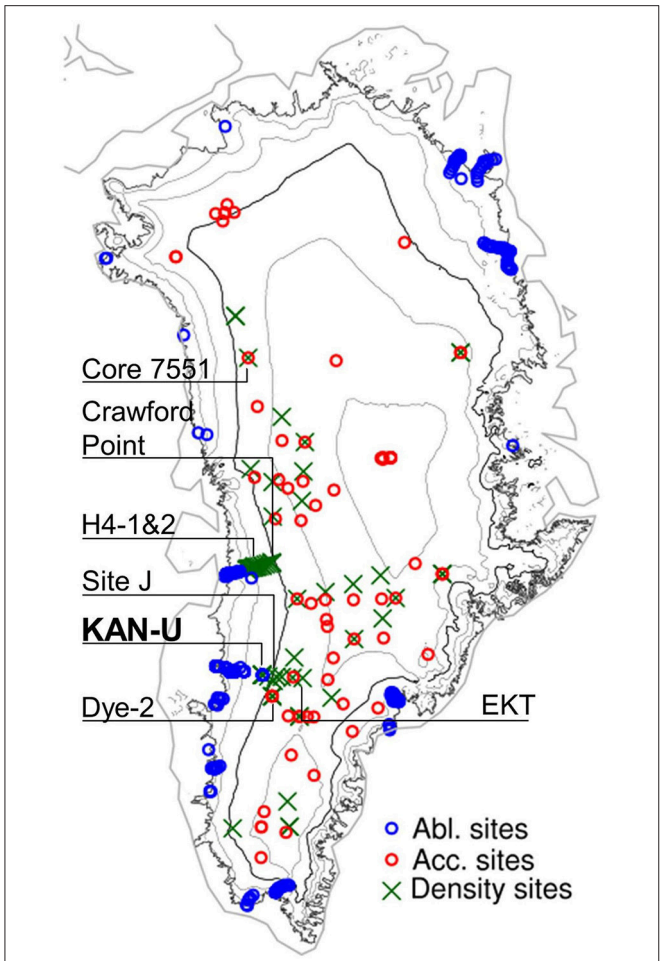

FIGURE 2 | The position of the 68 ice cores used for accumulation evaluation (red circles), 351 SMB observation sites in the ablation area (blue circles) and 75 firn cores used in density evaluation (names of 7 sites included in Figure 7 are shown) with elevation contours (1000-3000 m a.s.l. in steps of 500 m with 2000 m a.s.l. highlighted) and outline of the contiguous ice sheet.

observations (in m w.e.) of varying time span enter with equal weights.

Automatic Weather Stations

Interpretation of model-observation discrepancies is aided by the use of automatic weather station data from the PROMICE network (Ahlstrøm et al., 2008, see Supplementary Table S2). From these stations we use near-surface air temperature, surface temperature, downwelling longwave, downwelling shortwave, net incoming shortwave and albedo.

Surface Melt

We use the MEaSUREs Greenland Surface Melt Daily 25 km EASE-Grid 2.0 data set (Mote, 2014) from 1988 to 2012 to compare with modeled melt extent. After 1987, the product has daily resolution and derives from brightness temperatures measured with the Special Sensor Microwave Imager (SSM/I) and

TABLE 2 | Statistics of comparison between 1041 observed (Machguth et al., 2016b) and simulated SMBs from 351 ablation area sites.

Experiment	Slope	Intcpt (m w.e.)	R^2	RMSE (m w.e.)	Bias (m w.e.)	Bias (%)
MOD-ref	0.97	0.00	0.74	0.74	0.04	−3
MOD-w01	0.97	0.00	0.74	0.74	0.05	−3
MOD-Swi02	0.97	−0.01	0.74	0.74	0.04	−3
MOD-NoDarcy	0.97	0.00	0.74	0.74	0.04	−3
LIN-ref	0.95	−0.02	0.57	0.98	0.04	−3
LIN-Swi02	0.95	−0.02	0.57	0.98	0.05	−3

*Slope and intercept are of orthogonal linear fits (as in **Figure 4**). Biases (in m w.e. and in %) are mean model minus observation. Since SMBs are mostly negative, a positive bias (in m w.e.) indicates that the net mass loss is underestimated and the relative bias (%) is accordingly negative.*

Special Sensor Microwave Imager/Sounder (SSMIS) on board Defense Meteorological Satellite Program (DMSP) satellites. Measured brightness temperatures are compared to thresholds found using a microwave emission model to simulate brightness temperatures of a melting snowpack (Mote and Anderson, 1995; Mote, 2007). The result is a daily melt or no-melt field on the 25 km resolution Equal-Area Scalable Earth (EASE) grid.

Subsurface Temperature

Subsurface temperatures were recorded at the western ice sheet percolation area PROMICE site KAN-U (67.0003 N, 47.0243 W, marked in bold in **Figure 2**) 1840 m above sea level. The station has a thermistor string measuring subsurface temperature to 8–10 m depth (Charalampidis et al., 2015) and we use temperatures interpolated linearly between the thermistors. The depth of each sensor is calculated from maintenance reports and observed surface height changes from acoustic height sensors on the station boom and on a stake assembly few meters away. Between May and August 2012, the stake assembly tilted severely and the station was standing on (and lowering along with) the surface meaning that neither of them could monitor ablation accurately. For that period, we use five firn cores drilled at KAN-U in May 2012 and April 2013 and derive surface lowering between those two dates as the vertical offset that maximizes the correlation of their density profiles (Machguth et al., 2016a).

Density

Simulated subsurface density is evaluated against field measurements using a total of 75 firn cores spanning 1989 to 2013 (green crosses in **Figure 2** and Supplementary Table S4). This dataset comprises 14 cores from the Arctic Circle Traverse 2009 to 2013 (Machguth et al., 2016a), 32 cores from the PARCA campaigns in 1997-1998 (Mosley-Thompson et al., 2001), one core drilled at Site J in 1989 (Kameda et al., 1995) and 28 cores from 2007 to 2008 along the EGIG line (Harper et al., 2012). Resolution and accuracy vary for each dataset and are detailed in the studies above. Each core was compared to the modeled density profile of the grid cell it is located in. Different cores can

therefore be compared to the same modeled density profile and illustrate within-cell variability of firn density.

Surface Mass Balance and Melt Extent

The observed annual w.e. net accumulation rates compare with simulated net accumulation (calculated in the model as snowfall-minus-sublimation) with an average model bias of −5%, correlation coefficient of 0.90 and orthogonal linear regression slope of 1.01 indicating that the average magnitude and spatial variations are reliably reproduced by the model (**Figure 3**). Biases are locally both positive and negative and nearly cancel out in the mean but give a 25% root-mean-square-error, with no clear pattern in the distribution of positive and negative biases with elevation.

Figure 4 and **Table 2** compare the Machguth et al. (2016b) SMB measurements to nearest-neighbor interpolated simulated daily SMB sums over the dates reported in the observations. The MOD-ref experiment compares favorably with observations (slope 0.97, intercept 0.00 m w.e., R^2 0.74 and relative bias −3%, i.e., underestimated net mass loss). The LIN-ref experiment compares almost as well (slope 0.95, intercept −0.02 m w.e., R^2 0.57 and relative bias −3%). Comparing across model versions using MOD albedo in **Table 2**, they are all similar and no clear winner may be identified. The same applies across the two LIN albedo experiments.

To investigate the elevation dependence of the SMB comparison, statistics are redone for sites above and below 700 m a.s.l. (above 700 m shown in blue in **Figure 4**). At high elevation sites, the MOD-ref and LIN-ref experiments on average underestimate the net mass loss by 8 and 16%, respectively. At low elevation sites, they overestimate net mass loss by 1 and 7%, respectively. The small negative bias found for all sites (−3%), is thus a result of cancelation of under- and overestimates at high and low elevation sites. To gauge the overall impact of the low- and high-elevation biases, we calculate the total long-term runoff deriving from elevations above and below 700 m a.s.l. in the MOD-ref and LIN-ref experiments. We find that in both experiments, about 38% of the total ice sheet-wide runoff derives from below 700 m a.s.l. Considering the biases (+1 and +7% at low elevations for MOD and LIN, and −8 and −16% at high) together with 38% runoff from low areas and 62% from high, suggests weighted mean ice sheet-wide mass loss biases in the ablation area of −5 and −7% for the MOD and LIN cases, respectively.

For the very largest negative observed SMBs, the model has a pronounced tendency to underestimate the mass loss, see e.g., the leftmost points in both panels of **Figure 4** corresponding to the PROMICE QAS_L site in southern Greenland [see Supplementary Table S2). In fact, considering solely the lower ablation area PROMICE sites (KAN_L, KPC_L, NUK_L, NUK_N, QAS_L, SCO_L, TAS_L, and UPE_L, situated at 468 ± 240 m a.s.l. (mean ± stddev)] yields mean underestimates of 29 and 37% for MOD and LIN, respectively.

Reasons for the significant ablation underestimation at very low-elevation sites include: (i) The 5.5 km grid size which cannot resolve some fine-scale land-ice differences near the lowest sites

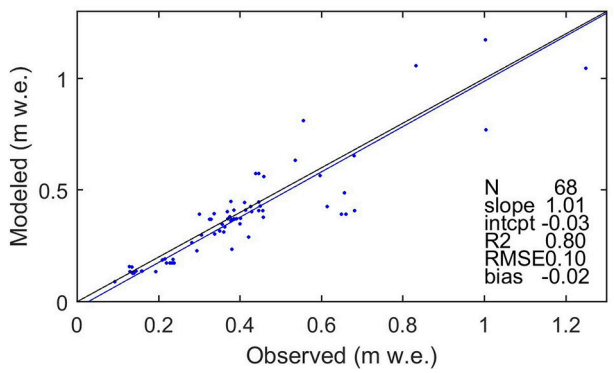

FIGURE 3 | Comparison of modeled and observed annual net accumulation (snowfall-minus-sublimation) for 68 ice cores with elevation greater than 1000 m a.s.l. The black line is 1:1 and the blue line is an orthogonal linear regression with statistics of the fit provided in the table. These are unitless except RMSE and bias (m w.e.).

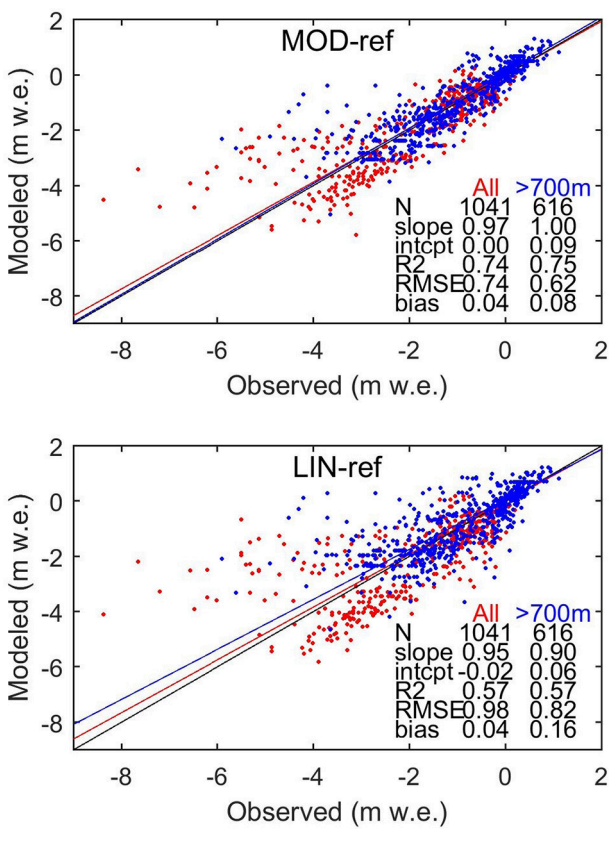

FIGURE 4 | Comparison of modeled and observed SMB at 351 ablation area sites providing a total of 1041 observations. Red dots are at sites below 700 m a.s.l. and blue above 700 m a.s.l. The red line (and the statistics in the "All" column) is an orthogonal linear fit to all 1041 observations, while the blue line is for sites above 700 m a.s.l. The statistics of the fits provided in the tables are unitless except RMSE and bias (m w.e.). The black line is 1:1. Units on the axes are in m w.e. and the observations cover uneven time intervals: some are a few months, some are 1 year and some are 2 years. Model numbers are integrated over the exact dates of the observation intervals.

(e.g., QAS_L); (ii) Jun-Aug observed vs. HIRHAM5 near-surface air temperatures at the L-sites indicate simulated cold biases of 2–3 degrees (Supplementary Table S3) giving biases in the air-to-surface temperature contrast typically of similar magnitude (ΔT bias Supplementary Table S3), which are expected to yield underestimated sensible heat input to the surface; (iii) A simplistic representation of surface roughness elements (crevasses, sub-grid undulations) may lead to underestimation of boundary layer turbulence and turbulent heat transfer (Fausto et al., 2016a,b); (iv) Average simulated albedo is overestimated at the low-level sites (Langen et al., 2015; Fausto et al., 2016b) as also shown in Supplementary Table S3. In the LIN case, the fixed bare-ice albedo of 0.4 is too high for sites like QAS_L where, for instance, July 2012 had an average *in situ* albedo of 0.21 (van As et al., 2013). Even in the MOD case, such a low value is not captured on the HIRHAM5 grid with a mean July 2012 value of 0.44 (Fausto et al., 2016b). Comparing Jun-Aug mean observed and simulated net incoming shortwave radiation (incoming minus reflected) over 2008-2014, QAS_L has model biases of −16 and −44% for MOD and LIN, respectively, as a result of positive mean albedo biases of 0.16 and 0.34 (Supplementary Table S3).

The U-sites also display a tendency for simulated near-surface air temperature cold biases but these are generally smaller than at the L-sites. At the KPC_U site (Northwest Greenland), however, where particularly the LIN case overestimates mass loss, there is a Jun-Aug mean 1.7 degree warm bias. The warm conditions allow a positive feedback between warming surface snow and lowered albedo to be activated resulting in a positive net incoming shortwave bias of 41%. Such a feedback is not active with the specified MOD albedo resulting in a small (−5%) net shortwave bias.

The 1988-2012 brightness temperature-derived melt days are compared to the simulations on the 25 km EASE grid to avoid artifacts of comparison of smoothly varying observations to finer scale variations in the model. Daily simulated fields of melt (value 1) vs. no-melt (value 0) on the 5 km HIRHAM5 grid (defined by daily total melt above 5 mm w.e. as in MAR and RACMO) are bi-linearly interpolated to the 25 km EASE grid and the resulting fractional (0–1) field is converted to melt vs. no-melt using a threshold of 0.5. Counting the melt days annually gives 25 2D fields which are compared between observations and simulations in cells where both have ice. In **Table 3**, "Bias" shows the long-term mean, ice sheet-wide sum of melt day counts as simulated relative to observation. The "Spatial" correlation and slope of orthogonal linear regression is found by calculating the long-term mean field of annual melt day counts, and the statistics are done on grid cells where either observations or model show melt (shown in **Figure 5**). The "Temporal" statistics are calculated by summing each year the melt day counts across the entire ice sheet.

The MOD versions have ∼18% too low long-term mean, ice sheet-wide melt day totals, while the LIN versions match observations closely (bias −4 to +2%). In all models, inter-annual variability in ice sheet-wide sums of melt day counts shows high correlation coefficient (∼0.9) but with too shallow slope (∼0.7) indicating that year-to-year differences are underestimated. The time-mean spatial pattern compares well in terms of correlation coefficient (∼0.9) but with too steep slopes (∼1.2), indicating too large differences between high and low melt day counts. **Figure 5** illustrates the spatial patterns and statistics of the long-term average fields. The simulated patterns are similar to observations, with the main differences related to the steep spatial regression slopes: The model tends to have too few points with few melt days and too many points with many melt days.

TABLE 3 | Statistics of comparison between observed (Mote, 2014) and simulated annual melt day counts (see text for details) over the period 1988-2012.

1988-2012		Spatial $N = 2683$		Temporal $N = 25$	
Experiment	**Bias (%)**	***r***	**Slope**	***r***	**Slope**
MOD-ref	−18	0.89	1.18	0.89	0.71
MOD-w01	−18	0.89	1.18	0.89	0.71
MOD-Swi02	−19	0.89	1.17	0.89	0.71
MOD-NoDarcy	−18	0.89	1.18	0.89	0.71
LIN-ref	+2	0.93	1.22	0.90	0.73
LIN-Swi02	−4	0.93	1.18	0.91	0.69

Slopes are for orthogonal linear fits and r denotes the correlation coefficient.

Comparing the LIN and MOD models, correlation coefficients (spatial and temporal) and slopes (spatial and temporal) are very similar, while the LIN models have a better match in terms of mean, ice sheet-wide totals. Within the LIN and MOD groups the statistics do not give a clear winner.

Subsurface Temperature and Density

Figure 6 shows the 8–10 m depth observed and simulated subsurface temperature records at the percolation area site KAN-U 1840 m above sea level (**Figure 2**). The subsurface model is generally too warm at these depths during winter (**Figure 6**) due to some combination of (i) a surface temperature warm bias (not shown) and (ii) excessive retention in the top 5 m which heats the modeled subsurface during winter. Given that the Swi02 versions of the experiments (which have a fixed S_{wi} of 0.02) display the same warm bias (not shown), excessive retained water is likely not the primary cause. In the early melt season, modeled temperatures are too low, indicating that the simulated wetting front advance is too slow. Once the wetting front has reached its maximum depth, the early-season cold bias subsides. The MOD-Swi02 and LIN-Swi02 experiments (not shown) allow, as discussed in the next section, a more rapid percolation to depth and the early melt season cold bias is less pronounced.

Two main differences between MOD-ref and LIN-ref at KAN-U are that the latter has a larger surface meltwater supply and produces a perched ice layer near 6 m depth beginning in summer 2011 (see **Figure 8**). Prior to that, the LIN experiment has a warm bias throughout the year below 5 m, while the MOD experiment is colder. In the summers following the ice layer formation in 2011, the LIN experiment is more in line with observations while the MOD experiment is too warm at depth. This difference agrees with the observed existence of an ice layer at the site in those years (Machguth et al., 2016a).

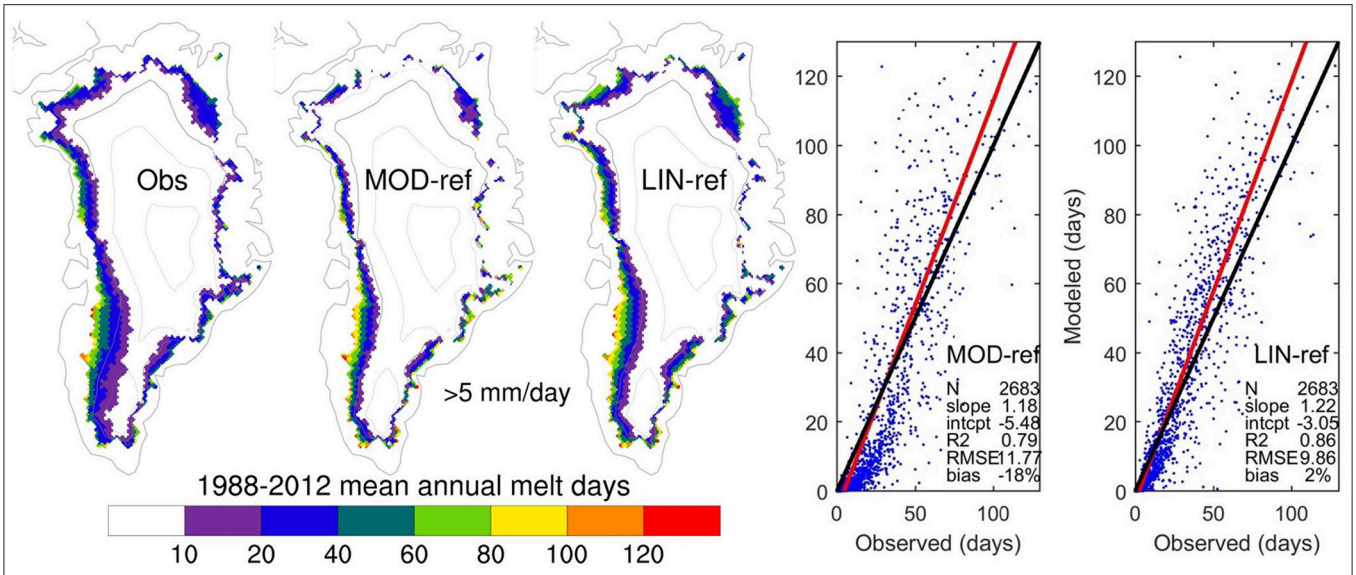

FIGURE 5 | Comparison of 1988-2012 mean observed and modeled spatial distribution of annual melt day counts on the 25 km EASE-grid (see text for details). The maps show melt day counts in grid cells where both the observed and interpolated model fields have ice. The scatter plots include only points where either observations or model show melt. The black line is 1:1 and the red line is an orthogonal linear regression with statistics of the fit provided in the table. These are unitless except RMSE (m w.e.).

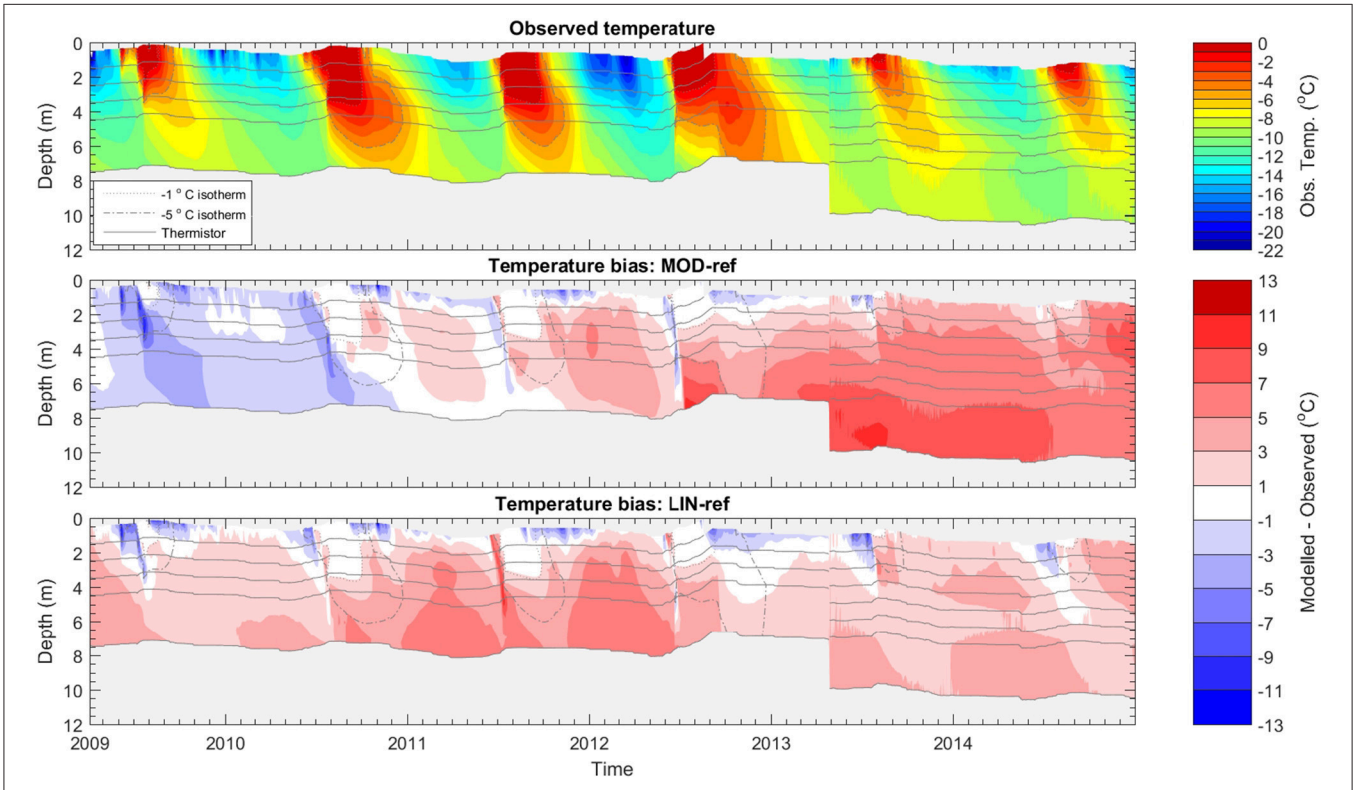

FIGURE 6 | Comparison between modeled and observed subsurface temperatures at KAN-U for 2009-2014. The positions of the thermistors are indicated by solid gray lines. In the lower panels, showing the difference between modeled and observed temperatures, the −1 and −5°C isotherms from the top panel are repeated for reference. Major ticks mark the beginning of the year.

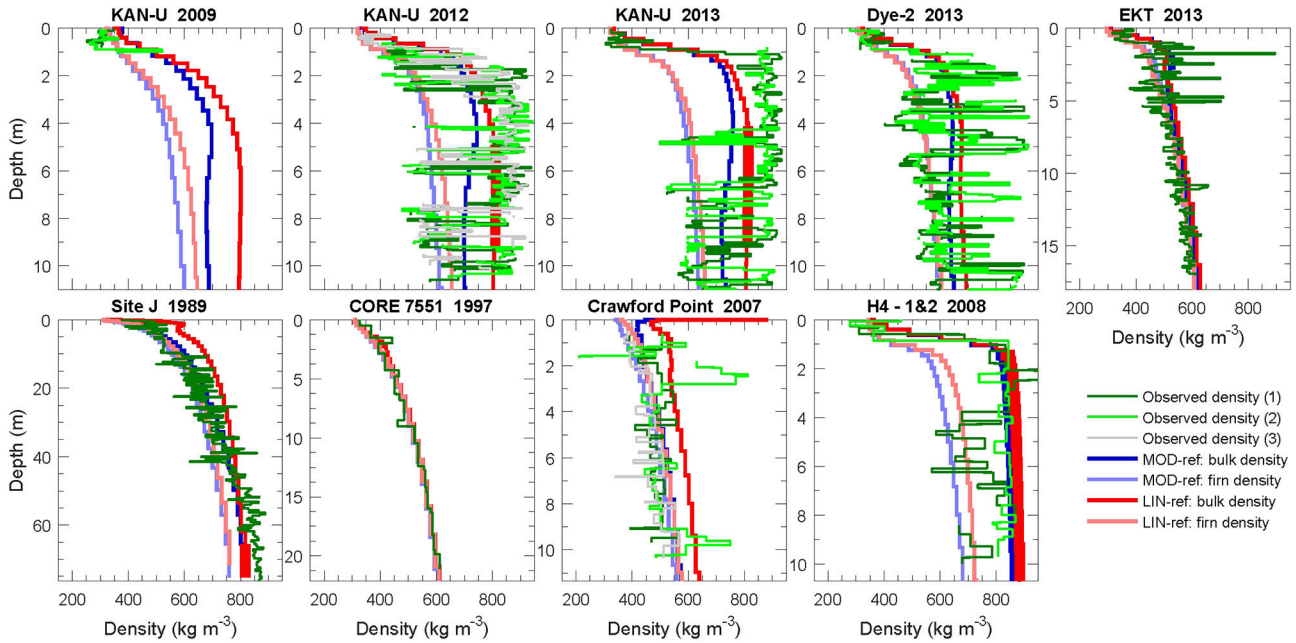

FIGURE 7 | Comparison between observed (green, light green, and gray) and modeled (blue for MOD-ref, red for LIN-ref) density profiles. Modeled bulk densities, ρ_{bulk} (Equation 12), are shown in darker blue or red while dry firn density, ρ_S, is shown in lighter shades. Modeled densities exceeding pore close-off density (810 kg m^{-3}) are shown with thicker lines.

Figure 7 shows nine comparisons of simulated and observed density profiles from MOD-ref and LIN-ref. More cores are presented in Supplementary Figures S1 and S2, showing that the following discussions apply more generally. The model gives realistic density profiles in dry snow areas such as core 7551 in **Figure 7**. In these areas, MOD-ref and LIN-ref give similar results due to limited melt.

In areas where more melt and refreezing occurs (all other panels in **Figure 7**), ice lenses of various thicknesses appear in the firn, and density profiles no longer increase monotonically with depth. At Site J for example, the smooth dry compaction profile is superimposed with sequences of higher and lower density peaks. Due to the model vertical resolution, it is not possible to recreate these thin features. However, agreement between the smoothed observed density (not shown) and modeled bulk density allows the model to accurately translate mass loss to surface lowering and calculate the thermal properties of the firn for that given resolution. On the other hand, the modeled firn density (shown in lighter shades) should match the ice-free sections of the observed density profile. In many cases, observed density profiles have low peak densities that are smaller than the modeled values, but with measurement uncertainty this overestimation of ice-free firn densities is perhaps less clear.

Wherever surface melt occurs, LIN-ref tends to give higher densities than MOD-ref because of the differences in meltwater input. In some cases it allows the LIN-ref model to reproduce observed ice lenses as shown with thick lines at KAN-U in 2012 and 2013. At other sites, such as Site J, LIN-ref clearly overestimates subsurface densities while MOD-ref fits the observed profile better.

The KAN-U core from 2009 only recorded densities to 1 m depth and stratigraphy down to 3 m and did not show any major ice lenses at shallow depth. In the cores from spring 2012, numerous ice layers are observed with some spatial variability (differences between multiple observed profiles). There, LIN-ref has reached pore close off at 5 m depth and replicates this densification process. The cores from spring 2013 show how the ice lens complexes had merged into a consistent ice layer. Accordingly the impermeable layer in LIN-ref also increased in thickness. A good spatial match is also visible on the EGIG line (first 15 panels in Supplementary Figure S2, ordered in decreasing altitude). The LIN-ref model reaches pore close off at the same sites where ice lenses and higher densities become frequent in the cores (from GGU163 to H2-1, differing only by 100 m in altitude). The MOD-ref model, however, reaches pore close off lower on this transect.

The observed density profiles at DYE-2 show a similar stratigraphy to what was observed at KAN-U before saturation of the near-surface firn and may potentially undergo a similar transformation. The EKT and Crawford Point cores also show increased ice features and density near the surface and can also potentially follow the same path. It is satisfactory to see the simulated density profile represent this near-surface densification due to increased refreezing in recent years. On the other end of the spectrum, sites like H4 show a stratigraphy where meltwater refreezing has filled most pore space except for isolated firn pockets at depth. Accordingly, simulated densities have reached pore close off at that site and surface melt is unable to percolate to depth.

SENSITIVITY RESULTS

Subsurface Temperature and Water Profiles

Figure 8 shows the simulated development of the subsurface (uppermost 10 m) temperature at KAN-U in different experiments. The long term variability in MOD-ref indicates relatively cold conditions in the 1990s, a somewhat warmer subsurface in the 2000s and widespread near-temperate conditions throughout the top 10 m in the 2010s. The 2000s heating is even more pronounced in the MOD-Swi02 experiment which differs from MOD-ref only in the parameterization for S_{wi} allowing considerably less water to be retained by capillary forces. As a result, surface meltwater is transferred more readily to depth thereby eroding the cold content. The MOD-NoDarcy experiment has the same irreducible saturation as MOD-ref but allows instantaneous downward percolation of water in excess of irreducible saturation. While this leads to differences between the two experiments on daily timescales (evident for liquid water content in the zoomed **Figure 9**), their resulting temperature structures are practically indistinguishable in **Figure 8**, even though daily values are, in fact, plotted.

Using the LIN albedo results in a larger meltwater supply at the KAN-U site leading to higher subsurface temperatures than in the corresponding MOD experiments, i.e., LIN-ref is warmer than MOD-ref and LIN-Swi02 is warmer than MOD-Swi02. The deeper penetration of latent heating with Swi02 than with SwiCL is seen also for LIN in the summers 2008-2010. In July 2011, however, a drastic difference emerges in that the 810 kg m^{-3} contour becomes visible in LIN-ref indicating the presence of impermeable layers. The larger capacity of the SwiCL formulation to retain water allows enough of the percolating meltwater to refreeze and initiate an ice layer. As the season progresses with latent heat supply cut off from above, the ice layer can grow from below from retained meltwater supplied before it was formed. In the following winter, the layer is gradually cooled and buried by snow accumulation. However, when the 2012 meltwater front reaches the layer, the thickness grows again from above. The subsequent summers 2013 and 2014 add further mass to the layer from above (in accordance with observations; Machguth et al., 2016a) but not enough to compensate the winter burial. The net effect is therefore a downward motion of the ice layer after the end of the 2012 melt season.

Figure 9 illustrates the differences in subsurface liquid water content ($L = p_w/p_s$) arising due to the presence of the perched ice layer in LIN-ref but also to different choices of w_h/w_{ice} and Darcy vs. NoDarcy. The presence of the ice layer in LIN-ref leads to an accumulation of liquid water on top which increases as long as supply from percolation continues. Two large melt events took place in July 2012 (Fausto et al., 2016b) during which this accumulation of liquid water is evident. In the intervening period, July 12 (day 194) to July 26 (day 208), runoff from the column lowers the liquid water level. The high levels of water in excess of the irreducible saturation leads to runoff from the time water starts accumulating atop the ice layer until late in the autumn season rather than being distributed over large depths as in the three left panels.

The distribution of liquid water content in MOD-ref vs. MOD-w01 shows the impact of reducing the hydraulic conductivity of the layers. Reduced conductivity in MOD-w01 slows the downward flow and allows for greater vertical gradients in liquid water to build up before being released. Such buildup of vertical gradients leads to a more intermittent downward flow

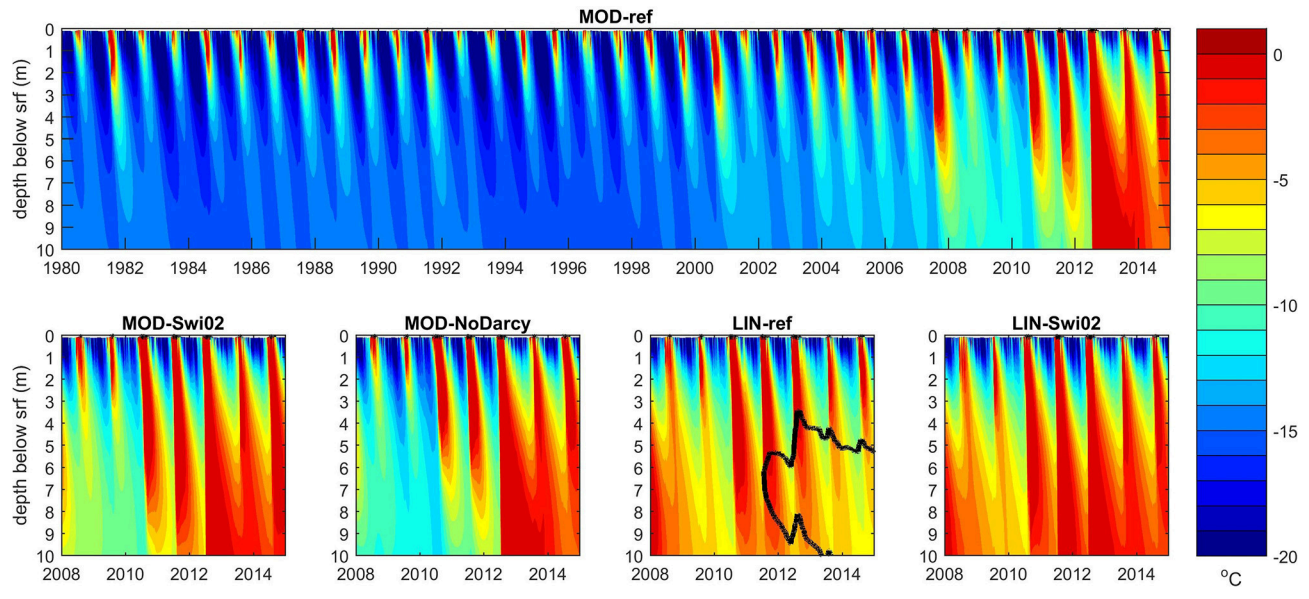

FIGURE 8 | Daily mean temperature at KAN-U of the upper 10 m for 1980-2014 for MOD-ref and for 2008-2014 for other selected experiments. The black solid line marks the $\rho_{bulk} = 810\,kg\,m^{-3}$ contour indicating the presence of impermeable layers.

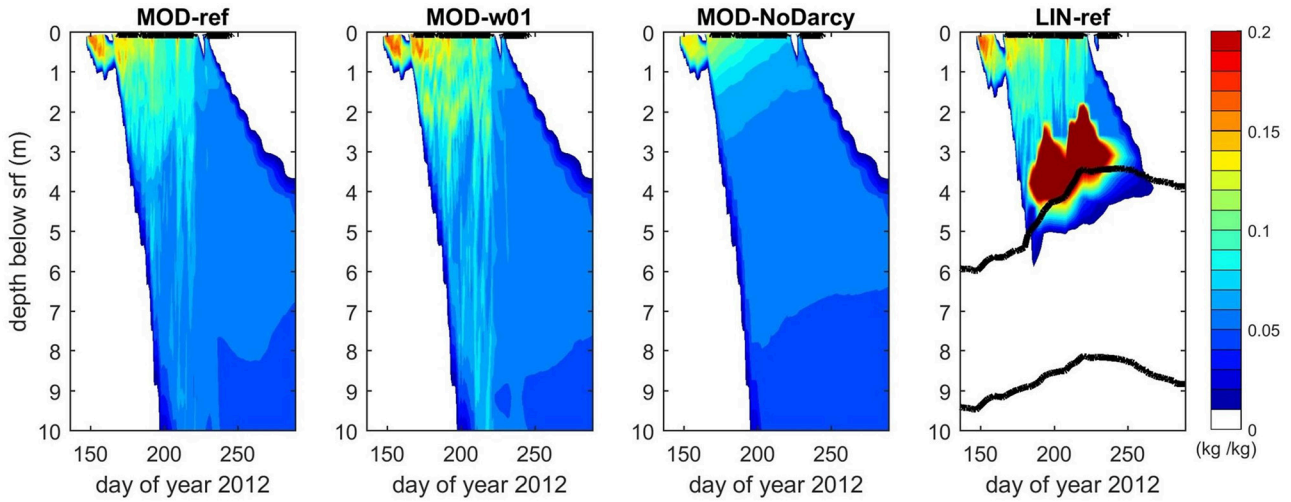

FIGURE 9 | Mass liquid water content (L = p_w/p_s) of the upper 10 m at KAN-U for days 136–289 (May 15–Oct 15) of 2012 for selected experiments. The black solid lines mark the ρ_{bulk} = 810 kg m^{-3} contour indicating the presence of impermeable layers. In the rightmost panel, the accumulating water leads to values of up to 0.5, beyond the range of the color bar.

pattern but not to formation of an impermeable layer. Opposite is the MOD-NoDarcy experiment in which excess water percolates instantaneously, leading to a gradual rather than intermittent evolution of the water field.

Since surface accumulation and percolation leads to simulated vertical shifting of mass, an ice layer effectively diffuses with time if no new mass is top-accreted after formation. A greater amount of meltwater is thus needed for the buildup of an ice layer that can survive the winter and still block percolation the next melt season. This could explain why MOD models do not form a sustainable ice layer at KAN-U.

Large-Scale Patterns of Perched Ice, Liquid Water, and Runoff

Figure 10 shows the distribution of perched ice layers over the years 2012-2014 along with the April 2014 distribution of perennial firn aquifers. Perched ice layers are identified from the three-dimensional field of ρ_{bulk} averaged over April: searching from the surface and downward, if one or more layers have ρ_{bulk} $\geq$810 kg m^{-3} followed by ρ_{bulk} $<$810 kg m^{-3}, then that grid cell has an identified perched ice layer. Perched ice layers determined in this manner are present in a narrow band (typically 3–6 grid cells) going from the southwest up the west coast and around the north and northeast, and in some cases interrupted in the west and northwest by perennial firn aquifers.

The spatial distribution of perennial firn aquifers in the south matches qualitatively that found by Forster et al. (2014) in firn cores, airborne radar surveys and the regional climate model RACMO2. As in RACMO2, the modeled perennial firn aquifers consist entirely of water held within the irreducible saturation, since excess water has percolated further and refrozen or run off during autumn. The column total water content is thus tightly controlled by the parameterization of S_{wi} and our Swi02 experiments are directly comparable to the RACMO2 results. As discussed by Kuipers Munneke et al. (2014), the existence of perennial firn aquifers requires high annual accumulation rates and moderate to high summer melt or rainfall. In addition to the areas in the southeast discussed by Forster et al. (2014), our model simulates these conditions also in several places in the west and northwest.

Comparing cases with SwiCL and Swi02 (i.e., MOD-ref vs. MOD-Swi02 and LIN-ref vs. LIN-Swi02), the perched ice layers are more widespread with SwiCL. The KAN-U site is, as illustrated in **Figure 8**, one such location where SwiCL, but not Swi02, allows an ice layer to emerge (in the LIN case). The higher retention of water in still cool near-surface layers apparently favors the formation of the perched ice layer.

Even though **Figure 9** showed how daily variations in the subsurface water field and downward flow depend crucially on the implementation of hydraulic conductivity (MOD-ref vs. MOD-w01 vs. MOD-NoDarcy), it is apparently not important for the large-scale distribution of perched ice layers and perennial firn aquifers. It appears that the seasonal supply of meltwater, accumulation and irreducible saturation are important and not the exact timing of the downward flow on time-scales of days. This is a useful result for climate models, as it implies that capturing short-term variability is not as important as accurately capturing longer-term precipitation and snowpack processes.

Figure 11 shows differences in total runoff averaged over the years 2012-2014 arising due to the different model implementations. The top row shows the runoff in the MOD-ref and LIN-ref experiments and below is shown the difference between them. The LIN albedo promotes higher melting across the north, likely contributing to the more widespread occurrence of perched ice layers in that area in LIN-ref (**Figure 10**). In most of the west, south and east, however, the MOD experiment produces larger runoff rates. One exception is the green band

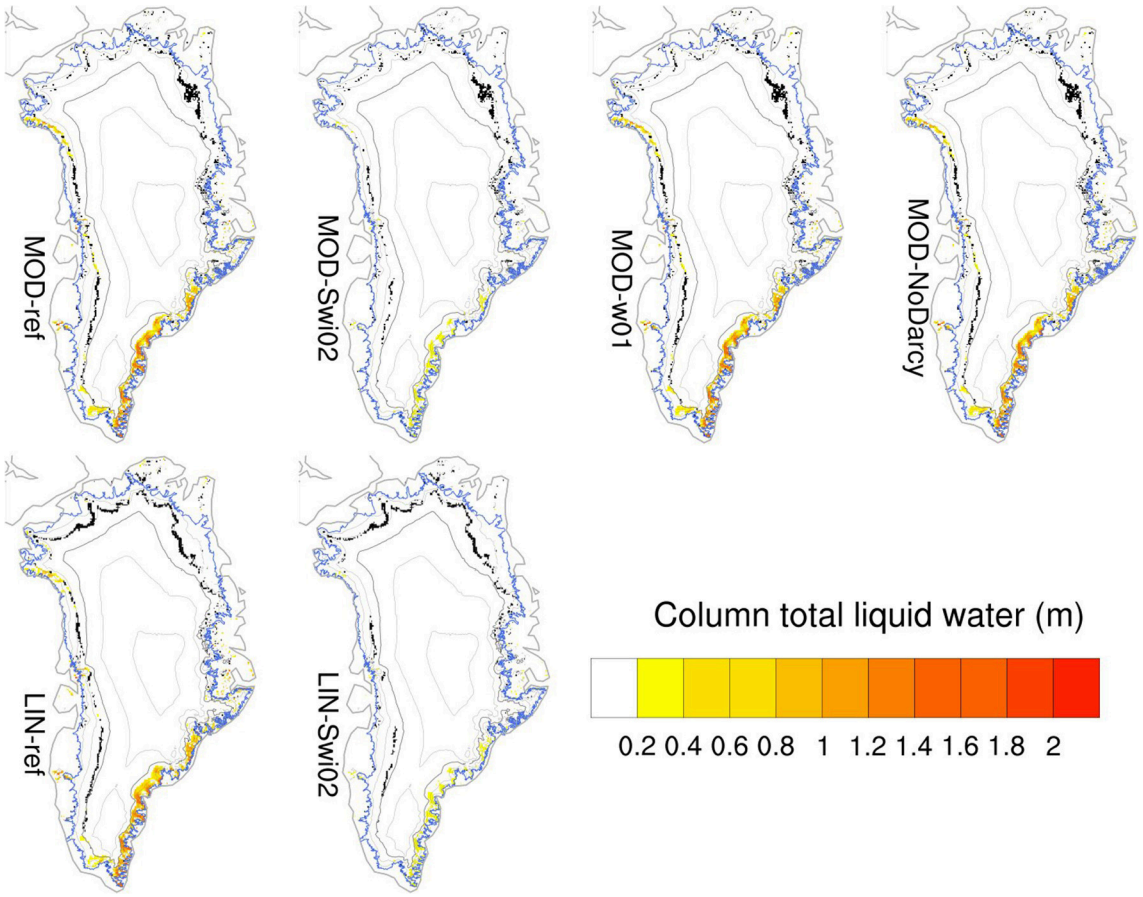

FIGURE 10 | Distribution of ice layers (i.e., existence of layers with $\rho_{bulk} \geq 810\,kg\,m^{-3}$ above less dense layers) in April of years 2012-2014 in black, and distribution of total column liquid water in April 2014 in reds. All panels include elevation contours (1000–3000 m a.s.l. in steps of 500 m with 2000 m a.s.l. highlighted) and outline of the contiguous ice sheet (blue).

inland of the yellow band in the west, indicating a higher runoff line in the LIN case.

The choice of albedo implementation is by far the most important factor for runoff. This is illustrated by the three remaining panels which have been multiplied by a factor of 10 for differences to appear. Again, the choice of Darcy vs. NoDarcy is particularly unimportant. In both the MOD (bottom left) and LIN (bottom right) cases, the choice of SwiCL vs. Swi02 has some impact. With exceptions, there is a general pattern of areas with perennial firn aquifers (south and southeast) giving less runoff with SwiCL and areas with perched ice layers (west and north) giving more runoff with SwiCL. This is to be expected since, in the absence of an ice layer, a higher S_{wi} allows more water to be retained in the column and refrozen during the following winter. In the presence of an ice layer, the meltwater accumulating on top (as seen in **Figure 9**) leads to runoff rather than deep percolation.

Greenland-wide time-series of calendar-year total runoff and SMB are shown in **Figure 12**. Clearly discernible are the differences between the MOD and LIN cases, while the differences between SwiCL and Swi02 are very small. This is due both to the smallness of the differences in the lower row of **Figure 11** (multiplied by a factor of 10) but also the competing effects from the perennial firn aquifer and perched ice layer areas. The MODIS-driven experiments employ an average 2000-2006 daily albedo climatology in the period before 2000. This reduces the inter-annual variability and leads to larger differences from the LIN experiments in runoff (and, consequently, SMB) in the pre-2000 period. In the post-2000 period with direct MODIS-derived albedos, there is better agreement on the variability.

CONCLUSIONS

The subsurface scheme of the regional climate model HIRHAM5 has been extended to include firn densification, grain size growth, snow state-dependent hydraulic conductivity and irreducible water saturation as well as retention of water in excess of the irreducible saturation and superimposed ice formation. Sensitivity experiments have been performed to gauge both small- and large-scale effects of these additions as well as the impact of different parameterization choices.

The model results compare favorably with 68 ice core-derived annual net accumulation rates (spatial correlation coefficient

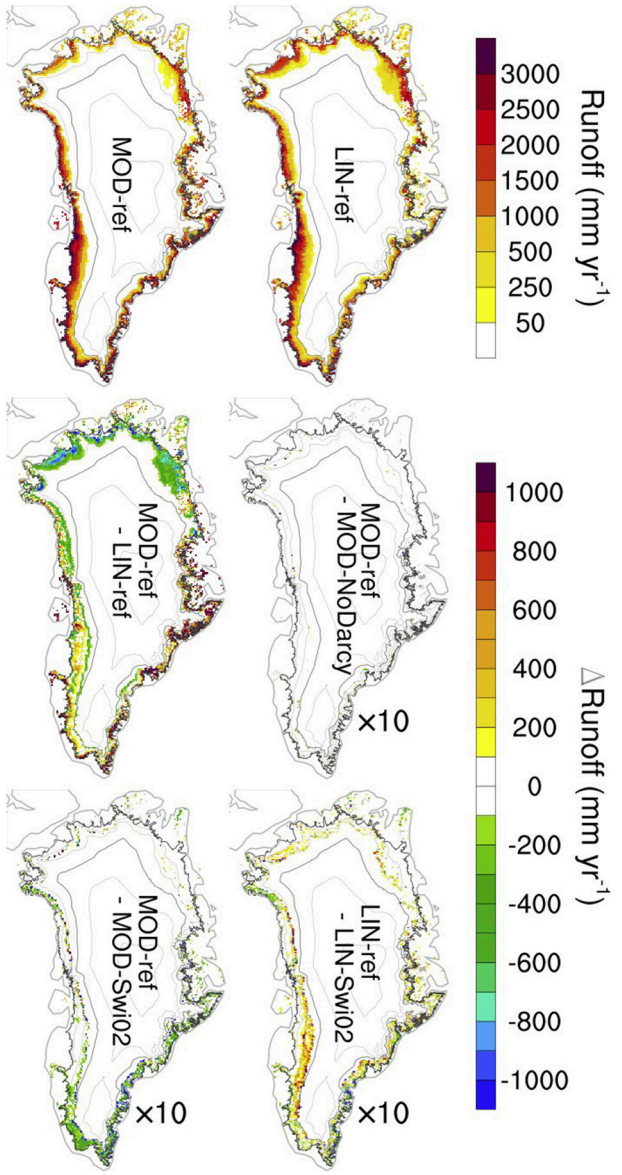

FIGURE 11 | (Upper row) Annual runoff (averaged over years 2012-2014) for experiments MOD-ref and LIN-ref. (Lower rows) Runoff differences between selected experiments. The last three have been multiplied by 10 to aid visualization. All panels include elevation contours (1000–3000 m a.s.l. in steps of 500 m with 2000 m a.s.l. highlighted) and outline of the contiguous ice sheet.

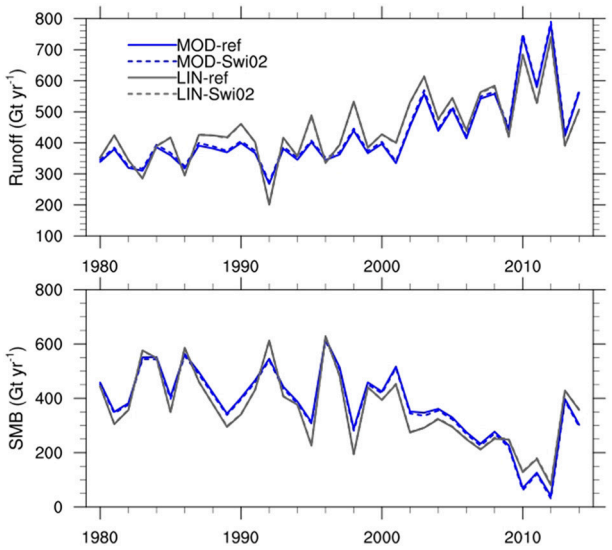

FIGURE 12 | Greenland-wide annual runoff and SMB from selected experiments.

of 0.90 and mean bias −5%). In the ablation area, simulated SMBs compare very well with 1041 observations with regression slopes of 0.97 and 0.95, and correlation coefficients of 0.86 and 0.75 for MOD-ref and LIN-ref, respectively. Mean biases are −3%, indicating only slightly underestimated net mass loss rates. The low mean bias is, however, partially due to a cancelation of under- and overestimates at high and low elevation sites. Splitting the sites between those above and below 700 m a.s.l. and weighting the resulting biases with the amount of runoff deriving from low vs. higher elevations results in weighted ice sheet-wide mass loss biases in the ablation area of −5 and −7% for MOD and LIN, respectively. These numbers do not depend significantly on other model choices (Darcy, S_{wi} and w_h/w_{ice}).

Comparing observed and simulated annual melt day counts shows that the spatial and temporal patterns of variability are reliably represented in the model, while it tends to underestimate the magnitude of inter-annual variability and overestimate that of spatial variability. As for the SMB comparison, the choice of albedo dominates the differences and the statistics do not allow for a best choice of the other model settings to be determined.

The mechanism for vertical flow (Darcy vs. NoDarcy and w_h/w_{ice} set to 1 vs. 0.1) has an impact on short time-scale features of the subsurface liquid water field, but appears unimportant for the seasonal-scale temperature structure and for the large-scale mass balance field.

Two model choices do influence the subsurface temperature at KAN-U on longer time-scales, namely albedo and S_{wi}. Prior to the formation of the ice lens, a larger meltwater production in LIN leads to a perennial warm bias below 5 m. Setting S_{wi} to 0.02, rather than parameterized according to Coleou and Lesaffre (1998), allows water to percolate more readily to depth in the early melt season and reduces the cold bias otherwise present in the model at that time of year with both LIN and MOD. On the other hand, using the Coleou and Lesaffre (1998) parameterization in combination with LIN albedo allows for formation of an ice layer in agreement with observations (**Figure 7** and Machguth et al., 2016a). This, in turn, shields the deeper part from latent heating from refreezing and reduces the warm bias at depth.

The model combinations without a perched ice layer at KAN-U do not produce runoff there over the 2009-2014 period, while LIN-ref generates 132 mm in 2010 and 583 mm in 2012. This agrees with the 690 ± 150 mm runoff in 2012 derived from

comparison of spring 2012 and 2013 firn core stratigraphies by Machguth et al. (2016a) at KAN-U. This increase in runoff line altitude with the LIN-ref combination (also seen in **Figure 11**) is a direct consequence of the perched ice layer formation, and modeling this accurately appears crucial in a warming climate where more meltwater would be available in the percolation area. While the appearance of the perched ice layer at KAN-U is in line with observations, this does not necessarily imply that the LIN-ref combination is better than the others. As seen in **Figure 10**, perched ice layers do form also with MOD and Swi02 in different combinations; just not exactly at KAN-U.

Perennial firn aquifers occur in the south and southeast in patterns corresponding to those found by Forster et al. (2014) and continue up the west coast interrupted by areas with perched ice layers. These areas with perennial firn aquifers are not much impacted by the choice of SwiCL vs. Swi02, but the total amount of water in the aquifers is. This is because the perennial firn aquifer water consists entirely of water held within the irreducible saturation. In areas of perennial firn aquifers, SwiCL generally leads to less runoff because more water is held back against runoff in the summer and fall and remains available for refreezing in winter.

The fact that water exits the model domain once it runs off from a column may influence our results. If water instead flowed to neighboring grid columns (at the surface or at the depth from which it runs off), it would become part of the water budget of that cell. This could potentially increase the magnitude or areal extent of both perched ice layers and perennial firn aquifers. Addition of a representation of lateral flow and routing of water along with vertical piping could potentially alter the current conclusions and should be the focus of further developments.

As perched ice layers form, water which would otherwise have percolated and refrozen at deeper levels end up contributing to runoff instead. This is visible in large-scale runoff maps, but in a Greenland-wide accumulated sense, this is more or less negligible in the model's current climate. In general, the same is true for details of the percolation mechanism and retention parameterizations: they matter for local-scale subsurface temperature, snow, ice and water fields; but for the Greenland-wide runoff and SMB, the major impact is from the choice of albedo implementation. Whether the large-scale effects of perennial firn aquifers and perched ice layers will change in a warmer climate is not yet clear.

AUTHOR CONTRIBUTIONS

PL led the development of the subsurface model, performed the subsurface experiments and led writing of the manuscript. RF, BV, and RM contributed to development of the subsurface model and RM performed the HIRHAM5 atmospheric model experiment. PL, BV, and JB performed comparisons of model output to observations. All authors contributed to discussions and writing of the manuscript.

FUNDING

This work is supported by the Retain project, funded by the Danish Council for Independent research (Grant no. 4002-00234).

ACKNOWLEDGMENTS

We are grateful to the three reviewers for their thorough and insightful input that lead to considerable improvements of the paper. We thank J. Harper, T. Kameda, M. Macferrin, H. Machguth, E. Mosley-Thompson, and D. van As for providing density profiles. The PARCA cores are available at http://research.bpcrc.osu.edu/Icecore/data/ and their collection was supported by NASA grants NAG5-5032 and 6817 to the Ohio State University, NASA grants NAG5-5031 and 6779 to the University of Arizona, and NASA grant NAGW-4248 and NSF/OPP grant 9423530 to the University of Colorado. The ACT campaigns were supported by NASA (grant NNX10AR76G), by the Greenland Analog Project (GAP), by the REFREEZE project, by the RETAIN project (DFF grant 4002-00234) and by the Programme for Monitoring of the Greenland Ice Sheet (PROMICE). PROMICE data are freely accessible at http://promice.org as is HIRHAM5 output at http://prudence.dmi.dk/data/temp/RUM/HIRHAM/GL2.

SUPPLEMENTARY MATERIAL

The Supplementary Material for this article can be found online at: http://journal.frontiersin.org/article/10.3389/feart.2016.00110/full#supplementary-material

REFERENCES

Ahlstrøm, A., Gravesen, P., Andersen, S., Van As, D., Citterio, M., Fausto, R., et al. (2008). A new programme for monitoring the mass loss of the Greenland ice sheet. *Geol. Surv. Den. Greenland Bull.* 15, 61–64. Available online at: http://www.geus.dk/DK/publications/geol-survey-dk-gl-bull/15/Documents/nr15_p61-64.pdf

Benson, C. S. (1962). *Stratigraphic Studies in the Snow and Firn of the Greenland Ice Sheet*. SIPRE, (CRREL) Research Report 70, reprinted with revisions by CRREL, 1996.

Box, J. E., Cressie, N., Bromwich, D. H., Jung, J.-H., van den Broeke, M., van Angelen, J. H., et al. (2013). Greenland ice sheet mass balance reconstruction. Part I: net snow accumulation (1600–2009). *J. Climate* 26, 3919–3934. doi: 10.1175/JCLI-D-12-00373.1

Box, J. E., Fettweis, X., Stroeve, J. C., Tedesco, M., Hall, D. K., and Steffen, K. (2012). Greenland ice sheet albedo feedback: thermodynamics and atmospheric drivers. *Cryosphere* 6, 821–839. doi: 10.5194/tc-6-821-2012

Braithwaite, R. J., W. Tad Pfeffer, Blatter, A., and Humphrey, N. F. (1992). "Meltwater refreezing in the accumulation area of the Greenland Ice Sheet, Pakitsoq Region, Summer 1991," in *Current Research, Greenland Geological Survey Report of Activities,* Report No. 155, 13–17.

Braithwaite, R., Laternser, M., and Pfeffer, W. (1994). Variations of near-surface firn density in the lower accumulation area of the Greenland ice sheet, Pakitsoq, West Greenland. *J. Glaciol.* 40, 477–485.

Brun, E. (1989). Investigation on wet-snow metamorphism in respect of liquid-water content. *Ann. Glaciol.* 13, 22–26.

Calonne, N., Geindreau, C., Flin, F., Morin, S., Lesaffre, B., Rolland du Roscoat, S., et al. (2012). 3-D image-based numerical computations of snow permeability: links to specific surface area, density, and microstructural anisotropy. *Cryosphere* 6, 939–951. doi: 10.5194/tc-6-939-2012

Charalampidis, C., van As, D., Box, J. E., van den Broeke, M. R., Colgan, W. T., Doyle, S. H., et al. (2015). Changing surface–atmosphere energy exchange and refreezing capacity of the lower accumulation area, West Greenland. *Cryosphere* 9, 2163–2181. doi: 10.5194/tc-9-2163-2015

Christensen, O., Drews, M., Christensen, J., Dethloff, K., Ketelsen, K., Hebestadt, I., et al. (2006). *The HIRHAM Regional Climate Model, Version 5*. Available online at: http://www.dmi.dk/fileadmin/Rapporter/TR/tr06-17.pdf

Church, J. A., Clark, P. U., Cazenave, A., Gregory, J. M., Jevrejeva, S., Levermann, A., et al. (2013). "Sea level change," in *Climate Change 2013: The Physical Science Basis. Contribution of Working Group I to the Fifth Assessment Report of the Intergovernmental Panel on Climate Change*, eds T. F. Stocker, D. Qin, G.-K. Plattner, M. M. B. Tignor, S. K. Allen, J. Boschung, A. Nauels, Y. Xia, V. Bex, and P. M. Midgley (Cambridge; New York, NY: Cambridge University Press), 1137–1216. Available online at: www.climatechange2013.org

Cogley, J. G., Hock, R., Rasmussen, L. A., Arendt, A. A., Bauder, A., Braithwaite, R. J., et al. (2011). *Glossary of Glacier Mass Balance and Related Terms*. IHP-VII Technical Documents in Hydrology No. 86, IACS Contribution No. 2, UNESCO-IHP, Paris.

Colbeck, S. (1972). A theory of water percolation in snow. *J. Glaciol.* 11, 369–385.

Colbeck, S. (1974). The capillary effects on water percolation in homogeneous snow. *J. Glaciol.* 13, 85–97.

Colbeck, S. (1975). A theory for water flow through a layered snowpack. *Water Resour. Res.* 11, 261–266. doi: 10.1029/WR011i002p00261

Coleou, C., and Lesaffre, B. (1998). Irreducible water saturation in snow: experimental results in a cold laboratory. *Ann. Glaciol.* 26, 64–68.

Cuffey, K. M., and Paterson, W. S. B. (2010). *The Physics of Glaciers*. Amsterdam: Elsevier Science, 704.

Dee, D. P., Uppala, S. M., Simmons, A. J., Berrisford, P., Poli, P., Kobayashi, S., et al. (2011). The ERA-Interim reanalysis: configuration and performance of the data assimilation system. *Q. J. R. Meteorol. Soc.* 137, 553–597. doi: 10.1002/qj.828

de la Peña, S., Howat, I. M., Nienow, P. W., van den Broeke, M. R., Mosley-Thompson, E., Price, S. F., et al. (2015). Changes in the firn structure of the western Greenland Ice Sheet caused by recent warming. *Cryosphere* 9, 1203–1211. doi: 10.5194/tc-9-1203-2015

Dumont, M., Brun, E., Picard, G., Michou, M., Libois, Q., Petit, J.-R., et al. (2014). Contribution of light-absorbing impurities in snow to Greenland's darkening since 2009. *Nat. Geosci* 7, 509–512. doi: 10.1038/ngeo2180

Eerola, K. (2006). About the performance of HIRLAM version 7.0. *HIRLAM Newslett.* 51, 93–102. Available online at: http://hirlam.org/index.php/hirlam-documentation/doc_view/473-hirlam-newsletter-no-51-article14-eerola-performance-hirlam7-0

Fausto, R. S., van As, D., Box, J. E., Colgan, W., and Langen, P. L. (2016a). Quantifying the surface energy fluxes in south Greenland during the 2012 high melt episodes using *in situ* observations. *Front. Earth Sci.* 4:82. doi: 10.3389/feart.2016.00082

Fausto, R. S., van As, D., Box, J. E., Colgan, W., Langen, P. L., and Mottram, R. H. (2016b). The implication of nonradiative energy fluxes dominating Greenland ice sheet exceptional ablation area surface melt in 2012. *Geophys. Res. Lett.* 43, 2649–2658. doi: 10.1002/2016GL067720

Fettweis, X. (2007). Reconstruction of the 1979–2006 Greenland ice sheet surface mass balance using the regional climate model MAR. *Cryosphere* 1, 21–40. doi: 10.5194/tc-1-21-2007

Forster, R. R., Box, J. E., van den Broeke, M. R., Miege, C., Burgess, E. W., van Angelen, J. H., et al. (2014). Extensive liquid meltwater storage in firn within the Greenland ice sheet. *Nat. Geosci.* 7, 95–98. doi: 10.1038/ngeo2043

Gascon, G., Sharp, M., Burgess, D., Bezeau, P., and Bush, A. B. G. (2013). Changes in accumulation-area firn stratigraphy and meltwater flow during a period of climate warming: Devon Ice Cap, Nunavut, Canada. *J. Geophys. Res. Earth Surf.* 118, 2380–2391. doi: 10.1002/2013jf002838

Gregory, J. M., White, N. J., Church, J. A., Bierkens, M. F. P., Box, J. E., van den Broeke, M. R., et al. (2013). Twentieth-century global-mean sea level rise: is the whole greater than the sum of the parts? *J. Climate* 26, 4476–4499. doi: 10.1175/JCLI-D-12-00319.1

Gregory, S. A., Albert, M. R., and Baker, I. (2014). Impact of physical properties and accumulation rate on pore close-off in layered firn. *Cryosphere* 8, 91–105. doi: 10.5194/tc-8-91-2014

Harper, J., Humphrey, N., Pfeffer, W. T., Brown, J., and Fettweis, X. (2012). Greenland ice-sheet contribution to sea-level rise buffered by meltwater storage in firn. *Nature* 491, 240–243. doi: 10.1038/nature11566

Hirashima, H., Yamaguchi, S., Sato, A., and Lehning, M. (2010). Numerical modeling of liquid water movement through layered snow based on new measurements of the water retention curve. *Cold Regions Sci. Technol.* 64, 94–103. doi: 10.1016/j.coldregions.2010.09.003

Howat, I. M., de la Peña, S., van Angelen, J. H., Lenaerts, J. T. M., and van den Broeke, M. R. (2013). Brief Communication "Expansion of meltwater lakes on the Greenland Ice Sheet." *Cryosphere* 7, 201–204. doi: 10.5194/tc-7-201-2013

Humphrey, N. F., Harper, J. T., and Pfeffer, W. T. (2012). Thermal tracking of meltwater retention in Greenland's accumulation area. *J. Geophys. Res. Earth Surf.* 117:F01010. doi: 10.1029/2011jf002083

Janssens, I., and Huybrechts, P. (2000). The treatment of meltwater retention in mass-balance parameterisations of the Greenland ice sheet. *Ann. Glaciol.* 31, 133–140. doi: 10.3189/172756400781819941

Kameda, T., Narita, H., Shoji, H., Nishio, F., Fujii, Y., and Watanabe, O. (1995). Melt features in ice cores from Site J, southern Greenland: some implications for summer climate since AD 1550. *Ann. Glaciol.* 21, 51–58.

Katsushima, T., Kumakura, T., and Takeuchi, Y. (2009). A multiple snow layer model including a parameterization of vertical water channel process in snowpack. *Cold Regions Sci. Technol.* 59, 143–151. doi: 10.1016/j.coldregions.2009.09.002

Keegan, K. M., Albert, M. R., McConnell, J. R., and Baker, I. (2014). Climate change and forest fires synergistically drive widespread melt events of the Greenland Ice Sheet. *Proc. Natl. Acad. Sci. U.S.A.* 111, 7964–7967. doi: 10.1073/pnas.1405397111

Koenig, L. S., Miège, C., Forster, R. R., and Brucker, L. (2014). Initial *in situ* measurements of perennial meltwater storage in the Greenland firn aquifer. *Geophys. Res. Lett.* 41, 81–85. doi: 10.1002/2013GL058083

Kuipers Munneke, P. M., Ligtenberg, S. R., van den Broeke, M. R., van Angelen, J. H., and Forster, R. R. (2014). Explaining the presence of perennial liquid water bodies in the firn of the Greenland Ice Sheet. *Geophys. Res. Lett.* 41, 476–483. doi: 10.1002/2013GL058389

Langen, P. L., Mottram, R. H., Christensen, J. H., Boberg, F., Rodehacke, C. B., Stendel, M., et al. (2015). Quantifying energy and mass fluxes controlling Godthåbsfjord freshwater input in a 5 km simulation (1991–2012). *J. Climate.* 28, 3694–3713. doi: 10.1175/jcli-d-14-00271.1

Lefebre, F., Gallée, H., van Ypersele, J.-P., and Greuell, W. (2003). Modeling of snow and ice melt at ETH Camp (West Greenland): a study of surface albedo. *J. Geophys. Res.* 108:4231. doi: 10.1029/2001jd001160

Ligtenberg, S. R. M., Helsen, M. M., and van den Broeke, M. R. (2011). An improved semi-empirical model for the densification of Antarctic firn. *Cryosphere* 5, 809–819. doi: 10.5194/tc-5-809-2011

Lucas-Picher, P., Wulff-Nielsen, M., Christensen, J. H., Aðalgeirsdóttir, G., Mottram, R., and Simonsen, S. B. (2012). Very high resolution regional climate model simulations over Greenland: identifying added value. *J. Geophys. Res.* 117:D02108. doi: 10.1029/2011jd016267

Machguth, H., MacFerrin, M., van As, D., Box, J. E., Charalampidis, C., Colgan, W., et al. (2016a). Greenland meltwater storage in firn limited by near-surface ice formation. *Nature Clim. Change* 6, 390–393. doi: 10.1038/nclimate2899

Machguth, H., Thomsen, H. H., Weidick, A., Ahlstrøm, A. P., Abermann, J., Andersen, M. L., et al. (2016b). Greenland surface mass-balance observations from the ice-sheet ablation area and local glaciers. *J. Glaciol.* 62, 861–887. doi: 10.1017/jog.2016.75

Mosley-Thompson, E., McConnell, J. R., Bales, R. C., Li, Z., Lin, P.-N., Steffen, K., et al. (2001). Local to regional-scale variability of annual net accumulation on the Greenland ice sheet from PARCA cores. *J. Geophys. Res.* 106, 33839–33851. doi: 10.1029/2001JD900067

Mote, T. L. (2007). Greenland surface melt trends 1973–2007: evidence of a large increase in 2007. *Geophys. Res. Lett.* 34, L22507. doi: 10.1029/2007GL031976

Mote, T. L. (2014). MEaSUREs Greenland Surface Melt Daily 25km EASE-Grid 2.0. Boulder, CO: NASA DAAC at the National Snow and Ice Data Center. doi: 10.5067/MEASURES/CRYOSPHERE/nsidc-0533.001

Mote, T. L., and Anderson, M. R. (1995). Variations in snowpack melt on the Greenland ice sheet based on passive microwave measurements. *J. Glaciol.* 41, 51–60.

Müller, F. (1976). On the thermal regime of a high arctic valley glacier. *J. Glaciol.* 16, 119–133.

Oerlemans, J., and Knap, W. (1998). 1 year record of global radiation and albedo in the ablation zone of Morteratschgletscher, Switzerland. *J. Glaciol.* 44, 231–238.

Parry, V., Nienow, P., Mair, D., Scott, J., Hubbard, B., Steffen, K., et al. (2007). Investigations of meltwater refreezing and density variations in the snowpack and firn within the percolation zone of the Greenland ice sheet. *Ann. Glaciol.* 46, 61–68. doi: 10.3189/172756407782871332

Pfeffer, W. T., Meier, M. F., and Illangasekare, T. H. (1991). Retention of Greenland runoff by refreezing: implications for projected future sea level change. *J. Geophys. Res.* 96, 22117–22124. doi: 10.1029/91JC02502

Polashenski, C., Courville, Z., Benson, C., Wagner, A., Chen, J., Wong, G., et al. (2014). Observations of pronounced Greenland ice sheet firn warming and implications for runoff production. *Geophys. Res. Lett.* 41:2014GL059806. doi: 10.1002/2014GL059806

Reeh, N. (1989). Parameterization of melt rate and surface temperature on the Greenland ice sheet. *Polarforschung* 59, 113–128.

Reijmer, C. H., van den Broeke, M. R., Fettweis, X., Ettema, J., and Stap, L. B. (2012). Refreezing on the Greenland ice sheet: a comparison of parameterizations. *Cryosphere* 6, 743–762. doi: 10.5194/tc-6-743-2012

Roeckner, E., Bäuml, G., Bonaventura, L., Brokopf, R., Esch, M., Giorgetta, M., et al. (2003). *The Atmospheric General Circulation Model ECHAM5. Part I: Model Description*. Available online at: http://www.mpimet.mpg.de/fileadmin/publikationen/Reports/max_scirep_349.pdf

Shimizu, H. (1970). Air permeability of deposited snow. *Contribut. Instit. Low Temp. Sci.* A22, 1–32.

Tedesco, M., Doherty, S., Fettweis, X., Alexander, P., Jeyaratnam, J., and Stroeve, J. (2016). The darkening of the Greenland ice sheet: trends, drivers, and projections (1981–2100). *Cryosphere* 10, 477–496. doi: 10.5194/tc-10-477-2016

van Angelen, J. H., Lenaerts, J. T. M., Lhermitte, S., Fettweis, X., Kuipers Munneke, P., van den Broeke, M. R., et al. (2012). Sensitivity of Greenland Ice Sheet surface mass balance to surface albedo parameterization: a study with a regional climate model. *Cryosphere* 6, 1175–1186. doi: 10.5194/tc-6-1175-2012

van Angelen, J. H. M., Lenaerts, J. T., van den Broeke, M. R., Fettweis, X., and van Meijgaard, E. (2013). Rapid loss of firn pore space accelerates 21st century Greenland mass loss. *Geophys. Res. Lett.* 40, 2109–2113. doi: 10.1002/grl.50490

van Angelen, J. H., van den Broeke, M. R., Wouters, B., and Lenaerts, J. T. M. (2014). Contemporary (1960–2012) evolution of the climate and surface mass balance of the Greenland Ice Sheet. *Surv. Geophysi.* 35, 1155–1174. doi: 10.1007/s10712-013-9261-z

van As, D., Box, J., and Fausto, R. (2016). Challenges of quantifying meltwater retention in snow and firn: an expert elicitation. *Front. Earth Sci.* 4:101. doi: 10.3389/feart.2016.00101

van As, D., Fausto, R., Colgan, W., Box, J., and PROMICE Project Team (2013). Darkening of the Greenland ice sheet due to the meltalbedo feedback observed at PROMICE weather stations. *Geol. Sur. Den. Greenland Bull.* 28, 69–72. Available online at: http://www.geus.dk/publications/bull/nr28/nr28_p69-72.pdf

van den Broeke, M., Bamber, J., Ettema, J., Rignot, E., Schrama, E., van de Berg, W. J., et al. (2009). Partitioning recent greenland mass loss. *Science* 326, 984–986. doi: 10.1126/science.1178176

van Genuchten, M. T. (1980). A closed-form equation for predicting the hydraulic conductivity of unsaturated soil. *Soil Sci. Soc. Am. J.* 44, 892–898. doi: 10.2136/sssaj1980.03615995004400050002x

Vernon, C. L., Bamber, J. L., Box, J. E., van den Broeke, M. R., Fettweis, X., Hanna, E., et al. (2013). Surface mass balance model intercomparison for the Greenland ice sheet. *Cryosphere* 7, 599–614. doi: 10.5194/tc-7-599-2013

Vionnet, V., Brun, E., Morin, S., Boone, A., Faroux, S., Le Moigne, P., et al. (2012). The detailed snowpack scheme Crocus and its implementation in SURFEX v7.2. *Geosci. Model Dev.* 5, 773–791. doi: 10.5194/gmd-5-773-2012

Wever, N., Schmid, L., Heilig, A., Eisen, O., Fierz, C., and Lehning, M. (2015). Verification of the multi-layer SNOWPACK model with different water transport schemes. *Cryosphere* 9, 2271–2293. doi: 10.5194/tc-9-2271-2015

Wright, A. P., Wadham, J. L., Siegert, M. J., Luckman, A., Kohler, J., and Nuttall, A. M. (2007). Modeling the refreezing of meltwater as superimposed ice on a high Arctic glacier: a comparison of approaches. *J. Geophys. Res.* 112:F04016. doi: 10.1029/2007JF000818

Yamaguchi, S., Katsushima, T., Sato, A., and Kumakura, T. (2010). Water retention curve of snow with different grain sizes. *Cold Regions Sci. Technol.* 64, 87–93. doi: 10.1016/j.coldregions.2010.05.008

Yen, Y. (1981). *Review of Thermal Properties of Snow, Ice and Sea Ice*. Hanover, NH: United States Army Cold Regions Research and Engineering Laboratory. Report number: CRREL Report 81-10.

Zuo, Z., and Oerlemans, J. (1996). Modelling albedo and specific balance of the Greenland ice sheet: calculations for the Søndre Strømfjord transect. *J. Glaciol.* 42, 305–317.

Conflict of Interest Statement: The authors declare that the research was conducted in the absence of any commercial or financial relationships that could be construed as a potential conflict of interest.

The reviewer PA and handling Editor declared their shared affiliation, and the handling Editor states that the process nevertheless met the standards of a fair and objective review.

frontiers in Earth Science

ORIGINAL RESEARCH
published: 27 January 2017
doi: 10.3389/feart.2017.00003

Firn Meltwater Retention on the Greenland Ice Sheet: A Model Comparison

Christian R. Steger[1], Carleen H. Reijmer[1], Michiel R. van den Broeke[1], Nander Wever[2,3], Richard R. Forster[4], Lora S. Koenig[5], Peter Kuipers Munneke[1], Michael Lehning[2,3], Stef Lhermitte[6], Stefan R. M. Ligtenberg[1], Clément Miège[4] and Brice P. Y. Noël[1]*

[1] *Institute for Marine and Atmospheric Research, Utrecht University, Utrecht, Netherlands,* [2] *School of Architecture, Civil and Environmental Engineering, École Polytechnique Fédérale de Lausanne, Lausanne, Switzerland,* [3] *WSL Institute for Snow and Avalanche Research SLF, Davos Dorf, Switzerland,* [4] *Department of Geography, University of Utah, Salt Lake City, UT, USA,* [5] *National Snow and Ice Data Center, Cooperative Institute for Research in Environmental Sciences, University of Colorado, Boulder, CO, USA,* [6] *Department of Geoscience & Remote Sensing, Delft University of Technology, Delft, Netherlands*

Runoff has recently become the main source of mass loss from the Greenland Ice Sheet and is an important contributor to global sea level rise. Linking runoff to surface meltwater production is complex, as meltwater can be retained within the firn by refreezing or perennial liquid water storage. To constrain these uncertainties, the outputs of two offline snow/firn models of different complexity (IMAU-FDM and SNOWPACK) are compared to assess the sensitivity of meltwater retention to the model formulation (e.g., densification, irreducible water content, vertical resolution). Results indicate that model differences are largest in areas where firn aquifers form, i.e., particularly along the south-eastern margin of the ice sheet. The IMAU-FDM simulates higher densification rates for such climatic conditions and prescribes a lower irreducible water content than SNOWPACK. As a result, the model predicts substantially lower amounts of refreezing and liquid water storage. SNOWPACK performs better for this area, confirmed both by density profiles from firn cores and radar-inferred observations. Refreezing integrated over the entire ice sheet and averaged for the period 1960–2014 amounts to 216 Gt a^{-1} (IMAU-FDM) and 242 Gt a^{-1} (SNOWPACK), which is 41 and 46% of the total liquid water input (snowmelt and rainfall). The mean areal extents of perennial firn aquifers for 2010–2014 simulated by the models are 55,700 km^2 (IMAU-FDM) and 90,200 km^2 (SNOWPACK). Discrepancies between modeled firn profiles and observations emphasize the importance of processes currently not accounted for in most snow/firn models, such as vertical heterogeneous percolation, ponding of water on impermeable layers, lateral (sub-)surface water flow, and the issue of ill-constrained refreezing conditions at the base of firn aquifers.

Keywords: firn modeling, refreezing on Greenland, meltwater retention, firn aquifer, ice layer

OPEN ACCESS

Edited by:
William Tad Pfeffer, University of Colorado Boulder, USA

Reviewed by:
Evgeny Andreevich Podolskiy, Hokkaido University, Japan
Leigh A. Stearns, University of Kansas, USA

****Correspondence:***
Christian R. Steger
c.r.steger@uu.nl

Specialty section:
This article was submitted to Cryospheric Sciences, a section of the journal Frontiers in Earth Science

Received: *20 September 2016*
Accepted: *11 January 2017*
Published: *27 January 2017*

Citation:
Steger CR, Reijmer CH, van den Broeke MR, Wever N, Forster RR, Koenig LS, Kuipers Munneke P, Lehning M, Lhermitte S, Ligtenberg SRM, Miège C and Noël BPY (2017) Firn Meltwater Retention on the Greenland Ice Sheet: A Model Comparison. Front. Earth Sci. 5:3. doi: 10.3389/feart.2017.00003

1. INTRODUCTION

The Greenland Ice Sheet (GrIS) is the largest freshwater reservoir in the Northern Hemisphere and its complete deglaciation would cause a sea level rise of 7.4 m (Bamber et al., 2013). Studying the GrIS mass balance is important, since surface melt along the margins is rapidly increasing, and its current mass loss is more than double that of the Antarctic Ice Sheet (van den Broeke et al., 2016).

Between 2000 and 2008, ice discharge and runoff contributed equally to the total mass loss of the GrIS (van den Broeke et al., 2009). In recent years (2009–2012), the relative contribution of meltwater runoff to total mass loss increased to 68% (Enderlin et al., 2014). It is likely that this trend will continue in the future, especially as progressively more outlet glaciers of the GrIS will lose contact with the ocean when the ice sheet retreats further inland (Goelzer et al., 2012).

Runoff is related to the amount of surface melt, which increased significantly in recent years (van Angelen et al., 2014). Primary causes of enhanced melting are atmospheric warming, which is further enhanced by polar amplification (Bekryaev et al., 2010), and the darkening of the ice sheet (van As et al., 2013). The darkening is caused by dust, glacial cyanobacteria, and algae (Wientjes et al., 2011; Yallop et al., 2012) and by snow grain growth (Tedesco et al., 2016). Expansion of the melt area is additionally amplified by the hypsometry of the ice sheet, with the surface slope decreasing toward higher elevations (Mikkelsen et al., 2016). However, the effect of increased surface meltwater on runoff is not straightforward, as meltwater can be retained within the firn due to refreezing and liquid water storage, or in supra- and subglacial hydrological systems (Livingstone et al., 2013). Understanding the short- and long-term effects of meltwater buffering is hence crucial for projecting future contributions of the GrIS to global sea level rise.

The surface of the GrIS can be divided into an ablation and accumulation area, separated at the equilibrium line altitude (ELA). Refreezing in the ablation area happens mainly at the beginning of the melt season, when meltwater percolates into the cold snowpack accumulated during the previous winter. This storage is however only temporary due to the negative annual surface mass balance (SMB). Still, refreezing delays the exposure of bare ice in the ablation zone (Reijmer et al., 2012) and hence reduces melt by maintaining a higher surface albedo. As soon as all available pore space in the snow is saturated, meltwater may laterally run off through an efficient drainage system (Smith et al., 2015) and accumulate in supraglacial lakes or drain into crevasses or moulins. The accumulation zone can be further divided into the dry snow and the percolation zone. The former is not affected by surface melt and/or rainfall and is hence irrelevant for liquid water retention. On the GrIS, this zone is vanishing, as e.g., in mid-July 2012, almost the entire ice sheet experienced surface melt (Nghiem et al., 2012; Bennartz et al., 2013). The percolation zone is demarcated by the dry snow line at its upper boundary and the ELA at its lower limit and it is divided in two parts by the runoff line. In the upper part, all melt is retained locally whereas a certain fraction of meltwater drains laterally into the lower part. These areas are of particular interest for studying refreezing processes as they may have the potential to buffer a considerable amount of meltwater (Harper et al., 2012).

Vertical meltwater percolation happens through a homogeneous wetting front (Colbeck, 1972) and/or through heterogeneous piping, where water (and latent energy) is efficiently transported to greater depth. Piping events seem to be linked to layer transitions (in terms of density or grain size) with ponding water conditions (Humphrey et al., 2012). A further important effect of refreezing is the formation of ice layers. Thick ice layers, with a vertical extent of up to several meters, may prevent meltwater from reaching greater depths and hence induce lateral runoff before all pore space is filled (Machguth et al., 2016). At the end of the melt season, low surface temperatures induce conductive heat loss in the firn and thereby refreeze liquid water that is held by capillary forces (irreducible water). At some locations however, refreezing is suppressed by high annual snowfall rates that isolate the liquid water from the cold winter atmosphere (Kuipers Munneke et al., 2014). These perennial water bodies are called firn aquifers and their abundance is particularly high along the south-eastern margin of the GrIS (Forster et al., 2014).

Many unknown factors, including current and future rates of rainfall (Doyle et al., 2015), remain in quantifying past, current and future refreezing on the GrIS. A study by Reijmer et al. (2012), where refreezing is compared between two regional climate models (RCMs) that explicitly simulate refreezing and different refreezing parameterizations, indicates that the RCMs agree reasonably well with respect to the amount of refreezing, whereas the parameterizations differ substantially. Currently, most models that simulate refreezing explicitly do not account for processes such as impermeable layers, vertical heterogeneous percolation (Hirashima et al., 2014; Avanzi et al., 2016) or lateral water movement within the firn (Cox et al., 2015). Uncertainty about the total amount of pore space in the firn for refreezing is also rather large: Harper et al. (2012) assume that all pore space is available for refreezing and that lateral runoff only occurs if the underlying firn is totally saturated. Machguth et al. (2016) however suggest that thick ice layers, which seem to form on large horizontal scales and after substantial surface melt, could render the underlying pore space unavailable for surface melt water, enhancing runoff. Furthermore, our lack of knowledge about sub- and englacial water storage introduces additional uncertainties in the amount of runoff predicted by climate models (Rennermalm et al., 2013; Smith et al., 2015). A study by Vernon et al. (2013) also highlights the importance of accurately modeling refreezing and indicates that the relatively good model agreement in terms of GrIS integrated SMB may be the result of regionally compensating errors.

In this study, we compare the results of two one-dimensional numerical snow/firn models of different complexity, with a special focus on refreezing and liquid water retention on the GrIS. Both models are forced with the most recent outputs of the regional atmospheric climate model RACMO2.3 (Noël et al., 2015). The primary goal is to assess the sensitivity of refreezing and liquid water storage to the model formulation. A more comprehensive understanding of these processes is highly relevant in estimating current and particularly future GrIS runoff amounts, which contribute substantially to the rise in global sea level. The following section provides an overview of the snow/firn models used, a description of the forcing and spin-up procedure, and a brief description of the observational data. Subsequently, the model's performance is assessed with density profiles from firn cores. Finally, the spatial and temporal patterns of refreezing, liquid water storage, and near-surface ice layers in the models are analyzed and discussed.

2. MODELS, METHODS, AND DATA

The snow/firn models considered in this study are the IMAU-FDM (Ligtenberg et al., 2011) and SNOWPACK (Bartelt and Lehning, 2002; Lehning et al., 2002a,b). Both models are one-dimensional, i.e., there is no lateral exchange of mass and energy between neighboring grid cells, and they are formulated in a Lagrangian framework, in which the coordinate system moves vertically with the ice matrix. The largest difference between the models concerns the densification scheme, the amount of irreducible water content, the vertical resolution and the general complexity.

2.1. IMAU-FDM

The IMAU-FDM was developed for interactive coupling to an RCM to simulate firn on polar ice sheets (Ligtenberg et al., 2011). It contains a semi-empirical scheme to compute dry firn densification (Arthern et al., 2010):

$$\frac{d\rho}{dt} = M_o\, C\, \dot{b}\, g\, (\rho_i - \rho)\, \exp\left(\frac{-E_c}{R\,T} + \frac{E_g}{R\,T_{av}}\right). \quad (1)$$

Equation (1) contains a calibration factor (M_o), which is specifically derived for the GrIS and depends on annual mean accumulation (Kuipers Munneke et al., 2015). Here, ρ is the firn density and ρ_i the density of ice, t is time, $\dot{b}$ is the mean annual accumulation over a reference period, g is the gravitational acceleration, C is a coefficient depending on density, T is the instantaneous local firn temperature and T_{av} the mean annual temperature at the surface, E_c and E_g are the activation energies for self-diffusion of water molecules through the ice lattice and for grain growth, and R is the ideal gas constant. The model time step depends on the occurrence of melt and is reduced from 3600 s (dry snow) to 300 s (wet snow) to capture vertical water percolation more accurately. Heat conduction (k) through the snow/firn is computed as (Anderson, 1976):

$$k = 0.021 + 2.5\left(\frac{\rho}{1000}\right)^2. \quad (2)$$

The specific heat capacity of ice is computed as a function of temperature. The vertical water percolation is simulated with a bucket scheme where melt water runs through all layers within one model time step and water is retained as ice or liquid water based on the availability of pore space and cold content. The irreducible water content is set to a relatively low value of 2% of the pore volume to mimic processes that allow an effective vertical water transport to lower layers, such as piping (Greuell and Konzelmann, 1994; Reijmer et al., 2012). Layer merging and splitting is constrained to the upmost layer of the model. If the upper layer thickness exceeds 0.2 m due to a positive SMB (snowfall, sublimation, snow drift), the layer is split into two equal parts. If the layer thickness is reduced to below 0.1 m due to a negative SMB (sublimation, snowdrift, melt), the layer is merged with the one below.

2.2. Snowpack

SNOWPACK, a state-of-the-art snow model, was originally designed to model seasonal snow cover in alpine areas and as a tool to study avalanche formation and snow hydrology. Recently, it has also been successfully applied to polar regions (Dadic et al., 2008; Groot Zwaaftink et al., 2013; Van Tricht et al., 2016). SNOWPACK simulates microstructural snow properties such as grain size, bond size, dendricity, and sphericity and links these quantities to thermal and mechanical snow properties. Densification of snow is calculated by combining the constitutive relation for snow (Lehning et al., 2002b):

$$\dot{\varepsilon} = -\frac{\sigma_s}{\eta_s}, \quad (3)$$

with the definition of strain rate ($\dot{\varepsilon}$):

$$\dot{\varepsilon} = \frac{d}{dt}\left(\frac{dL}{L}\right) = \frac{1}{L}\frac{dL}{dt}, \quad (4)$$

to yield:

$$\frac{dL}{L} = \frac{-\sigma_s}{\eta_s}\, dt\,. \quad (5)$$

L is thereby the thickness of a snow layer, σ_s the overburden pressure and η_s the viscosity of snow. The viscosity is a function of microstructural snow properties, temperature, overburden pressure, and liquid water content (the presence of liquid water decreases viscosity) and can be computed for temperatures ranging from -80° to 0°C (Groot Zwaaftink et al., 2013). Close to the surface, SNOWPACK considers the influence of wind speed on snow compaction. A formulation simulating an enhanced impact of wind speed on near-surface snow compaction, which was implemented for Antarctic experiments (Groot Zwaaftink et al., 2013), is not used, as the fresh snow density scheme (Equation 6) is already calibrated to yield snow densities valid for the topmost couple of centimeters on the GrIS. Thermal conductivity is computed as a function of (I) conduction through ice, pore space, and liquid water and (II) latent heat transport, which is induced by a water vapor gradient. Additionally, the effect of wind pumping is considered by linking the thermal conductivity near the surface to the vertical wind velocity gradient in the snow. Above a volumetric ice content of 0.55, a simpler formulation is used where the effective conduction is the sum of conduction through ice, water, and air. In the version we use, vertical water transport can be simulated by the bucket scheme or by the Richards equation. In contrast to the bucket scheme, Richards equation solves explicitly for the balance between capillary suction and gravity (Wever et al., 2014). Recently, a scheme for simulating preferential flow was implemented (Wever et al., 2016), but this version has not yet been applied to Greenland. For this study, the bucket scheme is chosen to enable a direct comparison with the IMAU-FDM and because this scheme is computationally less demanding. The irreducible water content is computed as a function of snow density (Coléou and Lesaffre, 1998; Wever et al., 2014) and is limited to a maximum volumetric value of 8%. This value is based on an expert judgment on maximal water retention by capillary suction.

Layer merging and splitting criteria are checked for every layer in SNOWPACK. Splitting ensures a sufficient near-surface

resolution to capture small-scale temperature and moisture gradients. Merging depends on a threshold for thickness, which is a linear function of depth, and the similarity of layer properties (volumetric contents and microstructural properties). The reduction of layers by merging is necessary to limit the computational demand of the model. SNOWPACK runs, in contrast to the default value of 900 s, with a time step of 1800 s to increase computational efficiency. Sensitivity experiments with the larger time step confirmed the numerical stability and revealed no significant deviation in the output compared to a run with the default time step. The intermittent use of a smaller time step (300 s) for the IMAU-FDM is possible due to the model's lower computational demand. Minor modifications are introduced to the model to use it for the GrIS and to allow a direct comparison with the IMAU-FDM:

- A SMB forcing mode is implemented to drive the model with SMB-components instead of meteorological observations (see subsection Model Forcing and Spin-up). The internal energy balance scheme of SNOWPACK is hence switched off. This ensures equal SMB fluxes (including melt amounts) for both models.
- The density of the uppermost element is kept constant during sublimation, snowdrift and melt.
- The layer merging thresholds for sphericity, grain size, and volumetric ice content are no longer constants but functions of depth. The thresholds for sphericity and grain size start to linearly increase from a depth of 10 m and the threshold for volumetric ice content from a depth of 50 m. The resulting decrease in vertical resolution at greater depth is necessary to keep the number of layers in a computationally reasonable range.
- The IMAU-FDM approach of dealing with layers that are depleted of pore space but contain both ice and liquid water is adapted. For such layers, additional compaction leads to a decrease in the liquid water content of the layer until the density of ice is reached. The excess water is moved to the subjacent layer.
- To improve the agreement with observations, the tunable factors in the snow viscosity scheme (Groot Zwaaftink et al., 2013) for the activation energy of snow Q_s and the critical exponent β are set to 16,080 J mol^{-1} and 0.3, respectively.

2.3. Model Forcing and Spin-Up

Both models are forced at the upper boundary with output from the regional atmospheric climate model RACMO2.3. This model is specifically adapted to simulate climate conditions over ice sheets and contains a multilayer snow model, physically identical to the IMAU-FDM but with fewer vertical layers, an albedo scheme based on prognostic snow grain size (Kuipers Munneke et al., 2011) and a drifting snow routine (Lenaerts et al., 2012). RACMO2.3 was run for the period 1958–2015 on an 11 km horizontal resolution grid and a domain including Greenland, Iceland, Svalbard, and part of arctic Canada. Evaluations of RACMO2.3 indicate that the model is capable of realistically simulating present-day surface characteristics on the GrIS and that it improves upon previous RACMO versions (Noël et al., 2015).

Three-hourly time series of RACMO2.3 cumulative snowfall, rainfall, evaporation/sublimation, snowdrift erosion/deposition, surface melt, and instantaneous skin temperature are used to force both models. Applying the same boundary conditions to both models allows an objective comparison of the internal processes. A minor difference in the forcing concerns sublimation and evaporation. In the IMAU-FDM, the sum of these mass fluxes is exclusively treated as sublimation. In SNOWPACK, deposition depends on the skin temperature, where ice is added at skin temperatures below 0°C and water under melting conditions. When mass is removed, all liquid water is removed before sublimating the ice matrix. The forcing data are linearly interpolated to the model time step. By using three-hourly data, the diurnal temperature cycle is reasonably well captured—a relevant process for near-surface refreezing. The heat equation is solved with a Dirichlet boundary condition at the top (skin temperature) and a Neumann condition at the bottom (zero heat flux) in both models. A further required boundary condition is the fresh snow density. For this study, a simple parameterization is used where fresh snow density (ρ_0) is related to the mean annual surface temperature (T_{av}) (Kuipers Munneke et al., 2015):

$$\rho_0 = 481.0 + 4.834\ (T_{av} - 273.15)\,. \tag{6}$$

Both models are run on the RACMO2.3 spatial grid and ice mask (**Figure 1**). However, to decrease computational time, the models are run on a checkerboard grid in the interior of the ice sheet, i.e., only every second RACMO2.3 cell is simulated. Within approximately 40 km of the ice sheet margins, all grid cells are run to resolve the greater climate gradients.

A spin-up for both snow/firn models is conducted to initialize the models with reasonable firn profiles in 1960. In accordance with Kuipers Munneke et al. (2015), we assume that a 20-year reference period (1 January 1960–31 December 1979) is representative for the pre-1960 climate. The spin-up for an individual location is performed by iterating over the reference period for an appropriate number of times (n_{iter}) to refresh the entire firn layer. Due to the individual densification schemes of the models (Equations 1, 5), n_{iter} is determined differently for the IMAU-FDM and SNOWPACK:

- IMAU-FDM: A steady-state solution of Equation (1) can be computed (Ligtenberg et al., 2011) and applied to the reference period. This yields an approximation of the firn thickness for each location and allows the calculation of n_{iter} together with the surface mass flux over the reference period. For locations with a negative SMB, n_{iter} is set to 2 to initialize a reasonable winter snow cover over bare ice.
- SNOWPACK: Equation (5) does not allow the derivation of a steady-state solution and hence another spin-up strategy is adopted. It is assumed that the firn layer at each location is entirely refreshed after accumulating 70 m water equivalent of solid input. Combining this assumption with the surface solid mass flux over the reference period yields n_{iter} for each location. To decrease computational time,

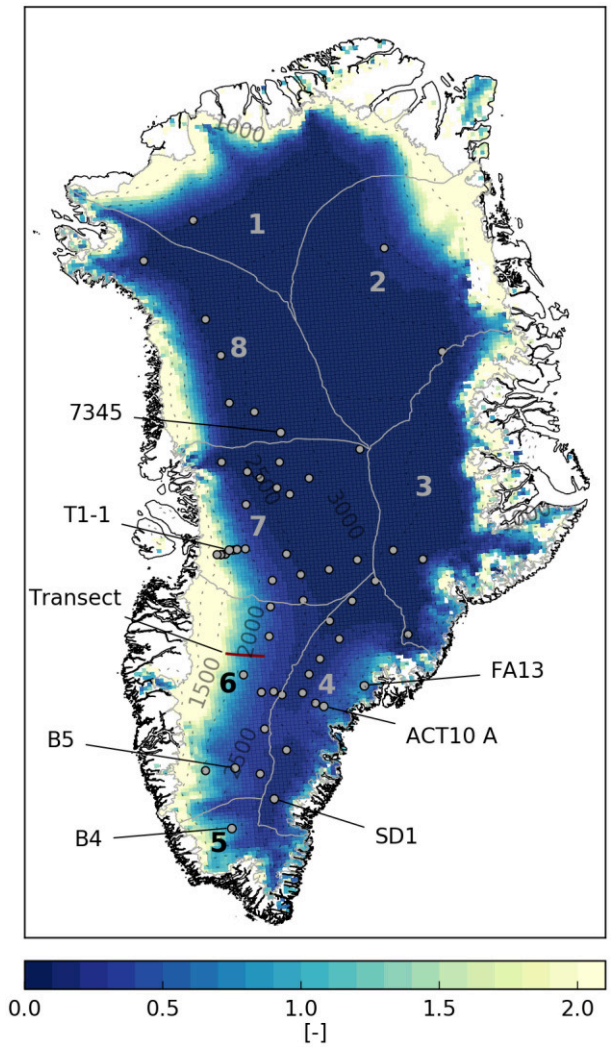

FIGURE 1 | Map of Greenland with ratio of liquid to solid surface mass input ($R_{liq/sol}$) averaged over 1960–2014 for the RACMO2.3 ice mask. Additionally, the 8 drainage basins, the location of the firn cores (gray) and the transect (red) used in this study are shown. Firn cores that are discussed in detail are labeled.

n_{iter} is limited to 2 for locations with a liquid (snowmelt, rainfall) to solid (snowfall, sublimation, snowdrift) surface mass input ratio ($R_{liq/sol}$) higher than 2.5. These locations are situated in the ablation zone where only seasonal snow but no firn is present. An analysis of the density profiles obtained by the spin-up confirmed that all n_{iter}-values were selected sufficiently large to refresh the firn layer at each location.

The spin-up in both models is initialized with firn density profiles computed with the steady-state solution of Equation (1) and with vertically constant temperatures that are equal to the average surface temperature over the reference period. These temperatures are additionally corrected for latent heat release by refreezing according to Reeh (2008).

2.4. Observational Data

All firn cores, except the one for location FA13 (**Figure 1**), are taken from the data set compiled by Kuipers Munneke et al. (2015). Density values of these profiles are usually calculated over a vertical distance of 0.5–2 m, hence the data of these cores do not capture thin layer variations such as ice lenses. The core used for location FA13 is described in Koenig et al. (2014). Evaluation of the models with firn cores is performed by selecting the closest grid cell and available time step of the models. The locations of all firn cores are shown in **Figure 1**. We also use data from airborne radar, which was on board the NASA Operation IceBridge (OIB) aircraft spring campaigns between 2010 and 2014 before the onset of surface-melt (Miège et al., 2016). The data are used to evaluate the horizontal extent of firn aquifers and ice layers simulated by the two numerical models. The Accumulation Radar was built and is operated by the Center for Remote Sensing of Ice Sheets (CReSIS) at the University of Kansas to image near-surface (up to approximately 400 m depth) internal structure of the ice sheet with a 65 cm vertical resolution (Rodriguez-Morales et al., 2014). The Accumulation Radar is well suited to image the presence of a water table in the firn characterized by a bright reflector in the radar images (Forster et al., 2014; Miège et al., 2016).

2.5. Model Output Processing

Both models provide time series and vertically resolved data for each grid cell. The vertically resolved data are first mass-conservatively resampled to a common grid. Subsequently, these data and the time series are bilinearly interpolated from the checkerboard grid to the full ice mask. Temporal resampling is either done mass-conservatively for flux quantities or with linear interpolation for the remaining data.

3. RESULTS AND DISCUSSION

3.1. Evaluation of Models with Vertical Density Profiles

A summary of the model performances in simulating average firn density in the topmost 30 m is shown in **Figure 2**, with the colors indicating the ratio of liquid to solid mass input at the surface ($R_{liq/sol}$). Generally, the skills are comparable, with both models overestimating density in regions with relatively high amounts of liquid water input. It is important to note that the firn core samples shown in **Figure 2** do not capture all occurring surface conditions on the GrIS, with some regions being rather over- or underrepresented. Despite the similar patterns shown in **Figure 2**, there are some notable differences, which are subsequently addressed by means of selected firn cores in **Figure 3**. First of all, the IMAU-FDM shows a better agreement with observed profiles for locations with low $R_{liq/sol}$-values where SNOWPACK exhibits a larger scattering with mean densities being typically slightly underestimated. The lower scattering in the IMAU-FDM can be explained by the tuning of the model's densification scheme with these cores. Density biases in SNOWPACK, particularly at greater depth, are likely related to the fact that its densification scheme was developed for alpine snow cover (Lehning et al., 2002b). Seasonal snow has a relatively short lifetime and hence overburden pressures that occur on

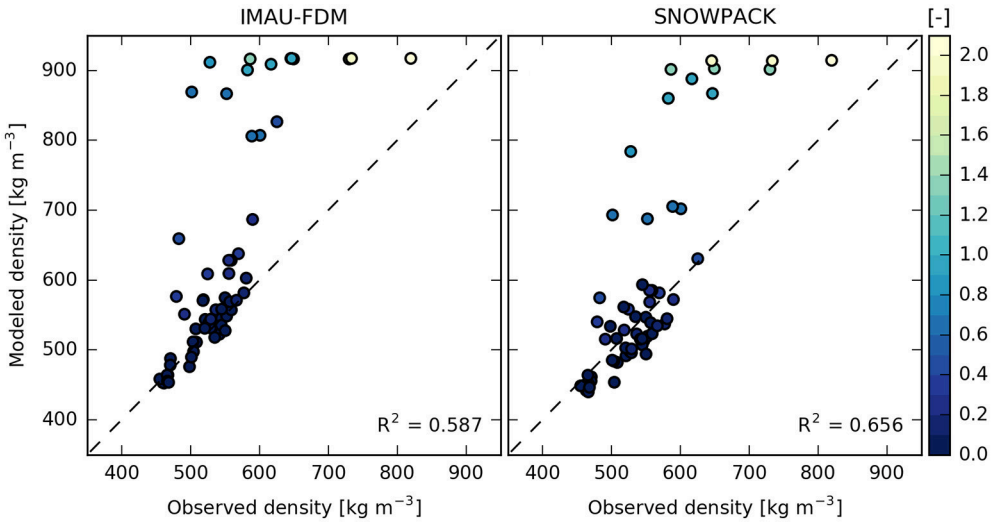

FIGURE 2 | Modeled vs. observed average firn density of the topmost 30 m. Colors indicate the ratio of liquid to solid surface mass input ($R_{liq/sol}$). Note that some shallow firn cores do not extend down to 30 m and hence only the available part is considered.

an ice sheet are never reached. Relevant processes for the later densification stages are therefore likely not fully incorporated in the densification scheme. SNOWPACK overestimates near-surface densities for the firn cores with the lowest mean annual surface temperatures (<−28°C), which are located in the north-eastern part of the GrIS. For locations with temperatures between −26° and −28°C, near-surface density is generally in line with observations (**Figure 3A**), whereas for higher temperatures, SNOWPACK tends to underestimate near-surface densities (**Figure 3B**).

For locations with $R_{liq/sol}$-values larger than approximately 0.2, the IMAU-FDM reveals a positive bias in mean density where SNOWPACK indicates a better agreement (**Figure 3C** and following Figures). The simulation of surface melt-freeze crusts and ice layers in SNOWPACK, which occurs at locations with considerable amounts of surface melt is addressed in subsection Formation of Ice Layers. Location ACT10 A (**Figure 3D**) has a relatively high mean annual surface temperature and accumulation rate and is located relatively close to observed firn aquifers. At this site, the IMAU-FDM reveals a particularly pronounced density overestimation whereas SNOWPACK is in better agreement with the observed density. The high-density spike around 10 m depth in the SNOWPACK profile is caused by a recent (around 2005) increase in liquid surface input and subsequent refreezing. Its absence in the observed density profile suggests an underestimation of vertical water transport in SNOWPACK, which does not account for vertical heterogeneous percolation in the used version. The relevance of the mismatch between the models under these climate conditions will be further discussed in subsection Perennial Firn Aquifers.

For locations with even higher $R_{liq/sol}$-values (>0.6), both models consistently overestimate mean density (**Figures 3E,F**), but SNOWPACK exhibits a lower bias. For relatively high $R_{liq/sol}$-values (close to 1 and above), the IMAU-FDM generally simulates bare ice profiles. As discussed in Kuipers Munneke et al. (2015), the overestimated density at high-melt locations could be caused by inaccurate atmospheric forcing, i.e., too much refreezing caused by an overestimation of surface melt or too little pore space caused by an underestimation of accumulation. Alternatively, errors in the snow/firn models could be responsible for this density bias due to an overestimation of refreezing caused by underestimating vertical water flow or ignoring lateral runoff due to impermeable ice layers. However, it seems likely that the IMAU-FDM overestimates densification rates for such locations as SNOWPACK still simulates available pore space for locations with an $R_{liq/sol}$-value close to 1 (**Figure 3F**). The pore space in the upper part of this density profile was recently filled with refreezing meltwater, where the low density spike at around 7 m depth was caused by an intermediate period with a lower $R_{liq/sol}$-value. This mismatch between the modeled and observed density may suggest again an underestimation of vertical water transport in SNOWPACK or points to the inability of the model to allow for lateral runoff at the surface.

Finally, a bias in fresh snow density could also contribute to density overestimations. This is supported by the fact that the uppermost measured firn densities are lower than values simulated by both models for the majority of the locations (not shown). Compared to other parameterizations [e.g., Groot Zwaaftink et al. (2013)], the fresh snow density formulation used in this study indeed predicts rather high values (between 320 and 480 kg m^{-3}). However, it is challenging to formulate an accurate and robust parameterization due to the numerous influencing factors (temperature, wind speed, humidity) and the sparse availability of observational data for the GrIS when it comes to real surface density, instead of the average over the first tens of centimeters.

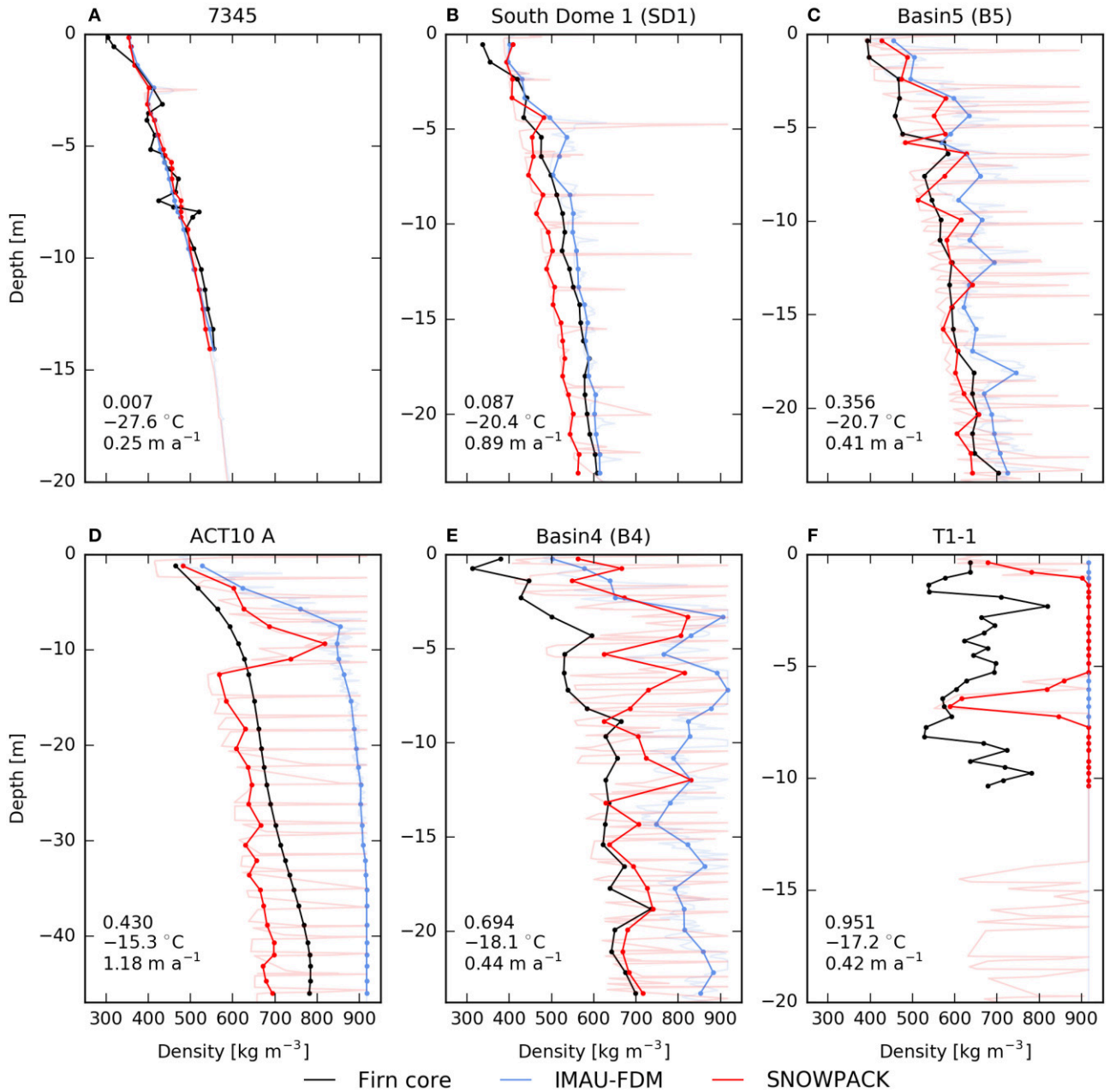

FIGURE 3 | Observed (black) and modeled (IMAU-FDM: blue, SNOWPACK: red) firn density profiles for 6 locations from different surface climate zones (A–F). The numbers in the lower left corner state the ratio of liquid to solid surface mass input ($R_{liq/sol}$), the mean annual surface temperature and the mean annual solid accumulation. The shaded profiles are model outputs at native vertical resolution whereas the thick lines represent profiles resampled to the vertical resolution of the firn cores.

3.2. Refreezing and Runoff

The mean spatial refreezing patterns of both models are similar (**Figure 4**), although the absolute magnitude differs significantly in some regions. In the northern and north-eastern part of the GrIS (basins 1 and 2), basin-integrated amounts of refreezing are slightly higher in the IMAU-FDM. This can be explained by lower refreezing amounts in SNOWPACK in the ablation zone and for some regions close to the ELA (**Figures 5A,B**). The model difference in the ablation zone is caused by two factors: (I) in SNOWPACK, part of the surface melt evaporates whereas in the IMAU-FDM, a latent-heat flux is always linked to a mass change of the ice matrix and (II) a combined effect of model differences in vertical resolution and merging of summer snowfall into subjacent ice layers. In contrast to SNOWPACK, merging in the IMAU-FDM is performed regardless of differences in layer properties. Hence, snowfall is merged into subjacent ice layers,

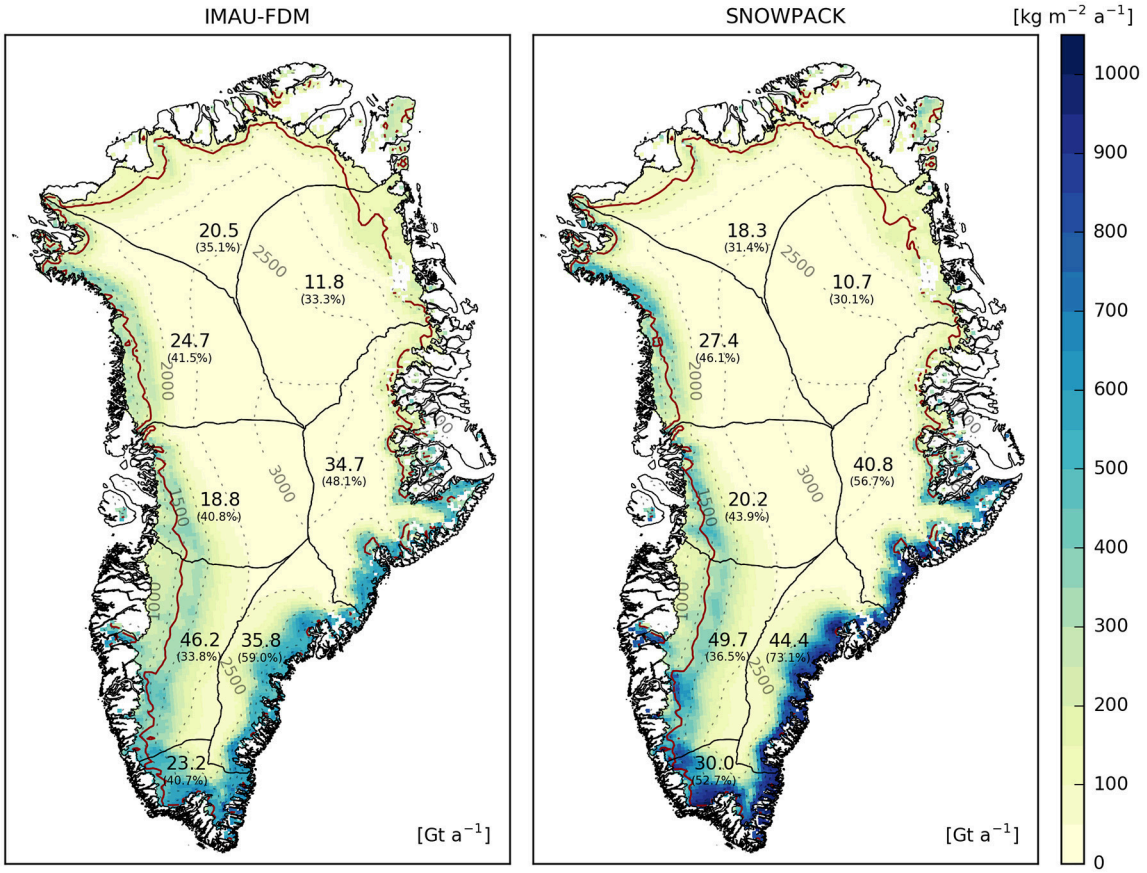

FIGURE 4 | Refreezing amounts averaged over the years 1960–2014 for both models. The red line marks the ELA derived with SMB components from RACMO2.3 but runoff is taken from the respective snow/firn model. Numbers provided in the drainage basins represent basin-integrated values of refreezing. The values in brackets express refreezing as a fraction of liquid surface mass input (melt and rainfall).

which results in comparably thick surface layers (approximately 0.1 m) with pore space available for liquid water retention and refreezing. During subsequent surface melt, this void space remains available longer than in SNOWPACK. The difference close to the ELA is caused by SNOWPACK simulating higher mean densities in the upmost 20 m. This leads to less available pore space for refreezing during the melt season. SNOWPACK therefore also predicts higher runoff amounts for these two basins (**Figures 6D–F**).

Refreezing in the three basins on the eastern, south-eastern, and southern GrIS (basins 3–5) is substantially larger (approximately 18–29%) in SNOWPACK. In early June, the discrepancy is small because both models provide mostly enough pore space and cold content to refreeze percolating meltwater. In July, when surface snowmelt amounts peak, SNOWPACK simulates considerably higher refreezing values (**Figure 5B**). In both models, near-surface firn in the vicinity of the ice sheet margins is temperate at this time, hence the difference is mainly caused by the higher irreducible water content and vertical resolution in SNOWPACK, which leads to more near-surface refreezing due to diurnal temperature variations (**Figures 6A,B**). For all three basins, the difference in refreezing peaks in late July or early August with a decay toward autumn (**Figure 6C**). This decaying difference is caused by the higher amounts of irreducible water in SNOWPACK, which refreeze in autumn when firn temperatures steadily decrease. Runoff generation is thus persistently smaller for basins 3–5 compared to the IMAU-FDM (**Figures 6D–F**).

For basins 6–8, SNOWPACK simulates slightly higher mean area-integrated refreezing values. These higher values are primarily restricted to the accumulation zone. There, deeper firn temperatures are well below 0°C in both models, and SNOWPACK simulates layers with porous firn, in contrast to the IMAU-FDM. This void space is subsequently filled with percolating meltwater that refreezes, particularly during the last decade of the simulation period when liquid mass input at the surface increases significantly. In the ablation area, refreezing is generally lower in SNOWPACK; especially in August (**Figure 5C**). Hence runoff in SNOWPACK is lower for these basins at the beginning of the melt season but this pattern reverses in August when the refreezing difference in the ablation zone starts to dominate. The reason behind the generally lower amounts of refreezing in SNOWPACK in the ablation zone is the same as for basins 1 and 2. Mean annual GrIS integrated values of

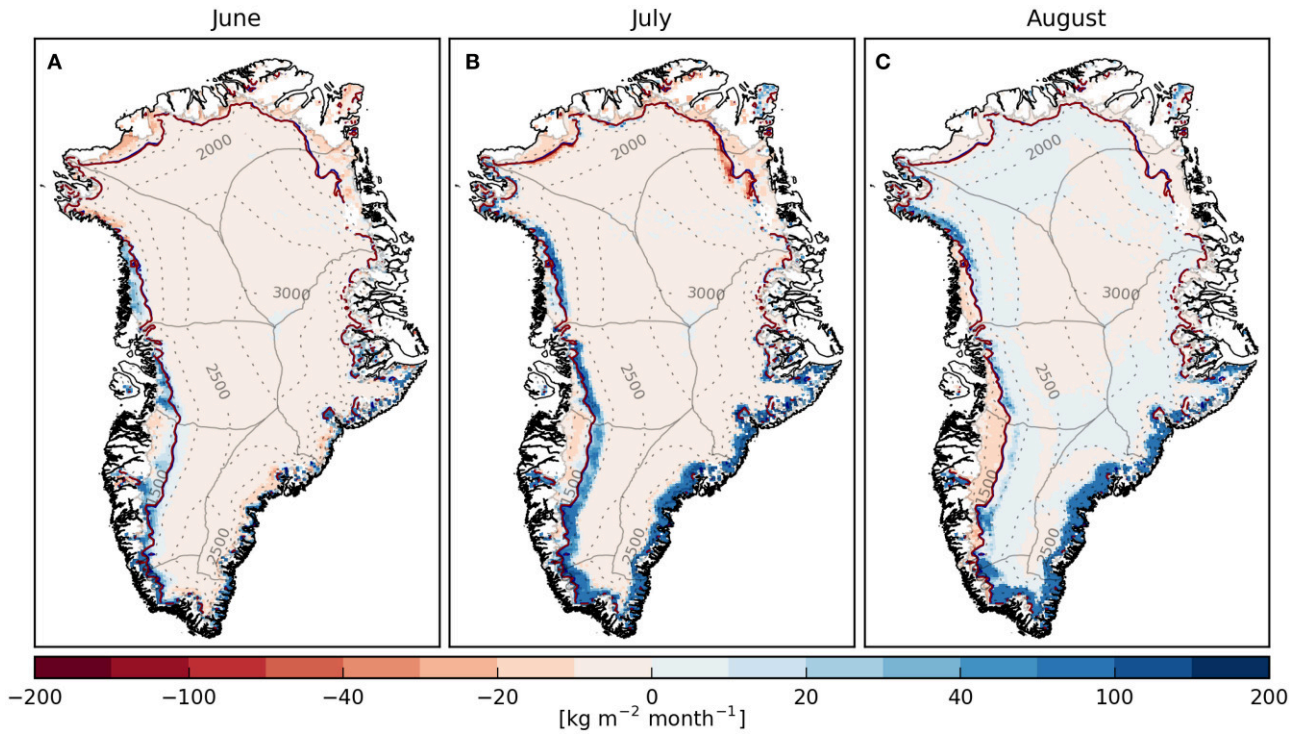

FIGURE 5 | Difference (SNOWPACK–IMAU-FDM) in monthly refreezing amounts for June (A), July (B), and August (C) averaged over the years 1960–2014. The blue (IMAU-FDM) and red (SNOWPACK) lines mark the ELA derived with SMB components from RACMO2.3 but with runoff taken from the respective snow/firn model.

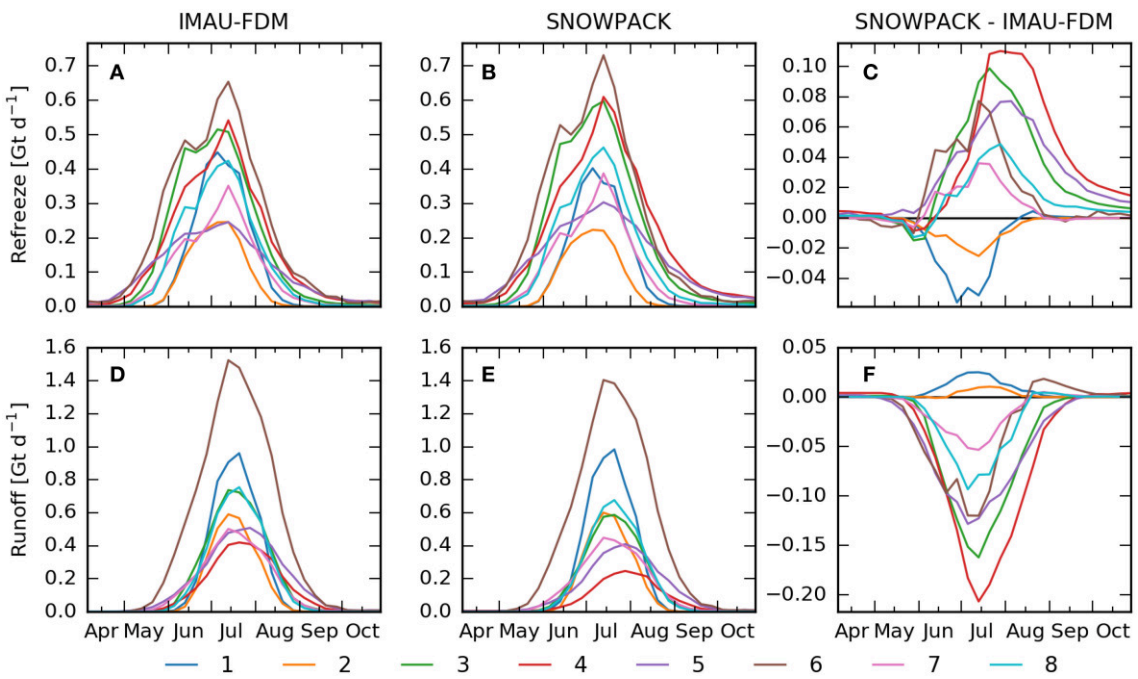

FIGURE 6 | Mean (1960–2014) seasonal cycle of refreezing (A–C) and runoff (D–F) for the 8 GrIS drainage basins and the two models. The right column represents the difference of these two variables between the models.

refreezing are 216 Gt a^{-1} (123 mm w.e. a^{-1}) for the IMAU-FDM and 242 Gt a^{-1} (138 mm w.e. a^{-1}) for SNOWPACK, respectively. Reijmer et al. (2012) found refreezing values for the GrIS in the range of 54–151 mm w.e. a^{-1} averaged over the period 1958–2008; depending on the RCM, refreezing parameterization, and ice mask used. The values obtained in this study are comparable but in the higher part of the range; particularly the one simulated by SNOWPACK.

3.3. Perennial Firn Aquifers

In this study, perennial firn aquifers are defined as liquid water bodies in the firn that persist throughout the winter. Observed firn aquifers on the GrIS normally reveal saturated conditions, i.e., the entire pore space is filled with liquid water (Forster et al., 2014; Koenig et al., 2014). The models applied in this study are however not capable of simulating such conditions in the used configuration, because ponding of liquid water within the firn is not allowed. To compare observed and modeled firn aquifer locations, we therefore apply the term perennial firn aquifer to both saturated and unsaturated conditions.

Both models simulate firn aquifers, but there are significant differences in the horizontal extent and the stored liquid water mass (**Figure 7**). Apart from the south-eastern GrIS, SNOWPACK produces extensive firn aquifers on the southern tip of the GrIS, along the north-western edge, and on Sukkertoppen ice cap. The IMAU-FDM fails to predict significant firn aquifers in the northwest and the general amount of liquid water stored is small compared to SNOWPACK. Comparing the spatial occurrence of firn aquifers in the models with radar-derived locations (Miège et al., 2016) indicates a good agreement;

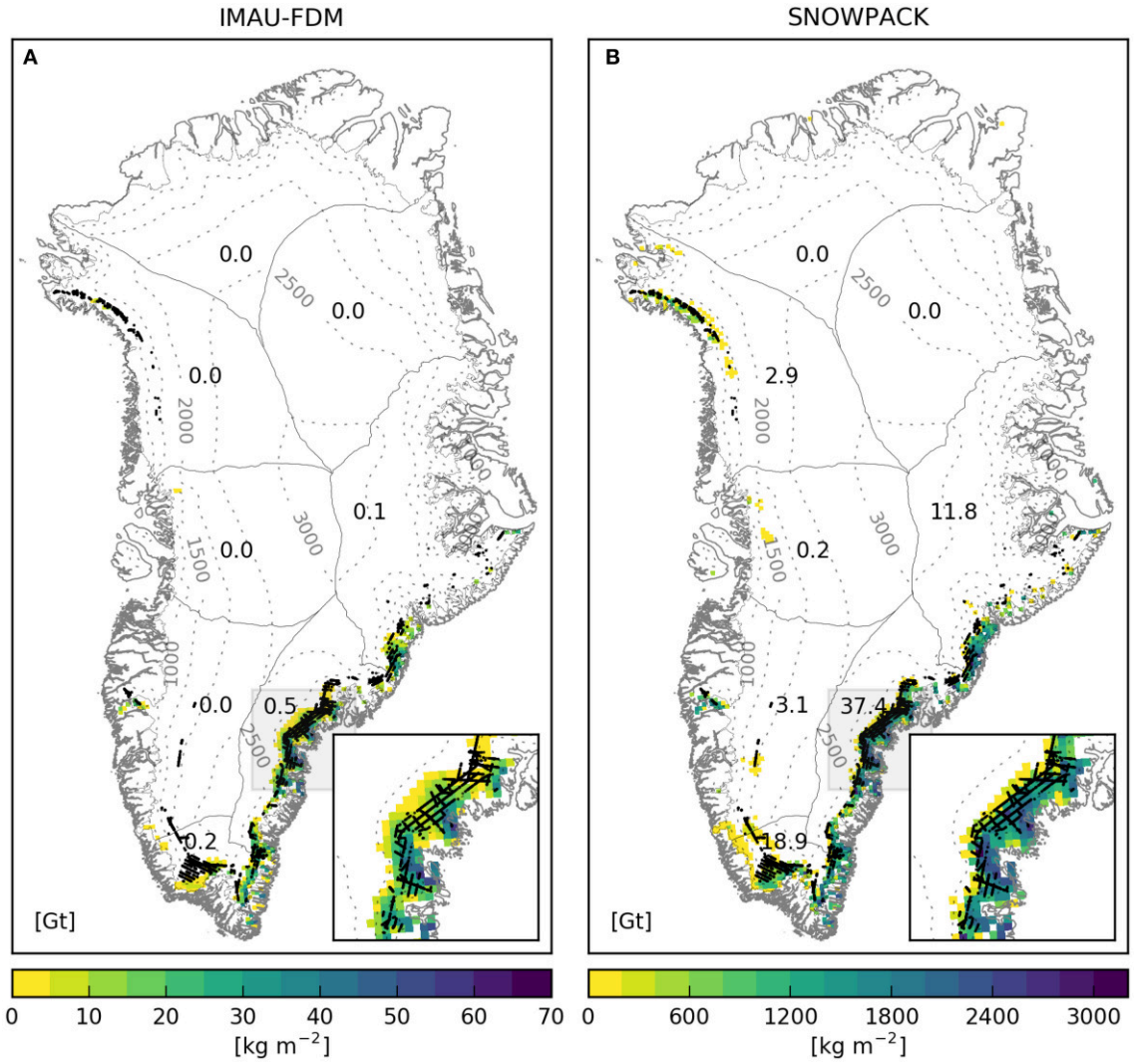

FIGURE 7 | Vertically integrated liquid water content averaged over April (2010–2014) before the onset of the melt season for IMAU-FDM (A) and SNOWPACK (B). Numbers provided in the drainage basins represent basin-integrated values of liquid water mass. Black dots mark the position of radar-derived firn aquifers from Operation IceBridge Accumulation Radar flights 2010–2014 (Miège et al., 2016). The sub-panels in the lower right corner show a zoom-in of the south-eastern margin of the GrIS. Note the different color scales for both panels.

TABLE 1 | Modeled firn aquifer characteristics averaged over April (2010–2014) before the onset of the melt season.

			IMAU-FDM	SNOWPACK
Area	Extent	km^2	55,700	90,200
	(liquid water >200 kg m^{-2})		(0)	(60,900)
	Coverage of observed firn aquifers by models	–	48.2%	67.7%
Liquid mass	Irreducible water	Gt	0.8	75.8
	Pore space saturation	Gt	44.5	299.7
	Observational constrained pore space saturation	Gt	22.7	158.2

Storage amounts assuming pore space saturation are derived by adding model runoff to void pore space of wet layers until full saturation is established. The observational constrained values are derived by limiting the areal extent of firn aquifers by radar-derived observations.

particularly for SNOWPACK (**Table 1**). Compared to this version of the IMAU-FDM, the previous better agreement of RACMO2.1 data with firn aquifer observations (Forster et al., 2014) can be attributed to a different densification scheme, as described by Reijmer et al. (2012). By comparing radar-inferred with modeled data, it is important to remember that observations indicate detections of water tables (saturated conditions) whereas the models show the occurrence of perennial liquid water without pore space saturation. The models' (particularly SNOWPACK's) apparent overestimation of the firn aquifer's horizontal extent downstream of the mapped locations may be explained by: (I) crevasses that evacuate stored liquid water and prevent the realization of a water table, (II) complex bedrock topography, which is not captured by the model's horizontal resolution and hinders the formation of firn aquifers, and (III) flight tracks not covering the entire area near the ice margin. The IMAU-FDM also indicates some areal overestimation upstream of the mapped locations, especially along the south-eastern margin (inset panel **Figure 7A**). This is caused by near-surface temperate firn conditions. In SNOWPACK, densification rates are lower, implying stronger downward advection of cold winter snowfall and hence cold conditions where all percolating meltwater refreezes. SNOWPACK indicates some areal overestimation on the western GrIS. Generally, these amounts of stored liquid water are rather small (<200 kg m^{-2}) and hence likely below the detection limit of the radar (Miège et al., 2016). Some isolated locations of radar-inferred firn aquifers are not captured by both models. This might be due to errors in RACMO2.3 forcing or the horizontal resolution of the models being too coarse to resolve small-scale climatic conditions required for firn aquifer formation.

To account for the models' inability to allow for saturation of pore volume by liquid water, estimates of water storage considering saturation are provided, which form an upper boundary for the stored mass (**Table 1**). However, these estimates are likely too high, because no water tables were detected for large areas in the vicinity of the ice sheet margin where both models simulate firn aquifers (inset panels **Figure 7**). As mentioned, this is most likely related to the presence of crevasses and/or complex bedrock topography. To address this issue, observation-constrained storage volumes are derived where water saturation is only computed for grid boxes where firn aquifers have been observed. The corrected storage amounts are 22.7 Gt for the IMAU-FDM and 158.2 Gt for SNOWPACK, respectively. The value simulated by SNOWPACK is in the same range as an earlier derived estimate of 140 ± 20 Gt for 2013 (Koenig et al., 2014).

The large difference in the amount of liquid water stored in both models can be attributed to two factors: (I) densification rates in areas with substantial amounts of refreezing are considerably higher in the IMAU-FDM (**Figure 3D**) and (II) the irreducible water content, which is larger in SNOWPACK. The first factor is related to applying Equation (1) to areas where refreezing causes a considerable amount of latent heat release within the firn. This equation is derived by approximating the local temperature with the mean annual surface temperature (Arthern et al., 2010) and hence likely overestimates densification rates for locations where the vertically averaged firn temperature significantly exceeds the mean annual surface temperature. This was confirmed by experiments where the steady-state solutions of Equation (1) was applied to firn aquifer areas with varying T_{av}. The comparably high densification rates in the IMAU-FDM result in a shallow firn layer whose vertical extent is often too small to insulate liquid water from the cold winter surface temperatures. If the vertical extent is large enough, the storage capacity is still lower compared to SNOWPACK due to the smaller irreducible water content. The issue of firn aquifers forming in the IMAU-FDM at too shallow depths was also discussed by Kuipers Munneke et al. (2014) and the deficiency of modeling vertical preferential flow was mentioned as a possible explanation. It seems however that the overestimation of densification rates in the IMAU-FDM in these areas also largely contributes to this bias. Additionally, firn aquifer formation in SNOWPACK is favored by the near-surface thermal conductivity. In winter, mean snow densities over the topmost couple of meters are lower than in the IMAU-FDM, implying lower values of heat conduction and hence less heat loss to the atmosphere. During the melt season, thermal conductivity in SNOWPACK is larger than in the IMAU-FDM because it is a function of the liquid water content, which is additionally higher in SNOWPACK.

A more in-depth validation of the models based on in-situ data is possible for location FA13, where a firn core was extracted in April 2013 (Koenig et al., 2014). As mentioned above, the high densification rate in the IMAU-FDM results in a density profile reaching bare ice already at a depth of approximately 5 m (**Figure 8D**). In this model, the formation of a perennial firn aquifer is thus not possible, as the overlaying snow/firn is not thick enough to insulate the seasonally occurring liquid water from refreezing in winter. As a result, a relatively constant amount of surface melt is refrozen in the IMAU-FDM and the excess water is running off (**Figure 8C**). SNOWPACK on the other hand simulates the formation of a perennial firn aquifer. At the start of the simulation period, the firn column is cold (not shown) and provides enough pore space to refreeze all surface melt (**Figures 8A,C**). In other words, the $R_{liq/sol}$-value is not high enough for a firn aquifer to form. Towards the end of the simulation period, this value increases

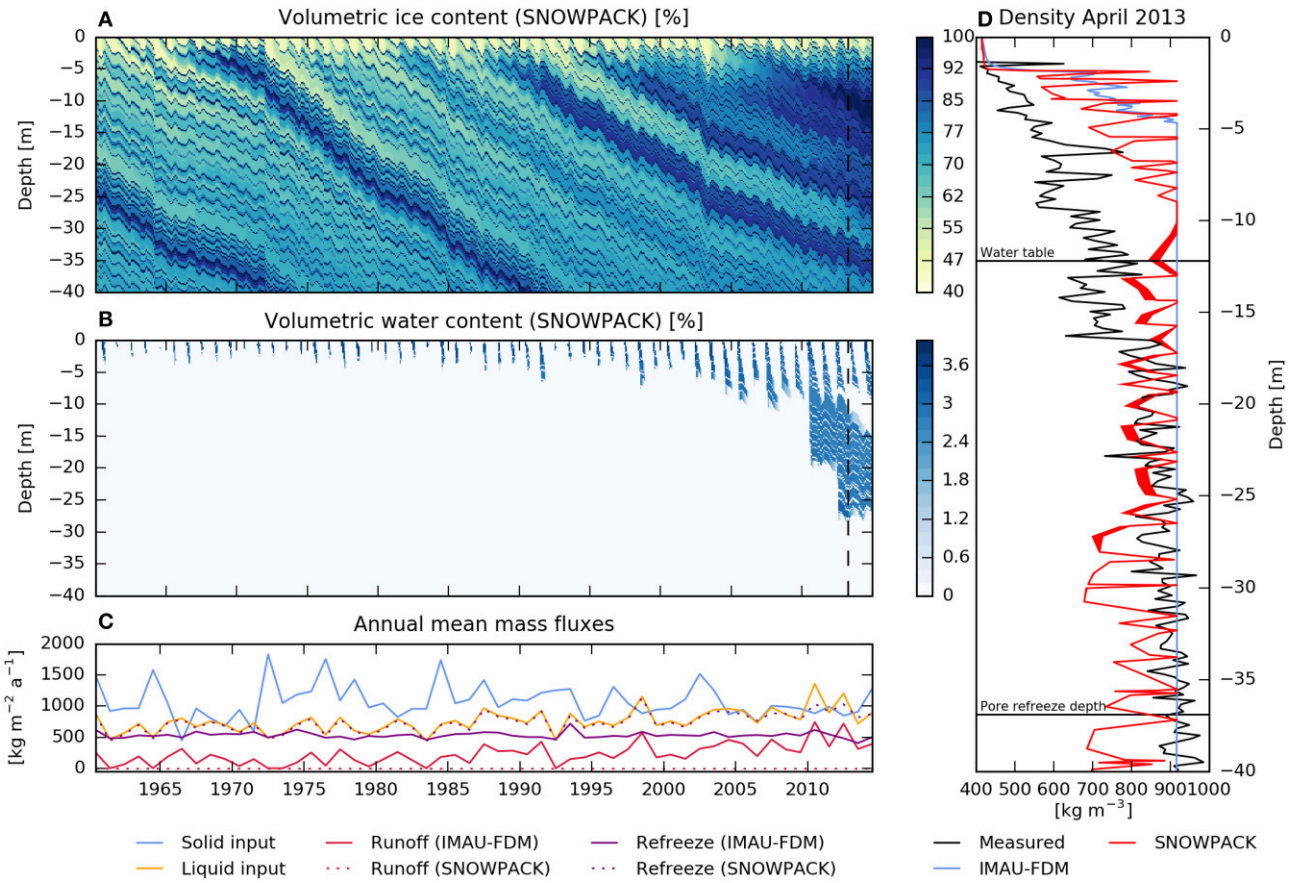

FIGURE 8 | Firn evolution between 1960 and 2014 for the modeled grid cell where firn core FA13 (39.04° W, 66.18° N, 1563 m a.s.l.) was extracted. The panels on the left show the temporal evolution of the volumetric ice **(A)** and water content **(B)** and the mass fluxes **(C)**. The panel on the right **(D)** shows the density profiles of the models at the time when the firn core was retrieved. The shaded area indicates the range of dry (only ice matrix) and wet (ice matrix with liquid water) firn density.

until a firn aquifer appears in the warm summer of 2010 (**Figure 8B**). Comparing this modeled aquifer with the in-situ observation of April 2013 yields a reasonable agreement in terms of vertical liquid water extent; especially the depth of the water table is accurately simulated (within approximately 2 m; **Figure 8D**). Evaluating the density profile of SNOWPACK indicates two major discrepancies: First of all, the model reveals a positive density bias in the uppermost 12 m. The temporal evolution of volumetric ice content (**Figure 8A**) shows that density recently increased due to enhanced refreezing caused by an increase in the surface liquid input (**Figure 8C**). This positive density bias might suggest that near-surface refreezing is overestimated in SNOWPACK. In nature, part of the liquid water that refreezes in the model may percolate into the subjacent firn aquifer, a process that would also explain the mismatch in the vertical extent of the modeled and observed aquifer. Position FA13 therefore appears to be an interesting location to test a heterogeneous water percolation scheme. Secondly, SNOWPACK seems to underestimate density in the deeper part of the core. This could be linked to the densification scheme underestimating compaction rates at high overburden pressure and/or the underestimation of the influence of liquid water on snow viscosity.

Modeling firn aquifers with the current, one-dimensional column models and model settings remains challenging for several reasons: First of all, both models only allow for irreducible amounts of water in the firn without considering full saturation due to water ponding on impermeable layers. However, implementing this feature without allowance for subsurface lateral water flow would likely lead to complete saturation of all available pore space at some locations, with the water table raising above the firn surface. Secondly, the implemented approach of compacting layers that are depleted of pore space and contain both ice and liquid water needs more detailed consideration. In our simulations, mean firn temperatures below aquifers are mostly at the melting point as a result of the initial firn temperature and the lower boundary condition for the heat equation (zero heat flux). Hence, the implemented approach prevents the continuous accumulation of liquid water at greater depth in temperate firn. In reality, it is likely that part of this liquid water refreezes as superimposed ice due to sub-zero temperatures either caused by cold initial firn/ice

or a downward-directed heat flux at the bottom of the model domain. However, these thermodynamic conditions, which co-determine the lower boundary of firn aquifers, are poorly known. Thirdly, there are indications that the bucket scheme, at least when used in combination with the irreducible water formulation by Coléou and Lesaffre (1998), is not able to transport water efficiently enough to greater depths; hence an improved model should also allow for preferential water flow.

3.4. Formation of Ice Layers

Figures 3B–F show that, when surface melt rates are sufficiently high, SNOWPACK simulates thin annual melt-freeze crusts or ice lenses at the surface that are subsequently buried under winter accumulation. These high-density layers are not simulated by the IMAU-FDM due to its coarser vertical resolution and less discriminating layer merging scheme. Modeling such sharp layer transitions is important because their occurrence has been linked to meltwater ponding and subsequent piping events (Marsh and Woo, 1984; Humphrey et al., 2012). However, SNOWPACK likely overestimates the density of such layers with the SMB forcing mode, which was implemented to force both models with the same mass fluxes at the upper boundary. In alpine conditions, SNOWPACK only generates melt-freeze crusts but not actual ice layers at the surface during the melt season. Tests with running SNOWPACK in the default mode generally reduce the formation of these high density layers because the subsurface temperature profile is allowed to exceed the melting point after solving the heat equation, which induces melt in several layers. In the implemented SMB forcing mode however, melt is applied by subsequently and completely melting layers from the top downwards (equal to the IMAU-FDM). This mode enhances the formation of surface ice layers at locations that experience periodic amounts of melt, for instance the day-night-cycle, and could hence be considered a model artifact. On the other hand, there are physical interpretations that support the formation of surface ice lenses in polar conditions as (I) the snowpack is generally cooler than the seasonal snowpack (higher refreezing capacity), (II) the surface energy loss due to longwave radiative cooling at elevated surfaces is larger, and (III) the daily melt cycles are more regular and persistent. Thin ice layers are also found in firn cores (Machguth et al., 2016), however there are indications that such layers also form below the surface due to meltwater percolation (Humphrey et al., 2012). In the current SNOWPACK configuration, the model is relatively insensitive to thin, high-density layers as the vertical water transport is simulated by the bucket scheme. Using more complex schemes such as the recently implemented preferential flow scheme (Wever et al., 2016), which allows downward water percolation in sub-freezing snow and is sensitive to marked layer transitions, would require a more detailed study of this feature. A GrIS-wide evaluation of this phenomenon is currently difficult due to the limited availability of firn cores with high vertical resolution.

Thicker ice layers, with a vertical extent of several meters, are simulated by both models, especially after the extreme melt events in 2012. A cross-section of simulated firn density along a transect in west Greenland for April 2014 is shown in **Figure 9**. The IMAU-FDM, simulating higher densification rates in regions with considerable amounts of refreezing, predicts continuous ice in the topmost 20 m until an elevation of approximately 2000 m a.s.l. Higher up, an area where porous firn is covered by a thick near-surface ice layer is simulated. SNOWPACK models this transition at a somewhat lower elevation of approximately 1850 m a.s.l., in spite of the higher irreducible water content. The radar-inferred observation indicates a better agreement with SNOWPACK but suggest that this transition is located at an even lower elevation. Additionally, both models overestimate the thickness of near-surface ice layers. This is probably related to the neglecting of lateral runoff at the surface and the application of the bucket scheme, which fills available pore space in a sequential top-down-mode.

4. CONCLUSIONS

Two numerical models, the IMAU-FDM, developed for coupling to an RCM, and SNOWPACK, developed as a stand-alone model, have been used offline to simulate firn evolution on the GrIS for the period 1960–2014. Forcing was provided by 3-h output of mass fluxes and skin temperature from RACMO2.3. Model evaluation using observed density profiles indicates that the IMAU-FDM slightly outperforms SNOWPACK for relatively cold and dry locations. For locations with intermediate ratios of liquid to solid mass inputs at the surface ($R_{liq/sol}$), SNOWPACK performs better than the IMAU-FDM. This is also true for locations where perennial firn aquifers form. For locations with high $R_{liq/sol}$-values (>0.6), both models overestimate near-surface density. This is either related to the snow/firn models deficiency to account for inhomogeneous vertical percolation and/or lateral surface runoff or to inaccurate meteorological forcing.

Our evaluation suggests that areas where firn aquifers form exhibit the highest sensitivity to the model's parameterization of liquid water retention (refreezing and perennial liquid water storage). Three factors are thereby of major relevance: (I) The snow/firn densification rate determines the amount of available pore space for refreezing or liquid water storage. These rates are apparently overestimated in the IMAU-FDM and more accurately simulated by SNOWPACK. It seems however that at least for location FA13, SNOWPACK underestimates densification rates at greater depths. Beside densification, the prescribed values of irreducible water content (II) co-determine the amounts of retained meltwater. The values prescribed in SNOWPACK are considerably higher than in the IMAU-FDM and are in better agreement with observed values (Coléou and Lesaffre, 1998; Schneider and Jansson, 2004). However, it seems that SNOWPACK overestimates near-surface refreezing with these comparably high amounts of prescribed irreducible water content–at least in combination with the bucket scheme. Finally, refreezing at the base of firn aquifers (and hence the formation of superimposed ice) is determined by the thermodynamic conditions (III) at the base of the aquifers. These conditions are largely unknown and it is probable that the models underestimate refreezing at the bottom of firn aquifers as temperatures below are predominantly at the melting point in both simulations.

This study also indicates that SNOWPACK is a suitable tool to perform offline firn simulations for the GrIS. Due to the

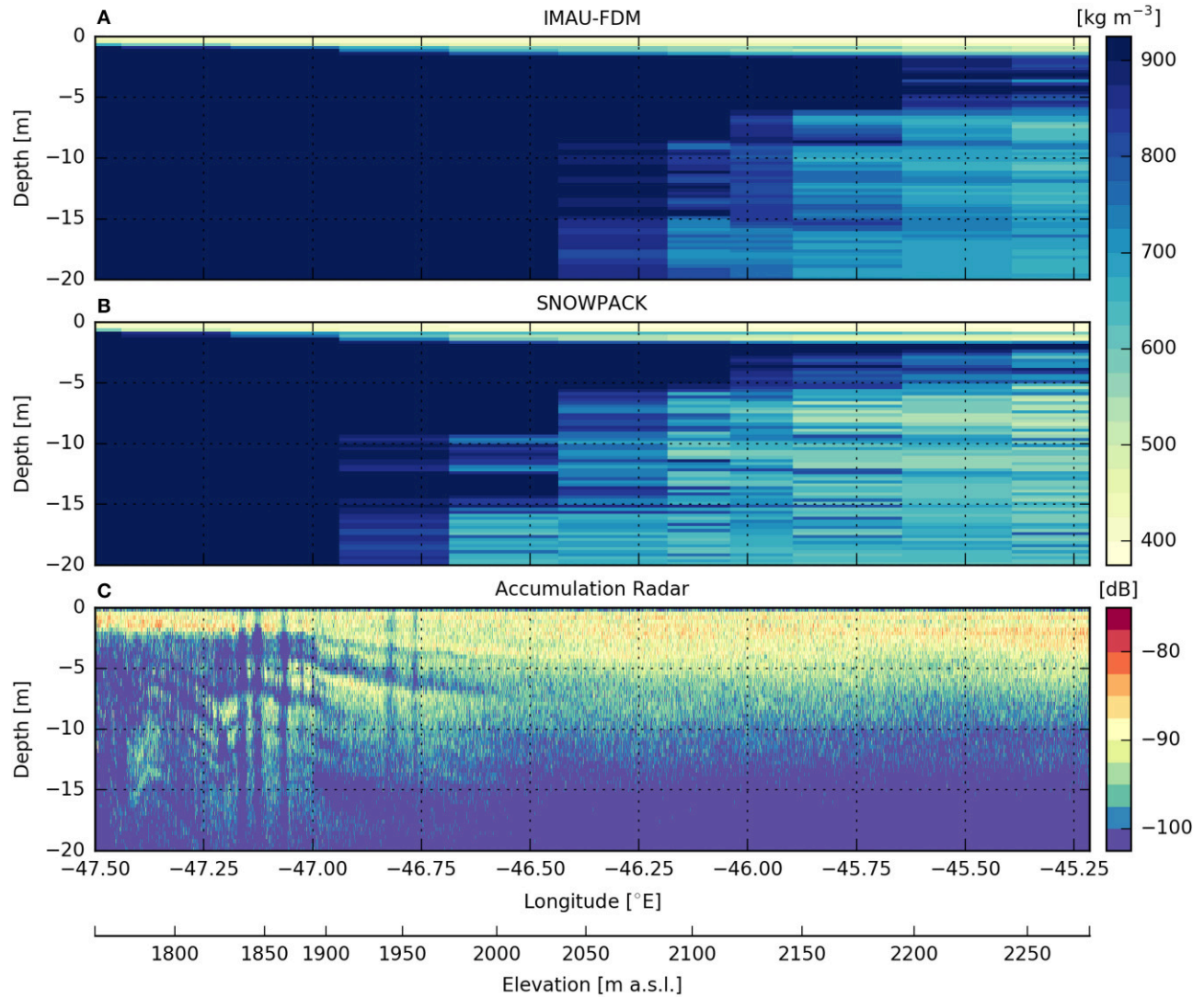

FIGURE 9 | Firn cross-section along the transect (66.97° N/−47.50° E – 66.97° N/−45.21° E) for April 2014. The upper two panels **(A,B)** show firn densities simulated by the models and the lower panel **(C)** the relative power return measured by the OIB Accumulation Radar. This cross-section partially overlaps with the radar transect described in Machguth et al. (2016) and its geographical extent is shown in **Figure 1**.

dynamical layer merging, which was used in a more aggressive setting in this study, it is feasible to perform multi-century long spin-up runs while maintaining thin heterogeneous layers, which are crucial factors for preferential water flow. With the aggressive layer merging switched on, the computational time is comparable to that required by the IMAU-FDM. Furthermore, SNOWPACK also models microstructural snow properties and includes a recently implemented preferential flow algorithm (Wever et al., 2016).

Considering the findings of this study, there are several processes that should be improved or included in future large-scale numerical snow/firn models: First of all, the densification schemes of both models should be further improved. Both schemes reveal inaccuracies under certain conditions; therefore it would be advantageous to have one formulation that is accurate for all climatic conditions and overburden pressures on the GrIS. Further research should also focus on the influence of liquid water on snow viscosity, as there is currently no direct empirical evidence to support this link. However, the validation of a densification scheme for locations with considerable amounts of surface melt remains challenging, as density profiles evolve as a combination of compaction and mass gain due to refreezing. Secondly, tests with impermeable layers could be conducted which are both relevant for saturated conditions within firn aquifers and lateral surface runoff. However, the relationship between vertical water permeability and ice layer thickness is, especially on the horizontal scale of a current regional climate model, rather uncertain. The feature of ponding water conditions is already integrated in SNOWPACK and was tested for superimposed

ice formation on the Kongsvegen glacier in Svalbard (Obleitner and Lehning, 2004). Furthermore, alternative (heterogeneous) vertical water percolation schemes should be tested as our results indicate that SNOWPACK, and likely other models that compute the irreducible water content according to Coléou and Lesaffre (1998), tend to overestimate near-surface liquid water retention and subsequent refreezing. Finally, the fresh snow density parameterization, which has a strong effect on the availability of near-surface pore space for refreezing, should be further refined.

AUTHOR CONTRIBUTIONS

CS carried out the SNOWPACK experiments, model comparison and wrote the manuscript. CR and MV supervised this study, NW provided SNOWPACK support, RF provided the Operation IceBridge Accumulation Radar data, LK provided the firn core data for location FA13, PK carried out the IMAU-FDM run and provided the firn core dataset, ML co-developed SNOWPACK, SL provided experience and support in applying SNOWPACK to the GrIS, SRML co-developed the IMAU-FDM, CM processed and provided the Operation IceBridge Accumulation Radar data, and BN provided the RACMO2.3 forcing data. All authors revised the manuscript.

FUNDING

CS received financial support from the Netherlands Polar Programme (NPP) of the Netherlands Organization for Scientific Research (NWO). MV is supported by the Netherlands Earth System Science Center (NESSC).

ACKNOWLEDGMENTS

ECMWF at Reading (UK) is acknowledged for use of the supercomputing system. Charles Fierz (WSL Institute for Snow and Avalanche Research SLF) is acknowledged for additional SNOWPACK support and advice. Graphics were made using Python Matplotlib (version 1.5.1).

REFERENCES

Anderson, E. A. (1976). *A Point Energy and Mass Balance Model of a Snow Cover.* Technical Report NWS19, NOAA.

Arthern, R. J., Vaughan, D. G., Rankin, A. M., Mulvaney, R., and Thomas, E. R. (2010). *In situ* measurements of Antarctic snow compaction compared with predictions of models. *J. Geophys. Res. Earth Surf.* 115:F03011. doi: 10.1029/2009JF001306

Avanzi, F., Hirashima, H., Yamaguchi, S., Katsushima, T., and De Michele, C. (2016). Observations of capillary barriers and preferential flow in layered snow during cold laboratory experiments. *Cryosphere* 10, 2013–2026. doi: 10.5194/tc-10-2013-2016

Bamber, J. L., Griggs, J. A., Hurkmans, R. T. W. L., Dowdeswell, J. A., Gogineni, S. P., Howat, I., et al. (2013). A new bed elevation dataset for Greenland. *Cryosphere* 7, 499–510. doi: 10.5194/tc-7-499-2013

Bartelt, P., and Lehning, M. (2002). A physical SNOWPACK model for the Swiss avalanche warning: Part I: numerical model. *Cold Regions Sci. Technol.* 35, 123–145. doi: 10.1016/S0165-232X(02)00074-5

Bekryaev, R. V., Polyakov, I. V., and Alexeev, V. A. (2010). Role of polar amplification in long-term surface air temperature variations and Modern Arctic Warming. *J. Clim.* 23, 3888–3906. doi: 10.1175/2010JCLI3297.1

Bennartz, R., Shupe, M. D., Turner, D. D., Walden, V. P., Steffen, K., Cox, C. J., et al. (2013). July 2012 Greenland melt extent enhanced by low-level liquid clouds. *Nature* 496, 83–86. doi: 10.1038/nature12002

Colbeck, S. C. (1972). A Theory of water percolation in snow. *J. Glaciol.* 11, 369–385.

Coléou, C., and Lesaffre, B. (1998). Irreducible water saturation in snow: experimental results in a cold laboratory. *Ann. Glaciol.* 26, 64–68.

Cox, C., Humphrey, N., and Harper, J. (2015). Quantifying meltwater refreezing along a transect of sites on the Greenland ice sheet. *Cryosphere* 9, 691–701. doi: 10.5194/tc-9-691-2015

Dadic, R., Schneebeli, M., Lehning, M., Hutterli, M. A., and Ohmura, A. (2008). Impact of the microstructure of snow on its temperature: a model validation with measurements from Summit, Greenland. *J. Geophys. Res. Atmospheres* 113:D14303. doi: 10.1029/2007JD009562

Doyle, S. H., Hubbard, A., van de Wal, R. S. W., Box, J. E., van As, D., Scharrer, K., et al. (2015). Amplified melt and flow of the Greenland ice sheet driven by late-summer cyclonic rainfall. *Nat. Geosci.* 8, 647–653. doi: 10.1038/ngeo2482

Enderlin, E. M., Howat, I. M., Jeong, S., Noh, M.-J., van Angelen, J. H., and van den Broeke, M. R. (2014). An improved mass budget for the Greenland ice sheet. *Geophys. Res. Lett.* 41, 866–872. doi: 10.1002/2013GL059010

Forster, R. R., Box, J. E., van den Broeke, M. R., Miège, C., Burgess, E. W., van Angelen, J. H., et al. (2014). Extensive liquid meltwater storage in firn within the Greenland ice sheet. *Nat. Geosci.* 7, 95–98. doi: 10.1038/ngeo2043

Goelzer, H., Huybrechts, P., Raper, S. C. B., Loutre, M.-F., Goosse, H., and Fichefet, T. (2012). Millennial total sea-level commitments projected with the Earth system model of intermediate complexity LOVECLIM. *Environ. Res. Lett.* 7:045401. doi: 10.1088/1748-9326/7/4/045401

Greuell, W., and Konzelmann, T. (1994). Numerical modelling of the energy balance and the englacial temperature of the Greenland Ice Sheet. Calculations for the ETH-Camp location (West Greenland, 1155 m a.s.l.). *Global Planet. Change* 9, 91–114. doi: 10.1016/0921-8181(94)90010-8

Groot Zwaaftink, C. D., Cagnati, A., Crepaz, A., Fierz, C., Macelloni, G., Valt, M., and Lehning, M. (2013). Event-driven deposition of snow on the Antarctic Plateau: analyzing field measurements with SNOWPACK. *Cryosphere* 7, 333–347. doi: 10.5194/tc-7-333-2013

Harper, J., Humphrey, N., Pfeffer, W. T., Brown, J., and Fettweis, X. (2012). Greenland ice-sheet contribution to sea-level rise buffered by meltwater storage in firn. *Nature* 491, 240–243. doi: 10.1038/nature11566

Hirashima, H., Yamaguchi, S., and Katsushima, T. (2014). A multi-dimensional water transport model to reproduce preferential flow in the snowpack. *Cold Reg. Sci. Technol.* 108, 80–90. doi: 10.1016/j.coldregions.2014.09.004

Humphrey, N. F., Harper, J. T., and Pfeffer, W. T. (2012). Thermal tracking of meltwater retention in Greenland's accumulation area. *J. Geophys. Res. Earth Surf.* 117:F01010. doi: 10.1029/2011JF002083

Koenig, L. S., Miège, C., Forster, R. R., and Brucker, L. (2014). Initial *in situ* measurements of perennial meltwater storage in the Greenland firn aquifer. *Geophys. Res. Lett.* 41, 81–85. doi: 10.1002/2013GL058083

Kuipers Munneke, P., Ligtenberg, S. R., van den Broeke, M. R., van Angelen, J. H., and Forster, R. R. (2014). Explaining the presence of perennial liquid water bodies in the firn of the Greenland Ice Sheet. *Geophys. Res. Lett.* 41, 476–483. doi: 10.1002/2013GL058389

Kuipers Munneke, P., Ligtenberg, S. R. M., Noël, B. P. Y., Howat, I. M., Box, J. E., Mosley-Thompson, E., et al. (2015). Elevation change of the Greenland Ice Sheet due to surface mass balance and firn processes, 1960–2014. *Cryosphere* 9, 2009–2025. doi: 10.5194/tc-9-2009-2015

Kuipers Munneke, P., van den Broeke, M. R., Lenaerts, J. T. M., Flanner, M. G., Gardner, A. S., and van de Berg, W. J. (2011). A new albedo parameterization for use in climate models over the Antarctic ice sheet. *J. Geophys. Res. Atmospheres* 116:D05114. doi: 10.1029/2010JD015113

Lehning, M., Bartelt, P., Brown, B., and Fierz, C. (2002a). A physical SNOWPACK model for the Swiss avalanche warning: Part III: meteorological forcing,

thin layer formation and evaluation. *Cold Reg. Sci. Technol.* 35, 169–184. doi: 10.1016/S0165-232X(02)00072-1

Lehning, M., Bartelt, P., Brown, B., Fierz, C., and Satyawali, P. (2002b). A physical SNOWPACK model for the Swiss avalanche warning: Part II. Snow microstructure. *Cold Reg. Sci. Technol.* 35, 147–167. doi: 10.1016/S0165-232X(02)00073-3

Lenaerts, J. T. M., van den Broeke, M. R., van Angelen, J. H., van Meijgaard, E., and Déry, S. J. (2012). Drifting snow climate of the Greenland ice sheet: a study with a regional climate model. *Cryosphere* 6, 891–899. doi: 10.5194/tc-6-891-2012

Ligtenberg, S. R. M., Helsen, M. M., and van den Broeke, M. R. (2011). An improved semi-empirical model for the densification of Antarctic firn. *Cryosphere* 5, 809–819. doi: 10.5194/tc-5-809-2011

Livingstone, S. J., Clark, C. D., Woodward, J., and Kingslake, J. (2013). Potential subglacial lake locations and meltwater drainage pathways beneath the Antarctic and Greenland ice sheets. *Cryosphere* 7, 1721–1740. doi: 10.5194/tc-7-1721-2013

Machguth, H., MacFerrin, M., van As, D., Box, J. E., Charalampidis, C., Colgan, W., et al. (2016). Greenland meltwater storage in firn limited by near-surface ice formation. *Nat. Clim. Change* 6, 390–393. doi: 10.1038/nclimate2899

Marsh, P., and Woo, M. (1984). Wetting front advance and freezing of meltwater within a snow cover 1. Observations in the Canadian Arctic. *Water Resour. Res.* 20, 1853–1864. doi: 10.1029/WR020i012p01853

Miège, C., Forster, R. R., Brucker, L., Koenig, L. S., Solomon, D. K., Paden, J. D., et al. (2016). Spatial extent and temporal variability of Greenland firn aquifers detected by ground and airborne radars. *J. Geophys. Res. Earth Surf.* 121, 2381–2398. doi: 10.1002/2016JF003869

Mikkelsen, A. B., Hubbard, A., MacFerrin, M., Box, J. E., Doyle, S. H., Fitzpatrick, A., Hasholt, B., Bailey, H. L., Lindbäck, K., and Pettersson, R. (2016). Extraordinary runoff from the Greenland ice sheet in 2012 amplified by hypsometry and depleted firn retention. *Cryosphere* 10, 1147–1159. doi: 10.5194/tc-10-1147-2016

Nghiem, S. V., Hall, D. K., Mote, T. L., Tedesco, M., Albert, M. R., Keegan, K., Shuman, C. A., DiGirolamo, N. E., and Neumann, G. (2012). The extreme melt across the Greenland ice sheet in 2012. *Geophys. Res. Lett.* 39:L20502. doi: 10.1029/2012GL053611

Noël, B., van de Berg, W. J., van Meijgaard, E., Kuipers Munneke, P., van de Wal, R. S. W., and van den Broeke, M. R. (2015). Evaluation of the updated regional climate model RACMO2.3: summer snowfall impact on the Greenland Ice Sheet. *Cryosphere* 9, 1831–1844. doi: 10.5194/tc-9-1831-2015

Obleitner, F., and Lehning, M. (2004). Measurement and simulation of snow and superimposed ice at the Kongsvegen glacier, Svalbard (Spitzbergen). *J. Geophys. Res. Atmospheres* 109:D04106. doi: 10.1029/2003JD003945

Reeh, N. (2008). A nonsteady-state firn-densification model for the percolation zone of a glacier. *J. Geophys. Res. Earth Surf.* 113:F03023. doi: 10.1029/2007JF000746

Reijmer, C. H., van den Broeke, M. R., Fettweis, X., Ettema, J., and Stap, L. B. (2012). Refreezing on the Greenland ice sheet: a comparison of parameterizations. *Cryosphere* 6, 743–762. doi: 10.5194/tc-6-743-2012

Rennermalm, A. K., Moustafa, S. E., Mioduszewski, J., Chu, V. W., Forster, R. R., Hagedorn, B., et al. (2013). Understanding Greenland ice sheet hydrology using an integrated multi-scale approach. *Environ. Res. Lett.* 8:015017. doi: 10.1088/1748-9326/8/1/015017

Rodriguez-Morales, F., Gogineni, S., Leuschen, C. J., Paden, J. D., Li, J., Lewis, C. C., et al. (2014). Advanced Multifrequency Radar Instrumentation for Polar Research. *IEEE Trans. Geosci. Remote Sens.* 52, 2824–2842. doi: 10.1109/TGRS.2013.2266415

Schneider, T., and Jansson, P. (2004). Internal accumulation in firn and its significance for the mass balance of Storglaciaren, Sweden. *J. Glaciol.* 50, 25–34. doi: 10.3189/172756504781830277

Smith, L. C., Chu, V. W., Yang, K., Gleason, C. J., Pitcher, L. H., Rennermalm, A. K., et al. (2015). Efficient meltwater drainage through supraglacial streams and rivers on the southwest Greenland ice sheet. *Proc. Natl. Acad. Sci. U.S.A.* 112, 1001–1006. doi: 10.1073/pnas.1413024112

Tedesco, M., Doherty, S., Fettweis, X., Alexander, P., Jeyaratnam, J., and Stroeve, J. (2016). The darkening of the greenland ice sheet: trends, drivers, and projections (1981–2100). *Cryosphere* 10, 477–496. doi: 10.5194/tc-10-477-2016

van Angelen, J. H., van den Broeke, M. R., Wouters, B., and Lenaerts, J. T. M. (2014). Contemporary (1960–2012) evolution of the climate and surface mass balance of the greenland ice sheet. *Surv. Geophys.* 35, 1155–1174. doi: 10.1007/s10712-013-9261-z

van As, D., Fausto, R. S., William, T. C., and Box, J. E. (2013). Darkening of the Greenland ice sheet due to the meltalbedo feedback observed at PROMICE weather stations. *Geol. Surv. Denmark Greenl. Bull.* 28, 69–72. doi: 10.5167/uzh-131201

van den Broeke, M., Bamber, J., Ettema, J., Rignot, E., Schrama, E., van de Berg, W. J., et al. (2009). Partitioning Recent Greenland Mass Loss. *Science* 326, 984–986. doi: 10.1126/science.1178176

van den Broeke, M. R., Enderlin, E. M., Howat, I. M., Kuipers Munneke, P., Noël, B. P. Y., van de Berg, W. J., et al. (2016). On the recent contribution of the Greenland ice sheet to sea level change. *Cryosphere* 10, 1933–1946. doi: 10.5194/tc-10-1933-2016

Van Tricht, K., Lhermitte, S., Lenaerts, J. T. M., Gorodetskaya, I. V., L'Ecuyer, T. S., Noël, B., et al. (2016). Clouds enhance Greenland ice sheet meltwater runoff. *Nat. Commun.* 7:10266. doi: 10.1038/ncomms10266

Vernon, C. L., Bamber, J. L., Box, J. E., van den Broeke, M. R., Fettweis, X., Hanna, E., and Huybrechts, P. (2013). Surface mass balance model intercomparison for the Greenland ice sheet. *Cryosphere* 7, 599–614. doi: 10.5194/tc-7-599-2013

Wever, N., Fierz, C., Mitterer, C., Hirashima, H., and Lehning, M. (2014). Solving Richards Equation for snow improves snowpack meltwater runoff estimations in detailed multi-layer snowpack model. *Cryosphere* 8, 257–274. doi: 10.5194/tc-8-257-2014

Wever, N., Würzer, S., Fierz, C., and Lehning, M. (2016). Simulating ice layer formation under the presence of preferential flow in layered snowpacks. *Cryosphere* 10, 2731–2744. doi: 10.5194/tc-10-2731-2016

Wientjes, I. G. M., Van de Wal, R. S. W., Reichart, G. J., Sluijs, A., and Oerlemans, J. (2011). Dust from the dark region in the western ablation zone of the greenland ice sheet. *Cryosphere* 5, 589–601. doi: 10.5194/tc-5-589-2011

Yallop, M. L., Anesio, A. M., Perkins, R. G., Cook, J., Telling, J., Fagan, D., et al. (2012). Photophysiology and albedo-changing potential of the ice algal community on the surface of the greenland ice sheet. *Int. Soc. Microb. Ecol.* 6, 2302–2313. doi: 10.1038/ismej.2012.107

Conflict of Interest Statement: The authors declare that the research was conducted in the absence of any commercial or financial relationships that could be construed as a potential conflict of interest.

The handling Editor declared a shared affiliation, though no other collaboration, with one of the authors LK and states that the process nevertheless met the standards of a fair and objective review.

frontiers in Earth Science

ORIGINAL RESEARCH
published: 07 February 2017
doi: 10.3389/feart.2017.00010

Investigation of Firn Aquifer Structure in Southeastern Greenland Using Active Source Seismology

Lynn N. Montgomery[1], Nicholas Schmerr[1], Scott Burdick[1], Richard R. Forster[2], Lora Koenig[3], Anatoly Legchenko[4], Stefan Ligtenberg[5], Clément Miège[2], Olivia L. Miller[6] and D. Kip Solomon[6]*

[1] Department of Geology, University of Maryland, College Park, MD, USA, [2] Department of Geography, University of Utah, Salt Lake City, UT, USA, [3] National Snow and Ice Data Center, University of Colorado, Boulder, CO, USA, [4] Laboratoire d'etude des Transferts en Hydrologie et Environment, Institute of Research for Development, Grenoble, France, [5] Institute for Marine and Atmospheric Research Utrecht, Utrecht University, Utrecht, Netherlands, [6] Department of Geology and Geophysics, University of Utah, Salt Lake City, UT, USA

In spring of 2011, a perennial storage of water was observed in the firn of the southeastern Greenland Ice Sheet (GrIS), a region of both high snow accumulation and high melt. This aquifer is created through percolation of surface meltwater downward through the firn, saturating the pore space above the ice-firn transition. The aquifer may play a significant role in sea level rise through storage or draining freshwater into the ocean. We carried out a series of active source seismic experiments using continuously refracted P-waves and inverted the first P-arrivals using a transdimensional Bayesian approach where the depth, velocity, and number of layers are allowed to vary to identify the seismic velocities associated with the base of the aquifer. When our seismic approach is combined with a radar sounding of the water table situated at the top of the firn aquifer, we are able to quantify the volume of water present. In our study region, the base of the aquifer lies on average 27.7 ± 2.9 m beneath the surface, with an average thickness of 11.5 ± 5.5 m. Using a Wyllie average for porosity, we found the aquifer has an average water content of 16 ± 8%, with considerable variation in water storage capacity along the studied east-west flow line, 40 km upstream of the Helheim glacier terminus. Between 2015 and 2016, we observed a 1–2 km uphill expansion of the aquifer system, with a site dry in summer 2015 exhibiting a water content of 530 kg m^{-2} in summer 2016. We estimate the volume of water stored in the aquifer across the entire region upstream of Helheim glacier to be 4.7 ± 3.1 Gt, ∼3% of the total water stored in firn aquifers across the GrIS. Elucidating the volume of water stored within these recently discovered aquifers is vital for determining the hydrological structure and stability of the southeastern GrIS.

Keywords: firn aquifer, seismology, active source, ice, meltwater, water retention, mass balance

OPEN ACCESS

Edited by:
Horst Machguth, University of Zurich, Switzerland

Reviewed by:
Jake Walter, University of Texas at Austin, USA
Anja Diez, Norwegian Polar Institute, Norway

****Correspondence:***
Lynn N. Montgomery
lynn.montgomery@colorado.edu

Specialty section:
This article was submitted to Cryospheric Sciences, a section of the journal Frontiers in Earth Science

Received: *03 October 2016*
Accepted: *23 January 2017*
Published: *07 February 2017*

Citation:
Montgomery LN, Schmerr N, Burdick S, Forster RR, Koenig L, Legchenko A, Ligtenberg S, Miège C, Miller OL and Solomon DK (2017) Investigation of Firn Aquifer Structure in Southeastern Greenland Using Active Source Seismology. Front. Earth Sci. 5:10. doi: 10.3389/feart.2017.00010

INTRODUCTION

The mass balance of the Greenland Ice Sheet (GrIS) is negative and mass loss is accelerating as melt and subsequent runoff increases (Ettema et al., 2009; Rignot et al., 2011; Enderlin et al., 2014). The recent acceleration of mass loss, driven by meltwater runoff overtaking ice discharge (e.g., van den Broeke et al., 2009; Enderlin et al., 2014; Jeffries et al., 2015), suggests that the GrIS

will be a dominant contributor to sea level change in upcoming decades (Fettweis et al., 2013) as temperatures continue to increase across the Arctic and surface albedo decreases (e.g., Jeffries et al., 2015). Though it is clear that surface melt is increasing across the GrIS, tracking meltwater as it travels across the ice sheet to the sea is complicated and imprecisely known (Rennermalm et al., 2013). For instance, it is estimated that retention and refreezing prevents ∼40% of the meltwater from reaching the ocean, however, large discrepancies still exist between models (van Angelen et al., 2013; Vernon et al., 2013). Humphrey et al. (2012) and Harper et al. (2012) made observations of meltwater storage capacity and refreezing in the firn across the western GrIS by firn coring and through temperature modeling. Additional observations, however, are necessary to accurately constrain surface mass balance and the storage of water within the GrIS as the Arctic warms.

In 2011, a perennial storage of liquid water, i.e., a firn aquifer, was observed in the southeastern GrIS through ice coring and radar measurement (Forster et al., 2014; Koenig et al., 2014). Aquifers are formed by meltwater percolating into the firn in high-accumulation, high-melt regions (Forster et al., 2014; Munneke et al., 2014) and are located extensively in the southeastern and southern parts of the GrIS according to NASA Operation IceBridge airborne radar and ground based radar measurements (Miège et al., 2016). Though extensive in some regions of the ice sheet, the exact flux and stability of meltwater into and out of firn aquifer systems remains uncertain.

The water stored within a firn aquifer is ultimately either drained out of the system or freezes into ice. If meltwater within the aquifer is replenished at nearly the same rate as outflow, then a stable aquifer system develops (Christianson et al., 2015). This requires drainage through crevasses or similar features, leading to meltwater addition to the bed of the ice sheet and eventually to the sea. If meltwater flux into the aquifer system exceeds outflow and saturates the pore space, the aquifer will buffer sea level rise until storage capacity is reached and, a sudden release event could happen (Koenig et al., 2014). In both cases, firn aquifers likely play a role in sea level rise but also on ice dynamics, and hence ice discharge, in the region by constantly supplying water to the base of the ice sheet and/or by storing and then briefly releasing large amounts of fresh water to the sea. Thus, improving the spatial and temporal volume estimates of the water stored in a firn aquifer is essential to quantify the aquifer's contribution to sea level change.

The compressional velocity of seismic waves in snow/firn (500–2000 m s^{-1}) and water (1450 m s^{-1}) is less than their velocity in ice (3500–3900 m s^{-1}) (e.g., Albert, 1998). Firn velocity will increase as pore space is removed via compaction and/or the addition of liquid water. Seismic velocities are also expected to increase if any liquid water in the pore space freezes out. Active source seismic experiments have been used to determine the stratigraphy and thickness of Antarctic ice streams (e.g., Blankenship et al., 1986; Jarvis and King, 1995; Johnson and Smith, 1997; Winberry et al., 2009; Horgan et al., 2012; Smith et al., 2013). Seismic experiments can be executed on meters to kilometer scales, using mechanical and/or explosive sources to generate seismic waves for imaging tens to thousands of meters into an ice sheet. Continuously refracted seismic waves that turn or bottom within the upper 100 m of ice sheets are sensitive to firn velocity structure and the properties of the underlying ice. Active source seismic studies are a valuable complement to ground/ice penetrating radar (GPR) measurements and ice core studies for the study of firn aquifers, as seismic waves can penetrate into liquids where the radar signal is attenuated. In addition, ice coring is comparably challenging as most drills are not adapted for a transition of water and then colder ice temperatures where refreezing in the borehole may occur (McMahon and Lackie, 2006; Neff et al., 2012). Therefore, seismic studies can provide information on ice properties in regions of the ice sheet where meltwater infiltration and firn aquifers dominate the firn column.

Here we use active-source seismic experiments to study the uppermost 100 m of the GrIS along a flow line at Helheim Glacier to investigate the structure of a firn aquifer. Seismic velocities are sensitive to the relative proportion of liquid water to ice and provide a tool for mapping lateral variations in aquifer water content and thickness. Our goal is first to constrain the local thickness of the aquifer layer and then provide seismological estimates for the volume fraction of water that can be compared to other geophysical and hydrological estimates.

METHODS

Field Site

During two field seasons in July and August of 2015 and 2016, we investigated the structure of a firn aquifer using seismic in the southeastern GrIS, situated 70 km west from Sermilik Fjord in the upper portion of Helheim Glacier, 40 km west from its terminus (**Figure 1A**). Our field site was chosen based on the presence and structure of the firn aquifer determined by NASA Operation IceBridge airborne radar measurements and ice core data from the region (Forster et al., 2014; Miège et al., 2016). This field site was positioned to assess the impact of the firn aquifer on a tide-water glacier contributing to sea-level rise through ice discharge and melt (Enderlin et al., 2014). Past field campaigns using radar soundings established that the water table is varying spatially between 10 and 20 m below the surface (Forster et al., 2014; Miège et al., 2016), and ice-coring placed the firn-ice transition at 30 m depth (Koenig et al., 2014). Gogineni (2012) used multi-channel coherent radar sounding to determine the ice sheet is 800–1000 m above sea level (a.s.l.) in the region. During the two field seasons, the aquifer site was also assessed by a range of hydrological and other geophysical methods, including hydrological conductivity measurements from slug tests, magnetic resonance soundings, density determined from ice cores, and aquifer depth from radar profiling (Miller et al., in review).

Seismic Refraction Experiment

To assess the structure of the firn aquifer and measure the depth of the aquifer-ice transition, we used a series of active source seismic refraction experiments situated every 1–2 km over a profile 15 km in length (**Figure 1C**). Each experiment was positioned parallel to the local east-west ice flow line defined by past radar investigations. We used two linear array geometries with geophones spaced every 5 m; (i) a 115 m long array in 2015

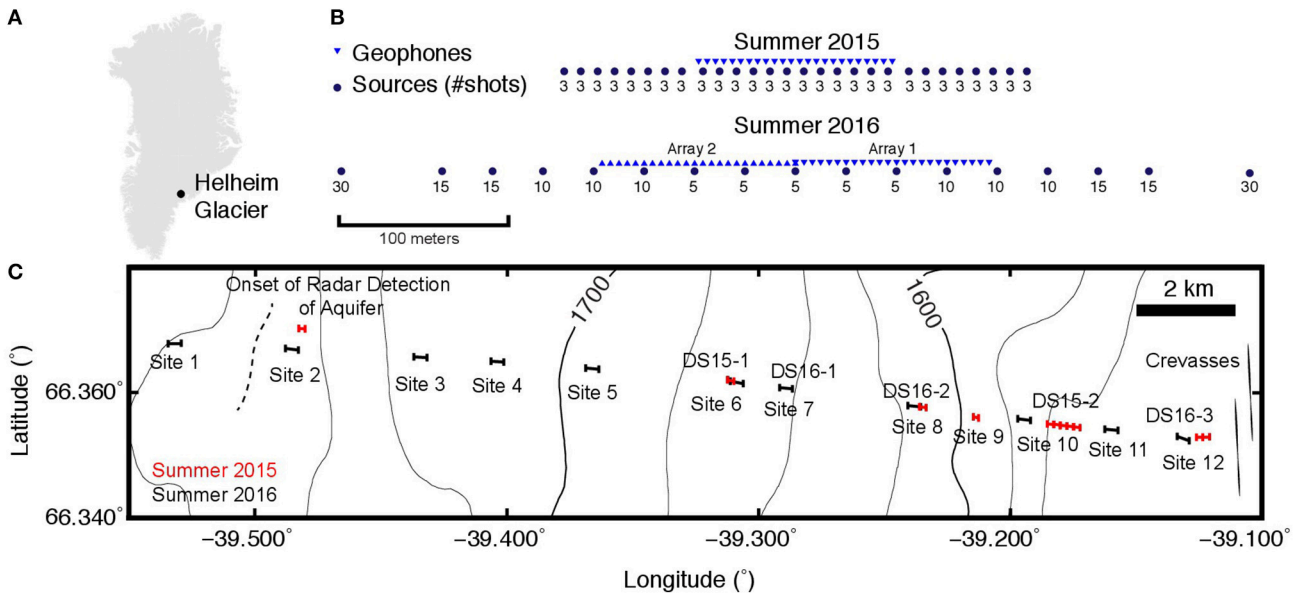

FIGURE 1 | Location of the firn aquifer field site in southeastern Greenland. (A) Geographic context of the field site, Helheim Glacier (black circle). **(B)** Geometry of seismic deployments; geophones (blue triangles) and source locations (black circle) for summers of 2015 and 2016. Note that in 2016 there were two overlapping arrays (inverted and regular triangles) and the source locations were occupied twice. Values beneath each source indicate the number of shots stacked at the location. **(C)** Locations of seismic refraction lines; hatches indicate location of first and last geophone in the station geometry shown in **(B)**. Drill sites (DS) from each year are also indicated. Surface topography is obtained from a WorldView-1 (DigitalGlobe©) digital elevation model generated by the Polar Geospatial Center; elevation contour interval is 25 m.

(24 stations) and (ii) two 115 m arrays that overlapped at the first station in 2016 (47 unique stations, 1 duplicated location) (**Figure 1B**). The seismic line was instrumented with Sercel 40 Hz vertical-component geophones. We buried the geophones 5–25 cm into the firn to improve the signal quality and isolate them from noise sources. The burial depth introduced 0.10–0.25 ms of uncertainty into seismic wave travel times, but this uncertainty is similar to or less than the error in picking the P-wave onsets (0.5–1.0 ms) and surface roughness, and is not considered further. In general, the sources of noise at each site were minimal, consisting of blowing wind or snow, distant generator noise, small disturbances in the firn from daily melt, or human movement. Noise conditions were typically better in the morning when the firn was still frozen, and deteriorated in the afternoon as the surface became softer and underwent melt. Seismograms were recorded on a Geometrics Geode multichannel data recorder using a record length of 1 s with a sampling rate of 62.5 μs.

For the active source, we manually struck a 30 × 30 cm, 1.5 cm thick steel plate with a 8-kg sledgehammer, producing seismic waves with a dominant frequency of 150–200 Hz. Where appropriate, multiple hammer strikes (or "shots") were stacked to enhance the signal-to-noise ratio of waves recorded from the shot location. The initial hammer strike would typically settle the plate into the surface, and subsequent shots would compact the underlying snow by 1–2 cm. Any uncertainties in travel time introduced by the settling of the plate between shots is expected to be minimal, and similar to the uncertainty introduced by the burial of the geophones (0.10–0.25 ms). The attenuation in this environment is quite high ($Q = 5$–10) so more shots were needed as we moved the source further from the geophone array to produce high signal-to-noise arrivals for analysis.

Two separate source configurations were used in the field experiment. In 2015, sources were spaced regularly with a separation of 10 m and with each consisting of a stack of 3 shots. The number of shots was determined experimentally in the field by determining the minimum number of hammer strikes needed to confidently identify the P-wave onset arriving at the most distant station. The first source was collected 80 m off the line from the first geophone, while the last source was positioned 80 m off the line from the last geophone (**Figure 1B**). This produced a maximum source-station offset of 195 m in the 2015 array geometry.

In 2016, we modified the source geometry to allow us to sample deeper into the ice sheet, with sources spaced 30 m apart and up to 270 m from the first station in our double array geometry, for a maximum source-station offset of 385 m. Each source location was occupied twice; the line was reshot after repositioning the 24 geophones into the second 115 m array configuration (array 1 and 2 in **Figure 1B**). The initial source was positioned 270 m from the first geophone, with multiple shots stacked to produce an acceptable signal-to-noise in the recordings. The numbers beneath each source location in **Figure 1B** indicates the number of shots stacked at each source. The number of shots was determined by experimentation in the field and designed to equalize data quality across different

hammer operator abilities and endurance, and to optimize the unfiltered signal-to-noise quality of the seismograms (e.g., **Figure 2**).

The final dataset consisted of operators stacking over 7000 shots, 18 separate seismic lines, and 21,312 individual seismogram recordings from the geophone stations.

Data Processing

Continuous refractions of P-waves are produced by a gradational increase in seismic velocity that bends downward diving waves gradually back upwards toward the surface (e.g., Shearer, 2009). The travel time of the wave is dependent upon the velocities encountered along the raypath of the seismic wave. If any seismic discontinuities are present at depth, a head wave forms along the interface with a travel time slope proportional to the underlying layer seismic velocity. A simple model of a water saturated layer within a gradually increasing firn velocity is shown in **Figure 2B**, and illustrates how the raypaths of continuous refractions are sensitive to velocity changes in such a medium. Therefore, using travel times of the first arriving P-wave, it is possible to recover the underlying seismic velocities.

Seismograms were visually examined to select the onset travel times of the refracted P-waves arrivals and determine the underlying seismic velocities. Each seismogram was Butterworth band-pass filtered between 40 and 200 Hz. This filtering range was chosen to remove high and low frequency environmental noise and isolate the seismic arrivals. Each P-wave arrival was selected manually according to the first coherent swing deviating from zero amplitude. Consistency between picks was achieved by examining all data for a shot simultaneously and picking on the same polarity across all seismograms (**Figure 2**). The picking error was defined by pixel accuracy of our picking tool (2–3 pixels), and was less than 0.5 ms.

Inversion for Ice Seismic Velocity Models

To determine the seismic structure of the firn and aquifer, we invert the travel time picks of the continuously refracted waves for one-dimensional (1D) velocity models. Past active source surveys of glacial ice have fit refraction data with an exponential function (e.g., Kirchner and Bentley, 1979). In this study, sharp increases in velocity from the top and bottom of the firn aquifer were anticipated, so we chose to represent the glacier with constant velocity layers in depth (e.g., Shearer, 2009). A further assumption is that the first arriving refracted waves are insensitive to decreases in velocity. In effect, the data could be equally well fit by models with an arbitrary number of low velocity layers. We therefore look for models with velocity increasing with depth. In order to constrain decreasing velocities, other parts of the seismic wavefield—particularly reflected waves and surface waves—could be incorporated in future efforts.

The inversion of first arrivals for layered structure is non-unique in that many velocity models could adequately explain the observations. Instead of inverting for the singular best fitting velocity model, our approach is to instead generate a large number of 1D models that fit the data to within the variance in the travel time picks.

We generate this chain of models using a reversible-jump Markov chain Monte Carlo algorithm (Green, 1995). New models in the chain are proposed by changing the properties of one layer in the current model. In addition to the varying the depth and velocity a layer, we also allow layers to be added or removed (i.e., the transdimensional approach, Bodin and Sambridge, 2009). Proposed changes in velocity and layer depth are randomly drawn from a normal distributions around their current values with standard deviations of 50 m s^{-1} and 2 m respectively. The depth of proposed new layers is chosen at random, and the velocity drawn at random from between the layers above and below. The velocities are constrained to be between 0 and 4500 m s^{-1} and the layer depths between 0 and 75 m.

For each proposed new model, the misfit between the observed and modeled travel times is calculated. The model is accepted or rejected based on the change to the misfit and the number of layers (Metropolis et al., 1953). The preferred models explain the data with the fewest number of layers. At regular intervals, the current model is added to an ensemble solution, and in the long term, the frequency with which a model appears in the ensemble is proportional to the probability that it explains the data.

We interpret these the model ensembles to estimate the base of the aquifer and the velocity of the solid ice underlying it. There are two main properties that we can derive from the ensemble of 1D models. First, we find the distribution of possible velocities at each depth (**Figure 3A**), which allows us to compute a mean velocity and standard deviation. Second, by finding the number of models that place a layer boundary within a certain depth range, we find the probability that there is an increase in velocity at each depth (**Figure 3B**). From this, we can estimate the confidence intervals on the depths of different interfaces.

RESULTS

Overview of Results

The velocity profiles and discontinuity histograms derived from the inversion are interpreted to estimate aquifer bottom depth (**Figure 4**). We define the base of the aquifer as the transition from liquid saturated pore space to where the liquid is frozen into ice, which manifests as a transition from increasing to a higher, nearly constant seismic velocity with depth. This definition is derived from ice cores in our study area that showed the base of the aquifer is associated with the onset of clear ice layers resulting from the freezing of aquifer water. We manually select the deepest, most probable discontinuity associated with this boundary (e.g., **Figure 3B**) and use the surrounding shape of the discontinuity histogram to select the minimum and maximum depths defining the uncertainty in the pick (**Table 1**). We also derive the local seismic velocity of the ice by selecting the velocity 3–4 m beneath the aquifer layer. As our experimental design was not optimized for imaging the top of the aquifer, we independently obtained depth to the water table from ground penetrating radar reflections that were collected in the field in tandem with the seismic data (Miège et al., 2016). The GPR depths to the water table are estimated from the two-way-travel

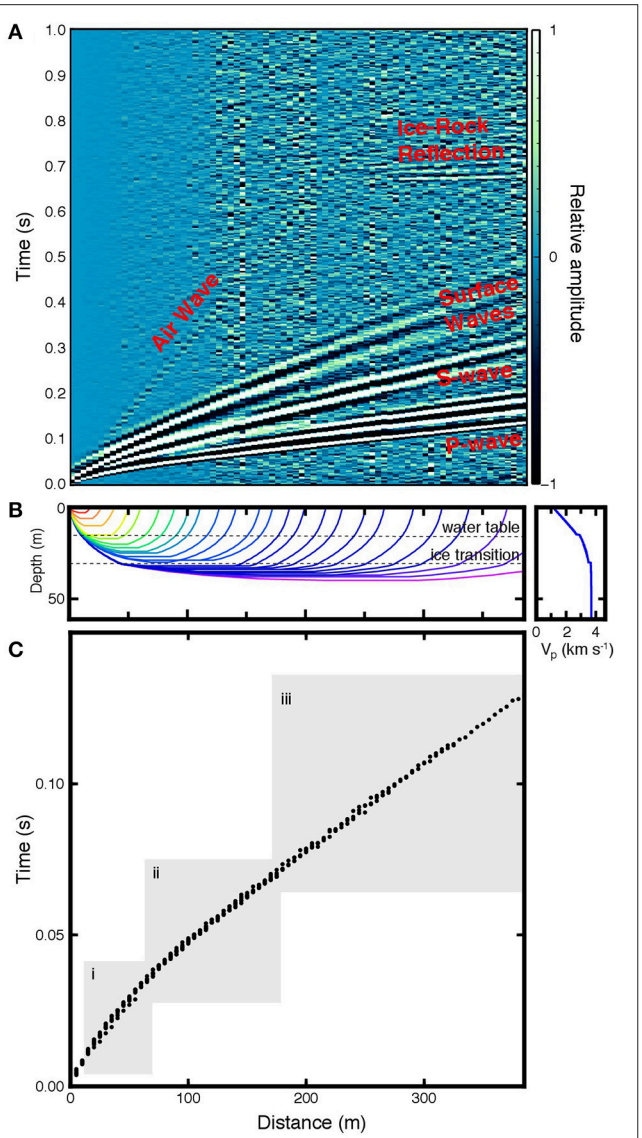

FIGURE 2 | Example active source seismograms, raypaths, and P-wave travel times measured at Site 3 of the study area. (A) Vertical component seismograms with the maximum amplitude of each trace normalized to unity. Interpreted seismic arrivals are labeled in the plot. **(B)** Theoretical raypaths for P-waves traveling in the hypothetical velocity model on the right. **(C)** Travel time picks for first arrivals of P-waves at Site 3. The gray regions indicate the distances where P-waves turn and refract: (i) at the water table, (ii) within the firn aquifer and at the ice transition, (iii) within the underlying glacial ice.

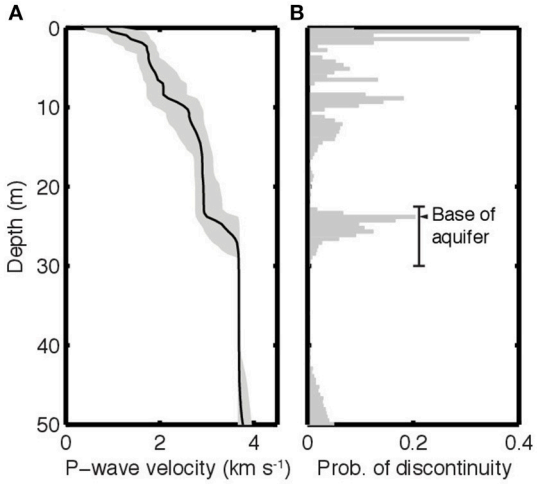

FIGURE 3 | Example model output from Site 11 from the transdimensional reversible-jump Markov chain Monte Carlo inversion. (A) Velocity profile. The mean velocity of models in the ensemble solution is shown as a black line, and the gray region shows the 95% confidence interval. **(B)** Histogram showing the proportion of models in the ensemble with an increase in velocity at each depth. We interpret this to find the likelihood that a boundary between layers occurs in a given depth range.

time of the radar electromagnetic wave between the snow surface and the water-table surface, with a calculated error of ±0.5 m. The aquifer thickness is then the difference between the GPR-derived water table depth and the seismically derived base of the aquifer. A summary of these measurements for each site in our study region is presented in **Table 1**.

Aquifer Thicknesses

The depth from both the radar-obtained measurements of the top and seismic-derived measurement of the bottom of the aquifer are summarized in **Figure 5**. On average, the base of the aquifer lies at 27.7 ± 2.9 m, with an average aquifer thickness of 11.5 ± 5.5 m. While there is temporal and spatial variations in the depth of the water table (Miège et al., 2016), the base of the aquifer appears stable between the 2015 and 2016 field seasons. We note that there is greater uncertainty in the 2015 measurements; this owes to the different array design, as the shorter effective apertures used in 2015 (**Figure 1B**) had less sensitivity to the base of the aquifer than the 2016 design. This is illustrated for 2015 by the two coincident seismic and GPR depths of the aquifer bottom and top in **Figure 5**. In this case, the inversion produced results with the largest velocity change near the depth of the water table, but seismic sampling was apparently not deep enough to capture the base, an issue rectified by the larger aperture of the 2016 measurements.

Ice Seismic Velocity

At each site, the seismic velocity of the glacial ice and its standard deviation were derived from the 1D inversion at a depth 3–4 m below the inferred base of the aquifer (**Figure 6**). We find significant variation between the ice velocities as a function of location along the profile (**Figure 1B**). On average, the ice in our study region has a velocity of 3590 ± 133 m s^{-1}, however we note that in 2015 we observed more variability in ice seismic velocities (3400–3900 m s^{-1}) than in 2016 (3700–3800 m s^{-1}) for the downslope regions. We attribute this difference to the larger array aperture in 2016 that provided improved sensitivity to the deeper ice structure compared to the 2015 array. We calculate that the deepest continuously refracted waves for the 2015 array reached a depth of 30–35 m, while the

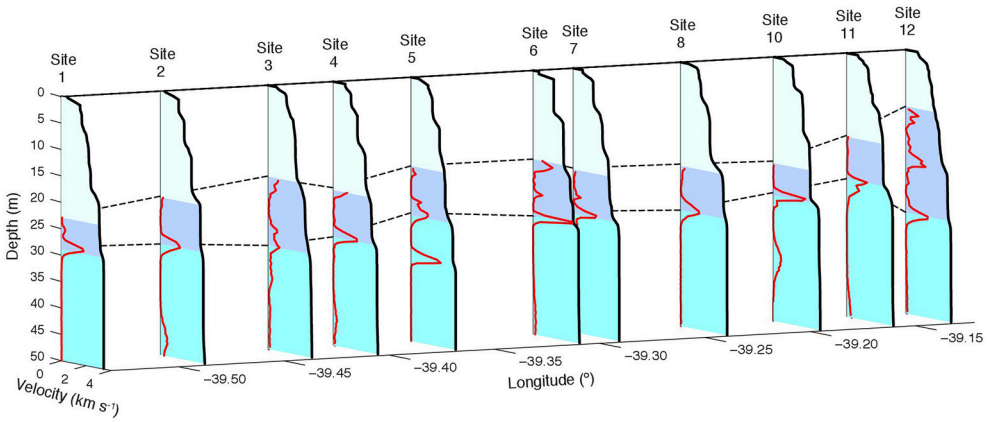

FIGURE 4 | Mean 1D velocity profiles derived from the inversion of travel times measured in the 2016 seismic experiments (solid black lines). The sites locations are as indicated in **Figure 1**. Light blue is the unsaturated firn, dark blue bands indicate the aquifer layer, and cyan the underlying ice. The water table depth (top dashed line) is derived from radar data, while the aquifer base (lower dashed line) is inferred from the probability of a seismic velocity increase (from 0 to 0.4) associated with the base of the aquifer (**Figure 3B**).

TABLE 1 | Aquifer and ice properties of our seismic survey sites upstream of Helheim glacier.

Site	Latitude	Longitude	Year	E	D	H	Err	V_{aq}	V_{ice}	Φ
1	66.367	−39.532	2016	1770	18.35	6	+1/−1	3111	3403	8
2 (a)	66.366	−39.485	2016	1755	16.27	9	+1/−2	3222	3452	6
2 (b)[a]	66.366	−39.481	2015	1753	16.07	–	+4/−3	–	3505	–
3	66.365	−39.434	2016	1711	13.99	13	+2/−3	2984	3506	17
4	66.365	−39.403	2016	1710	12.63	9	+2/−2	3097	3532	12
5	66.363	−39.366	2016	1691	10.94	17	+2/−3	2792	3600	22
6 (a)	66.362	−39.311	2015	1663	8.42	14	+3/2	3195	3631	15
6 (b)	66.361	−39.308	2016	1661	8.37	11	+1/−1	3007	3668	20
7	66.360	−39.289	2016	1647	7.50	8	+3/2	3001	3711	22
8 (a)	66.357	−39.238	2016	1618	5.20	8	+2/−3	3458	3751	6
8 (b)	66.357	−39.234	2015	1615	4.99	1	+6/−4	3200	3580	10
9[b]	66.355	−39.212	2015	1589	4.14	–	+3/−3	–	3448	–
10 (a)	66.355	−39.194	2016	1560	3.24	6	+3/−1	3000	3689	21
10 (b)	66.355	−39.184	2015	1545	2.83	17	+2/−2	3056	3812	22
10 (c)	66.354	−39.181	2015	1544	2.71	14	+3/−3	2854	3626	28
10 (d)	66.354	−39.178	2015	1543	2.59	21	+7/−6	3117	3883	21
10 (e)	66.354	−39.176	2015	1542	2.36	6	+6/−2	2779	3414	25
10 (f)	66.354	−39.173	2015	1542	2.25	8	+1/−2	2974	3467	16
11	66.354	−39.159	2016	1538	1.69	8	+5/−2	2925	3683	25
12 (a)	66.352	−39.131	2016	1518	0.41	20	+3/−3	3017	3631	19
12 (b)	66.352	−39.122	2015	1519	0	16	+3/−4	2918	3417	19
12 (c)	66.352	−39.124	2015	1519	0	19	+3/−2	2969	3563	17

Sites sharing similar locations are labeled with a–f. Measurements and observations are defined as: E surface elevation (m a.s.l.), D the relative distance from Site 12 (km), H the computed thickness of aquifer (m) and Err is the uncertainty in the thickness measurement (m) (Section Aquifer Thicknesses), V_{aq} is the average velocity of aquifer (m s^{-1}) lying between the radar top and seismic base, V_{ice} is the average velocity of ice in the underlying glacier (m s^{-1}) (Section Ice Seismic Velocity), and Φ is our estimated water content (%) (Section Water Content and Volume).

[a] *No aquifer detected by GPR measurements.*

[b] *Unconstrained bottom of aquifer by seismic measurements.*

continuously refracted wave in the 2016 survey reached a depth of 50–55 m. We also observed a systematic increase in ice velocity moving downslope to Site 9; this may represent the addition of ice lenses, compaction processes, increased ice flow or frozen aquifers (Harper et al., 2012). We explore this further in the discussion.

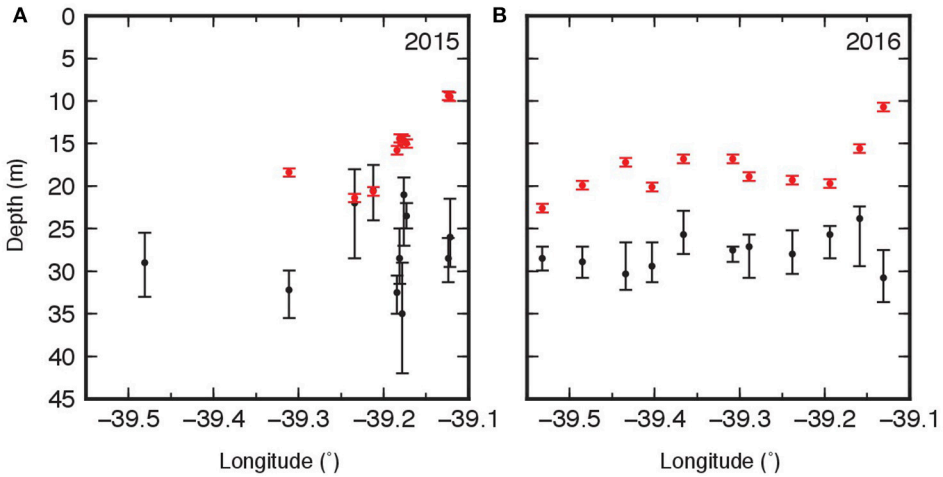

FIGURE 5 | Summary of measurements of the top of aquifer from GPR (red, error ± 50 cm) and seismic determined bottom of aquifer (black; errors from Table 1) along the (A) Summer 2015 and **(B)** Summer 2016 field sites.

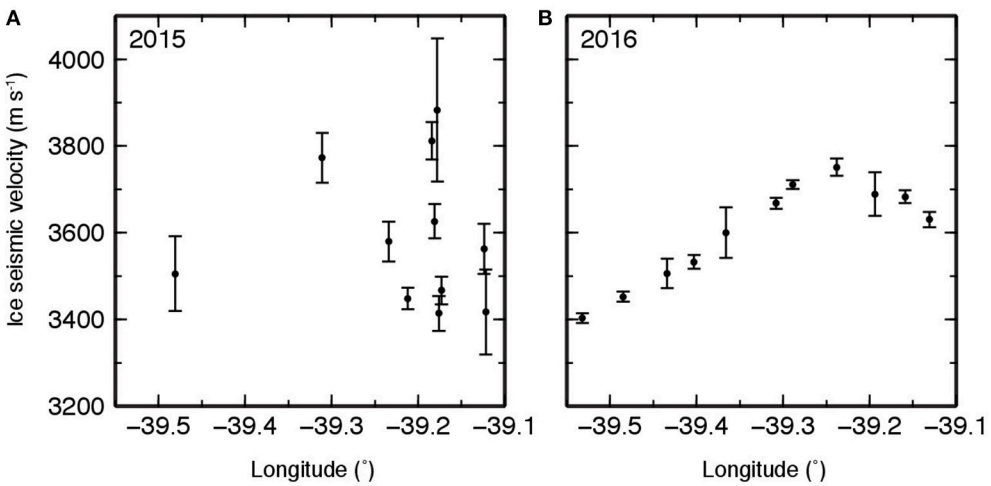

FIGURE 6 | Velocity of the ice underlying the firn aquifer, as measured in the summer of (A) 2015 and **(B)** 2016. Error bars are derived from the 1D inversion (**Figure 3B**).

Water Content and Volume

Seismic velocities are sensitive to the relative fraction of liquid and solid in a two-phase interconnected mixture (Biot, 1956; Hajra and Mukhopadhyay, 1982). We can relate these two quantities using (Equation 1) (Wyllie et al., 1956), which describes the contribution of water content (ϕ) to the P-wave velocity (v_{aq}) observed in the aquifer layer of each seismic site.

$$\phi = \frac{v_{H_2O}\left(v_{ice}/v_{aq} - 1\right)}{\left(v_{ice} - v_{H_2O}\right)} \times 100\% \quad (1)$$

The value of ϕ is proportional to the relative seismic velocity of the water in the saturated pore space, ($v_{H_2O} = 1450\,\mathrm{m\ s^{-1}}$; Shearer, 2009), the seismic velocity of ice (v_{ice}) that we derive from our inversion results (**Table 1**), and the average seismic velocity of the aquifer V_{aq}, also in **Table 1**. Our porosity estimate from this method is an upper bound as we exclude the effects of air bubbles trapped within the saturated pore space (∼6% on average, Koenig et al., 2014), which would further reduce seismic velocity.

We observe spatial and temporal changes in water content within the aquifer (**Figure 7**). We omit locations where we could not determine the aquifer base or water table, and sampling of the aquifer at higher altitudes further to the west was limited to one site in 2015 (Site 2b). At this location, no reflection in the GPR data corresponding to the water table was identified, so we interpret this region as having minimal water content in 2015. In 2016, Site 1 was dry, while Site 2a situated near Site 2b indicated the presence of water in both the seismic and radar investigations (**Figure 7**). These observations confirm that the

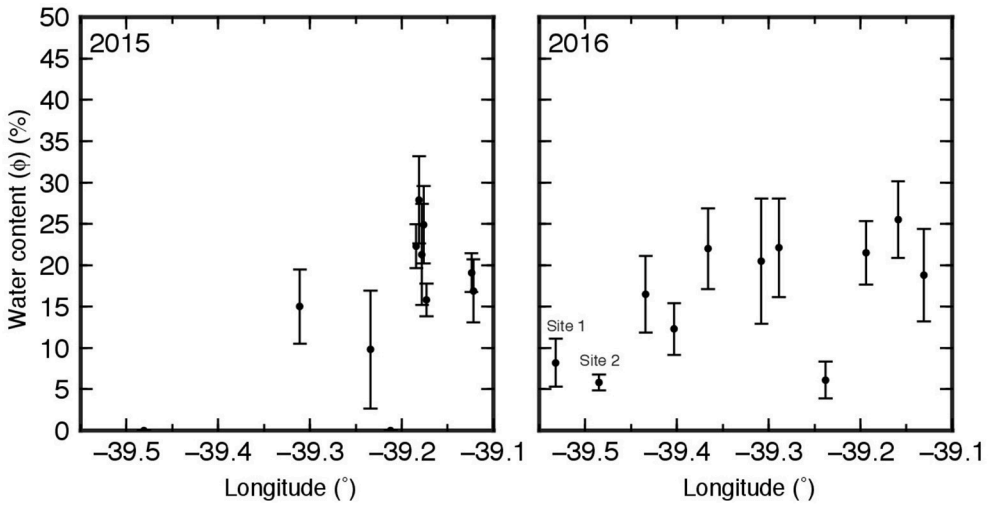

FIGURE 7 | Seismic velocity-derived water content (Φ) of the saturated pore space within the firn aquifer for years 2015 and 2016. Error bars are derived from the uncertainty in the thickness measurements.

aquifer is expanding inland to the west and at higher elevations, which is in agreement with airborne radar and remote sensing observations (Jeffries et al., 2015; Miège et al., 2016). In both years, we calculate that the average water content of the aquifer saturated zone ranges from 8 to 24%.

We then use aquifer water content to calculate firn storage capacity M_{H_2O} (in kg m^{-2}) for each site by estimating the total mass of water stored per 1 m^2 of aquifer:

$$M_{H_2O} = \phi H \rho. \quad (2)$$

where H is aquifer thickness (m), ϕ is the water content (%), and ρ is the density of water (1000 kg m^{-3}). **Figure 8** shows the result of this calculation for firn water storage capacity at each site. We calculate that the aquifer in our study region has an average storage capacity of 2070 $\pm$ 1360 kg m^{-2}. There is a general increase in water storage capacity within the aquifer, moving from a minimum at the highest elevations to the west, and increasing downslope to the east.

DISCUSSION

Effective media estimations require knowledge of the matrix and fluid velocities to determine the bulk velocity of a fluid-filled medium (e.g., Biot, 1956; Wyllie et al., 1956). Here we assign a value of 1450 m s^{-1} for liquid water and 343 m s^{-1} for air (Shearer, 2009). An assembled dataset of laboratory and *in situ* measurements of firn and ice velocity presented in Kohnen (1974) show that polycrystalline ice at 0°C should have a seismic velocity of 3795 m s^{-1}. This is comparable, given the uncertainties, to the highest velocities observed in our study region in 2015, 3883 $\pm$ 165 m s^{-1} at site 10 days; in 2016, 3751 $\pm$ 20 m s^{-1} at site 8a. However, the majority of sites across our study region are systematically slower than this expected value for ice, up to 10% less at Site 1. In the 2015 active source experiments, this discrepancy can be attributed to the 195 m effective array aperture and incomplete sampling of the region beneath the aquifer. The continuously refracted seismic waves in these experiments refracted very near the base of the aquifer (25–30 m) and may not have sampled deep enough to resolve ice velocity. This is supported by the comparably higher errors derived from the inversions of the ice seismic velocity in 2015 vs. 2016 (**Figure 6**). In the 2016 experiments, there is a systematic increase in seismic velocity derived from Site 1 (3403 $\pm$ 11 m s^{-1}) eastward and downslope to Site 8a (3751 $\pm$ 20 m s^{-1}), and then a small decrease moving eastward and downslope to Site 12a (3631 $\pm$ 18 m s^{-1}). For these experiments the effective array aperture is 385 m, with the deepest diving rays sampling near 50–55 m depth, well below the base of the aquifer. Given this deeper sampling, we interpret the pattern of ice velocities in 2016 as a well-resolved feature of the study region. Furthermore, since these ice velocities are up to 10% less than that of polycrystalline ice, we suggest that the base of the firn aquifer in these locations cannot correspond to the pore closure depth within the firn, and is associated with a different mechanism.

In situ measurements of firn and ice velocity from Kohnen and Bentley (1973) show that dry firn velocities increase exponentially with depth and are related to the mechanisms driving compaction within the firn. Densification in the upper 11–14 m of firn is driven by mechanical rearrangement of grain boundaries, and then switches to recrystallization of grains down to 56–64 m depth. Below these depths, any further densification results from the compression of air bubbles in the ice. Liquid water percolating into and through the firn would descend to a depth where it either reaches an impermeable boundary (e.g., pore closure at the firn-ice transition) or falls below 0°C and freezes into the pore space. The freezing depth in our study region occurs near 30–35 m depth (Koenig et al., 2014) and is shallower than the expected depth of pore closure (56–64 m)

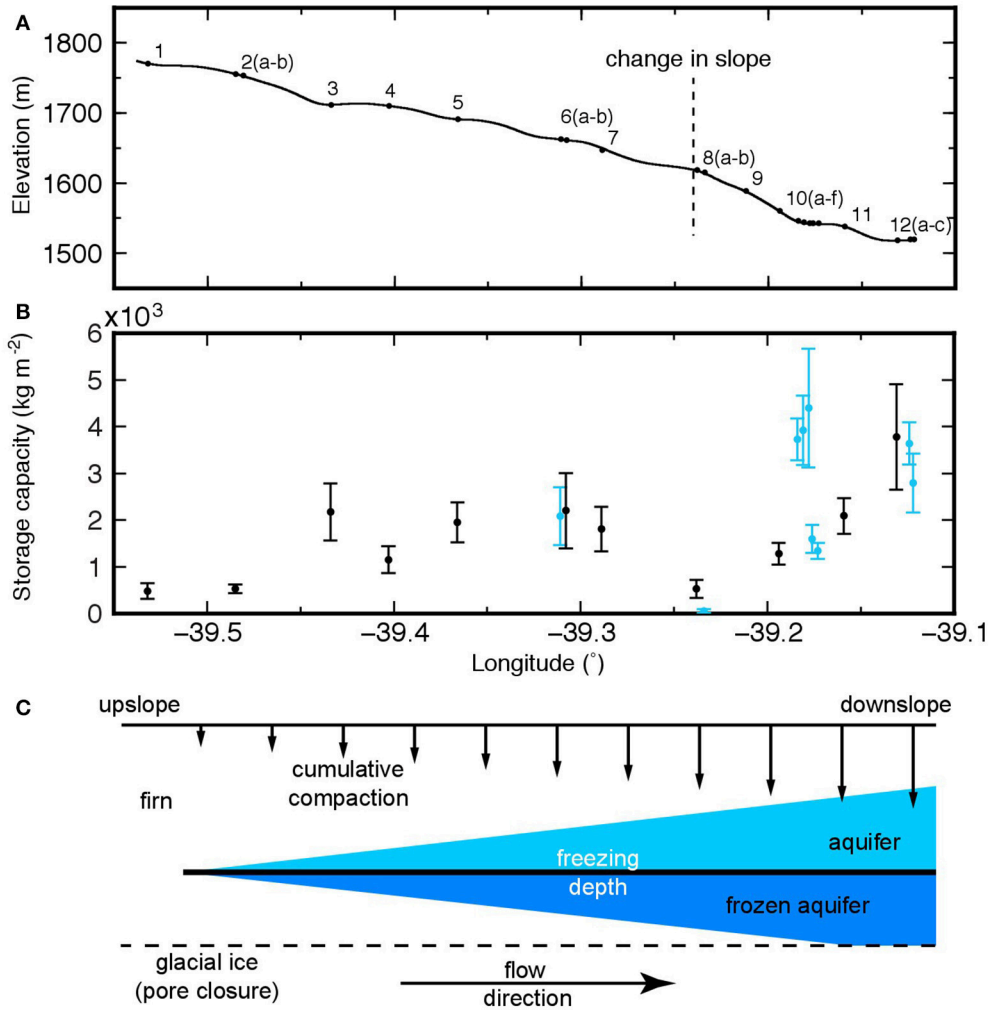

FIGURE 8 | Aquifer water storage capacity across our study region. (A) Elevation profile along flow line and location of the major change in slope across our study region. Surface topography is obtained from a WorldView-1 (DigitalGlobe©) digital elevation model generated by the Polar Geospatial Center. **(B)** 2015 measurements shown in cyan, 2016 measurements shown in black. Error bars are determined from the uncertainty in the water content measurements. **(C)** Inferred structure of the Greenland ice sheet aquifer.

reported by Kohnen and Bentley (1973). The base of the aquifer in our study (27.7 ± 2.9 m) is therefore closer to the freezing depth than the pore closure depth, so we infer that the seismic velocity jump at the base of the aquifer corresponds to freezing of liquid water into the pore space. Since the firn at this depth has not completely recrystallized into ice, the effective velocity is dependent upon the amount of frozen water added at the base of the aquifer. We also observe multiple 0.2–0.5 m layers of clear ice in cores drilled in the summers of 2015 and 2016 down to depths of 55 m (Koenig et al., 2014). The clear ice layers are more abundant in cores drilled further eastward and downslope (**Figure 1C**). Clear ice forms by freezing of a layer of older aquifer water; addition of material to the ice sheet will compact and drive the aquifer layer below the freezing isotherm. It is expected that regions with older aquifer would therefore be underlain by a series of frozen clear ice layers. Subsequent addition of these layers each year would increase seismic velocity as the number of frozen-in clear ice layers increases with the velocity of the ice beneath the aquifer and is expected to increase as the ice moves the aquifer to lower elevation (**Figure 8**).

Our estimate of water content in the aquifer is dependent upon several assumptions about the relationship between seismic velocity, porosity, and fluid content. First, we use the velocity of the ice directly below the aquifer layer rather than the expected velocity of polycrystalline ice at 0°C (3795 m s^{-1}). The Wyllie average assumes prior knowledge about the velocity of the fluid and matrix; using the velocity of polycrystalline ice would overestimate water content as it assumes the unsaturated firn matrix would behave as fully recrystallized ice (Kohnen and Bentley, 1973). The firn is still undergoing compaction and thus will have a lower effective velocity than pure ice. We therefore

choose to use the velocity of the ice directly beneath the aquifer to derive a porosity estimate to minimize any offset expected from the incomplete compaction of the firn matrix. Second, we use the average of the velocity across the aquifer layer to compare to the underlying ice. This is obtained by finding the mean velocity lying between the GPR-defined top of the aquifer, and seismically defined base. This does not take into account vertical variations of water content that could be present within the aquifer. Integrating the porosity across the layer would provide a more appropriate estimate; however the resolution of our inversion typically places a singular layer at aquifer range of depths, so any attempt to refine the stratification in the aquifer layer would be better served by allowing the inversion to fit gradients rather than layers. This will be incorporated into future work. Third, we neglect the effect of air bubbles on the seismic velocity, making our estimate of porosity an upper bound on the water content within the aquifer layer. The addition of air bubbles will reduce the amount of water required to explain the inversion-derived seismic velocity within the aquifer layer. For example, adding 6% air to the pore space in the aquifer at site 12a will reduce the derived porosity from 18.8 to 10.5% and our storage capacity down from 3780 to 1946 kg m^{-2}. Since we do not have a way to independently evaluate air content within the aquifer layer, we choose to report the upper bound estimate of water content assuming no contribution from the air.

Past estimates of water content in the aquifer obtained by Koenig et al. (2014) via ice cores found a firn capacity (in kg m^{-2}) of 2150 kg m^{-2} assuming a 14-m thick aquifer with an aerial extent of 70 $\pm$ 10 $\times$ 10^3 km^2 or 980 $\pm$ 140 km^3. Using radar mapping of the lateral extent of the firn aquifer, they estimated the total mass of Greenland aquifer to contain 140 $\pm$ 20 gigatons (Gt) of liquid water. With our seismic methodology, we are able to examine the lateral variability in aquifer thickness and water content along an elevation 2-D transect and refine this volume estimate (**Figure 8**). With these improved estimates of aquifer thickness (11.5 $\pm$ 5.5 m) and seismically-derived water content (8–24%), we find that water volume ranges from 0 to 4400 kg m^{-2}; with an average value of 2070 $\pm$ 1360 kg m^{-2}, similar to the Koenig et al. (2014) value. Furthermore, in 2016, the spatial extent of the Helheim Glacier aquifer is estimated at 2286 km^2 (Miège et al., 2016). With these values, we estimate that the total volume of water in the Helheim aquifer is 4.7 $\pm$ 3.1 Gt, similar to the ice core estimates of Koenig et al. (2014).

The values reported above represent bulk averages; we also detect spatial variability in the water content of the aquifer layer. This value evolves from 530 kg m^{-2} at Site 2 up to 3800 kg m^{-2} at Site 12 (**Figure 8**). Site 12 is 250 m lower in elevation than Site 2, with undulations in the surface topography (and underlying water table) with wavelengths of 1–2 km. The increase in water content generally mirrors the topography and is expected to increase due to more melt percolating into the system at lower and presumably warmer elevations. The water table approaches the surface (10.7 m) at Site 12 (**Figure 5**) where we seismically estimate the highest water storage capacities for the aquifer. There is also a large decrease in water content near Sites 8 and 9 (530 and 50 kg m^{-2}, respectively) where there is a noticeable change in surface slope (marked in **Figure 8**). Cores drilled at Site 8a in 2016 revealed a very thin (<1 m) aquifer at this location. The lack of water at this location could reflect a 3-dimensional change in the aquifer, including increased flow rates at the higher slope, drainage into a buried crevasse, diversion around a local geographic feature, or a locally shallow firn-ice transition and lack of permeability within the ice. We cannot distinguish between these possibilities without further investigation of this feature in the field.

At most sites with seismic measurements in both years (e.g., Sites 6, 8, 12), there is agreement between the estimated water storage capacities. However, at Site 10, we observed a discrepancy in the estimated storage capacities from 2015 to 2016 (**Figure 8**). Sites 9 and 10 were our noisiest sites, with both data collected during active drill site and team operations in 2015 (individuals walking, generators, etc.). In the resulting inversions, we were unable to uniquely derive aquifer properties at Site 9 owing to coincidence of the radar selected water table and seismological discontinuities. This discrepancy was also observed in the seismic velocity measurements of the ice; in general the sites expressed much lower ice seismic velocity than their 2016 counterparts (**Figure 6**). These uncertainties were not identified until after the 2015 field season, to which we responded by the expansion of the effective array aperture length of the seismic array from 195 m to 385 m. To offset any potential site noise, we also increased the number of stacked shots in 2015 (3 shots) to >5 in 2016 (**Figure 1B**). These measures improved the overall quality of the deepest diving seismic waves that sample the base of the aquifer. The combined effects of higher signal-to-noise and deeper sampling thus make us more confident in the 2016 results.

To summarize, in 2015 and 2016, we used refraction seismology to temporally and spatially sample the structure of a firn aquifer on the southeastern GrIS, and determined that the base of this aquifer lies on average 27.7 $\pm$ 2.9 m beneath the surface, with an average thickness of 11.5 $\pm$ 5.5 m. We relate the change in seismic wave speed across the aquifer to pore saturation of water, finding the aquifer has an average pore space of 16 $\pm$ 8%, with considerable variation in storage capacity of water along the studied east-west regional flow line. We also find that the seismic base of the aquifer corresponds to the freezing point of liquid water within the pore space. Subsequent addition of these frozen layers beneath the aquifer from year-to-year produces a high velocity seismic layer directly beneath the aquifer. From 2015 to 2016, we observed a 1–2 km uphill expansion of the aquifer system, with a dry site seismically investigated in 2015 now having a 530 kg m^{-2} water content in 2016 (Site 2). We estimate that the volume of water stored in the aquifer across the entire region upstream of Helheim glacier to be 4.7 $\pm$ 3.1 gigatons, a value comparable to prior estimates by Koenig et al. (2014) from ice core sampling of the aquifer. Using seismics, we reveal the relationship between the percolation of meltwater through the aquifer system, the addition of frozen surface melt at depth beneath the aquifer layer, and ultimately constrain the impact of ice sheet aquifers on sea level rise.

AUTHOR CONTRIBUTIONS

The manuscript was written by LM and NS and edited by all the authors. Data analysis was performed by LM and NS; and SB wrote the THB inversion. CM provided the radar depth of the aquifer and estimates of aquifer extent. Seismic data were collected by LM, NS, RF, CM, SL, OM, AL, and DS. All authors agree to be accountable for the content of this work.

FUNDING

Support for this research was provided by the National Science Foundation; LM and NS were supported by PLR-1417993. SB was supported by EAR-1349771; and DS, RF, OM, and CM were supported by PLR-1417987. LK was supported by NASA Cryospheric Sciences program NASA Award NNX15AC62G. SL was supported by an NWO ALW Veni grant number 865.15.023.

ACKNOWLEDGMENTS

We thank Kyli Cosper and the entire CH2MHILL PFS Team for excellent field logistics and support. We thank our two review editors for providing thorough and insight commentary that helped to greatly improve the quality of the manuscript. Seismic instruments were provided by the Incorporated Research Institutions for Seismology (IRIS) through the PASSCAL Instrument Center at New Mexico Tech. Seismic data collected will be made available through the IRIS Data Management Center as an assembled data set. GPR data will be made available through the Arctic Data Center. The facilities of the IRIS Consortium are supported by the National Science Foundation under Cooperative Agreement EAR-1261681 and the DOE National Nuclear Security Administration. Figures in this manuscript were constructed using the Generic Mapping Toolkit (Wessel et al., 2013).

REFERENCES

Albert, D. (1998). Theoretical modeling of seismic noise propagation in firn at the south pole, Antarctica. *Geophys. Res. Lett.* 25, 4257–4260. doi: 10.1029/1998gl900155

Biot, M. A. (1956). The theory of propagation of elastic waves in a fluid-saturated porous solid. I. Low frequency range. II. Higher frequency range. *J. Acoust. Soc. Am.* 28, 168–178, 179–191. doi: 10.1121/1.1908239

Blankenship, D. D., Bentley, C. R., Rooney, S. T., and Alley, R. B. (1986). Seismic measurements reveal a saturated porous layer beneath an active Antarctic ice stream. *Nature* 322, 54–57. doi: 10.1038/322054a0

Bodin, T., and Sambridge, M. (2009). Seismic tomography with the reversible jump algorithm. *Geophys. J. Int.* 178, 1411–1436. doi: 10.1111/j.1365-246X.2009.04226.x

Christianson, K., Kohler, J., Alley, R. B., Nuth, C., and Pelt, W. J. J. (2015). Dynamic perennial firn aquifer on an Arctic glacier. *Geophys. Res. Lett.* 42, 1418–1426.doi: 10.1002/2014GL062806

Enderlin, E. M., Howat, I. M., Jeong, S., Noh, M. J., van Angelen, J. H., and van den Broeke, M. R. (2014). An improved mass budget for the Greenland ice sheet. *Geophys. Res. Lett.* 41, 866–872. doi: 10.1002/2013GL059010

Ettema, J., van den Broeke, M. R., van Meijgaard, E., van de Berg, W. J., Bamber, J. L., Box, J. E., et al. (2009). Higher surface mass balance of the Greenland ice sheet revealed by high-resolution climate modeling. *Geophys. Res. Lett.* 36:L12501. doi: 10.1029/2009GL038110

Fettweis, X., Franco, B., Tedesco, M., van Angelen, J. H., Lenaerts, J. T. M., van den Broeke, M. R., et al. (2013). Estimating the Greenland ice sheet surface mass balance contribution to future sea level rise using the regional atmospheric climate model MAR. *Cryosphere* 7, 469–489. doi: 10.5194/tc-7-469-2013

Forster, R. R., Box, J. E., van den Broeke, M. R., Miège, C., Burgess, E. W., van Angelen, J. H., et al. (2014). Extensive liquid meltwater storage in firn within the Greenland ice sheet. *Nat. Geosci.* 7, 95–98. doi: 10.1038/ngeo2043

Gogineni, S. P. (2012). *CReSIS RDSData with Digital Data.* Lawrence. Available online at: http://data.cresis.ku.edu/

Green, P. J. (1995). Reversible jump Markov chain Monte Carlo computation and Bayesian model determination. *Biometrika* 82, 711–732. doi: 10.1093/biomet/82.4.711

Hajra, S., and Mukhopadhyay, A. (1982). Reflection and refraction of seismic waves incident obliquely at the boundary of a liquid-saturated porous solid. *Bull. Seismol. Soc. Am.* 72, 1509–1533.

Harper, J., Humphrey, N., Pfeffer, W. T., Brown, J., and Fettweis, X. (2012). Greenland ice-sheet contribution to sea-level rise buffered by meltwater storage in firn. *Nature* 491, 240–243. doi: 10.1038/nature11566

Horgan, H. J., Anandakrishnan, S., Jacobel, R. W., Christianson, K., Alley, R. B., Heeszel, D. S., et al. (2012). Subglacial Lake Whillans—Seismic observations of a shallow active reservoir beneath a West Antarctic ice stream. *Earth Planet. Sci. Lett.* 331–332, 201–209. doi: 10.1016/j.epsl.2012.02.023

Humphrey, N. F., Harper, J. T., and Pfeffer, W. T. (2012). Thermal tracking of meltwater retention in Greenland's accumulation area. *J. Geophys. Res.* 117:F01010. doi: 10.1029/2011JF002083

Jarvis, E. P., and King, E. C. (1995). Seismic investigation of the Larsen Ice Shelf, Antarctica: in search of the Larsen Basin. *Antarct. Sci.* 7, 181–190. doi: 10.1017/S0954102095000241

Jeffries, M. O., Richter-Menge, J., and Overland, J. E. (Eds.). (2015). *Arctic Report Card 2015.* Available online at: http://www.arctic.noaa.gov/Report-Card

Johnson, M. R., and Smith, A. M. (1997). Seabed topography under the southern and western Ronne Ice Shelf, derived from seismic surveys. *Antarct. Sci.* 9, 201–208. doi: 10.1017/S0954102097000254

Kirchner, J. F., and Bentley, C. R. (1979). Seismic short-refraction studies on the Ross Ice Shelf, Antarctica. *J. Glaciol.* 24, 313–319.

Koenig, L. S., Miège, C., Forster, R. R., and Brucker, L. (2014). Initial *in situ* measurements of perennial meltwater storage in the Greenland firn aquifer. *Geophys. Res. Lett.* 41, 81–85. doi: 10.1002/2013GL058083

Kohnen, H. (1974). Temperature dependence of seismic waves in ice. *J. Glaciol.* 13, 144–147.

Kohnen, H., and Bentley, C. (1973). Seismic refraction and reflection measurements at "byrd" station, Antarctica. *J. Glaciol.* 12, 101–111.

McMahon, K. L., and Lackie, M. A. (2006). Seismic reflection studies of the Amery Ice Shelf, East Antarctica: delineating meteoric and marine ice. *Geophys. J. Int.* 166, 757–766. doi: 10.1111/j.1365-246X.2006.03043.x

Metropolis, N., Rosenbluth, A. W., Rosenbluth, M. N., Teller, A. H., and Teller, E. (1953). Equation of state calculations by fast computing machines. *J. Chem. Phys.* 21, 1087–1092. doi: 10.1063/1.1699114

Miège, C., Forster, R. R., Brucker, L., Koenig, L. S., Solomon, D. K., Paden, J. D., et al. (2016). Spatial extent and temporal variability of Greenland firn aquifers detected by ground and airborne radars, *J. Geophys. Res. Earth Surf.* 121, 2381–2398. doi: 10.1002/2016JF003869

Munneke, P. K., Ligtenberg, S. R. M., van den Broeke, M. R., van Angelen, J. H., and Forster, R. R. (2014). Explaining the presence of perennial liquid water bodies in the firn of the Greenland Ice Sheet. *Geophys. Res. Lett.* 41, 476–483. doi: 10.1002/2013GL058389

Neff, P. D., Steig, E. J., Clark, D. H., McConnell, J. R., Pettit, E. C., and Menounos, B. (2012). Ice-core net snow accumulation and seasonal snow chemistry at a temperate-glacier site: Mount Waddington, southwest British Columbia, Canada. *J. Glaciol.* 58, 1165–1175. doi: 10.3189/2012JoG12J078

Rennermalm, A. K., Moustafa, S. E. Mioduszewski, J., Chu, V. W., Forster, R. R., Hagedorn, B., et al. (2013). Understanding Greenland ice sheet hydrology using an integrated multi-scale approach. *Environ. Res. Lett.* 8:015017. doi: 10.7916/D88K7916

Rignot, E., Velicogna, I., van den Broeke, M. R., Monaghan, A., and Lenaerts, J. T. (2011). Acceleration of the contribution of the Greenland and Antarctic ice sheets to sea level rise. *Geophys. Res. Lett.* 38:L05503. doi: 10.1029/2011GL046583

Shearer, P. M. (2009). *Introduction to Seismology*. Cambridge: Cambridge University Press.

Smith, A. M., Jordan, T. A., Ferraccioli, F., and Bingham, R. G. (2013). Influence of subglacial conditions on ice stream dynamics: seismic and potential field data from Pine Island Glacier, West Antarctica. *J. Geophys. Res. Solid Earth* 118, 1471–1482. doi: 10.1029/2012JB009582

van Angelen, J. H., Lenaerts, J. T. M., van den Broeke, M. R., Fettweis, X., and van Meijgaard, E. (2013). Rapid loss of firn pore space accelerates 21st century Greenland mass loss. *Geophys. Res. Lett.* 40, 2109–2113. doi: 10.1002/grl.50490

van den Broeke, M., Bamber, J., Ettema, J., Rignot, E., Schrama, E., van de Berg, W. J., et al. (2009). Partitioning recent greenland mass loss. *Science* 326, 984–986. doi: 10.1126/science.1178176

Vernon, C. L., Bamber, J. L., Box, J. E., van den Broeke, M. R., Fettweis, X., Hanna, E., et al. (2013). Surface mass balance model intercomparison for the Greenland ice sheet. *Cryosphere* 7, 599–614. doi: 10.5194/tc-7-599-2013

Wessel, P., Smith, W. H. F., Scharroo, R., Luis, J. F., and Wobbe, F. (2013). Generic Mapping Tools: improved version released, EOS Trans. *AGU* 94, 409–410. doi: 10.1002/2013EO450001

Winberry, J. P., Anandakrishnan, S., and Alley, R. B. (2009). Seismic observations of transient subglacial water-flow beneath MacAyeal Ice Stream, West Antarctica. *Geophys. Res. Lett.* 36:L11502. doi: 10.1029/2009GL037730

Wyllie, M. R. J., Gregory, A. R., and Gardner, L. W. (1956). Elastic wave velocities in heterogeneous and porous media. *Geophysics* 21, 41–70. doi: 10.1190/1.1438217

Conflict of Interest Statement: The authors declare that the research was conducted in the absence of any commercial or financial relationships that could be construed as a potential conflict of interest.

frontiers in Earth Science

ORIGINAL RESEARCH
published: 26 May 2017
doi: 10.3389/feart.2017.00038

Hydraulic Conductivity of a Firn Aquifer in Southeast Greenland

Olivia L. Miller[1], D. Kip Solomon[1], Clément Miège[2], Lora S. Koenig[3], Richard R. Forster[2], Lynn N. Montgomery[4], Nicholas Schmerr[4], Stefan R. M. Ligtenberg[5], Anatoly Legchenko[6] and Ludovic Brucker[7,8]*

[1] Department of Geology and Geophysics, University of Utah, Salt Lake City, UT, United States, [2] Geography Department, University of Utah, Salt Lake City, UT, United States, [3] National Snow and Ice Data Center, University of Colorado Boulder, Boulder, CO, United States, [4] Department of Geology, University of Maryland, College Park, College Park, MD, United States, [5] Institute for Marine and Atmospheric Research Utrecht, Utrecht University, Utrecht, Netherlands, [6] Institute of Research for Development, University Grenoble Alps, IGE, Grenoble, France, [7] Cryospheric Sciences Laboratory, Goddard Space Flight Center (NASA), Greenbelt, MD, United States, [8] Goddard Earth Sciences Technology and Research Studies and Investigations, Universities Space Research Association, Columbia, MD, United States

OPEN ACCESS

Edited by:
William Tad Pfeffer, University of Colorado Boulder, United States

Reviewed by:
Stefan W. Vogel, Glaciology Tasmania, Australia
Henning Löwe, WSL Institute for Snow and Avalanche Research SLF, Switzerland
Andrew Fountain, Portland State University, United States

***Correspondence:**
Olivia L. Miller
olivia.miller@utah.edu

Specialty section:
This article was submitted to Cryospheric Sciences, a section of the journal Frontiers in Earth Science

Received: *30 September 2016*
Accepted: *28 April 2017*
Published: *26 May 2017*

Citation:
Miller OL, Solomon DK, Miège C, Koenig LS, Forster RR, Montgomery LN, Schmerr N, Ligtenberg SRM, Legchenko A and Brucker L (2017) Hydraulic Conductivity of a Firn Aquifer in Southeast Greenland. Front. Earth Sci. 5:38. doi: 10.3389/feart.2017.00038

Some regions of the Greenland ice sheet, where snow accumulation and melt rates are high, currently retain substantial volumes of liquid water within the firn pore space throughout the year. These firn aquifers, found between ~10 and 30 m below the snow surface, may significantly affect sea level rise by storing or draining surface meltwater. The hydraulic gradient and the hydraulic conductivity control flow of meltwater through the firn. Here we describe the hydraulic conductivity of the firn aquifer estimated from slug tests and aquifer tests at six sites located upstream of Helheim Glacier in southeastern Greenland. We conducted slug tests using a novel instrument, a piezometer with a heated tip that melts itself into the ice sheet. Hydraulic conductivity ranges between 2.5×10^{-5} and 1.1×10^{-3} m/s. The geometric mean of hydraulic conductivity of the aquifer is 2.7×10^{-4} m/s with a geometric standard deviation of 1.4 from both depth specific slug tests (analyzed using the Hvorslev method) and aquifer tests during the recovery period. Hydraulic conductivity is relatively consistent between boreholes and only decreases slightly with depth. The hydraulic conductivity of the firn aquifer is crucial for determining flow rates and patterns within the aquifer, which inform hydrologic models of the aquifer, its relation to the broader glacial hydrologic system, and its effect on sea level rise.

Keywords: hydraulic conductivity, mass balance, aquifer test, slug test, meltwater flow

INTRODUCTION

Across the percolation zone of the southeast portion of the Greenland ice sheet, surface meltwater infiltrates to depth within the ice sheet, where it currently forms an extensive firn aquifer. The firn aquifer contains liquid water within the pore space of the compacting snow/firn throughout the year at depths of ~10–30 m. Initially documented in 2011 (Forster et al., 2014), the aquifer has been identified and monitored with ground penetrating radar, airborne radar, and *in situ* measurements since then (Koenig et al., 2014; Miège et al., 2016; Montgomery et al., this issue). Over the entire ice sheet, firn aquifers are estimated to cover an area between 20,000 and 70,000 km^2, with ~50% of this total extent located in the southeastern portion of the ice sheet (Forster et al., 2014; Miège et al., 2016). Firn aquifers form in areas with a combination of high accumulation and high melt

rates (Forster et al., 2014; Kuipers Munneke et al., 2014). Complete drainage of the aquifer could contribute up to 0.4 mm to sea level rise globally (Koenig et al., 2014).

In a firn aquifer, water storage occurs as meltwater fills firn pore space until the residual liquid water content of the firn is achieved, which allows horizontal flow to occur (Freeze and Cherry, 1979; Pfeffer et al., 1991). Water flow within the firn aquifer may allow surface meltwater originating far from the edge of the ice sheet to discharge to the ocean. The saturation of the firn allows more meltwater that would otherwise rest in pore spaces if the firn remained unsaturated to flow laterally. Crevasses at the edge of the ice sheet represent one possible pathway for aquifer water to discharge to the ocean (Alley et al., 2005; Chu, 2014; Koenig et al., 2014). Transport of liquid water to the base of the ice sheet, likely via crevasses (Miège et al., 2016; Poinar et al., 2017) may also influence ice dynamics and ice discharge to the ocean (e.g., Zwally, 2002; Joughin et al., 2008; Sole et al., 2011). The hydrologic properties of the aquifer and its connections to the broader glacier hydrologic system remain unclear. The aquifer may be storing meltwater and buffering sea level rise, or it may be constantly draining and routing water toward the ocean. To characterize the connection between surface melt and discharge to the ocean, and quantify water flow, hydraulic properties of the aquifer are required.

This process of water storage and transport differs from meltwater discharge to the ocean in other parts of Greenland, where inland meltwater is routed through surface lakes and streams to crevasses and moulins (Das et al., 2008; Lewis and Smith, 2009; Chu, 2014; Smith et al., 2015). In some areas outside of firn aquifer regions, thick ice layers prevent meltwater percolation to depth and surface runoff is favored, contributing to sea level rise (Machguth et al., 2016). In other areas, meltwater storage occurs by refreezing in the firn, buffering sea level rise (Pfeffer et al., 1991; Harper et al., 2012).

The storage and transmission of meltwater through firn is similar in many ways to water flow through a rocky or unconsolidated porous media, where water flows from recharge to discharge areas (high hydraulic head to low hydraulic head). The undulating water table observed in radar profiles (Forster et al., 2014) resembles the topographically driven flow of an unconfined aquifer (Tóth, 1963). In the unsaturated zone above the water table, where fluid pressures are less than atmospheric, pores can contain both gas and liquid. The aquifer is defined as the saturated zone below the water table, where fluid pressures are positive. Isolated gas phases within the saturated zone can exist. We conceptualize saturated groundwater flow to follow Darcy's law:

$$q = \frac{Q}{A} = -K\frac{\partial h}{\partial x} \tag{1}$$

where q is the specific discharge (length/time), Q is the discharge (length^3/time), A is the cross sectional area across which flow occurs (length^2), K is the hydraulic conductivity (length/time), h is the hydraulic head (length), and x is the distance (length). To quantify aquifer discharge, the hydraulic gradient can be estimated from ground penetrating radar surveys of the aquifer but site-specific *in-situ* measurements of hydraulic conductivity are needed.

Hydraulic conductivity is typically measured *in situ* by two major techniques: aquifer tests and piezometer tests (Freeze and Cherry, 1979). Each test introduces a different hydraulic stress to the system. Aquifer tests involve injecting or pumping water from or into an aquifer at a controlled rate and observing the change in water level over time. Slug tests, a type of piezometer test, involve instantaneously changing the hydraulic head within a well and recording recovery in that well over time (Hvorslev, 1951; Butler, 1997). Both tests induce horizontal flow within the aquifer, and therefore indicate horizontal hydraulic conductivity. Slug tests can provide depth-specific measurements of hydraulic conductivity within a formation. However, the conditions immediately surrounding the piezometer have a larger influence on slug test results.

Aquifer tests assess the hydraulic properties, including hydraulic conductivity, of an aquifer over a larger area (∼m–km) than slug tests because they perturb a larger volume of water over a longer period of time (Ferris et al., 1962). Thus, aquifer tests are less subject to formation disturbance caused by the drilling or melting processes that may alter hydraulic conductivity close to the borehole or piezometer. As a result, aquifer tests generally provide a better estimate of the effective hydraulic parameters of an aquifer than slug tests. However, they are technically more difficult to conduct, require more equipment, and take longer than slug tests. The water level response during the recovery period of an aquifer test can provide the most accurate estimate of hydraulic conductivity as it is generally independent of well construction or pumping effects. A comparison of slug and aquifer test results, as is presented in this manuscript, can provide a comprehensive estimate of the hydraulic conductivity within an aquifer.

Firn aquifers have been observed in mountain glaciers, and their hydraulic conductivities have been measured using slug tests and aquifer tests (Oerter and Moser, 1982; Oerter et al., 1983; Fountain, 1989; Fountain and Walder, 1998; Schneider, 1999; Jansson et al., 2003). Slug tests have also been used to estimate subglacial hydraulic properties (Stone and Clark, 1972; Iken et al., 1996; Kulessa et al., 2005; Meierbachtol et al., 2008). Hydraulic conductivity depends on properties of both the porous media (grain size, shape, distribution, and packing) and the fluid (viscosity and density). Firn permeability, which only depends on porous media properties, has been measured at various sites across Greenland using permeameters (Albert and Shultz, 2002; Adolph and Albert, 2014; Keegan et al., 2014) and Antarctica (Albert et al., 2000, 2004). Hydraulic conductivity (K) is related to permeability (k) as

$$K = \frac{k\rho g}{\mu} \tag{2}$$

where ρ is fluid density, g is the acceleration due to gravity, and μ is the fluid dynamic viscosity. These parameters can shed light on the depositional and metamorphic history of the firn.

In this manuscript, we describe the methods and results of field experiments conducted to determine, for the first time,

the hydraulic conductivity of a firn aquifer in the southeastern area of the Greenland ice sheet. Mathematical solutions to determine hydraulic conductivity involve matching curves to water displacement data. These results, combined with aquifer geometry, are essential to developing a hydrologic model of the firn aquifer and understanding the impact of the aquifer on ice sheet mass balance estimates.

MATERIALS AND METHODS

Site Description

The study site is located along an elevation gradient of an ice flow line upstream of Helheim Glacier in southeast Greenland (**Figure 1**). Field work was conducted ∼40 km west of the glacier front in April, July, and August 2015, and July and August 2016. Five 6.4 cm diameter boreholes were drilled with an electrothermal drill to ∼50 m depth, and a heated piezometer, described in Section Heated Piezometer, was installed at 6 sites (**Table 1**) to a maximum depth of almost 40 m. At two of those drilling sites, piezometers were installed <5 m away from the borehole to perform aquifer tests. The 6.4 cm diameter holes were enlarged with a heated reamer to 8 cm diameter in order to accommodate the pump inside the borehole.

We determined the thickness of the aquifer using *in-situ* and geophysical methods. We measured the depth to the water table with both a chalked steel tape (Garber and Koopman, 1968) and ground penetrating radar (Forster et al., 2014; Miège et al., 2016). We also determined the bottom of the aquifer with a borehole dilution test. Briefly, during the borehole dilution test, we mixed a small amount of saltwater into the 8 cm diameter borehole and measured the specific conductance of the water within the borehole at 30 cm intervals over ∼20 h. The reduction in specific conductance due to inflow of freshwater is proportional to the specific discharge through the borehole. Within the aquifer, the change in specific discharge was significant, but below a certain depth, the specific discharge did not change, indicating the bottom of the flow zone. We only did this test in 2016. The other method to determine the bottom of the aquifer is with a seismic survey, described in Montgomery et al. this issue. The depth to the water table and aquifer bottom and aquifer thickness using each method at each site are shown in **Table 2**. The thickness of the saturated zone determined by the borehole dilution test was used where available. The seismic bottom depths were also used. The borehole dilution and seismic thicknesses do not perfectly agree (5–17 m differences) and so a range of thicknesses were used for the hydraulic conductivity estimates.

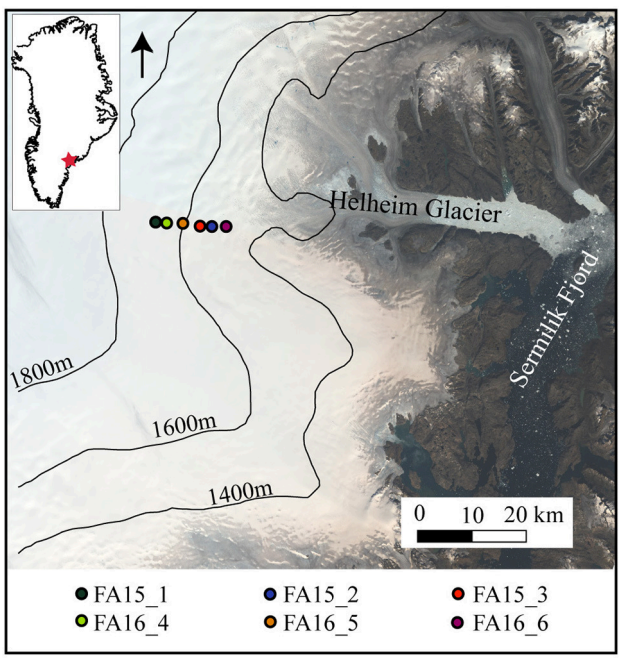

FIGURE 1 | Site map. Landsat 8 composite image (August 21, 2014) showing sites in southeast Greenland where slug tests and aquifer tests were conducted in April, July, and August 2015 and July and August, 2016. Elevation contours from Cryosat-2 DEM (Helm et al., 2014).

Heated Piezometer

A piezometer, commonly used in groundwater hydrology, consists of a sealed pipe with an open end installed in the porous media to measure depth-specific hydraulic heads. We adapted a piezometer to penetrate the numerous ice lenses within the firn through the addition of a heated tip that allows the piezometer to advance by melting through the firn and ice (**Figure 2**). The 3 cm diameter piezometer standpipe is closed along its entire length except for a 32 cm screened interval near the tip which allows water to enter or exit when advanced below the water table. The casing radius is 1.5 cm, and the well radius is 1.5 cm. The piezometer also features a 108 cm long packer made of rubber surgical tubing, which can be inflated from the surface and allows for depth-specific measurements and water sampling. A generator at the surface powers the 500 W heated tip. A power cable and hollow tube to inflate the packer run from the surface to the heated tip and packer along the inside of the metal pipe above the packer. A bicycle pump is used to inflate the packer, which surrounds a section of the metal pipe above the screened interval, to a pressure of ∼1.7 atm (25 psi) above the water pressure.

TABLE 1 | Site locations.

Site name	Latitude (°)	Longitude (°)	Elevation (m)	Tests conducted and field season
FA15_1	66.362	−39.312	1,664	Slug tests, April 2015
FA15_2	66.355	−39.179	1,543	Slug tests, July 2015
FA15_3	66.355	−39.190	1,553	Slug tests, August 2015
FA16_4	66.360	−39.287	1,648	Slug tests and aquifer tests, July 2016
FA16_5	66.358	−39.239	1,619	Slug tests, July 2016
FA16_6	66.353	−39.135	1,519	Slug tests and aquifer tests, August 2016

Description of sites where boreholes were drilled, piezometers were installed, and hydraulic testing was conducted.

TABLE 2 | Depth to water table and aquifer bottom, and aquifer thickness measurements from *in-situ* and geophysical methods.

Site name	FA15_1	FA15_2	FA15_3	FA16_4	FA16_5	FA16_6
Name of nearest seismic line*	6a	10d	10a	7	8a	12a
Water table depth from chalked steel tape (m)	19.9	14.6	20.8	20.1	22.5	10.0
Bottom of aquifer depth from borehole dilution (m)				33.25	30.15	47.78
Aquifer thickness from *in-situ* measurements (m)				13.2	7.7	37.8
Radar water table depth (m)	18.4	14.4	19.7	18.9	19.3	10.7
Seismic bottom (m)	32.2	35.0	25.7	27.1	28.0	30.8
Minimum bottom depth (m)	29.9	29.0	24.7	25.7	25.2	27.5
Maximum bottom depth (m)	35.5	42.0	28.5	30.8	30.3	33.6
Seismic thickness (m)	13.8	20.6	6	8.2	8.7	20.1
Minimum thickness (m)	11.5	14.6	5.1	6.8	5.9	16.8
Maximum thickness (m)	17.1	27.6	8.8	11.9	11.0	22.9
Thickness used for hydraulic conductivity estimate (m)	13.8, 17.1	20.6, 27.6	6, 8.8, 11.06	13.2	7.7, 11	37.8

**Seismic line names are from Montgomery et al. this issue.*

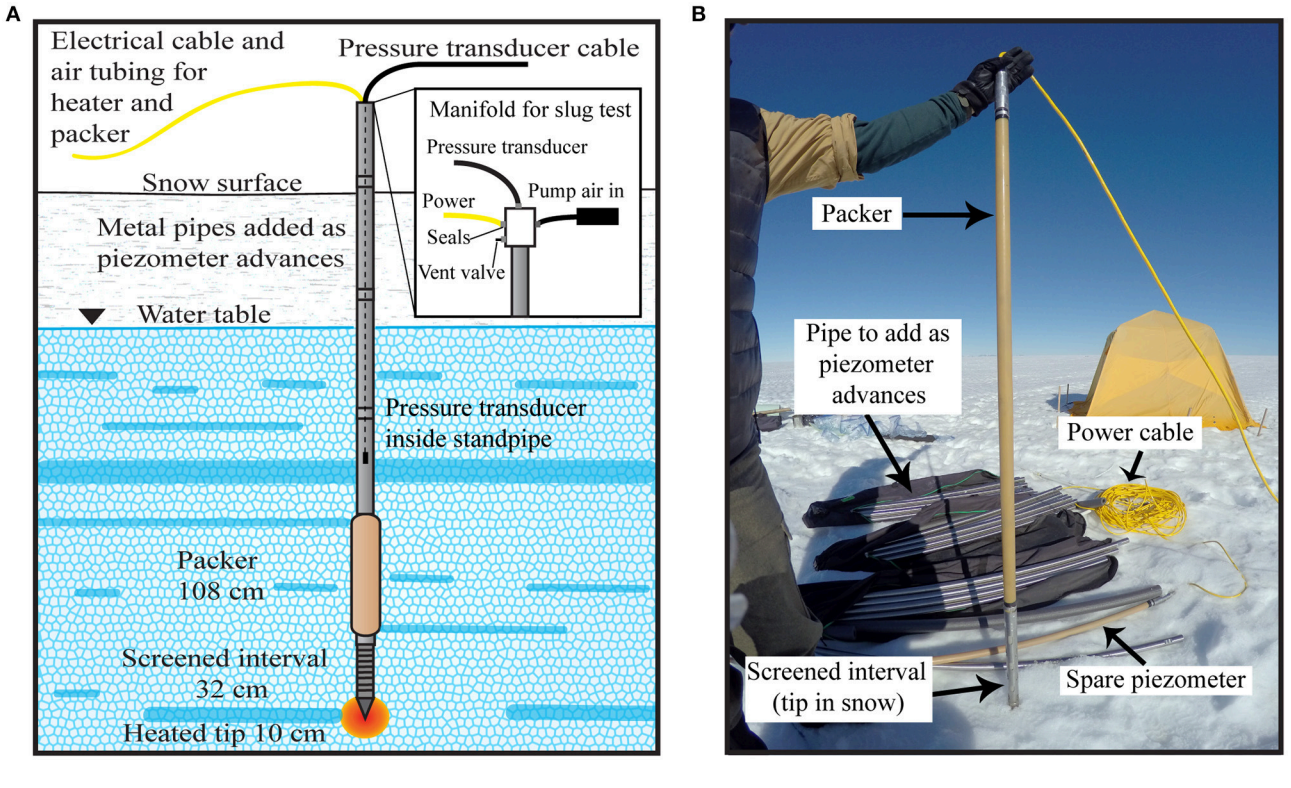

FIGURE 2 | The heated piezometer. Diagram **(A)** and photo **(B)** of the heated piezometer. The piezometer, consisting of a sealed pipe above an inflatable packer, screened interval, and heated tip at depth, advances to greater depth as the heated tip melts through the firn and ice lenses. Lengths of threaded pipe can be added at the surface as the tip moves downward. A power cable and hollow tube run the length of the pipe to power the heater and allow for packer inflation from the surface. Tubing can be lowered into the piezometer to collect water samples. The screened interval allows for hydraulic testing and water sampling from the entire thickness of firn/ice that the screened interval is open to.

As the piezometer melts through the firn, additional lengths (1.5 m) of threaded pipe are added at the surface. The pipe allows the creation of a sealed volume required to accumulate enough pressure to displace water during the slug tests. The walls of the piezometer were flush to the firn. The piezometer advances at a rate of ~13 cm/min in firn with a density below ~600 kg/m^3 and ~3 cm/min in firn and ice above a density of ~600 kg/m^3. We advanced the piezometer to a maximum depth of 38 m, limited by the length of pipe available in the field, but in concept could go deeper. The temperature at the maximum piezometer depth was 0°C (±0.2°C), from borehole temperature sensors. Although, never encountered, firn or ice temperatures below 0°C could cause the piezometer to freeze into the ice.

We removed the piezometer with a tripod equipped with a hand winch. The pipe can be pulled out by hand, but can be heavy enough that the tripod pulley system is safer. The piezometer standpipes were commercially available while the tip and packer were custom fabricated. Prior to use on the Greenland ice sheet, the piezometer was tested in ice blocks and on a frozen lake.

Slug Tests

Slug tests are widely used to determine hydraulic conductivity in the saturated zone (Kruseman et al., 1994). During a slug test, water within a piezometer is displaced, and the recovery, which depends on the hydraulic properties of the aquifer, is recorded (**Figure 3**). These tests are made depth-specific when a seal is formed between the screened interval of the piezometer and the porous media above.

At each site, the piezometer was used to conduct depth-specific slug tests, resulting in profiles of hydraulic conductivity with depth. After the piezometer melted to a desired depth below the water table, the packer was inflated and a pressure transducer was inserted into the piezometer standpipe until it was below the water table but above the screened interval. The piezometer was closed at the top using a PVC manifold with seals around the power and pressure transducer cables. Air was then pumped into the metal standpipes using a bicycle pump to displace water out of the screened interval (the only outlet in the piezometer) at the bottom of the piezometer. Once the water level was lowered to the pressure transducer, a valve at the surface was opened to instantaneously release the air pressure and allow water to flow back into the piezometer through the screened interval. Displacement ranged from 0.3 to 6 m, depending on the depth of the piezometer tip (less for shallower tests). The pressure transducer recorded pressure at 1 s intervals. Tests were repeated at each depth between 1 and 3 times. Sampling frequency varied from site to site. Slug tests were conducted every 0.3 m at FA15_1, every 3 m at FA15_2, every 4.5 m at FA15_3, every 3 m at FA16_4, and FA16_5, and ∼every 7 m at FA16_6. A total of 145 slug tests were conducted across the 6 sites.

The hydraulic conductivity of an aquifer can be estimated from slug test data through several curve fitting techniques. The firn aquifer is considered unconfined because no continuous, impermeable boundaries above the water table have been observed. The methods of both Hvorslev (1951), originally developed for a confined aquifer, and Bouwer and Rice (1976), developed for unconfined aquifers, are used in this study. The Hvorselv method for a confined aquifer can be applied to an unconfined aquifer because the water table boundary in an unconfined aquifer does not greatly affect the slug test response as long as the well screen is fully below the water table (Hvorslev, 1951; Bouwer and Rice, 1976). Both the Hvorslev method and the Bouwer and Rice solution for slug test analysis of an unconfined aquifer assume the aquifer has an infinite aerial extent and is homogeneous, and of uniform thickness (Bouwer and Rice, 1976; Hvorslev, 1951). Further, they are both applicable for a fully or partially penetrating test well, and neglect any aquifer storage (flow to the well is quasi-steady state). The Bouwer and Rice method also assumes that drawdown at the well is negligible, flow above the water table can be ignored, and well losses are negligible. The equations used for the Hvorselv and Bouwer and Rice methods are shown in the Supplementary Methods.

Aquifer Tests

Although, slug tests are simple and relatively reliable, the results are sensitive to conditions immediately surrounding the piezometer and are generally considered less reliable than aquifer pumping tests (Kruseman et al., 1994). During an aquifer test, the water level is lowered by pumping water out at a constant rate

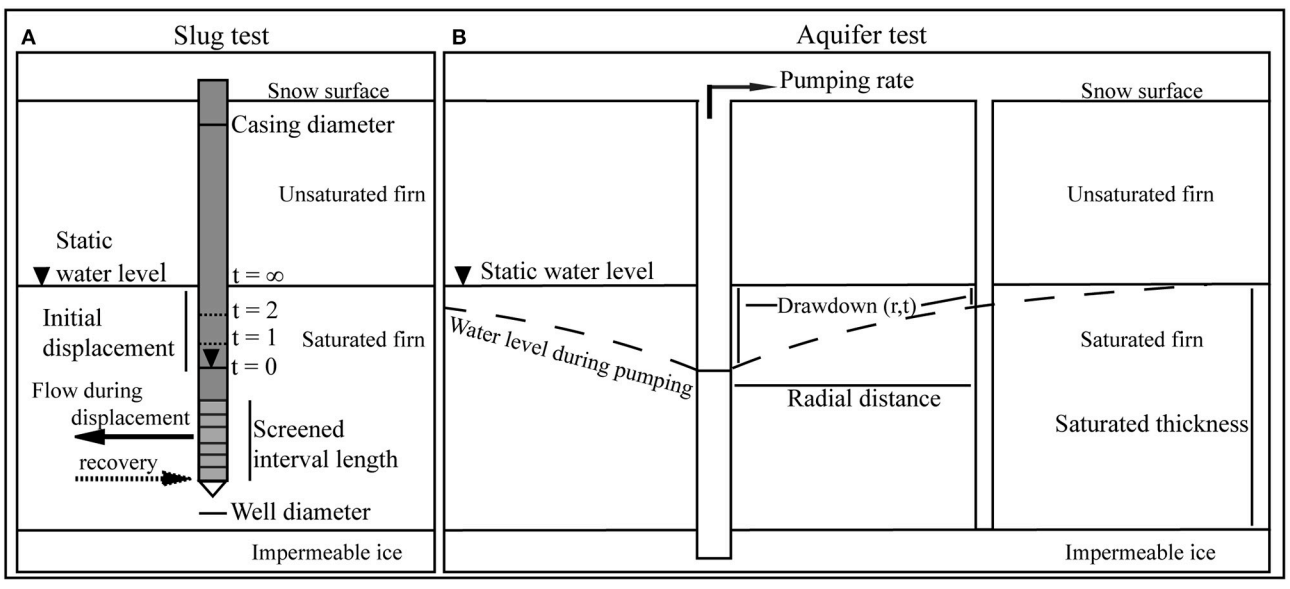

FIGURE 3 | Diagrams of slug and aquifer tests. The aquifer and well geometry for slug **(A)** and aquifer **(B)** tests used in analysis of slug and aquifer tests.

(**Figure 3**). The removal of water causes the water level to lower. This response, which depends on the hydraulic properties of the aquifer, is measured in the pumping well and/or an observation well some distance away (1–5 m). Aquifer pumping tests are more complex to conduct (they require multiple boreholes and more equipment) and take longer to conduct than slug tests, but they provide insight into the hydraulic conductivity over a larger volume of the aquifer.

Aquifer tests were conducted at two sites 7 km apart (FA16_4, upstream, and FA16_6, downstream). To conduct aquifer tests within the firn aquifer, 8 cm diameter boreholes formed from ice core drilling and widened with a heated reamer were used as fully penetrating pumping wells and piezometers were installed and removed to create observation wells. Water was pumped from the borehole at a constant rate (0.0011 m^3/s at FA16_4 and 0.0012 m^3/s at FA16_6) and discharged ∼30 m downslope. The water level change was measured with pressure transducers lowered down the pumping and observation wells. Pressure was measured at 1 min intervals, and at 1 s intervals for some of the periods around the time the pump was turned off. The higher frequency was employed to capture water level during times of rapid change in water level.

At FA16_4 the water level was monitored in the pumping well and in one fully penetrating observation well 1 m away. At FA16_6 the water level was monitored in the pumping well and in two observation wells 2 m (fully penetrating) and 5 m (partially penetrating, screen length is 460 cm) away. Drawdown from pumping forms a cone of water level depression surrounding the pumping well. The shape of this cone depends on the storage and transmissive properties of the aquifer. A more permeable aquifer will develop a narrower, shallower cone of depression than a less permeable aquifer. The observation wells were placed close to the pumping wells to capture drawdown in a highly permeable material.

The Theis theoretical response curves for unconfined aquifers were compared to observed water level changes to estimate aquifer transmissivity and storativity (Theis, 1935). The Theis solution of aquifer parameters for the drawdown distribution surrounding a well at any time is shown in the Supplementary Material.

Prior to curve fitting, the drawdown data was adjusted according to Equation (3) because the Theis solution was originally developed for confined aquifers where the saturated thickness remains constant with pumping. The saturated thickness of an unconfined aquifer changes due to pumping. The adjusted drawdown, which accounts for changing saturated thickness, is calculated as:

$$s' = s - s2/2b \tag{3}$$

where *s'* is the corrected displacement (length), *s* is the observed displacement, and *b* is the saturated aquifer thickness (length) (Jacob, 1944; Kruseman et al., 1994). The aquifer thickness was obtained from ground penetrating radar, seismic investigations (Montgomery et al., this issue), water level measurements, and borehole dilution tests (Freeze and Cherry, 1979). The observed displacements were small (<2 m), causing this correction to be minimal.

Hydraulic conductivity (K), can then be calculated as:

$$K = \frac{T}{b} \tag{4}$$

where T is transmissivity (length^2/time). The Theis solution assumes that the aquifer has an infinite aerial extent and is homogeneous, isotropic, and of uniform thickness. The diameter of the pumping well must be relatively small so that storage in the pumping well is assumed to be negligible. The pumping well can be fully or partially penetrating. Further, the method assumes that flow to the pumping well is horizontal when the pumping well is fully penetrating, and there is no delayed response to gravity within the aquifer.

Hydraulic Conductivity Estimation

Solutions of aquifer parameters to the Bouwer–Rice, Hvorselv, and Theis equations can be obtained through a curve matching method. The publicly available program AQTESOLV, by HydroSOLVE, Inc.© (Duffield[1]), was used to estimate hydraulic conductivity from slug and aquifer test data. AQTESOLV has both automatic and visual curve matching options. The automatic curve matching option uses a nonlinear least squares method to match theoretical to observed data by minimizing the sum of squared residuals. The visual curve matching option allows the user to manually match solutions to the observed data. The automatic curve matching was applied, and visually checked to ensure a match between observed slug test data and test solution line within the recommended normalized head ranges (0.15–0.25 for Hvorslev method and 0.2–0.3 for Bouwer and Rice method) (Butler, 1996).

The water level rose several centimeters over the course of the longer duration aquifer tests (∼hours), likely due to aquifer recharge from surface melt. A linear relationship between water level and time was used to calculate the water level change at a given time due to recharge. This additional water level rise was removed from the water level data prior to input into AQTESOLV in order to isolate the water level change effects (lowering water level) induced by pumping from those due to recharge (rising water level).

The correction to apply the Theis solution for a confined aquifer to data from an unconfined aquifer is automatically applied to drawdown data by AQTESOLV. However, to analyze the recovery data, the correction was manually applied and the residual recovery Theis solution for a confined aquifer was used.

RESULTS

Slug Tests

Several types of water level response curves to the slug test were noted (**Figure 4**). Generally, the early time response, within the recommended normalized head ranges, fits the Hvorslev and Bouwer and Rice solutions well. A few tests mostly followed

[1]Duffield, G. M. *AQTESOLV*. HydroSOLVE, Inc. Available online at: http://www.aqtesolv.com/

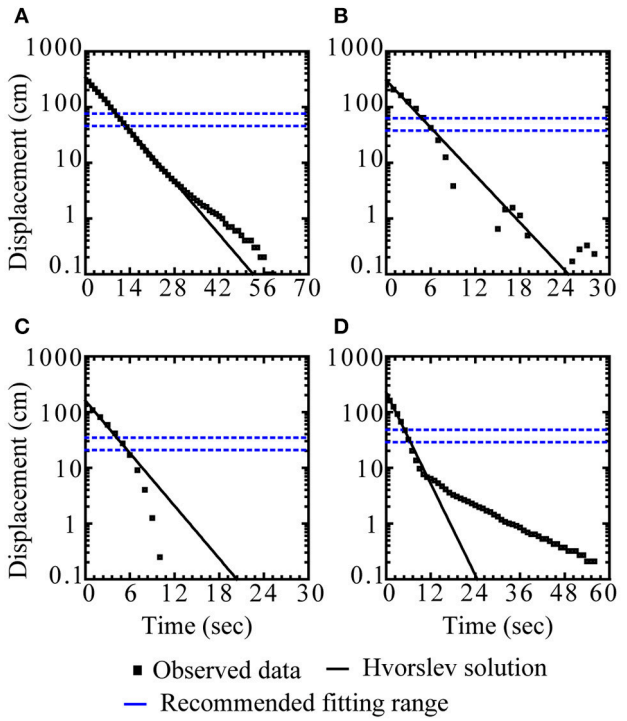

FIGURE 4 | Slug test curve fitting. Water level responses over time (squares), Hvorslev solution (lines) for representative slug tests, and recommended fitting range (blue dashed lines). Water levels generally match the predicted recovery **(A)**, recover rapidly, and sometimes oscillate slightly **(B)**, recover more quickly than predicted **(C)**, or recover more slowly than predicted **(D)**.

the response predicted by the Hvorslev method (1%; **Figure 4A**). The oscillatory (**Figure 4B**), water level response to the slug test, which reflects the high permeability of the firn (Bredehoeft et al., 1966; Van der Kamp, 1976), occurred in 25% of responses. For some tests (65%), the later time water levels recovered more quickly than predicted (**Figure 4C**), and for other tests (10%), the late time water levels took longer to recover than predicted (**Figure 4D**). The concave up response (**Figure 4D**) is often observed in confined and unconfined aquifers, and is likely due to a storage parameter of the aquifer and the piezometer (Butler, 1996). This could look like the double straight line effect, which has been observed when the well is screened across the water table (Bouwer, 1989). However, the screened interval of the piezometer was always below the water table and so we do not think this contributes to the poor fit. About 8% of responses showed a quicker than predicted and oscillatory response. Individual sites tend to have dominant response types, but can have a variety of responses. The dominant response type does not correspond to site location or slope of the water table. Overall, we found good fits within the recommended normalized head ranges.

Initial water level displacements within the piezometer ranged from 0.3 to 6 m. Despite initial displacements up to 6 m for some slug tests, the Reynolds number is still within the laminar flow range. For this analysis, we assumed that K_z/K_r was 1. A sensitivity analysis showed that decreasing ratio of K_z/K_r from 1 to 0.01 changed the hydraulic conductivity of one slug test from 1.6×10^{-4} to 2.7×10^{-4} m/s, which is within the range of variation observed between repeat tests.

Hydraulic conductivity within the firn aquifer was estimated from slug tests using two analysis methods (Supplementary Table 1). Hydraulic conductivity estimated using the Hvorslev method ranges from 1.1×10^{-3} to 2.5×10^{-5} m/s, with a geometric mean of 2.8×10^{-4} m/s and geometric standard deviation of 1.6. Hydraulic conductivity estimated using the Bouwer and Rice method ranges from 8.8×10^{-4} to 2.4×10^{-5} m/s, with a geometric mean of 2.5×10^{-4} m/s and geometric standard deviation of 1.7 (**Table 3**). The geometric mean is reported because hydraulic conductivity tends to be log normally distributed (Neuman, 1982). The Hvorselv method yields a larger range in hydraulic conductivity estimates (1.1×10^{-3} m/s) than the Bouwer and Rice method (8.5×10^{-4} m/s). The effective radius over which the water level change occurred ranges from 0.16 m for a test at 12 m depth to 1.18 m for a test at 38 m.

Hydraulic conductivity varies slightly between sites. The hydraulic conductivity decreases slightly with depth through the firn aquifer, although the relationship is weak ($r^2 = 0.17$; **Figure 5**). The greatest decrease with depth occurs at FA16_4. Ice layer stratigraphy does not seem to dramatically influence hydraulic conductivity within the aquifer. This is likely because the horizontal flow induced by the slug test is controlled by the firn with the highest hydraulic conductivity within the screened interval of the piezometer. Further, ice layers can be permeable (Keegan et al., 2014). Humphrey et al. (2012) describe meltwater bypassing ice layers in the percolation zone, a more similar setting to our work than Keegan et al. (2014). Still the general decrease in hydraulic conductivity can be attributed to a gradual increase in density with depth, indicating an increase in ice, which may be more uniformly distributed as opposed to distributed in layers. This is addressed in further detail in Section Discussion.

The Hvorslev method and Bouwer and Rice methods for estimating hydraulic conductivity yield similar results (**Figure 6**). The linear fit between the estimates from both methods ($y = 0.84 \times + 2 \times 10^{-5}$ m/s) indicates that the Bouwer and Rice method predicts hydraulic conductivity estimates that are roughly 20% lower than the Hvorslev method. This is consistent with the findings described in Butler (1996) of Hyder et al. (1994) and Hyder and Butler (1995) in terrestrial groundwater systems. The average percent difference between estimates is 8%. The Bouwer and Rice method has been found to underestimate hydraulic conductivity, and yield superior estimates relative to the Hvorslev method (Brown et al., 1995). The largest uncertainty in the hydraulic conductivity estimates from slug tests is that both the Hvorselv and Bouwer and Rice methods ignore the storage properties (specific storage) of the aquifer, which can contribute to uncertainties of over 60% (Brown et al., 1995). However, the difference between the estimates from both methods in this study is ∼20%, smaller than the uncertainty from ignoring storage. The mean hydraulic conductivity estimated using both methods are not statistically different, as indicated by a t-test (at $p = 0.05$). The similarity to each other and to the aquifer test results, described below, indicates that both methods seem to represent the firn aquifer well.

TABLE 3 | Hydraulic conductivity results.

Test			Hydraulic conductivity geometric mean (m/s)	Geometric standard deviation
Slug tests	Hvorselv method		2.8E-04	1.6
	Bouwer and Rice method		2.5E-04	1.7
Aquifer tests	All results		1.8E-04	2.1
	Turbulent flow excluded		2.3E-04	1.4
	Recovery period only		2.4E-04	1.4
Slug tests and aquifer tests together	Hvorselv method	All results	2.6E-04	1.7
		Turbulent flow excluded	2.7E-04	1.6
		Recovery period only	2.7E-04	1.6
	Bouwer and Rice method	All results	2.4E-04	1.7
		Turbulent flow excluded	2.5E-04	1.6
		Recovery period only	2.5E-04	1.6

Summary of geometric mean and standard deviations of slug tests and aquifer tests analyzed using different methods, excluding turbulent flow, and focusing on the recovery period of the aquifer tests.

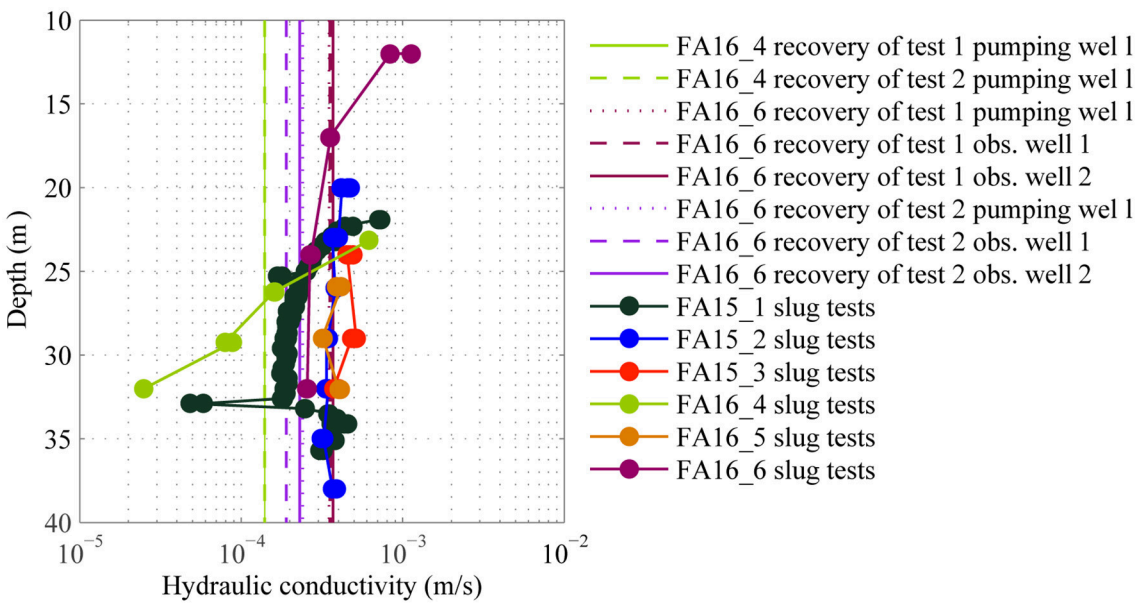

FIGURE 5 | Hydraulic conductivity across ~10 km and between 10–40 m depth. Hydraulic conductivity estimates determined using the Hvorslev method for slug test data and the Theis method for aquifer test data. The slug test measurements were taken at specific depths while the aquifer test data are not depth-specific. Water level rise due to recharge during the aquifer tests has been removed, as has data from the pumping well at site FA16_4 (see Section Aquifer Tests). Data points are larger than standard error of estimate.

Aquifer Tests

Aquifer test drawdown and recovery over time, and predicted displacements for a range of hydraulic conductivities are show in **Figure 7**. The comparisons between observed drawdown and recovery data to theoretical curves predicted by the Theis solution are shown in **Figure 8**. The hydraulic conductivity estimated from all aquifer tests ranges from 3.7×10^{-4} to 2.8×10^{-5} m/s, with a geometric mean of 1.8×10^{-4} m/s and geometric standard deviation of 1.6 (**Tables 3, 4**). Changing the ratio of K_z/K_r does not affect hydraulic conductivity estimates. The observed drawdown is close to the predicted drawdown for a hypothetical aquifer test in a 15 m thick aquifer with hydraulic conductivity of 2×10^{-4} m/s, a pumping rate of 0.001 m^3/s and a radial distance of 1 m between the pumping and observation well (**Figure 7**). Increasing or decreasing the hydraulic conductivity by an order of magnitude results in much larger or smaller displacements than what we observed.

The fit between observed and theoretical drawdown for some tests varies. A generally poor fit to early time data probably results from wellbore storage of water and transience in the pumping

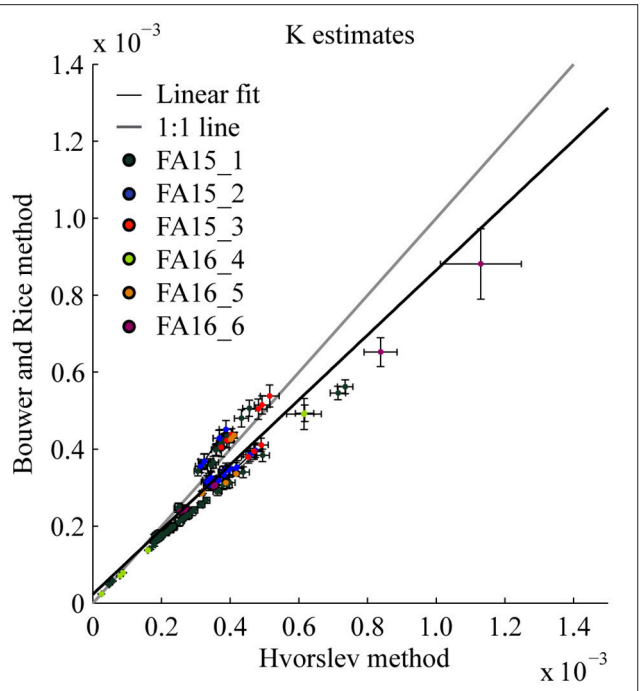

FIGURE 6 | Comparison of hydraulic conductivity estimated using Hvorslev's method and Bouwer and Rice's method for each site. Error bars represent standard error of the hydraulic conductivity estimates. A linear fit of these estimates (black line) has a slope of 0.84, intercept of 2×10^{-5}, and an r^2 of 0.89 ($r = 0.94$). The gray line indicates a 1:1 fit.

rate at very early times. The pump gradually increases the pumping rate over the first minute, which violates the constant pumping rate assumption. Wellbore storage serves as the primary source of pumped water at early times, but as pumping continues, wellbore storage decreases and the aquifer becomes the primary source of pumped water. Therefore, many of the early time data (∼min) were discarded.

The pumping well at site FA16_4 experienced drawdown below the pressure transducer, causing a loss of data. These data were excluded from hydraulic conductivity estimates. Further, the observation well at site FA16_4 is located only 1 m from the pumping well, and may have been subject to turbulent flow effects caused by pumping as observed in the significantly greater drawdown at this site compared to FA16_6 and the difference between the hydraulic conductivity estimates during the drawdown and recovery periods. Increased and turbulent flow causes head loss in the borehole (Jacob, 1947), which would lead to an underestimation of hydraulic conductivity during the drawdown period. Excluding data influenced by turbulent flow (excluding data from FA16_4 pumping well, and observation well during the drawdown period) results in a range of hydraulic conductivity between 3.7×10^{-4} and 1.4×10^{-4} m/s, with a geometric mean of 2.3×10^{-4} m/s and geometric standard deviation of 1.4.

The displacement data from the recovery period were not influenced by turbulent effects as the pump is not used during this period. Therefore, the recovery data likely result in a more accurate estimate with a range between 3.7×10^{-4} and 1.4×10^{-4} m/s, with a geometric mean of 2.4×10^{-4} m/s and geometric standard deviation of 1.4.

The distance between the pumping and observation wells was measured at the surface, and if the boreholes deviated from vertical, then the true distance between the boreholes may vary. A sensitivity analysis comparing the hydraulic conductivity estimated from the observation well at site FA16_4 showed that increasing the distance between the wells from 1 to 20 m had no effect on the hydraulic conductivity estimate. This is likely because in a highly permeable system, the cone of depression is wide and shallow, and therefore insensitive to the distance between the wells.

The geometric mean of hydraulic conductivity estimated using both slug tests (Hvorselv method) and aquifer tests (only recovery period) is 2.7×10^{-4} m/s with a geometric standard deviation of 1.4. The hydraulic conductivity decreases most with depth at site FA16_4, shown in the slug test results. The aquifer test at this site indicates that the hydraulic conductivity at this site is roughly the average of the depth-specific slug test measurements.

DISCUSSION

To our knowledge, these are the first hydraulic conductivity measurements of a firn aquifer in the southeastern Greenland ice sheet and these are the first depth specific slug tests conducted in a firn aquifer. We find relatively homogeneous hydraulic conductivity between measurement sites, and a slight decrease with depth. While ice layers within the firn aquifer may reduce vertical hydraulic conductivity, we did not test for this. Ice layers within the aquifer do not appear to dramatically reduce horizontal hydraulic conductivity and thus horizontal flow. Any horizontal fluid flow within the aquifer and discharge into the englacial hydrologic system is controlled by the horizontal firn layers with the highest hydraulic conductivity. Quantifying hydraulic conductivity and its spatial variation is a crucial step in developing realistic hydrologic models of the aquifer systems, and for understanding the impact the firn aquifer has on ice sheet mass balance. The observed spatial and vertical homogeneity should reduce firn aquifer hydraulic modeling complexity.

The largest uncertainties in the hydraulic conductivity estimates from slug tests result from ignoring the storage properties of the aquifer, and possible leakage around the packer. This could contribute to the weak vertical gradient in hydraulic conductivity. However, water level differences were observed as the packer was inflated, suggesting that the seal was strong enough to counter the hydraulic gradient. The largest uncertainties in the hydraulic conductivity estimates from the aquifer tests likely result from turbulent effects in this highly permeable system. The high permeability of the aquifer meant that the observation wells had to be placed close to the pumping well in order to observe any measurable drawdown. However, this also resulted in some turbulent effects in the water level data (much lower hydraulic head than predicted), leading to a poor fit to theoretical solutions, particularly in the pumping well.

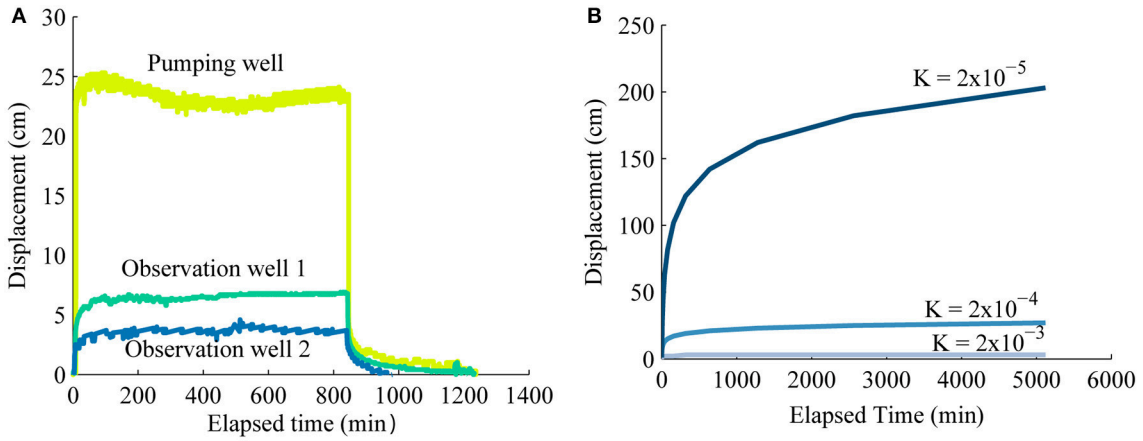

FIGURE 7 | Observed and theoretical drawdown. Displacement over time at site FA16_6 in the pumping and observation wells during the first test **(A)** and predicted drawdown in an observation well for a hypothetical aquifer test with varying hydraulic conductivity **(B)**. For this scenario, the aquifer is 15 m thick, the pumping rate is 0.0011 m^3/s, the storativity is 0.2, and the distance between the pumping and observation well is 1 m. The predicted drawdown when hydraulic conductivity is 2×10^{-4} m/s is most similar to the drawdown we observed.

This was addressed by discarding data where these effects were obvious, and by fitting the theoretical curves to the later time data and the recovery period data.

Although, the very early time recovery data (∼seconds) may be subject to turbulent effects, most of it is not. The recovery data, particularly in the observation wells, are also not subject to influences by well construction. These data depend solely on aquifer parameters. The recovery data are also not subject to any turbulent effects from pumping and are therefore the more reliable data and provide the most reliable estimate of hydraulic conductivity. Further, the general agreement with the hydraulic conductivity estimates from multiple sites and methods suggests that the hydraulic conductivity of the system is generally well-represented. The agreement between the slug tests and the aquifer tests, which perturb a larger volume of the aquifer (over 10 m diameter), suggests that meltwater from the installation of the piezometer or drilling of the borehole does not seem to impact the hydraulic conductivity estimates. Numerical modeling combined with an independent measurement of fluid flow, can better constrain hydraulic conductivity. In the absence of an independent measurement of flow, the *in situ* measurements described in this manuscript represent the best estimates of hydraulic conductivity. The overall range of hydraulic conductivity values seems to capture the uncertainty.

The porosity and permeability of the firn could be altered by the melting caused by the heated piezometer or the heated thermoelectric drill. This would particularly bias the slug test results toward a higher hydraulic conductivity because they perturb a relatively smaller volume of the aquifer. However, the aquifer test results, which perturb a much larger volume of the aquifer (>10 m diameter), are less subject to significant alteration from melting and provide a good comparison to, and generally agree with, the slug test results. The agreement between multiple complementary methods (slug tests and aquifer tests during pumping and recovery periods in particular) suggests that the hydraulic conductivity estimates are robust.

No seasonal changes were observed in hydraulic conductivity. However, only one site was tested in the spring, prior to surface melt onset. The other five sites were tested in the summer. Still, we do not expect substantial changes to hydraulic conductivity within the saturated zone because the temperature within the saturated zone remains at 0°C throughout the year. Thus, we do not expect significant freezing or thawing to occur within the saturated zone, which could alter the hydraulic conductivity by reducing or enhancing pore connectivity. However, longer time monitoring in different seasons would be required to identify seasonal impacts.

Our measurements of the hydraulic conductivity of the firn aquifer in southeast Greenland overlap with estimates for a firn aquifer in the Holtedahlfonna ice field, Svalbard, between 3.2×10^{-5} and 1.8×10^{-4} m/s (Christianson et al., 2015). The hydraulic conductivities measured in southeast Greenland, however, are approximately an order of magnitude higher than those taken from firn aquifers in various mountain glaciers where hydraulic conductivities show a relatively narrow range from 1.2×10^{-5} to 5×10^{-5} m/s (Oerter and Moser, 1982; Oerter et al., 1983; Fountain, 1989; Fountain and Walder, 1998; Schneider, 1999; Jansson et al., 2003). Hydraulic conductivity depends on the properties of the porous media (e.g., grain size, shape, or packing) and the fluid flowing through the porous media. Christianson et al. (2015) hypothesized that aquifers at deeper locations within an ice sheet/glacier will have decreased conductivities as firn densifies and pore space decreases. While this hypothesis may generally hold for a firn column in a single location, the growing number of spatially distributed hydraulic conductivity measurements of firn show variations across glaciers and ice sheets. This is expected as firn stratigraphy and microstructure vary across climates.

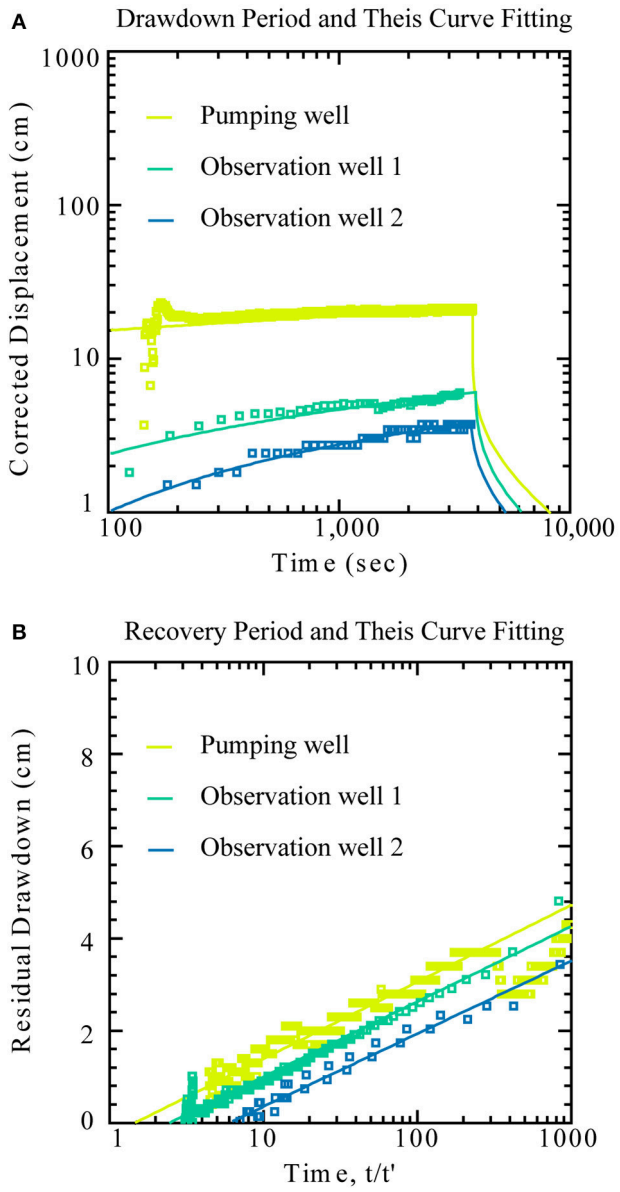

FIGURE 8 | Aquifer test curve fitting. (A) Recharge-corrected drawdown over time and Theis solution curves in the pumping and two observation wells during the second aquifer test at FA16_6. The squares represent water level displacement from the water level prior to pumping in different wells. The lines represent the Theis solution to the drawdown data. **(B)** Residual drawdown vs. time elapsed since the start of pumping relative to the time since pumping stopped (t/t′) and the Theis solution curves for aquifer test 1 at FA16_6 and FA16_6 The squares represent water level measurements after pumping stops and the lines represent the Theis solution to the recovery data.

We can also compare permeability, which is only a function of the porous media, to sites where no aquifer exists. Permeability increases from mountain glaciers ($\sim 10^{-12}$ m^2) to the southeast Greenland firn aquifer ($\sim 10^{-12}$ to 10^{-10} m^2) to dry firn ($\sim 10^{-10}$ m^2) (Oerter and Moser, 1982; Oerter et al., 1983; Fountain, 1989; Fountain and Walder, 1998; Schneider, 1999; Albert et al., 2000; Luciano and Albert, 2002; Adolph and Albert, 2014; Keegan et al., 2014). We attribute the difference in permeability across regions to the ice content represented in density profiles of the different locations where average density decreases from mountain glaciers to southeast Greenland firn aquifer to dry firn (Fountain, 1989; Adolph and Albert, 2014; Koenig et al., 2014). Although, Keegan et al. (2014) and Adolph and Albert (2014), and Albert et al. (2000) report vertical permeability, Keegan et al. (2014) note that differences between lateral and vertical permeability are smaller than differences between vertical permeability of different layers (see Luciano and Albert, 2002), and are therefore adequate for a general comparison. Also, the horizontal and vertical permeability are within the same order of magnitude. The density profiles recorded at measurement sites offer an initial explanation, as follows, for the changes in permeability; however, detailed microstructure measurements are needed, specifically to resolve pore interconnectivity and orientation, to more fully describe permeability differences.

TABLE 4 | Hydraulic conductivity estimates from aquifer tests during drawdown and recovery periods in each well.

Site	Well	Hydraulic conductivity (m/s)			
		Drawdown		Recovery	
		Test 1	Test 2	Test 1	Test 2
FA16_4	Observation	3.1E-05*	2.8E-05*	1.4E-04	1.4E-04
FA16_6	Pumping	1.6E-04	1.6E-04	3.5E-04	2.4E-04
FA16_6	Observation 1	1.6E-04	2.5E-04	3.6E-04	1.9E-04
FA16_6	Observation 2	3.2E-04	3.1E-04	3.7E-04	2.3E-04

Asterisk indicates estimates likely subject to turbulent flow effects caused by pumping.

The differences in ice content, and therefore densities, between mountain glaciers and the southeast Greenland firn aquifer are in part due to the long-term (decades), perennial nature of the aquifer in southeast Greenland. Aquifers in mountain glaciers are generally smaller, thinner, and steeper, allowing for annual drainage and more refreeze when air temperatures dip below 0°C in the winter (Vallon et al., 1976; Oerter et al., 1983; Fountain, 1989, 1996; Jansson et al., 2003). The perennial aquifer in southeast Greenland is in general deeper (10's of m) and thicker (10's of m), which limits refreezing in the saturated zone (**Table 2**). This increased annual refreezing in mountain glaciers likely leads to more ice and reduced pore connectivity.

The differences in ice content between dry firn and the southeast Greenland firn aquifer are due to climatic and geographic differences (Kuipers Munneke et al., 2014). The dry-firn sites experience little to none of the surface melt and subsequent freezing that occurs at our site, in the percolation zone of southeast Greenland. Therefore, the dry-firn sites do not accumulate as much refrozen ice, leading to more permeable firn.

The lateral homogeneity of hydraulic conductivity observed in the Greenland firn aquifer has also been observed in South Cascade Glacier (Fountain, 1989). This similarity likely reflects the homogenizing effect of saturating firn at 0°C on firn microstructure. While the ice layer stratigraphy at a specific location doesn't seem to dramatically influence the horizontal

hydraulic conductivity, as shown in our measurements and noted by Keegan et al. (2014), increases in overall ice content of the firn column do seem to reduce hydraulic conductivity and permeability (e.g., from mountain glaciers to water saturated firn to dry firn).

This study provides estimates on hydraulic parameters for a newly discovered firn aquifer and proves the effectiveness of the heated piezometer, particularly as a light weight (∼200 kg), fast method to access an aquifer from the snow surface for *in situ* physical measurements and water sampling. The heated piezometer is a unique tool developed to study firn hydrology in Greenland, but can be used in any firn aquifer setting. The hydraulic conductivities measured can be used to improve models of water flow within, and discharge from, firn aquifers and further constrain the storage and retention time estimates for aquifers within the Greenland ice sheet. As melt is projected to increase under a predicted warmer climate, the firn aquifer could have an increasingly important effect on Greenland ice sheet mass balance by efficiently transporting meltwater through firn to the ocean.

AUTHOR CONTRIBUTIONS

OM collected field data, conducted analysis and interpretation, and wrote the manuscript. DS designed and built heated piezometer, collected field data, and consulted on data analysis and manuscript writing and editing. CM, LK, RF, LM, NS, SL, AL, and LB assisted with field work, contributed to intellectual content, and contributed to manuscript writing.

FUNDING

This work was supported by NSF grant number PLR-1417987. LM and NS were supported by PLR-1417993. LK and LB were supported by NASA Cryospheric Sciences program NASA Award NNX15AC62G. SL was supported by an NOW ALW Veni grant, number 865.15.023.

ACKNOWLEDGMENTS

The authors thank Kyli Cosper, Kathy Young, and the entire CH2M Polar Field Services team for logistical assistance. Thanks also to Josh Goetz and IDDO for drilling support in April, 2015 and Jay Kyne for drill consultation and development. We also thank the editor and reviewers for thoughtful comments that greatly improved this manuscript.

SUPPLEMENTARY MATERIAL

The Supplementary Material for this article can be found online at: http://journal.frontiersin.org/article/10.3389/feart.2017.00038/full#supplementary-material

REFERENCES

Adolph, A. C., and Albert, M. R. (2014). Gas diffusivity and permeability through the firn column at Summit, Greenland: measurements and comparison to microstructural properties. *Cryosphere* 8, 319–328. doi: 10.5194/tc-8-319-2014

Albert, M. R., and Shultz, E. F. (2002). Snow and firn properties and air–snow transport processes at Summit, Greenland. *Atmos. Environ.* 36, 2789–2797. doi: 10.1016/S1352-2310(02)00119-X

Albert, M. R., Shultz, E. F., and Perron, F. E. (2000). Snow and firn permeability at Siple Dome, Antarctica. *Ann. Glaciol.* 31, 353–356. doi: 10.3189/172756400781820273

Albert, M., Shuman, C., Courville, Z., Bauer, R., Fahnestock, M., and Scambos, T. (2004). Extreme firn metamorphism: impact of decades of vapor transport on near-surface firn at a low-accumulation glazed site on the East Antarctic plateau. *Ann. Glaciol.* 39, 73–78. doi: 10.3189/172756404781814041

Alley, R. B., Dupont, T. K., Parizek, B. R., and Anandakrishnan, S. (2005). Access of surface meltwater to beds of sub-freezing glaciers: preliminary insights. *Ann. Glaciol.* 40, 8–14. doi: 10.3189/172756405781813483

Bouwer, H. (1989). The bouwer and rice slug test - an update. *Groundwater* 27, 304–309. doi: 10.1111/j.1745-6584.1989.tb00453.x

Bouwer, H., and Rice, R. C. (1976). A slug test for determining hydraulic conductivity of unconfined aquifers with completely or partially penetrating wells. *Water Resour. Res.* 12, 423–428. doi: 10.1029/WR012i003p00423

Bredehoeft, J. D., Cooper, H. H., and Papadopulos, I. S. (1966). Inertial and storage effects in well-aquifer systems: an analog investigation. *Water Resour. Res.* 2, 697–707. doi: 10.1029/WR002i004p00697

Brown, D. L., Narasimhan, T. N., and Demir, Z. (1995). An evaluation of the Bouwer and Rice method of slug test analysis. *Water Resour. Res.* 31, 1239–1246. doi: 10.1029/94WR03292

Butler, J. J. J. (1996). Slug tests in tite characterization: some practical considerations. *Environ. Geosci.* 3, 154–163.

Butler, J. J. J. (1997). *The Design, Performance, and Analysis of Slug Tests*. New York, NY: CRC Press.

Christianson, K., Kohler, J., Alley, R. B., Nuth, C., and van Pelt, W. J. J. (2015). Dynamic perennial firn aquifer on an Arctic glacier. *Geophys. Res. Lett.* 42, 1418–1426. doi: 10.1002/2014GL062806

Chu, V. W. (2014). Greenland ice sheet hydrology: a review. *Prog. Phys. Geogr.* 38, 19–54. doi: 10.1177/0309133313507075

Das, S. B., Joughin, I., Behn, M. D., Howat, I. M., King, M. A., Lizarralde, D., et al. (2008). Fracture propagation to the base of the Greenland ice sheet during Supraglacial Lake drainage. *Science* 320, 778–781. doi: 10.1126/science.1153360

Ferris, J. G., Knowles, D. B., Brown, R. H., and Stallman, R. W. (1962). *Theory of Aquifer Tests*. Water Supply Paper U.S. Geological Survey, 174.

Forster, R. R., Box, J. E., van den Broeke, M. R., Miège, C., Burgess, E. W., van Angelen, J. H., et al. (2014). Extensive liquid meltwater storage in firn within the Greenland ice sheet. *Nat. Geosci.* 7, 1–4. doi: 10.1038/ngeo2043

Fountain, A. G. (1989). The storage of water in, and hydraulic characteristics of, the firn of South Cascade Glacier, Washington State, USA. *Ann. Glaciol.* 13, 69–75.

Fountain, A. G. (1996). Effect of snow and firn hydrology on the physical and chemical characteristics of glacial runoff. *Hydrol. Process.* 10, 509–521. doi: 10.1002/(SICI)1099-1085(199604)10:4<509::AID-HYP389>3.0.CO;2-3

Fountain, A. G., and Walder, J. S. (1998). Water flow through temperate glaciers. *Rev. Geophys.* 36:299. doi: 10.1029/97RG03579

Freeze, A., and Cherry, J. (1979). *Groundwater*. Englewood Cliffs, NJ: Prentice Hall.

Garber, M. S., and Koopman, F. C. (1968). *Methods of Measuring Water Levels in Deep Wells*. U.S. Geological Survey Techniques of Water-Resources Investigations, 23.

Harper, J., Humphrey, N., Pfeffer, W. T., Brown, J., and Fettweis, X. (2012). Greenland ice-sheet contribution to sea-level rise buffered by meltwater storage in firn. *Nature* 491, 240–243. doi: 10.1038/nature11566

Helm, V., Humbert, A., and Miller, H. (2014). Elevation and elevation change of Greenland and Antarctica derived from CryoSat-2. *Cryosphere* 8, 1539–1559. doi: 10.5194/tc-8-1539-2014

Humphrey, N. F., Harper, J. T., and Pfeffer, W. T. (2012). Thermal tracking of meltwater retention in Greenland's accumulation area. *J. Geophys. Res.* 117, F01010. doi: 10.1029/2011JF002083

Hvorslev, M. J. (1951). *Time Lag and Soil Permeability in Ground-Water Observations*. Bull. no. 36 (Vicksburg, MS: Waterways Experiment Station, U.S. Army Corps of Engineers), 53.

Hyder, Z., and Butler, J. J. J. (1995). Slug tests in unconfined formations: an assessment of the Bouwer and Rice technique. *Ground Water* 33, 16–22. doi: 10.1111/j.1745-6584.1995.tb00258.x

Hyder, Z., Butler, J. J. J., McElwee, C. D., and Liu, W. (1994). Slug tests in partially penetrating wells. *Water Resour. Res.* 30, 2945–2957. doi: 10.1029/94WR01670

Iken, A., Fabri, K., and Funk, M. (1996). Water storage and subglacial drainage conditions inferred from borehole measurements on Gornergletscher, Valais, Switzerland. *J. Glaciol.* 42, 233–248.

Jacob, C. E. (1944). *Notes on Determining Permeability by Pumping Tests under Watertable Conditions*. US Geological Survey Open File Report.

Jacob, C. E. (1947). Drawdown test to determine effective radius of artesian well. *Trans. Am. Soc. Civ. Eng.* 112, 1047–1064.

Jansson, P., Hock, R., and Schneider, T. (2003). The concept of glacier storage: a review. *J. Hydrol.* 282, 116–129. doi: 10.1016/S0022-1694(03)00258-0

Joughin, I., Das, S. B., King, M. A., Smith, B. E., Howat, I. M., and Moon, T. (2008). Seasonal speedup along the Western flank of the Greenland ice sheet. *Science* 320, 781–783. doi: 10.1126/science.1153288

Keegan, K., Albert, M. R., and Baker, I. (2014). The impact of ice layers on gas transport through firn at the North Greenland Eemian Ice Drilling (NEEM) site, Greenland. *Cryosphere* 8, 1801–1806. doi: 10.5194/tc-8-1801-2014

Koenig, L. S., Miege, C., Forster, R. R., and Brucker, L. (2014). Initial *in situ* measurements of perennial meltwater storage in the Greenland firn aquifer. *Geophys. Res. Lett.* 41, 81–85. doi: 10.1002/2013GL058083

Kruseman, G. P., De Ridder, N. A., and Verwei, J. M. (1994). *Analysis and Evaluation of Pumping Test Data*, *2nd Edn*. Wageningen: ILRI Publication.

Kuipers Munneke, P., Ligtenberg, S. R. M., van den Broeke, M. R., van Angelen, J. H., and Forster, R. R. (2014). Explaining the presence of perennial liquid water bodies in the firn of the Greenland Ice Sheet. *Geophys. Res. Lett.* 41, 476–483. doi: 10.1002/2013GL058389

Kulessa, B., Hubbard, B., Williamson, M., and Brown, G. H. (2005). Hydrogeological analysis of slug tests in glacier boreholes. *J. Glaciol.* 51, 269–280. doi: 10.3189/172756505781829458

Lewis, S. M., and Smith, L. C. (2009). Hydrologic drainage of the Greenland Ice Sheet. *Hydrol. Process.* 23, 2004–2011. doi: 10.1002/hyp.7343

Luciano, G. L., and Albert, M. R. (2002). Bidirectional permeability measurements of polar firn. *Ann. Glaciol.* 35, 63–66. doi: 10.3189/172756402781817095

Machguth, H., MacFerrin, M., van As, D., Box, J. E., Charalampidis, C., Colgan, W., et al. (2016). Greenland meltwater storage in firn limited by near-surface ice formation. *Nat. Clim. Chang.* 6, 390–393. doi: 10.1038/nclimate2899

Meierbachtol, T. W., Harper, J. T., Humphrey, N. F., Shaha, J., and Bradford, J. H. (2008). Air compression as a mechanism for the underdamped slug test response in fractured glacier ice. *J. Geophys. Res.* 113:F04009. doi: 10.1029/2007JF000908

Miège, C., Forster, R. R., Brucker, L., Koenig, L. S., Solomon, D. K., Paden, J. D., et al. (2016). Spatial extent and temporal variability of Greenland firn aquifers detected by ground and airborne radars. *J. Geophys. Res. Earth Surf.* 121, 2381–2398. doi: 10.1002/2016JF003869

Neuman, S. P. (1982). Statistical characterization of aquifer heterogeneities: an overview. *GSA Spec. Pap.* 189, 81–102. doi: 10.1130/SPE189-p81

Oerter, H., and Moser, H. (1982). "Water storage and drainage within the firn of a temperate glacier (Vernagtferner, Oetztal Alps, Austria)," in *Hydrological Aspects of Alpine and High Mountain Areas*, ed J. W. Glen (Exeter: Proceedings Exeter Symposium), 71–81.

Oerter, H., Reinwarth, O., and Rufli, H. (1983). Core drilling through a temperate alpine glacier (Vernagtferner, Oetztal Alps) in 1979. *Z. Gletscherkd. Glazialgeol.* 18, 1–11.

Pfeffer, W. T., Meier, M. F., and Illangasekare, T. H. (1991). Retention of Greenland runoff by refreezing: implications for projected future sea level change. *J. Geophys. Res.* 96:22117. doi: 10.1029/91JC02502

Poinar, K., Joughin, I., Lilien, D., Brucker, L., Kehrl, L., and Nowicki, S. (2017). Drainage of Southeast Greenland firn aquifer water through crevasses to the bed. *Front. Earth Sci.* 5:5. doi: 10.3389/FEART.2017.00005

Schneider, T. (1999). Water movement in the firn of Storglaciaren, Sweden. *J. Glaciol.* 45, 286–294. doi: 10.3189/002214399793377211

Smith, L. C., Chu, V. W., Yang, K., Gleason, C. J., Pitcher, L. H., Rennermalm, A. K., et al. (2015). Efficient meltwater drainage through supraglacial streams and rivers on the southwest Greenland ice sheet. *Proc. Natl. Acad. Sci. U.S.A.* 112, 1001–1006. doi: 10.1073/pnas.1413024112

Sole, A. J., Mair, F. D. W., Nienow, P. W., Bartholomew, I. D., King, M. A., Burke, M. J., et al. (2011). Seasonal speedup of a Greenland marine-terminating outlet glacier forced by surface melt–induced changes in subglacial hydrology. *J. Geophys. Res.* 116:F03014. doi: 10.1029/2010JF001948

Stone, D. B., and Clark, G. C. (1972). Estimation of subglacial hydraulic properties frotn induced changes in basal water pressure: a theoretical fratnework for borehole-response tests. *J. Glaciol.* 39, 327–340.

Theis, C. V. (1935). The relation between the lowering of the piezometric surface and the rate and duration of discharge of a well using ground-water storage. *Trans. Am. Geophys. Union* 16, 519–524. doi: 10.1029/TR016i002p00519

Tóth, J. (1963). A theoretical analysis of groundwater flow in small drainage basins. *J. Geophys. Res.* 68, 4795–4812. doi: 10.1029/JZ068i016p04795

Vallon, M., Petit, J.-R., and Fabre, B. (1976). Study of an ice core to the bedrock in the accumulation zone of an Alpine glacier. *J. Glaciol.* 17, 13–28.

Van der Kamp, G. (1976). Determining aquifer transmissivity by means of well response tests: the underdamped case. *Water Resour. Res.* 12, 71–77. doi: 10.1029/WR012i001p00071

Zwally, H. J. (2002). Surface melt-induced acceleration of greenland ice-sheet flow. *Science* 297, 218–222. doi: 10.1126/science.1072708

Conflict of Interest Statement: The authors declare that the research was conducted in the absence of any commercial or financial relationships that could be construed as a potential conflict of interest.

The handling Editor declared a shared affiliation, though no other collaboration, with one of the authors LK and states that the process nevertheless met the standards of a fair and objective review.

frontiers in Earth Science

ORIGINAL RESEARCH
published: 07 February 2017
doi: 10.3389/feart.2017.00005

Drainage of Southeast Greenland Firn Aquifer Water through Crevasses to the Bed

Kristin Poinar[1], Ian Joughin[2], David Lilien[2,3], Ludovic Brucker[1,4], Laura Kehrl[2,3] and Sophie Nowicki[1]*

[1] Cryospheric Sciences Laboratory, NASA Goddard Space Flight Center, Greenbelt, MD, USA, [2] Polar Science Center, Applied Physics Laboratory, University of Washington, Seattle, WA, USA, [3] Department of Earth and Space Sciences, University of Washington, Seattle, WA, USA, [4] Goddard Earth Sciences Technology and Research Studies and Investigations, Universities Space Research Association, Columbia, MD, USA

A firn aquifer in the Helheim Glacier catchment of Southeast Greenland lies directly upstream of a crevasse field. Previous measurements show that a 3.5-km long segment of the aquifer lost a large volume of water (26,000–65,000 m^2 in cross section) between spring 2012 and spring 2013, compared to annual meltwater accumulation of 6000–15,000 m^2. The water is thought to have entered the crevasses, but whether the water reached the bed or refroze within the ice sheet is unknown. We used a thermo-visco-elastic model for crevasse propagation to calculate the depths and volumes of these water-filled crevasses. We compared our model output to data from the Airborne Topographic Mapper (ATM), which reveals the near-surface geometry of specific crevasses, and WorldView images, which capture the surface expressions of crevasses across our 1.5-km study area. We found a best fit with a shear modulus between 0.2 and 1.5 GPa within our study area. We show that surface meltwater can drive crevasses to the top surface of the firn aquifer (~20 m depth), whereupon it receives water at rates corresponding to the water flux through the aquifer. Our model shows that crevasses receiving firn-aquifer water hydrofracture through to the bed, ~1000 m below, in 10–40 days. Englacial refreezing of firn-aquifer water raises the average local ice temperature by ~4°C over a ten-year period, which enhances deformational ice motion by ~50 m $year^{-1}$, compared to the observed surface velocity of ~200 m $year^{-1}$. The effect of the basal water on the sliding velocity remains unknown. Were the firn aquifer not present to concentrate surface meltwater into crevasses, we find that no surface melt would reach the bed; instead, it would refreeze annually in crevasses at depths <500 m. The crevasse field downstream of the firn aquifer likely allows a large fraction of the aquifer water in our study area to reach the bed. Thus, future studies should consider the aquifer and crevasses as part of a common system. This system may uniquely affect ice-sheet dynamics by routing a large volume of water to the bed outside of the typical runoff period.

Keywords: firn aquifer, crevasse, englacial hydrology, meltwater runoff, meltwater retention

OPEN ACCESS

Edited by:
Horst Machguth, University of Zurich, Switzerland

Reviewed by:
Baptiste Vandecrux, Technical University of Denmark, Denmark
Ruth Mottram, Danish Meteorological Institute, Denmark

****Correspondence:***
Kristin Poinar
kristin.poinar@nasa.gov

Specialty section:
This article was submitted to Cryospheric Sciences, a section of the journal Frontiers in Earth Science

Received: *01 October 2016*
Accepted: *17 January 2017*
Published: *07 February 2017*

Citation:
Poinar K, Joughin I, Lilien D, Brucker L, Kehrl L and Nowicki S (2017) Drainage of Southeast Greenland Firn Aquifer Water through Crevasses to the Bed. Front. Earth Sci. 5:5. doi: 10.3389/feart.2017.00005

INTRODUCTION

Water at the bed of the Greenland Ice Sheet has a substantial influence on ice velocity. The transport of surface meltwater to the bed, via moulins formed from supraglacial lakes and rivers, has been well studied in western Greenland (Das et al., 2008; Clason et al., 2015). In Southeast Greenland, surface melt has been found to correlate with ice motion over only limited time periods and spatial extents, for the few outlet glaciers studied (Andersen et al., 2011; Sundal et al., 2013; Moon et al., 2014). Over inland ice, the scarcity of supraglacial lakes in Southeast Greenland is also thought to limit the effect of surface melt on basal motion (Selmes et al., 2011).

Surface melt rates can reach 3 m year^{-1} in some areas of Southeast Greenland (Franco et al., 2013), but high accumulation rates (Miège et al., 2013) and cold wintertime temperatures help retain much of the meltwater in regional firn aquifers (Kuipers Munneke et al., 2014). Springtime radar observations (Forster et al., 2014) and climate model outputs (Kuipers Munneke et al., 2014) indicate that firn-aquifer water persists englacially in liquid form year-round. Such firn aquifers cover 20,000–70,000 km^2 of the ice sheet in Southeast Greenland (Forster et al., 2014; Miège et al., 2016) and store up to approximately 140 km^3 of water or, equivalently, 0.4 mm global sea level (Koenig et al., 2014).

The volume of water stored by the aquifer can vary in time and space (Miège et al., 2016). In particular, observations of the water level in a portion of the Southeast Greenland firn aquifer in the upstream reaches of Helheim Glacier indicate a loss of water volume between spring 2012 and spring 2013 (Miège et al., 2016). This portion of the aquifer sits at approximately 1520–1550 m elevation (**Figure 1**), directly upstream of a crevasse field. It is suspected that the water drained into crevasses (Miège et al., 2016), but the depth to which this water was able to drive the crevasses, and whether the firn-aquifer water reached the bed or refroze englacially, are unknown.

Here, we use a thermo-visco-elastic model for crevasse propagation to investigate the plausibility of firn-aquifer water draining to the bed through crevasses. The model is well-suited for crevasses that terminate above the ice-sheet bed, but we extend its application, with some caution, to full-thickness hydrofractures when required. We use the crevasse model to explore multiple scenarios, including the behavior of crevasses in the absence of a firn aquifer and when fed by a range of water fluxes from the firn aquifer, and multiple values for certain physical parameters. We conclude by discussing the effect that the crevasse field—firn aquifer system may have on ice dynamics at this location.

METHODS

We study a ~1.5-km segment along an approximate flowline in the onset of the southern branch of Helheim Glacier (**Figure 1**), centered at 66.35°N, 39.07°W at surface elevation s ~1490–1520 m above sea level (a.s.l.). Radar measurements indicate that a portion of the Southeast Greenland firn aquifer terminates abruptly in this region, just above a crevasse field (Miège et al., 2016). WorldView satellite imagery (courtesy of Digital Globe, Inc.) indicates that this crevasse field comprises narrow crevasses (~1–2 m) at 1520 m a.s.l. and wider crevasses (>10 m) less than 1 km downstream, at 1510 m a.s.l. (**Figure 2A**). We generalize our study area into a conceptual model (Section "Conceptual model of firn aquifer—crevasse field system"), then apply a physically based numerical model (Section "Thermo-Mechanical Model for Crevasse Propagation") to investigate the widths and depths of crevasses within our conceptual model. **Table 1** contains all variables and physical constants used in the numerical model.

Conceptual Model of Firn Aquifer—Crevasse Field System

We represent our study area in two-dimensional model space, with a vertical dimension and a down-surface-gradient horizontal dimension (**Figures 2B–C**). We thus report model-generated volumes in two dimensions (m^2), i.e., as cross-sectional volumes. In our model, we feed the crevasses with water from different sources in turn: (1) locally generated meltwater, and (2) water from the firn aquifer.

Crevasses Fed by Local Surface Melt Only

First we consider the case of crevasses whose only water source is local snowmelt. We approximate the local catchment of a single

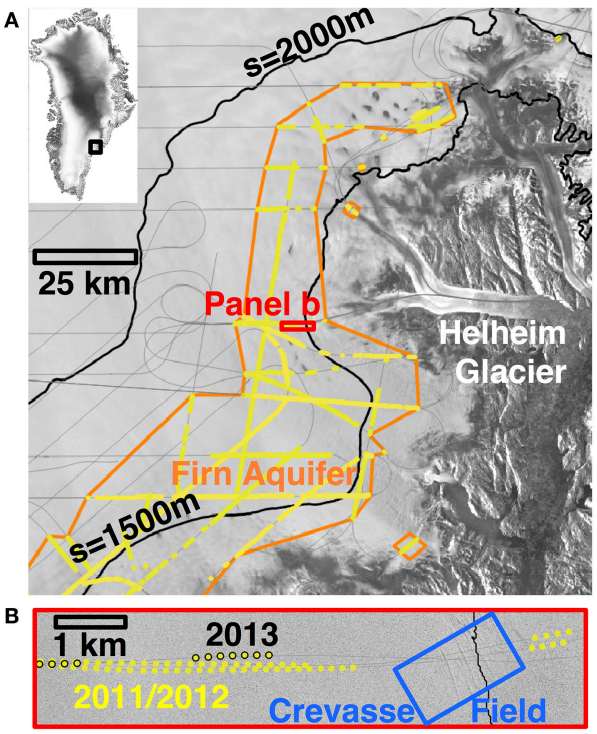

FIGURE 1 | The region in Southeast Greenland where the firn aquifer overlies the upper reaches of Helheim Glacier. (A) Operation IceBridge flight lines (2010–2014) where firn-aquifer water is detected (yellow) and is not detected (gray), with the firn aquifer extent outlined in orange (Miège et al., 2016). Background is a radar mosaic from winter 2009–2010 (Joughin et al., 2016). Image dimensions are 140 × 150 km. **(B)** An 8 × 1.5 km section of a 24 June 2016 WorldView image that includes the study area (blue box; **Figure 2A**).

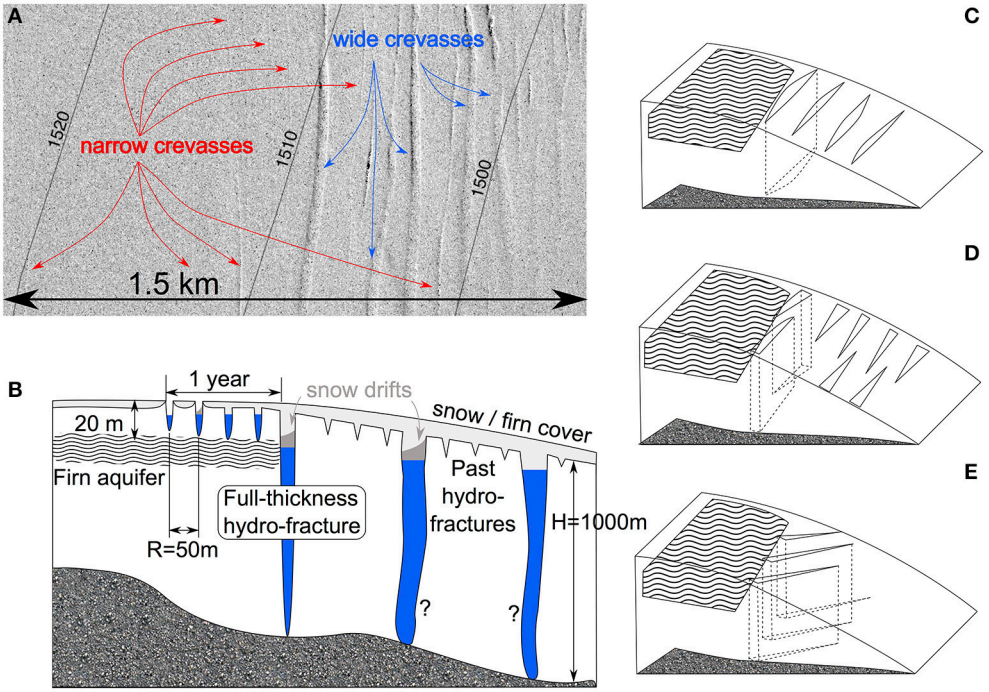

FIGURE 2 | (A) Detail of the crevasse field within our study area (blue box in **Figure 1B**). Elevation contours (Howat et al., 2014) are in m. Background is a WorldView image from 24 June 2016, courtesy of DigitalGlobe. **(B)** Conceptual model of the firn aquifer—crevasse field system. Crevasses initiate above the firn aquifer (wavy lines), which begins at a depth of 20 m. Firn aquifer water may fill the crevasses, forming a train of wide hydrofractures. **(C)** Simplified 3D view of the conceptual model of the firn aquifer—crevasse field system. **(D,E)** Alternatives to the conceptual model presented here.

crevasse within a crevasse field as the area that is closer to that crevasse than any other crevasse. That is, in a field of crevasses spaced by a distance R, each crevasse collects snowmelt that originates from the small, one-dimensional catchment of $R/2$ to either side of the crevasse. We limit the meltwater input to a crevasse to that produced within this small catchment because other crevasses collect melt generated nearby and because crevasses are usually found on topographic highs (Price et al., 2008), which isolates them from non-local meltwater sources such as supraglacial rivers.

To quantify the annual snowmelt for our study area, we use reanalysis data from MERRA-2 (Rienecker et al., 2011), which we average over 1980–2015. MERRA-2 uses a simple snowpack model for the ice-sheet surface, from which it generates surface meltwater production rates (Cullather et al., 2014). The MERRA-2 melt season is slightly longer, however, than that indicated from field observations (Forster et al., 2014). We thus adjust the model output by setting snowmelt to zero on days when the MERRA-2 average 2-m air temperature (1980–2012) is below 0°C. After this correction, the MERRA-2 output indicates an average of 0.5 m year^{-1} water equivalent of annual snowmelt in our study area, in agreement with previous mass-balance modeling of this area (McNerney, 2016).

We quantify the influx of local surface melt, Q_{local}, that enters each crevasse as

$$Q_{local} = R\,\dot{b} \qquad (1)$$

where $\dot{b}$ is the MERRA-2-derived local snow melt rate and R is the spacing between adjacent crevasses. We set R to 50 m based on our examination of WorldView imagery for our study area.

Crevasses Fed by Firn-Aquifer Water

Next, we consider the case where a firn aquifer is present ~20 m below the surface and crevasses propagate deep enough to intersect it, as illustrated in **Figures 2B–C**.

Although crevasses initiate as narrow, dry fractures in the top ~10–30 m of the ice sheet (Nye, 1955; Cuffey and Paterson, 2010), they can propagate deeper if they collect water (Weertman, 1973). We consider the firn aquifer as a possible water source to crevasses. Because the top surface of the firn aquifer in our study area lies 12–30 m below the ice-sheet surface (Forster et al., 2014; Miège et al., 2016), any water flow from the aquifer into a crevasse likely occurs below the ice-sheet surface, as suggested in **Figure 2B**.

In our model, we approximate the firn aquifer depth in our study area as a constant 20 m. When a surface-meltwater-filled crevasse reaches this depth, we assign it an influx of Q_{aq}, a value we define based on the estimated water flux through the segment of the aquifer shown in **Figure 1B**, where it abuts the crevasse field (Miège et al., 2016). This segment, and our study area as a whole, represents only a small portion of the Southeast Greenland firn aquifer (**Figure 1A**); thus, we directly analyze the influence of only a small fraction of the firn-aquifer water. In addition, the data in **Figure 1B** indicate the intermittent

TABLE 1 | Symbols and values of model parameters, variables, and physical constants.

	Symbol	Value
MODEL PARAMETERS		
Ice thickness	H	1000 m
Surface elevation	s	∼1490–1520 m a.s.l.
Crevasse spacing	R	50 m
Surface runoff rate	$\dot{b}$	0.5 m year^{-1}
Water depth in crevasse	w	Equation S3
Longitudinal stress	$\sigma_y^{'}$	Determined using Elmer (Section S1)
Shear modulus	μ	0.07–3.9 GPa
Surface boundary condition	T_{skin}	From MERRA-2 (Section S3)
Water flux	Q	
Without firn aquifer	Q_{local}	Equation 1
Firn aquifer, normal year	Q_{aq0}	5000–15,000 m^2 year^{-1}
Firn aquifer, 2012–2013	$Q_{aq12–13}$	20,000–60,000 m^2 year^{-1}
MODEL OUTPUTS		
Crevasse depth	d	
Crevasse width	$2W$	
Ice temperature	T	Section S3
Deformational velocity	u_d	Equation 4
MODEL COMPONENTS		
Elastic component		Section S1
Elastic deformation over one timestep	$e(z)$	Equation S1
Total elastic deformation over model time	$E(z)$	Equation S4
Viscous (creep) component		Section S2
Total creep deformation over model time	$C(z)$	Determined using Elmer
Freezing component		Section S3
Total thickness refrozen over model time	$F(z)$	Equation S6
PHYSICAL CONSTANTS		
Density of water	ρ_w	1000 kg m^{-3}
Density of ice	ρ_i	910 kg m^{-3}
Thermal conductivity of ice	k_i	2.1 J m^{-1}K^{-1}s^{-1}
Latent heat of freezing	L_f	335,000 Jkg^{-1}
Specific heat capacity of ice	C_p	2115.3 Jkg^{-1}°C^{-1}
Gravitational constant	g	9.8 m s^{-2}
Flow-law parameter	$A(T)$	Cuffey and Paterson (2010), Equation 3.30
Driving stress	τ_d	100 kPa
Poisson's ratio	ν	0.3
Fracture toughness	K_{IC}	0.1 MPa m$^{1/2}$

presence of a ∼500 m long firn aquifer downstream of the crevasse field we study. Water in this small aquifer may be sourced from the aquifer upstream (i.e., the water travels through the crevasse field) or from local surface melt (i.e., the water is distinct from upstream aquifer water). Our present model setup cannot constrain these hypotheses; we thus eliminate from our analysis the area downstream of the blue box in **Figure 1B**.

We assume in our two-dimensional model that only one crevasse can intersect the firn aquifer at a given time. That is, any upstream crevasse with depth greater than 20 m will cut off all downstream crevasses from the firn-aquifer water (**Figure 2B**). In a three-dimensional world, however, two or more crevasses at similar elevations could connect to the firn aquifer (**Figure 2D**). Alternately, crevasses may strike obliquely to the firn-aquifer boundary, so that firn-aquifer water could enter many crevasses simultaneously (**Figure 2E**). WorldView imagery (**Figure 1B**) suggests, however, that crevasses strike approximately parallel to the firn-aquifer boundary, supporting our assumption, in two dimensions, that the firn-aquifer water flows into one crevasse at a time (**Figures 2B–C**). Therefore, we discard the alternate scenarios (**Figures 2D–E**) from this analysis, although future, more detailed studies should consider them.

We vary the value of Q_{aq} to reflect two specific scenarios. First, we define Q_{aq0} as the background water flux through the aquifer. We base Q_{aq0} on estimates of snowmelt directly upstream of this portion of the firn aquifer and on the results of a groundwater flow model constrained with radar observations and field estimates (Miège et al., 2016). There is considerable uncertainty in this value due to the assumption of spatially uniform aquifer thickness, uncertainties in the value of hydraulic conductivity, and steady-state 2D modeling that does not include seasonal variations in water input or 3D effects such as catchment extent and lateral water flow. We use a range of Q_{aq0} estimates between 6000 m^2 year^{-1} (determined by summing snowmelt) and 15,000 m^2 year^{-1} (determined by McNerney, 2016 from groundwater flow modeling) to define the range of values we test: Q_{aq0} = 5000, 10,000, and 15,000 m^2 year^{-1}. We vary Q_{aq0} over this wide range to reflect the uncertainties in its estimation.

We also consider $Q_{aq12–13}$, which represents the enhanced water flux during the 2012–2013 aquifer drainage event. We define this quantity based on differences in the water levels identified in springtime radar observations for these 2 years (Miège et al., 2016). We subtract the observed level (top surface) of the firn aquifer in 2013 from that in 2012 over the ∼3.5-km segment of the aquifer where the water surface dropped or disappeared completely (**Figure 1B**). This method yields a water flux $Q_{aq12–13} \sim$ 65,000 m^2 year^{-1}. However, groundwater flow modeling suggests that some of the water from this 3.5-km segment may discharge at the surface at topographic inflection points, where it would refreeze (Miège et al., 2016) before reaching the crevasse field. If such discharge occurs, our initial estimate of $Q_{aq12–13}$ may be too high. Thus, we also consider a scenario where water from only the lower 1–1.5 km of the transect, which is downstream of the lowest modeled hydraulic discharge point (McNerney, 2016), drains into the crevasse field. This second scenario gives $Q_{aq12–13} \sim$ 26,000 m^2 year^{-1}. To reflect uncertainties, we test three values of $Q_{aq12–13}$: 20,000, 40,000, and 60,000 m^2 year^{-1}.

Even using the smallest values, the aquifer-sourced water flux into crevasses ($Q_{aq} \sim 10^3$–10^4 m^2 year^{-1}) exceeds the flux from local snowmelt ($Q_{local} \sim 10^1$–10^2 m^2 year^{-1}) by approximately two orders of magnitude. We use these estimates of water flux to drive our model for the geometry of crevasses.

Thermo-Mechanical Model for Crevasse Propagation

When a sufficient volume of water flows into a crevasse, it will elastically open and deepen the crevasse (Weertman, 1996). Over a longer timescale (days to years), the crevasse walls will close viscously (through creep) as well as elastically, narrowing the crevasse and making it shallower. The meltwater inside will also steadily refreeze onto the crevasse walls, which diffusively warms the surrounding ice and contributes further to the closing and shoaling of the crevasse. Our crevasse model calculates the shape and depth of crevasses based on these elastic, viscous, and refreezing processes, which we model independently:

$$W(z) = E(z) + C(z) - F(z) \quad (2)$$

Here, *W(z)* denotes the half-width of a crevasse, symmetric about its vertical axis, as a function of the vertical coordinate *z*. The terms *E(z)*, *C(z)*, and *F(z)* represent the elastic deformation, creep (viscous) deformation, and refreezing, respectively, that have occurred cumulatively over the model time. Details of these components of the model can be found in the Supplementary Material. The elastic component of our model has previously been applied to calculate the propagation of full-thickness hydrofractures in western Greenland (Krawczynski et al., 2009). That study considered crevasses in bare ice in the ablation zone, whereas we consider crevasses in a firn-covered portion of the ice sheet. This approach introduces some limitations, which we discuss in Section "Influence of firn on crevasse width and shear modulus."

The model runs for 10 years or until any one crevasse reaches the bed. At each timestep of the model, we first calculate V_{water}, the cross-sectional volume of water that the crevasse is required to hold at that timestep, from the time-integrated water influx minus the total volume of water that has exited the crevasse by refreezing englacially onto the crevasse walls. We then solve for the crevasse depth *d* for which the volume of the crevasse, integrated from the crack tip *d* to the water line *w*, equals V_{water}:

$$2\int_d^w W(z)\, dz = V_{water} \quad (3)$$

Crevasse Water Balance and Cryo-Hydrologic Warming

The propagation of a water-filled crevasse brings meltwater into contact with cold englacial ice, causing some of that water to refreeze, which warms and softens the ice and allows further deformation to occur. This process, cryo-hydrologic warming, has been observed in western Greenland (Phillips et al., 2010; Lüthi et al., 2015) in crevassed ice in the ablation zone. Here, we evaluate whether cryo-hydrologic warming likely is occurring in our study area, which is higher on the ice sheet than previous studies of cryo-hydrologic warming have considered. Our thermal model calculates the quantity of water refrozen englacially over time and the effect of the consequent release of latent heat on ice temperature across the modeled crevasse field (i.e., in ice between and below crevasses). We use these temperatures to calculate the expected deformational velocity of ice within our model domain, through a standard Arrhenius relation for the flow-law parameter, *A(T)* (Cuffey and Paterson, 2010). For a given driving stress τ_d, warmer ice will deform at a faster rate than colder ice. We calculate the deformational velocity u_d of ice with temperature profile *T(z)* over the thickness *H* as follows:

$$u_d = \tau_d^3 \int_b^s \left[A(T(z)) \left(1 - \frac{z}{H}\right)^3 \right] dz \quad (4)$$

We average u_d over all ice columns in the model (i.e., across a crevasse field) to calculate the deformational velocity of ice in our study area.

Shear Modulus and Other Model Parameters

The visco-elastic model incorporates a number of material parameters, the values of some of which are poorly constrained for glacial ice. For instance, studies have approximated the fracture toughness K_{IC} from 30 kPa $m^{1/2}$ (Mottram and Benn, 2009) to 150 kPa $m^{1/2}$ (Sassolas et al., 1996). Model runs over a range of values of these and other parameters (Poinar, 2015) indicate that the modeled crevasses are less sensitive to K_{IC} (as also found by van der Veen, 1998; Alley et al., 2005; Mottram and Benn, 2009) and background longitudinal stress σ_y' (consistent with Krawczynski et al., 2009), and more sensitive to crevasse spacing *R* (consistent with Sassolas et al., 1996) and shear modulus μ (consistent with Krawczynski et al., 2009). Crevasse spacing often varies widely across a single crevasse field, but we approximate it as a constant value in our model. Because of this limitation, we do not explore sensitivity to crevasse spacing. We focus instead on the shear modulus μ.

Vaughan (1995) summarized field and laboratory studies of μ and used μ = 0.2–0.5 GPa to model the flexure of Antarctic ice shelves. Krawczynski et al. (2009) proposed values of μ = 0.32, 1.5, and 3.9 GPa for hydrofractures in western Greenland. We use the Krawczynski et al. (2009) values as a starting point in our model but also test lower values of μ (0.18, 0.10, and 0.07 GPa). We discuss the reasons for and implications of varying μ across this range in Section "Influence of firn on crevasse width and shear modulus."

Remote Sensing of Crevasse Widths

We quantify crevasse widths from remotely sensed data to validate our model output.

ATM Data

NASA Operation IceBridge (OIB) has flown the Airborne Topographic Mapper (ATM) laser altimeter since 2009 (Krabill, 2010). The ATM scans the ice-sheet surface in a conical pattern and returns a swath of dense topographic measurements with vertical accuracy ~10 cm and horizontal accuracy ~3 cm (Martin et al., 2012). We used ATM observations from 17 April 2012 of wide crevasses in our study area to compare to crevasse widths predicted in our model. Because this flight, and most other OIB flights over our study area, occurred in spring, we expect the accumulated snow to bridge any shallow, narrow crevasses and to mute the surface expression of wider, deeper crevasses. We thus

use the ATM data to indicate the shapes and approximate sizes of the widest and deepest crevasses in our study area.

WorldView Imagery

We used high-resolution (pixel size ∼0.5 m) imagery from the WorldView-1 satellite, courtesy of DigitalGlobe, Inc., to study the widths of crevasses within our study area. We surveyed images from 7 August 2014, 1 August 2015, and 19 July 2016 for crevasses and outlined each crevasse from tip to tip, when possible. Image borders, snow cover, and image resolution (for very narrow crevasses) sometimes limited the extent of our digitization. We calculated the average width of each crevasse by dividing its two-dimensional area in the image by its length. We identified 30, 38, and 56 crevasses from the 2014, 2015, and 2016 images, respectively, for a total of 124 crevasses. Because a crevasse will advect ∼200 m downstream over the course of a year and our study area spans ∼3 km, our dataset likely includes many of the same crevasses reappearing from year to year.

Because we average the width over the entire crevasse, including very narrow end points, our technique should yield a smaller crevasse width than what is usually reported at the widest central span. At the same time, our dataset also likely omits a number of the narrowest crevasses, which the 0.5 m resolution of the imagery does not adequately resolve. We thus use this dataset, which excludes narrower crevasses that we did not model, to outline an approximate distribution of crevasse width in our study area.

RESULTS

We ran our model forced with various meltwater sources and using various values for certain parameters. We then compared our model results for crevasse width at the ice-sheet surface to observations of crevasse width at the ice-sheet surface. Here we present the results of these simulations.

Evidence for Water-Filled Crevasses

Previous observations suggest that dry (non-water-filled) crevasses in grounded ice can reach widths of 2–3 m (Cook, 1956; Holdsworth, 1969) in northern Greenland and Antarctica, respectively. Crevasses observed near the calving faces of tidewater glaciers, on the other hand, are typically very wide: ∼20–30 m on Jakobshavn Isbræ, for instance (Echelmeyer et al., 1991). These large widths are due to both high extensive stresses and the widening pressure from liquid water that fills these crevasses. Meier et al. (1957) observed 30-m-wide crevasses in northwest Greenland far from any calving faces; these crevasses, however, were exceptional in their age and flow history (Colgan et al., 2016) and may have contained moderate amounts of water (Meier et al., 1957). Based on these previous observations, we take 2–3 m as an approximate maximum width for dry crevasses.

OIB data from 17 April 2012 show multiple wide (>5 m) crevasses at $s \sim 1490$–1510 m a.s.l. in our study region. Images from the Digital Mapping System (DMS; **Figure 3A**) show sastrugi extending off of the southeast ends of three of the deepest crevasses. ATM data, collected concurrently, show that three crevasses are approximately 7, 11, and 10 m wide at the surface (**Figures 3B–D**, respectively), substantially wider than the 2–3 m we identify for dry crevasses. Thus, we hypothesize that these crevasses are water-filled. The top surface of this water would likely freeze over winter, providing a platform onto which windblown snow could collect (**Figure 3E**). Alternately, a snow bridge may form between the crevasse walls in the uppermost tens of m, independent of any such seasonal ice layer. The ATM and DMS data show that snow fills these crevasses to depths of 6–12 m, likely blown in by the wintertime winds that formed the sastrugi.

These wide crevasses are located <1 km downstream of the lower border of the firn aquifer in this area (**Figure 1B**). As noted above, the firn aquifer is the largest source of water in the area, greatly exceeding the local melt supply (Section "Crevasses Fed by Firn-Aquifer Water"). Based on this observation, we hypothesize that these crevasses may have been widened by firn-aquifer water. We use our crevasse model to test this hypothesis.

Modeled Crevasses Isolated from the Firn Aquifer

We first investigate the expected springtime widths of crevasses if the firn aquifer were not present by running our model with a meltwater influx of Q_{local} (Equation 1). That is, only snowmelt generated within $R = 50$ m of each crevasse is fed to the crevasse. We make this assumption because crevasses tend to form on or near local rises; therefore, their meltwater catchments are topographically limited.

We run our model with Q_{local} for 10 years allowing ice to advect through our 2-km-wide study area at 200 m year^{-1}. **Figure 4** shows the time series of crevasse depth, modeled using various values for the shear modulus of ice (colors). Crevasses in ice with high shear moduli ($\mu = 1.5$ GPa) seasonally penetrated to depths up to 500 m, while crevasses in ice with lower shear moduli ($\mu = 0.32$ GPa) reached depths of ∼200–300 m. In all cases, the crevasses refroze all their water and closed up each winter. Ice with a high shear modulus (stiff ice) cannot open wide, and thus a crevasse must extend relatively deep to hold the volume of water produced by local snow melt. The variation of our results with shear modulus is consistent with the modeling conclusions of Krawczynski et al. (2009).

We found that crevasses modeled in ice with high shear moduli ($\mu = 1.5$–3.9 GPa) had surface widths of 0.1–0.2 m. These widths are smaller than the 0.5 m pixel size of the 2016 WorldView imagery, which clearly shows ∼1-m-wide crevasses initiating at high elevations ($s \sim 1520$ m; **Figure 2A**). Crevasses modeled with $\mu = 0.32$ GPa were 0.5 m wide, slightly narrower than indicated by the imagery. To produce crevasses with widths consistent with our imagery observations, we also tested lower shear moduli ($\mu = 0.18$, 0.10, and 0.07 GPa), which may reflect the influence of the firn layer, as we discuss further in Section "Influence of firn on crevasse width and shear modulus". These values yielded crevasses with surface expressions of 0.7–1.0 m, a better match to the high-elevation crevasses. We use this full set of shear moduli (μ ranging over 0.07–3.9 GPa) in subsequent model runs.

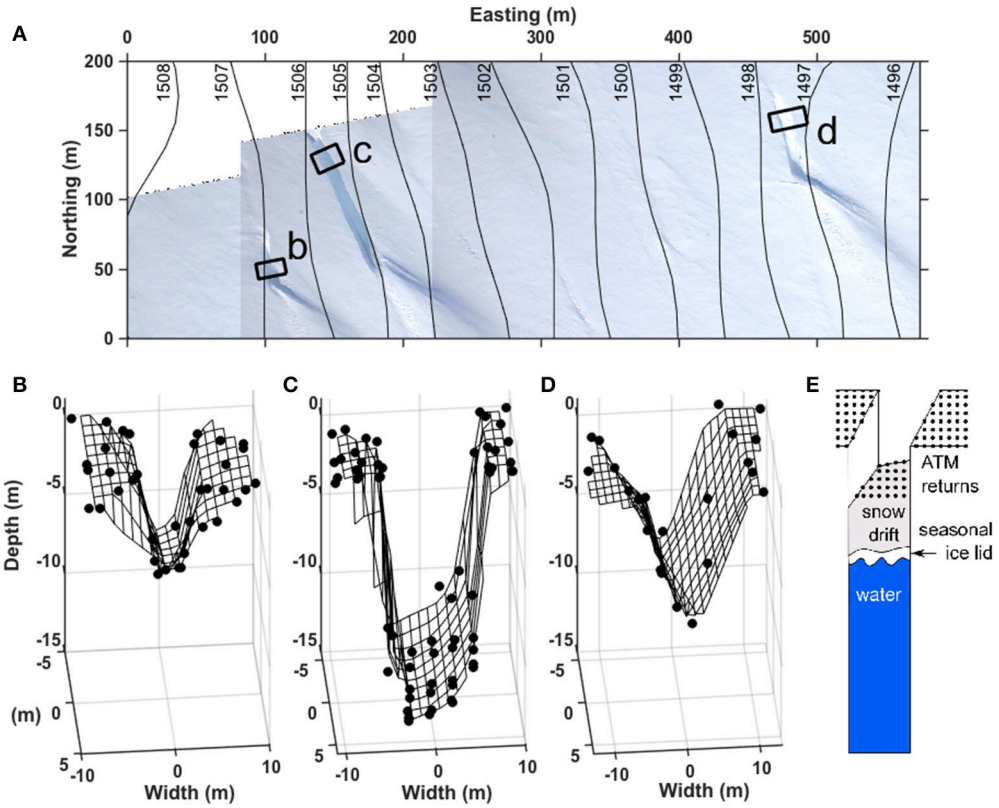

FIGURE 3 | (A) Mosaic of Digital Mapping System (DMS) images from 17 April 2012 of the crevasse field study area. Elevations from the GIMP DEM (Howat et al., 2014) are overlain. **(B–D)** Returns from the Airborne Topographic Mapper (ATM) from 17 April 2012 for the three areas outlined in panel a. Black dots indicate level-1 returns, with a triangulation-based, linearly interpolated mesh to guide the eye. Crevasse widths are **(B)** 7, **(C)** 11, and **(D)** 10 m. **(E)** Schematic interpretation of the surfaces that give ATM returns.

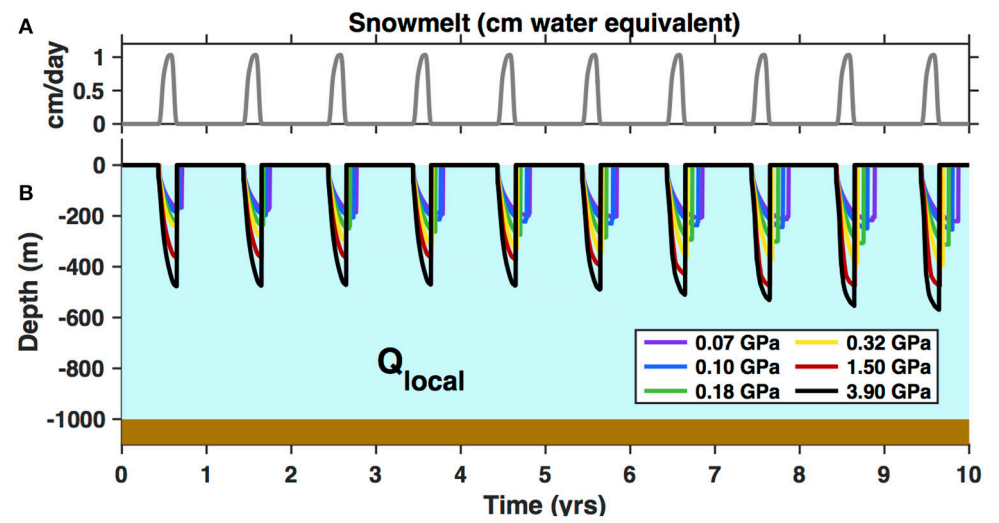

FIGURE 4 | (A) MERRA-2-derived surface melt rates, in water-equivalent units, averaged over 1980–2015 at our study site, which we used to inform Q_{local}, the meltwater influx into crevasses in the absence of a firn aquifer (Equation 1). **(B)** Time series of the depth of crevasses receiving Q_{local}. Colors indicate the values for shear modulus tested and are consistent across other figures.

We were unable to reproduce the observed crevasse widths of 6–11 m at $s \sim 1500$ m a.s.l. (**Figure 3**) using Q_{local}; in fact, our modeled widths are almost an order of magnitude too low. Thus, we conclude that Q_{local} provides an insufficient meltwater volume to explain these observations. We do find, however, that crevasses fed by local snowmelt (Q_{local}) reach well beyond the depth of the firn aquifer (20 m), for all values of the shear modulus we tested (**Figure 4**). Thus, firn aquifer water should drain into crevasses in this area, consistent with our conceptual model (**Figure 2B**).

Modeled Crevasse Field—Firn Aquifer System

We next run our model with higher water fluxes, Q_{aq0} and $Q_{aq12-13}$, which represent the water fluxes through the firn aquifer in our study area in typical years and in 2012–2013, respectively.

Penetration to the Bed

We first investigate how deep the water fluxes from the firn aquifer can drive crevasses in our model. For all values of the shear modulus we tested ($\mu = 0.07$–3.9 GPa) and for all values for firn-aquifer-sourced water flux that we tested ($Q_{aq0} = 5000$–$15{,}000$ m^2 year^{-1} and $Q_{aq12-13} = 20{,}000$–$60{,}000$ m^2 year^{-1}), we found that crevasses hydrofractured through the full thickness of the ice sheet ($H = 1000$ m) in less than 180 days. We use observations of the surface widths of crevasses in our study area to adjust the shear modulus we use in our model, in an effort to better constrain the amount of time required for firn-aquifer water to drive crevasses to the bed.

Comparison to Observed Surface Widths

We compare the surface widths of crevasses modeled using the median value of Q_{aq0}, 10,000 m^2 year^{-1}, to the dataset of observed surface widths. **Figure 5A** shows ATM data from $s \sim 1500$ m a.s.l. (**Figure 3C**) alongside the walls of crevasses modeled using all values of the shear modulus we tested. Once again, previously accepted values of μ (0.32–3.9 GPa) produce crevasses (0.3–5 m) that are substantially narrower than this crevasse (11 m). While lower values of μ (0.07–0.18 GPa) generate wider crevasses, we seek further evidence that these values, which are outside the previously published range (Vaughan, 1995), are realistic for our study area.

Figures 5B,C compare the modeled crevasse widths to the set of 124 observed crevasse widths in our study area. The observed crevasses show a general widening trend along flow (**Figure 5B**; $r^2 = 0.8$). The calculated longitudinal stress at the ice-sheet surface (Section S1) increases smoothly from 120 to 150 kPa across the first kilometer of **Figure 5B**, as the crevasses widen, then decreases smoothly to 110 kPa along the next kilometer while the crevasses continue to widen. This lack of correlation suggests that the local stress field is unlikely the cause of the observed along-flow increase in crevasse width. We also consider enhanced ablation of crevasse walls (Cathles et al., 2011) due to trapping of solar radiation (Pfeffer and Bretherton, 1987). Using results from Cathles et al. (2011) appropriate for our study area, we estimate that this effect (<0.5 m year^{-1} widening) accounts for up to approximately half of the trend we see (1.2 m year^{-1} widening).

We note an asymmetry in the along-flow crevasse width data (**Figure 5B**). Very few narrow crevasses (<5 m wide) occur downstream of the first ~500 m of our study area; in contrast, wide crevasses (>10 m wide) appear throughout the study area.

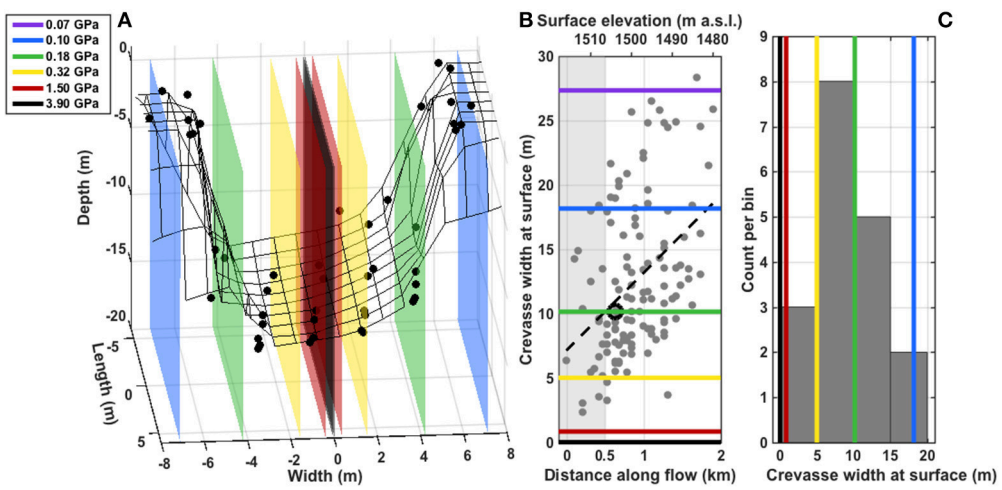

FIGURE 5 | (A) ATM data (black points) from 17 April 2012 for the crevasse shown in **Figure 3C**. Colored surfaces show the modeled crevasse walls for $Q_{aq0} =$ 10,000 m^2 year^{-1} using various values of the shear modulus. **(B)** Average surface width of 124 crevasses (identified in WorldView images) versus elevation (Howat et al., 2014) and horizontal distance along flow. Dashed black line shows the linear fit; black circle shows the crevasse detailed in panel **(A)**. The colored lines show modeled crevasse widths at the surface for $Q_{aq0} = 10{,}000$ m^2 year^{-1} and various values of the shear modulus. **(C)** Histogram of the average surface widths of the 18 crevasses within the first 500 m downstream of the firn-aquifer boundary (gray area in panel **B**). The colored lines show modeled crevasse widths at the surface for $Q_{aq0} = 10{,}000$ m^2 year^{-1} and various shear moduli.

We hypothesize that the narrower crevasses penetrate to less than the full ice thickness (that is, they are in the process of hydrofracturing), and that wider crevasses have reached the bed. The physics behind our model assume an infinite ice thickness, which is violated as the crevasses approach the bed. Hence, we are cautious about comparing modeled crevasse widths with observations in regions where crevasses may extend to the bed, as we discuss later (Sections "Effect of Finite Ice-Sheet Thickness and S1"). We therefore confine our analysis to the ~500 m segment at the upstream end of our study area (gray area in **Figure 5B**), where the narrower observed widths are more likely to represent crevasses ($d < H$) than full-thickness rifts ($d = H$). These data are fit best by the model results with $\mu = 0.32$ GPa, for which crevasse width varies from 3 to 7 m over the 5000–60,000 m^2 $year^{-1}$ range of Q we consider (**Figure 6A**). We thus focus our analysis on model results generated with $\mu = 0.32$ GPa while also considering our results for the full range of shear modulus we test.

Hydrofracture Driven by Average Firn-Aquifer Water Flux

Over many years, the average water flux through this section of the firn aquifer should balance the average annual snowmelt volume in the catchment, 6000–15,000 m^2 $year^{-1}$ (Miège et al., 2016), if the firn aquifer is in mass balance. For $\mu = 0.32$ GPa, we find that a full-thickness hydrofracture can form in just 22–37 days (**Figure 6B**), depending on the influx Q_{aq0} (5000, 10,000, or 15,000 m^2 $year^{-1}$). Immediately before reaching the bed, the cross-sectional volume of water held in the modeled crevasse is 500–900 m^2, depending on Q_{aq0} (**Figures 7A,B**).

Hydrofracture Driven by 2012–2013 Firn-Aquifer Water Flux

The drop in the firn-aquifer water level observed over 2012–2013 (Miège et al., 2016) suggests that a much larger volume of water, 26,000–65,000 m^2, exited the firn aquifer over this one-year period. Model results with $Q_{aq12-13} = 20{,}000$, 40,000, and 60,000 m^2 $year^{-1}$ suggest that this higher volume may have generated slightly wider crevasses (5–7 m; **Figure 6A** with $\mu = 0.32$ GPa) than did Q_{aq0} (3–5 m), and that these crevasses reached the bed more quickly (11–18 days for $\mu = 0.32$ GPa; **Figures 6B**, **7C, D**). Extensive snow cover obscures these crevasses in the 2013–2015 OIB campaigns, so it was not possible to compare crevasse widths modeled with $Q_{aq12-13}$ to ATM measurements.

Englacial Refreezing and Deformational Ice Motion

We track the volume of meltwater refrozen within each crevasse over its lifetime in the model (i.e., until it reaches the bed). For Q_{local}, the entirety of the meltwater refreezes each winter, and because crevasses penetrate only to depths of <500 m (**Figure 4**), no water is lost to the bed. Thus, in the scenario where the firn aquifer does not exist, 100% of the surface meltwater would refreeze englacially. **Figure 8A** shows that this would warm the ice by 1.8°C, averaged over all depths

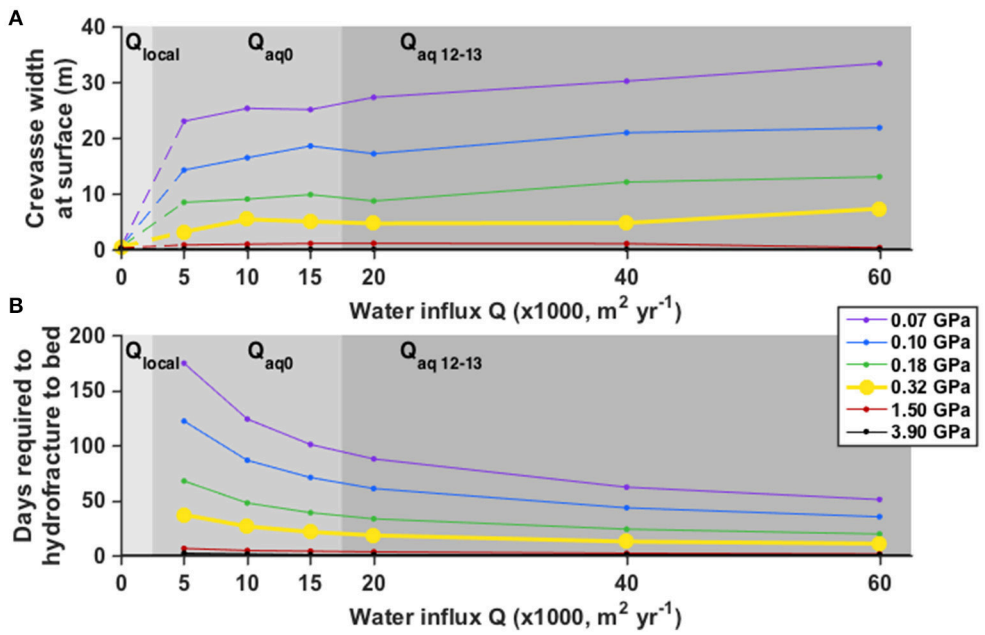

FIGURE 6 | Model results for various influx values *Q* (x-axis) and shear moduli (colored curves). Results for the best-fit shear modulus, $\mu = 0.32$ GPa (yellow), are in bold. Influx regimes are indicated by the gray shading: lightest gray, local snowmelt only (Q_{local}); medium gray, background aquifer flux (Q_{aq0}); dark gray, 2012–2013 aquifer flux ($Q_{aq12-13}$). **(A)** Modeled crevasse width at the ice-sheet surface at the timestep just before the crevasse reaches the bed. For Q_{local} (dashed lines), crevasse widths at model time of 10 years are shown. **(B)** Model results for the time required for firn aquifer water to drive a crevasse 1000 m deep to the bed. For Q_{local}, crevasses did not reach the bed.

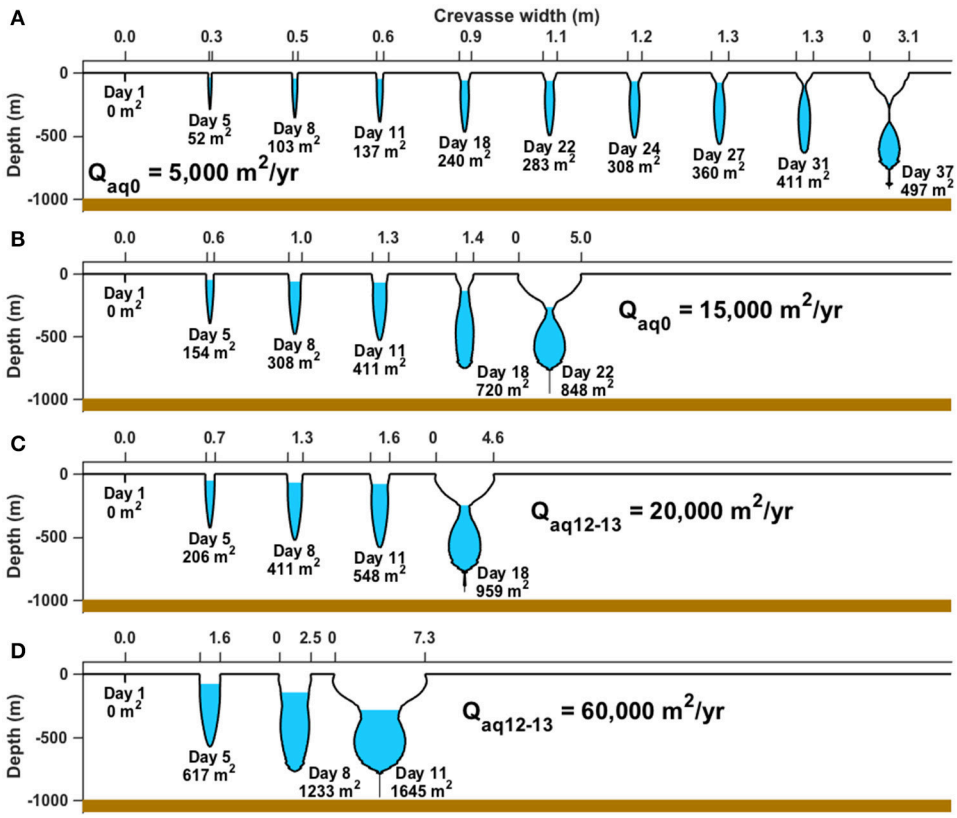

FIGURE 7 | Evolution of modeled crevasse geometry over time (increasing rightward) for $\mu = 0.32$ GPa (all panels) and (A) $Q_{aq0} = 5000$ m^2 year^{-1}, **(B)** $Q_{aq0} = 15{,}000$ m^2 year^{-1}, **(C)** $Q_{aq12–13} = 20{,}000$ m^2 year^{-1}, and **(D)** $Q_{aq12–13} = 60{,}000$ m^2 year^{-1}. Labels at each crevasse show the crevasse life time and the total volume of water accepted by the crevasse at that time.

and the full horizontal extent of the modeled crevasse field. This would enhance deformational ice motion by 6.5 m year^{-1} (**Figure 8A**).

For Q_{aq0} and $\mu = 0.32$ GPa, we find that a cross-sectional meltwater volume of 50–80 m^2 refreezes in the ∼20–40 days over which the crevasse hydrofractured to the bed. For $Q_{aq12–13}$, the modeled crevasses refroze 30–40 m^2 over ∼10–20 days. These volumes are less than 10% of the volume of firn-aquifer water that went into the crevasse over these time periods (∼1000–3000 m^2). After a crevasse reaches the bed, its heat balance becomes more complicated due to unknown influxes and outfluxes of water with the basal system. Thus, we do not calculate refreezing rates within crevasses after this point, but we do continue to calculate the temperature of the ice between crevasses, assuming that the crevasse walls remain in contact with water and thus provide 0°C boundary conditions (see Section S3). Performing these calculations over the duration of the ten-year model run shows a 4°C increase in ice temperature averaged over all ice within the crevasse field, which enhances ice deformation by ∼50 m year^{-1}. This is a substantial portion of the observed surface velocity, which includes both deformation and sliding, of ∼200 m year^{-1} in our study area.

DISCUSSION

Model Assumptions

We make a number of approximations in our representation of this problem. Here we discuss some of the limitations of our approach.

Influence of Firn on Crevasse Width and Shear Modulus

Our model was developed for application to exposed glacial ice in the ablation zone, in the absence of firn. Our application of this model to our study area, where approximately 35 m of firn overlies the ice, therefore may introduce errors: the weak firn layer should be less able to support the high stresses that fractures generate. Thus, in the presence of firn, crevasses must propagate deeper to balance these stresses, compared to a scenario of uniform glacial ice (van der Veen, 1998). In our model, fracture propagation depths therefore may be too shallow. Thus, the lack of a firn layer in our model may cause us to overestimate the time required for water to hydrofracture to the bed.

We also speculate on the influence of the firn layer on our value of the shear modulus, which we adjusted to match observed crevasse widths. Our model assumes a constant shear modulus

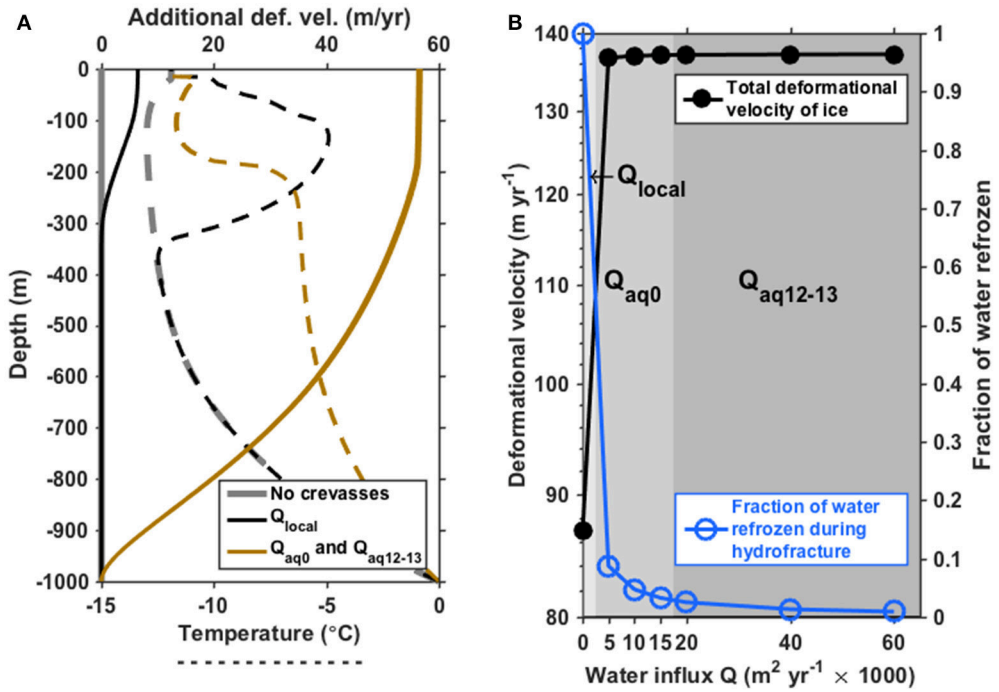

FIGURE 8 | (A) The effect of crevassing on mean englacial temperature (dashed lines; bottom axis) and deformational velocity (solid lines; top axis) for shear modulus $\mu = 0.32$ GPa. Velocity difference is the difference between deformational velocity calculated based on the temperature profile of uncrevassed ice (gray dashed line) and that calculated for each influx Q (brown and black dashed lines). **(B)** Total deformational velocity averaged over the crevasse field (black; left axis) and fraction of firn-aquifer water that refreezes onto the crevasse walls (blue; right axis), as a function of water influx Q, for a 10-year model run with $\mu = 0.32$ GPa. Influx regimes are indicated by the gray shading, as in **Figure 6**.

with depth, yet the range of shear moduli for snow ($\mu = 8.5 \times 10^{-4} - 0.02$ GPa; Sigrist, 2006) is at least two orders of magnitude lower than the accepted values for ice, suggesting that firn should have a substantially lower shear modulus than ice. Because we chose μ to match surface widths, where the crevasses outcrop through firn, our value of $\mu = 0.32$ GPa, which is at the low end of previously published values for ice, may partially reflect the influence of firn. This value, which we borrowed from a previous study (Krawczynski et al., 2009), implies a level of precision that is inconsistent with our confidence in its value. However, considering the relatively poor fit of the results of our model using other values of μ, we have confidence in the bounds of $0.2 < \mu < 1.5$ GPa, averaged over the ice column in our study area.

Effect of Finite Ice-Sheet Thickness

We find a wide distribution of crevasse width in our study area (**Figure 5B**) and identified a set of values of shear modulus that fit these observations. Because wider crevasses appear farther along flow, the best-fit shear modulus appears to decrease along flow (**Figure 5C**). In reality, the shear modulus is unlikely to vary greatly between crevasses within our relatively small study area; instead, the apparent need for lower shear moduli likely reflects the limitations of our model.

Our model assumes that crevasses exist within an ice sheet of infinite thickness, which provides cryostatic resistance at the crack tip that limits the opening width of the crevasse. A nearby basal boundary, however, alters the stress field around the crack tip (Weertman, 1996; van der Veen, 2007), which may limit the accuracy of our model for crevasses that approach the bed. This limitation of our crevasse model precludes our ability to explore the along-flow variability in crevasse width (Section "Comparison to observed surface widths").

Figure 7 shows that as a crevasse approaches the bed, our model starts to predict unusual shapes that require rapid deformation of the crevasse walls. In general, crevasse geometries evolve smoothly until the crevasse reaches a depth of approximately $0.8H$, at which point the crevasses widen considerably, exhibit increased necking at the water line, and sometimes develop isolated reservoirs (e.g., **Figure 7A**). Although the latter two features are consistent with the model results of Weertman (1973) in infinite ice, our awareness of the basal boundary effects compels us to interpret the modeled shapes of deep crevasses ($d > 0.8H$) with caution.

Volumetric Constraints on Englacial Water Storage

The results of our model show that the influx of firn-aquifer water into the crevasse field is sufficient to drive our modeled crevasses to the ice-sheet bed 1000 m below. Here, we introduce a second line of reasoning to add to our confidence that firn-aquifer water reaches the bed.

We consider a hypothetical case where firn-aquifer water resides permanently within crevasses that are shallower than $H =$ 1000 m. Were this to occur, the firn-aquifer water would slowly refreeze englacially without reaching the bed. To perform this test, we compare the volume of crevasses in our model to the volume of water lost by the firn aquifer in the scenarios Q_{aq0} and Q_{12-13}.

Figure 7 shows the time evolution of the geometry of crevasses modeled using Q_{aq0} and Q_{12-13}. As the crevasses collect more water over time, they widen and deepen. We calculate the volume of meltwater that a crevasse holds at the penultimate timestep of our model (rightmost crevasses on **Figure 7**), when the crevasse has reached its maximum depth before breaking through to the bed. **Figure 7** shows these cross-sectional volumes for each crevasse. These volumes are the sum of the volume of liquid water held inside the crevasse and the water-equivalent volume that has refrozen onto the crevasse walls. These span ∼900–1600 m^2, depending on Q_{aq0}. These volumes are less than the annual volume flux of water through the firn aquifer (5000–15,000 m^2 for Q_{aq0}) by approximately a factor of 5–10, suggesting that it would take 5–10 such crevasses to englacially store the annual volume of water lost by the firn aquifer.

In our conceptual model, shallow crevasses spaced by 50 m advect across the firn aquifer at ∼200 m $year^{-1}$; thus, only 4 crevasses annually can receive firn-aquifer water. It is possible, within uncertainties, that firn-aquifer water could reach 5 or more crevasses in 1 year and drive them to within tens of m of the bed. Such deep hydrofractures, however, would be likely to ultimately reach the bed through additional creep deformation, by intersecting with a basal fracture, by advecting onto a bedrock high, or by the addition of more meltwater beyond our one-year model time. Thus, we reason that firn-aquifer water likely reaches the ice-sheet bed near the downstream end of the aquifer, and that this happens regularly (i.e., with Q_{aq0}).

We repeat this analysis for the higher water fluxes $Q_{aq12-13}$. The cross-sectional water volumes that each crevasse holds immediately before reaching the bed range over ∼1800–3100 m^2, larger than crevasse capacities modeled with Q_{aq0}. At the same time, the volume of firn-aquifer water lost (20,000–60,000 m^2) is a factor of 10–20 larger than this. Using similar arguments as above, we conclude that the firn-aquifer water lost between 2012 and 2013 OIB measurements is even more unlikely to have been contained englacially in crevasses.

Although **Figure 7** presents volumetric results for only $\mu =$ 0.32 GPa, our results for all six values of shear modulus that we tested ($\mu =$ 0.07–3.9 GPa) also suggest that the annual volume generated from $Q_{aq12-13}$ is unlikely to be held englacially (i.e., it exceeds the volume of ∼5 crevasses). For Q_{aq0}, this is also the case for shear moduli $\mu =$ 0.18 GPa. This result further strengthens our confidence that firn-aquifer water regularly reaches the bed in our study area.

Our model assumes that each crevasse evolves mechanically independently from its neighboring crevasses. However, the short distance ($R =$ 50 m) between crevasses compared to the much greater ice thickness ($H =$ 1000 m) suggests that crevasses may interact. In the presence of a deep crevasse downstream, a newly formed crevasse may not fracture directly downwards but instead may propagate toward the thin ice block between crevasses. This would be analogous to faulting observed at sites of supraglacial lake drainage (Doyle et al., 2013). Lateral fracturing some tens or hundreds of m below the surface may connect new crevasses with existing downstream hydrofractures. Over many such connections, firn-aquifer water could form an englacial fracture network similar to those observed on mountain glaciers (Fountain et al., 2005). This scenario is outside of the capabilities of our crevasse model, but we note that it may be possible for such a network to store a large volume of firn-aquifer water annually, without it reaching the bed. At the same time, this network of deep hydrofractures would be susceptible to the same processes mentioned above that would be likely to connect near-full-thickness fractures to the bed.

It is also possible that the fate of the 2012–2013 firn-aquifer water was not tied to the crevasse field: perhaps the water flowed to the ice-sheet surface at an unidentified hydraulic discharge point, or perhaps the aquifer expanded laterally along-strike of the crevasse field, or even flowed around the crevasse field and reconverged in the downstream reaches of our study area (**Figure 1B**). These scenarios could occur outside the bounds of our flowline model and the 1D OIB radar flight lines. While we cannot rule out these possibilities, our model results for the observed water-filled crevasses at the downstream end of the firn aquifer provide a compelling argument that drainage of the firn-aquifer water into the subglacial system is plausible.

We study only a 3.5 km transect within the vast Southeast Greenland firn aquifer (∼10,000 km^2; Miège et al., 2016). While we have shown that crevasses provide the firn-aquifer water in our study area with a credible, rapid path to the bed, crevasse fields do not necessarily exist at the lower boundary of the firn aquifer across all of Southeast Greenland. Thus, other drainage mechanisms or englacial refreezing may occur in other areas of the firn aquifer.

Contribution of the Firn Aquifer—Crevasse Field System to Ice Deformation

Our results show that if the firn aquifer were absent, crevasses would carry meltwater to depths of ∼300–500 m annually (**Figure 4B**), where it would refreeze. Over the ten-year period we model, this refreezing would warm the top few hundred m of the ice column by up to 8°C (**Figure 8A**). In this upper portion of the ice column, vertical shear stresses are relatively low, which limits the effect that this warming would have on ice velocities (Lüthi et al., 2015) to an additional 6 m $year^{-1}$ (**Figure 8A**), for a total deformational velocity ∼87 m $year^{-1}$ (**Figure 8B**). This is consistent with the observed (deformational plus sliding) ice velocity of ∼200 m $year^{-1}$ in our study area. WorldView imagery (**Figure 1B**) shows that the crevasse field we study spans 1–2 km, equivalent to 5–10 years of advection; thus, our ten-year model time is likely an upper bound. Furthermore, some fraction of the surface meltwater would likely refreeze within the snow and firn (Humphrey et al., 2012) without reaching the crevasses. Thus, our estimates of enhanced ice deformation from Q_{local} are likely upper bounds.

We find that for Q_{aq0} and $Q_{aq12-13}$, a relatively small fraction of firn-aquifer water refreezes englacially (1–10%; **Figure 8B**); this warms the ice by 4°C and enhances deformation by 56 m year^{-1} (**Figure 8A**) over a 10-year period. This represents an additional warming of ∼2°C and additional deformation of ∼50 m year^{-1} compared to the base case Q_{local}. These values are robust across our tested ranges for Q_{aq0} and $Q_{oq12-13}$ (**Figure 8B**). If these processes act regionally such that the 4°C warming occurs over a horizontal scale of multiple ice thicknesses, then our results suggest that the firn aquifer—crevasse field system may contribute a considerable portion (∼20%) of the observed surface velocity in our study area by enhancing ice deformation.

Potential Influence of Firn Aquifer Water at the Bed

We have demonstrated that the firn aquifer—crevasse field system in our study area likely delivers surface meltwater to the bed through crevasses. We compare this to the formation of similar full-thickness hydrofractures in western Greenland. There, the wide ablation zone and the large number of visually obvious meltwater lakes and streams make the surface hydrology (Box and Ski, 2007; Smith et al., 2015) and the formation of full-thickness hydrofractures well-studied topics (Das et al., 2008; Stevens et al., 2015). The community has thus made great progress in understanding the effects of meltwater reaching the bed seasonally in western Greenland, but this question has been less addressed in East Greenland.

A primary consideration is whether the full-thickness hydrofractures we infer in our study area bring water to a bed that is frozen or thawed. Existing knowledge (MacGregor et al., 2016) gives high confidence that a melted bed underlies our study area and the area 80–100 km upstream. While we have shown that the firn aquifer—crevasse field system most likely contributes to the basal water supply in our study area, other heat sources (frictional dissipative or geothermal) are likely to produce basal melt upstream, where no crevasses are visible. It therefore appears likely that the bed in our study area would be thawed even in the absence of the firn aquifer—crevasse field system.

To estimate the water flux from the firn aquifer to the bed, we scale the average annual 2D flux of water out of the firn aquifer (Q_{aq0} = 5000–15,000 m^2 year^{-1}) over the median length of the crevasses we observe in our study area (600 m) to reach a 3D water flux of 3–9 × 10^6 m^{3}year^{-1}. This is on the low end of the range of water volumes that fast-draining Greenland supraglacial lakes deliver to the bed: 7–40 × 10^6 m^3 (Das et al., 2008; Doyle et al., 2013) in approximately annual occurrences. However, many lakes drain more slowly, over periods comparable to the melt season (Selmes et al., 2011); these and other western Greenland catchments drain through rivers, which ties the basal water flux more closely to surface melt rates (Smith et al., 2015), leading to lower but sustained inputs to the bed.

The rate of water delivery to the bed is of fundamental importance to its effect on basal hydrology (Schoof, 2010). High water fluxes to the bed can channelize the basal system over the course of a melt season (Bartholomew et al., 2011); however, channelization may fail to occur during episodes of extremely high water flux such as rapid lake drainages (Dow et al., 2015) or when the water flux is too low (Bartholomew et al., 2011). Thus, if we are to understand the effect of firn-aquifer water on the subglacial system, we must first know its rate of input to the bed. The water fluxes we use are constrained by observations of firn-aquifer water level (2016) that are currently performed on an annual basis. The water flux at any one time, however, may well differ from the annual average, and with higher or lower instantaneous Q_{aq}, crevasses may hydrofracture and deliver water to the bed at different rates.

The annual average water flux through the firn aquifer (∼0.1–0.3 m^{3}s^{-1}) is comparable to observed daily flow rates through supraglacial streams during the melt season (0.5–8 m^{3}s^{-1}, McGrath et al., 2011; Chandler et al., 2013) but 4–5 orders of magnitude less than instantaneous water fluxes during rapid supraglacial lake drainages (3300–8700 m^{3}s^{-1}, Das et al., 2008; Doyle et al., 2013). However, in a hypothetical scenario where the firn-aquifer water is delivered to the bed over a 90-min period similar to a rapid supraglacial lake drainage (Das et al., 2008), the basal water flux for $Q_{aq12-13}$ would be similar to that from a fast-draining lake. Such a rapid timescale is likely an upper bound, as the diffusive nature of the firn aquifer would likely impede such rapid evacuation of water; instead, the firn aquifer may provide a steadier flux of water into the crevasse field and therefore to the bed. The travel time through the firn aquifer could introduce an offset between the timing of delivery of water to the bed and the timing of the melt season. This would further differentiate this system from western Greenland, where basal water fluxes peak roughly with the melt season (Bartholomew et al., 2011; Smith et al., 2015). Further remote sensing or field observations are required to better constrain any intra-annual variability in water flux.

Overall, we show that the volume of water that a segment of the firn aquifer—crevasse field system delivers to the bed is comparable to water volumes from supraglacial lakes and streams in western Greenland. Current observations, however, limit our ability to know the temporal character of the water flux and thus its effect on basal hydrology.

CONCLUSION

Our results show that the water flux through the Southeast Greenland firn aquifer is likely sufficient to hydrofracture to the bed through crevasses. Without the firn aquifer, crevasses filled with meltwater would not reach the bed. Similarly, without the adjacent downstream crevasse field, the firn-aquifer water would lack a delivery mechanism to the bed. Thus, the firn aquifer and the crevasse field should be thought of together, as a single system that brings surface meltwater to the bed under relatively high-elevation ice (s ∼ 1500 m a.s.l.) in this area. Refreezing over the weeks-long hydrofracture period in our study area raises ice temperature by ∼4°C and contributes ∼50 m year^{-1} of ice deformation to the observed surface velocity of ∼200 m year^{-1}.

We study here only one specific transect (∼3.5 km) of the Southeast Greenland firn aquifer, which covers

$\sim$10,000 km^2 (Miège et al., 2016) over a broad range of elevations and ice speeds. The fast flow of Helheim Glacier directly adjacent to our study area likely aids the formation of crevasses; other areas of the Southeast Greenland firn aquifer also border smaller fast-flowing outlet glaciers (Moon et al., 2012). Other firn-aquifer areas may therefore also encounter crevasse fields that could seed hydrofractures and deliver surface-sourced meltwater to the bed in areas of the ice sheet that lack visible supraglacial lakes or rivers.

AUTHOR CONTRIBUTIONS

KP devised the project, performed all model runs and analysis, and wrote the manuscript. KP and IJ conceived and developed the crevasse model. DL implemented and ran the creep component of the crevasse model. LB guided the application of the crevasse model to the study area. LK provided separate model results that constrained parameters for use in the crevasse model. All authors contributed to the organization, focus, and editing of the manuscript.

FUNDING

CReSIS funded the model development (NSF ANT-0424589) and the NASA Postdoctoral Program funded its application to the Southeast Greenland firn aquifer (NNH15CO48B).

ACKNOWLEDGMENTS

We thank Clément Miège, Laura McNerney, Rick Forster, and Lauren Andrews for helpful discussions and Clément Miège for feedback on the manuscript. We acknowledge DigitalGlobe, Inc. for providing WorldView images. We thank Michael Studinger for suggesting the use of the ATM data to examine crevasse geometries. We are grateful to the reviewers for constructive criticism that improved and clarified the manuscript.

SUPPLEMENTARY MATERIAL

The Supplementary Material for this article can be found online at: http://journal.frontiersin.org/article/10.3389/feart.2017.00005/full#supplementary-material

REFERENCES

Alley, R. B., Dupont, T. K., Parizek, B. R., and Anandakrishnan, S. (2005). Access of surface meltwater to beds of sub-freezing glaciers: preliminary insights. *Ann. Glaciol.* 40, 8–14. doi: 10.3189/172756405781813483

Andersen, M. L., Nettles, M., and Elosegui, P. (2011). Quantitative estimates of velocity sensitivity to surface melt variations at a large Greenland outlet glacier. *J. Glaciol.* 57, 609–620. doi: 10.3189/002214311797409785

Bartholomew, I. D., Nienow, P., Sole, A., Mair, D., Cowton, T., King, M. A., et al. (2011). Seasonal variations in Greenland Ice Sheet motion: inland extent and behaviour at higher elevations. *Earth Planet. Sci. Lett.* 307, 271–278. doi: 10.1016/j.epsl.2011.04.014

Box, J. E., and Ski, K. (2007). Remote sounding of Greenland supraglacial melt lakes: implications for subglacial hydraulics. *J. Glaciol.* 53, 257–265. doi: 10.3189/172756507782202883

Catania, G. A., and Neumann, T. A. (2010). Persistent englacial drainage features in the Greenland Ice Sheet. *Geophys. Res. Lett.* 37, 1–5. doi: 10.1029/2009GL041108

Cathles, L. M., Abbot, D. S., Bassis, J. N., and MacAyeal, D. R. (2011). Modeling surface-roughness/solar-ablation feedback: application to small-scale surface channels and crevasses of the Greenland ice sheet. *Ann. Glaciol.* 52, 99–108. doi: 10.3189/172756411799096268

Chandler, D. M., Wadham, J. L., Lis, G. P., Cowton, T., Sole, A., Bartholomew, I., et al. (2013). Evolution of the subglacial drainage system beneath the Greenland Ice Sheet revealed by tracers. *Nat. Geosci.* 6, 195–198. doi: 10.1038/ngeo1737

Clason, C. C., Mair, D., Nienow, P., Bartholomew, I., Sole, A., Palmer, S., et al. (2015). Modelling the transfer of supraglacial meltwater to the bed of Leverett Glacier, southwest Greenland. *Cryosphere* 9, 123–128. doi: 10.5194/tc-9-123-2015

Colgan, W., Rajaram, H., Abdalati, W., McCutchan, C., Mottram, R., Moussavi, M., et al. (2016). Glacier Crevasses: observations, models and mass balance implications. *Rev. Geophys.* 54, 1–43. doi: 10.1002/2015RG000504

Cook, J. C. (1956). Some observations in a Northwest Greenland Crevasse. *EOS* 37, 715–718.

Cuffey, K. M., and Paterson, W. S. B. (2010). *The Physics of Glaciers*. Available online at: http://booksite.elsevier.com/9780123694614/?ISBN=9780123694614

Cullather, R. I., Nowicki, S. M. J., Zhao, B., and Suarez, M. J. (2014). Evaluation of the surface representation of the Greenland Ice Sheet in a general circulation model. *J. Clim.* 27, 4835–4856. doi: 10.1175/JCLI-D-13-00635.1

Das, S. B., Joughin, I., Behn, M. D., Howat, I. M., King, M. A., Lizarralde, D., et al. (2008). Fracture propagation to the base of the Greenland Ice Sheet during supraglacial lake drainage. *Science* 320, 778–781. doi: 10.1126/science.1153360

Dow, C. F., Kulessa, B., Rutt, I. C., Tsai, V. C., Pimentel, S., Doyle, S. H., et al. (2015). Modeling of subglacial hydrological development following rapid supraglacial lake drainage. *J. Geophys. Res. Earth Surf.* 120, 1127–1147. doi: 10.1002/2014JF003333

Doyle, S. H., Hubbard, A. L., Dow, C. F., Jones, G. A., Fitzpatrick, A., Gusmeroli, A., et al. (2013). Ice tectonic deformation during the rapid in situ drainage of a supraglacial lake on the Greenland Ice Sheet. *Cryosphere* 7, 129–140. doi: 10.5194/tc-7-129-2013

Echelmeyer, K., Clarke, T. S., and Harrison, W. D. (1991). Surficial glaciology of Jakobshavns Isbræ, West Greenland: Part I. Surface morphology. *J. Glaciol.* 37, 368–382.

Forster, R. R., Box, J. E., van den Broeke, M. R., Miège, C., Burgess, E. W., van Angelen, J. H., et al. (2014). Extensive liquid meltwater storage in firn within the Greenland ice sheet. *Nat. Geosci.* 7, 95–98. doi: 10.1038/ngeo2043

Fountain, A. G., Jacobel, R. W., Schlichting, R., and Jansson, P. (2005). Fractures as the main pathways of water flow in temperate glaciers. *Nature* 433, 618–621. doi: 10.1038/nature03296

Franco, B., Fettweis, X., and Erpicum, M. (2013). Future projections of the Greenland ice sheet energy balance driving the surface melt. *Cryosphere* 7, 1–18. doi: 10.5194/tc-7-1-2013

Gagliardini, O., Zwinger, T., Gillet-Chaulet, F., Durand, G., Favier, L., de Fleurian, B., et al. (2013). Capabilities and performance of Elmer/Ice, a new-generation ice sheet model. *Geosci. Model Dev.* 6, 1299–1318. doi: 10.5194/gmd-6-1299-2013

Holdsworth, G. (1969). Primary transverse crevasses. *J. Glaciol.* 8, 107–129. doi: 10.3198/1969JoG8-52-107-129

Howat, I. M., Negrete, A., and Smith, B. E. (2014). The Greenland Ice Mapping Project (GIMP) land classification and surface elevation data sets. *Cryosphere* 8, 1509–1518. doi: 10.5194/tc-8-1509-2014

Humphrey, N. F., Harper, J. T., and Pfeffer, W. T. (2012). Thermal tracking of meltwater retention in Greenland's accumulation area. *J. Geophys. Res.* 117, F01010. doi: 10.1029/2011JF002083

Joughin, I., Smith, B. E., Howat, I. M., Moon, T., and Scambos, T. A. (2016). A SAR record of early 21st century change in Greenland. *J. Glaciol.* 62, 62–71. doi: 10.1017/jog.2016.10

Koenig, L. S., Miège, C., Forster, R. R., and Brucker, L. (2014). Initial *in situ* measurements of perennial meltwater storage in the Greenland firn aquifer. *Geophys. Res. Lett.* 41, 81–85. doi: 10.1002/2013GL058083

Krabill, W. B. (2010). *IceBridge ATML1B Qfit Elevation and Return Strength*. Boulder: NASA DAAC at the National Snow and Ice Data Center.

Krawczynski, M. J., Behn, M. D., Das, S. B., and Joughin, I. (2009). Constraints on the lake volume required for hydro-fracture through ice sheets. *Geophys. Res. Lett.* 36:L10501. doi: 10.1029/2008GL036765

Kuipers Munneke, P., Ligtenberg, S. M., van den Broeke, M. R., van Angelen, J. H., and Forster, R. R. (2014). Explaining the presence of perennial liquid water bodies in the firn of the Greenland Ice Sheet. *Geophys. Res. Lett.* 41, 476–483. doi: 10.1002/2013GL058389

Lüthi, M. P., Ryser, C., Andrews, L. C., Catania, G. A., Funk, M., Hawley, R. L., et al. (2015). Excess heat in the Greenland Ice Sheet: dissipation, temperate paleo-firn and cryo-hydrologic warming. *Cryosphere* 9, 245–253. doi: 10.5194/tcd-8-5169-2014

MacGregor, J. A., Fahnestock, M. A., Catania, G. A., Aschwanden, A., Clow, G. D., Colgan, W. T., et al. (2016). A synthesis of the basal thermal state of the Greenland Ice Sheet. *J. Geophys. Res. Earth Surf.* 121, 1328–1350. doi: 10.1002/2015JF003803

MacGregor, J. A., Li, J., Paden, J. D., Catania, G. A., Clow, G. D., Fahnestock, M. A., et al. (2015). Radar attenuation and temperature within the Greenland Ice Sheet. *J. Geophys. Res. Earth Surf.* 120, 983–1008. doi: 10.1002/2014JF003418

Martin, C. F., Krabill, W. B., Manizade, S. S., Russell, R. L., Sonntag, J. G., Swift, R. N., et al. (2012). *Airborne Topographic Mapper Calibration Procedures and Accuracy Assessment*. NASA/TM-2012-215891.

McGrath, D., Colgan, W., Steffen, K., Lauffenburger, P., and Balog, J. (2011). Assessing the summer water budget of a moulin basin in the Sermeq Avannarleq ablation region, Greenland ice sheet. *J. Glaciol.* 57, 954–964. doi: 10.3189/002214311798043735

McNerney, L. (2016). *Constraining the Greenland Firn Aquifer's Ability to Hydrofracture a Crevasse to the Bed of the Ice Sheet*. Master's Thesis, 1–54, University of Utah. Available online at: https://content.lib.utah.edu/cdm/ref/collection/etd3/id/4086

Meier, M. F., Conel, J. E., Hoerni, J. A., Melbourne, W. G., Pings, C. J. J., and Walker, P. T. (1957). *Preliminary Study of Crevasse Formation*. Wilmette, IL: Snow Ice and Permafrost Research Establishment (SIPRE). Available online at: http://acwc.sdp.sirsi.net/client/search/asset/1022260

Miège, C., Forster, R. R., Box, J. E., Burgess, E. W., McConnell, J. R., Pasteris, D. R., et al. (2013). Southeast Greenland high accumulation rates derived from firn cores and ground-penetrating radar. *Ann. Glaciol.* 54, 322–332. doi: 10.3189/2013AoG63A358

Miège, C., Forster, R. R., Brucker, L., Koenig, L. S., Solomon, D. K., Paden, J. D., et al. (2016). Spatial extent and temporal variability of Greenland firn aquifers detected by ground and airborne radars. *J. Geophys. Res. Earth Surf.* 121, 2381–2398. doi: 10.1002/2016JF003869

Moon, T., Joughin, I., Smith, B., and Howat, I. (2012). 21st-Century evolution of greenland outlet glacier velocities. *Science* 336, 576–578. doi: 10.1126/science.1219985

Moon, T., Joughin, I., Smith, B., van den Broeke, M., van de Berg, W. J., Noel, B., et al. (2014). Distinct patterns of seasonal Greenland glacier velocity. *Geophys. Res. Lett.* 41, 7209–7216. doi: 10.1002/2014GL061836

Morlighem, M., Rignot, E., Mouginot, J., Seroussi, H., and Larour, E. (2014). Deeply incised submarine glacial valleys beneath the Greenland ice sheet. *Nat. Geosci.* 7, 418–422. doi: 10.1038/ngeo2167

Mottram, R. H., and Benn, D. I. (2009). Testing crevasse-depth models: a field study at Breiğamerkurjökull, Iceland. *J. Glaciol.* 55, 746–752. doi: 10.3189/002214309789470905

Nye, J. F. (1955). Comments on Dr Loewe's letter and notes on crevasses. *J. Glaciol.* 2, 512–514.

Pfeffer, W. T., and Bretherton, C. S. (1987). The effect of crevasses on the solar heating of a glacier surface. *IAHS Publ.* 170, 191–205.

Phillips, T., Rajaram, H., and Steffen, K. (2010). Cryo-hydrologic warming: a potential mechanism for rapid thermal response of ice sheets. *Geophys. Res. Lett.* 37, 1–5. doi: 10.1029/2010GL044397

Poinar, K. (2015). *The Influence of Meltwater on the Thermal Structure and Flow of the Greenland Ice Sheet*. Ph.D. thesis, 1–166, University of Washington. Available online at: https://digital.lib.washington.edu/researchworks/handle/1773/35062

Poinar, K., Joughin, I., Lenaerts, J. T. M., and van den Broeke, M. R. (2017). Englacial latent-heat transfer has limited influence on seaward ice flux in western Greenland. *J. Glaciol.* 63, 1–16. doi: 10.1017/jog.2016.103

Price, S. F., Payne, A. J., Catania, G. A., and Neumann, T. A. (2008). Seasonal acceleration of inland ice via longitudinal coupling to marginal ice. *J. Glaciol.* 54, 213–219. doi: 10.3189/002214308784886117

Rienecker, M. M., Suarez, M. J., Gelaro, R., Todling, R., Bacmeister, J., Liu, E., et al. (2011). MERRA: NASA's modern-era retrospective analysis for research and applications. *J. Clim.* 24, 3624–3648. doi: 10.1175/JCLI-D-11-00015.1

Sassolas, C., Pfeffer, T., and Amadei, B. (1996). Stress interaction between multiple crevasses in glacier ice. *Cold Reg. Sci. Technol.* 24, 107–116.

Schoof, C. (2010). Ice-sheet acceleration driven by melt supply variability. *Nature* 468, 803–806. doi: 10.1038/nature09618

Selmes, N., Murray, T., and James, T. D. (2011). Fast draining lakes on the Greenland Ice Sheet. *Geophys. Res. Lett.* 38, 1–5. doi: 10.1029/2011GL047872

Sigrist, C. (2006). *Measurement of Fracture Mechanical Properties of Snow and Application to Dry Snow Slab Avalanche Release*. ETH Dissertation No. 16736. Available online at: http://www.wsl.ch/fe/warnung/projekte/snow_fracture_mechanics/phd_thesis_sigrist.pdf

Smith, L. C., Chu, V. W., Yang, K., Gleason, C. J., Pitcher, L. H., Rennermalm, A. K., et al. (2015). Efficient meltwater drainage through supraglacial streams and rivers on the southwest Greenland ice sheet. *Proc. Natl. Acad. Sci. U.S.A.* 112, 1001–1006. doi: 10.1073/pnas.1413024112

Stevens, L. A., Behn, M. D., McGuire, J. J., Das, S. B., Joughin, I., Herring, T., et al. (2015). Greenland supraglacial lake drainages triggered by hydrologically induced basal slip. *Nature* 522, 73–76. doi: 10.1038/nature14480

Sundal, A. V., Shepherd, A., van den Broeke, M., Van Angelen, J., Gourmelen, N., and Park, J. (2013). Controls on short-term variations in Greenland glacier dynamics. *J. Glaciol.* 59, 883–892. doi: 10.3189/2013JoG13J019

van der Veen, C. J. (1998). Fracture mechanics approach to penetration of surface crevasses on glaciers. *Cold Reg. Sci. Technol.* 27, 31–47. doi: 10.1016/S0165-232X(97)00022-0

van der Veen, C. J. (2007). Fracture propagation as means of rapidly transferring surface meltwater to the base of glaciers. *Geophys. Res. Lett.* 34, 1–5. doi: 10.1029/2006GL028385

Vaughan, D. G. (1995). Tidal flexure at ice shelf margins. *J. Geophys. Res.* 100, 6213–6224.

Weertman, J. (1973). Can a water-filled crevasse reach the bottom surface of a glacier? *IASH Publ.* 95, 139–145.

Weertman, J. (1996). *Dislocation Based Fracture Mechanics*. London: World Scientific.

Conflict of Interest Statement: The authors declare that the research was conducted in the absence of any commercial or financial relationships that could be construed as a potential conflict of interest.

Advantages of publishing in Frontiers

OPEN ACCESS
Articles are free to read for greatest visibility and readership

FAST PUBLICATION
Around 90 days from submission to decision

HIGH QUALITY PEER-REVIEW
Rigorous, collaborative, and constructive peer-review

TRANSPARENT PEER-REVIEW
Editors and reviewers acknowledged by name on published articles

Frontiers
Avenue du Tribunal-Fédéral 34
1005 Lausanne | Switzerland

Visit us: www.frontiersin.org
Contact us: info@frontiersin.org | +41 21 510 17 00

REPRODUCIBILITY OF RESEARCH
Support open data and methods to enhance research reproducibility

DIGITAL PUBLISHING
Articles designed for optimal readership across devices

FOLLOW US
@frontiersin

IMPACT METRICS
Advanced article metrics track visibility across digital media

EXTENSIVE PROMOTION
Marketing and promotion of impactful research

LOOP RESEARCH NETWORK
Our network increases your article's readership